Modelling of Oxide Failure in Hot Metal Forming Operations

by

Mikhail Trull

Thesis submitted for the degree of Doctor of Philosophy

Department of Engineering Materials

The University of Sheffield

May 2003

To Liudmila, Karyna and Victoria

Those who fall in love with practice without science are like a sailor who steers a ship without a helm or compass, and who never can be certain whither he is going.

Leonardo

It is easier to write ten volumes on theoretical principles than to put one principle into practice.

L.N. Tolstoy

Contents

Summary

Oxide scale can affect many aspects of hot metal forming operations, such as heat transfer, friction and the final surface finish of the rolled product. Surface oxide scale is always present on the steel slab and sometimes on cold rolls. Therefore, the study of the thermo-mechanical behaviour of oxide scale, particularly under conditions as close as possible to the steel manufacturing process is very important.

In order to undertake a detailed study of oxide scale behaviour, several high-temperature testing techniques were applied. First, high-temperature tensile tests were carried out to investigate the brittle fracture and cracking of the surface oxide scales. Second, high-temperature compression tests were developed and the results obtained revealed many different failure mechanisms that are present in the compressed oxide scale. Finally, a tensile-compressive test was developed and performed under thermal conditions which were as close as possible to hot rolling. The best results in the understanding of oxide scale failure were achieved by closely linked combination of laboratory testing and measurements coupled with detailed finite element analysis. A close microstructural examination of the morphology of oxides was carried out after each experiment and finite element modelling was performed. The three-dimensional finite element simulations helped to improve the interpretation of the thermo-mechanical testing and to obtain more accurate heat transfer and stress-strain relationships.

In this work the following thermo-mechanical failure modes of the oxide scales were observed and investigated: brittle fracture (through-thickness cracking, blister failure), indications of plastic behaviour (arrested cracks, unbroken top layers of the oxide scale) and a sticking effect (equivalent to the mill pick-up).

Acknowledgements

I would like to express my gratitude to Professor J.H. Beynon for his guidance, kind help and encouragement during the research and the preparation period of this thesis.

I would like to thank EPSRC and the IMMPETUS for providing the financial support of the research project.

I am also very grateful to Dr. M. Krzyzanowski for his advice, beneficial discussion and help.

I am also grateful to Dr. B.P. Wynne for useful suggestions and help.

I thank Mr J. Goodliffe, technician at the Mechanical Engineering Department and Mr. A. Marshall technician at the Engineering Materials Department for their technical help and collaboration.

I would like to thank all my colleagues and friends in IMMPETUS who have made my staying in Sheffield very pleasant.

Finally, my loveliest thanks are for Liudmila, my wife and best friend, who has constantly been close to my side and supporting me during all this period.

Chapter 1

Introduction

The market is continually demanding a higher level of quality in the final products of the metal industry. Examples of parameters under consideration are surface finish, flatness and dimensional control. The 5th International Rolling Conference that took place in London in 1990 points out difficulties in the dimensional control of finishing products [1]. Despite the automatic control, the tolerance on the thickness, profile and flatness of hot rolled coils is about ±50 microns [2]. All these problems remain unsolved or partially solved so far [3].

The most common hot-forming process is hot rolling in the hot strip mill. During hot rolling, a heated steel slab is passed between two water-cooled metal rolls revolving in opposite directions. Blistering, creep, oxidation, embrittlement, and thermal fatigue are common sources of failure in metal hardware and unpredictable, brittle failure of non-metallic parts. Therefore, the critical parameters for steel finishing and forming include temperature, uniformity of temperature during hot operations, flatness, steel chemistry, and surface finish. The demand for improved quality has produced an increased emphasis on monitoring temperature, surface finish, microstructure, and metal thickness throughout the process [4]. Surface oxide scale is always present on the steel slab and sometimes on cold rolls. The thickness of the scale varies between several microns and several hundred microns. Oxide scale can affect many aspects, such as heat transfer, friction and the final surface finish. Finishing processes (pickling and oiling) are used to clean the surface of the semi-

finished, hot rolled steel prior to cold rolling, forming, or coating operations. Mill scale, rust, oxides, and soil are chemically removed by a variety of chemical and physical processes. Additional finishing steps (i.e., tube rolling or wire drawing) are performed integrally to the steel making process or as secondary operations at specialty vendors. Ceramic-coated metals and advanced ceramics are currently used in a number of these operations to provide the desired surface finish and dimensional tolerances while increasing throughput and reducing downtime. The mechanical behaviour of ceramic coatings is very similar to the oxide scales. While the performance of ceramic-coated metals and advanced ceramics is considered superior to that of hard steels, high incidences of failure occur from spallation of the ceramic coatings and unpredictable failure of the advanced ceramics [4]. Consequently, the study of oxide scale (ceramic coating) behaviour under steel making conditions is very important nowadays. The best results in the understanding of oxide scale failure can be achieved by closely linked combination of laboratory testing and measurements coupled with detailed finite element analysis. It should be noted that only a physically based model of oxide scale would be suitable for successful simulation of real processes. Therefore, a close examination of the oxide formation, chemistry and morphology of oxides, and their thermo-mechanical properties is essential.

The oxide properties and behaviour under different loading conditions have been well discussed in the literature, especially for temperatures up to 800°C. However, a lack of data on mechanical failure of oxide scales at elevated temperatures exists. Therefore, Chapter 2 of the present research consists of general information about the oxide formation, such as defect structures, diffusion, the process of oxidation of metals and the mechanical behaviour of oxide scales at elevated temperatures as well as the hot rolling process and multi-scale modelling of materials. In Chapter 3, the experimental procedures of high-temperature tensile and newly developed compression tests are explained in detail. In addition, the microstructural techniques and finite element modelling that have been used are described. The results obtained during the high-temperature tensile and compression tests of the mild steel flat specimens with oxide scale and a microstructural analysis of fractured and deformed oxide scales are presented in Chapter 4. The temperature range used for tests was from 800 up to 1070°C with equivalent strain 0.012…0.035

and strain rate 0.06...0.15 s^{-1}. The thickness of the oxide scales was varied between 10 and 260 μm. Chapter 5 is concerned with the three-dimensional finite element simulations carried out to improve the interpretation of the thermo-mechanical testing and to obtain more accurate heat transfer and stress-strain relationships. All information on behaviour of the oxide scales that was obtained from the present research and the literature (reviewed in Chapter 2) is discussed in Chapter 6. To finish, Chapter 7 draws the main conclusions and Chapter 8 makes suggestions for further work. In addition, there are three appendices presented in the thesis citing some useful calculations and properties of materials, and the schedules of tests are also given.

Chapter 2

Literature Review

2.1. Introduction

It is well known that during high temperature metalworking it is almost impossible to avoid the formation of thin or sometimes even thick oxide scales, which significantly affects heat transfer, friction and the final surface finish. All these parameters have a direct influence on the quality of metal products. One of the most complicated metal-forming processes in terms of oxide scale behaviour is hot rolling. The properties of oxide scale on hot rolled steel are receiving increasing attention nowadays. Customers of hot strip mills place increasingly stiff requirements on the properties of unpickled hot rolled steel strip. Thermo-mechanical properties of scale can only be controlled systematically when a more coherent understanding is gained of the relation between the process parameters in the hot strip mill, steel composition and scale properties. In the past, most attention has been paid to scale thickness and composition. Consequently, the important aspects of adherence and failure have been underexposed. That is why it is very important to study the physical nature and possible behaviour of the surface oxide scales under hot rolling conditions. Plastic deformations transform not only metals, but also have an influence on oxide scales. Moreover, the mechanical and hydraulic descaling processes are more preferable environmentally than acid pickling. Hence, a knowledge of the adherence and

mechanical properties of oxide scales becomes very important for developing these descaling processes.

During the hot rolling operations, the range of temperatures for semi-finished products is disposed between 800 and 1200°C. Also, the process of oxidation of steel takes place under high temperature and under a time limitation. The oxidation mechanism, properties and failure of oxide scales are investigated and considered under these conditions.

2.2. Oxidation of solids

2.2.1. Defect structures in oxides

Classical crystallography gives an idealized conception of the composition and structure of inorganic materials. It assumes that the atoms or structural units are arranged in ideal structures where all the structural sites are occupied. However, real materials are not ideally built up. At any temperature, they contain many structural imperfections and defects. These defects might be divided into three main groups [5]: point defects, line defects and plane defects. The point defects include vacancies, interstitial atoms and misplaced atoms. The line defects include dislocations that are characterized by displacements in particular directions in the periodic structure. The plane defects comprise stacking faults, grain boundaries and outer surfaces. Besides the structural defects, crystals also contain electronic or valence imperfections. It is well known that deviations from ideal structure and composition determine a number of properties of solids. For example, diffusion in solids is greatly accelerated by the presence of imperfections. Point defects are responsible for lattice diffusion, and grain boundary and surface diffusion take place along the plane defects. Moreover, solid state diffusion determines many properties or processes in solids such as mass transport in solids, solid state reaction, high temperature creep, and gas-metal reactions, resulting in the formation of compact layers of reaction products, etc.

i) Point defects

There are several systems of notation in use to describe point defects in solids [6] and [7]. The symbols introduced by Kröger [7] are used in the following discussion. In a compound metal-oxygen (*MO*), the point defects are written as V_O – anion vacancies, V_M – cation vacancies, O_i – anion interstitials, M_i – cation interstitials. In that case, atoms on normal lattice positions can be determined O_O and M_M.

According to many authors [6], [8] and [9], if a point defect is created in a perfect crystal, the internal energy and the entropy of the system increases, and the equilibrium concentration of the defects can be reached when the free energy of the system is at a minimum. However, the values of free energies of formation of the different types and systems of defects usually spread widely, and often one type of defect structure commonly predominates in a particular solid. The relative concentration of other defects will be a function of temperature and variables which influence the state and the composition of the compound. Therefore, defect equilibria with a large positive enthalpy of formation, for example, which are negligible at low temperatures, may become important at high temperatures.

Point defects may be neutral or charged. Also several point defects usually form to maintain the electrical neutrality of a crystal.

When a crystal is stoichiometric, two most common defects can be observed: Schottky and Frenkel disorder (Figure 2.1).

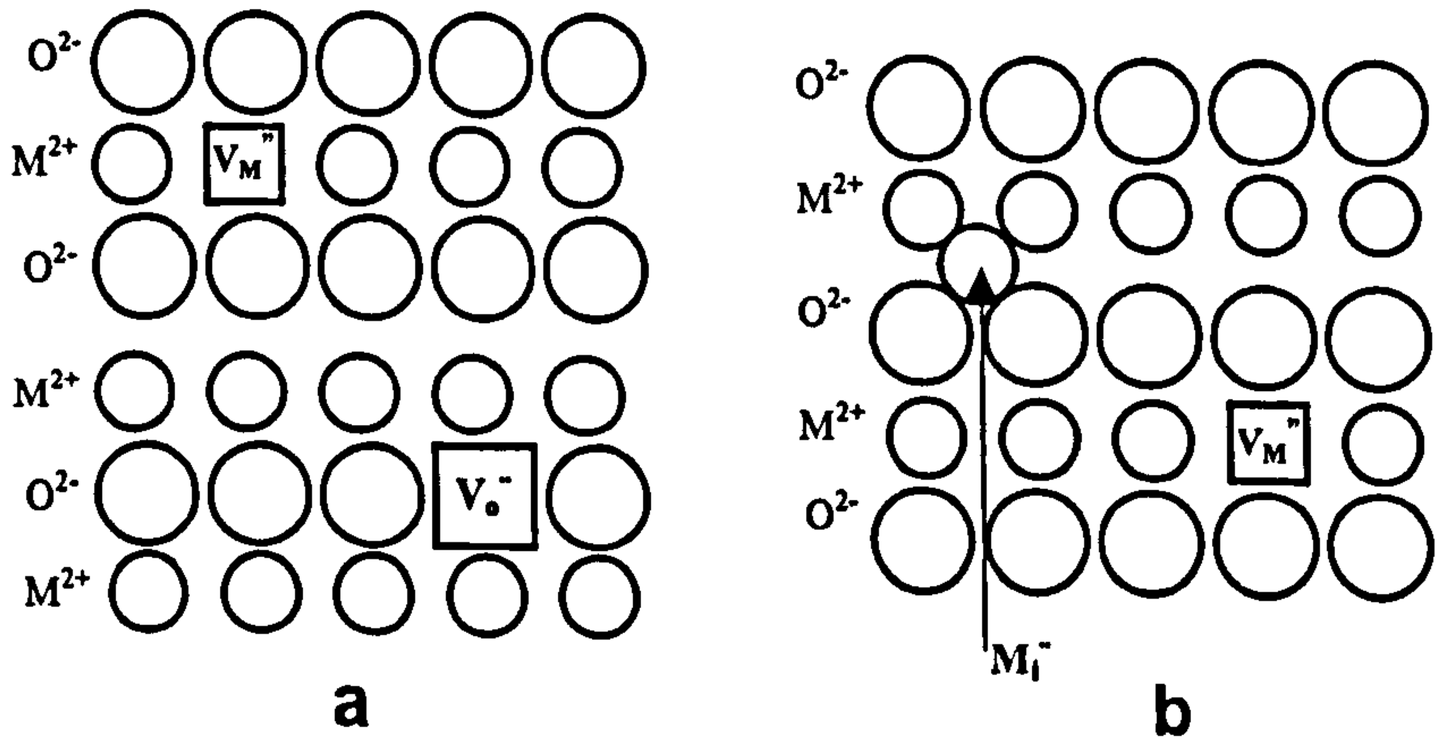

Figure 2.1. Schematic illustration of a) Schottky and b) Frenkel defects.

A crystal with Schottky defects contains equivalent concentrations of anion (V_O) and cation (V_M) vacancies as shown in Figure 2.1a. This type of disorder allows the anion and the cation lattice defects to form. Meanwhile, in the Frenkel disorder a defect pair could involve vacancies or interstitial atoms for the same component ($V_O + O_i$ or $V_M + M_i$) as illustrated in Figure 2.1b.

As is frequently mentioned in the literature [10] and [6], many chemical compounds have deviations from stoichiometric composition.

ii) Nonstoichiometry and defects in oxides

Nonstoichiometric compounds do not contain an equivalent concentration of complementary point defects and neutrality of the crystal is conserved through the formation of complementary valence or electronic defects. In addition, defects can interact with each other or with impurity atoms to produce more complex defects.

There is a number of deviations from stoichiometry that might be revealed for oxides. An example of such a compound could be wüstite. Ideal wüstite *FeO* has under all conditions lack of iron and its real formula is $Fe_{1-m}O$.

Defects in nonstoichiometric oxides can predominate in the oxygen or metal lattice. However, oxides may contain relatively equal concentration of both cation and oxygen defects. The relative concentration of different defects will also be a function of temperature and oxygen pressure [8].

Therefore, oxides can be with anion defects, cation defects and both anion and cation defects. The general formula for oxides with anion defects is MO_{a-x}, where x is a small fraction of a. Examples of such oxides are Nb_2O_5 and Ta_2O_5. Oxides with cation defects are metal-deficient oxides and the general formula may be written as $M_{b-m}O$, where m is a small fraction of b. Examples of such oxides are *NiO*, *CoO* and *FeO*.

iii) Defect Equilibria

Since oxides may have appreciable disorder on both the anion and the cation lattices, it is important to determine equilibrium concentrations of the different defects with temperature and partial pressures of the compounds. According to

Kofstad [10], the defect equilibria may be calculated using the law of mass action or by statistical mechanics.

The thermodynamic approach gives us the free energy of a system, G, as

$$G = H - TS \tag{2.1}$$

where T is the absolute temperature, H is the enthalpy and S is the entropy of the system.

A system will be in equilibrium at a constant given temperature and pressure when its free energy is minimal. Therefore, at equilibrium

$$dG_{T,p} = 0 \tag{2.2}$$

Stoichiometric oxides

The formation of a pair of doubly charged Schottky defects in a stoichiometric oxide, MO, will be as follows [8]

Perfect crystal = $V^{\cdot\cdot}_O + V^{''}_M$

where each superscript dot indicates positive charge and each prime sign denotes a negative charge on the defects. If the defect concentrations are small, relative to the total numbers of lattice sites, the defect equilibrium is

$$N_{V_M^{''}} \cdot N_{V_O^{\cdot\cdot}} = K_S \tag{2.3}$$

where $N_{V_M^{''}}$ and $N_{V_O^{\cdot\cdot}}$ represent the mole fraction of doubly charged cation and anion vacancies, respectively, and K_S is the equilibrium constant.

K_S is related to the molar free energy of formation of a pair of doubly charged Schottky defects, ΔG_S, as follows [8]

$$K_S = \exp\left(-\frac{\Delta G_S}{RT}\right) = \exp\frac{\Delta S_S}{R}\exp\left(-\frac{\Delta H_S}{RT}\right) \tag{2.4}$$

where ΔH_S is the molar enthalpy and ΔS_S is the molar entropy of formation of Schottky defect pairs, and R is the universal gas constant.

For Frenkel defects the equilibrium constant could be obtained similarly and the relationship will be as follows

$$N_{M_i^{\bullet\bullet}} \cdot N_{V_M^{''}} = K_F = \exp\left(-\frac{\Delta G_F}{RT}\right) = \exp\frac{\Delta S_F}{R}\exp\left(-\frac{\Delta H_F}{RT}\right) \qquad (2.5)$$

Nonstoichiometric oxides

Nonstoichiometry in compounds signifies the presence of point defects. Therefore, electrical neutrality may be maintained by creation of complementary valence or electronic defects. The degree of nonstoichiometry in an oxide is dependent on the temperature and on the partial pressure of its components.

2.2.2. Diffusion in oxides

Oxides, as all other materials, always contain defects. Therefore, diffusion takes place because of the presence of imperfections and defects in solids. Generally, diffusion is a kinetic process that guides to the homogenisation of the chemical components in a phase. That kind of process can happen as mixing on many length scales. In the case of solids, diffusion occurs on the atomic or molecular level [11], [10] and [12].

i) Fick's law of diffusion

The description of diffusion requires the definition of the diffusion coefficient, *D*. This was first introduced by Adolf Fick [13] in his first law

$$J = -D\left(\frac{\partial c}{\partial x}\right)_t \qquad (2.6)$$

where J is the instantaneous particle flow rate per unit area of the diffusing species across a plane, c is the concentration of the diffusing species at the plane, and $\partial c/\partial x$ is the concentration gradient normal to the plane.

The diffusion coefficient (Equation 2.6) can be measured only if a concentration gradient is fixed. Such a condition is experimentally difficult to achieve in a solid. The change in concentration with time might be measured more easily. This is given by Fick's second law which has the form

$$\frac{\partial c}{\partial t} = \frac{\partial}{\partial x}\left(D\frac{\partial c}{\partial x}\right) \tag{2.7}$$

In the most elementary form when the diffusion coefficient is independent of concentration, Equation 2.7 becomes

$$\frac{\partial c}{\partial t} = D\frac{\partial^2 c}{\partial x^2} \tag{2.8}$$

This type of equation may be solved explicitly under experimentally closely approximated boundary conditions [11].

ii) Lattice diffusion in oxides

Lattice diffusion ensues from the movement of point defects. The different types of defects that are present in solids give rise to different mechanisms of diffusion. These mechanisms can be illustrated schematically for elemental solids [6], [8], [10] and [11] as shown in Figure 2.2.

If an atom on a normal lattice site jumps into an adjacent unoccupied lattice site, the diffusion takes place by a vacancy mechanism (Fig.2.2a).

If an atom moves from an interstitial site to one of its nearest interstitial sites, the diffusion occurs by an interstitial mechanism (Fig. 2.2b). Such a relocation or jump of the atom can produce a substantial distortion of the lattice, and this mechanism is possible when the interstitial atom is smaller than the atoms on the normal lattice position. If the distortion during the jump becomes too large, the

interstitial atom may move by another type of mechanism. In the interstitialcy mechanism an interstitial atom pushes one of its nearest neighbours on a normal lattice site into another interstitial position and itself occupies the lattice site of the displaced atom (Fig. 2.2c). If an atom displaces several atoms along the line from their equilibrium positions, the diffusion occurs by a crowdion mechanism. Although the energy to move such a defect is small, the mechanism can shift only along the line or equivalent directions.

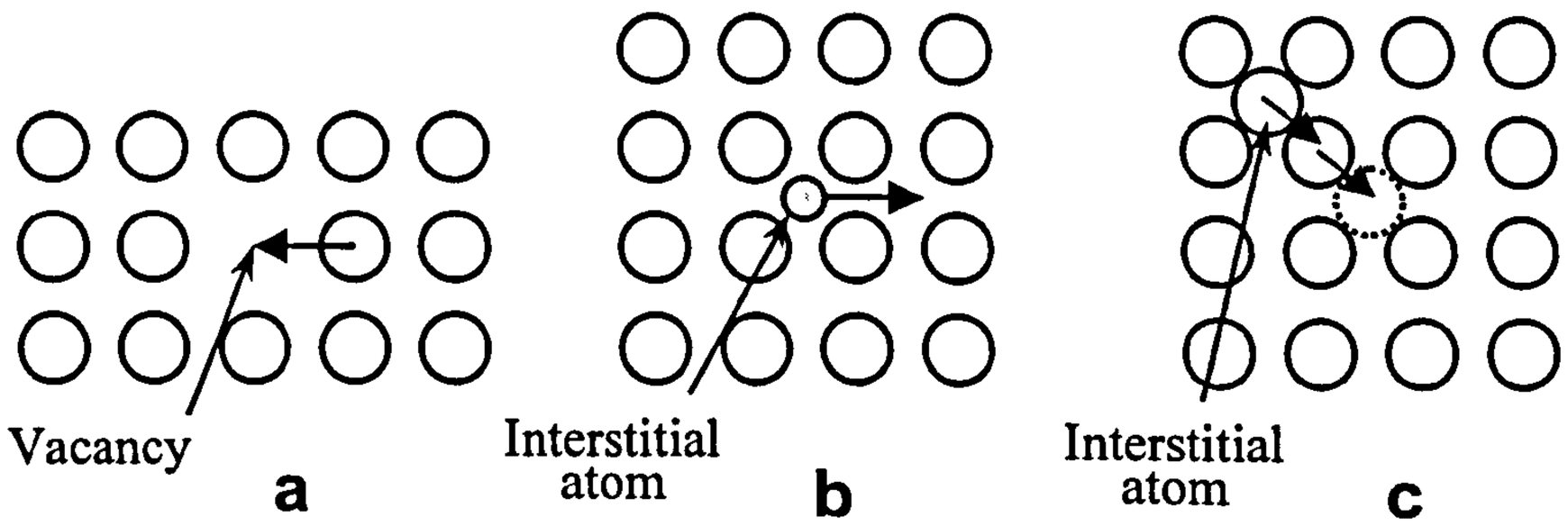

Figure 2.2. Schematic illustration of diffusion mechanisms in solids: a) vacancy diffusion, b) interstitial diffusion, c) interstitialcy diffusion.

Diffusion in crystalline solids is a random process, which involves movement of uncountable sets of atoms and defects in the crystal structure. It is not possible to observe or detect the individual atom jumps. Therefore, it is essential to find a relation between individual atom jumps and the macroscopic diffusion phenomena, which can be observed. Such relations may be derived statistically by the random-walk method. By this method and on the assumption that the individual jump distances s are equal, the diffusion coefficient may be expressed as follows [11]

$$D = \frac{1}{6}\frac{n}{t}s^2 = \frac{1}{6}\Gamma s^2 \qquad (2.9)$$

where n is the number of jumps during the time t, and Γ is the number of jumps per unit time.

The jump distance s is a function of the geometry of the crystal and may be introduced as a function of the lattice parameters. Γ is dependent on the mole fraction

of vacancy or defects in the crystal, N_d, the jump frequency ω of an atom to an adjacent vacancy, and is finally determined by the number of nearest positions to which an atom may jump. For a crystal with cubic symmetry and a lattice parameter a_0, Equation 2.9 can be rewritten as [8] and [11]

$$D = \alpha a_o^2 N_d \omega \tag{2.10}$$

Where α is geometric factor, which equals 1 for f.c.c. and b.c.c. metals.

According to Kofstad [8], the mole fraction of defects, N_d, may be expressed by

$$N_d = \exp\left(-\frac{\Delta G_d}{RT}\right) = \exp\frac{\Delta S_d}{R}\exp\left(-\frac{\Delta H_d}{RT}\right) \tag{2.11}$$

where ΔG_d, ΔS_d and ΔH_d represent the molar energy, entropy and enthalpy of formation of the defects. If the concentration of defects in oxides is a function of oxygen pressure, a pressure term must also be included in Equation 2.11.

The expression of the rate of transition from one equilibrium site to another, ω, based on statistical mechanics and the theory of activated complexes has been given by Zener [14]

$$\omega = \nu \exp\left(-\frac{\Delta G_m}{RT}\right) = \nu \exp\frac{\Delta S_m}{R}\exp\left(-\frac{\Delta H_m}{RT}\right) \tag{2.12}$$

where ΔG_m is the free energy change to move the atom from equilibrium position to the top of the potential barrier. ΔS_m and ΔH_m are the corresponding change in entropy and enthalpy. ν is the vibrational frequency of the atom in the direction of diffusion. The value of ν as a first approximation is taken to be equal to the Debye frequency or about 10^{13} sec^{-1}.

Combining Equations (2.10), (2.11), and (2.12) the diffusion coefficient of the atoms is given by

$$D = a_0^2 \nu \alpha \exp\left(\frac{\Delta S_d + \Delta S_m}{R}\right) \exp\left(-\frac{\Delta H_d + \Delta H_m}{RT}\right) \tag{2.13}$$

An experimentally determined diffusion coefficient is typically given by

$$D = D_0 \exp(-Q/RT) \tag{2.14}$$

where Q is termed the activation energy and D_0 is the frequency factor.

Comparing Equations 2.13 and 2.14 it is possible to determine the activation energy as

$$Q = \Delta H_d + \Delta H_m \tag{2.15}$$

where Q is the sum of the enthalpy of defect formation and motion of the defects.

iii) Grain boundary and surface diffusion

Apart from single crystals, polycrystalline materials contain not only atoms and vacancies, but also dislocations, grain boundaries, internal and external surfaces. Therefore, diffusion takes place along such lines and surface defects. Additionally it is commonly agreed that surface diffusion is more rapid than lattice diffusion. Hauffe [6] points out that with decreasing temperature the lattice diffusion is replaced by a more rapid diffusion. This more rapid process takes place through grain boundaries of the material. While at high temperatures the combination of this "short-circuit" diffusion is proportionally much less.

The effective rate of grain-boundary diffusion can be equal to the rate of lattice diffusion, but only at a critical temperature. This critical temperature depends largely on the total structure of the material. A mathematical solution of grain boundary diffusion was introduced by Fisher [15]. The model assumes that the material moves rapidly along the grain boundary and simultaneously diffuses into the grains from the grain boundary by lattice diffusion. An approximate solution has been given for the penetration of the activity into the material

$$\ln a = -\left[\frac{\sqrt{2D_l / \delta \cdot D_{gb}}}{(\pi \cdot D_l t)^{1/4}}\right] x + const \qquad (2.16)$$

where a is the activity in each section parallel to and at a distance x from the original surface, t is the time of diffusion anneal, δ is the width of the grain boundary, and D_l and D_{gb} represent the lattice diffusion and grain boundary coefficients, respectively. Fisher's solution predicts a linear relationship between activity and the penetration distance and the time dependence of the penetration amounts is smaller than for lattice diffusion. It should be noted that knowledge of D_l is necessary in order to evaluate the value of D_{gb}. The same mathematical analysis of surface diffusion may also be given, but experimental data on this object is still very limited.

Kofstad [10] suggests that the activation energies for lattice, grain boundary, and surface diffusion often decrease in the order $\Delta H_l > \Delta H_{gb} > \Delta H_s$, and diffusion coefficients increase as $D_l > D_{gb} > D_s$. The pre-exponential factor D_0 for surface diffusion may be ten times larger than that for lattice diffusion.

Most recent studies of grain boundary and surface diffusion on solids suggest models for interface motion are based on free energy approach [16], [17], [18] and [19].

2.2.3. The process of oxidation of metals

The result of high-temperature oxidation of metals is the formation of an oxide film or scale on the metal surface. The mechanism of oxidation depends on the nature of the scale. When solid scales are formed, the oxidation behaviour also depends on whether the scales are compact or porous. An oxide scale acts as a barrier which separates the metal surface and oxygen gas. Diffusion plays a very important role in oxidation. If sufficient oxygen is available at the oxide surface, the rate of oxidation at high temperature will be limited by a solid-state diffusion or short-circuit diffusion, through the compact scale. The diffusion distance increases as the oxide grows in thickness and the rate of reaction will decrease with time.

Kubaschewski and Hopkins [20] examine and suggest a number of oxidation mechanisms. The thickness of oxides can be between films <5 ... < 1000 nm and scales >1 mm. When an oxide film covers the surface of metal at low temperature, it is assumed in many models that a transport of electrons or ions through the film determines the oxidation rate. At high temperature, this transport is assumed to involve a diffusion, which is due to a chemical potential gradient across the scale and width, according to the Wagner mechanism, and leads to a parabolic oxidation [8]. Wagner's work [21] has provides a fundamental understanding of high-temperature oxidation of metals. His theory of a parabolic oxidation is widely applied today.

All effects of low temperature oxidation can be taken into account during a short period and then Wagner's mechanism predominates.

i) Models for thin films

It can be reasonably assumed that the domain of thin oxide films is situated up to 1000 nm. Logarithmic, inverse logarithmic relationships and the cubic rate law of oxidation are commonly suggested in this region [6] and [20]. The hypothesis that a strong electric field is set up in the thin oxide film was originally proposed by Mott [22]. In the theory developed by Mott and Cabrera [23] it is considered that a) oxygen atoms are adsorbed on the oxide surface; b) electrons can pass rapidly through the oxide by tunnelling (a quantum-mechanical process by which electrons of lower maximum energy than that of a barrier possess a finite probability of penetrating this barrier) to establish equilibrium between the metal and absorbed oxygen. The electric field set up during oxidation has a negative surface charge and can transport ions across the oxide film. It is supposed that a chemisorbed film exists on a metal and electrons and ions move independently in the film [20]. Any space charges in the oxide film are neglected and the defect concentrations are constant within the film [6].

Let us consider a film of the excess-cation type and denote the concentration of ions and electrons in the oxide at a distance (thickness) ξ from the metal-oxide interface by $n_i(\xi)$ and $n_e(\xi)$ respectively. W_i is the energy to remove an ion from its position and Φ is the energy to remove an electron from the metal into the conduction band of the oxide (see Figure 1.1). N_i is the number of interstitial

positions per unit volume in the oxide and $N_e = 2(2\pi mkT/h^2)^{3/2}$, where m – mass of electron, k – Boltzmann's constant and h – Planck's constant.

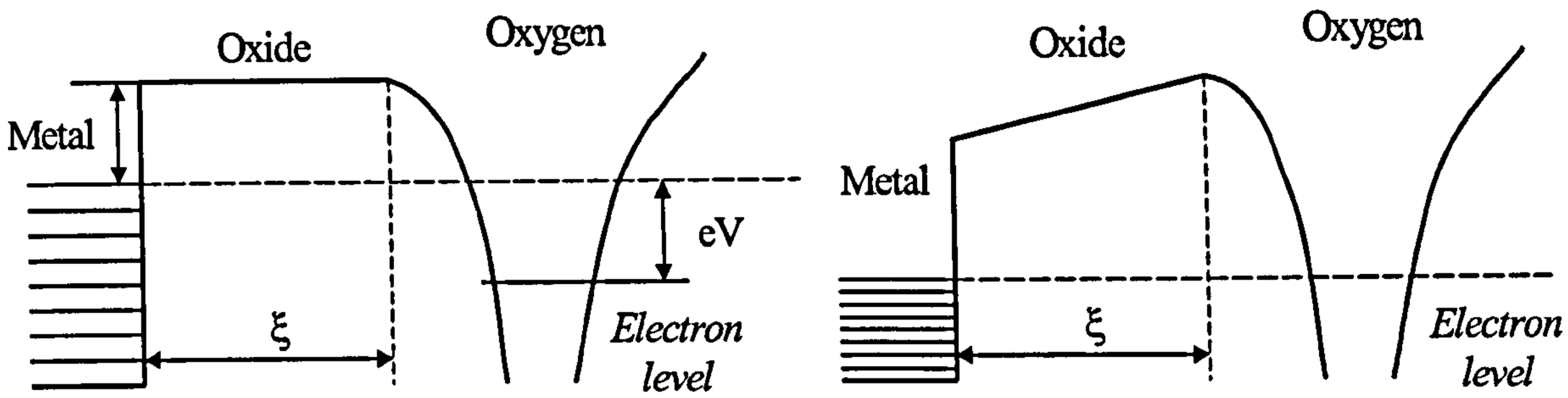

Figure 2.3. Schematic position of electron energy levels in a metal, oxide and oxygen: a) before electron transfer and b) after exchange of electrons, after Cabrera and Mott [23].

The concentrations of interstitial ions and electrons at the interface are given by

$$n_i\,(0) = N_i \exp\,(-W_i/kT)$$

and

$$n_e\,(0) = N_e \exp\,(-\Phi/kT) \qquad (2.17)$$

At large distance, the product of $n_i(\xi)$ and $n_e(\xi)$ must be constant and equal:

$$n = \sqrt{(N_i N_e)}\exp[-\tfrac{1}{2}(W_i + \Phi)/kT] \qquad (2.18)$$

At smaller distances the quantities $n_i(\xi)$ and $n_e(\xi)$ can be related to the electrostatic potential V by means of Boltzman's law:

$$n_i\,(\xi) = n \exp\,(-eV/kT); \qquad n_e\,(\xi) = n \exp\,(eV/kT), \qquad (2.19)$$

and, using Poisson's equation

$$d^2V/d\xi^2 = [n_i\,(\xi) - n_e\,(\xi)]4\pi e/\varepsilon \qquad (2.20)$$

the equation

$$\frac{d^2V}{d\xi^2} = \frac{8\pi \cdot n}{\varepsilon} e \sinh\left(\frac{eV}{kT}\right) \tag{2.21}$$

is obtained, where ε is the dielectric constant and the ions are supposed to carry unit charge. If ξ is large and V consequently small, equation (2.21) then becomes

$$\frac{d^2V}{d\xi^2} = \frac{V}{\xi_0^2} \tag{2.21a}$$

where

$$\xi_0 = \left(\frac{\varepsilon \cdot kT}{8\pi \cdot ne^2}\right)^{1/2} \tag{2.22}$$

For the following considerations, it is essential to distinguish in the solution of equation (2.22)

$$V = \text{const} \exp(-\xi/\xi_0), \tag{2.23}$$

Between a scaling system where $\xi > \xi_0$ and a tarnishing system where $\xi < \xi_0$. The situations can be as follows [20]:

a) $\xi >> \xi_0$: The concentration of interstitial ions and electrons can be treated as equal throughout the bulk of the oxide layer. The two constants k'_0 and Q of the equation $k'_p = k'_0 \exp\left(-\frac{Q}{kT}\right)$ assume the forms

$$k'_0 = 2a^2 \nu \upsilon e \sqrt{(N_i N_e)} \tag{2.24}$$

$$Q = ½(W_i + \Phi) + U \tag{2.25}$$

where U – the energy of activation for the transit of an ion from one equilibrium position to another, ν - frequency of oscillation ≈ 10^{12} s^{-1}, υ - the volume of metal oxide per ion, and a – the distance between the ions ≈ 0.3 nm.

b) $\xi << \xi_0$: Electrons can penetrate the thin oxide film by the tunnel effect, leaving the equivalent number of metal ions behind. The oxygen adsorbed at the surface is transformed into ions and an electric field is set up across the oxide layer.

The field strength would be $E = V/\xi$. The value of the potential V is approximately equal to 1 V. The electric field strength corresponding to a film thickness of 5 nm should be of the order of 10^7 V cm^{-1}. This strong field is necessary to enforce a directional movement of cations across the oxide film at temperatures where normal diffusion cannot accomplish this.

c) $\xi_1 < \xi < \xi_0$: If $zeaE \ll kT$ (where *ze* is the charge on the ion) or $\xi > \xi_1$ where $\xi_1 = zeaE / kT$ (ξ_1 = 50-100 atomic layers at room temperature) then the diffusion rate of the ions would be proportional to the field strength. If $\xi \gg \xi_1$ - the number of ions crossing a unit area in unit time is

$$n_i B_i E = n_i B_i V/\xi \tag{2.26}$$

where B_i is the mobility of an ion. The resulting rate law of film growth is

$$\frac{d\xi}{dt} = \frac{1}{\xi}(n_i B_i \upsilon V) = \frac{1}{\xi}(n_i D_i \upsilon \frac{eV}{kT}) \tag{2.27}$$

Considering the expressions in brackets as constants, we find that Equation (2.27) is a parabolic law. In systems where the oxide film has an electron deficit, however, the number of cation holes would be proportional to the number of excess atoms of oxygen at the surface, $n_{o..}$. Since $n_{o.}$ is related to the field strength by

$$n_{o.} = \frac{\varepsilon V}{4\pi e}\frac{1}{\xi} \tag{2.28}$$

This leads to an oxidation law of the type

$$\xi^3 = 3k't \tag{2.29}$$

where k' is the constant.

d) $\xi_1 > \xi < \xi_0$: If $\xi < \xi_1$ where $\xi_1 = zeaV / kT$, then the electric field strength is so great that the migration rate of the ions can no longer be assumed proportional to the field strength and no longer inversely proportional to the film thickness. An

interstitial ion can jump to the next interstitial lattice site as shown in Figure 2.4 if it is able to overcome the potential barrier U_2. For the thin layers the energy U_E which a defect with a z-fold charge within a lattice distance a can obtain from the field is comparable to its thermal energy U_{th} at low temperatures (a is as in Figure 2.4).

$$\mathrm{k}T = U_{th} \approx U_E = zea\mathrm{E} \tag{2.30}$$

The rate j at which a charge carrier moves through a constant field in the lattice is given by [24]

$$j = \frac{\mathrm{k}T}{\mathrm{h}} a \exp(-U_{th}/\mathrm{k}T)\left[\exp\left(\frac{U_E}{2\mathrm{k}T}\right) - \exp\left(-\frac{U_E}{2\mathrm{k}T}\right)\right] \tag{2.31}$$

where h is Planck's constant.

In the case of high temperatures ($U_E < \mathrm{k}T$) only terms of the first power in $U_E/\mathrm{k}T$ in the series expansion of the exponential function in Equation (2.31) need be considered. Therefore, the field current is the linear dependent on E. If $U_E > \mathrm{k}T$ the rate of migration j of the particles in the tarnishing layer is exponentially dependent on the field strength, which in turn is inversely proportional to the thickness of the film.

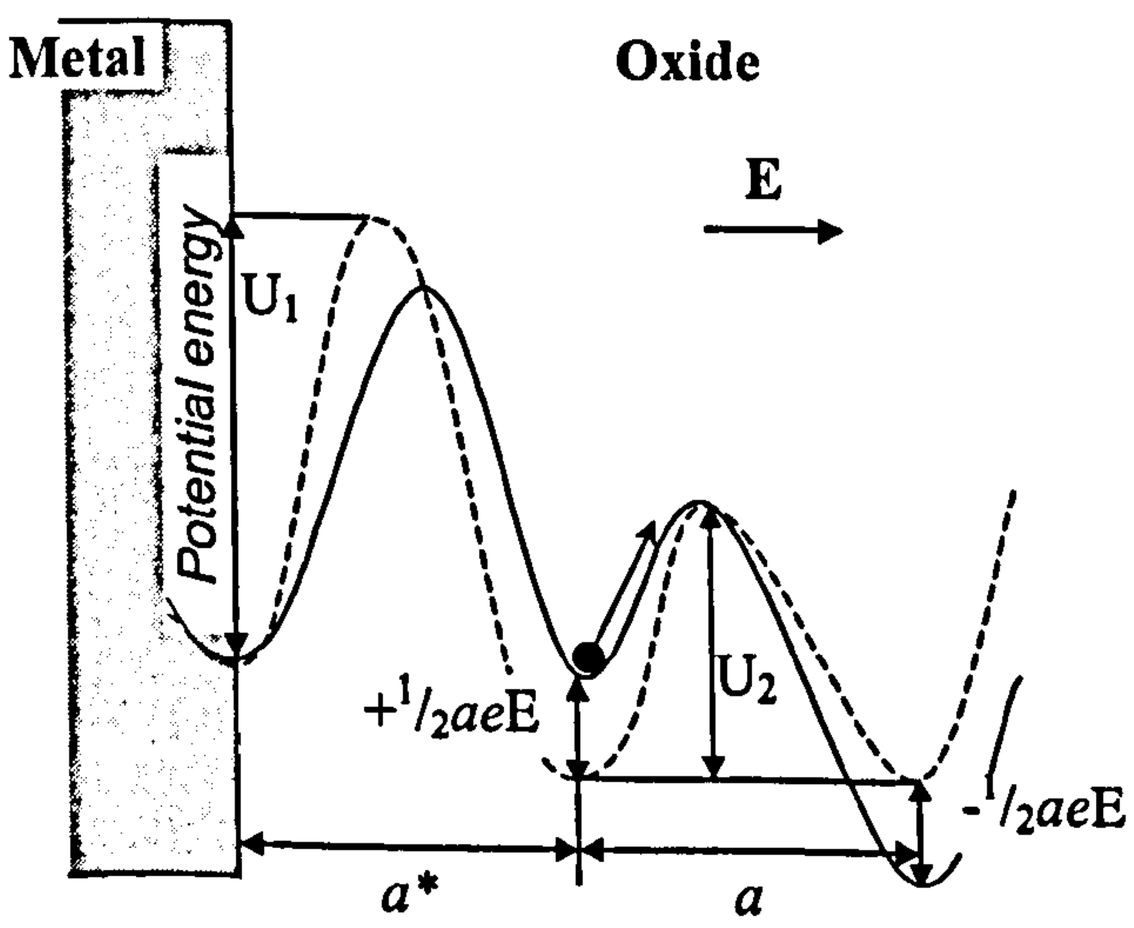

Figure 2.4. Schematic representation of potential energy levels of the metal ions for vacancy migration in the presence of an electric field. ($a^* \neq a$; $U_1 > U_2$);
$\mathrm{j} = \mathrm{j}_0 \exp\{-(U \pm \frac{1}{2} U_E)/\mathrm{k}T\}$ with $U_E = zea\mathrm{E}$

The following relationship is obtained for the growth of the oxide film thickness:

$$\frac{d\xi}{dt} = \mathrm{N}\nu\upsilon \cdot \exp(-\frac{\mathrm{W}}{\mathrm{k}T})\exp(\frac{zea\mathrm{E}}{\mathrm{k}T}) \qquad (2.32)$$

where N is the number of ions per cm^2 surface; $W = U_2 + \frac{1}{2}U_E$.

Equation (2.32) can be simplified to the following form:

$$\frac{d\xi}{dt} = u\exp(\frac{\xi_1}{\xi}) \qquad (2.33)$$

where $\xi_1 = zea\mathrm{V} / \mathrm{k}T$ and $u = \mathrm{N}\nu\upsilon \exp(-\mathrm{W} / \mathrm{k}T)$.

For $\xi << \xi_1$ an integration of Equation (2.33) can be made, which leads to an inverse logarithmic law:

$$\xi_1/\xi = \text{const.} - \ln t \qquad (2.34)$$

In practice however, inverse logarithmic relationships have been rarely observed, whilst a direct logarithmic relationship is more frequent.

According to Equation (2.31) the ionic current represented by $j_{ion} \propto \exp(\xi_1/\xi)$. On the other hand, the electronic current due to the tunnel effect is represented by $j_{el} \propto \exp(-\xi/\xi_0)$ so that for $\xi < \xi_0$,

$$\frac{d\xi}{dt} = const.\exp(-\frac{\xi}{\xi_0}) \qquad (2.35)$$

and after the integration of equation (2.35):

$$\xi = \xi_o \ln t + C \qquad (2.36)$$

where ξ_o and C are constants.

The currents thus depend on the thickness of the film formed. As can be seen from Figure 2.5 only the lower curves determine the overall rate of reaction.

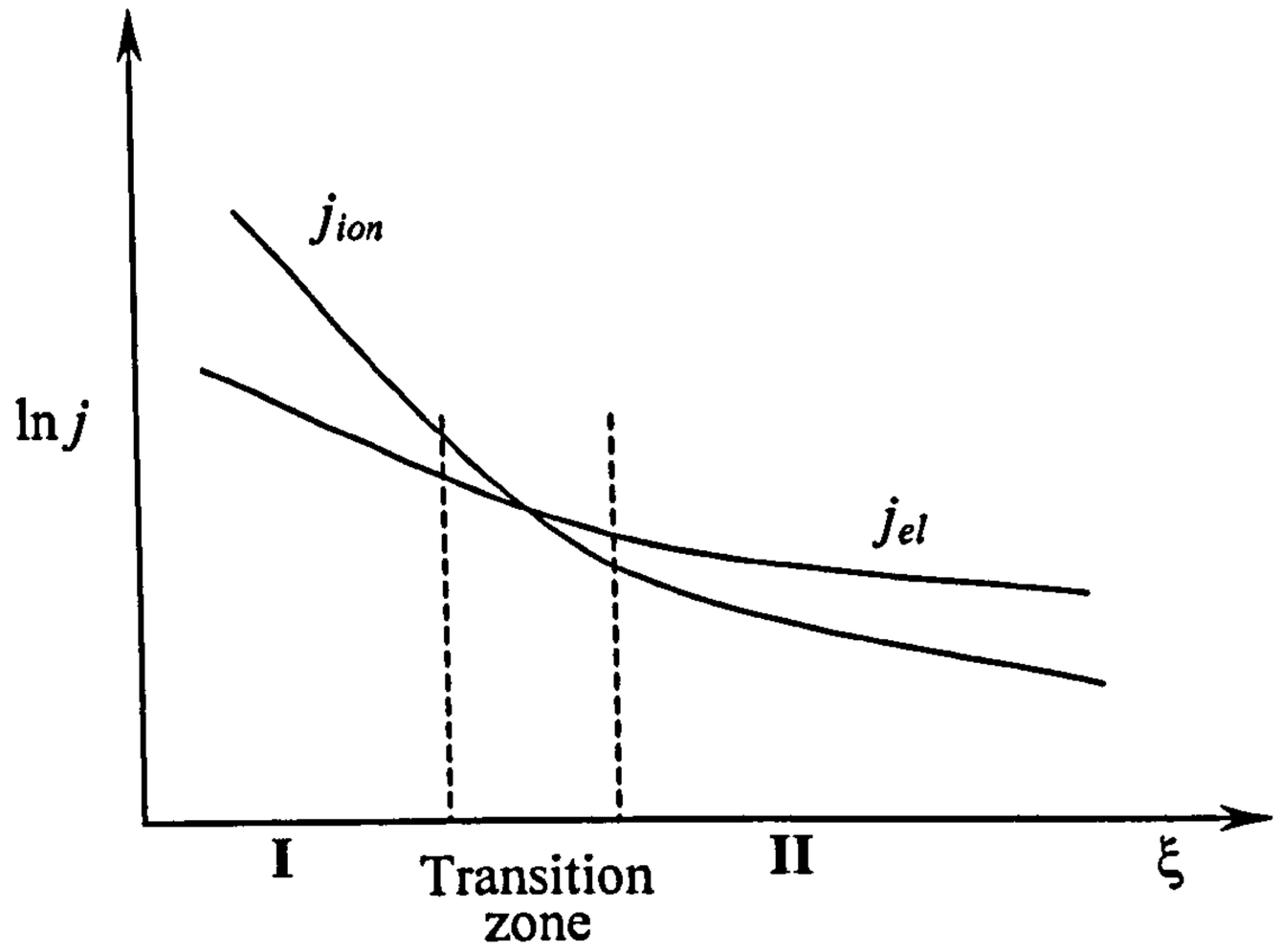

Figure 2.5. Local dependence of the ion and electron current in very thin oxide films [6].

The rate of electron tunneling (I) determines the formation of the thinnest layers and the rate of ionic transfer (II) that of the thicker films.

There is a number of suggested oxidation mechanisms for thin films. The growth process of the oxide layers will be different depending on film thickness and temperature. It can be cubic, logarithmic, inverse logarithmic, parabolic or even linear laws of oxidation.

ii) The Wagner theory of oxidation, models for scales

When oxidation leads to the forming of a thicker film on the surface of metal, the parabolic relationship becomes the time law most commonly observed. The theory of parabolic oxidation has been fully developed by Wagner [21] and it is the best understood and most important of the various oxidation mechanisms.

Wagner's theory assumed that a volume diffusion of the reacting ions or a transport of electrons across the growing scale is the rate-determining process of the total reaction. Electrons and ions have possibilities to move independently of each

other. It is assumed that thermodynamic equilibrium is established between the oxide and the oxygen gas at the oxide-oxygen interface and between the metal and the oxide at the metal-oxide phase boundary.

The driving force of the reaction is the free-energy change associated with the formation of the oxide and as a result, concentration gradients of the components are established in the oxide scale. Such concentration gradients are illustrated, according to Kofstad [8], in Figure 2.6.

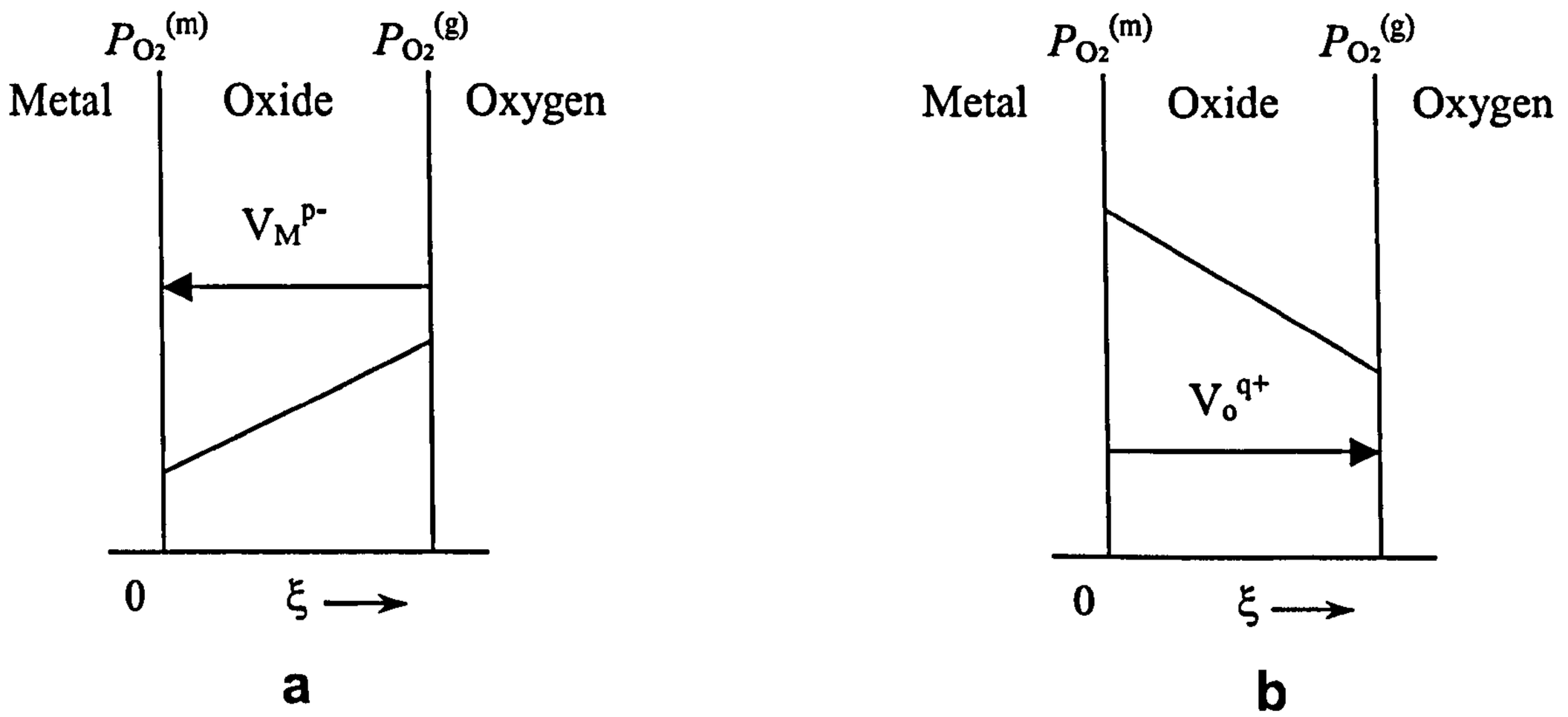

Figure 2.6. Schematic representation of concentration gradient of a) metal ion vacancies and the transport processes occurring in an oxide scale containing mostly metal ion vacancies (for instance Cu_2O, NiO); b) oxygen ion vacancies and the transport processes occurring in an oxide scale containing mostly oxygen ion vacancies (for instance ZnO).

For an oxide scale with metal ion vacancies, the metal ions diffuse outward from the metal-oxide to the oxide-gas interface. The vacancies migrate inversely, and their equilibrium concentrations at the interface are given by the defect equilibrium:

$$\tfrac{1}{2}\,O_2 = \text{oxide} + V_M^{p-} + pe^{+} \qquad (2.37)$$

As $P_{O_2}^{(g)} > P_{O_2}^{(m)}$, external gas pressure and equilibrium dissociation pressure of the oxide in contact with its metal respectively, the metal vacancies (V_M^{p-}) are

continuously produced at the oxide-gas interface and consumed at the metal-oxide interface.

Oxygen ion vacancies (V_o^{q+}) migrate in the direction opposite to the metal ions vacancies, and their equilibrium concentration at the interfaces is given by

$$O_o \leftarrow\rightarrow V_o^{q+} + qe^- + \tfrac{1}{2} O_2 \qquad (2.38)$$

Oxygen ion vacancies are correspondingly created continuously at the metal-oxide interface and consumed at the oxide-gas phase boundary.

The gradients and the rate of diffusion of the components determine the oxide growth rate. These mechanisms lead to a parabolic oxidation.

A separation of charges takes place in a growing oxide scale due to the difference of the diffusion coefficients for the cations, anions and electrons. In describing the transport of ions and electrons through the scale, both the diffusion due to the chemical potential (μ) and that due to the electrical potential (ϕ) must be taken into account.

On this basis the number of particles passing through cross-section unit of a plane per second is given by

$$j_i = c_i u_i = -c_i B_i \left(\frac{d\mu_i}{d\xi} + z_i e \frac{d\phi}{d\xi} \right) \qquad (2.39)$$

$d\mu_i/d\xi$ is the chemical potential gradient, $d\phi_i/d\xi$ is the electric field strength, e is electronic charge, z_i is the valence of the particle, c_i is the particle concentration, u_i their average drift velocity. B_i is related to the mobility of the particles, υ_i, through $B_i = \upsilon_i / z_i e$.

After several substitutions and elimination of B_i and $d\phi_i/d\xi$, the equation of the reaction rate dn/dt can be finally obtained

$$\frac{dn}{dt} = \left\{ \frac{1}{e^2 r^2 b^2} \int_{\mu_o^i}^{\mu_o^0} \Sigma t_e (t_M + t_O) b d\mu_O \right\} \frac{1}{\Delta\xi} = k_i \frac{1}{\Delta\xi} \qquad (2.40)$$

where the scale is assumed to consist of the compound M_aO_b forming the ions M^{m+} and O^{r-}, $\Delta\xi$ is the thickness of the scale, r and b are the constants related to the valence of nonmetal, Σ is the electrical conductivity, t_e, t_M and t_O – transport numbers ($t_e + t_M + t_O = 1$). μ_o° and μ_o^{i} represent the chemical potential of the nonmetal at the gas-oxide interface and metal-oxide interface, respectively. k_t is the parabolic rate constant for the reaction.

If the activity is approximated by the partial pressure, the chemical potential of oxygen in oxides is given by

$$d\mu_X = d\mu_O = \tfrac{1}{2}kTd\ln p_{O_2} \tag{2.41}$$

and in this case equation 2.40 takes the form

$$\frac{dn}{dt} = \left\{\frac{kT}{2e^2r^2b}\int_{p'_{O2}}^{p^0_{O2}}\Sigma t_e(t_M + t_O)dp_{O_2}\right\}\frac{1}{\Delta\xi} \tag{2.42}$$

where p°_{O2} represents the oxygen pressure in the gas phase and p^{i}_{O2} the oxygen partial pressure at the metal-oxide interface.

The formation of a non-uniform scale, that is porous or cracked, can take place on the surface of a metal. Evans [24] suggests a model in that case that would account for the logarithmic growth of scales. It is based on the assumption of the formation of mechanical imperfections in the oxide scale, in the form of minute blisters or cracks. If rifts are formed in a blister, they could conceivably be permeable or impermeable to oxygen molecules. The metal at the seat of the blister can build up a new film of oxide until fresh blisters form. If the varying rates of oxidation due to alternate breakdown and repair were smoothed out, the overall rate would be rectilinear. If, on the other hand, the rifts were insufficiently large to admit oxygen molecules, scale growth would be due to ionic diffusion. The blisters can prevent diffusion and then the area for diffusion would be restricted. Evans obtained the effective rate of thickening of the whole surface from the probability that a cavity barrier will not cover a representative point of the metal surface. If the chance of a barrier being situated within the thickness element $d\xi$ is defined as $k'd\xi$, the chance

that there will be no barrier in ξ must be $e^{-k'\xi}$ provided that k' is independent of ξ. The rate of mean thickening will be given by

$$d\xi/dt = \text{const}\ e^{-k'\xi} \qquad (2.43)$$

which gives upon integration

$$\xi = k' \ln (a't + b') \qquad (2.44)$$

where k', a' and b' are constants. Therefore, in such a way, a satisfactory explanation for the logarithmic law of scale growth was obtained. However, due to the assumptions that have been made the validity of this interpretation is still open to question until further arguments are presented.

It should be noted that the different oxidation mechanisms could be applied depending on the metal and conditions of oxidation.

iii) Formation of several oxides

Several different oxide layers may form on the surface when a metal has varying valence. In the ideal case, each compound will constitute a separate layer within which the concentration of metal decreases from the inside to the outside. The most metal-rich oxide will be next to the metal, and the most oxygen-rich oxide next to the gas phase. Growth of the oxidation layers will take place by diffusion. The relative thickness will depend on the diffusion rates through the different layers and on the porosity of individual layers.

Kubaschewski and Hopkins [20] note the difference between oxide layers; the one highest in oxygen is usually an n-type conductor, the one lowest in oxygen a p-type. If diffusion takes place via vacancies rather than interstitial sites, then for two oxide layers the cations diffuse in the inner and anions in the outer layer, both towards the interface between the two oxides. Therefore, the formation of new oxide is expected to take place mainly at the oxide-oxide interface in most cases.

Kofstad [8] points out that often the higher oxide forms a porous nonprotective scale growing on a compact scale of a lower oxide. Such oxidation

behaviour results in paralinear oxidation in which parabolic oxidation predominates only during initial stages, when the compact scale of the lower oxide is the main reaction product. In other cases, a different oxide layer may be compact. Similar oxidation behaviour was found on iron for FeO, Fe_2O_3 and Fe_3O_4 layers [25], [26], [27] and [28]. According to Wrazej [28], in terms of thickness, the ratio for Fe_2O_3/Fe_3O_4 is being about 1/1. Wrazej also supposes that Fe_2O_3 flakes off easily from the surface. However, Krzyzanowski and Beynon [29] indicate for high temperature oxidation of mild steel that separation of the oxide scales is sensitive to the temperature. The three-layer oxide also was found at the range of 830-1150°C.

If the diffusion through the different oxide layers is rate determining, the total oxidation will be parabolic. The relative thickness of the layers will be determined by the relative diffusion rates through the layers in that case. Then the relationship for the thickness of two layers, using Equation 2.40, can be given by

$$\frac{x_1}{x_2} = \frac{k_1}{k_2} \tag{2.45}$$

where x_1 and x_2 are the thickness of layer 1 and 2 respectively growing with a rate constant k_1 and k_2 respectively.

The oxygen pressure dependence can be a function of the relative growth rates. If the new oxide is mainly growth of the inner layer, the oxidation will be independent of oxygen pressure. On the other hand, if the outer layer represents the major part of the scale, the pressure dependence will approximate that predicted by Wagner's theory.

iv) Oxidation of iron and alloys

As the aim for this thesis is modelling oxide failure based on steel specimens and because of the great technical importance of iron alloys and steels, close consideration of their oxidation is necessary.

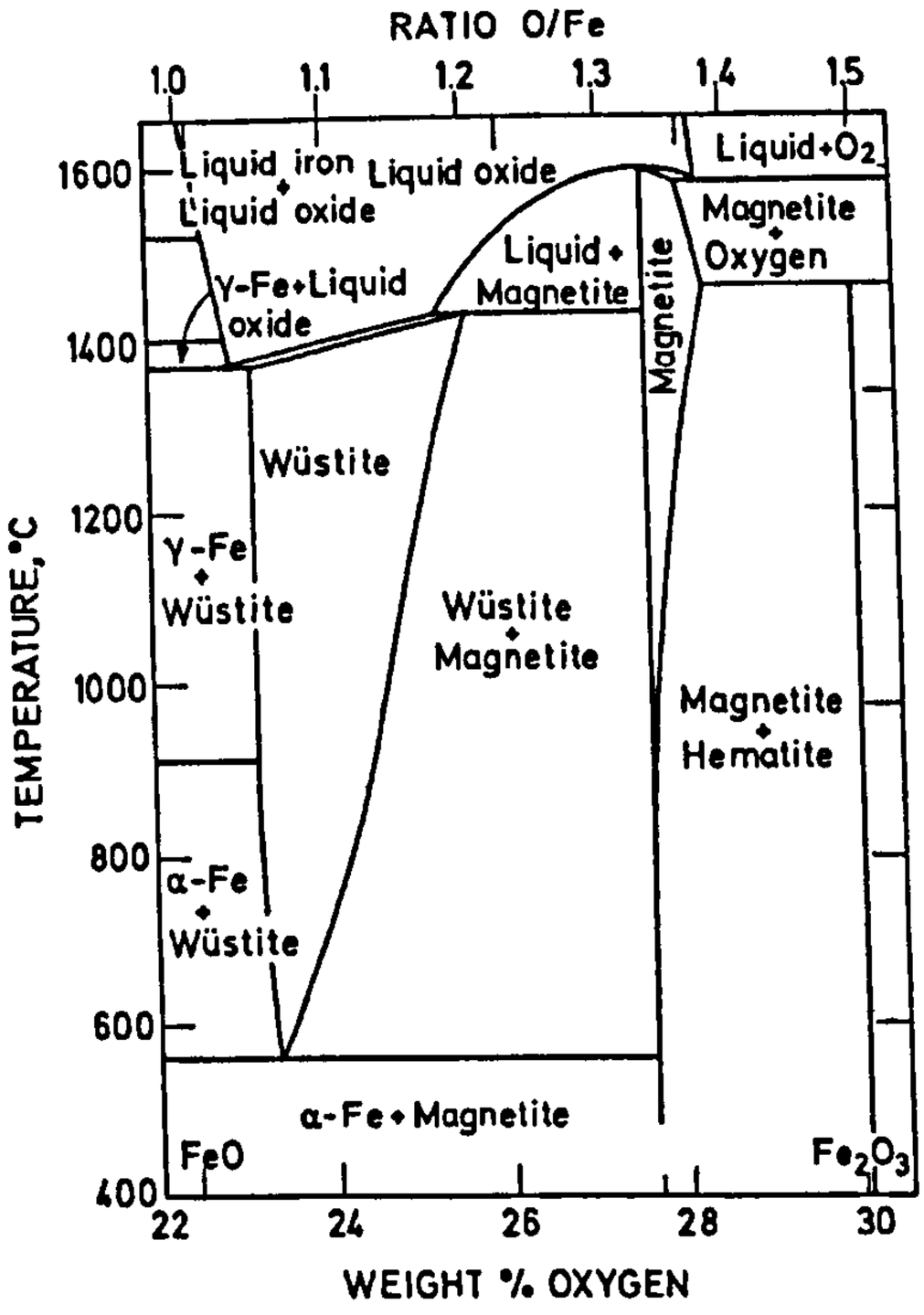

Figure 2.7. The iron-oxygen phase diagram [10].

Figure 2.7 shows the iron-oxygen phase diagram. Iron forms three stable oxides: wüstite ($Fe_{1-m}O$), magnetite (Fe_3O_4), and hematite (Fe_2O_3). Wüstite and magnetite both have a face centred cubic oxygen lattice, and hematite has the hexagonal crystal structure.

A schematic representation of the diffusion processes which can participate in iron oxidation are presented in Figure 2.8.

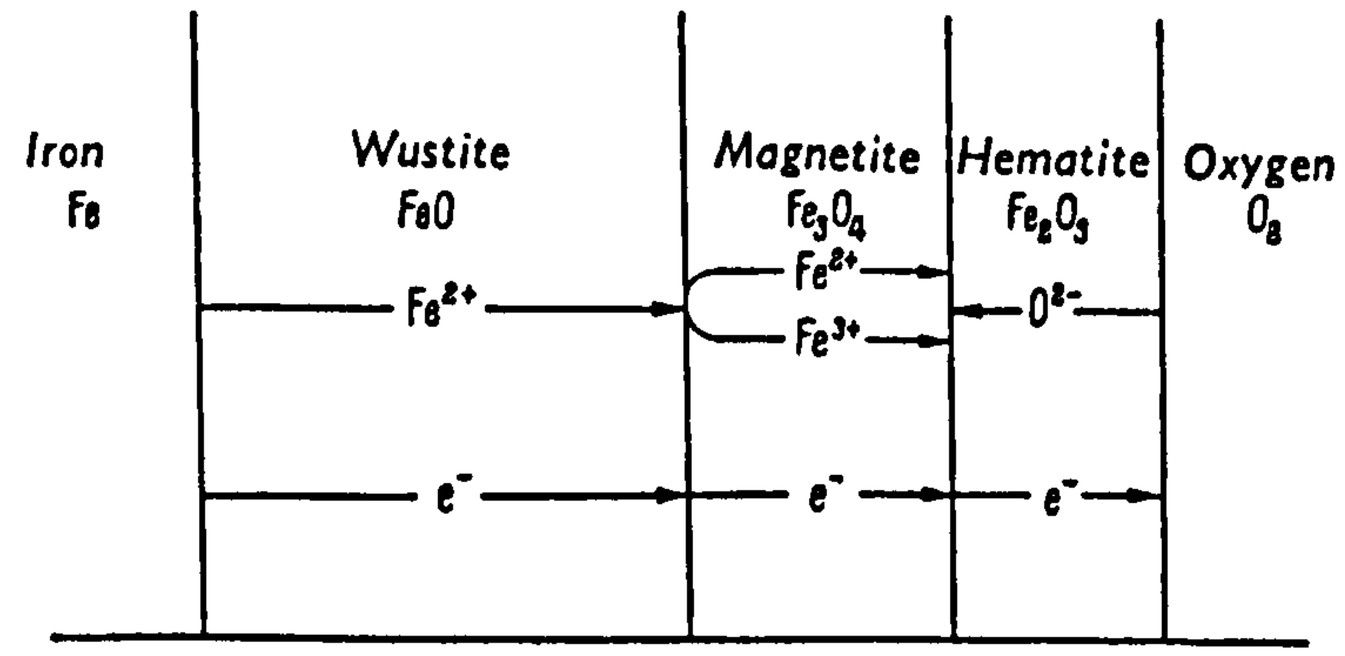

Figure 2.8. Schematic representation of the diffusion processes during the oxidation of iron [6].

Wüstite ($Fe_{1-m}O$) is a nonstoichiometric oxide and only stable at temperatures higher then 570°C. It is a p-type conductor with a relatively high concentration of holes and iron ion vacancies. The defects consist of vacant cation sites and an equivalent number of electron defects represented chemically by trivalent Fe^{3+} ions. The diffusion is essentially cationic via vacant cation sites. The diffusion rate is relatively high.

Magnetite (Fe_3O_4) also exists with an excess of oxygen, but the excess is much smaller than with wüstite and the defect concentration correspondingly less. Some authors [26] indicate that both cations and anions diffuse in Fe_3O_4.

Hematite (Fe_2O_3) is an n-type conductor in which anions largely diffuse [26]. It exhibits little or no deviation from stoichiometry.

Generally, alloys contain two or more oxidizable metals and as a result, oxidation mechanisms are more complex for alloys than for pure metals. Atoms in the components of alloys do not diffuse at the same rates. Consequently, oxide scales on alloys will not contain the same relative amounts of the alloy constituents, as does the alloy phase. Moreover, the structure and composition of oxide scales on an alloy often change with oxidation. Therefore, the oxidation kinetics are often far from ideal or simple rate equations [8].

v) Influence of chemical composition of steel on oxide properties

Steels typically contain small amounts of carbon, silicon and several alloying elements, for example, manganese, nickel, and copper. During oxidation, oxygen reacts with all these elements in the same way as with iron. Therefore, steel oxide scales could include enrichments of alloying elements, carbides and silicon. Oxides of alloying elements may affect the defect structure and the growth rate of the oxide scale and its mechanical properties, such as adhesion to the alloy. There is enough information in the literature in summarising the influence of elements, which is frequently under discussion.

Carbon. Carbon may react with metals and forms carbides that release the metal element as it becomes depleted during oxidation [30]. The overall effect of carbon in oxidation is relatively small. Some authors [31] and [32] suggested that the

presence of carbon decrease scale adhesion. However, Malik [33] studied the oxidation behaviour of *Fe-5M-C* alloys (where *M* is *Si*, *Ti*, *V*, *Nb*, *Ta*, *Cr*, *W*, or *Ni*) and indicates that the adherence of the oxide scale increases with carbon content. Also the same author states that the oxidation rates of the *Fe-5M-C* alloys at 850°C depend upon the thermodynamic state and the mobility of carbon in austenite. Sheasby and co-workers [34] reported that the effect of carbon is already important at low impurity levels. At temperatures up to 950°C, a solid scale is obtained on pure iron in air atmosphere, but when the iron contains as little as 50 ppm *C*, the scale formed is porous. This is in a good agreement with another author publication which states that blisters do not form in the scale on pure iron and they do form on *Fe-C* alloys [32].

Silicon. Silicon generates a quite stable oxide. A very thin continuous layer of SiO_2 may form at the scale base, developing down grain boundaries and as individual internal oxide particles. The influence of *Si* depends on the temperature range. Below 1177°C *FeO* reacts with SiO_2 to form fayalite (Fe_2SiO_4) at the metal/scale interface decreasing the oxidation rate. At higher temperatures, the formation of melting oxidation products (eutectics reactions) is possible, which leads to catastrophic oxidation. The liquid phase preferentially attacks the grain boundaries of the metal, making the scale highly adherent. This can produce surface defects of the embedded scale type during the hot rolling process [35]. Many studies indicate that silicon is often enriched in grain boundary regions [36], near the interface between oxide layers [37] and can govern the oxidation rates, for example *Mn-Cu* low carbon steels [38].

Manganese. The high mobility of *Mn* allows enough manganese to reach the surface to form the very stable oxide layer in the form of *MnO*. A large quantity of *Mn* was also observed in oxides formed on fine-grained material oxidized over long periods [39]. *Mn*-rich outer layers form very quickly on fine-grained stainless steel, but not on large-grained stainless steel [40]. In case of *Mn-Cu* low carbon steels (oxidation temperatures 800 and 1000°C), the element mappings indicate that *Mn* is not enriched in the scale nor in the substrate [37].

Nickel. *Ni* allows stabilising of the austenitic structure of stainless steels in the annealed condition. In addition, *Ni* might influence the oxidation resistance of *Fe-Cr* alloys. It is retained in the alloy or in the inner scale at the metal/scale interface. Although it does not enter the bulk scale in great quantities, it may enter

thin films, scale nodules at breakaway or thick oxidising scales as *Ni*-rich alloy particles. The enrichment of *Ni* in the alloy may well also restrict the rate of diffusion of *Fe* and *Cr* to the interface. Despite a relatively weak affinity for oxygen, nickel plays an important role in dictating the composition, adhesion and mechanical properties of the protective scale [41]. In recent studies [42], an addition of *Ni* to the 0.3% *Cu* bearing steel reveals that nickel eliminates most *Cu*-enriched liquid phases in the steel/scale interface at 1000-1200°C temperatures.

Chromium. In stainless steels, results show that a chromium oxide is mostly formed near grain boundaries [40]. Baer suggests that enhanced diffusion of *Cr* along grain boundaries allows small-grained material to form a protective oxide. The overall oxidation behaviour of small- and large-grained stainless steels at 800°C was consistent with formation of Cr_2O_3 at grain boundaries with following lateral diffusion of *Cr* and spreading of Cr_2O_3. A small-grained material forms continuous Cr_2O_3 films under conditions where such films may not form on larger-grained materials [40].

Copper. The *Cu*-enriched phases formed at mild steel (oxidation temperature 1000-1200°C) were closely observed at the scale/steel interface using back-scattered electron microscopy [42]. Taniguchi [37] also reports that during low carbon steel oxidation at 800-1100°C, *Cu* is enriched in the porous *FeO* layer, near the interface between oxide layers, and near the scale/steel interface. Several authors have reported that the *Cu* enrichments cause a better scale adhesion [31, 32] and [43]. One of the possible mechanisms is given by Grabke et al [44], who state that rugged interface is formed when the interdiffusivity in the enriched layer beneath the scale is lower than the self-diffusivity of iron in wüstite. The average scale growth rate will be reduced in this situation.

Titanium. *Ti* behaves in a similar manner to *Mn*. Its corresponding oxide is more stable than Cr oxide and it is detected in the outer regions of the protective scales indicating that it diffuses across them. It is also found as intergranular oxide, perhaps showing that it is less mobile than *Mn* [35].

Phosphorus. Phosphorus segregates to the scale/metal interface in oxidised form. It forms a low melting point phase at temperatures above 960°C and can lead to preferential attack of the metal grain boundaries [30].

Cerium. According to Seal [45], the presence of *Ce* restrains the formation of the Fe_2O_3 layer allowing the Cr_2O_3 layer to form uniformly in *Fe-Cr* steels.

The effect of addition of rare earth elements such as *Ce*, *Y*, *La*, etc. in their oxide form to Cr_2O_3 forming alloys for improving high temperature oxidation behaviour are reviewed in a detail in the literature [46], [47], [48] and [49].

vi) Atomistic approach to the metal/oxide interface

Atomistic modelling of materials using interatomic potentials within the shell model, which was introduced by Mayer [50], has made a significant contribution to the understanding of interfacial processes, such as bonding and oxidation. Examples of such modelling could be the calculations of the structure and energy of formation of the metal/oxide interface realized by Duffy [51, 52] and Stoneham [53]. Calculations of the formation and interaction energies of intrinsic defects in oxides near grain boundaries also are possible [54] and [55]. All these computations could be very important for understanding and modelling mechanical parameters such as adhesion, friction and wear, ductility, stress in oxides and metal/oxide interface [56]. However, computer simulation of mechanical failure of oxide scales or metal/oxide interface is not yet possible using atomistic modelling. Nevertheless, some calculations of growth modes of metal films on oxide surfaces have been done [57].

2.2.4. Morphology of oxide scales

During the oxidation of mild steel several layers of oxide usually form. Metcalfe [58] suggests that the interface between the two layers is the original metal surface as is shown in Figure 2.9. The outer layers consist of pure iron oxides, the phases present being a function of temperature and oxygen partial pressure. The top outer layer is the hematite (Fe_2O_3). It is a major factor determining the stresses in the scale during cooling [59]. The most common oxide formed is the spinel phase, Fe_3O_4. It grows in the form of long columnar crystals. The scale grows by the diffusion of iron in the form of Fe^{2+} or Fe^{3+} through the oxide to the scale/oxidant interface. The inner layer consists of a spinel structure, M_3O_4, where *M* comprises both *Fe* and the alloying elements. The inner layer occupies the same volume as the steel from which it is formed and the removal of iron to form the outer layer means

that the alloying elements become more concentrated in the inner layer spinel compared to the underlying metal. The grain structure of the inner layer is very fine and is often difficult to measure. It can usually be determined using electron microscopy.

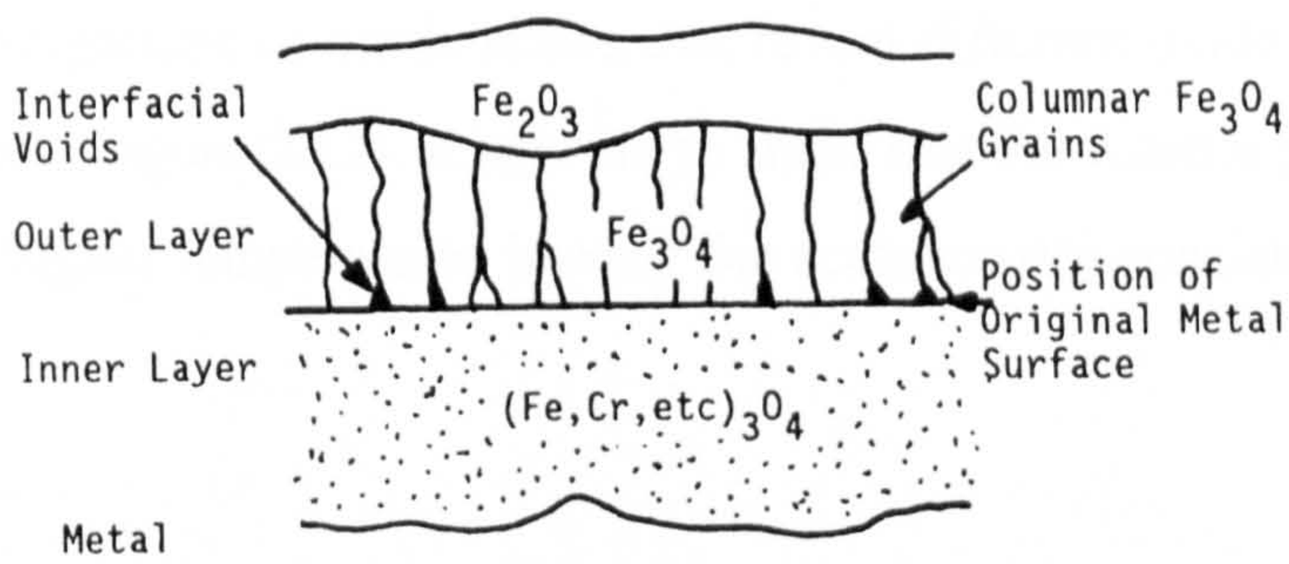

Figure. 2.9. Schematic diagram of a duplex oxide scale formed on steel [58].

Temperature has a leading role in the oxide scale formation. For instance, the scale formed below 570°C on low alloy steels should be very similar to that given in Figure 2.9. The layer of *FeO* is not expected due to its instabilities at this temperature. Above 570°C wüstite may predominate, and grow up to 90% of the total thickness of the scale. Therefore, the oxide scale could have a structure as shown in Figure 2.10. Time of oxidation also has a big influence on oxide scale morphology. As can be seen from Figure 2.10, the oxidation time is equal to 16 hours and in many studies as much as tens or even hundreds of hours [28], [39], [60], [61], etc.

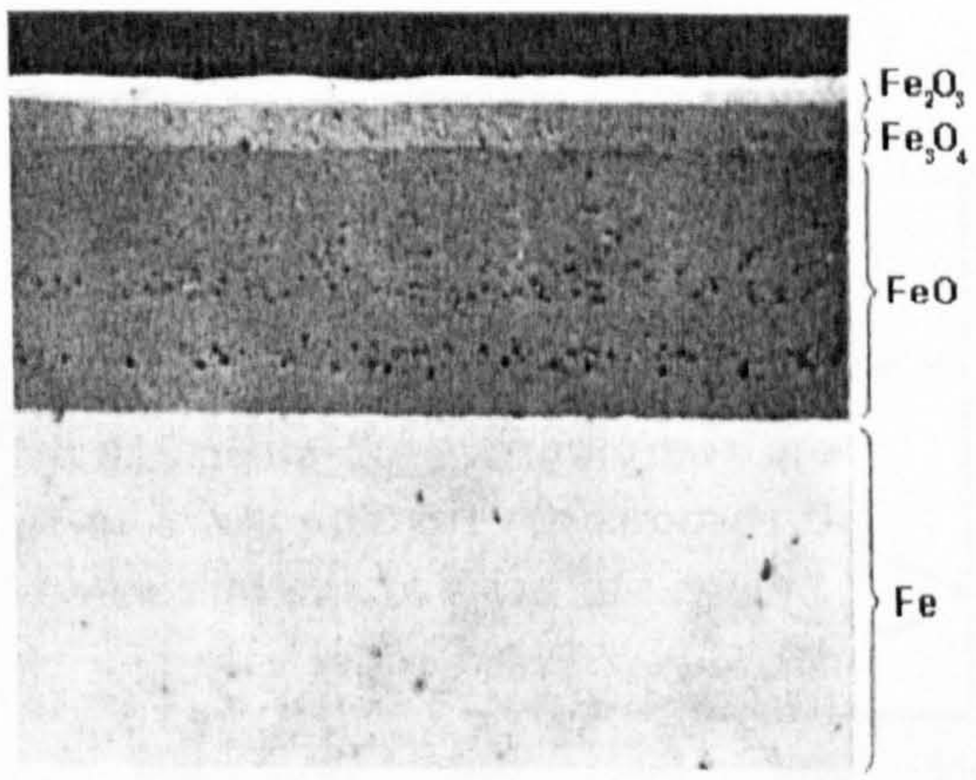

Figure. 2.10. Results of the oxidation of a pure iron sample, T = 600°C, t = 16h, after [6].

However, during most hot metal forming processes, because of the descaling phase, the time for oxide scale growing varies between seconds and tens of minutes. Therefore, the amount of wüstite in the scale may be different from that shown in Figure 2.10. Gittins [62] suggests that the surface layer of steel after a re-heat furnace has the structure shown in Figure 2.11. However, there is a variety of old [63-65] and recent [66] investigations of oxide scales that reveal different oxide compositions at high temperatures (Figure 2.12). It appears to show that the wüstite percentage drops dramatically at higher temperatures leaving the scale mostly consisting of magnetite and hematite.

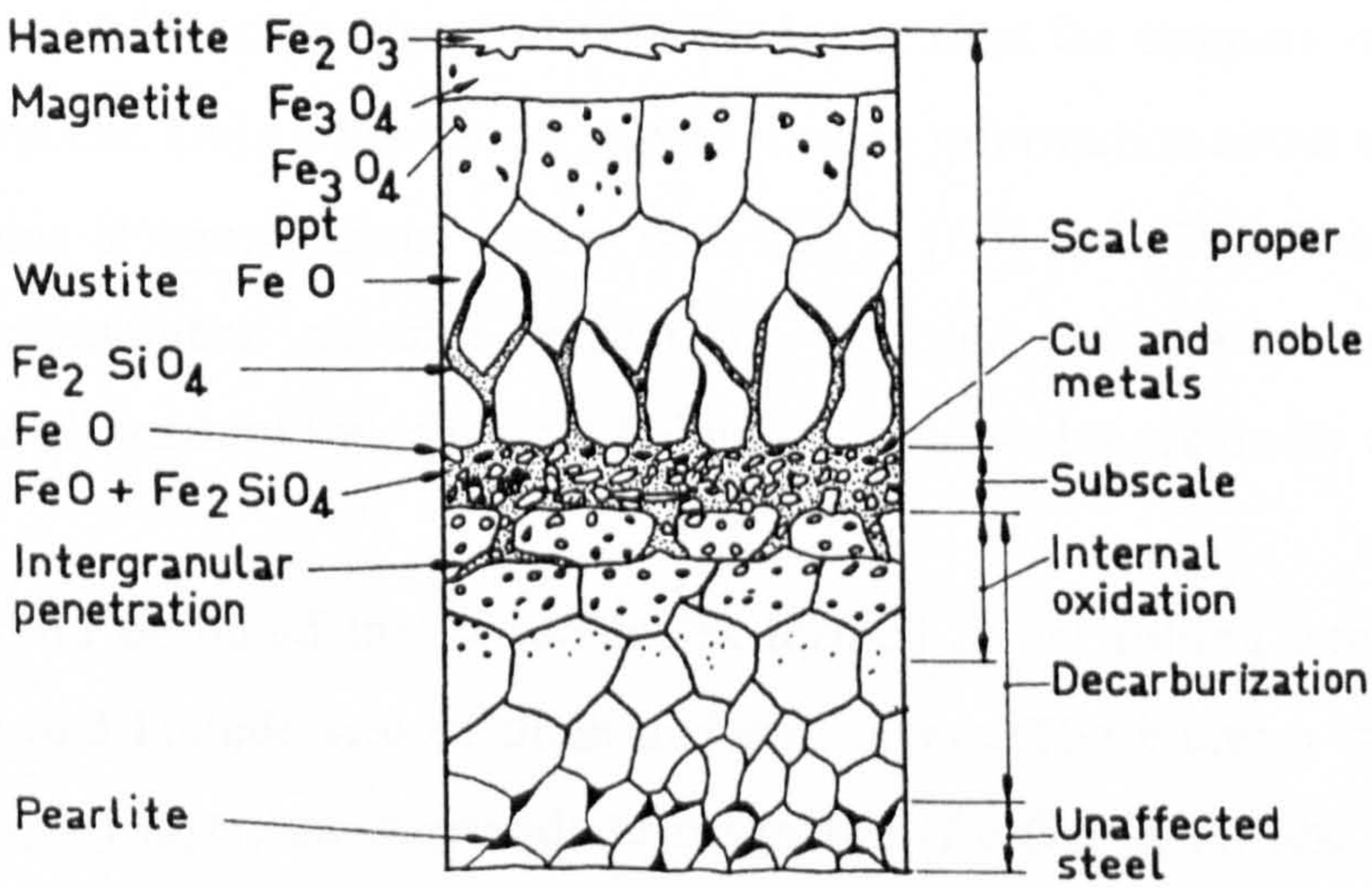

Figure. 2.11. Structure of the surface layer of steel after reheating [62].

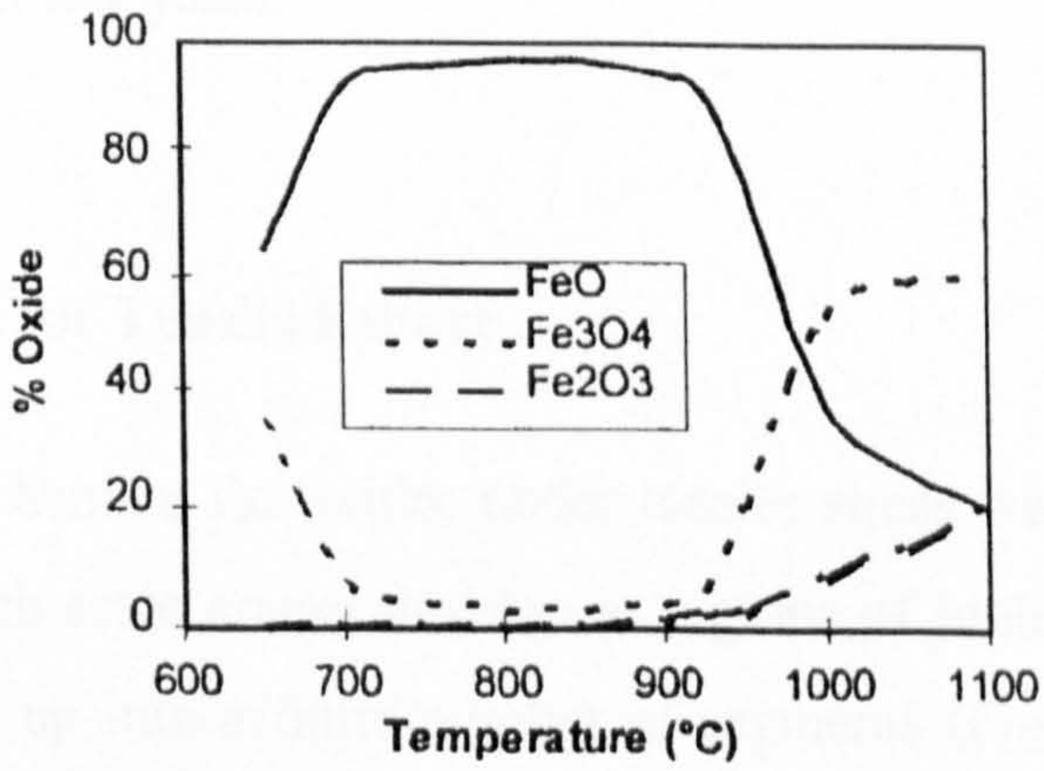

Figure. 2.12. Relation between oxide composition and temperature [66].

Also, different rates of oxidation and morphology of oxide scale have been reported in various atmospheres [67] and [68]. According to Abuluwefa et al., porosity and big voids formation in the oxide scale are strongly dependent on the atmosphere composition.

2.3. Mechanical behaviour of oxide scales

A number of literature sources contain models for tensile and compressive failures of oxides [69-71] and [72]. However, a limit of 800°C in the temperature range is present in most studies. This limit is lower than the temperature during the hot rolling process. Only a few recent papers contain information about the behaviour of oxide scales at temperatures higher than 800°C [60] and [29]. Therefore, many unexplored phenomena are still present for the high temperature oxide failure. Nevertheless, all modes of mechanical failure of oxide scales are under consideration in this study.

It should be noted that oxide scales formed at hot rolling temperatures are non-uniform and include two or three different layers. These are: a thin outermost hematite (Fe_2O_3) layer, an intermediate magnetite (Fe_3O_4) layer, and a thick inner wüstite ($Fe_{1-m}O$) layer [28], [73], [74] and [75]. However, most researchers model an oxide as one persistent layer [76-78] and [79]. Nevertheless, the multi-layer models are already under development [80] and [81] and one can expect their wide appearance in the next few years.

2.3.1. Models for Tensile Failure

A failure mechanism for oxides under tensile stress was proposed by Evans [82]. Initially, through-scale cracks develop at regions of high stress concentration, i.e. the oxide breaks up into a finite number of segments (Fig. 2.13). Elastic stress relaxation in the vicinity of these cracks can reduce the local stress concentration within the oxide segment. Plastic stress relaxation within the oxide is possible if sliding can occur at the oxide/metal interface [82]. The shear translation may induce

fracture damage at the interface which could result in delamination and subsequent spallation [82].

Another mechanism producing plastic stress relaxation exists, which is substrate yielding at the base of through-scale cracks [70]. However, in this case it should not lead to interface delamination. The proposed failure mechanism has found confirmation in a recent study of the tensile failure of oxide scales [29].

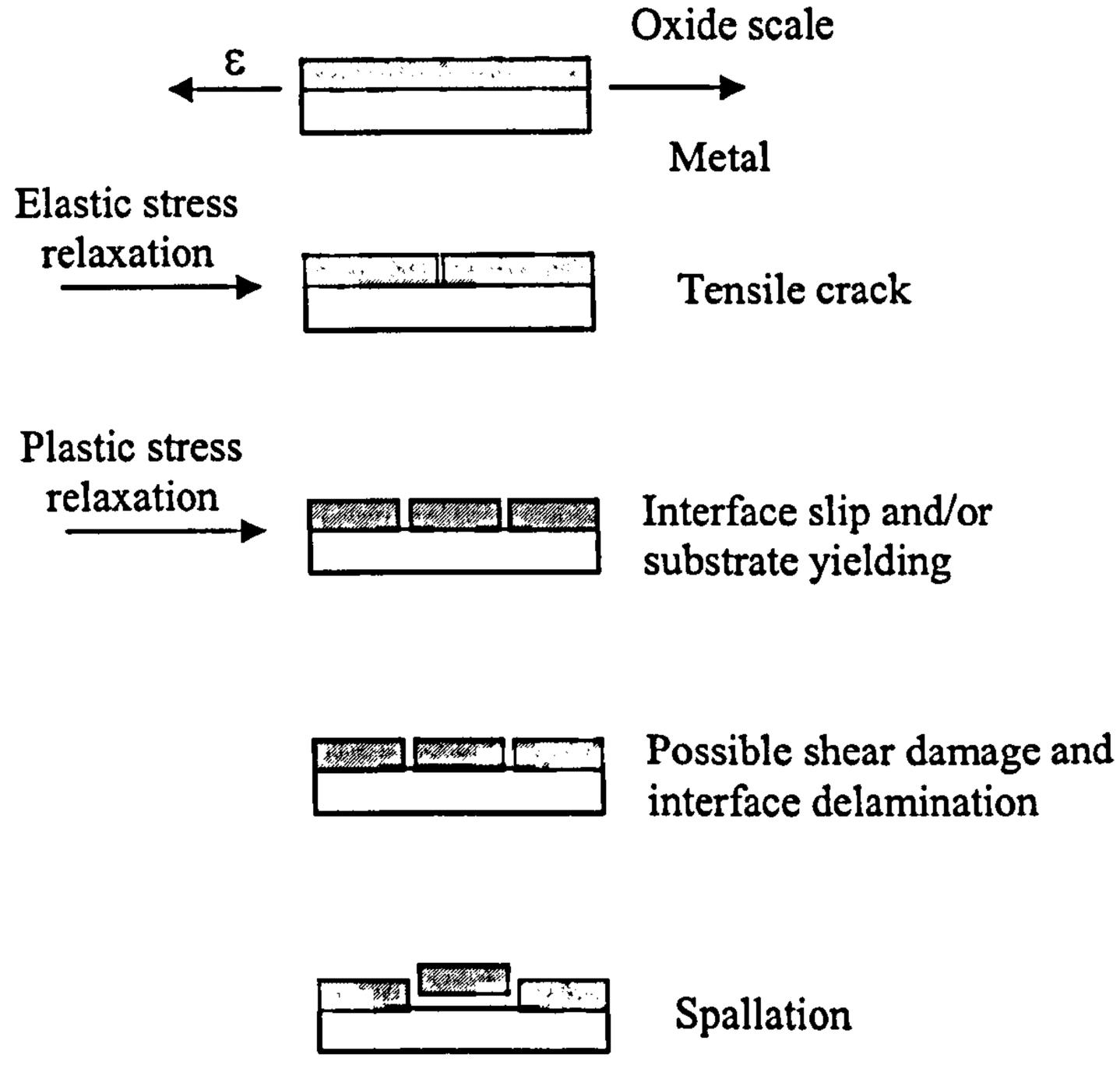

Figure 2.13. Schematic diagram of oxide failure caused by tensile stress, after [82].

Linear elastic fracture mechanics has been applied to determine the critical failure strains under tensile stress. This is justified at temperatures where creep is not expected ($T < 0.5T_m$). It should be noted, that in the present work temperatures were a little higher than $0.5T_m$. However, the previous research shows the brittle behaviour of the oxide scales for the temperature region 850-900°C [29]. Therefore, the LEFM approach is justified under used conditions. Through-thickness cracks are likely to develop by propagation of pre-existing defects either within or at the surface of the oxide layer [83]. The critical applied tensile strain ε_c, needed to produce unstable crack growth is [69]

$$\varepsilon_c = \frac{K_{IC}}{E_{ox} F \sqrt{\pi c}} \tag{2.46}$$

where K_{Ic} is the critical stress intensity factor, c is the size of the physical defect (length of a surface defect or half-length of an embedded defect), E_{ox} is the Young's modulus of the oxide. F is a numerical factor depending on shape, size and position of the void. It can take values of 1.12 for a surface notch of infinite length, of 1.0 for a buried defect and of $2/\pi$ for a semicircular surface notch of radius c [72]. K_{Ic} can be calculated from surface fracture energy values γ_0 of the oxide according to [72]

$$K_{IC} = \sqrt{2\gamma_0 E_{ox}} \tag{2.47}$$

From (2.46) and (2.47) follows equation

$$\varepsilon_c = \sqrt{\frac{2\gamma_0}{F^2 E_{ox} \pi c}} \tag{2.48}$$

The values of γ_0 are tabulated, for instance, in [70].

On the other hand, the critical stress, σ_{cr}, required to propagate a single crack in the oxide scale under plane strain conditions is [84]

$$\sigma_{cr} \geq 0.7 K_{IC} / \sqrt{d} \tag{2.49}$$

where d is the scale thickness. A number of cracks may propagate when the stress reaches this critical value. Thouless [84] suggests that the initial spacing should be less than about 8 film thicknesses. If the film stress exceeds the critical value, the crack density is increased. The minimum crack spacing is given by [84]

$$l_{\min} \approx 8d(1 - \sqrt{1 - 0.5(\sigma\sqrt{d} / K_{IC})^{-2}}) \tag{2.50}$$

In addition, a critical film thickness, d_{cr} could be calculated where no crack can grow across the film.

$$d_{cr} = 0.5K^2_{Ic}/\sigma_o^2 \qquad (2.51)$$

where σ_o is the constant stress.

If slip is assumed to occur at the interface then the minimum crack spacing is [85]

$$l_{min} = 2\sigma_o d/\tau \qquad (2.52)$$

where τ is the critical shear stress at which slip occur, and the critical scale thickness below which no cracks can propagates is [85]

$$d_{cr} = 3\tau K^2_{Ic}/\sigma_o^3 \qquad (2.53)$$

There are three main possible cases of the development of through-scale cracks:

- Multiple cracking with pure elastic stress relaxation,
- Multiple cracking with interfacial slip and/or plastic deformation of the substrate at the base of through-scale cracks,
- Delamination at suitable interfaces.

All these mechanisms are well discussed in the literature [69], [86], [87] and [88].

Recently, Krzyzanowski and Beynon [29] and [76] report the temperature dependence of the oxide scale failure during tension testing. The through thickness cracking has been observed up to 850-870°C for mild steel specimens and at higher temperatures sliding of the non-fractured oxide occurs in the oxide/metal interface (Figure 2.14).

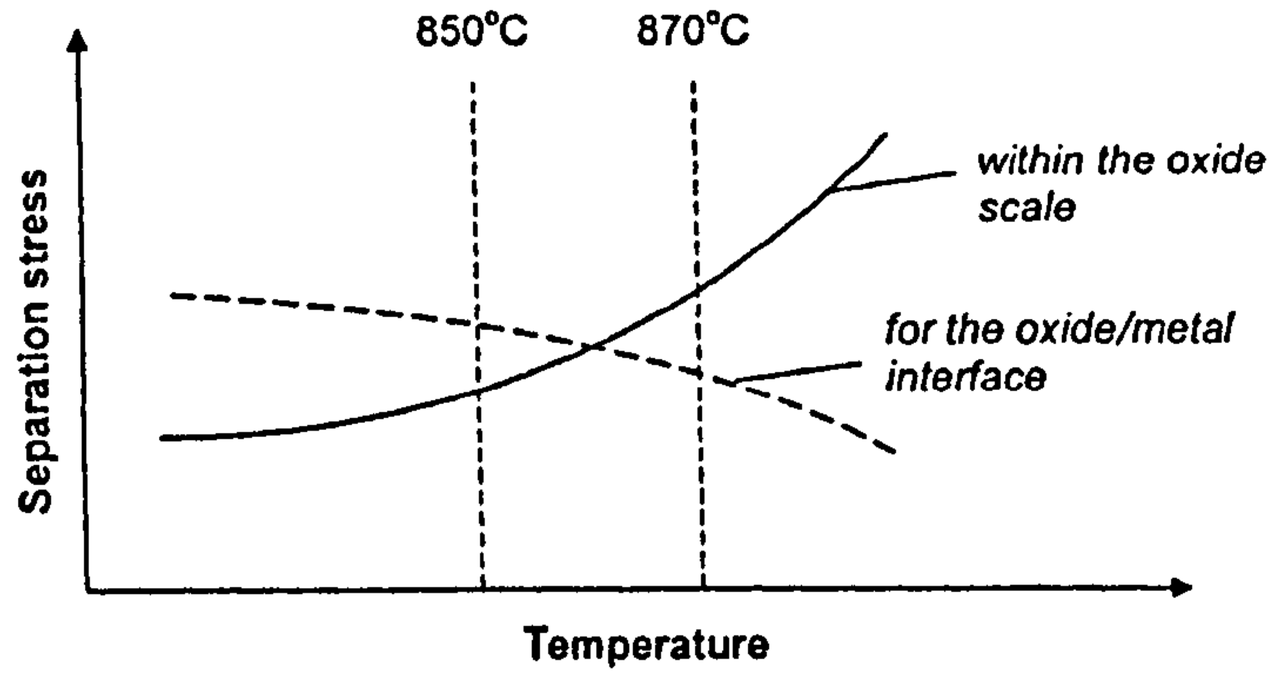

Figure 2.14. Schematic representation of temperature sensitivity of separation stresses of scale/metal system [76].

2.3.2. Models for Compressive Failure

As regards compression failure, it has to be divided into two different types. The first may be called tangential compression, where the load is applied parallel to the surface oxide scale. This type of compressive failure is examined in detail in the literature [69], [72], [82] and [89] including shear failure, buckling, delamination and damage by the substrate yielding. The second type may be called normal compression, where the load is applied perpendicular to the surface oxide scale. This kind of loading is very common in metal forming. Examples of the forming processes with normal compression are forging, rolling of metals and sheet-metal forming. The behaviour of the oxide scale under this type of compression is still not clear. It is quite possible that normal compression can lead to rupture damage similar to concrete failure under uniaxial compression [90, 91] and [92].

i) Tangential compressive failure of oxide scales

Figure 2.15 shows the observed behaviour of oxide scales under compressive stress.

Designation	Critical initiation condition	Schematic diagram of the failure mechanism
Case A: Route I (shear failure by wedging)	Critical shear strength	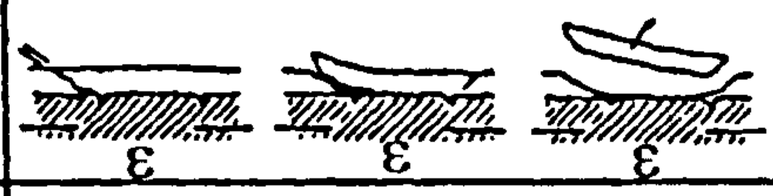
Case B: Route II (buckling)	Critical buckling stability	
Case C: (shear failure)	Critical shear strength	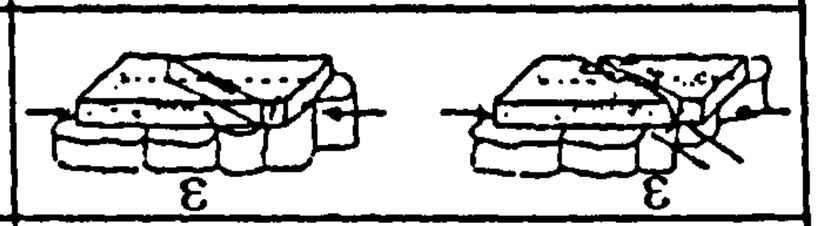
Case D:	Substrate yielding	
Case E:	Critical buckling stability	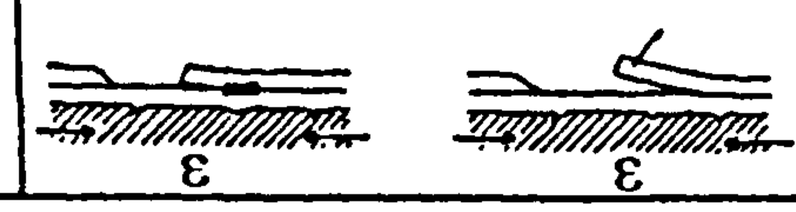

Figure 2.15. Schematic diagram of different oxide failure mechanisms observed under compressive stresses [69].

Many researchers observed the spallation of parts or the whole scale due to compression stress. Two general modes leading to oxide spallation are well developed [72]. Mode I assumes that the oxide/metal interface is intrinsically strong. Initial failure occurs from shear cracking (Figure 2.15 case A and C), followed by the nucleation and propagation of a crack along oxide/metal interface.

The critical strain ε^s_{cl} for spallation can be calculated by [69] or [72]

$$\varepsilon^s_{cl} = \sqrt{\frac{2\gamma_0}{dE_{ox}(1-\nu)}} \tag{2.54}$$

where $2\gamma_0$ is the fracture energy of the oxide/metal interface, d is the scale thickness, and ν is Poisson's ratio.

Mode II assumes weak oxide/metal interface and strong oxide. In this case, spallation is the result of proceeding decohesion at the interface and buckling of the oxide layer leading to through-thickness cracks (Figure 2.15 case B).

The critical strain for the initiation of buckling ε^{b}_{cII}, according to [69] or [72] is

$$\varepsilon^{b}_{cII} = \frac{1.22}{1-\nu^2}\left(\frac{d}{R}\right)^2 \tag{2.55}$$

with R as the initial radius of the zone of decohesion.

In case D, Figure 2.15, the oxide delaminates because of grain-boundary sliding in the substrate adjacent to the interface. For case E, the oxide layer delaminates along a line of least cohesive strength within the oxide.

Schutze [72] also considers the possibility of plastic oxide yield at a stress of

$$\sigma_y \approx E_{ox}/10 \tag{2.56}$$

If brittleness is assumed as a size dependent concept, a critical scale thickness is calculated from the yield stress, σ_y, below which the oxide does not fail only by cracking, but also in a ductile manner [72]

$$d_c = \frac{2.8\gamma_0 E_{ox}}{\sigma_y^2} \tag{2.57}$$

It is possible to take interfacial roughness into account in equation (2.54) by replacing γ_0 by γ_r according to [70] and [72]

$$\gamma_r = \gamma_0\left(1+\frac{0.1E_{ox}}{2\gamma_0}\frac{r}{\lambda}\right) \tag{2.58}$$

where r is the roughness height and λ is the roughness length.

It is possible to summarise the main mechanisms that exist for oxide failure under tangential compression as follows:

- Detachment at the oxide/metal interface,
- Buckling of detached parts of the scale,
- Through-scale fracture (critical shear strain),

- Failure due to substrate yielding,

Plasticity of the oxide (critical scale thickness below which the scale is expected to deform in a ductile manner).

Numerical calculations can be found in the following literature [69], [72], [93], [94], [95], [96], [97] and [98].

ii) Normal compressive failure of oxide scales

Oxide scale is porous and has multilayer and often non-uniform structure. Therefore, a description of normal compressive failure of oxide scales is more complicated then uniaxial compression of metals and remains a problem. Possible solutions for this problem are: use of damage mechanics [99], which include a rupture criterion; failure by void growth to coalescence [100] and [101]; or models for concrete fracture [102] and [103]. However, in order to approach the understanding of failure of oxide scales under uniaxial compression, the determination of failure mechanisms is necessary. For instance, Figure 2.16 shows uniaxial compression of the concrete and types of damage which characterizes its failure. Concrete is a heterogeneous material prone to localized failure. In compression, damage of concrete is initially characterized by axial splitting, which progresses until a sliding shear band forms and the cylinder stiffness rapidly degrades.

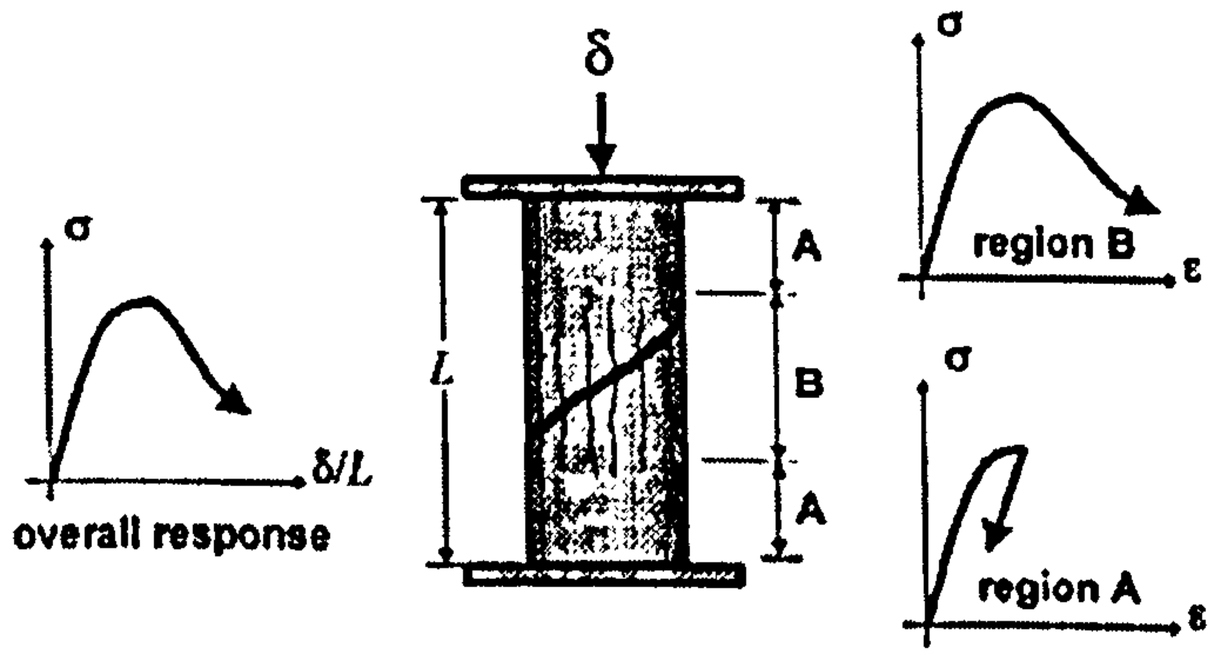

Figure 2.16. Uniaxial compression failure of concrete [92].

In general, what failure mechanism can one expect in oxide scales under normal compression at high temperatures? Admittedly, it could include: localized failure inside the scale where coarse imperfections occur; cracking and crushing of the crack edge; sliding in the metal/oxide interface or between oxide layers; and intrusion of oxide into the metal substrate.

2.3.3. Plastic behaviour of oxide scale at high temperatures

The property of solids that causes them to change permanently in size or shape as a result of the application of a stress in excess of a certain value, is called the yield point. In actual polycrystalline solids the lattice defects exist, and nucleation, annihilation and interaction of such lattice defects occur when the material deforms plastically. In the case of oxide scales, plasticity could be defined as any type of deformation where the strains are larger than those which can be expected from purely linear elastic behaviour.

Previously suggested forms of oxide scale plastic deformation include grain boundary sliding, mechanical twinning, and dislocation climb [104]. Plastic deformation of polycrystalline solids by dislocation glide requires five independent slip systems [105]. Generally, at room temperatures, most of the oxides contain less then five independent primary slip systems [106]. However, at elevated temperatures, the mechanical properties of oxides are different, and the amount of data is rather limited [72]. Nevertheless, Schutze [71] discusses creep deformation of the oxide scale and later introduces pseudoplasticity [107] as result of the combination of scale cracking and crack healing. He concludes that even at high temperatures not much 'genuine' plasticity can be expected in oxide scales, but 'pseudoplasticity' can be observed. Other authors [108] assume the yield stress as $\sigma_y = E_{ox}/10$. Based on this relation and experimental values of Young's modulus, Robertson and Manning [70] calculate the yield stresses for different oxides. The experimental data and verification of the model equations are still in an obvious deficit. Schutze [72] also suggests that more data is needed for the fracture toughness, K_{Ic}, of the different oxides as a function of temperature, and the measurement of the size and distribution of physical defects also requires further development.

Recent strain measurements in metal/oxide system at high temperature suggest that oxide may yield or creep in response to the stresses [109]. Zhang [110] studies surface steps and grooves on the faces of the oxide grains, using atomic force microscopy, and reports the evidence of highly localized plastic deformation of the oxide scales. All these studies indicate that plastic deformation in oxide scales at high temperatures exists, although, it is difficult to detect. Finally, Schmitz-Niederau and Schutze [60] point out that acoustic-emission measurements do not indicate extensive genuine plasticity below 1000°C for most oxides.

2.3.4. Influence of chemical composition of steel on oxide scale behaviour

The influence of chemical composition of the steel on oxide scale behaviour is even less explored than it was discussed in the paragraph 2.2.3 (v). Generally, the adherence of the oxide scale increases with carbon content [33]. Baer [40] and Imai [42] admit that nickel and chromium play an important role in adhesion and mechanical properties of the protective scale although few experimental data exists. Some elements, such as *Cu*, *Si* and *P*, form enriched phases at the scale/metal interface and can also affect the adherence [36, 37] and [42]. Krzyzanowski and Beynon [78] compare two steels with different chemical content in *Si*, *Mn* and *Nb* under high temperature tensile tests conditions. Their results show that the transition zone for oxide scale cracking and sliding (Figure 2.8) shifts to the high temperature region for the steel with higher content of *Si*, *Mn* and *Nb*. Moreover, Tan [80] confirms that previous studies result for *Si-Mn*, *Mn-Mo* and stainless steels. Another author [37] indicates that *Mn* does not enrich at the scale or in the scale/metal interface, hence its role in oxide scale failure not clear. All these studies give clear evidence that chemical composition of alloys is very important for the oxide scale behaviour and demands new experimental data.

2.3.5. Limitation of data on mechanical properties of oxide scale at high temperature

A relatively large amount of mechanical properties data on room temperature exists for oxide scales [72]. However, the amount of data at high temperatures is rather limited. Figure 2.17 shows, for example, experimentally determined values of the fracture toughness of the oxide scales. It is easy to conclude that there is no data available at higher then 1000°C temperatures. The situation is similar for Young's modulus of oxide scales, the fracture energy for oxide and oxide/metal interface and heat transfer coefficients. It should be mentioned that most of the models on scale cracking are based on the assumption of linear elastic behaviour of the oxide scale. However, some evidence of the plastic behaviour of oxides at high temperatures is mentioned in the literature [110] and needs more investigation. In conclusion, more data on physical defect sizes and morphology of multilayer oxide scales is desirable.

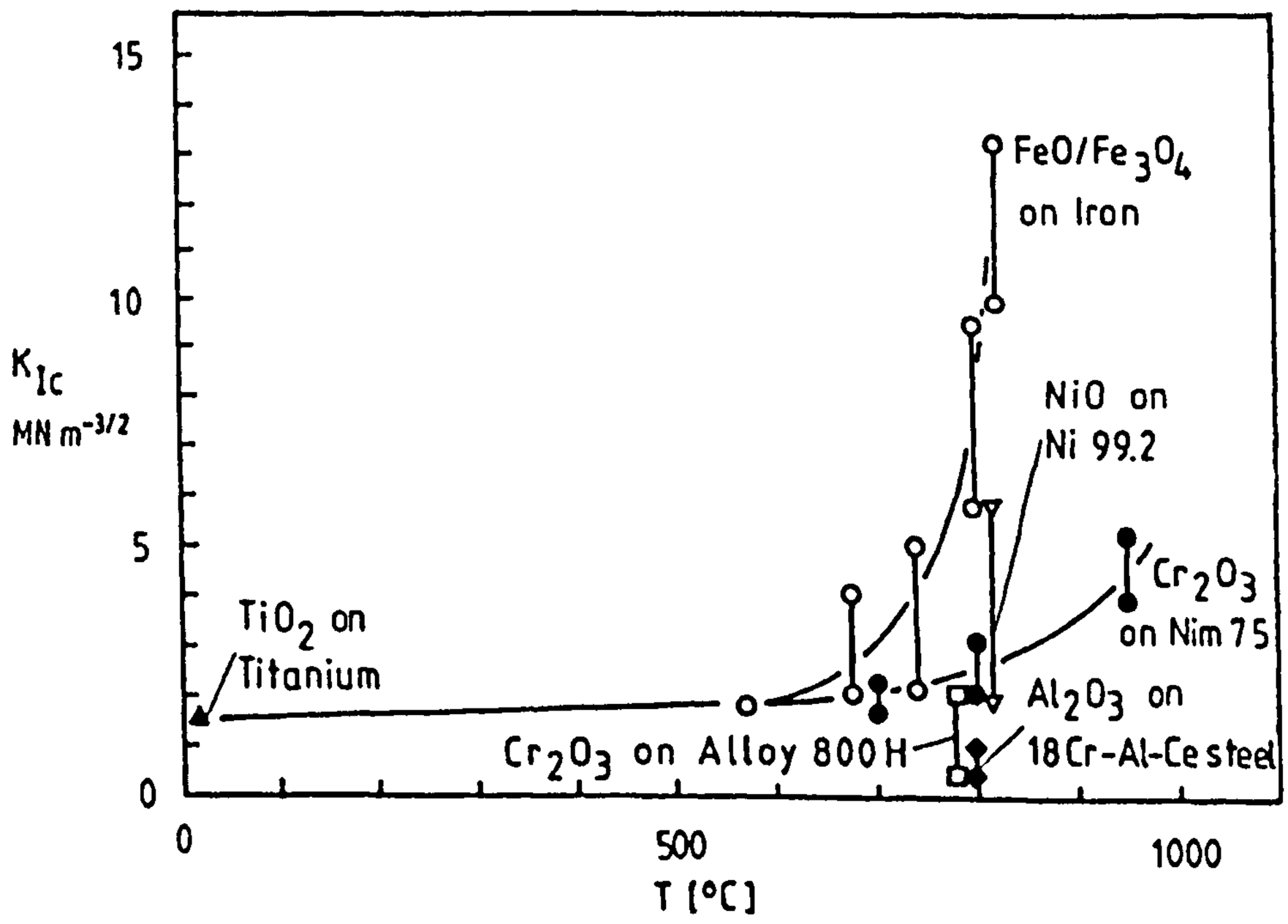

Figure 2.17. Experimentally determined values of the fracture toughness K_{Ic} of surface scale oxides as a function of temperature [107].

2.4. Hot rolling operation

In the steelmaking process, hot rolling occurs after continuous casting (Figure 2.18). During hot metal forming, the shape, microstructure and mechanical properties of steel undergo huge changes (Figure 2.19). Hot working operations are generally carried out in the temperature range 1300°C to 800°C, when the steel is in the austenitic condition. At these temperatures, work hardening is rapidly eliminated by the softening processes of recovery and recrystallisation. Therefore, the forces required to work the steel are relatively low and the ductility is generally high.

Semi-finished products called blooms, billets or slabs are transported from the steelmaking plant to the rolling mills. Steel products can be classified into two basic types according to their shape: flat products and long products. Slabs are used to roll flat products, while blooms and billets are mostly used to roll long products. Billets are smaller than blooms, and therefore are used for the smaller types of long product.

Semi-finished products are first heated in a re-heat furnace to around 1200°C for approximately three hours. On all types of mills the semi-finished products first go to a roughing stand. A stand is a collection of steel rolls (or drums) on which pressure can be applied to squeeze the hot steel passing through them, and arranged so as to form the steel into the required shape. The roughing stand is the first part of the rolling mill. The large semi-finished product is often passed backwards and forwards through it several times. Each pass gradually changes the shape and dimension of the steel closer to that of the required finished product [111]. It should be noted, that low-carbon and mild steels are most commonly used in the hot rolling operation.

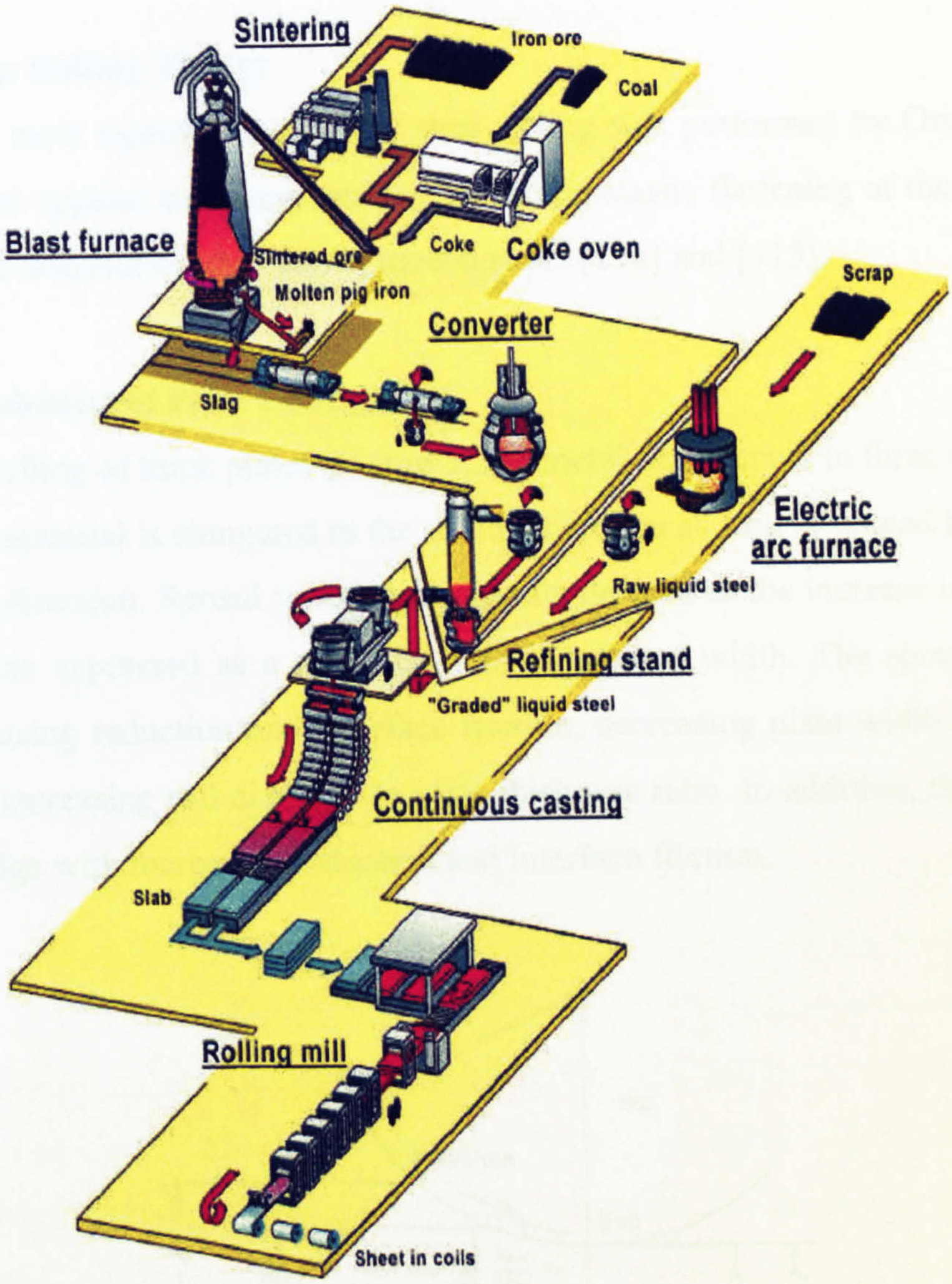

Figure 2.18. Steelmaking processes (www.virtualsteel.com).

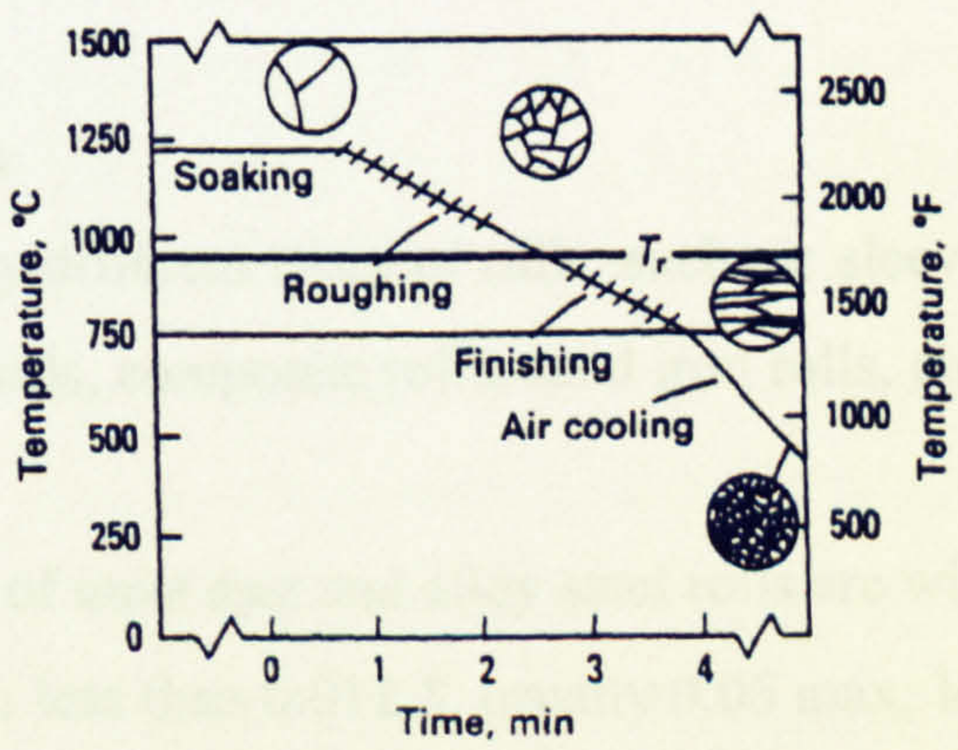

Figure 2.19. Temperature-time profile and microstructural changing for controlled rolling of high-strength low-alloy steel plate [112].

Strip Rolling Theory

The most rigorous analysis of strip rolling was performed by Orowan [113] and has been applied and computerized, including elastic flattening of the rolls and a temperature distribution, by various investigators [114] and [115].

Mechanics of Plate Rolling

In rolling of thick plates (Figure 2.20), metal flow occurs in three dimensions. The rolled material is elongated in the rolling direction as well as spread in the lateral (or width) direction. Spread in rolling is usually defined as the increase in width of a plate or slab expressed as a percentage of its original width. The spread increases with increasing reduction and interface friction, decreasing plate width to thickness ratio, and increasing roll diameter to plate thickness ratio. In addition, the free edges tend to bulge with increasing reduction and interface friction.

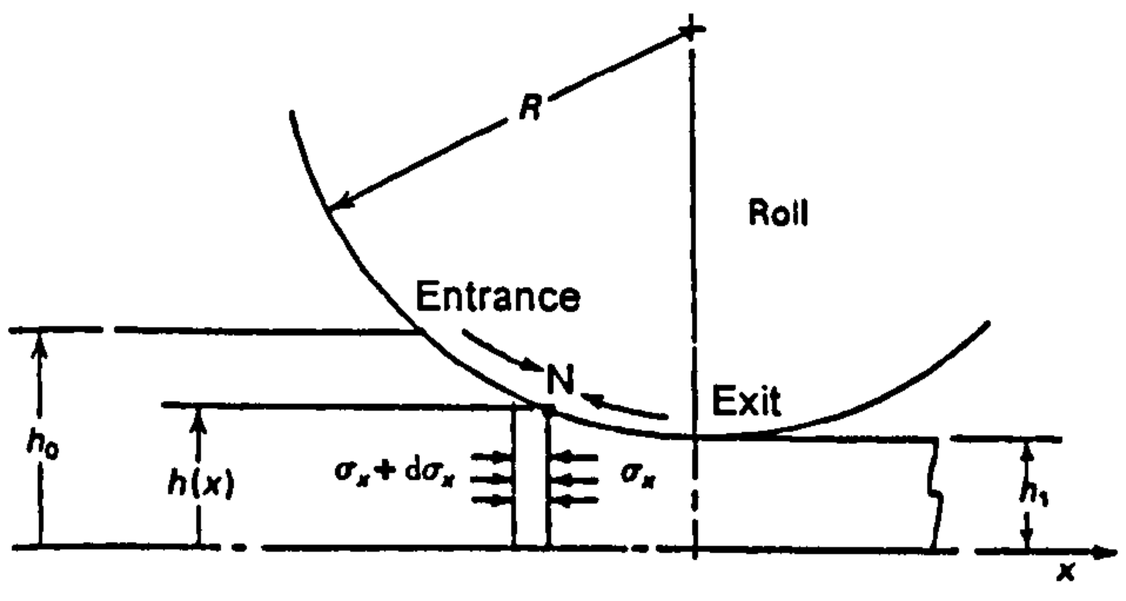

Figure 2.20. Schematic representation of strip rolling, after [116].

Roll Materials

There are many different types of rolls, such as: sleeve rolls, hardened forged steel rolls, cast steel rolls, composite rolls, sand iron rolls, chilled iron rolls, and cast iron rolls.

Compositions of most cast and alloy steel rolls are within the following limits (wt %): 0.40 to 2.0 *C*; less than 0.012 *S*, usually 0.06 max; less than 0.012 *P*, usually 0.06 max; up to 1.25 *Mn*: up to 1.50 *Cr*; up to 1.50 *Ni*; and up to 0.60 *Mo* [117]. Hardness of most rolls are between 250 and 800 HV. Higher carbon contents increase

hardness and wear resistance. Some rolls have higher alloy contents, but these are usually employed for special purposes.

2.4.1. Oxide scale behaviour during hot rolling

During hot rolling, changes on the surface of semi-finished products takes place along with changes in the microstructure. Since the steel is at high temperature, the oxide scales quickly grow as shown in Figure. 2.11. The oxide composition at elevated temperatures was investigated in detail [63-66]. Recent research [73-75] revealed forming of the oxide scales during hot rolling. Therefore, the oxide scales are present on the surface of the metal and involved in all thermo-mechanical transformations along with the steel. The oxide scale influences heat transfer during the hot metal forming operations. Köhler et al. [156 and 157] studied thermal properties of the iron oxides during cooling in the continuous casting process. However, heat-transfer coefficient values of the oxide-metal interface were hard to measure particularly in hot rolling and still have a big scatter. In addition, the oxide scale (or secondary oxide scales) can participate in all metal deformations that take place during hot rolling. The general approach to the mechanical behaviour of the oxide scales was made by Schütze [72] and Evans [158] who modelled oxide spallation. The deformation events might be divided in several stages or zones where failure of the oxide scale is possible [118]. First, the oxide scale is under tensile stress just before the entrance to the roll. Second, at the moment of the roll bite bending and cracking of the oxide scale can occur. Recently, Picque et al. [79] studied this behaviour of the oxide scales using the 4-point bending technique. Third, the most complicated zone is in the roll bite where normal compression and tension or normal compression and shear take place at the same time. In addition, the oxide scale, depending on thickness and crack spacing, has a huge influence on heat transfer between the hot workpiece and the cold roll [119]. Additionally the damaged oxide scale can allow the direct contact between hot metal and the roll [119 - 122]. Nevertheless, precise experimental data and analysis of oxide failure in the literature is lacking. Therefore, a more accurate experiment and full analysis of the oxide scale failure are desirable.

2.4.2. Hydraulic, mechanical and other descaling events

The problem of oxidation during the process of hot rolling arose long time ago, hence, removing the surface oxide scale from the metal is a way to partially solve that problem. In fact, it is not practicable to stop oxidation at high temperature and secondary oxide scales (see 2.4.1) will grow again after descaling events.

There are many ways to remove mill scale (or surface) oxide. Consider, for example, wire production. The oxide scale forms, on the wire as it cools following the rolling process, which needs to be removed prior to drawing.

There are five different methods for oxide removal:

- Acid pickling,
- Mechanical descaling,
- Hydraulic descaling,
- Abrasive Blasting or Sanding,
- Shaving.

Acid pickling can be divided up in two major sub-methods: chemical acid pickling and electrolytic pickling.

Conventional chemical acid pickling of the steel surface is carried out by submerging the rod bundles in sulphuric or hydrochloric acid. The iron ions will go into solution, the evolving hydrogen gas "blasting" off the iron oxide.

Electric current will always flow where the electrical resistance is the lowest. In an electrolytic bipolar cleaning tank (Figure 2.21), most of the current will flow from the cathode to through the electrolyte to the nearest point of the wire. The current will then pass through the wire to the point where the wire is closest to the anode, where it will exit the wire and again pass through the electrolyte on to the anode.

At the point where the current enters the wire oxygen gas will form on the steel surface and where the current exits the wire hydrogen gas will form on the steel surface (i.e at the cathode) breaking off the scale.

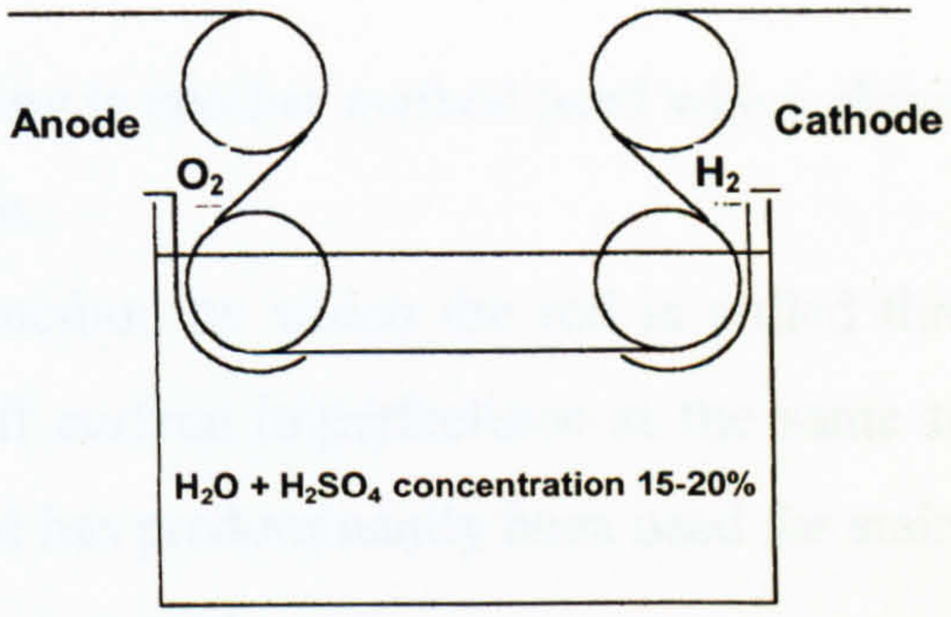

Figure 2.21. Schematic representation of electrolytic bipolar cleaning tank.

In order to reduce the amount of acid and electrical energy needed, it is common to first mechanically descale the rod before it enters the bipolar cleaning process.

In the mechanical descaling process the wire rod is pulled through a set of pulleys, guide wheels and breaker wheels with the axis of rotation offset 90 degrees. As the wire is bent over the breaker wheels as much as 80% of the mill scale is removed. Most of the remaining undesirable scale residue can then be removed by a water/air jet cleaner (Figure 2.22) using a combination of a water wash/air dry sequence. Hydro-mechanical descaling systems are nowadays an indispensable part of high quality hot rolling mills, continuous casting plants, rod and wire mills as well as closed die forging installations [123] and [124]. It is also common in certain applications, such as bedspring wire, to let the wire rod pass through a set of abrasive belt sanders that polishes the rod surface while removing any remaining scale residue.

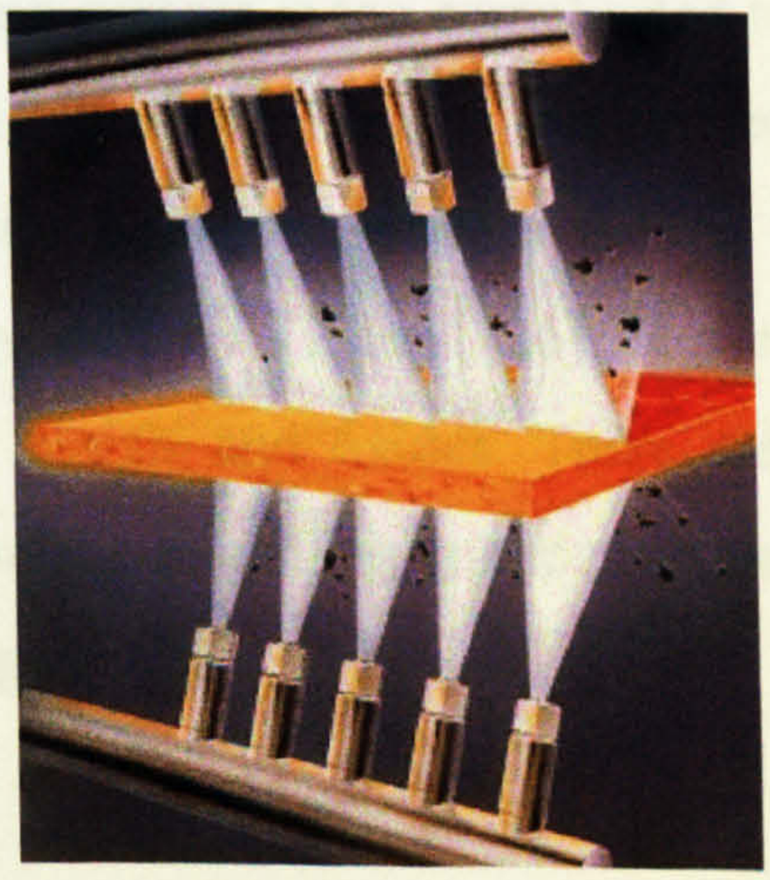

Figure 2.22. Hydraulic descaling process (www.wepuko.com).

Abrasive blasting is another method used where abrasive material is "blasted" on the wire rod surface.

Shaving is a method by which the rod is pulled through a shaving die that removes or shaves off surface imperfections at the same time as the mill scale is removed. This method has predominantly been used for stainless steel wire rods (on-line seminar at www.wireworld.com).

2.4.3. Hot mill pick-up of oxides

Another poorly understood phenomenon is hot mill pick-up or streak coating. The latest European Commission report [125] indicates a sticking effect during roll surface wear and degradation.

Streak coating might be defined as a banded condition caused by non-uniform adherence of roll coating to a work roll. It can be created during hot and cold rolling. If generated in the hot rolling process, it is also called hot mill pick-up. A streak on the sheet surface is in the rolling direction can be caused by transfer from the leveller rolls. This phenomenon also is quite common in aluminium hot rolling.

2.5. Multi-scale modelling of materials

Since the hot rolling process is too complicated to be studied experimentally in detail as a single entity, the modelling of this process becomes very important. Generally, the relationships between ceramics theory, simulation and experiment have been reviewed very well by Fisher [126]. However, these methods can be equally well applied for metals and oxides. There are three main levels for the computer simulation: atomistic modelling, microstructure modelling and macro-scale modelling as shown in Figure 2.23.

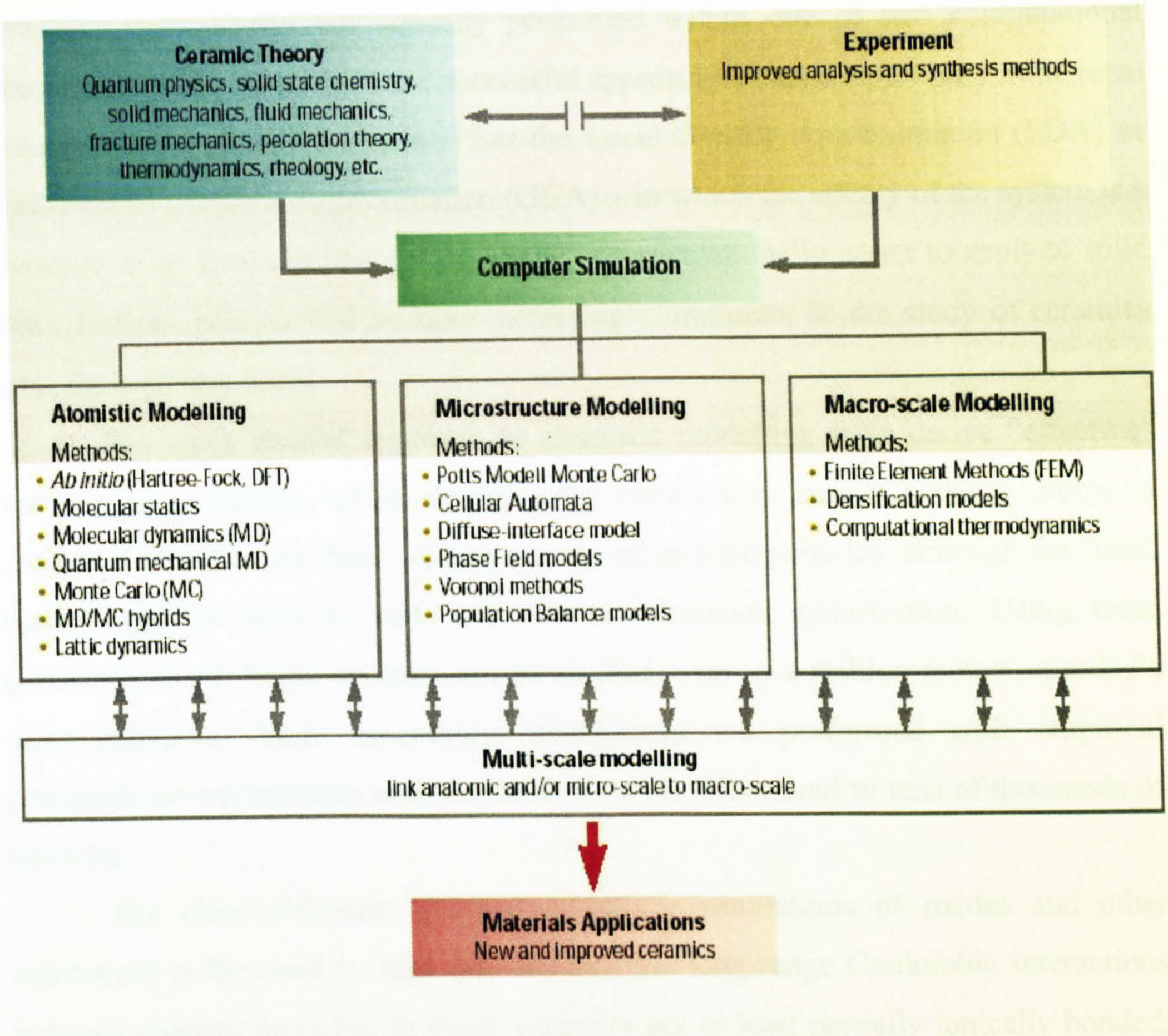

Figure 2.23. Idealized interaction between ceramics theory, simulation and experiment [126].

2.5.1. Atomistic modelling

This method starts from quantum mechanical (QM) calculations that take into account the electronic structure by solving the Schrödinger equation. Several academic and commercial software packages are available for performing QM calculations, such as CRYSTAL and GAUSSIAN. However, these methods are all computationally expensive; calculations are confined to at most a hundred atoms. Nevertheless, these methods are vital for the accurate determination of the fundamental physics and chemistry of solids, and are already being used by industry to solve problems where knowledge of electronic structure is important, e.g. molecule-surface adsorption during catalysis. Despite the large number of techniques

available, calculations are typically performed within one of two computational frameworks. Currently, the most successful approach is based on Density Functional Theory (DFT) – usually within either the Local Density Approximation (LDA) or Generalised Gradient Approximation (GGA) – in which the energy of the system is a function of its total electron density. DFT is computationally easier to apply to solid state systems, and so will become increasingly important in the study of ceramics over the next few years.

The more general approach to atomistic modelling is to derive "effective" interatomic potentials, which describe the variation in energy between atoms in analytical or numerical form. Atoms are treated as rigid particles, although the "shell model" can be used to take into account electronic polarization. Using these potentials, much larger systems can be studied – up to a million atoms on today's supercomputers. More commonly, simulations are performed with empirical potentials on workstations and the latest PC's for a thousand to tens of thousands of particles.

The chief difference between atomistic simulations of oxides and other substances is the need to take into account the long-range Coulombic interactions between charged particles, as many ceramics are at least partially ionically bonded. Once an atomic interaction model has been selected, essentially the same techniques for simulating metallic and polymeric systems can be applied to oxides. These methods are now used routinely to predict the properties of perfect crystals, bond states, defects, surfaces and grain boundaries, covering phenomena such as surface catalysis, solution energies, atomic diffusion, wetting, friction, crack growth and phase changes.

2.5.2. Meso-scale modelling

A major goal of current research is to develop, based on established theories of sintering and grain growth, simulation methods that can reliably reproduce the time-evolution of microstructures. Many simplified models have provided a sound basis for understanding the basic mechanisms involved in microstructural

development, and are an important step in the formulation of more sophisticated general theories.

Most techniques for modelling the meso-scale are continuum methods. These have been used to describe a vast range of phenomena from ceramic processing (extrusion, pressing, slip-casting, etc) and sintering to ferroelectric domain switching in magnetic ceramics and crack-bridging in composites. They are usually based on principles such as constitutive theory and balance laws from solid mechanics and thermodynamics. The Cellular Automaton method and Population Balance modelling are also being successfully applied to meso-scale modelling.

Unlike continuum techniques, the Potts Model Monte Carlo method does not rely on explicit input of thermodynamic and kinetic characteristics into the model. Methods have been developed for treating grain growth and crack propagation in multi-phase systems. 2D simulations can often reproduce the chief characteristics of microstructural evolution, while 3D models are often necessary, despite the large increase in computational costs they entail, for quantitative agreement with actual materials. The primary limitation of this method is in deciding on the range and relative size of the interface energies.

2.5.3. Macro-scale modelling

Many macro-scale processes, such as thermo-mechanical [121], have been successfully modelled using Finite Element Methods (FEM). This is one of the earliest techniques applied to materials modelling, and is used throughout industry today. Many powerful commercial software packages are available for calculating 2-D and 3-D thermo-mechanical, electromechanical and optical properties/processes. Recent developments in Continuum Damage Mechanics (CDM) theory allow FEM to be used to treat fracture, crack growth and related phenomena. FEM is the simulation method closest to real material, usually relying on a large database of measured materials properties as input.

Another successfully applied field of "macro-scale" modelling is computational thermodynamics. Software packages such as Thermo-Calc, Chemsage and Fact use the laws of thermodynamics and large databases of thermodynamic data

to predict phase diagrams and the chemical stability of single and multiple phase systems at various temperatures and pressures [126].

It should be noted that only macro-scale modelling results are presented in this thesis for an interpretation of obtained experimental results. However, the understanding of general multi-scale modelling approach is very important.

2.6. Summary

In this chapter the nature of oxidation, mechanical behaviour of oxide scales and the process of hot rolling have been reviewed. In addition, the general principles of multi-scale modelling are presented. The organisation of the literature review allows the reader gradually go from the principles of metal oxidation to the formation and mechanical failure of oxide scale on steels due to hot metal forming. Oxidation happens because of defects and diffusion exist in solid materials. In general, the parabolic law describes oxide scale growth. The process of hot rolling is also considered in some detail and particularly oxide scale behaviour. The mechanical failure of surface oxide scales during metal forming can take place due to tensile or compressive stresses. The high temperature of the deformation and a temperature gradient have dramatic influence on the oxide scale failure. General approaches to the computer simulation of physical phenomenon are presented as the three different scale modelling. There are atomistic modelling, microstructural modelling and macro-scale modelling.

Chapter 3

Experimental Procedure

3.1. Aims of Experiments

During the hot rolling of steel, the range of temperatures for semi-finished products lies between 700 and 1200°C, inevitably producing some oxidation of the steel surface. The deformation of a metal and, hence, the oxide scale begins at that range of temperature and before entry to the rolls. Flat rolling starts with tension as friction pulls the metal into the roll gap, which may lead to cracking of the surface oxide scale perpendicular to the rolling direction. More complicated tensile-compressive shear loads then appear under the roll. The behaviour of the oxide scale, situated between roll and stock, is very important. Heat-transfer, friction, roll wear and the final surface finish of the rolled product all depend directly on the oxide behaviour. The investigation of oxide scale failure under hot rolling conditions is the subject of this work.

The deformation of a metal and its oxide scale during the hot rolling process is too complicated to be reproduced and closely observed in one simple test. Hence, a combination of simple tests was suggested in order to replicate as closely as possible the required conditions. The deformation and fracture behaviour of oxide scales formed on mild steel have been studied using a high-temperature tensile test technique at the first stage of the work. The failure of oxide scales formed on round tensile specimens at high temperature has been investigated in previous studies [29].

In contrast to this axisymmetric case, a plane strain condition has been used for the modelling of flat hot rolling. This difference raised the concern that the radial contraction of the underlying steel in the tensile test could produce behaviour different to that experienced in a flat geometry. Therefore, oxide scale was formed on a specimen with flat surfaces and rectangular cross-section at the temperature range 800-880°C to compare with round specimen results and also to determine the appropriate specimen geometry. This temperature was chosen for the investigation of brittle fracture of oxide scales, based on previous research [29]. The investigation of heat transfer and oxide scale failure under pressure and high temperature conditions was the second stage of this work. The fractured oxide scales were investigated by a visual examination and using optical and scanning electron microscopy with energy dispersive spectroscopy and electron back-scattered diffraction. Subsequently three-dimensional finite element models were developed in order to simulate tensile and compression tests using commercial code, MSC.Marc2000. The final stage was the tensile-compressive tests, which modelled cracked oxide scales behaviour in the roll bite.

3.2. Materials

Since mild steels are most commonly used in hot rolling operations, this material has been chosen to investigate oxide scale formation and failure. In addition, a roll-imitation tool is essential for compression tests. This tool was made from high speed steel M2 that meets requirements for roll materials.

Table 3.1 show chemical contents for both materials. The roll-imitation tool was heat-treated in order to increase the hardness as shown in Figure 3.1.

Table 3.1. Composition of the steels (weight %, balance *Fe*)

Element	Mild steel	Steel M2	Accuracy	Method
C	0.15	0.88	± 0.01	Leco
S	0.032	0.007	± 0.001	"
P	0.015	-	± 0.002	ICP
Si	0.17	0.16	± 0.02	"
Mn	0.73	0.28	"	"
Cr	0.02	3.99	"	"
Ni	0.02	0.19	"	"
Cu	0.03	0.09	"	"
Co	<0.02	0.42	"	"
V	<0.02	1.88	"	"
Mo	<0.04	4.90	± 0.04	"
W	<0.04	5.66	"	"

The steels for the experiments were delivered in the form of 16 mm diameter rods.

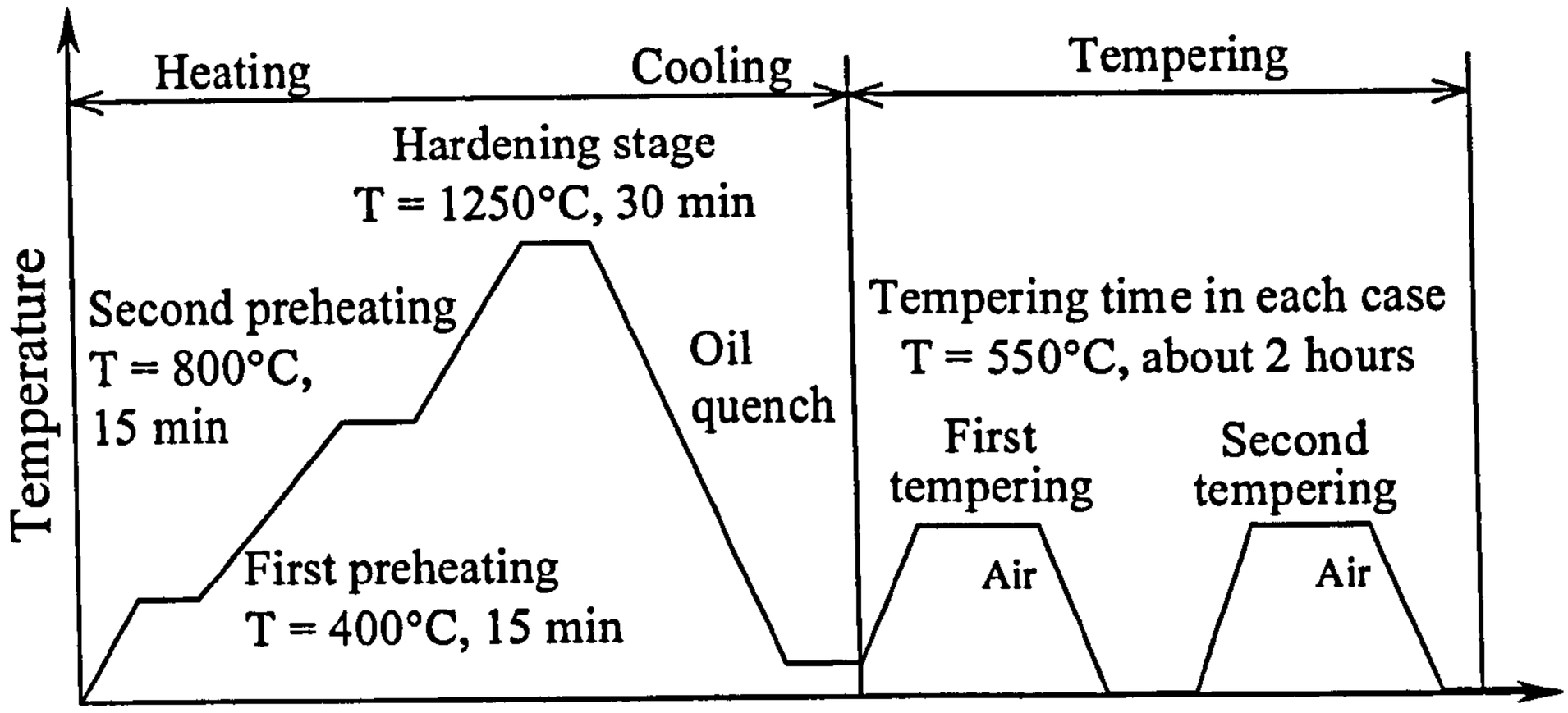

Figure 3.1. Complete heat treatment cycle for the high speed steel M2, after [127].

3.3. Specimen Design and Preparation

3.3.1. Tensile test

Mild steel in the form of a 16 mm diameter and 120 mm long rod was used for the tensile tests. The machining of all specimens was carried out by Ashmark Engineering (Sheffield). The gauge section of the specimens was a parallelepiped with dimensions of Z x 11 x 20 mm, where Z varied between 2 and 5.5 mm (Figure 3.2a). The surfaces of the gauge section were ground manually with 1200 grade *SiC* paper. The groove was drilled in the specimen for temperature measurements by a thermocouple as shown in Figure 3.2b.

3.3.2. Compression test

The aims of the compression tests were to investigate heat transfer from the top (compression tool) specimen through the oxide scale to the bottom (slab imitation) specimen with different thicknesses of the oxide scales and the

deformation of the oxide scale. In order to achieve these aims two different cylindrical specimens were required. The specimens had the following dimensions and materials, the slab imitation Ø11 x 80 mm was made from mild steel and the compression tool Ø13 x 80 mm was made from high speed steel M2 (Figure 3.3a). The difference in diameters was in order to achieve a better contact during the test. The grooves for temperature measurements were drilled in the specimens as shown in Figure 3.3b. The top surfaces of the specimens were roughly polished manually with a 1200 grit *SiC* paper. The compression tool was repolished after each test in the same way. This operation was essential to avoid an undesirable oxide scale and to obtain the repeatability of the required test conditions.

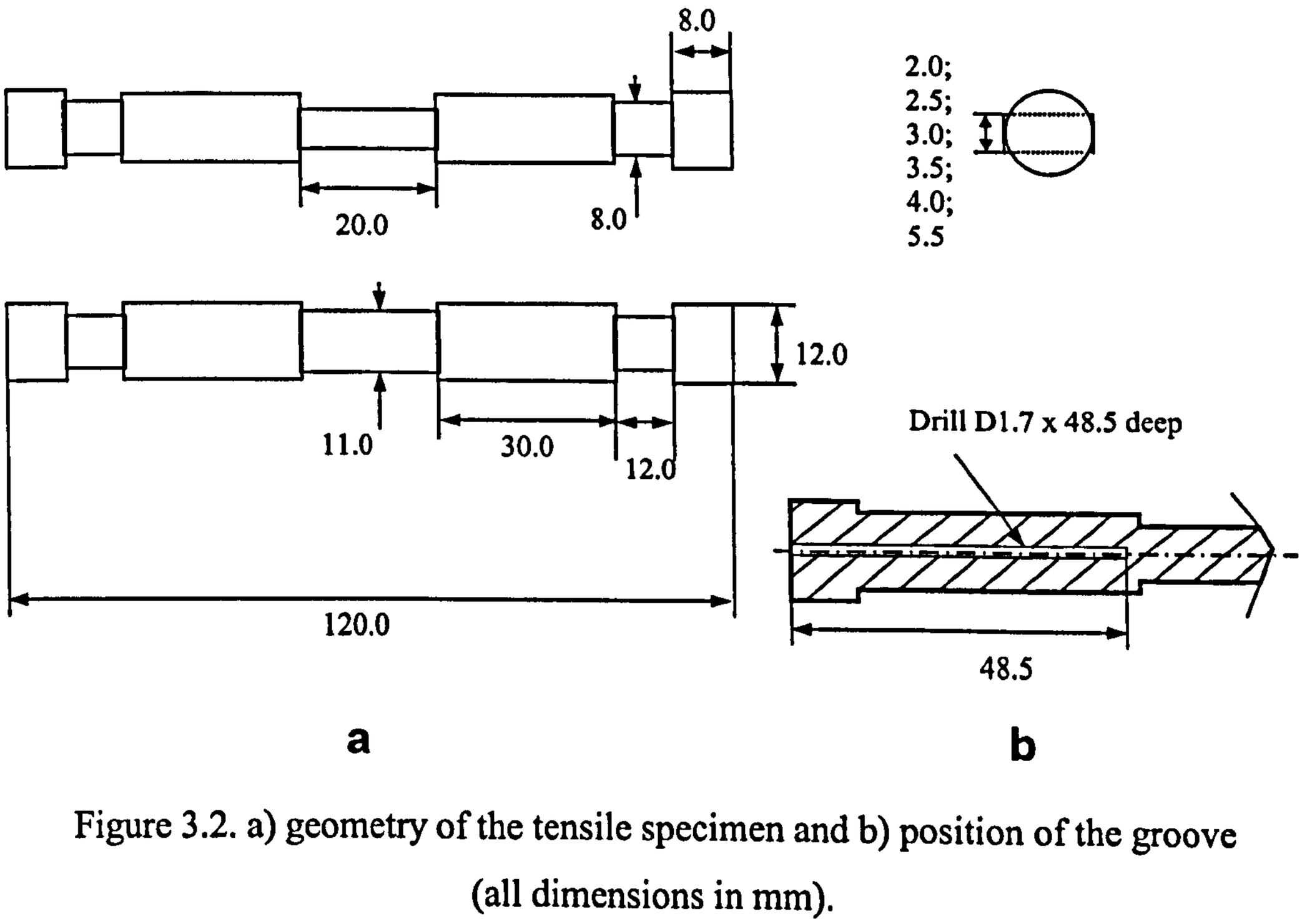

Figure 3.2. a) geometry of the tensile specimen and b) position of the groove (all dimensions in mm).

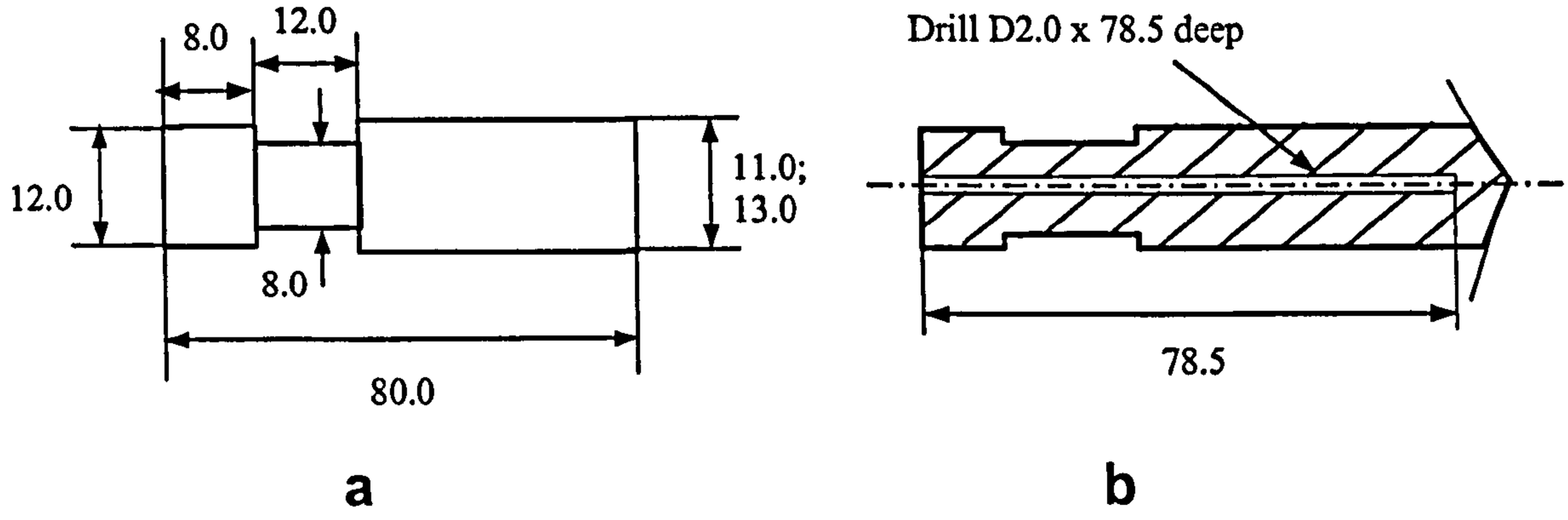

Figure 3.3. a) geometry of the compression specimen and tool and b) position of the groove (all dimensions in mm).

3.4. Thermo-Mechanical Testing Equipment

Computer-controlled MAYES and INSTRON servohydraulic testing machines fitted with induction-heating equipment TR8 (produced by Cheltenham Induction Heating ltd. with power = 8 kW and frequency = 50-200 kHz) were used for loading and oxidation (Figures 3.4a and 3.4b). Nitrogen, as a nominally inert atmosphere, was used for heating, cooling, tension and compression stages and only high temperature oxidation of specimens took place in air. A vertical cylindrical induction furnace was used for the heating (Figure 3.4a). The temperature of the specimens was controlled by a thermocouple. However, the alternative measurements of surface temperature were made by the radiative pyrometer, MINOLTA/LAND Cyclops 152, with a technical accuracy ± 0.5% of reading. However, the experimental accuracy was about ± 5% of reading due to the variation of the colour of the hot specimen. It should be noted, that the careful calibration of emissivity would be needed to achieve more precise temperature measurements. The main technical parameters of the machine were as follows: strain rate 0.001 - 5 s^{-1}; minimal strain 0.001; maximum load 50kN; controllable variables - load and displacement; temperature control 600 - 1400°C.

A JEOL-JSM-6400 scanning electron microscope was used for the microstructural investigations.

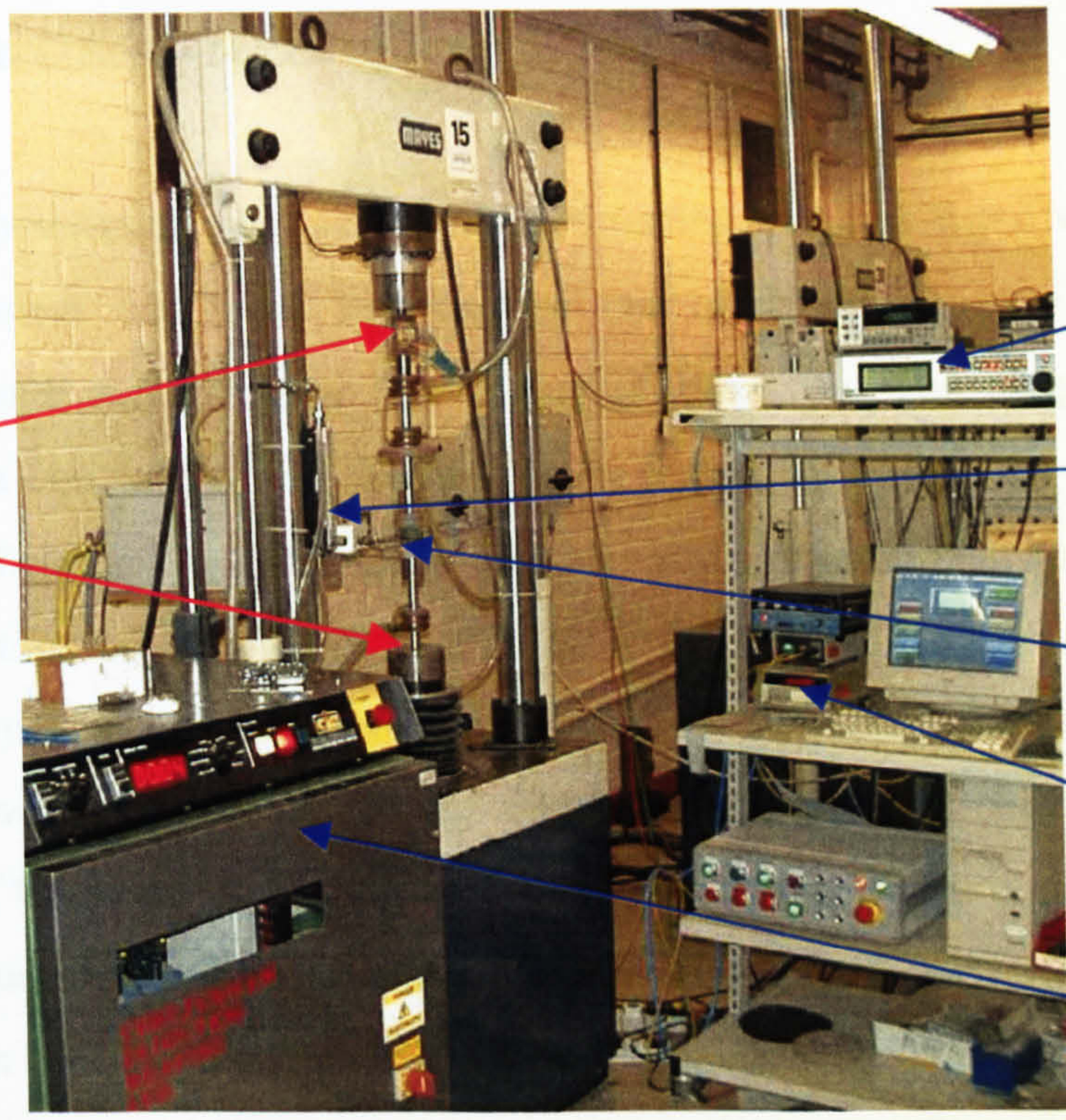

Figure 3.4a. MAYES test rig and heating equipment.

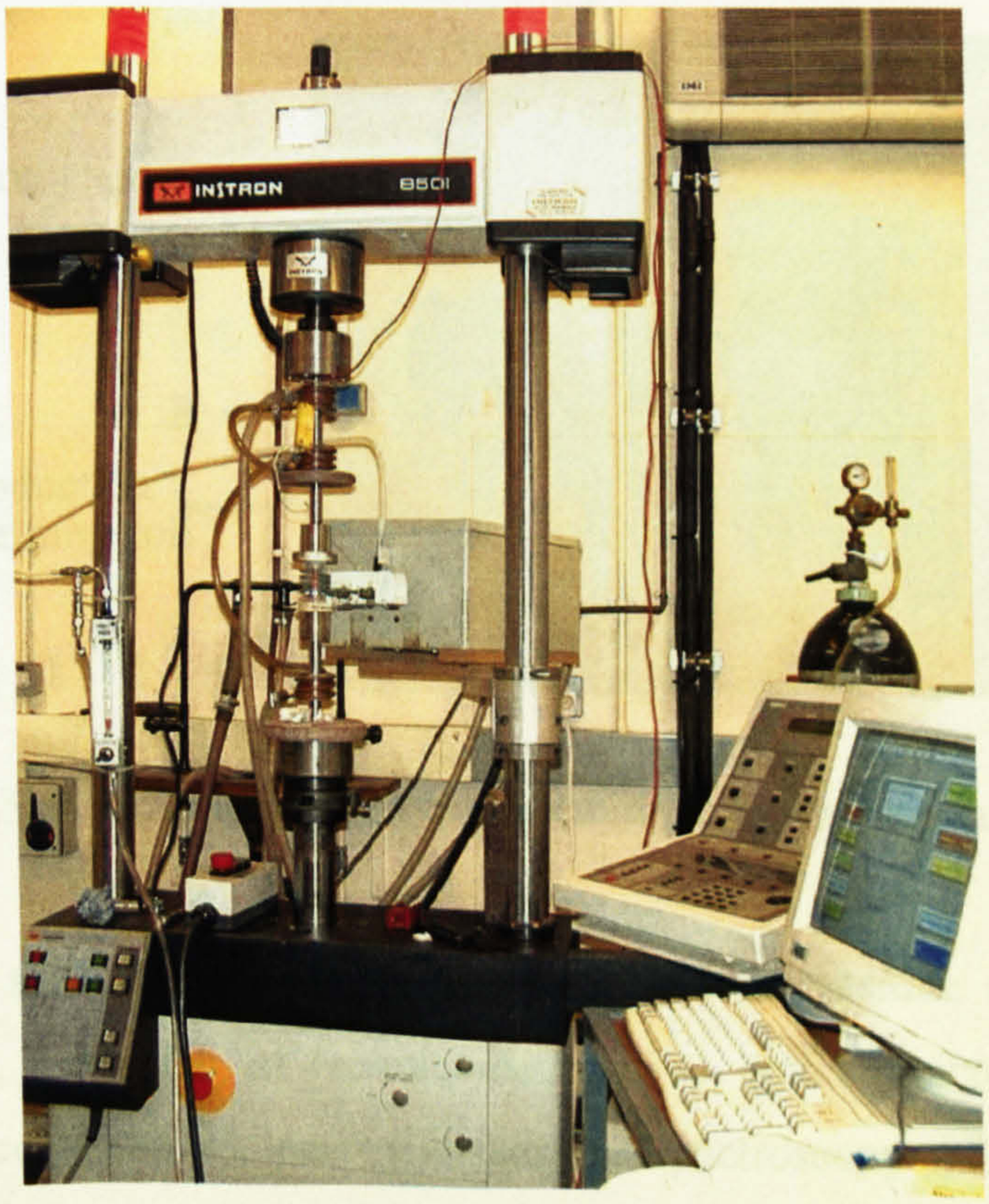

Figure 3.4b. INSTRON test rig.

3.5. Measurement Techniques

A computer-controlled servohydraulic testing machine fitted with induction-heating equipment was used for loading and oxidation. A vertical cylindrical induction furnace was used for the heating (Figure 3.5). The temperature of the specimens was controlled by a thermocouple. Figure 3.5 shows the specimen with schematic indications of the thermocouple and measurement points between induction heating coils. Points A and B were used for the measurements of temperature by a radiative pyrometer. Input data, including the temperature and crosshead movement, were set in the computer. Output data, including time (s), temperature (^{o}C), load (kN) and displacement (mm), were obtained from the multiple-channel digital servo-controller and written to the Microsoft Excel file. The data collection and control signals were simultaneous with a frequency of 1000 Hz with a dither at 195 ± 10 Hz (MAYES) and 500 ± 10 Hz (INSTRON).

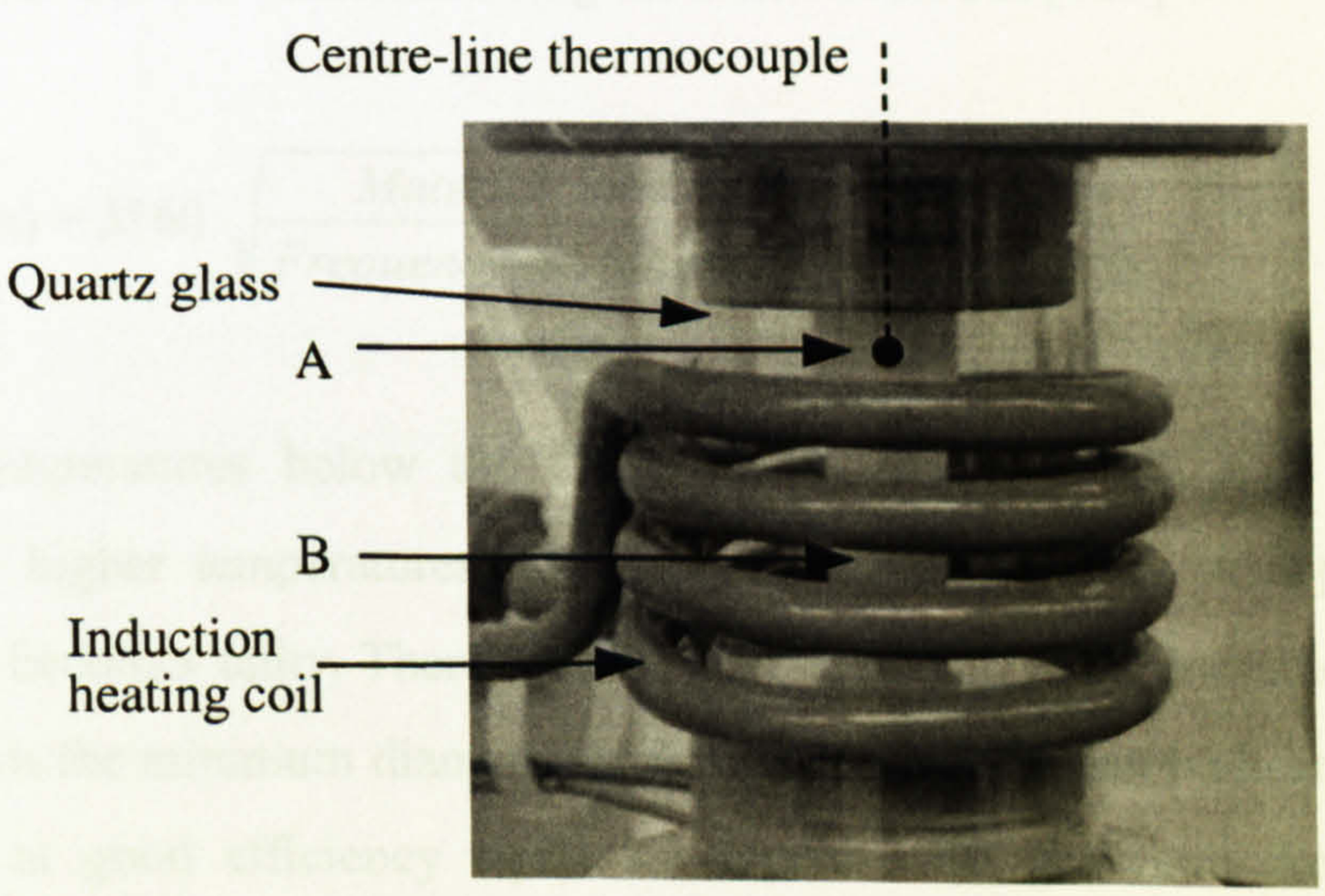

Figure 3.5. Actual view of the specimen in the tension machine grips.

Detailed studies of the oxide scale fracture necessitate a microstructural analysis. Hence, a number of techniques, such as optical microscopy, scanning electron microscopy (SEM), energy dispersive spectroscopy (EDS) and electron backscatter diffraction (EBSD), were used in order to study the oxide scale fracture, chemical contents and grain structure of the scales.

3.6. Tensile Testing

3.6.1. Induction-heating

The induction heating process is used in this work to heat all specimens. Generally, energy is transferred from the induction coil to the workpiece via alternating magnetic field. The induced electromagnetic field produces a circulating current, which generates heat. The current, and therefore the generation of heat, is concentrated at the surface because of skin effect. The depth and rate of heating depend on the frequency and duration of applied current and on the electrical and physical characteristics of the work material. The basic problem when heating steel through to forging temperature is the variation of the magnetic properties. The skin depth of current flow in a material being induction heated is [128]

$$d\,(\text{mm}) = 3160\sqrt{\frac{Material \cdot electrical \cdot resistivity}{Frequency \cdot \times \cdot Magnetic \cdot permeability}} \qquad (3.1)$$

At temperatures below the Curie temperature (780°C), d is very small. However, at higher temperatures, the ferromagnetic properties disappear and the permeability becomes unity. Therefore, the skin depth increases dramatically. Wright [128] suggests the minimum diameter of steel billets, which can be heated to forging temperature at good efficiency equal 3.3 mm for the generator frequency 100-350kHz.

3.6.2. Experimental procedure

The specimen was placed in the grips and a small tensile load was applied to avoid the effects connected with backlash in the grips. Each sample was under load control during the heating and cooling stages to prevent stresses that could arise due

to the thermal expansion and shrinkage. Nitrogen, as a nominally inert atmosphere, was used for heating, cooling and tension stages and only high temperature oxidation of the steel took place, in air. The whole experiment consisted of five stages as shown in Figure 3.6: in the first, heating was applied over 2 minutes to the maximum temperature. In the second, the temperature was stabilized during 5 min. After that, oxidation begins and continues for 25 min. In these three stages specimens were preparing under the hot rolling temperature conditions for the principal moment that is the tensile test. The fourth stage included a gas change and the tensile test itself after approximately 3 min. The tensile test lasted only one second with a thousand measurements each of load, displacement and temperature. The system was switched over from load control to position control just before and changed back after the tensile test. The following conditions were applied for the tensile stage of the tests: elongation 0.2...0.3 mm (strain 0.012...0.015) and strain rate 0.12...0.15 s^{-1}. The slow controlled cooling for 15 min to 100°C was the final stage of the experiment.

Natural strain and strain rate were calculated using the following equations

$$\varepsilon = \ln\frac{l}{l_0}; \qquad \dot{\varepsilon} = \frac{v}{l} \tag{3.2}$$

where l is the instantaneous gauge length, l_o is the initial gauge length and v is the instantaneous deformation velocity (crosshead speed).

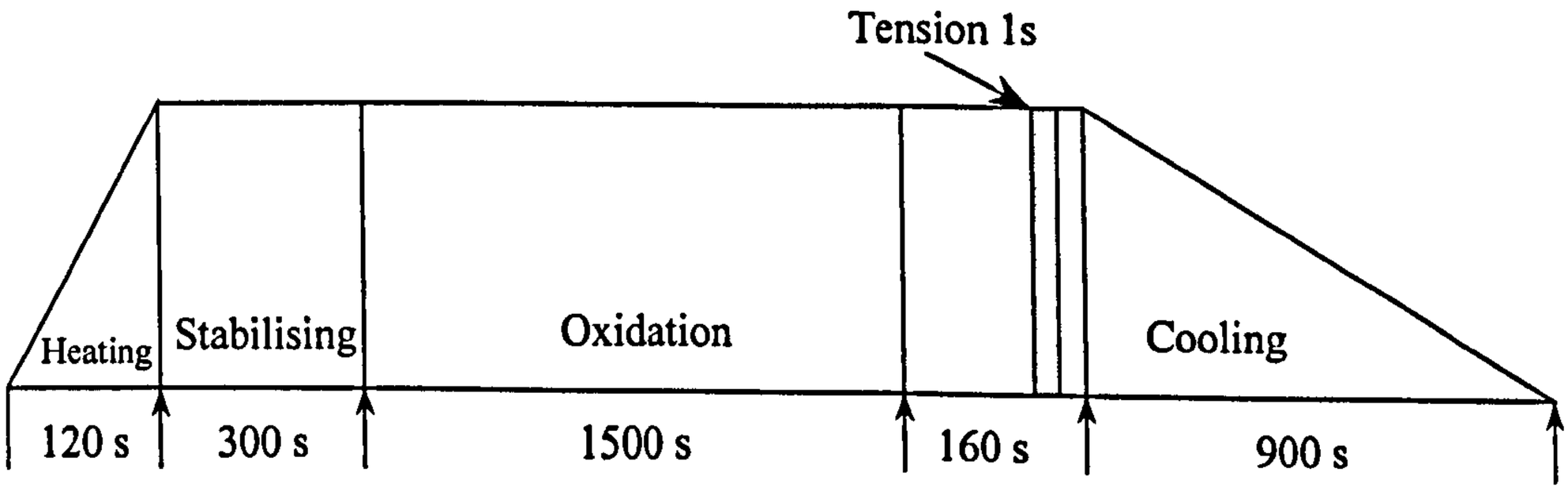

Figure 3.6. Time schedule for high temperature tensile tests.

All specimens were oxidised with the thermocouple reading a temperature of 830°C. Previous tests [29] showed a non-uniform temperature distribution with a

maximum at the centre of the round specimen. Hence, checking of the temperature distribution for a flat specimen was required. The two surface points were used for the measurements of temperature by a radiative pyrometer as shown in Figure 3.4.

Changing of the microstructure and decarburisation of 4-mm and 2-mm specimens was checked after the tests.

3.7. Compression Testing

3.7.1. Experimental procedure

The aims of the current test were to investigate heat transfer from the top (compression tool) specimen through the oxide scale to the bottom (slab imitation) specimen with different thicknesses of the oxide scales and the deformation of the oxide scale during a pure compression. In order to achieve these aims two different specimens, a temperature gradient and the compression were required. Two cylindrical specimens were fixed in the compression machine grips as shown in Figure 3.7.

The top specimen was situated outside the heating coil as far as possible to keep it at the lower temperature. The slab imitation specimen was placed inside of the induction-heating coil, where it was heated and oxidised. Both specimens were located in the vertical furnace, which consisted of a cylindrical quartz glass, a ceramic base and lid.

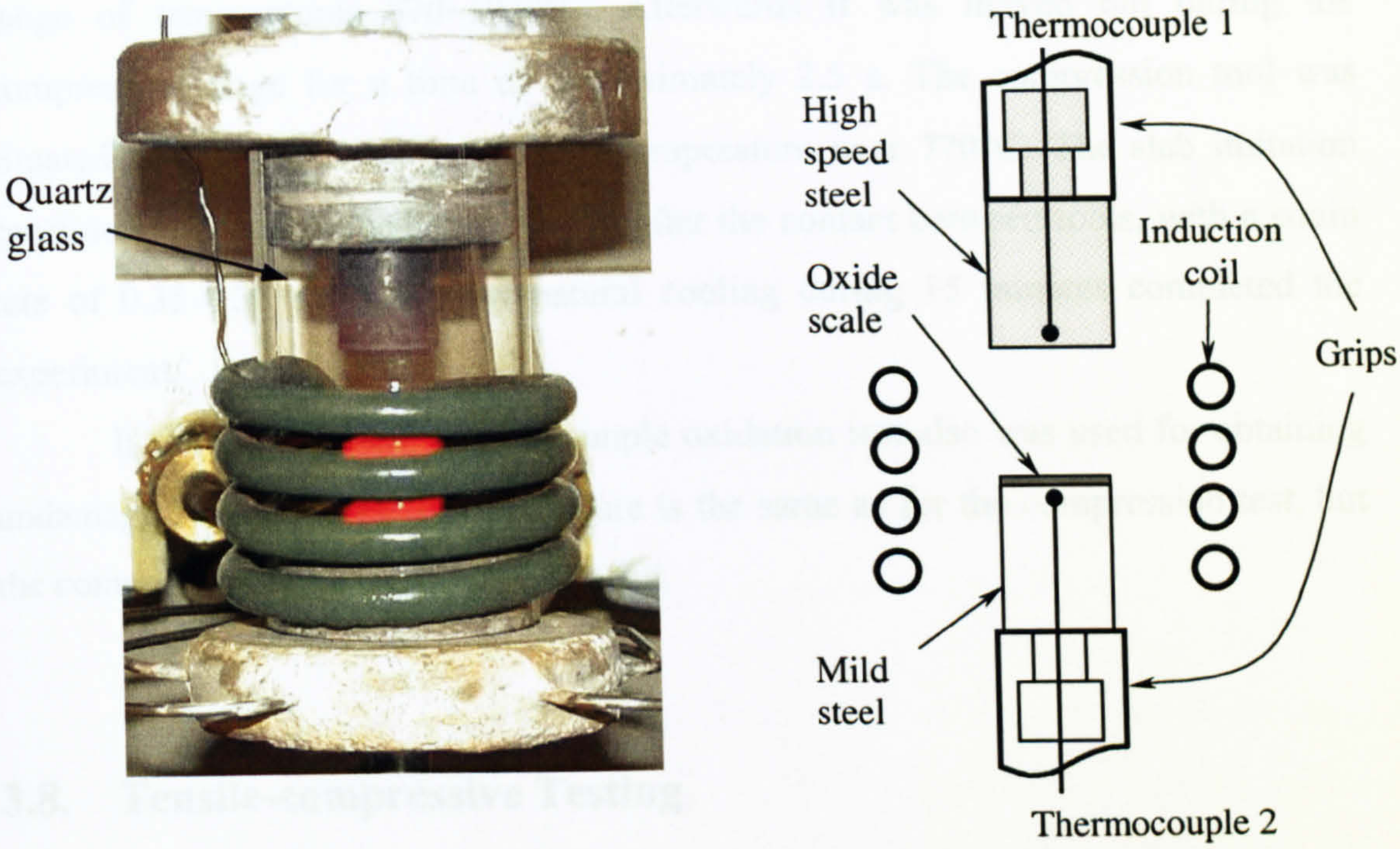

Figure 3.7. Actual (left) and schematic (right) view of the mounting of the compression test specimens.

Generally, the compression test contains the following stages: heating, temperature stabilisation, oxidation, gas change, compression and cooling. Figure 3.8 shows approximate times for each stage of the experiment.

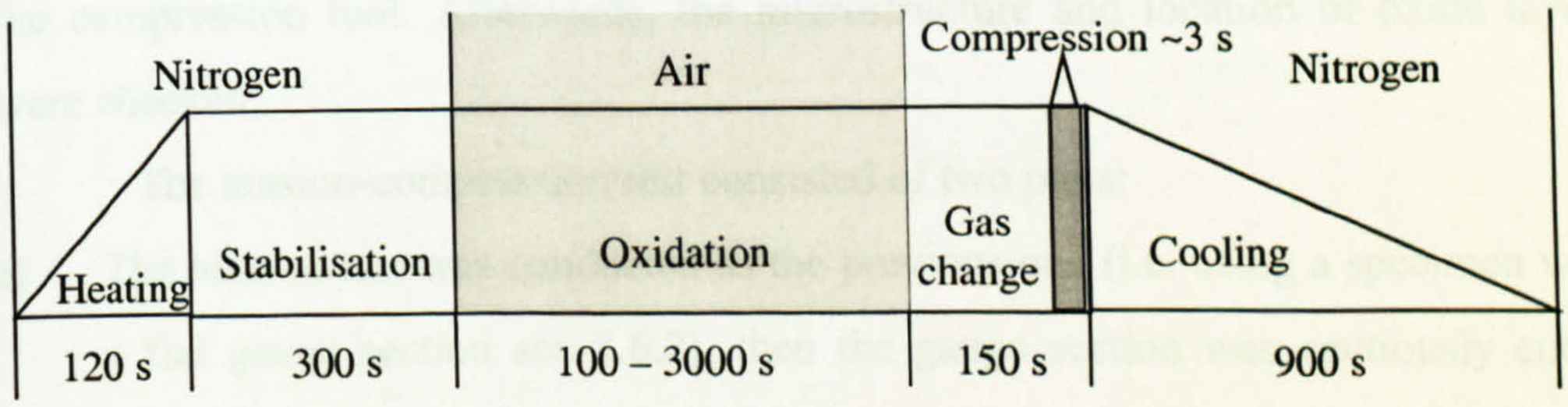

Figure 3.8. Complete experimental schedule.

The nitrogen inert atmosphere was used in the furnace for heating, cooling and compression stages and only high temperature oxidation of the steel took place in air. Two thermocouples (Figure 3.7) were used to simultaneously monitor and control the specimen's temperature and heating/cooling rates. The slab imitation specimen that was inside the induction-heating coil was heated and oxidised at the

range of temperatures 870–1070°C. Afterwards it was moved out during the compression stage for a time of approximately 2.5 s. The compression tool was situated outside the heating coil at a temperature near 770°C. The slab imitation specimen was compressed about 2 mm after the contact between tools, with a strain rate of 0.35-0.38 s^{-1}. The slow natural cooling during 15 minutes completed the experiment.

It should be noted, that the simple oxidation test also was used for obtaining undamaged oxide scales. The procedure is the same as for the compression test, but the compression stage itself was excluded.

3.8. Tensile-compressive Testing

3.8.1. Experimental procedure

The aims of the current test were to investigate: deformation of oxide scale during compression after a previous tension test (oxide could be cracked, spalled and separated) in conditions similar to those for hot rolling. This might involve heat transfer enhanced by extrusion of the hot metal up through the fissures in the oxide to the compression tool. Afterwards, the microstructure and location of oxide layers were checked.

The tension-compression test consisted of two parts:

a) The tension test was conducted as the previous one (i.e. using a specimen with a flat gauge section see 3.6.2), then the gauge section was cautiously cut at room temperature;

b) The specimen was heated and compressed in a nitrogen atmosphere at the same temperature as tension (780-900°C). The test procedure is similar to the pure compression test 3.7.1.

Figure 3.9 shows the principal scheme of the tension-compression test.

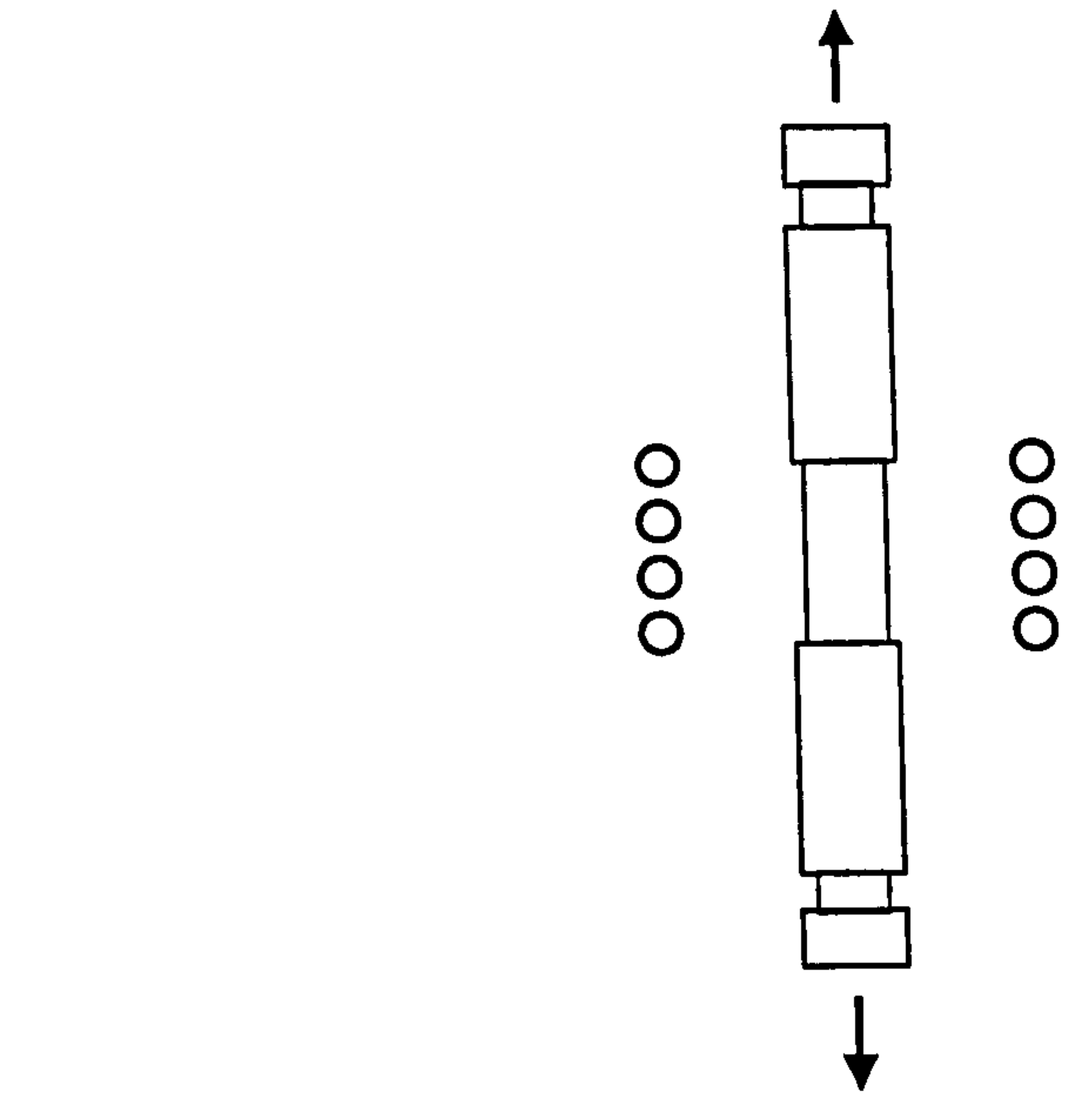

Specimen under tension

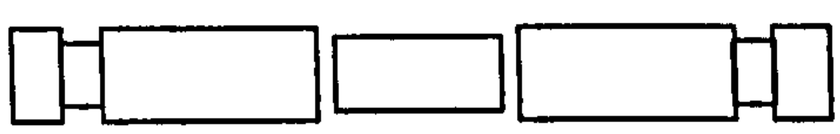

Cutting the specimen

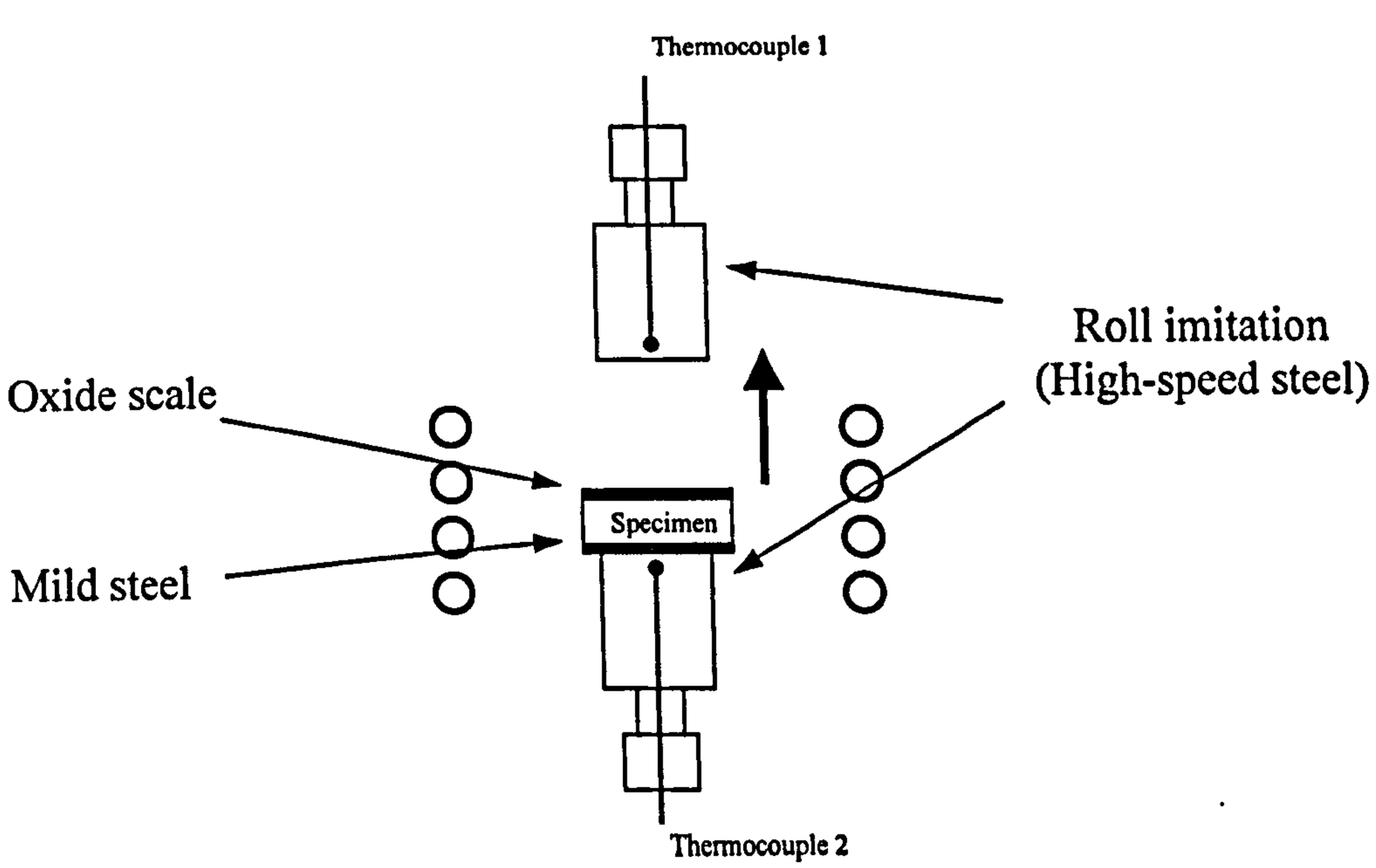

Specimen under compression

Figure 3.9. Tensile-compressive test.

3.9. Optical Microscopy

3.9.1. Sample preparation

The samples require some degree of mechanical polishing. There are four steps to a complete mechanical polish: Sectioning, Mounting, Grinding, and Polishing.

Sectioning

Sectioning is the removal of a representative area from a parent specimen. The final specimen must be small enough to allow examination. The samples were cautiously cut from the gauge section of the tensile specimens and the top 10 mm of the cylindrical compression specimens. The high-speed abrasive sectioning was carried out with the Struers Accutom-5 cutting machine. Proper wheel speed and cooling procedure (see Table 3.2) have been chosen to preserve the oxide scales and microstructure of the original specimen.

Table 3.2. Cutting parameters.

Wheel	357CA
Speed of cutting	3000 rpm
Feed	0.04 mm/s
Force	Medium
Cooling	Water

Mounting

All samples were cold mounted using an epoxy resin to avoid unnecessary damage of oxides.

Grinding

Grinding begins to remove the deformation layer introduced during sectioning, and produces a flat surface for examination. Typically, grinding has been started with 240 grit *SiC* paper in disk, and continued through about 1200 grit *SiC*.

Water is used as a lubricant to flush away removed material and keep fresh abrasive exposed.

Polishing

Polishing is used to remove any deformation introduced earlier during grinding. The procedure is similar to grinding, but diamond solutions were used for polishing. Polishing consisted of three steps, starting at about a 6 micron abrasive, and ending with a 0.25 micron abrasive.

Afterwards, etching in 2% Nital solution was used to observe the microstructures. Optical microscope Olympus CH-2 and a digital camera were used for observations.

3.10. Electron Microscopy

3.10.1. Scanning electron microscopy

Scanning Electron Microscopy (SEM) uses a focused electron beam to scan small areas of solid samples. Secondary electrons are emitted from the sample and are collected to create an area map of the secondary emissions. Since the intensity of secondary emission is very dependent on local morphology, the area map is a magnified image of the sample. Spatial resolution is as high as 1 nanometer for some instruments, but 4 nm is typical for most. Magnification factors can exceed 500,000. Secondary Electron Imaging (SEI) provides high-resolution imaging of fine surface morphology. Inelastic electron scattering caused by the interaction between the sample's electrons and the incident electron beam results in the emission of low-energy electrons from near the sample's surface. The orientation of surface features influences the number of electrons that reach the secondary electron detector, which creates variations in image contrast that represent the sample's surface topography. Backscattered electrons (BSE) and characteristic X-rays are also generated by the scanning beam and many instruments can utilize these signals for compositional analysis of microscopically small portions of the sample. Backscattered Electron Imaging (BEI) provides elemental composition variation, as well as surface

topography. Backscattered electrons are produced by the elastic interactions between the sample and the incident electron beam. These high-energy electrons can escape from much deeper than secondary electrons, so surface topography is not as accurately resolved. The efficiency of production of backscattered electrons is proportional to the sample material's mean atomic number, which results in image contrast as a function of composition - higher atomic number material appears brighter than low atomic number material.

i) Sample preparation

Initial mounting, grinding and polishing conditions were the same as for the optical microscopy except etching. A carbon coating in a vacuum was required to perform scanning electron microscopy of the oxide scales. Silver paint is used to cover the base of the sample and the epoxy to improve conduction and reduce charging effects in the SEM.

ii) Microscope used and technique

The microscope used for these observations was a JEOL-JSM-6400. The techniques were Scanning Electron Imaging and Backscattered Electron Imaging, also known as Electron-channelling contrast, which gave a very good contrast in the image, revealing different grey scales for different orientations or phases of the oxide scale. The conditions used were 20 kV, working distance 12-18 mm and probe size 8. Secondary electron image photomicrographs are recorded with a digital camera. Images are digitally stored in 'tiff' format.

3.10.2. Energy Dispersive Spectroscopy Microanalysis

Energy Dispersive Spectroscopy (EDS) is a standard procedure for identifying and quantifying elemental composition of sample areas as small as a few cubic micrometers. The characteristic X-rays are produced when a material is bombarded

with electrons in an electron beam instrument, such as a scanning electron microscope (SEM).

When the sample is bombarded by the electron beam of the SEM, electrons are ejected from the atoms comprising the sample's surface. A resulting electron vacancy is filled by an electron from a higher shell, and an X-ray is emitted to balance the energy difference between the two electrons.

The EDS X-ray detector measures the number of emitted X-rays versus their energy. The energy of the X-ray is characteristic of the element from which the X-ray was emitted. A spectrum of the energy versus relative counts of the detected X-rays is obtained and evaluated for qualitative and quantitative determinations of the elements present in the sampled volume.

Sample preparation is the same as for scanning electron microscopy. The microscope used for these observations was a JEOL-JSM-6400. EDS spectra were acquired using count times of 1-2 minutes.

3.10.3. Electron Backscatter Diffraction

Electron Backscatter Diffraction (EBSD) is a diffraction technique for obtaining microtextural information from bulk samples or thin layers in the scanning electron microscope. It provides information on the orientation of crystals with a spatial resolution of a few microns. Experimentally, the diffraction information is acquired via a low-light TV camera, which in turn is interfaced to a software package, which extracts the crystallographic information. The local grain orientation is measured and the orientation distribution is displayed as a map. Other measurements can then be derived such as misorientation maps, grain size maps, and texture maps.

i) Sample preparation

The near-incident energy backscattered electrons form the EBSD patterns. Therefore, backscattered electrons that have experienced inelastic events inside the bulk of the specimen do not contribute to the pattern. This fact, combined with the

high tilt angle of the specimen (70 degrees), results in a diffraction region that forms within the top 10-50 nanometers of the specimen. The crystal lattice in this region should be strain-free and clean from contamination or oxide layers for diffraction to occur. If these conditions are not met, the resulting EBSD patterns will be of poor quality or will not be visible at all. Therefore, a proper specimen preparation addresses these issues and helps in obtaining reliable data.

Initially, the samples were polished as for scanning electron microscopy. Subsequently, colloidal silica was used for 25 minutes, as fine polishing, just before going into the microscope. This commercially available solution consists of negatively charged particles of silicon dioxide (SiO_2) with a pH value between 8 and 11. The solution polishes and slightly etches the specimen, removing most of the surface deformation layer.

ii) Microscope used and technique

Through-thickness variation of the crystallographic orientation of the oxide grains was investigated by the electron backscattering diffraction (EBSD) technique using a JEOL-JSM-6400 operating at 20kV with a tungsten filament. The microscope is fitted with a h-k-l Technologies EBSD system. The electron beam is directed at the sample, whose surface is tilted to an angle of ~ 70° with respect to the electron beam (Figure 3.10). This angle improves the backscattering diffraction of the electrons. The backscattered electrons are directed at a phosphor screen, which is viewed using a low light television camera and displayed on a television monitor. The image is enhanced and the diffraction pattern is then analysed automatically by a computer attached to the system to identify the Euler angles of the scanned point [129]. The complete orientation of a crystal must be specified by at least three Euler angles, which are defined as follows (Figure 3.11); if the crystal frame of reference is aligned to the specimen coordinate system, the first angle, φ_1, rotates around the [001] z axis, the second angle, ϕ, about the new [100] x axis and the third angle, φ_2, about the new [001] z axis. The comparison of the Euler angles of adjacent points will determine their misorientation. The system is fully automatic, allowing scanning of areas previously selected and digitalised depending on the step size required.

The data handling and processing was undertaken using both the software provided by h-k-l Technologies and with the software designed and programmed in the Department of Engineering Materials, The University of Sheffield.

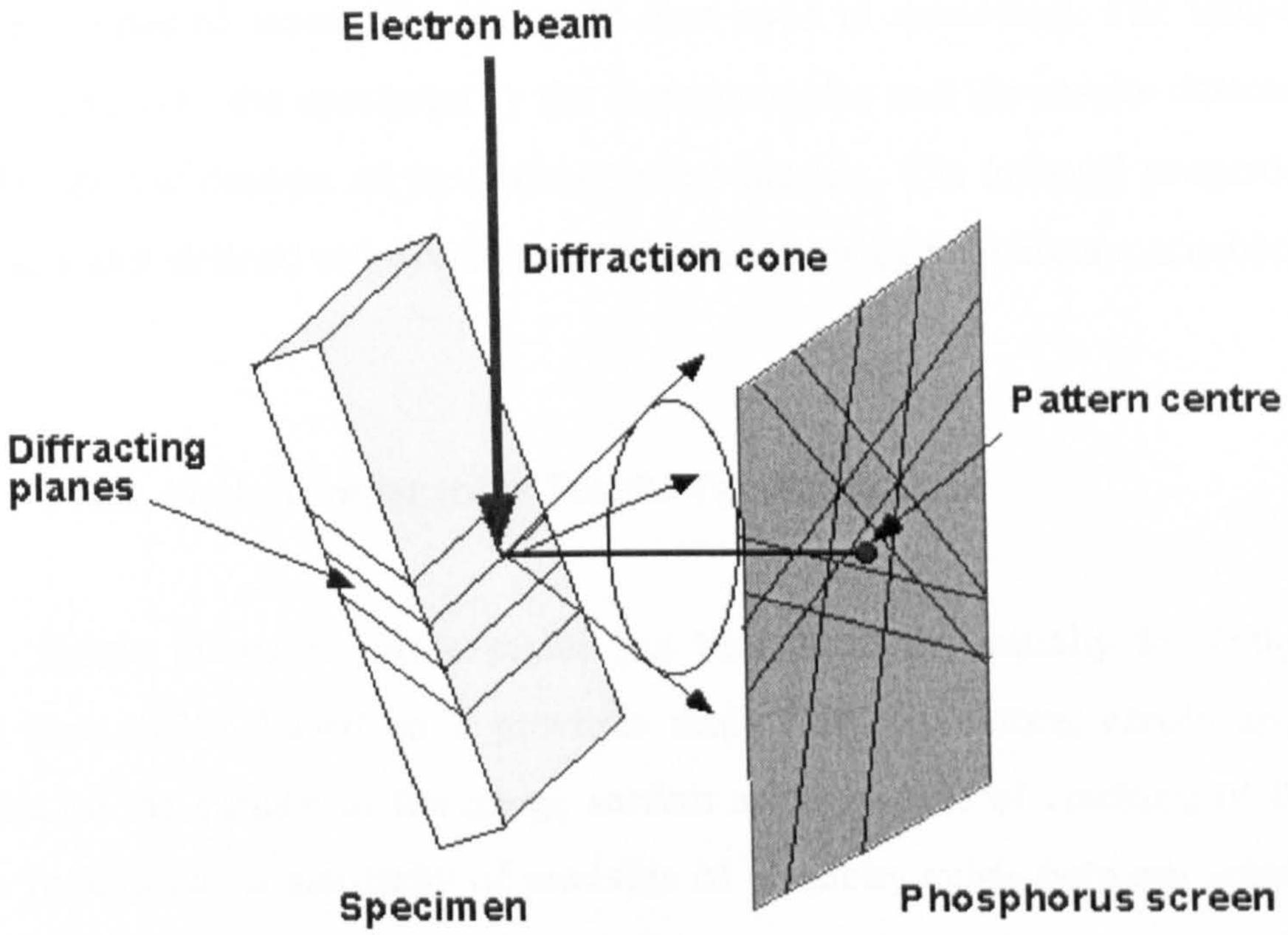

Figure 3.10. Schematic diffraction pattern formation.

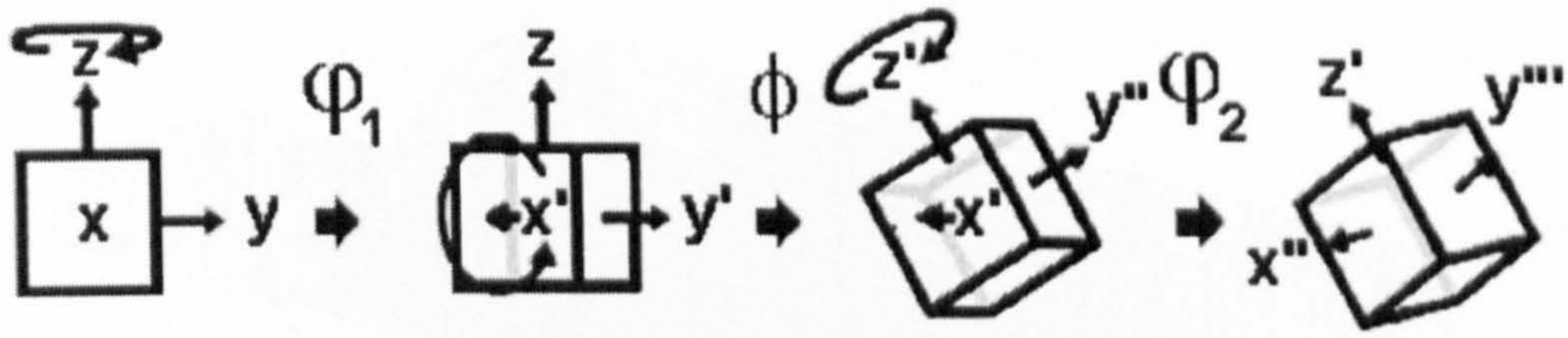

Figure 3.11. Definition of the Euler angles in a cubic system.

3.11. Finite Element Modelling

The high-temperature tensile and compression tests were simulated using the commercial code MSC.Marc 2000 (finite element) and MSC.Mentat 2000 (pre- and post- processor). The experimental results of tensile and compression tests were

interpreted using fully-coupled, thermo-mechanical finite element analysis The models consist of three-dimensional arbitrarily distorted finite elements. These elements are eight-node, isoparametric, arbitrary hexahedral. The displacement was set to simulate the actual testing conditions. Stress-strain curves and flow stresses that were obtained during the tests and then used in modelling. The temperatures were measured in the specimen by the thermocouples and the results obtained were used for the verification of the finite element models. The material properties were given as a user defined subroutine and tables considering temperature sensitivity.

3.11.1. High-Temperature Tensile Test Simulation

Brittle failure of oxide scales has been assumed initially for temperatures lower than 900°C based on a previous study [29]. Therefore, elastic and plastic stresses on the surface of the gauge section are the cause of cracking of the oxide scale. In addition, a similarity of modulus of elasticity exists between substrate and oxide (see Appendix 2, Figures A2.5 and A2.7), and the oxide represents only 5-10% of the overall thickness. Based on these assumptions, a coupled thermo-mechanical model was built as shown in Figure 3.12.

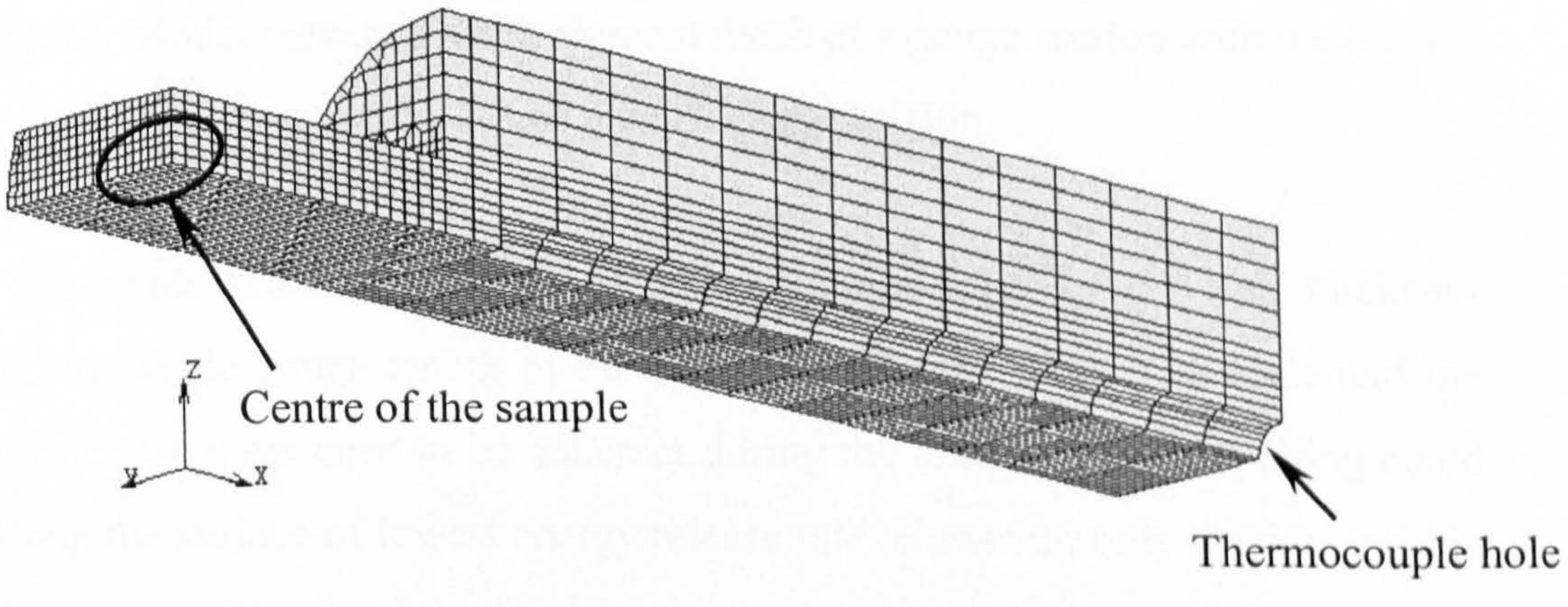

Figure 3.12. Model view and finite element mesh, 1/8 of the full specimen.

The model itself does not include any oxide scales. Surface stresses and strains were under investigation only for 2 and 4 mm thicknesses of gauge section. The cracking behaviour of the oxide scale was simulated separately and only for the gauge section of the specimen (Figure 3.13). The mathematical model for the

behaviour of mild steel used in this work was similar to that recently published [120] and [76]. The differences are in the stress-strain curve and Young's modulus dependencies on temperature. Young's modulus was included as a function of the temperature, taking into consideration published data [130]. Stress-strain curves and flow stresses that were obtained during the tensile tests were used in modelling and checked later with literature [131-133] and [134]. The MSC.Marc 2000 finite element code was used to simulate metal flow and heat transfer during hot tension. The functions for materials properties, which were used in the finite element models, are presented in Appendix 2.

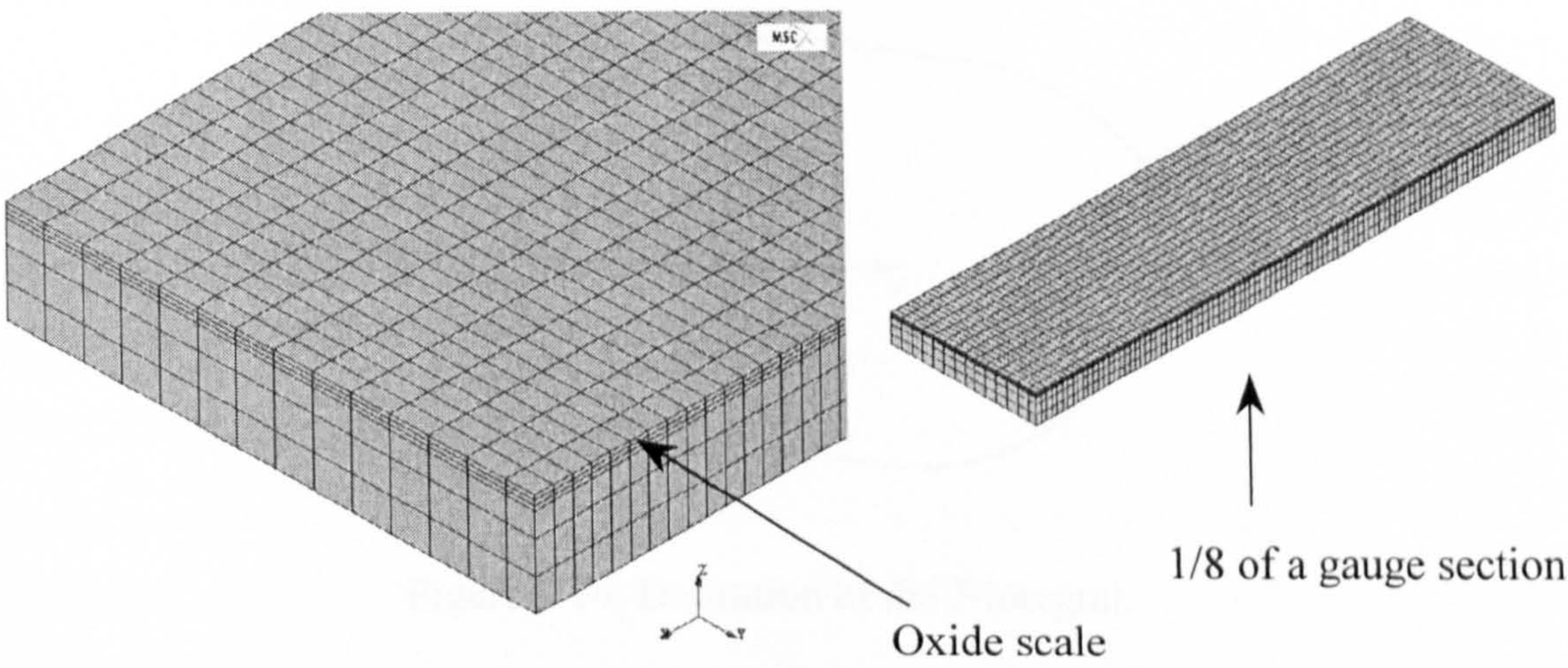

Figure 3.13. Model view and finite element mesh of a gauge section with the oxide scale, 1/8 of the full gauge section.

The oxide scale was simulated as continuous layer of 0.1 mm thickness covering the whole gauge length of the specimen (Figure 3.13). The scale and the metal surface were assumed to be adherent during the tensile test and spalling could occur along the surface of lowest energy release rate. However, only cracking within the scale was considered, while the delamination along the scale/metal interface was not allowed. The linear fracture mechanics approach was used in the model. The basic concept presented by Griffith and Irwin is an energy balance between the strain energy in the structure and the work needed to create a new crack surface [135]. This energy balance can be expressed using the energy release rate G as

$$G = G_{cr} \tag{3.3}$$

MSC.Marc uses the J-integral for evaluating the energy release rate. The J-integral is similar to G but is more general and is also used for nonlinear applications [136]. J is equivalent to G when a linear elastic material model is used. The J-integral evaluation in MSC.Marc is based upon the domain integration method as described by [137]. In the domain integration method for two dimensions, the line integral is converted into an area integration over the area inside the path Γ (Figure 3.14). This conversion is exact for the linear elastic case. By choosing this area as a set of elements, the integration is straightforward using the finite element solution.

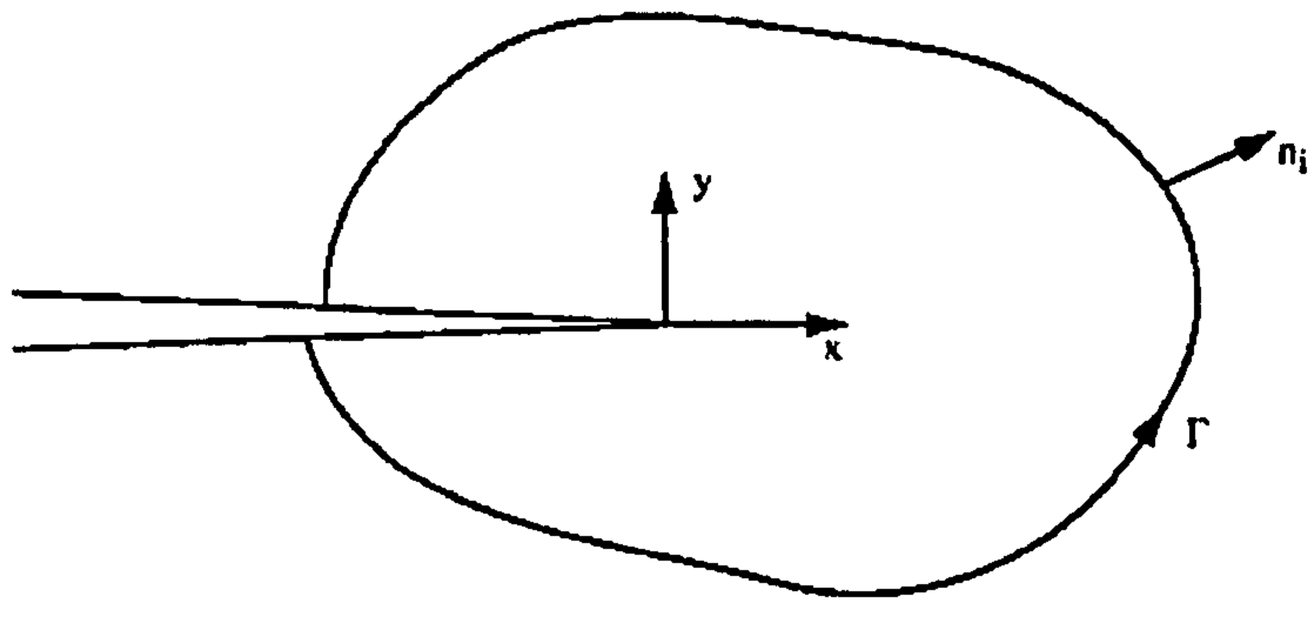

Figure 3.14. Definition of the J-integral.

In two dimensions, the converted expression of the J-integral is [138]

$$\overline{J} = \int_A \left(\sigma_{ij} \frac{\partial u_j}{\partial x_1} - W \delta_{1i} \right) \frac{\delta q_1}{\delta x_i} dA \tag{3.4}$$

for the simplified case of no thermal strains, body forces or pressure on the crack faces. A is the area inside Γ and q_1 is a function introduced in the conversion into an area integral. W is the strain energy density, σ_{ij} is the stress tensor and u_j is the displacement vector. The function q_1 can be chosen generally, as long it is equal to one at the crack tip and zero on Γ. The form of the function chosen in MSC.Marc is that it has the constant value of one at all nodes inside Γ, and decreases to zero over the outermost ring of elements in A. It can be interpreted as a rigid translation of the nodes inside Γ while the nodes on Γ remain fixed. Thus, the contribution to Equation

3.4 comes only from the elements in a ring away from the crack tip. The set of nodes moved rigidly is referred to as the rigid region and the function q_i as the shift function or shift vector.

In three dimensions, the line integral becomes an area integral where the area is surrounding a part of the crack front. In this case, the selection of the area is even more bulky than in two dimensions. The converted integral becomes a volume integral that is evaluated over a set of elements. The rigid region is a set of nodes, which contains a part of the crack front, and the contribution to the integral comes from the elements that have at least one but not all their nodes in the rigid region.

For the evaluation of the J-integral, MSC.Marc requires the nodes along the crack front, the shift vector, and the nodes of the rigid region. MSC.Marc allows three ways of defining the rigid region.

The first is direct input, the nodes in the rigid region are listed explicitly as well as the shift vector. The second and third variants use an automatic search for the nodes of the rigid region. The second variant is based on the mesh topology (connectivity) where a number of regions of increasing size are found by MSC.Marc. The first region for two dimensions consists of the nodes of all elements connected to the crack tip node. The second region consists of all nodes in the first region and the nodes of all elements connected to any node in the first region and so on for a given number of regions. This way, contours of increasing size are determined. In the third way (geometry based search) of determining the rigid region, a radius is given and all nodes within that radius are part of the rigid region. For the automatic search methods, the shift vector can also be determined automatically. It is then determined using the first element edge on the crack face. Symmetry at the crack face is automatically detected by MSC.Marc.

In three dimensions, the crack front is defined by an unsorted list of nodes. In order to obtain the variation of the J-integral along the crack front, a disk of nodes with the normal of the disk directed along the tangent to the crack front can be determined. The shift vector at each crack front node is automatically determined to be perpendicular to both the tangent to the crack front and the normal to the crack face at each crack front node. At the first and last crack front node, where a free surface is assumed to exist, the shift direction is projected to the tangent to the free

surface. This is important since the shift must not change the outer boundary of the model.

The geometry based search method here works with a cylinder with the axis aligned with the tangent of the crack front and centred at the crack front node. The relative length of the cylinder is given as a fraction of the distance to the neighboring crack front nodes. All nodes within the cylinder are part of the rigid region. The shift vector is determined in the same way as for the topology based search method [138].

The critical cracking stress (Equation 2.49) was used as a criterion for the occurrence of a through thickness crack.

3.11.2. High-Temperature Compression Test Simulation

Since the compression test was not plane strain and the temperature distribution had complexities, simulation with finite element analysis is required for proper interpretation of the results. The aims of the computer simulation were to check heat transfer and stress-strain distribution, based on results obtained during the test data. Figure 3.15 shows the model view and the orientation of the compression tool and the slab imitation specimen. The model does not include an oxide scale layer. However, the influence of the oxide scale was taken into account via selection of the heat transfer coefficient. Since the contact during the compression test was asymmetrical, this has been introduced in the finite element model. In addition, the contact under small angle due to misalignment has been considered (Figure 3.16) because some specimens were found to be bent after the compression test. Mild steel thermal and mechanical properties were the same as for the tensile test model. Compression tool properties were acquired from the literature [127] and implemented in the finite element code as tables based on the information shown in Appendix 2. Temperature and stress measurements have been used to tune and verify the model. The contact phenomena were modelled, including friction and heat transfer between the tool and workpiece. During the contact process, it is unlikely that a node actually comes into contact with the surface. For this reason, a contact tolerance is associated with each surface. If a node was within the contact tolerance, it was considered to be in contact with the segment. The contact tolerance

was calculated by the program as the smallest of 5% of the smallest element side or it could be manually defined through the input. The friction coefficient was assumed to equal 0.3 and the contact tolerance – 0.02 mm.

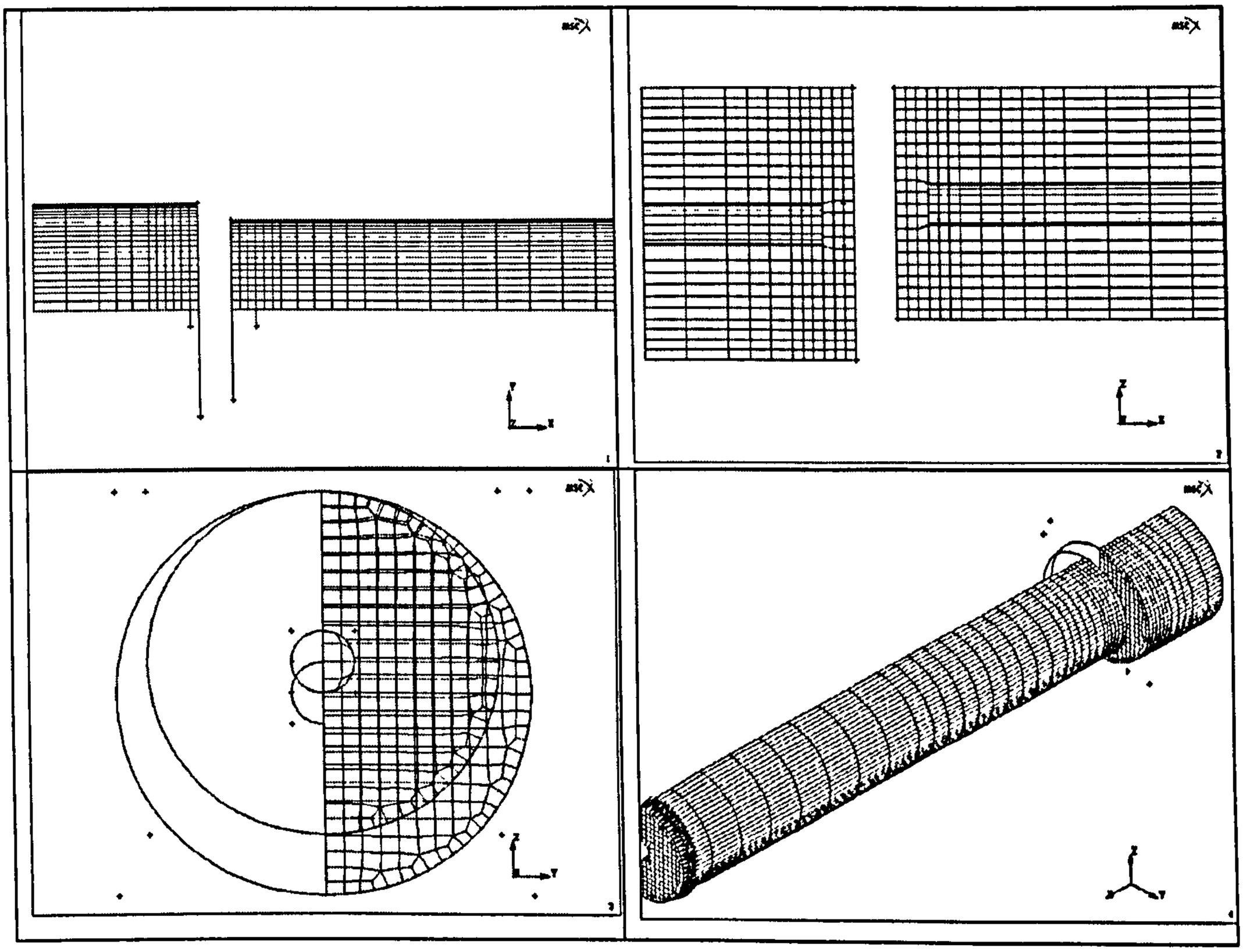

Figure 3.15. Model view and finite element mesh, half size of specimens.

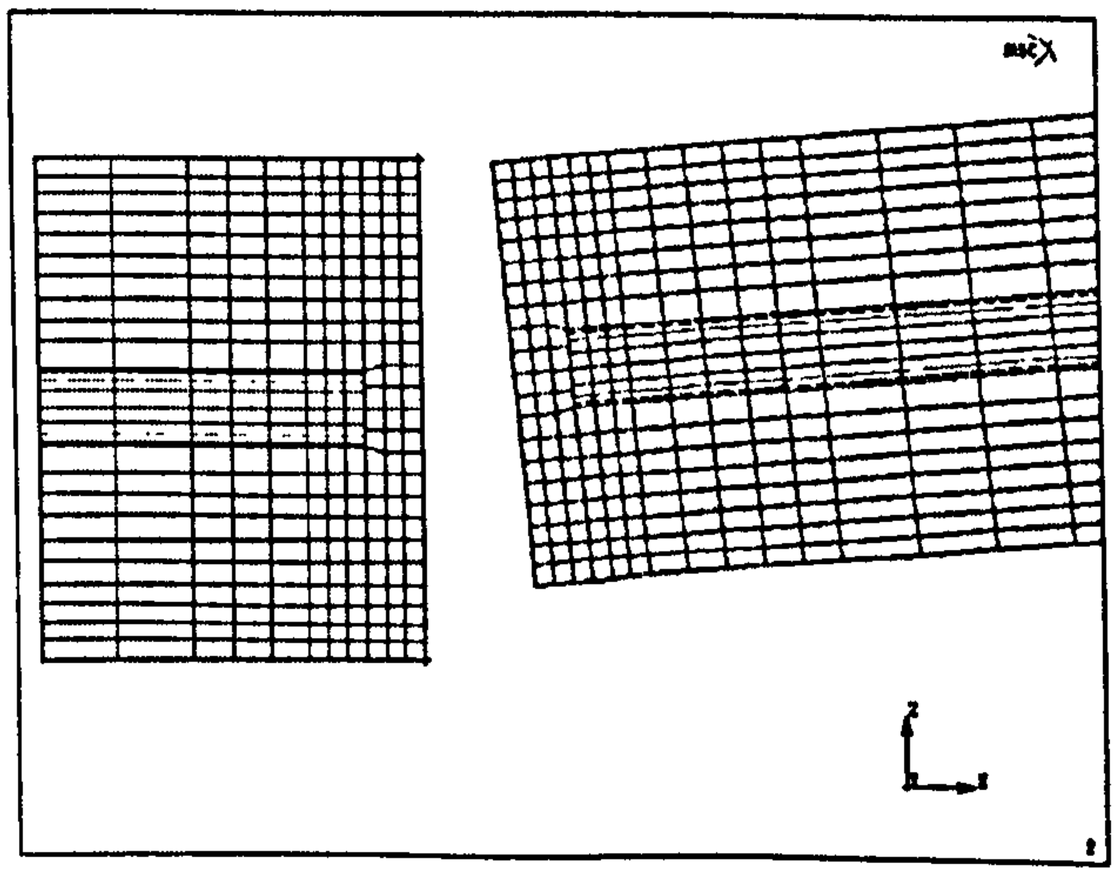

Figure 3.16. Model with the contact at small angle.

Chapter 4

Thermo-Mechanical Testing Results

4.1. Introduction

In the present chapter the results obtained during the high temperature mechanical tests of oxide scales formed on mild steel and the subsequent microstructural investigations are reviewed. The general objective of this study is the modelling of oxide scale behaviour in hot metal forming operations, such as hot rolling. The deformations of a metal and oxide scales during the hot rolling process are too complicated to be reproduced in one detailed test. Hence, a few simple tests were suggested in order to replicate the required conditions. The deformation and fracture behaviour of oxide scales formed on mild steel were studied using a high-temperature tensile test technique in the first stage of the work. The second stage was dedicated to the compression test. A high-temperature compression test has been developed using the same equipment as the tensile test (Figure 3.4). The new test technique was based on previous experience (see paragraph 3.7). Finally, the tensile-compressive test was carried out to investigate a complex compressive failure of the oxide scale with cracks. The oxide scales were formed on flat surfaces, as explained in section 3.3, to replicate more closely the flat rolling process.

Detailed studies of the oxide scale fracture required microstructural analysis. A number of techniques, such as optical microscopy, scanning electron microscopy (SEM), energy dispersive spectroscopy (EDS), electron backscatter diffraction (EBSD), and transmission electron microscopy (TEM) can be used in order to study

the oxide scale behaviour. TEM is useful for a very thin layer of oxide (< 2 nm) and SEM provides good resolution of surface (cross sectional) features up to 1 μm. Therefore, optical microscopy, SEM, EDS, and EBSD techniques were used to study features of the oxide scale fracture, chemical contents and a grain structure of scales after thermo-mechanical tests. However, TEM can be used for the atomic structure determination in thin oxide layers.

4.2. High-Temperature Tensile Test

The high-temperature tensile test, which will be presented in this section, has a direct relation to the oxide failure that happens before the entry into the roll gap during hot rolling.

4.2.1. Preliminary temperature mapping

The behaviour of oxide scales formed on round tensile specimens at high temperature has been investigated in recent studies [29], [76] and [80]. The induction heating coil design used in flat tensile tests was the same as for the round specimens. Previous tests show the non-uniform temperature map with the maximum in the centre of the round specimen. Therefore, checking the temperature map for a flat specimen was required. The actual view of the specimen with a thermocouple for temperature observation and the heating coil is shown in Figure 3.5. Initially only one specimen with 4-mm thickness was used for temperature mapping. No temperature gradient was detected near the corners in the gauge section of the specimen. Points A and B were used for the measurements of temperature by pyrometer. According to Table 4.1, the temperature map for the flat specimen with 4 mm thickness was very similar to that for round specimens. At point A, the temperature measured by pyrometer equals the thermocouple measurement. Therefore, no changes in the calculation of temperature in the centre of a flat specimen have been made in comparison with the round specimen.

Table 4.1. Average temperatures (in °C) for round and flat specimens; see Figure 3.5 for point location.

Thermocouple	Point C, round specimen	Point A, flat specimen	Point B, flat specimen
808	854	805	851

4.2.2. General experimental results

All tests were performed at the same temperature level (T_{th} = 830°C) and oxidation period (1500 seconds). Only specimen thickness was different and varied as shown in Figure 3.2. The exact time for each stage is given in Figure 4.1. The deviation from the schedule was ± 5 s. The temperature range and elongation were measured every 10 s (0.1 Hz) during the experiments other than during the tensile testing itself. The tensile test lasted only 1 s with a thousand measurements each of load, displacement and temperature (1 kHz). The system was switched over from load control to position control just before and changed back after the tensile test. The following conditions were applied for the tensile stage of the tests: elongation 0.2…0.3 mm (strain 0.012…0.014) and strain rate 0.12…0.14 s^{-1}.

Figure 4.2 shows the main experiment stages and a thermocouple temperature versus time plot for a typical experiment. As can be seen from the graph, there are two areas where temperature drops slightly from the average level at 830°C. This is due to the gas exchanging operation and requires a finite amount of time for the temperature to restabilize. Since the system was in load control during the heating and cooling stages, the displacement was tuned (to maintain the constant loading condition) during the experiment automatically as shown in Figure 4.3. It should be noted that even after temperature stabilisation, the displacement has changed by about a half millimetre. The explanation of this could be in the measurement system. Since all the data were obtained between crossheads and this distance is much longer than the heated part of the specimen. Therefore, the time required for stabilizing the temperature of the testing rig was longer than that of the specimen.

4.2.3. Tensile test results

The load and displacement data that were obtained during the tensile deformation are given in Figures 4.4 and 4.5. Four specimens with four different gauge thicknesses are presented. It is clear to see that all plots in Figure 4.4 have the maximum peak at about 0.1 second. These peaks arose due to the inertial movement of the crosshead. Therefore, only the first 0.1 second is important for the oxide scale failure. Results for this period are presented in Figure 4.6. The natural strain was calculated using the actuator displacement. The testing system produced a wide scatter of the displacement data during position control at the tensile stage. The data collection and control signals were simultaneous with a frequency of 1000 Hz with a dither at 195 ± 10 Hz. Dither can be superimposed over a command signal arising from a small vibration or barely detectable oscillation of the servo valve spool. The dither effect for the both tensile machines is shown in Figure 4.7. In this case, it is quite possible that the dither was the reason for the wide scatter of the displacement data (Figure 4.6b). Therefore, the strain results were smoothed by the 11-point running average technique. However, the load data were collected with a minimal noise through a different channel and do not need any transformations (Figure 4.6a). Figure 4.8 shows stress-strain curves after calculations. In addition, all specimens have different maximum stresses but the same elongations (strains). It should be noted that the measured loads were of most value to this investigation.

4.2.4. Surface temperature verification

After the initial analysis of the experimental results, additional measurements of surface temperatures were carried out. The measurements made by the pyrometer at the points A and B (see Figure 3.5) and by a thermocouple at point A are presented in Figure 4.9. ΔT is the difference between surface temperatures and the thermocouple at point A. The cylindrical specimen temperature was measured by the thermocouple and recalculated for point B as described in reference [29]. The flat specimen with 2.5 mm thickness has a different temperature map in the gauge section. It can be seen from Figure 4.9 that the temperature difference, ΔT, for the

gauge section with thickness 2.5 mm is less than for thickness 4 mm. Generally speaking, the thinner specimen has a lower temperature in the gauge section with respect to the thicker one for a given thermocouple temperature. Therefore, not only thickness of specimens influenced oxide scale cracking behaviour, but the temperature as well.

4.2.5. Macro observation of oxide scales

Photographs were taken after the tests for further macro analysis. The oxide scales on the surface were fractured during the test with various numbers of cracks. Through-scale cracks formed in the direction perpendicular to the tensile axis, but if the sample was heated and cooled without tension, crack formation was not directional (Figure 4.10).

Figure 4.10 shows one round [29], one undeformed and three deformed flat specimens with different numbers of cracks in the oxide scales. The ranges of the gauge sections the width/height ratio and the average crack spacing are between 0.18 – 0.49 and 1.2 – 5.0 mm respectively. After testing, the dependence of crack spacing on the thickness of the gauge section (Figure 4.11) and the crack spacing distribution (Figure 4.12) were determined.

In addition, the information of exact geometrical parameters of the tensile specimens before and after the tests is given in Table 4.2. (Note: Yield stresses in Table 4.2 were estimated using experimental stress-strain curves similar to those shown in Figure 4.8.)

Table 4.2. Tensile specimens parameters

Test No	Specimen No	Thickness, mm	l_0, mm	l_{end}, mm	Residual (plastic) elongation, %	Yield stress (estimated), MPa	Comments
1	1	4	~20	20.24-20.28	~1.3	55	l_0 has very approximate values to do the precise calculations
2	2	5.5	~20	20.21-20.32	~1.33	41	
3	3	3.54	~20	20.24-20.17	~1.03	47	
4	4	2.04	~20	20.47-20.54	~2.53	65	
5	5	5.42	~19.9	20.11-20.08	~0.98	41	-
6	6	3.5	~19.98	20.18-20.25	~1.18	47	-
7	7	2.45	19.98	20.21-20.27	1.30	57	-
8*	10	2.97	19.99	-	-	-	Without tension
9	9	2.94	20.05	20.87-20.90	4.16	-	To high initial stress
10	11	1.96	20.01-20.07	20.22-20.30	1.10	61	-
11	8	2.5	19.99	20.22-20.24	1.20	55	-
12	10	2.92	19.99	20.31-20.29	1.55	52	-
13	12	4.1	18.82-18.88	19.75-19.77	4.83	-	Initially damaged sample

Where l_o is the initial gauge length and l_{end} is the gauge length after the test.

4.3. Compression Test

The behaviour of oxide scales formed on flat tensile specimens at high temperature, which is related to entry into the roll gap, was investigated in a previous section. The current section takes into consideration compression under the roll. In order to simulate these conditions, high-temperature compressive tests were conducted in the temperature range 870 - 1070°C.

The compression test was elaborated upon in order to carry out measurements of the following parameters: temperature, load and displacement. The aims of the current tests were to investigate the deformation of the oxide scale during a pure compression and heat transfer from the top (compression tool) specimen through the oxide scale to the bottom (slab imitation) specimen with different thicknesses of the oxide scales.

4.3.1. Oxidation results

Initially, the oxidation tests were carried out to collect information about undamaged oxide scales. These oxides were compared with those that were compressed. Schedules of the oxidation tests are presented in Appendix 3. Figure 4.13 shows different oxide thicknesses depending on time of oxidation and temperatures. The oxide scales were heterogeneous at temperatures higher then 1000°C (Figure 4.14), hence the thickest measured scales are presented in Figure 4.13. Solid lines represent the prediction of scale thicknesses based on the parabolic character of oxidation. The published parabolic rate constant for iron oxidation based on completed experimental data [34] was used as follows

$$d^2 = k_p t \tag{4.1a}$$

$$k_p = 5.053 \cdot 10^{-4} \exp\left(-\frac{20419}{T^*}\right) \tag{4.1b}$$

where d is the oxide thickness (m), k_p is the rate constant for iron oxidation (m^2s^{-1}), t is the time of oxidation (s), and T^* is the temperature (K).

Figure 4.14 shows four specimens after oxidation at different temperatures. The outward oxides in the cases (*a*) and (*b*) were uniform while (*c*) and (*d*) were heterogeneous. Non-uniform oxides can be seen near the corners in Figure 4.14*c*, and the whole oxide scale was heterogeneous at the temperature 1070°C as shown in Figure 4.14*d*. It should be noted that in Figure 4.14*d* the oxide scale was removed from the top of the specimen and shown separately.

4.3.2. Compression results

Compression tests were carried out at three temperature levels, namely 870°C, 970°C and 1070°C. Specimens were oxidized to several different oxide scale thicknesses. The oxide scale thicknesses are given in Figure 4.13. The exact time and specimen temperatures for each test can be found in Appendix 3. The deviation from the schedule was the same as for the tensile tests (± 5 s). The system was under position control throughout the experiment. During the compression stage, the displacement changes as shown in Figure 4.15. The actual moment of contact between the tool and the slab imitation specimen was at approximately 0.5 s and the contact lasted about 2.5 s. The following conditions were applied for the compressive stage of the tests: displacement after the contact 1.7...2.5 mm and instantaneous deformation velocity (crosshead speed) 6.7 mm/s. The displacement, temperature and load were measured with a frequency of 1000 Hz during 5 s. Figure 4.16, 4.17 and 4.18 show raw applied load data of the specimens at temperatures 870°C, 970°C and 1070°C respectively.

Following this, the load data were processed as shown in Figure 4.19, 4.20 where moments of the contact for all the tests were matched together and time (or displacement) scale was shifted at that point. It can be seen from the figures that loading conditions were very similar for all specimens and there was only one difference in maximum values.

Finally, compressive stresses were calculated using obtained load data. The results are shown in Figure 4.21.

4.3.3. Heat transfer through oxide scale

The formation of the oxide scale reduces heat transfer between the tool and workpiece. The temperature alterations were measured using two thermocouples. Thermocouple 2 (Figure 3.7) was used for controlling the oxidation temperature, while thermocouple 1 was situated outside of the induction-heating coil. Therefore, the temperature of the tool was only measured and not controlled. Sharp steps in the slab imitation specimen temperature were observed due to design features of the temperature controlling equipment, which limited measurements. The results of the temperature alteration for the tool and slab imitation specimen are presented in Figures 4.22, 4.23, 4.24 and tables 4.3, 4.4. The contact between the tool and slab imitation specimens was obtained at about 0.5 s after the measurements started.

i) Oxidation temperature 870 °C

Figure 4.22 shows the change of temperatures of slab imitation specimens and the tool. The test with an oxidation time of 1500 s continued for 2 s. It can be seen from Figure 4.22 that the delay in the temperature change after the contact was 0.5 – 1 s. This delay was quite likely related to the thermocouples, which were used for temperature measurement. Afterwards a correction in the schedule was made and all other tests and measurements lasted 3 and 5 s respectively. The initial temperature difference between the tool and slab imitation specimen was about 110 degrees.

ii) Oxidation temperature 970 °C

Four compression tests with different oxide scale thicknesses were carried out at this temperature. Figure 4.23 shows the temperature changes that were measured for the tool and slab imitation specimens. The contact time lasted approximately 2.5 s. The initial temperature difference between the tool and slab imitation specimen was about 200 degrees. Average oxidation and tool temperatures and temperature changes for different oxide scale thicknesses are given in Table 4.3. Standard errors were calculated using the Sigma Plot 2001 software. It should be noted that the

specimen that was tested in nitrogen had a thin oxide scale (5 - 10 μm) due to air leaking into the furnace.

Table 4.3. Average temperatures and oxide thicknesses for the tool and specimens

Specimen	d_{ox}, μm	Max T, °C	Min T, °C	ΔT, °C	Std. Err.
Tool, ox.time 1500 s	5	785.3	770.3	15.0	0.15
Tool, ox.time 800 s	5	794.6	778.8	15.8	0.15
Tool, ox.time 100 s	5	784.2	765.0	19.2	0.15
Tool, nitrogen	-	788.8	767.8	21.0	0.15
Slab imitation, ox.time 1500 s	235	969.2	940.9	28.3	0.03
Slab imitation, ox.time 800 s	145	969.7	934.6	35.1	0.03
Slab imitation, ox.time 100 s	55	970.2	929.4	40.8	0.03
Slab imitation, nitrogen	10	970.4	929.0	41.4	0.03

iii) Oxidation temperature 1070 °C

Two specimens with different periods of the oxidation were tested at this temperature. The oxides at temperature higher then 1000°C grew very fast and heterogeneously. Therefore, the thickness measurements were carried out at the thickest oxide scale. However, the oxide scale thickness measurement at the oxidation temperature 1070°C was only approximate. Figure 4.24 shows the temperature changes that were measured for the tool and slab imitation specimens during the compression stage. The contact time lasted approximately 2.5 s. The initial temperature difference between the tool and slab imitation specimen was about 290 degrees. Average oxidation and tool temperatures and temperature changes for different oxide scale thicknesses are given in Table 4.4. Standard errors were calculated as mentioned above.

Table 4.4. Average temperatures and oxide thicknesses for the tool and specimens

Specimen	d_{ox}, μm	Max T, °C	Min T, °C	ΔT, °C	Std. Err.
Tool, ox.time 300 s	5	809.9	778.5	31.4	0.15
Tool, ox.time 800 s	5	808.7	779.7	29.0	0.15
Slab imitation, ox.time 300 s	100	1070.7	1019.7	51.0	0.03
Slab imitation, ox.time 800 s	260	1071.0	1027.4	43.6	0.03

iv) Comparison of three temperatures

Figure 4.25 shows that not only oxide thickness influenced heat transfer, but the oxidation temperature as well. Three specimens were oxidized to approximately the same oxide scale thicknesses still had the different temperature change.

Figure 4.26 shows the temperature drop, during the contact, for specimens that were oxidized at three different temperatures and having various oxide scale thicknesses.

4.3.4. Macro observation of oxide scales

Macro observations were made at different stages of the experiment using the digital camera Nikon CoolPix 900 (Fine mode picture: 1280x960 pixels).

i) Oxidation stage, before the compression test

Figure 4.27 shows red-hot slab imitation specimens and the tool at the top. It can be seen from this figure that the typical uniform oxide scale grew at the temperature of 970°C and heterogeneous one at 1070°C.

ii) Compression test

Figure 4.28 shows the moment of the contact between the tool and specimens. The oxide scale on the side of the specimen, which was fractured and peeled off, is

shown in Figure 4.28*a*. According to Figure 4.28*b* the oxide scale on the side of the specimen at the temperature of 970°C was only cracked and delaminated, but was not peeled off. Finally, at the temperature of 1070°C, more complicated fracture of non-uniform oxide scales are shown in Figure 4.28*c*.

iii) Oxide scales after the test

The condition of the oxide scale after the compression test depended on the oxidation temperature and scale thickness. Figure 4.29 shows three different specimens after the compression test. There was a slight bending of the specimens with increasing temperature. The top oxide might be the entire scale, as is shown in Figure 4.29*b*, or cracks and fracture might happen after the compression, as shown in Figure 4.29*c*. In addition, the oxide scale, in whole or in part, could be pulled out from the hot specimen by the cold tool, and the damage on the surface in such case is shown in Figure 4.29*a*.

iv) Sticking effect

A sticking effect similar to the hot mill pick-up was observed for specimens with oxide scale thicknesses of about 50 μm. Figure 4.30 shows the slab imitation specimen that was tested at 870°C and the tool. It is clear to see that a sticking effect happened directly after the compression stage (Figure 4.30*a*) and no other damage or cracks appeared after the cooling stage (Figure 4.30*b*). On the other hand, exactly the same shape of the oxide was observed on the tool at room temperature (Figure 4.30*c*). This test was particularly successful, because only the part of the oxide scale was transferred to the tool. Therefore, the boundary conditions for the sticking effect were obtained.

The sticking effect becomes stronger with increasing the temperature. The whole oxide scale (thickness 50 μm) was captured by the tool at 970°C as shown in Figure 4.31.

4.4. Tensile – Compression Test

Oxide scale is often damaged before the roll bite in the hot rolling process. Therefore, compression can be applied to the oxide scale that already was fractured and cracked. Additionally, the damaged oxide scale can allow the direct contact between hot metal and the roll [119], [120], [121] and [122]. Hence, deformation of the oxide scale during compression after a previous tension test was investigated in conditions similar to those for hot rolling. Heat transfer between the specimen and the compression tool and loading conditions were measured during the test. The microstructure of steel and location of oxide layers were checked after the experiment.

4.4.1. Tension stage

The tensile stage of the experiment was carried out using the same experimental technique as the tensile tests described in section 4.2.2. However, the unified size of the gauge section thickness of 3.5 mm was used for all specimens. Also, tests were conducted at several different temperatures (see section A3.3 in Appendix 3). The following conditions were applied for the tensile stage of the tests: elongation 0.35...0.4 mm (Figure 4.32) (strain 0.019...0.02) and strain rate 0.49...0.5 s^{-1}. It should be noted, that the INSTRON tensile machine was used for the tensile-compressive tests. The data collection and control signal were simultaneous with a frequency of 1000 Hz and with a dither frequency 500 ± 10 Hz.

The displacement and load data that were obtained during the tensile stage are given in Figures 4.32 and 4.33. Figure 4.34 shows typical stress-strain curve after calculations.

Photographs were taken after the tests to compare the results obtained with those shown in Figure 4.10. Figure 4.35 shows five specimens that were tested at four different temperatures. Through-scale cracks formed in the direction perpendicular to the tensile axis and the range of the average crack spacing was 0.7 - 5.0 mm.

4.4.2. Compression stage

Compression tests were carried out at the temperature 880°C. Specimens were prepared and placed between two tools as shown in Figure 3.9. The test schedule for each test is given in Appendix 3. The maximum deviation from the schedule was about 5 s and the system was under position control during the experiment as for the compression tests described in section 4.3. The following conditions were applied for the compressive stage of the tests: displacement after the contact 0.5...1.2 mm and strain rate 1.0...1.5 s^{-1}. The actual moment of contact between the top tool and the workpiece was at 0.3-0.6 s and the contact lasted about 2.5 s. It should be noted, that the top tool was about 400 degree cooler than the bottom tool (Figure 4.36), hence they were named the "cold" and "hot" tools respectively. The sides of the specimen were also named "cold" and "hot" according to the tool they contacted. The displacement, two temperatures and load were measured with a frequency 1000 Hz during 5 s. Figure 4.36 shows the history plot of temperature before and after the compressive stage. Figure 4.37 shows typical raw load data. Compressive stresses were calculated using the load data obtained and the results are shown in Figure 4.38. Figure 4.39 shows temperature alteration during the tool-specimen contact of several various oxide thicknesses. In addition, Figure 4.40 shows actual view of the specimen inside of the induction coil in different time of the experiment. Figure 4.40a shows the specimen before the compression test and the cracked oxide scale can be seen. Figure 4.40b shows the same specimen after the compression test.

4.5. Microstructural Analysis

4.5.1. Optical microscopy

Optical microscopy was carried out on the tensile, compression and tensile-compressive specimens to investigate the fracture surface of the oxide scale and to check decarburisation of steel. Decarburisation can affect the mechanical properties of steel and, hence, should be checked.

i) Tension results

Figure 4.41 shows the optical image of the fractured surface of the oxide scale after the high-temperature tensile test. The oxide scale was spalled from the metal after the cooling stage. Two different oxide layers were detected in the optical micrograph. According to the literature [6], [58] and [66], it was assumed that the top thin layer was hematite (Fe_2O_3) and the bottom thick layer possibly was magnetite (Fe_3O_4) or mixture of the magnetite and wüstite (FeO).

Optical microanalyses detected a decarburisation of the surface layer of steel. Figure 4.42 shows cross-sections of the two etched specimens near the surface. According to Figure 4.42, the depth of the decarburising zone was about 100 μm for all of the specimens. In this area, there is no pearlite (black spots) that can be seen. However, this zone is too small compared with the dimensions of the gauge section for the decarburisation to be a reason for the stress variation.

ii) Compression results

The cross-section of two specimens is shown in Figure 4.43. As can be seen from Figure 4.43*a* and *b*, there is no noticeable decarburisation near the surface at the optical micrographs of the short (300s) and long (3000s) periods of oxidation. Also, here is the evidence that the oxide scale obtained during the tests can be a dense oxide (Figure 4.43*a*) or a porous, multi-layer system with big voids and blisters (Figure 4.43*b*).

iii) Tension-compression results

Optical micrographs of the etched cross-section of the tensile-compressive specimen are shown in Figure 4.44. The depth of decarburisation was similar to that for the tensile specimens (about 100 μm). Figure 4.44a shows the "cold" side of the specimen with elongated grains near the surface. Figure 4.44b shows the "hot" side of the specimen with a slightly deeper decarburisation zone and smaller grains near the surface. Figure 4.45 shows the cracked oxide scale that was pressed in to the

metal substrate. Meanwhile, Figure 4.46 shows the surface area where the substrate was extruded between the oxide pieces. Optical micrographs in Figure 4.47 show damage of the metal in the form of the micro-cracks (of the order of a few μm long), which could be seen after the etching of the specimen near the oxide-metal interface.

4.5.2. Scanning Electron Microscopy

Further analysis of the oxide scales was performed using electron microscopy. The cross-section of the specimens and particularly the surface oxide scales were examined. Secondary electron images (SEI) and backscatter electron images (BEI) were obtained using a JEOL-JSM-6400 scanning electron microscope. BEI images allowed investigating the oxide scales in detail. For example, several intensities of the grey colour show the different phase of an oxide. The results are presented in the following order: first, the untested oxide scales (or oxidation test results) are examined, and second, the scanned electron images of the compressed oxide scales are shown. The oxidation test results were divided on three groups by temperature of oxidation namely 870°C, 1000°C and 1040°C. Similarly, the compressed oxide scales were divided on three groups (870°C, 970°C and 1070°C).

i) Consequences of the oxidation process

Oxidation at 870°C

At this temperature of oxidation, a complicated morphology of scales was observed. Such phenomena as a big pore, delamination within the scale, through-scale cracks and separation of the scale from the metal substrate were indicated. Figure 4.48 shows the porous oxide scale near the corner of the specimens. The backscatter electron image of the oxide scale (Figure 4.48*a*) appears to be more detailed than the secondary electron one (Figure 4.48*b*). It was possible to separate different oxide phases in the BEI (dark and light grey in Figure 4.48*a*). The shape of oxide near the corner was very close to the theoretical expectation (Figure 4.49).

The separation of scale from the metal substrate and delamination within the scale are shown in Figure 4.50. Both of the images in Figure 4.50 are the BEI, hence

it was possible to indicate up to three different oxide phases (grey intensity). In addition, through-layer cracks could be seen in Figure 4.50*a*.

The morphology of the dense oxide scale is shown in Figure 4.51*a*. It is clear that the top (dark grey) layer was a different phase (probably Fe_3O_4) from the rest of the oxide. The dense oxide scale grew up as well as the corner oxides according to the theory (Figure 4.52, [139]). In spite of the presence of the dense oxide scale, big blisters were observed, for example Figure 4.51*b*.

Oxidation at 1000°C

The scales observed after oxidation at temperatures closer to 1000°C were less porous, denser and even closer to the theoretical shape (Figure 4.49). However, the top layer (or layers) of the scale appeared to have big vertical voids or even blisters. Figure 4.53 is the secondary electron image and shows oxide morphology near the corners (Figure 4.53*a* and *c*) and in the central part of the specimen (Figure 4.53*b*). The oxide scale that includes big vertical voids or columns of small pores in the top part of the scale is shown in Figure 4.53*b*. The sizes of the void were up to 50 μm. The difference between oxide phases or layers was not indicated using backscatter electron images. Therefore, these micrographs (identical to SEI) are not shown.

Oxidation at 1040°C

At temperatures higher than 1000°C, oxide scales grew very fast and became laminated and heterogeneous (Figure 4.17). Figure 4.54 shows the oxide scale near the corner of the specimen, which was oxidised at the temperature of 1040°C. The separation of the oxide scale and a crack appearance can be seen in this figure. These cracks, which are shown in Figure 4.54*a*, were not through-thickness and could be a sign of plasticity or ductile behaviour of the oxide scale.

ii) Compressive stresses and oxide scale failure

Oxide scales after compression at 870°C

Many features were revealed in deformed oxide scales after high-temperature compressive testing. The morphology of oxides was generally the same as reported

above. The oxide scales had damages, failures and cracks, and also a sticking effect was detected. The sticking effect took place for the particular oxide scale thickness equal to 50 μm. Figure 4.55 shows damaged oxide scales near the corner of the specimens. This area consists of many big voids and blisters. Therefore, a destruction of such voids and blisters can be seen in Figure 4.55. The thin, unbroken, top oxide layer, possibly hematite (Fe_2O_3), is shown in Figure 4.55*a*, but the middle layer was damaged and locally cracked. Even more damaged oxide scale is revealed in Figure 4.55*b*.

Figure 4.56 shows a so-called blister failure for different sizes of blisters. Two inverted blisters are shown in Figure 4.56*a*. The top thin oxide layer remained intact while the oxide underneath crushed. The fracture in this figure was similar to the brittle crushing of ceramics or concrete (see [91] and [90]). Also two failed blisters and, as the result, the fractured oxide scale are shown in Figure 4.56*b*. The interesting point of this figure that the small blister is caused only local cracking underneath, but the big one is almost broke through the oxide scale.

Figure 4.57 shows through-thickness cracks in the oxide scale. This figure reveals the brittle behaviour at the different scale thicknesses (100 μm Figure 4.57*a* and 50 μm Figure 4.57*b*). Figure 4.58*a* reveals unusual non-perpendicular through-thickness cracks. Moreover, some cracks can deviate further and be the reason for a delamination process (Figure 4.58*b*). As can be seen in this figure, the inclined crack started the delamination of the top oxide layer.

The sticking phenomenon was observed during the high-temperature compression test with the thickness of the oxide scale equaling approximately 50 μm (oxidation time of 300s). Figure 4.59 shows partly separated oxide scale on the slab imitation specimen after the test. Further on the left side, the oxide stuck to the tool and was taken off. The remaining thin oxide layers on the specimen are shown in Figure 4.60. Despite the small thickness (3-5 μm), it was also delaminated and cracked (Figure 4.60*b*).

Figure 4.61 shows the verge of the oxide scale on the tool surface. It has the almost inverted shape of the oxide scale that is shown in Figure 4.59. Another evidence that the oxide scale actually adhered to the tool from the slab imitation specimen is shown in Figure 4.62. Figure 4.62*a* shows the oxide scale on the specimen, whereas Figure 4.62*b* shows the upside-down oxide scale on the tool. It is

easy to see that big vertical voids were at the bottom of the oxide scale in Figure 4.62*b* instead of the top as was in Figure 4.62*a*. Therefore, there are no doubts that this oxide scale was captured from the slab imitation specimen. Figure 4.63 shows the adhered oxide scale on the surface of the tool (case *a*) and the proper high-speed steel oxide on the side of the tool (case *b*). As can be seen in Figure 4.63*a*, the lower layer with thickness about 5-10 μm has the different porosity from the rest of the scale. This thin smooth layer was situated next to the metal/oxide interface. The thickness of the layer was equal to the high-speed oxide scale thickness on the side of the tool, where there was no contact. The higher magnification confirmed the rapid change in porosity of oxide scale near the oxide/metal interface (Figure 4.64*a*) and BEI revealed two types of oxides in the thin smooth layer (dark and light grey in Figure 4.64*b*).

Oxide scales after compression at 970°C

The oxide scales grew faster at this temperature level. The scale itself was dense with some big voids and blisters as mentioned above for the oxidation at 1000°C. Figure 4.65 shows the big and small crushed blisters. Big blisters can be the reason for through-thickness destruction of the oxide scale as shown in Figure 4.65*a*. Small blisters and vertical voids may damage only one-half or less of the scale (Figure 4.65*b*). The thin top layer of the oxide (probably hematite) unexpectedly survived without fracture after the compression test (Figure 4.65). Figure 4.66 shows damage of the scale near the corner. The closed crack was observed, in a similar place to that presented in Figure 4.54, and shown in Figure 4.66*b*. Perhaps this crack was closed during the compression test.

The sticking effect was detected at this temperature level as well as for the temperature of 870°C. The thickness of the oxide was about 50 μm and matched the previous test where sticking was detected. However, at 970°C the whole oxide scale was adhered to the tool during the contact and pulled away. Nevertheless, the thin oxide layer remained on the surface of the specimen (Figure 4.67*a*). This layer appeared to be brittle because through-thickness cracks were detected (Figure 4.67*b*).

Finally, the morphology of the thin oxide scale is shown in Figure 4.68. It was a dense, dual-phase oxide scale (Figure 4.68*a*). Oxide scales with thickness about 10

μm were fractured in the brittle manner and oxide islands can be formed which leads to the substrate yielding as shown in Figure 4.68*b*.

Oxide scales after compression at 1070°C

The oxide scale became heterogeneous at temperatures higher then 1000°C and a thickness of the scale can vary. The morphology of the scale was complicated and included all previously observed types. The thickest oxide scale is shown in Figure 4.69*a*. It was a dense oxide about 250 μm with some voids in the top layer. This scale was spalled from the metal substrate after the compression test, and only traces (not a film) of the oxide remained on the metal surface as shown in Figure 4.69*b*.

The remaining oxide scale was observed after the compression test, as shown in Figure 4.70*a*, in those places where the scale before the test was porous and had many voids. Also big blisters survived after compression, as shown in Figure 4.70*b*.

Figure 4.71 shows damaged, highly porous oxide scales. The oxide scale with "teeth"-shaped voids inside and many small vertical cracks is shown in Figure 4.71*a*, while a similar type of scale with horizontal cracks is shown in Figure 4.71*b*. In the process of deformation, voids can be merged into one big cavity as shown in Figure 4.72*a*. On the other hand, compression can be the reason for delamination in the scale, for instance as shown in Figure 4.72*b*. In addition it should be noted that oxide at temperatures of 1000°C and higher was observed as a heterogeneous delaminated formation with a large number of voids. Hence, the deformation of such structures was very complicated and only the most obvious mechanisms have been described.

iii) Cracked oxide scales after compression

Pressed in fragments of the oxide and the metal extrusion were revealed in deformed oxide scales after high-temperature tensile-compressive testing. The morphology of the oxides was the same as that reported above. The oxide scales were cracked during the tensile part of the test then, after the compression part, they were pressed into the metal substrate and sometimes delaminated. Figure 4.73 shows damaged oxide scales in the area of the contact with the edge of the "cold" tool. A thick oxide scale could rise uncracked if it was outside of the tool as shown in Figure

4.73a. A thin oxide scale behaved differently; it was cracked and not separated from the substrate as shown in Figure 4.73b. Figure 4.74 shows several pressed in fragments of the oxide scale after compression was applied. Figure 4.75a shows the cracked and delaminated but not picked up by the "cold" tool oxide scale fragment. Figure 4.75b shows the mild steel surface without the oxide scale (the scale was taken off by the "cold" tool), however the surface maintained the profile, which could reveal the places where the oxide scale was cracked and pressed in the substrate.

4.5.3. Energy Dispersive Spectroscopy Microanalysis

Energy Dispersive Spectroscopy (EDS) was used for identifying and quantifying elemental composition of oxide scales and particularly those where the sticking effect occurred. The sample areas for the investigation were the circle spot, on the surface of the specimen, with a diameter less than one micrometer.

The EDS X-ray detector measured the number of emitted X-rays versus their energy. The energy of the X-ray is characteristic of the element from which the X-ray was emitted. A spectrum of the energy versus relative counts of the detected X-rays was obtained and evaluated for qualitative and quantitative determinations of the elements present in the sampled area.

The minimum detection limit for the EDS analysis was about one weight percent.

i) Oxide scale on the slab imitation specimen

Initially the EDS spectrum of mild steel was obtained (Figure 4.76). It was expected that this spectrum should not include any maxima of intensity, except iron. However, a small peak near energy level 6 keV can be seen in Figure 4.76. This peak was related to manganese, whose mass content in the mild steel equalled to 0.73% (Table 3.1). Afterwards, spectra of the different oxide scales were acquired.

Figure 4.80 shows EDS spectra of the top and middle layers of the oxide scale that was compressed at 870°C. The same oxide scale also is shown in Figure 4.57*a*.

These spectra were very similar to the mild steel one and had only small peak of manganese.

Figure 4.81 shows two EDS spectra that were obtained from the surface oxide scale that was compressed at 970°C. There is no evidence of any other elements in these spectra. However, the difference appeared when one EDS spectrum was obtained from the separated scale on the side of the specimen and another from the thin remaining oxide layer as shown in Figure 4.79. It is clear to see silicon and manganese in the EDS spectra of the thin oxide scale. It should be noted that this specimen also is shown in Figure 4.67*a*.

Figure 4.80 shows two EDS spectra for oxides, which were given in Figure 4.69. These oxides were compressed at 1070°C. One spectrum (green line) was obtained from the middle of the scale (see Figure 4.69*a*), while another (pink line) came from the remaining oxide (see Figure 4.69*b*). According to these spectra, both oxides consisted of recognisable amounts of manganese, and in addition, the remaining oxide had the silicon peak (Figure 4.80).

ii) Oxide scale on the tool

The oxide scale, which adhered to the tool after the compression test at 870°C, was investigated with EDS and results are presented in this section. The EDS spectrum of the tool material was acquired first and shown in Figure 4.81. Several chemical elements namely tungsten, molybdenum, vanadium and chromium were recognized in this spectrum. All these elements were well above one weight percent in the chemical contents of steel M2 (Table 3.1). In addition, semi-quantitative analysis of the grain boundary (see Figure 4.64) of the steel was obtained. The EDS spectrum result, which revealed even higher content of the above-mentioned elements, is given in Figure 4.82.

Figure 4.83 shows two EDS spectra of high-speed steel oxides. The first spectrum (blue line) was obtained from the smooth bottom oxide layer (Figure 4.64*b*) and the peaks of tungsten, vanadium and chromium can be seen in Figure 4.83. The second spectrum (red line) was obtained from the oxide scale on the side of the tool (Figure 4.63*b*) and the peaks of tungsten, molybdenum and chromium can be seen in Figure 4.83. Therefore, these oxide scales undoubtedly were the proper tool oxides.

The EDS spectra, which were acquired for the middle and top layers of the tool oxide scale (Figure 4.63*a*) is shown in Figure 4.84. These two spectra were the same as for the mild steel oxide scale, which is shown, for instance, in Figure 4.80.

4.5.4. Electron Backscatter Diffraction

The electron backscatter diffraction (EBSD) technique was used to analyse the grain structure and to distinguish between the different phases in an oxide scale by the diffraction patterns produced by the phases. The 256-colour maps, in which the strengths of the primary colours are proportional to the three Euler angles, were obtained. The light green colour represents unindexed diffraction patterns for all figures. Iron, wüstite and magnetite have the body centre cubic systems, hence it created difficulties for indexing of the diffraction patterns. Since oxide scales were studied, the crystallographic data of iron was not included in the data file for the EBSD analysis to improve and simplify the automatic data processing.

i) Oxide scale on the slab imitation specimen

Figure 4.85 shows the secondary emission image of the oxide scale, which was prepared for EBSD analysis. A light grey colour in the figure is the oxide scale and dark grey is the metal substrate. The same area of the oxide scale with better resolution is shown in Figure 4.65*a*. Figure 4.86 shows an EBSD scan for this area of the oxide scale. The grain structure of the oxide scale and mild steel were identified. One layer of magnetite is clearly defined with the large grains. Another expected layer of hematite is not indexed, as the layer was found to be too thin or damaged for indexing the patterns. The fracture of oxide scale also shown in Figure 4.85 and it appears to have damaged or crushed-in pieces of grains.

Figure 4.87 shows inverse pole figures of magnetite grains orientation for the x, y and z axes. According to the figure, oxide grains were distributed quite randomly without any preferential orientation.

ii) Oxide scale on the tool

Figure 4.88 shows the EBSD Euler angles map of the oxide scale, which was adhered to the tool after the compression test at 870°C. Detailed scanning electron microscopy of this oxide scale is given in Figure 4.63*a*. The two layers of magnetite and hematite are defined with the large columnar grains of magnetite. The outer hematite layer was hardly identified by the system, possibly due to its small size. Therefore, the grain structure of the hematite layer was not obtained with a good resolution. However, two different phases of oxide were successfully distinguished as shown in Figure 4.89. The oxide/metal interface and the grain structure nearby are given in Figure 4.90. Figures 4.91 and 4.92 show the EBSD scan for the same oxide scale where the columnar structure of grains was observed even more clearly. These figures also show that some big grains (~50 μm) appeared to grow directly from the substrate (Figure 4.92 encircled) while the neighbour grains were as small as about 5 μm (see Figure 4.91 encircled). It should be noted that the more porous are oxides, the more difficulties for indexing diffraction patterns.

Figures

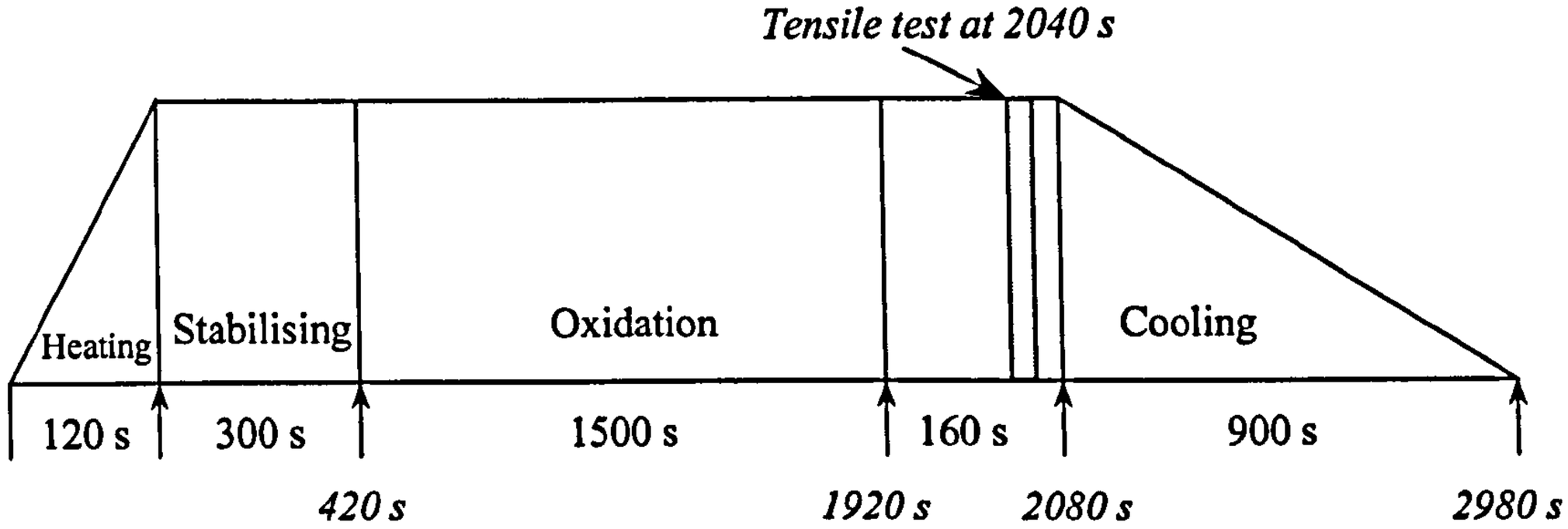

Figure 4.1. Time schedule for high temperature tensile tests.

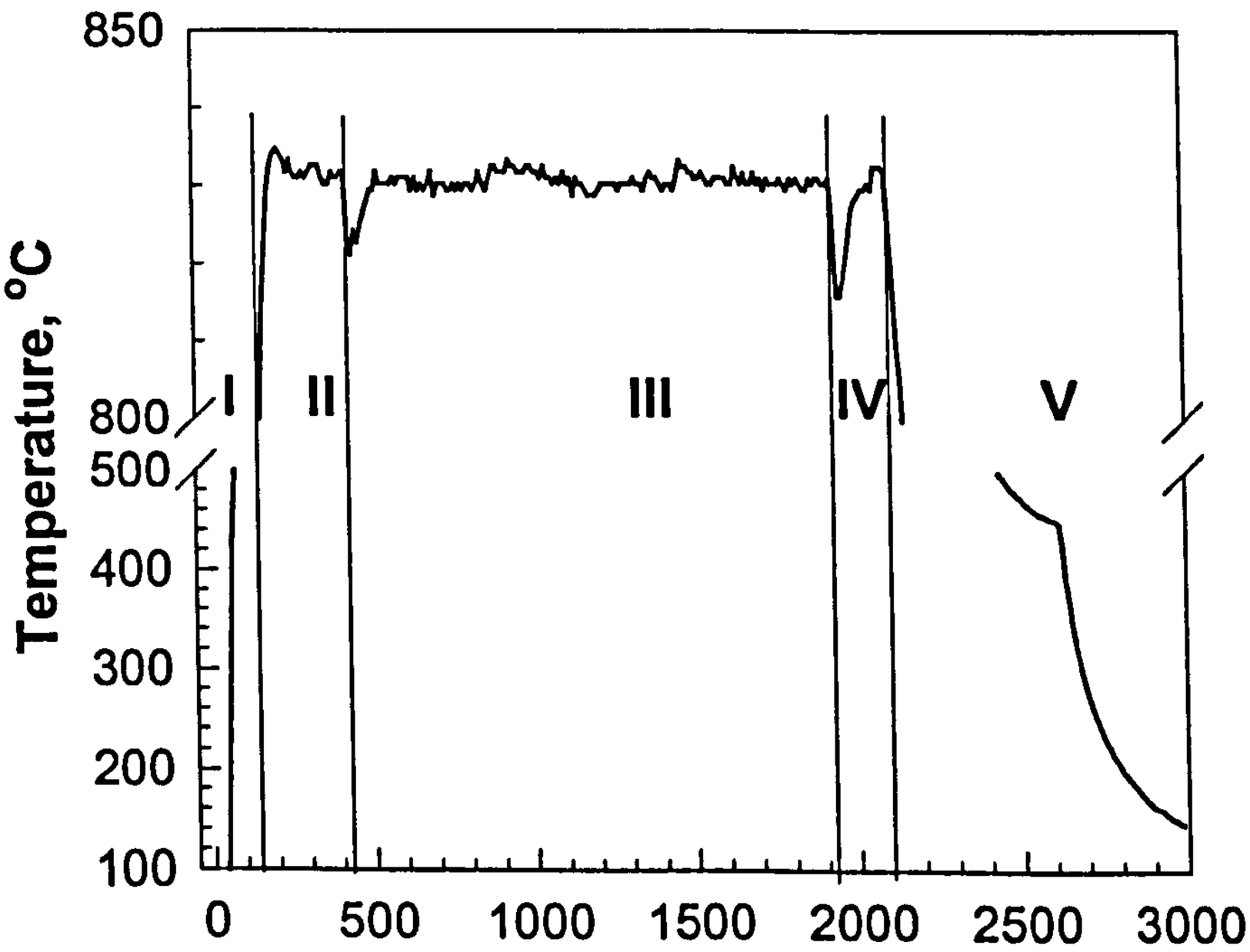

Figure 4.2. A thermocouple temperature by stages: I - heating; II - stabilizing; III - oxidation; IV - gas change stage and tension; V - cooling.

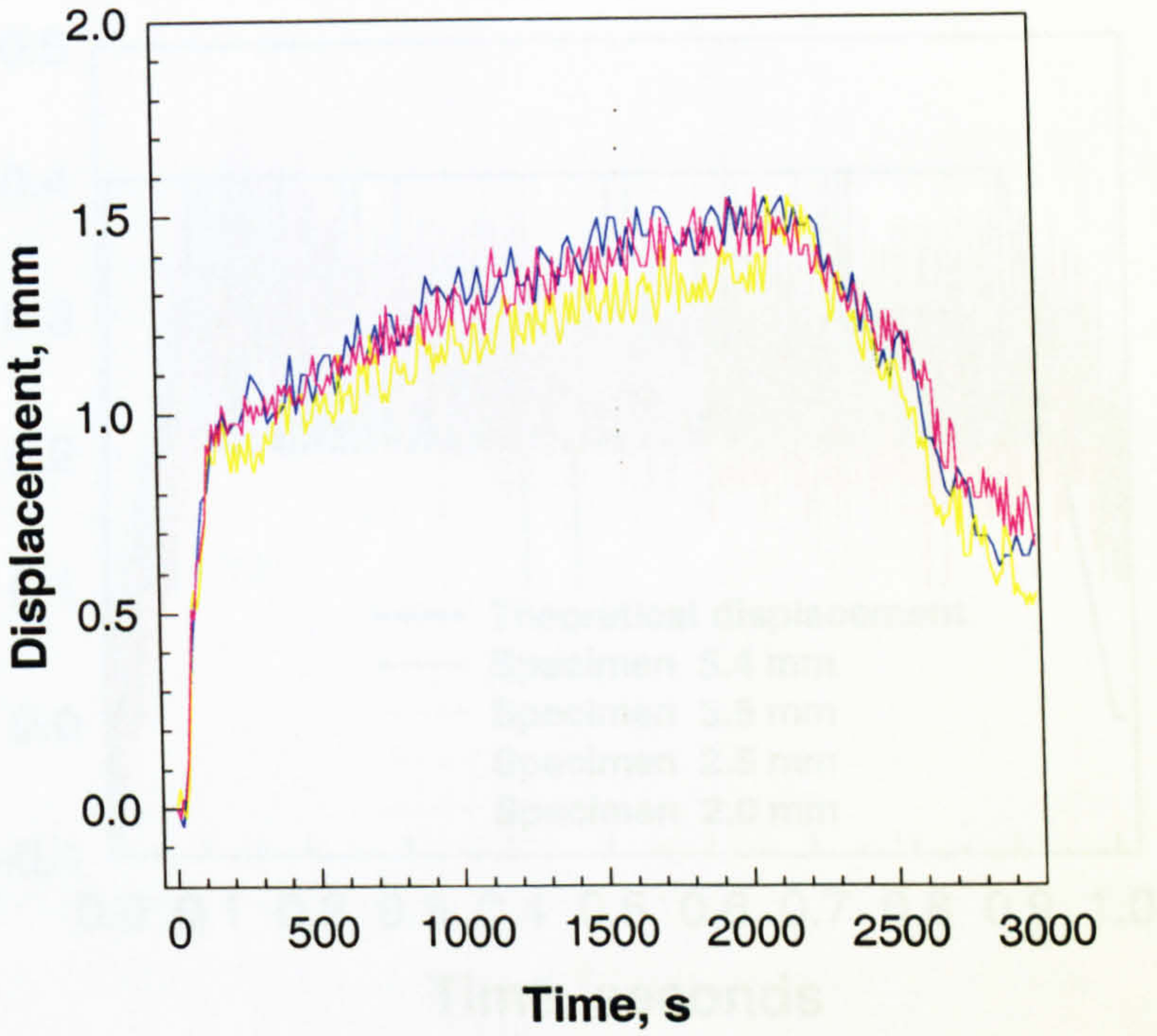

Figure 4.3. Displacement changes for several specimens.

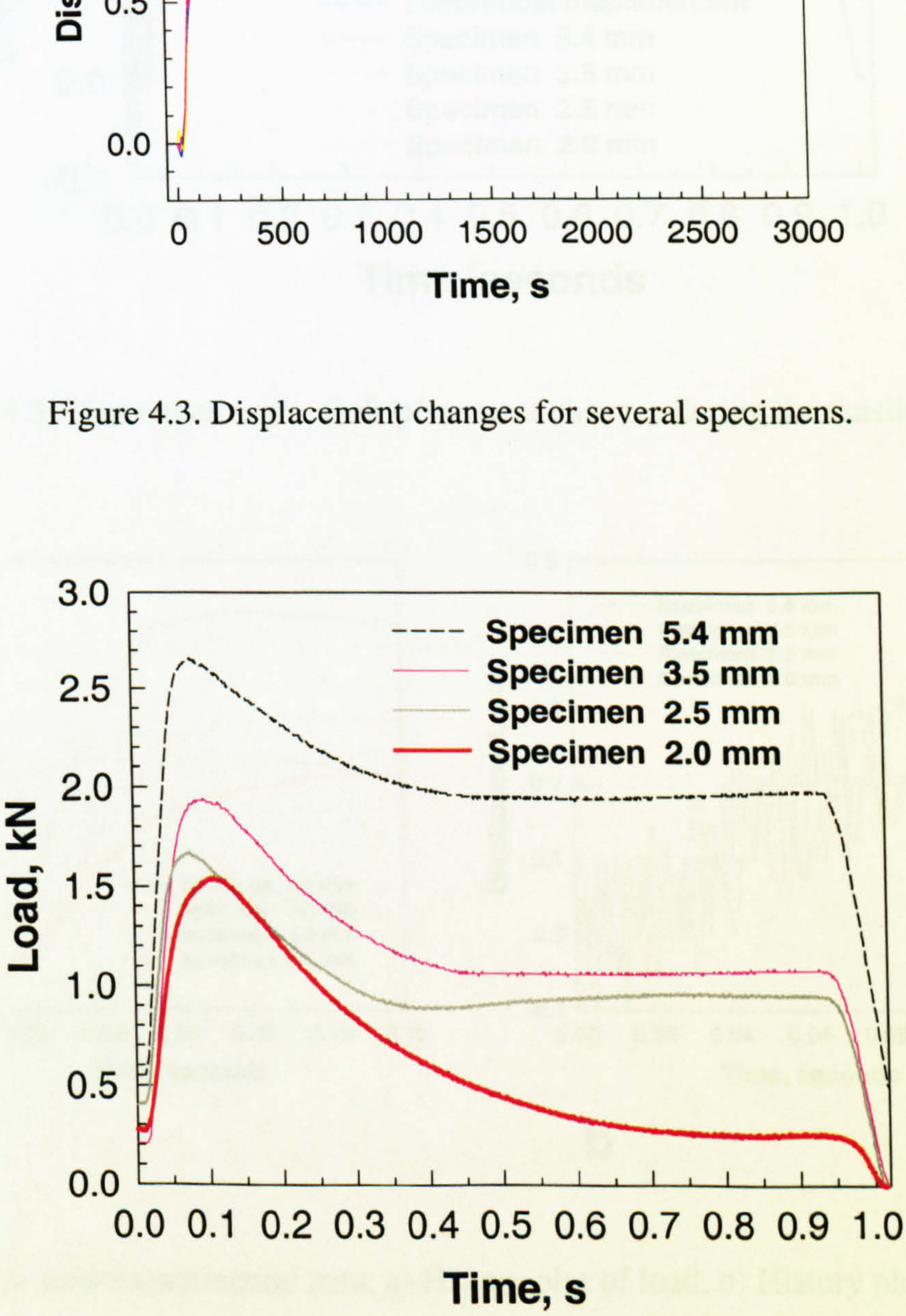

Figure 4.4. Measured loads.

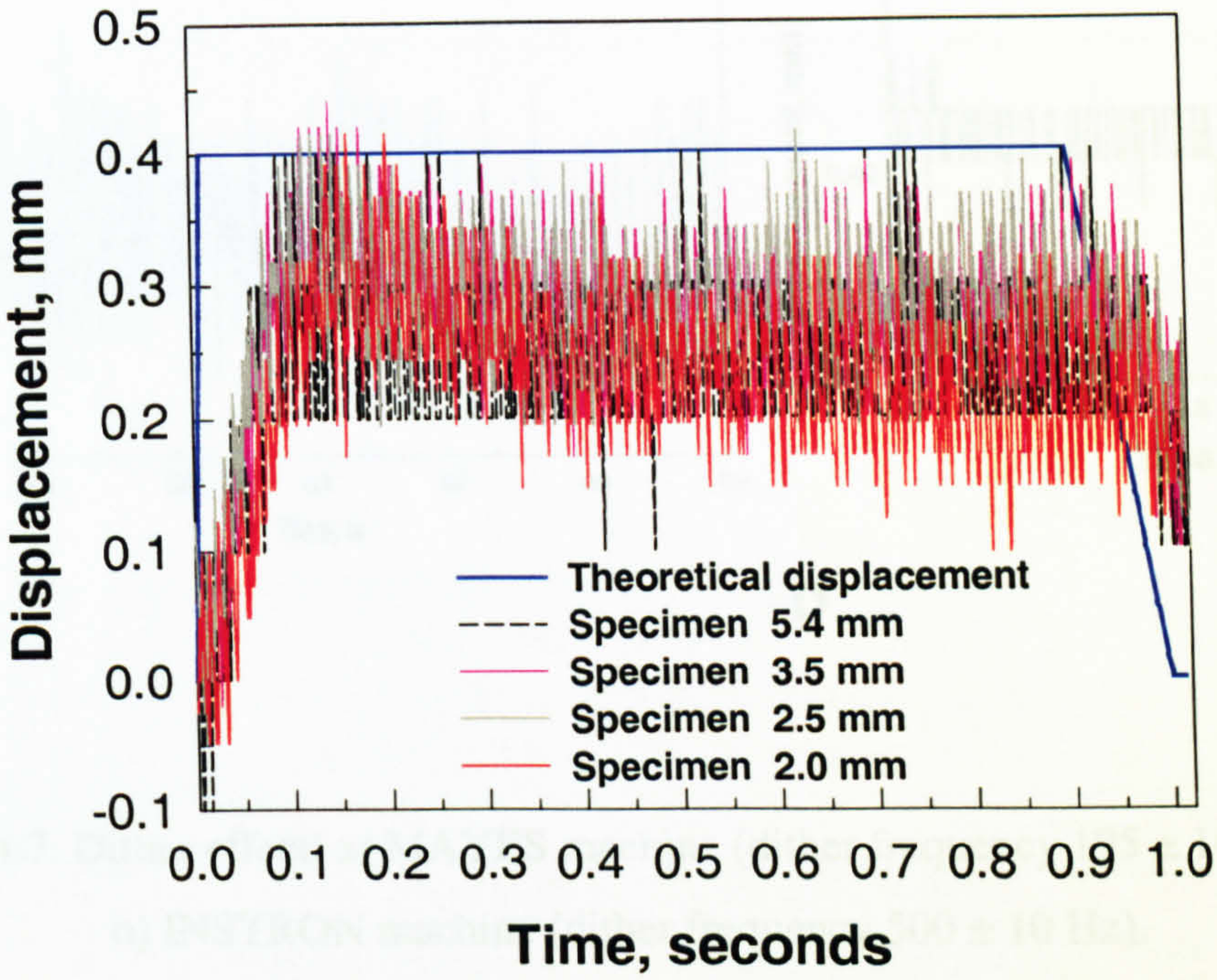

Figure 4.5. Theoretical and real displacement changes during the tensile tests.

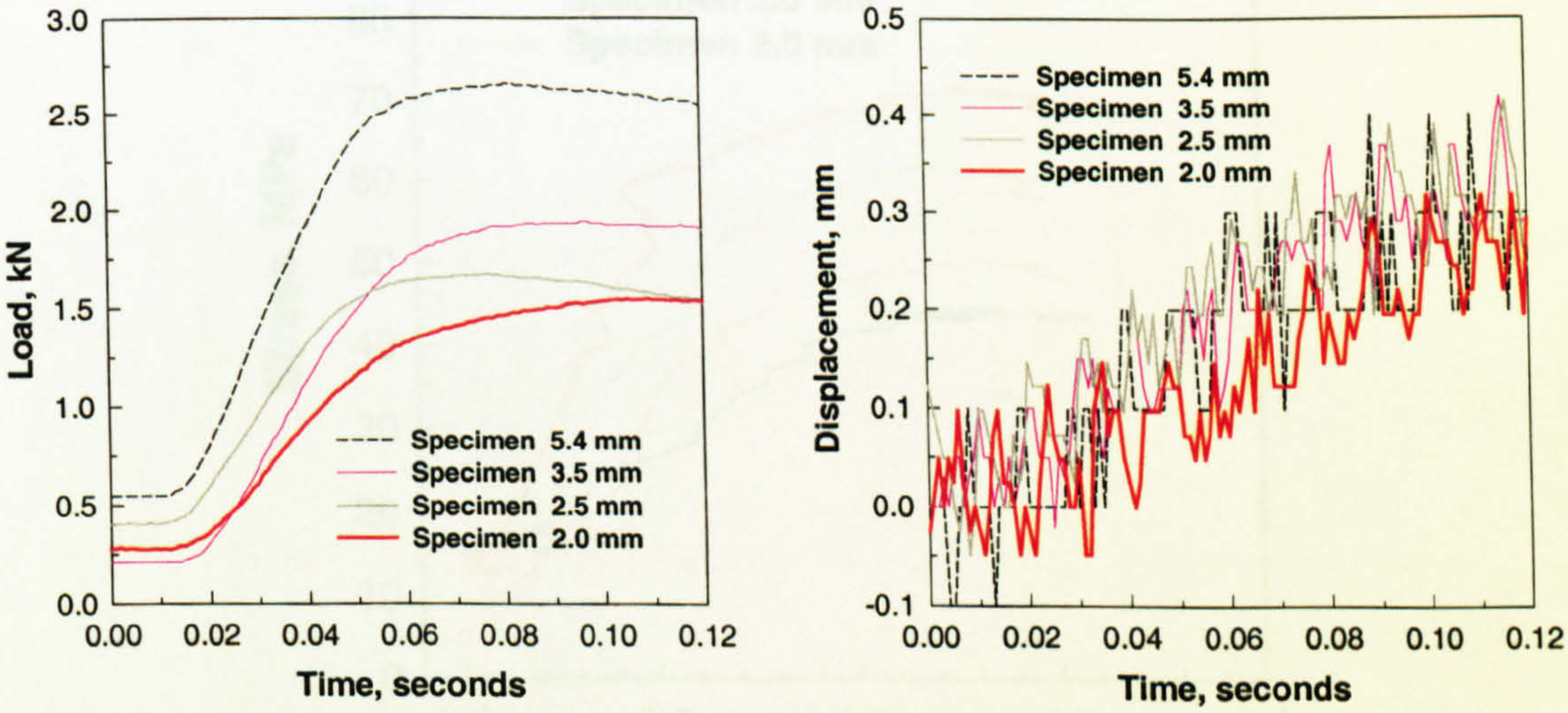

Figure 4.6. Raw experimental data: a) History plot of load, b) History plot of cross-head movement.

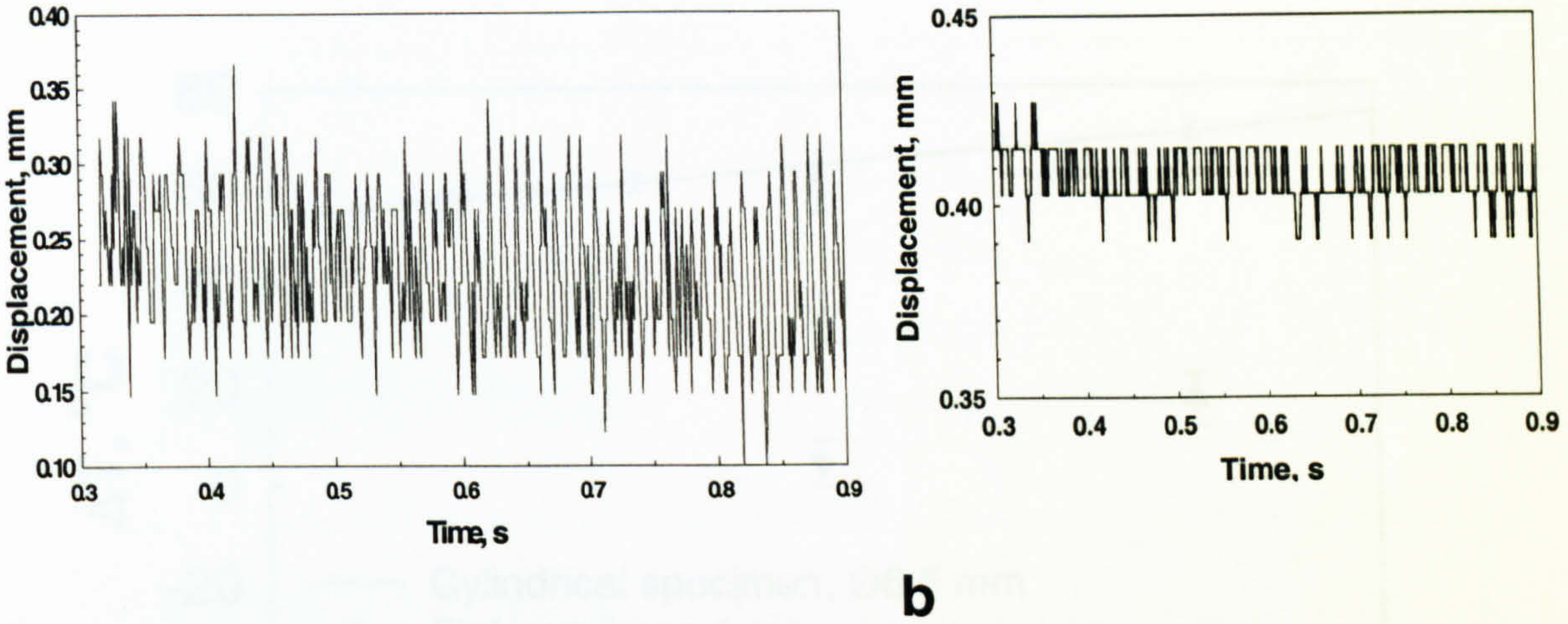

Figure 4.7. Dither effect: a) MAYES machine (dither frequency 195 ± 10 Hz) and b) INSTRON machine (dither frequency 500 ± 10 Hz).

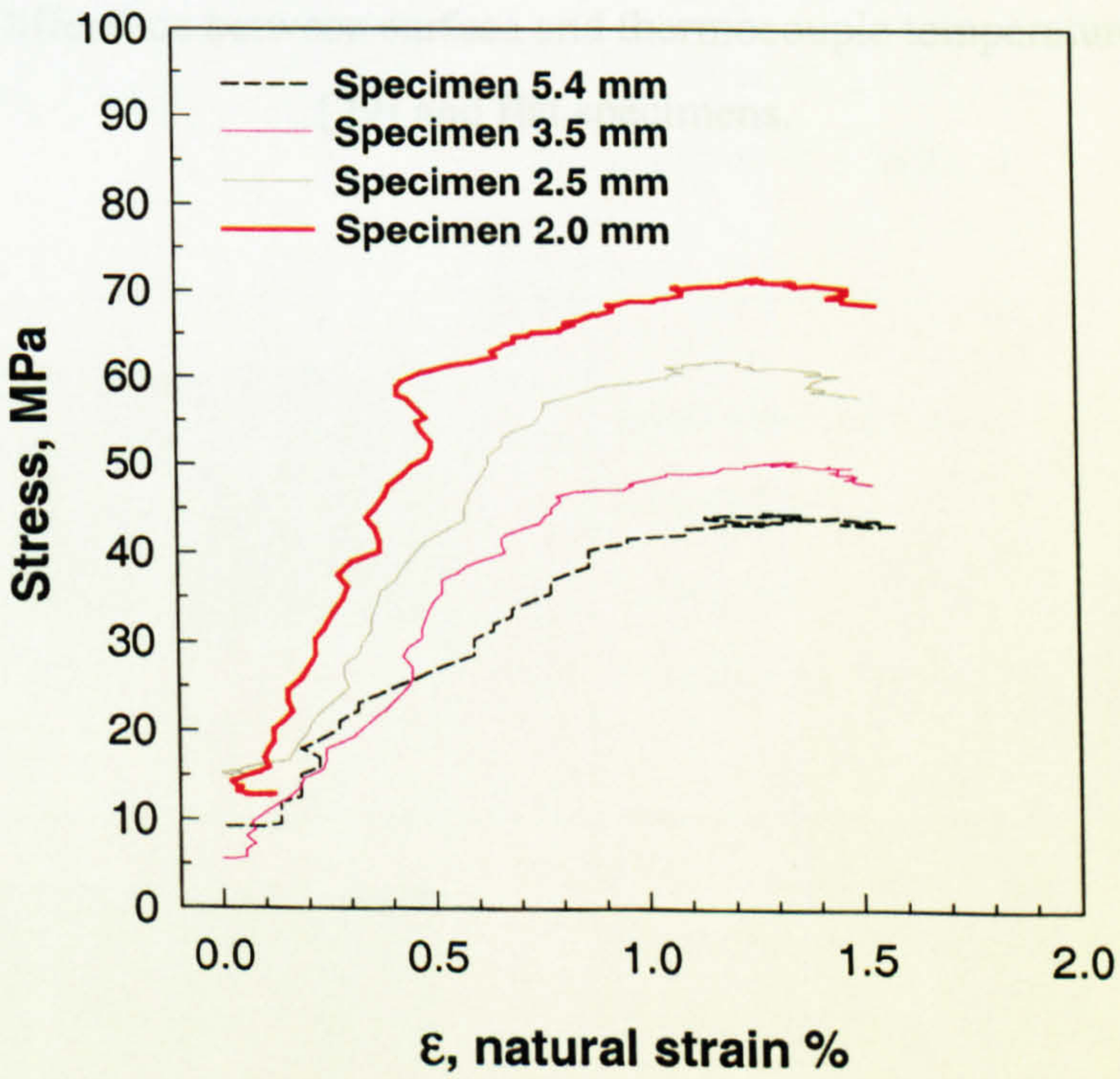

Figure 4.8. Smoothed stress-strain curves.

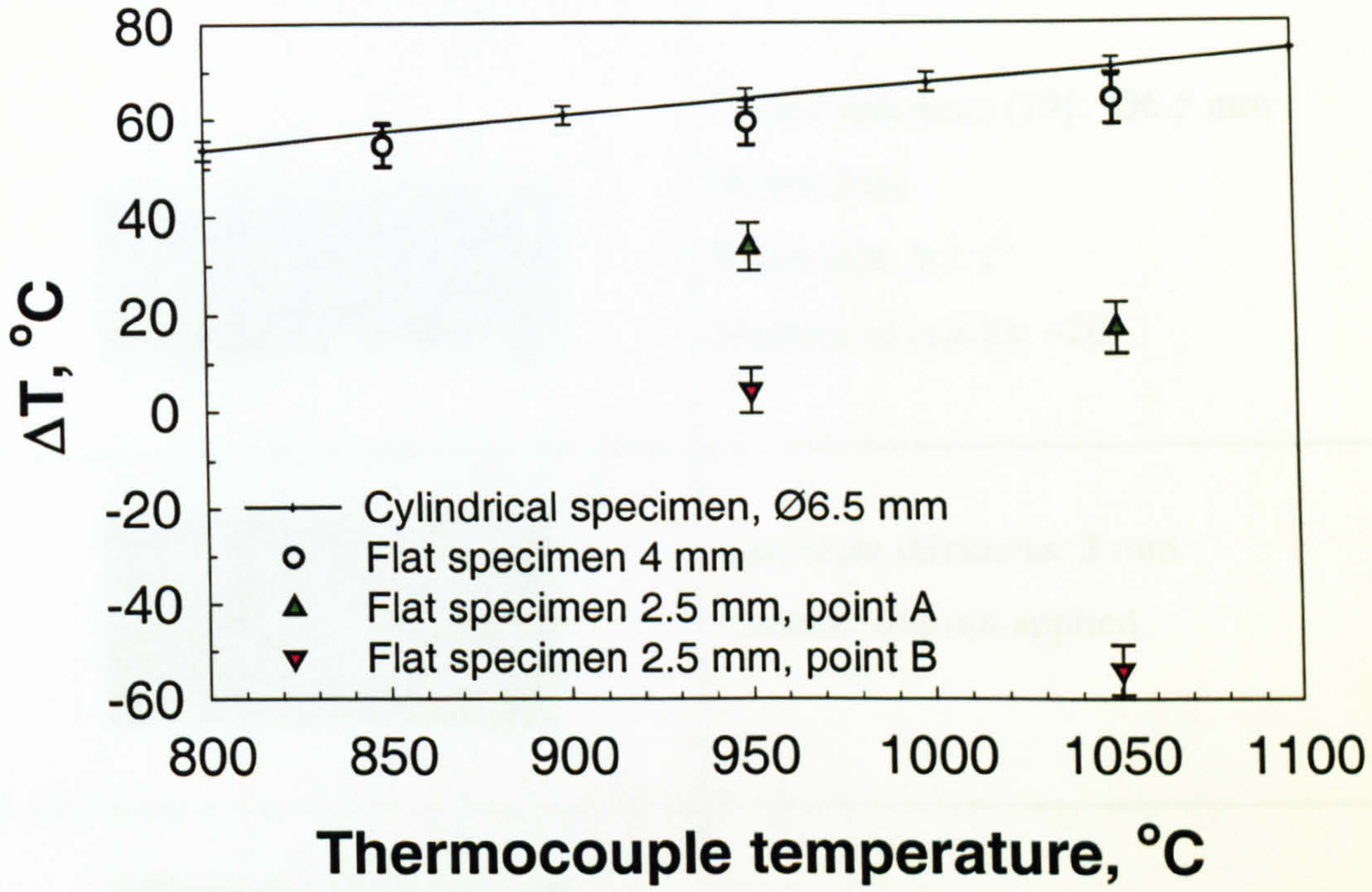

Figure 4.9. Difference between surface and thermocouple temperatures for round [29] and flat specimens.

	Round specimen [29]: Ø6.5 mm Strain: 0.02 Strain rate: 0.2 s^{-1} Number of cracks: ~20
	Specimen thickness: 3 mm Tension was not applied
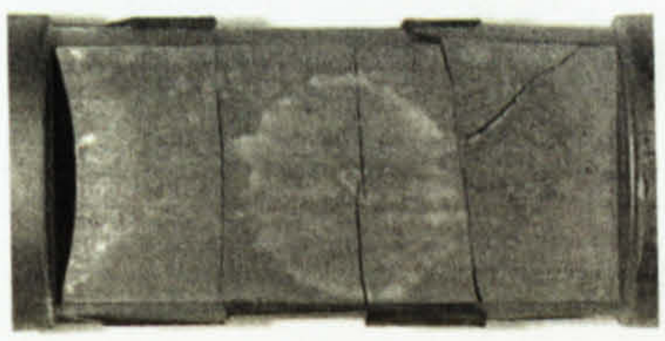	Specimen thickness: 5.4 mm Strain: 0.0125 Strain rate: 0.13 s^{-1} Number of cracks: 3
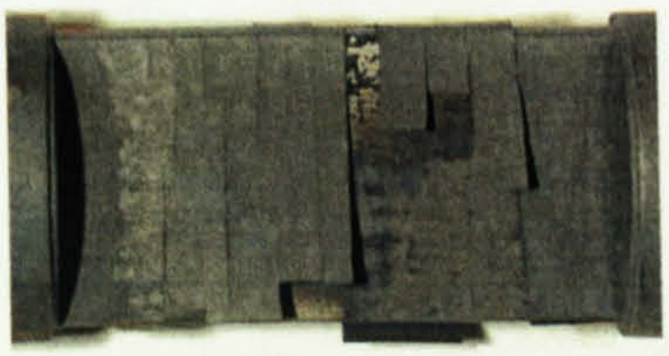	Specimen thickness: 3.5 mm Strain: 0.014 Strain rate: 0.14 s^{-1} Number of cracks: 12
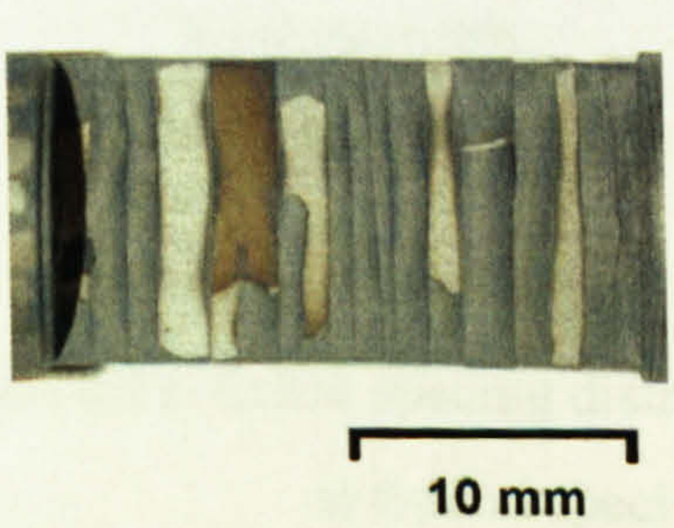	Specimen thickness: 2 mm Strain: 0.012 Strain rate: 0.12 s^{-1}; Number of cracks: 16

Figure 4.10. Specimens with different crack spacing value, $T_{thermocouple}$ = 830°C.

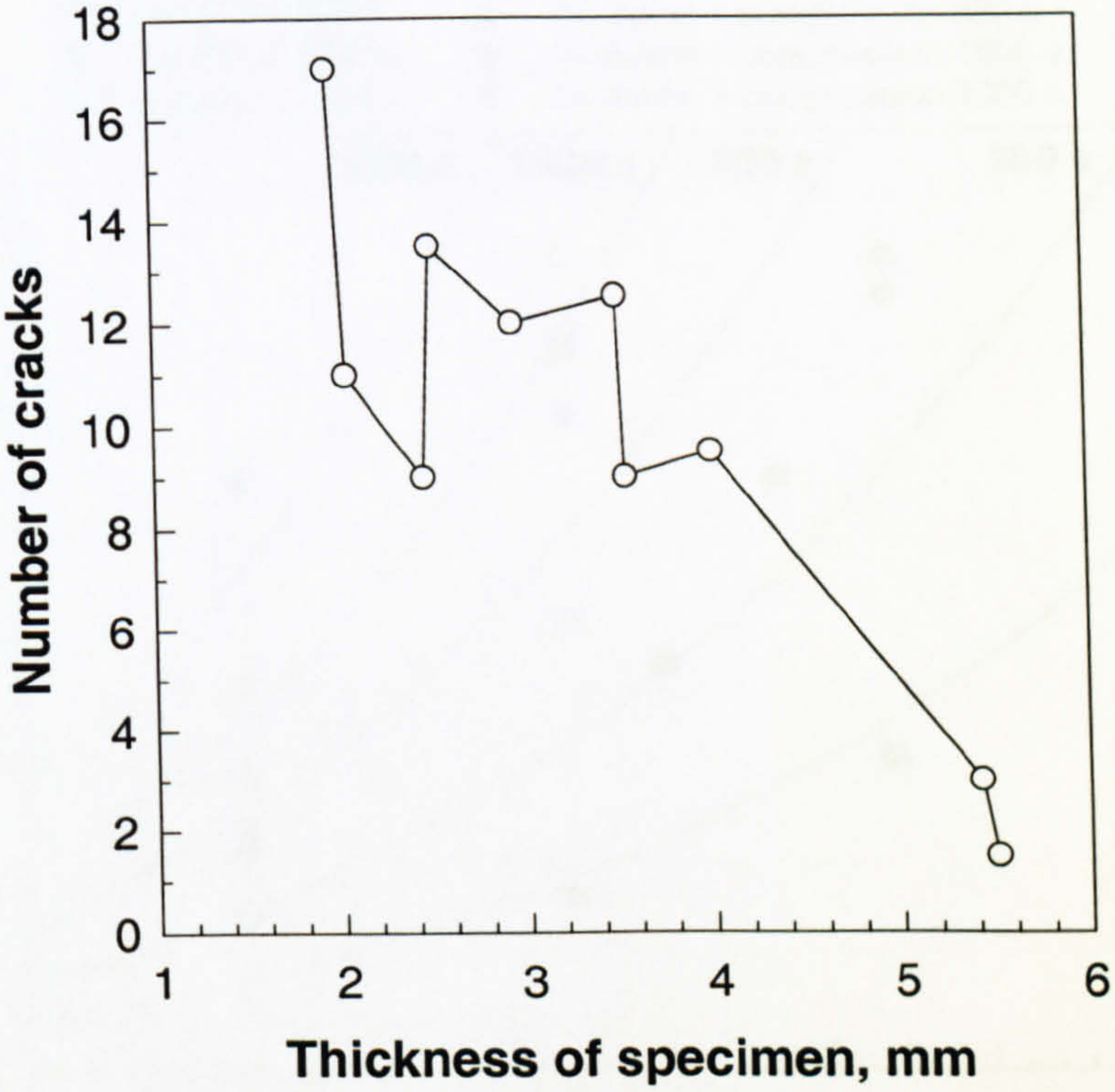

Figure 4.11. Number of cracks for different specimens.

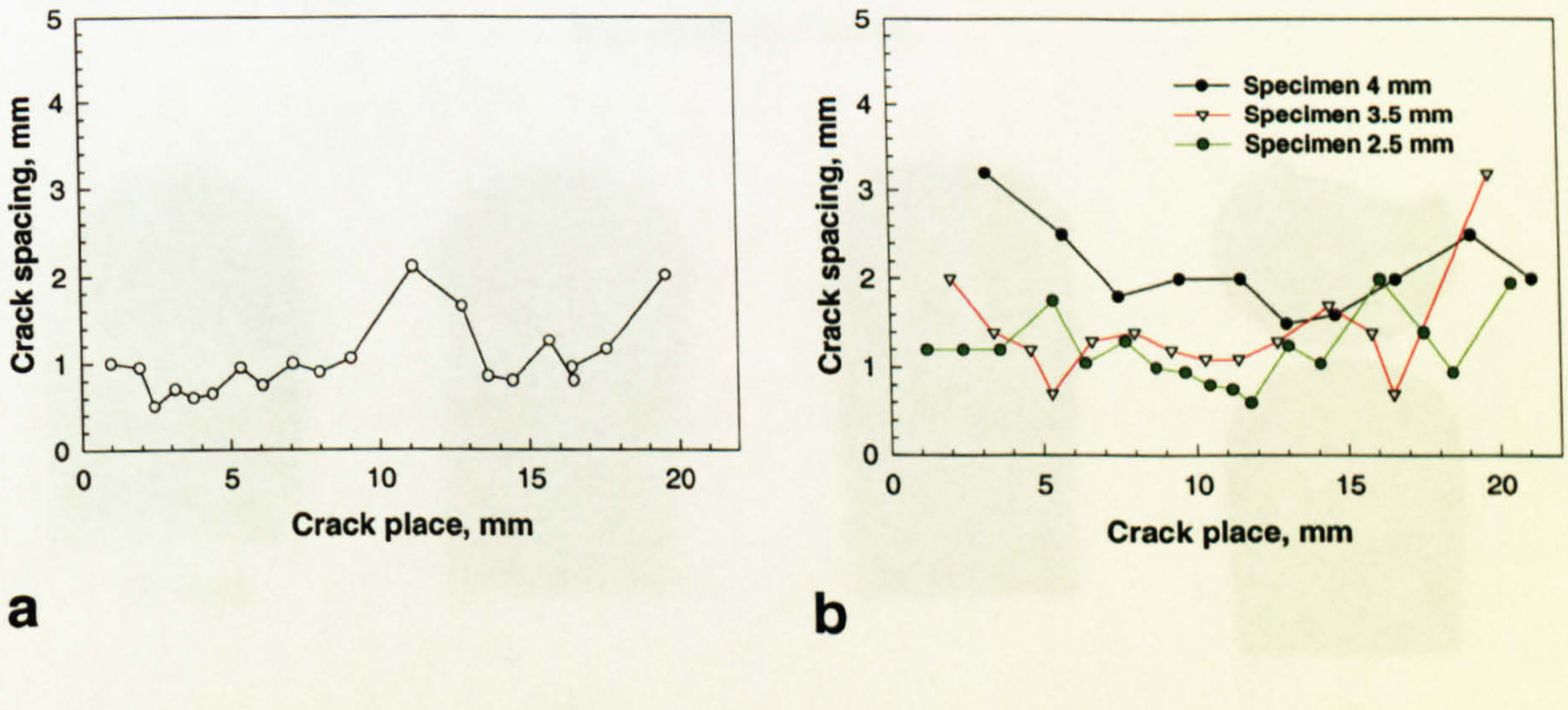

Figure 4.12. Crack spacing distribution in the gauge section area (0-20 mm);
a) Round specimen [29]; b) Flat specimens.

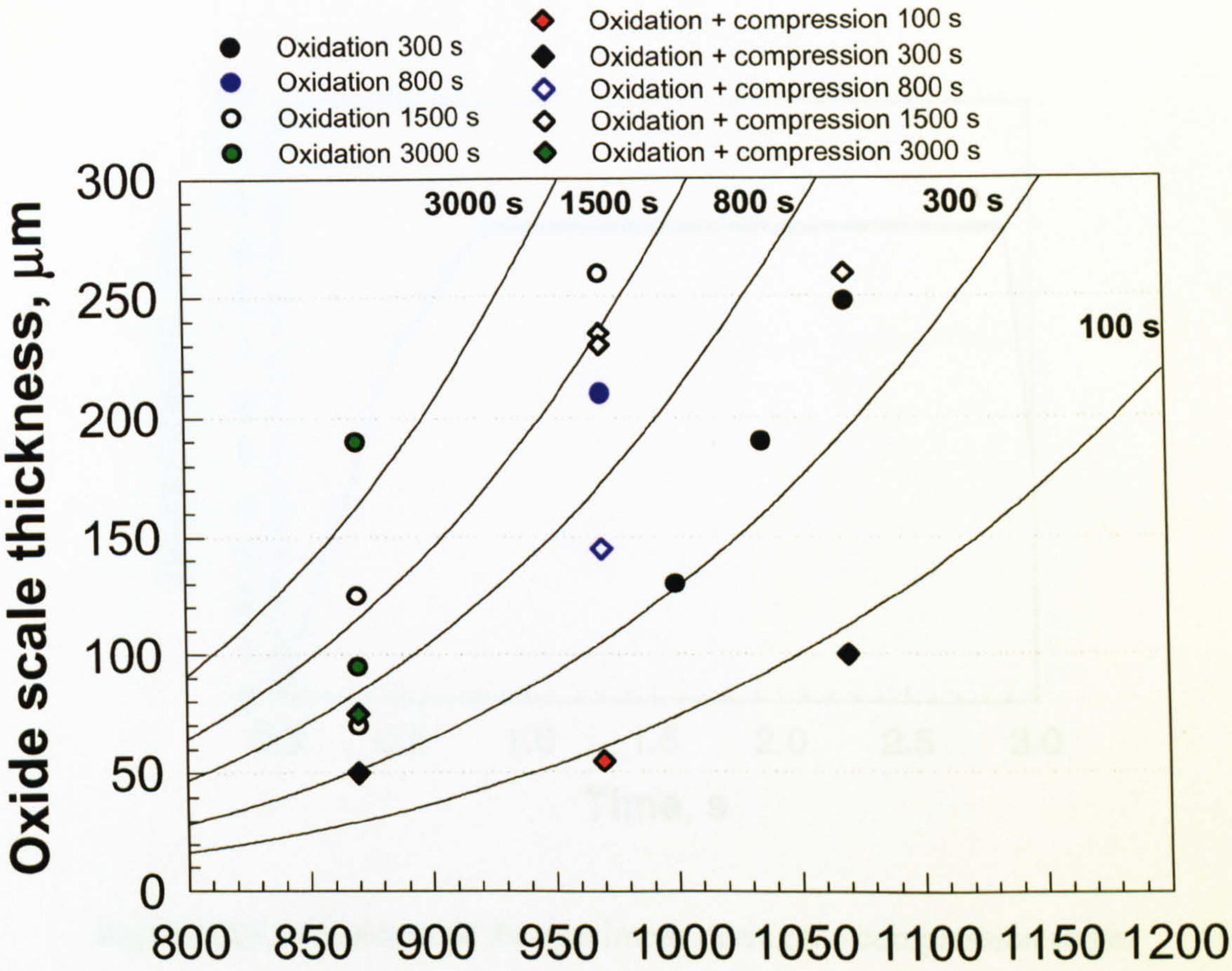

Figure 4.13. Prediction and experimental oxide thicknesses at different temperatures and oxidation times.

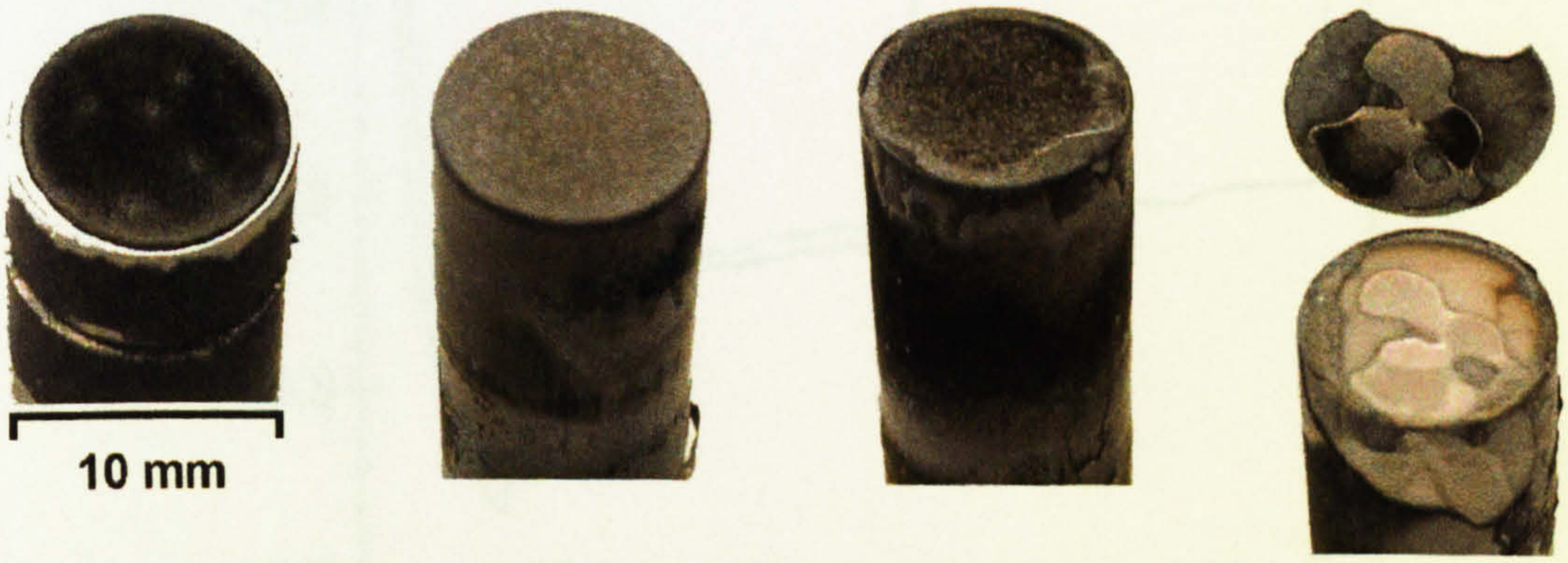

Figure 4.14. The appearance of the oxide scales at different temperatures: a) 970°C, b) 1000°C, c) 1040°C, d) 1070°C.

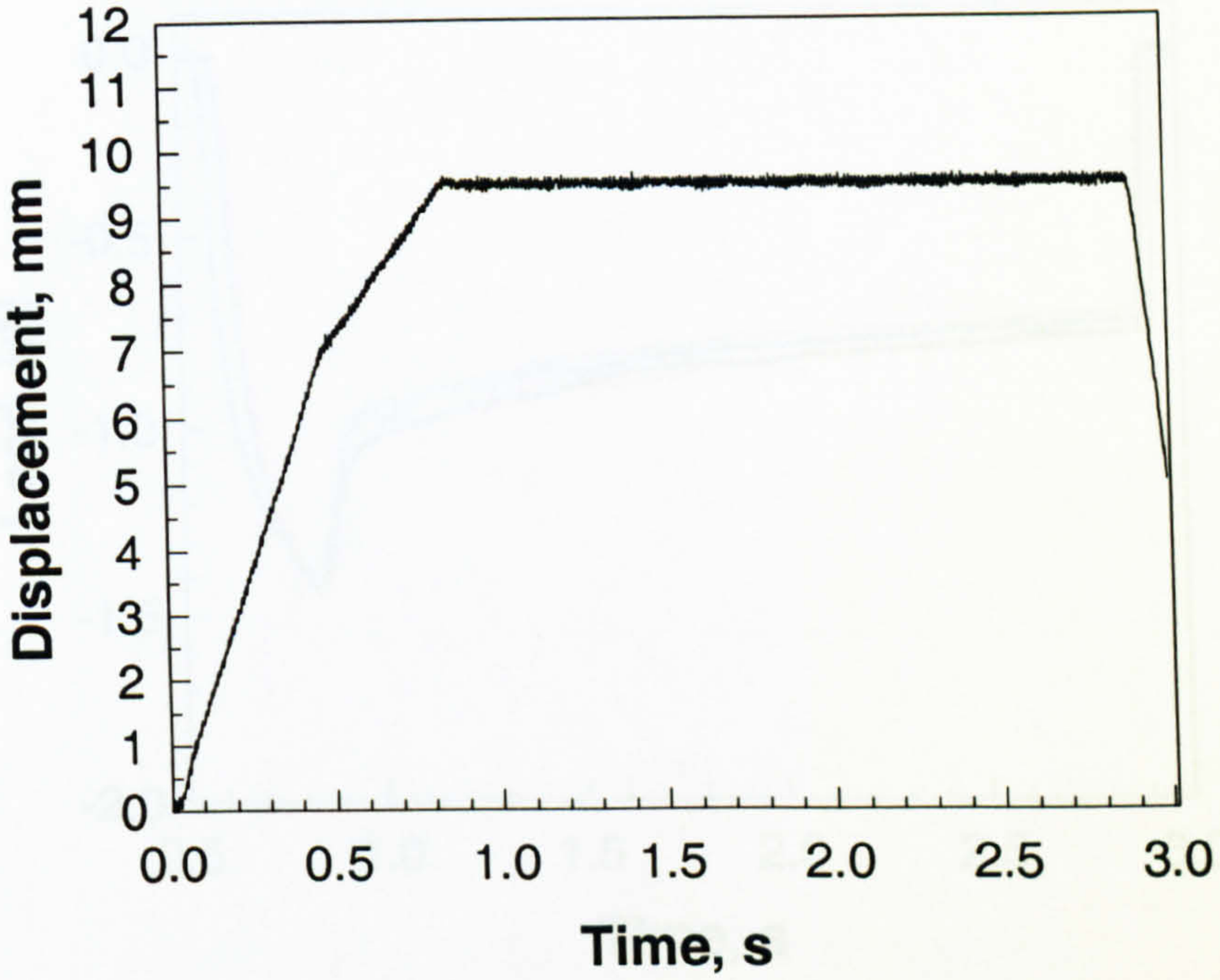

Figure 4.15. Movement of the specimens during the compression stage.

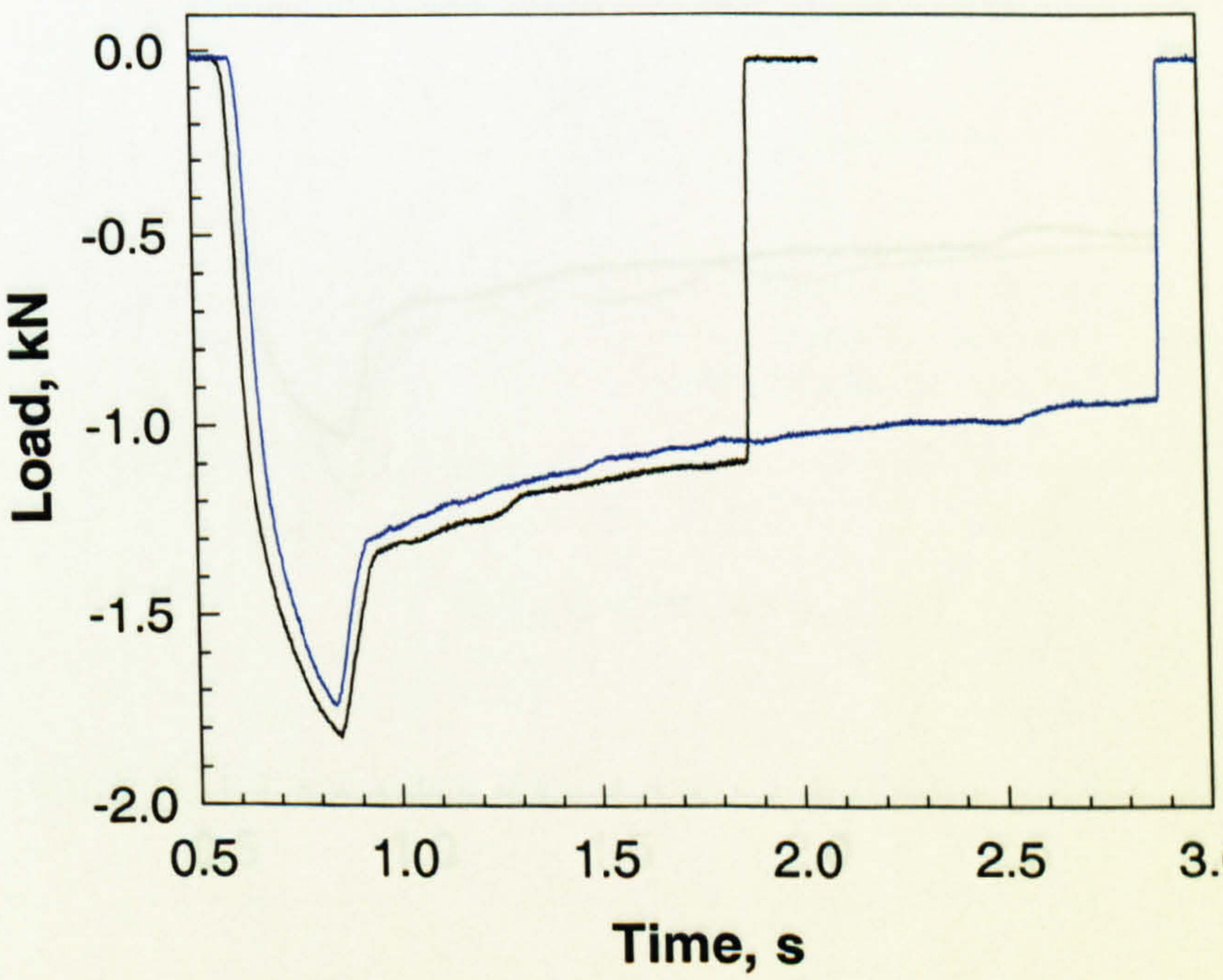

Figure 4.16. Raw data of measured load at 870°C.

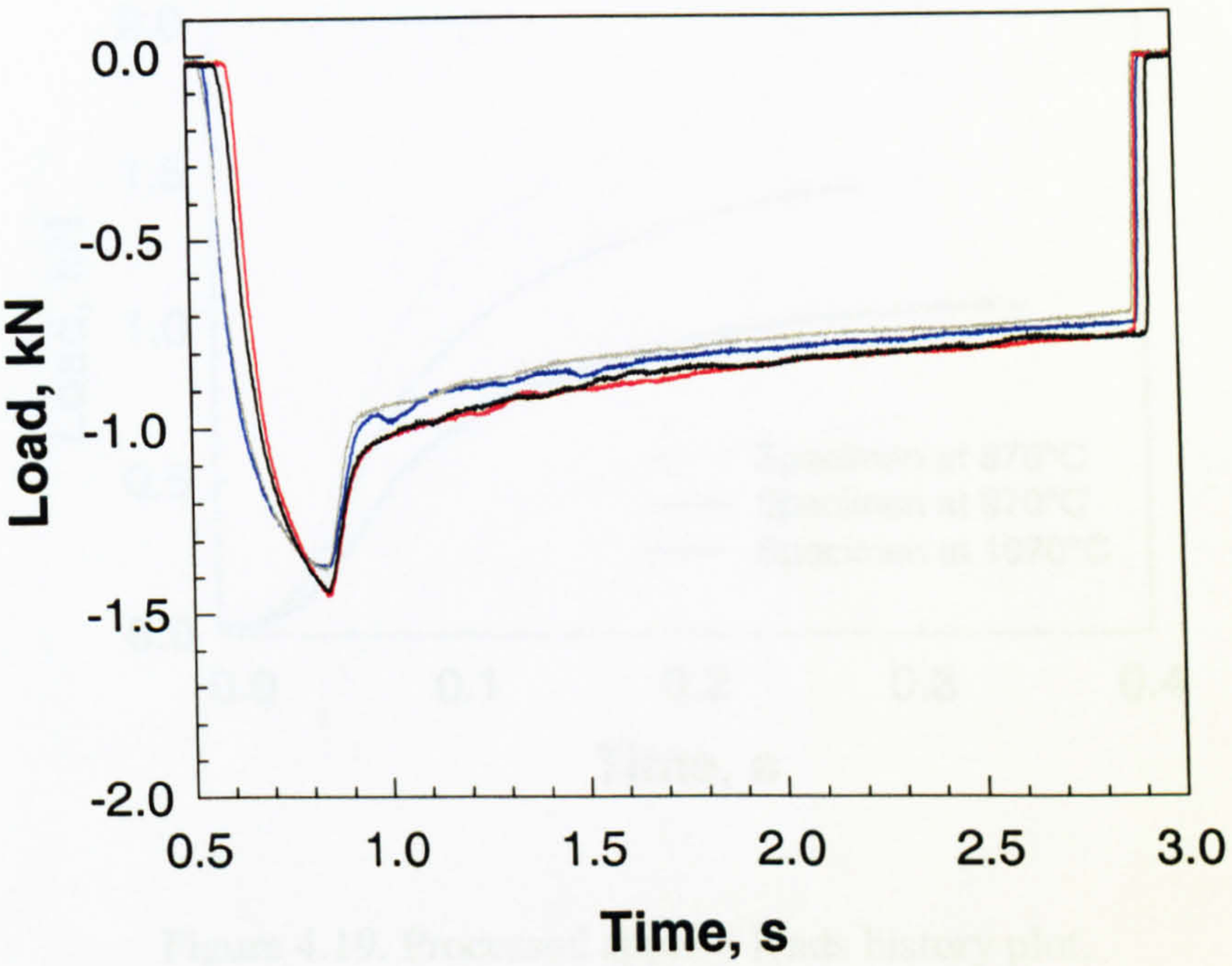

Figure 4.17. Raw data of measured load at 970°C.

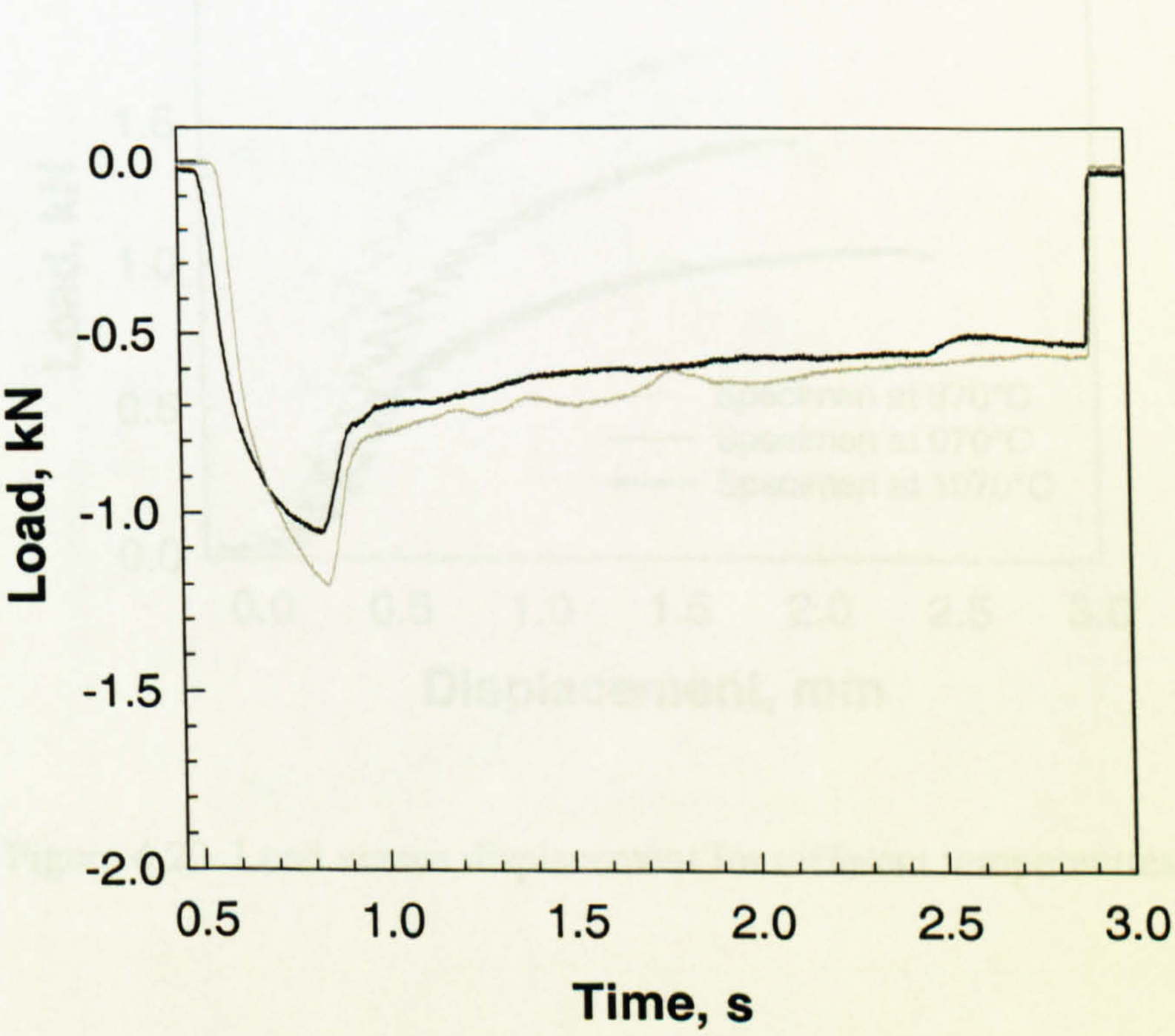

Figure 4.18. Raw data of measured load at 1070°C.

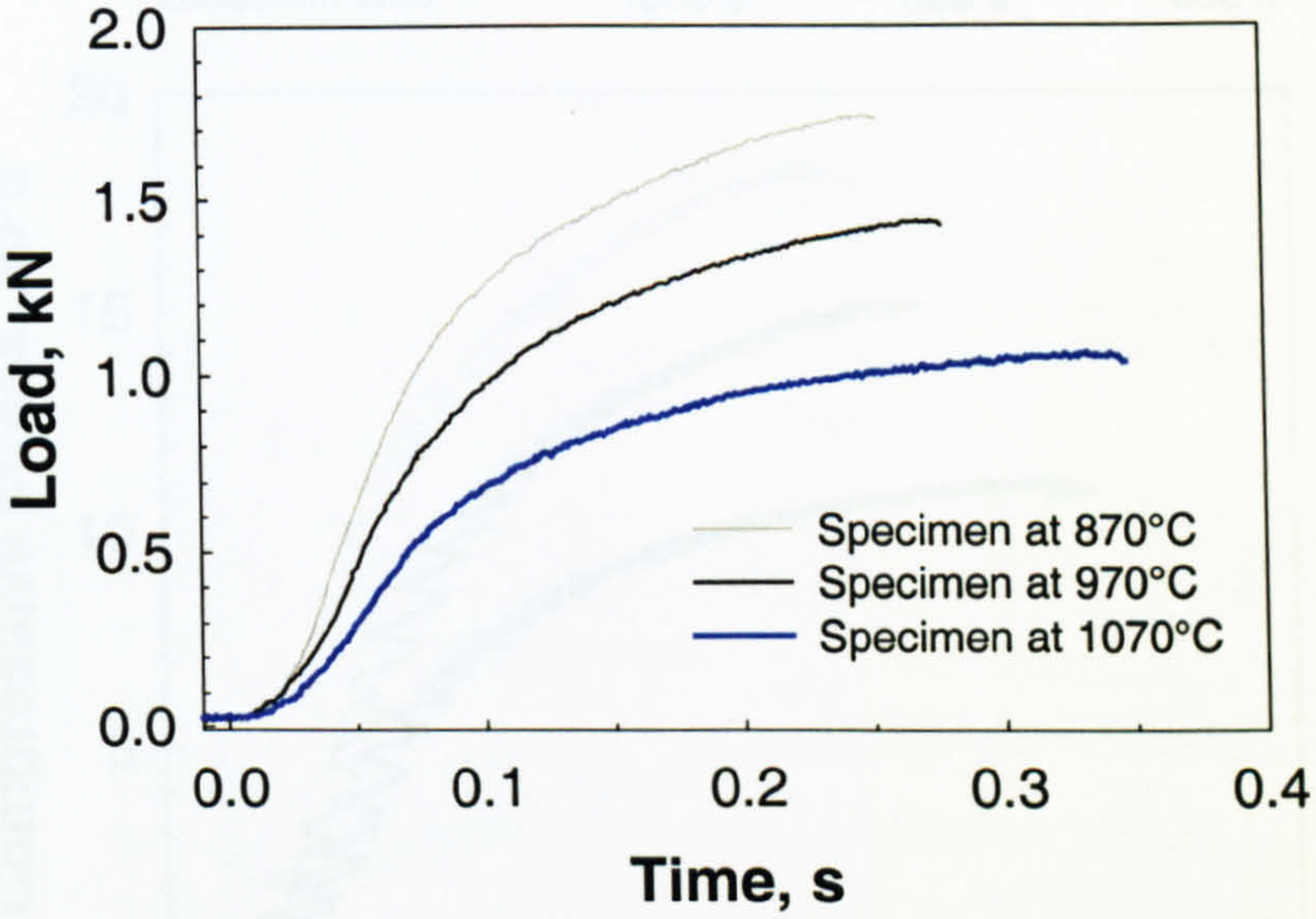

Figure 4.19. Processed applied loads history plot.

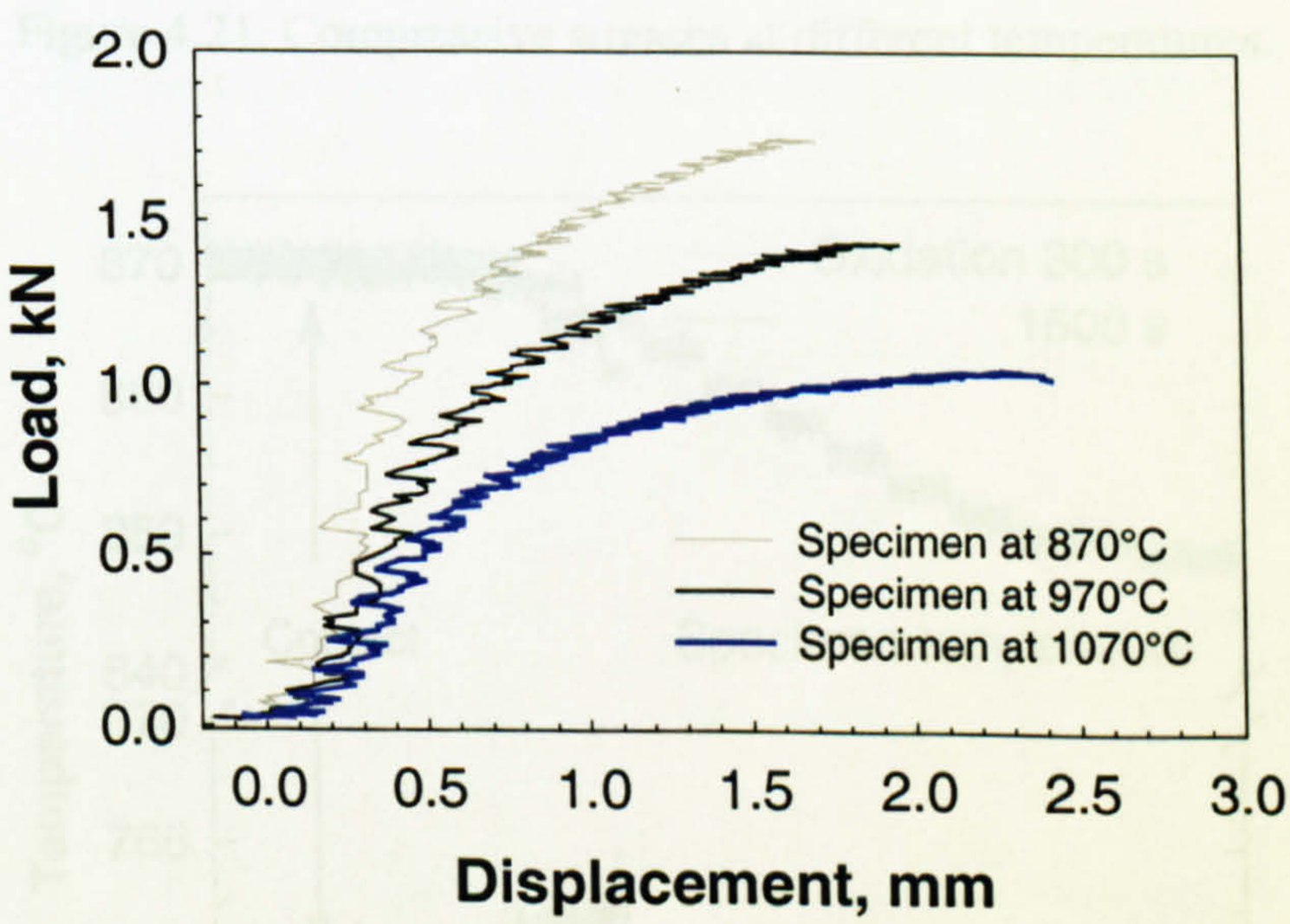

Figure 4.20. Load versus displacement for different temperatures.

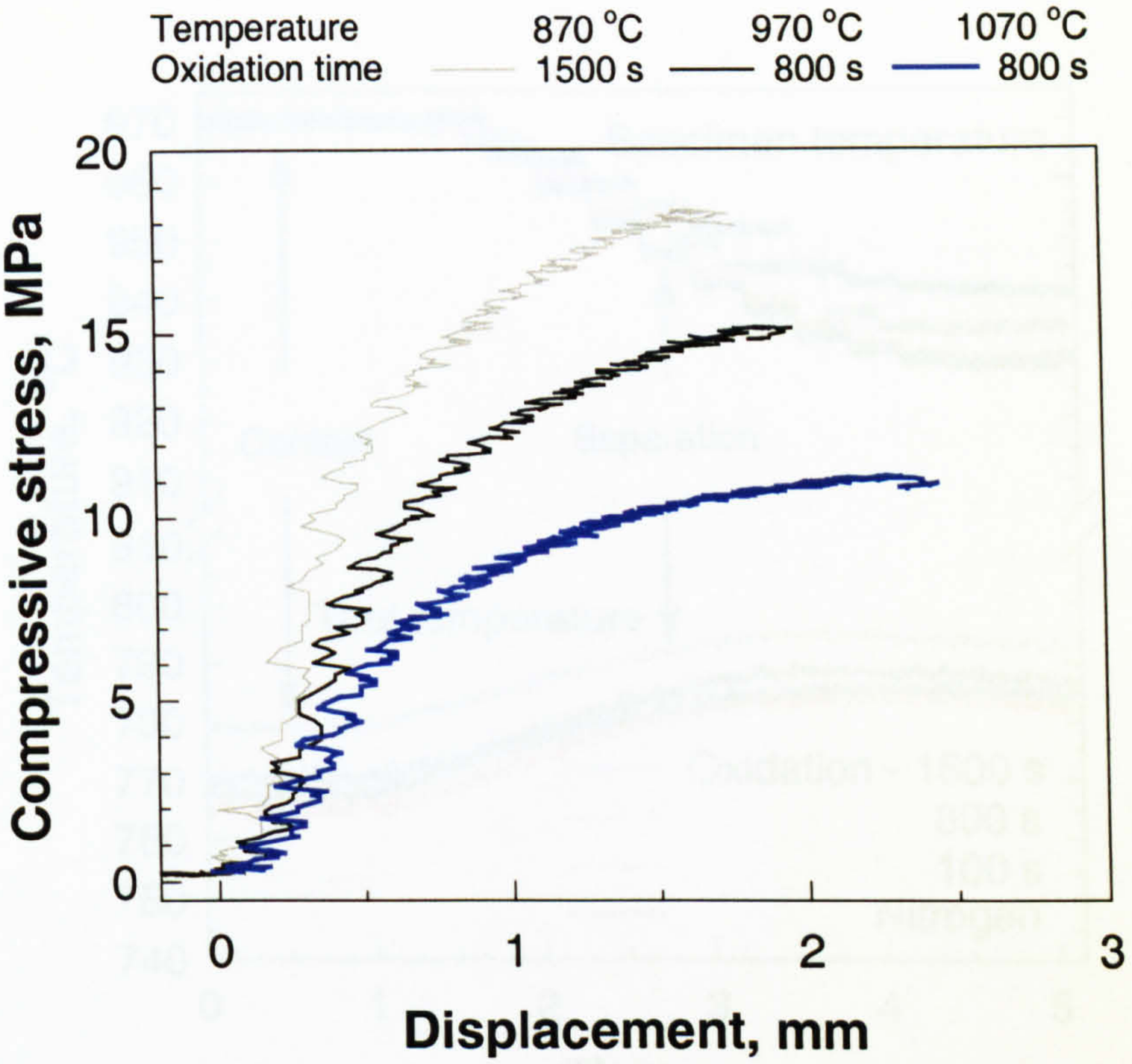

Figure 4.21. Compressive stresses at different temperatures.

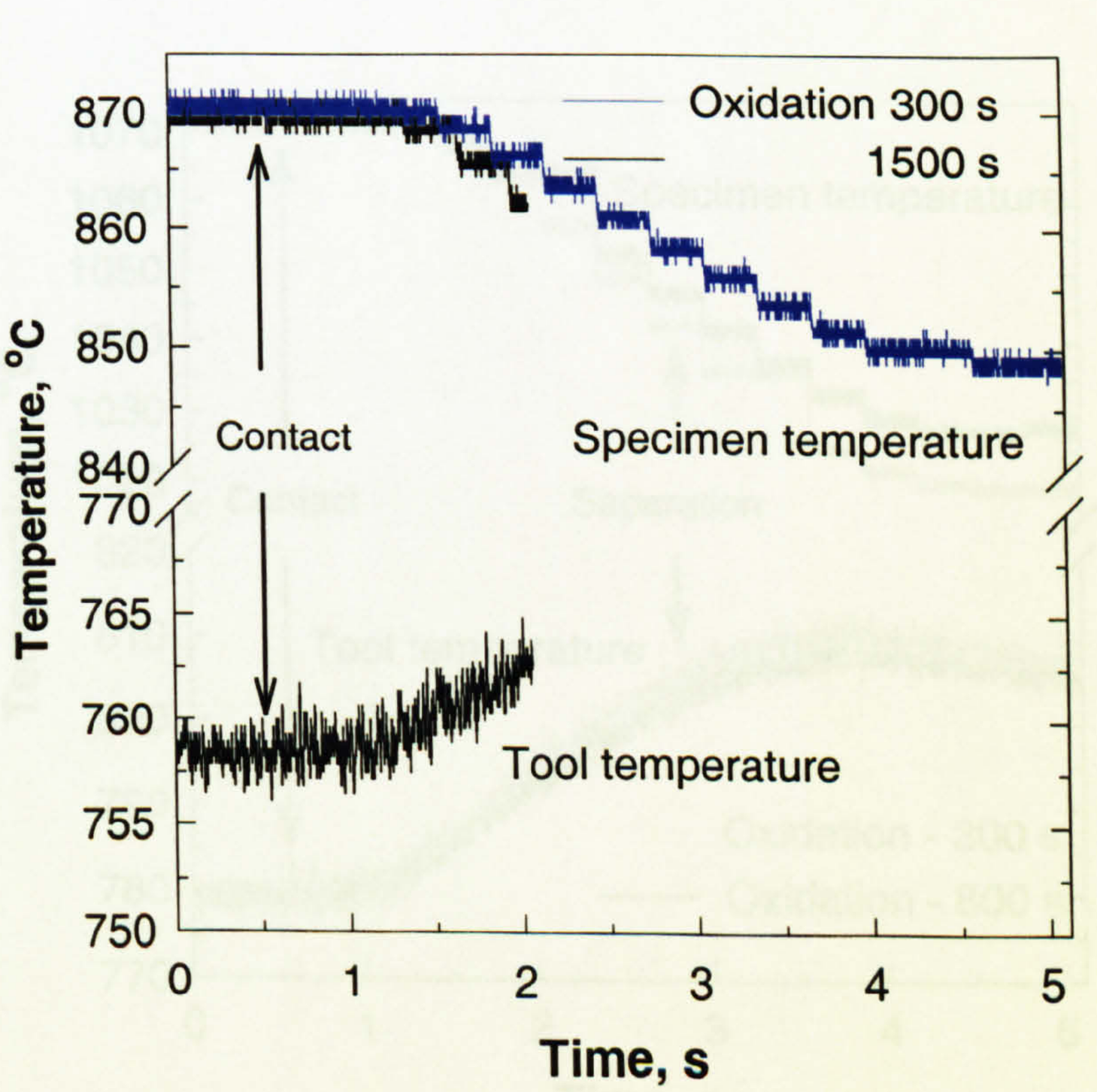

Figure 4.22. Temperature alteration, oxidation at 870°C.

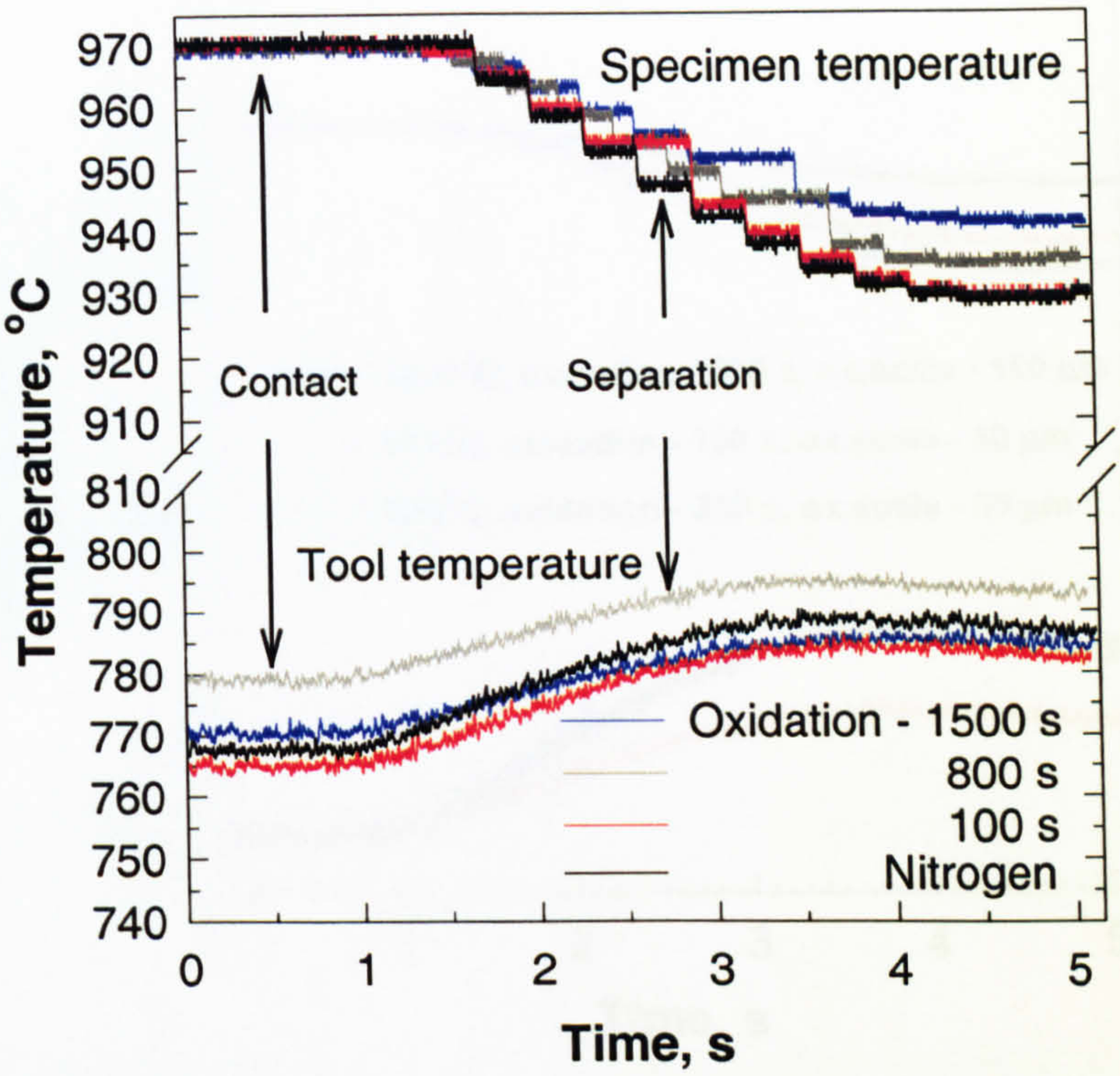

Figure 4.23. Temperature alteration, oxidation at 970°C.

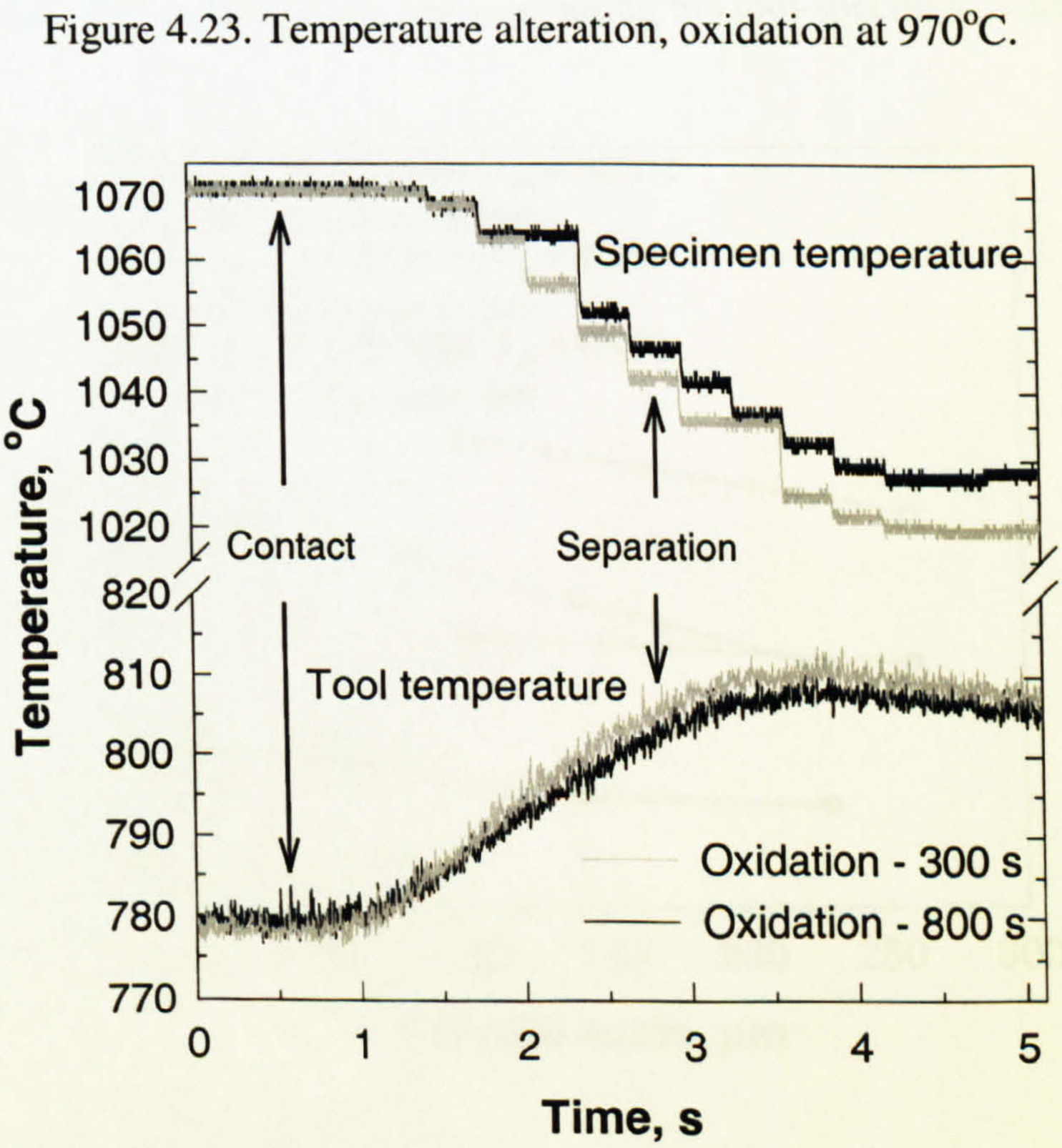

Figure 4.24. Temperature alteration, oxidation at 1070°C.

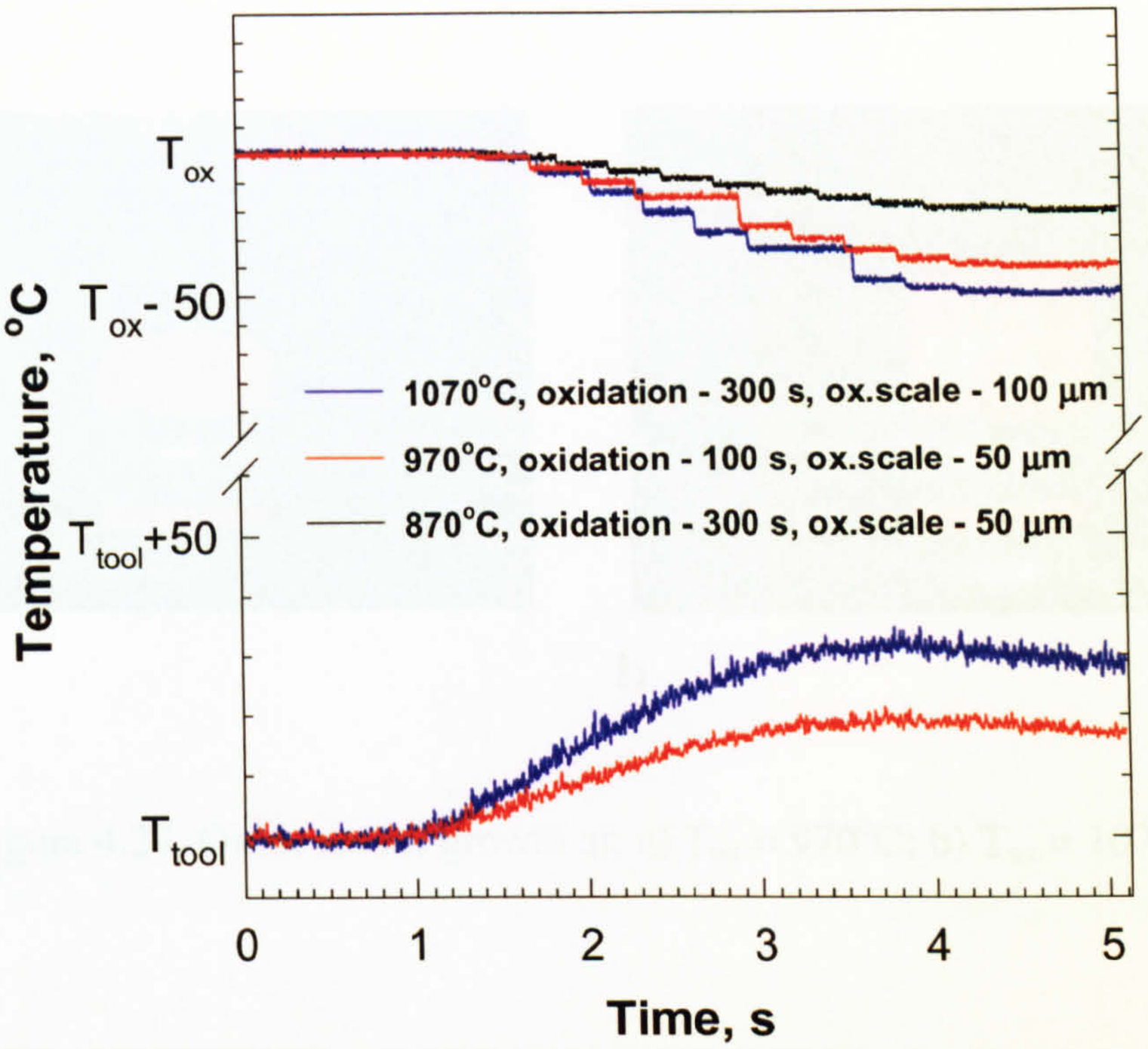

Figure 4.25. Temperature changes during the tool-specimen contact.

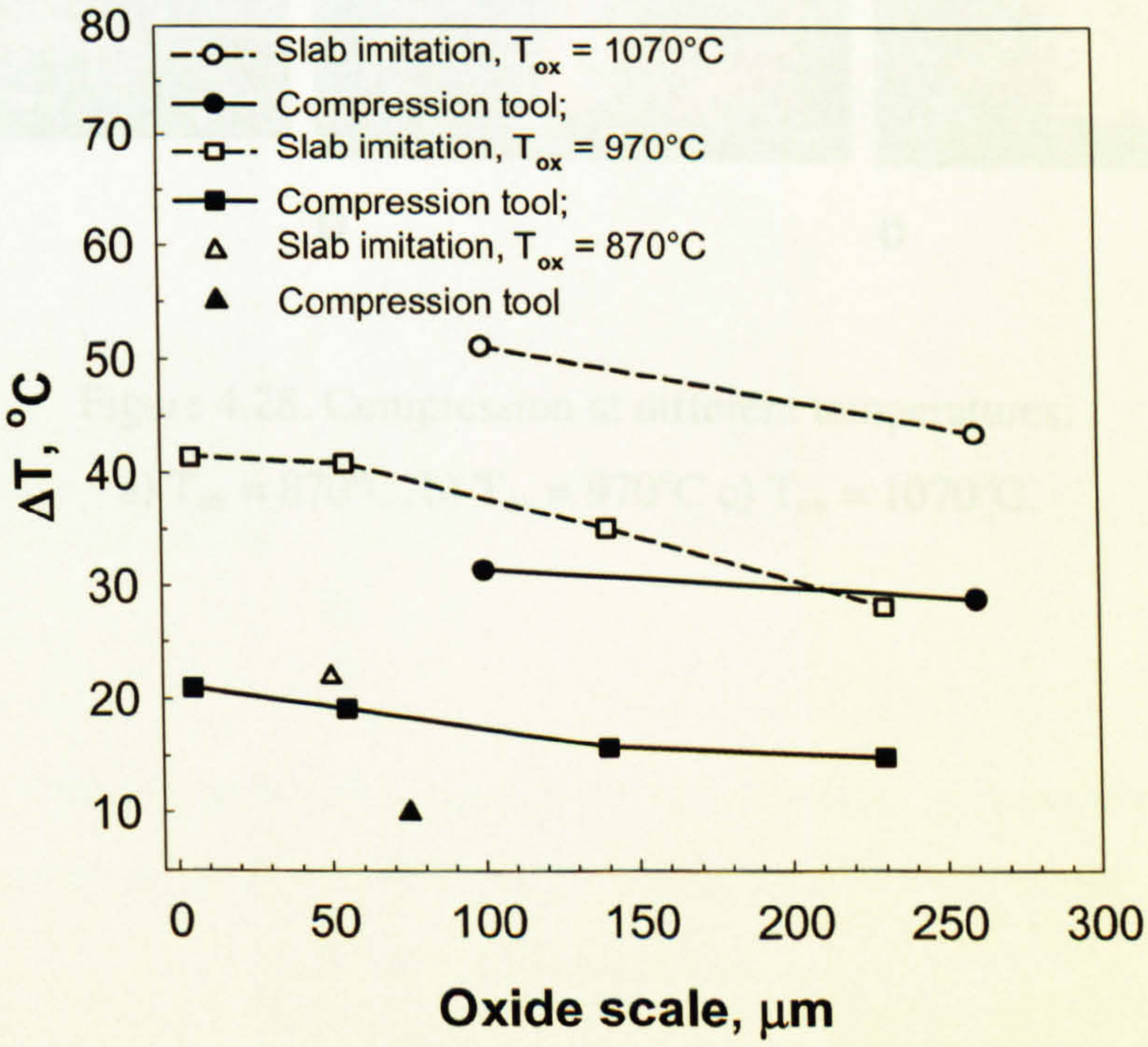

Figure 4.26. Numerical differences in temperature changes between specimens with oxide scale and the tool.

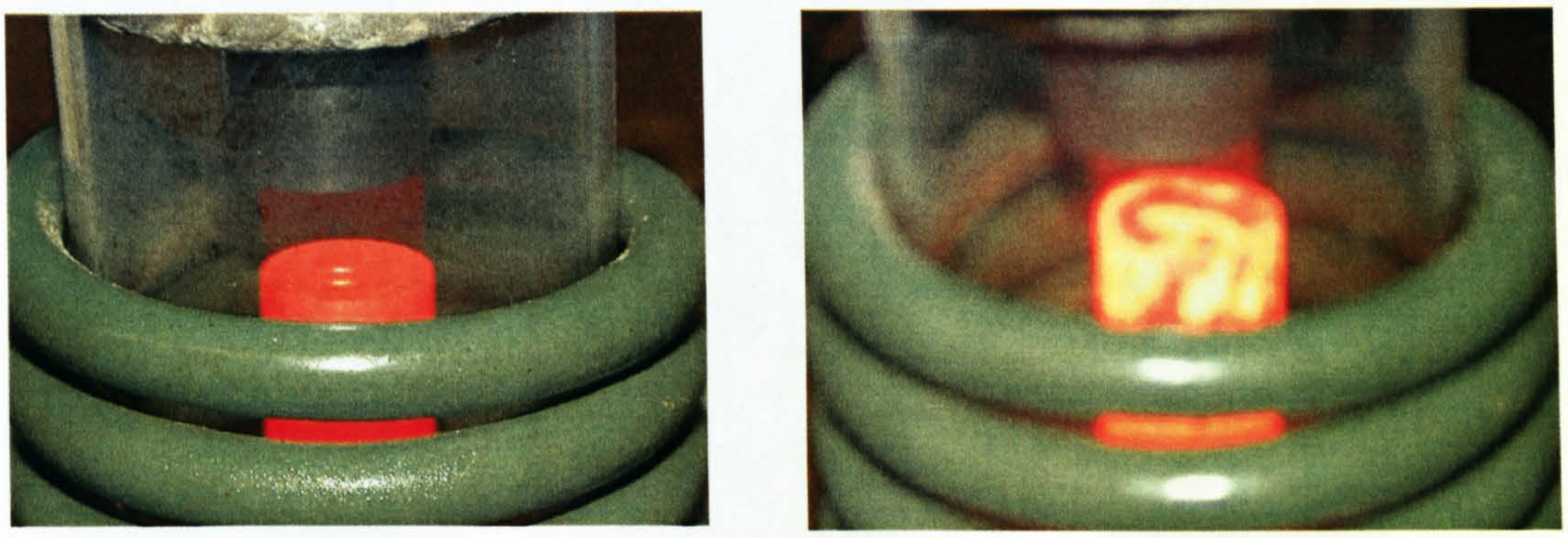

a b

Figure 4.27. Oxide scales growth at: a) T_{ox} = 970°C; b) T_{ox} = 1070°C.

a b c

Figure 4.28. Compression at different temperatures:
a) T_{ox} = 870°C, b) T_{ox} = 970°C c) T_{ox} = 1070°C.

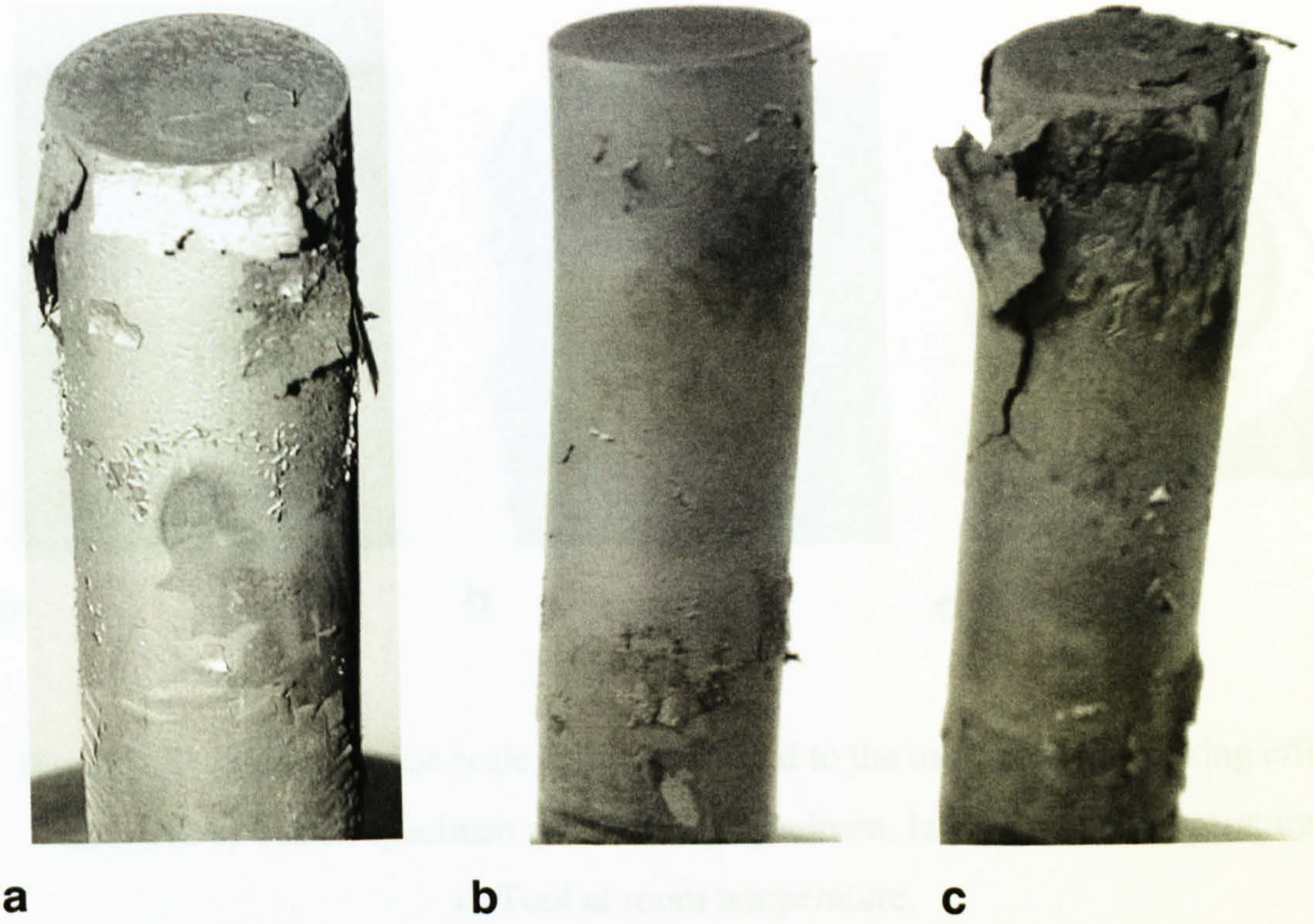

Figure 4.29. Specimens after the compression test at room temperature:

a) T_{ox} = 870°C, b) T_{ox} = 970°C c) T_{ox} = 1070°C.

Figure 4.30. Partially damaged surface oxide scale after the sticking effect occurred:

a) Tested specimen at 870°C, b) Specimen, later at room temperature,

c) Tool at room temperature.

Figure 4.31. Surface oxide scale fully transferred to the tool after the sticking effect occurred: a) Tested specimen at 970°C, b) Specimen, later at room temperature, c) Tool at room temperature.

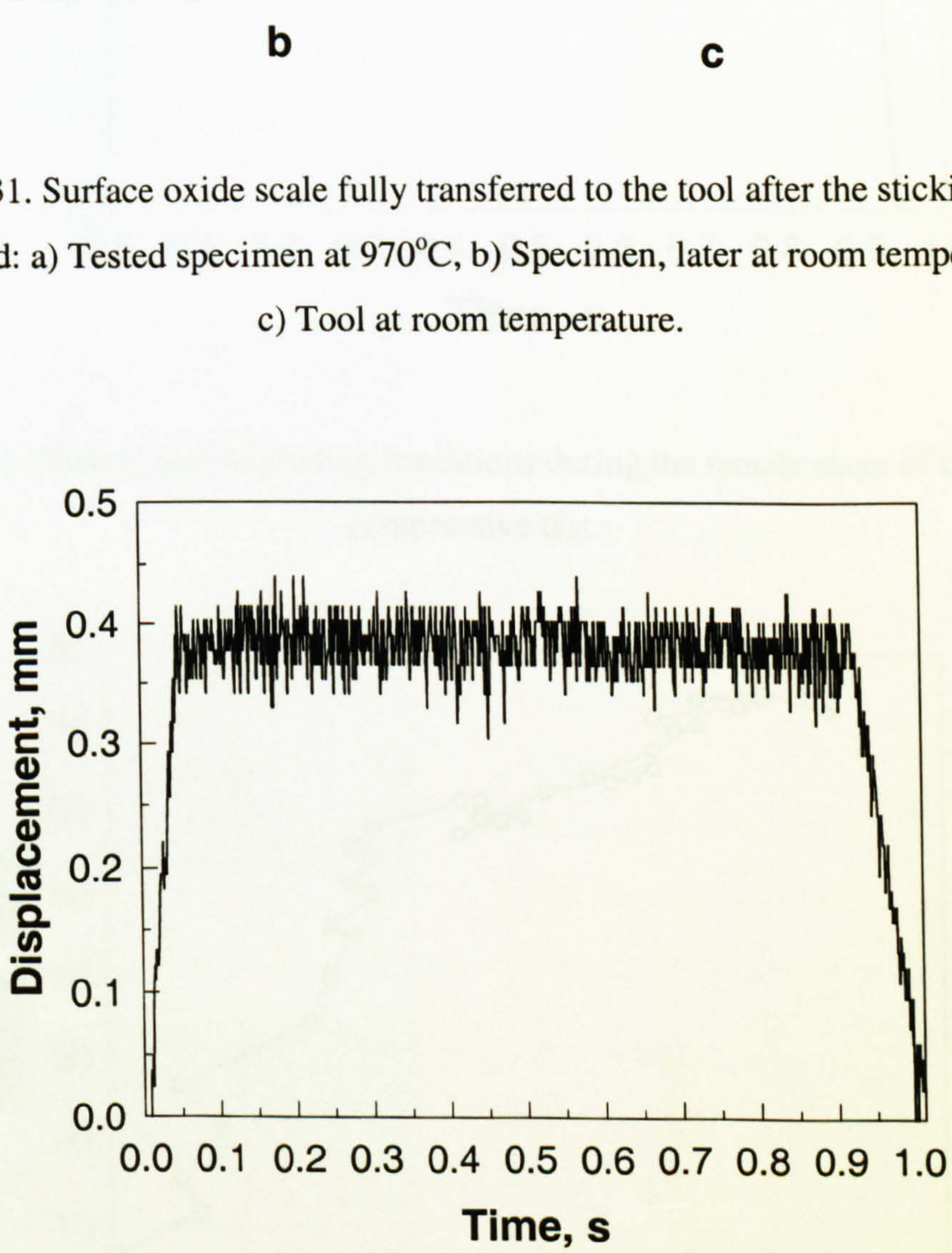

Figure 4.32. Displacement changes during the tensile stage of the tensile-compression test.

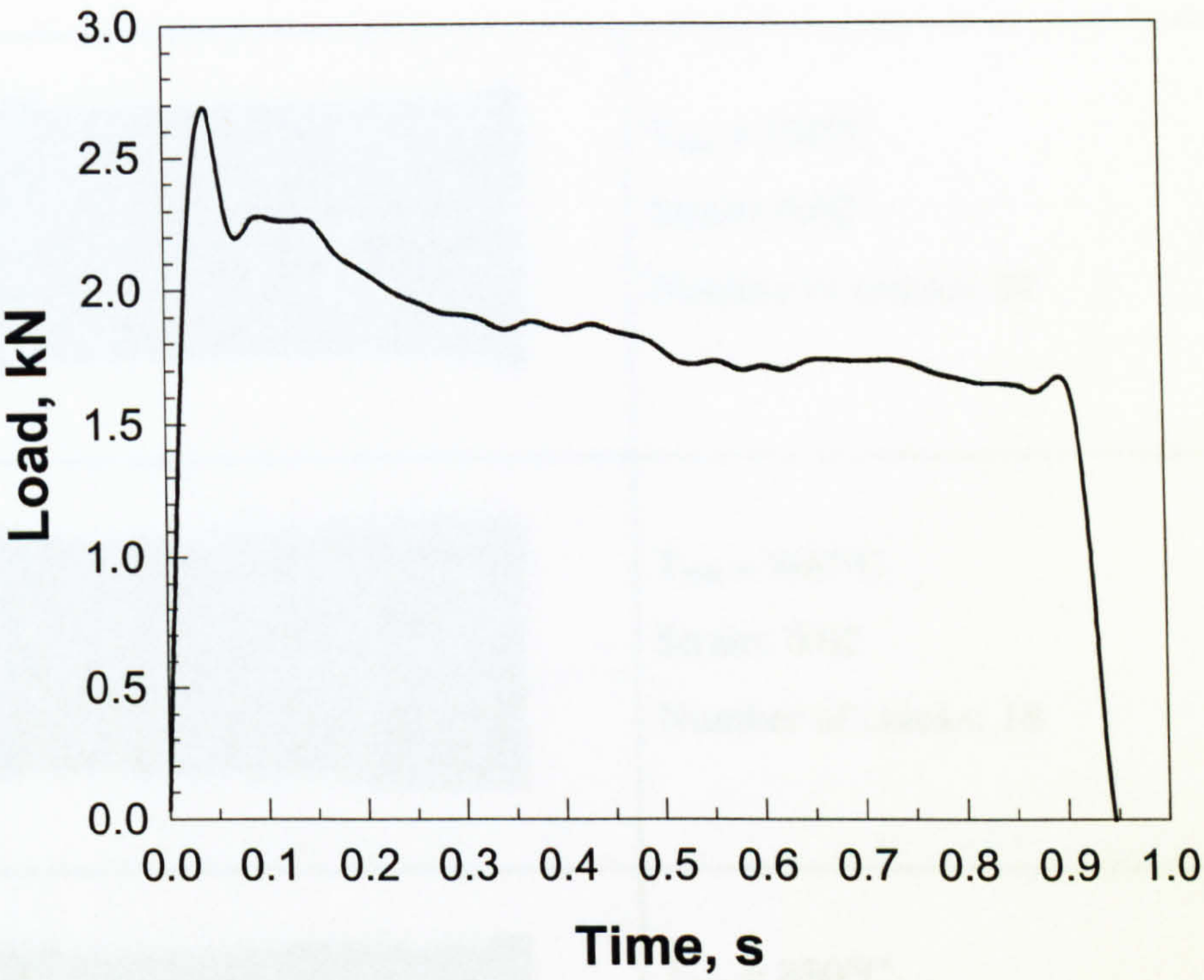

Figure 4.33. History plot of loading conditions during the tensile stage of the tensile-compressive test.

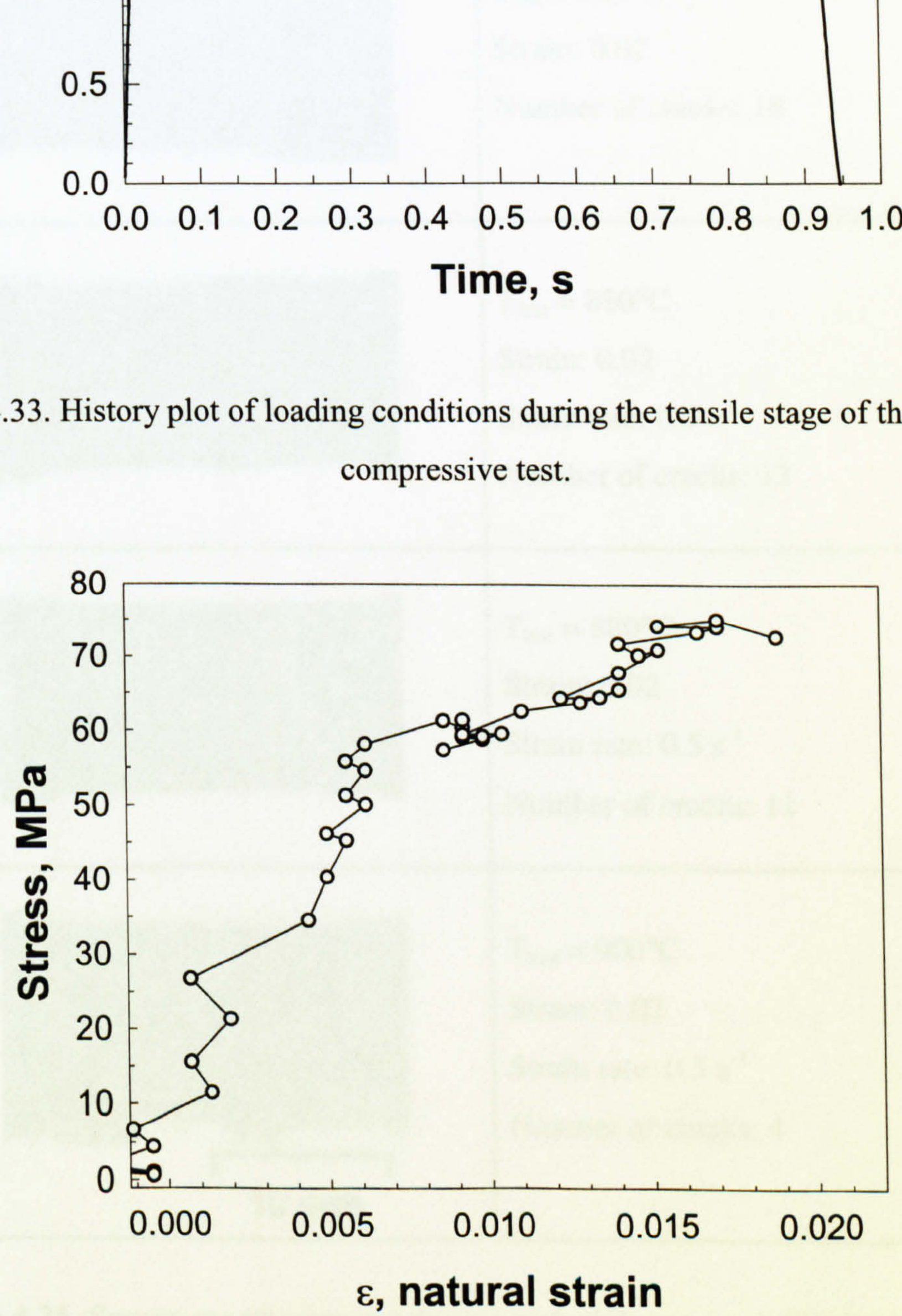

Figure 4.34. Typical stress-strain curve.

	T_{test} = 780°C Strain: 0.02 Number of cracks: 28
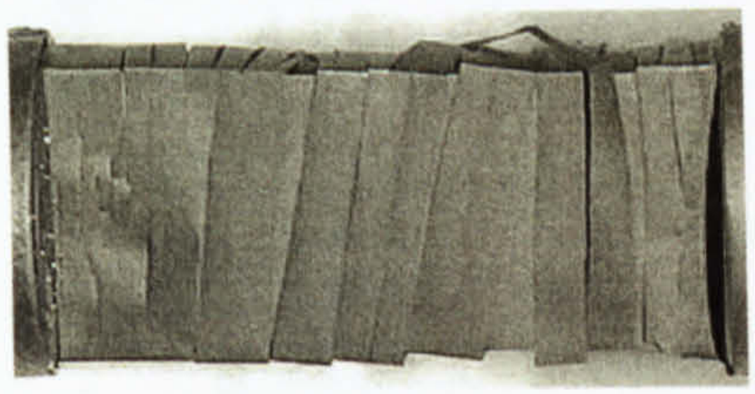	T_{test} = 800°C Strain: 0.02 Number of cracks: 18
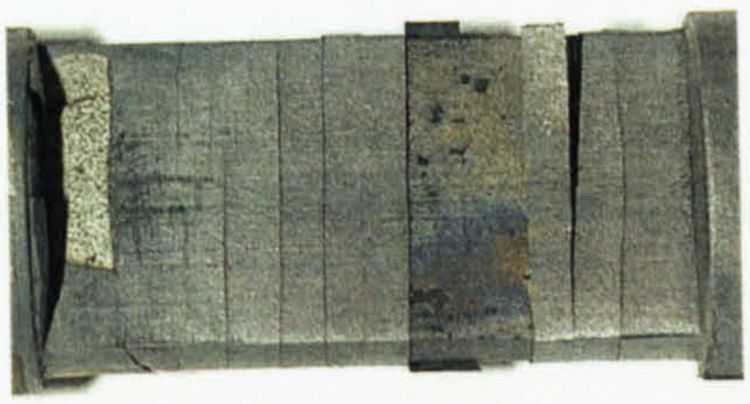	T_{test} = 880°C Strain: 0.02 Strain rate: 0.5 s^{-1} Number of cracks: 13
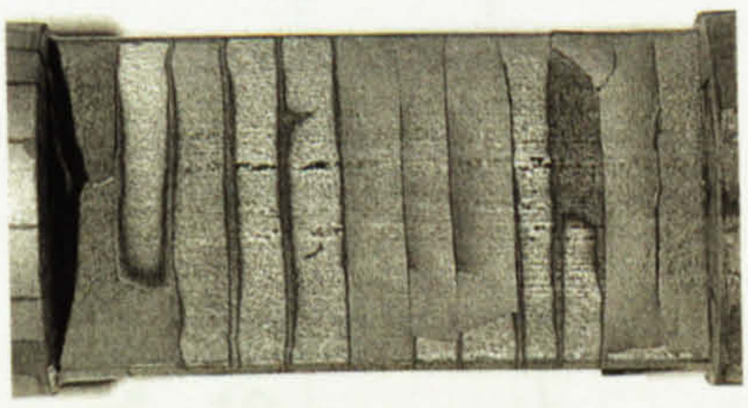	T_{test} = 880°C Strain: 0.02 Strain rate: 0.5 s^{-1} Number of cracks: 11
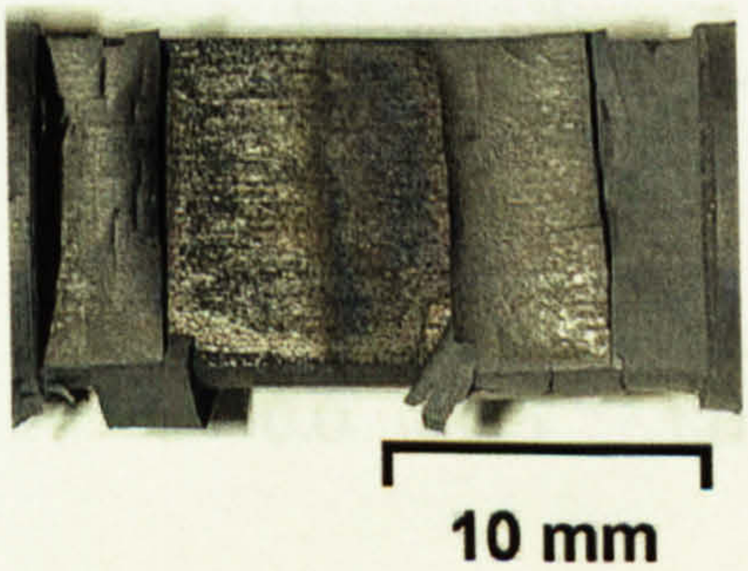	T_{test} = 900°C Strain: 0.02 Strain rate: 0.5 s^{-1} Number of cracks: 4

Figure 4.35. Specimens (thickness 3.5 mm) with different crack spacing value after they have been tested at different temperatures.

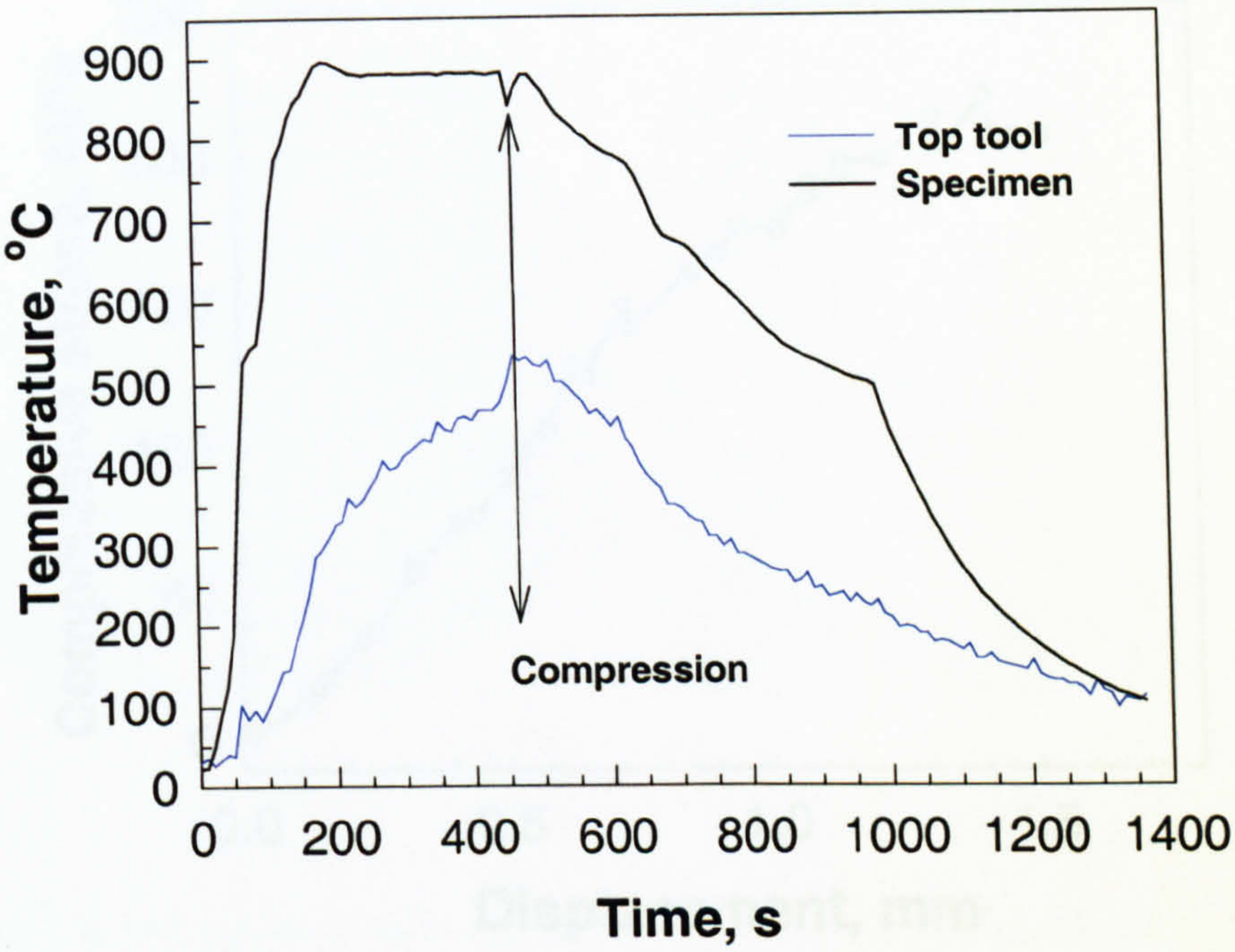

Figure 4.36. History plot of the temperatures before and after the compression test.

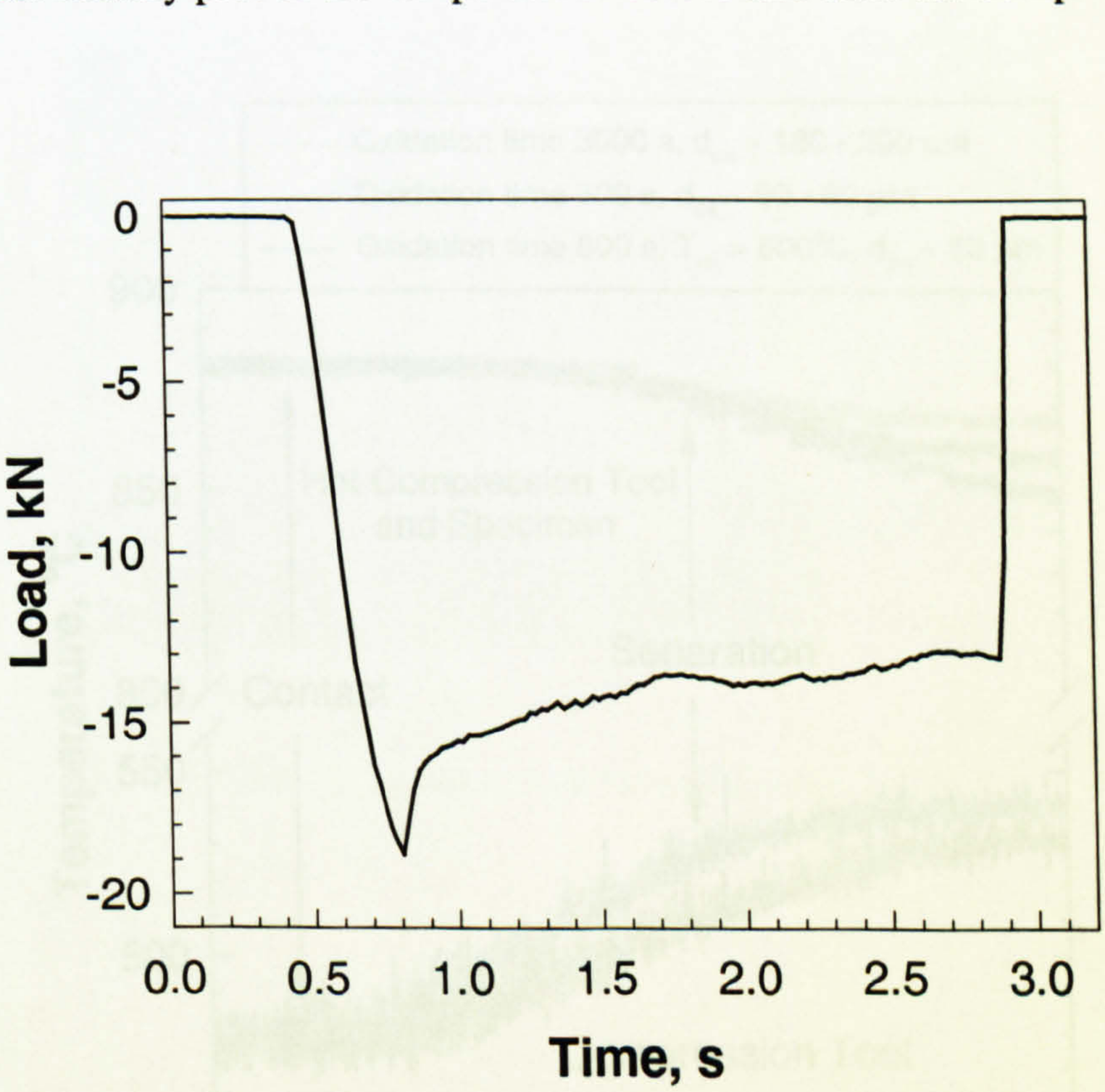

Figure 4.37. Raw data of measured load during the compression stage of the tension-compression test ($T_{specimen}$ = 880°C).

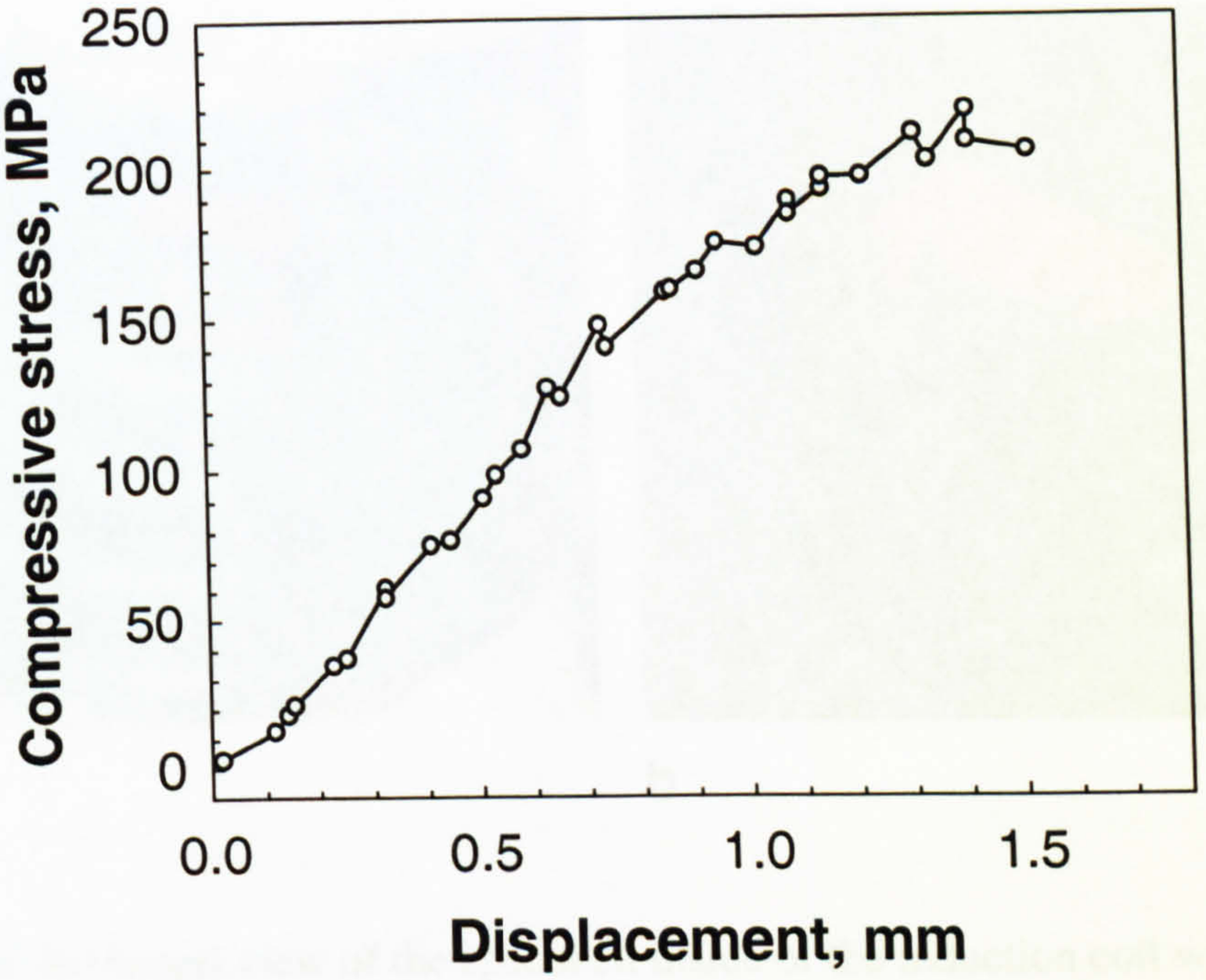

Figure 4.38. Compressive stresses at T_{test} = 880°C.

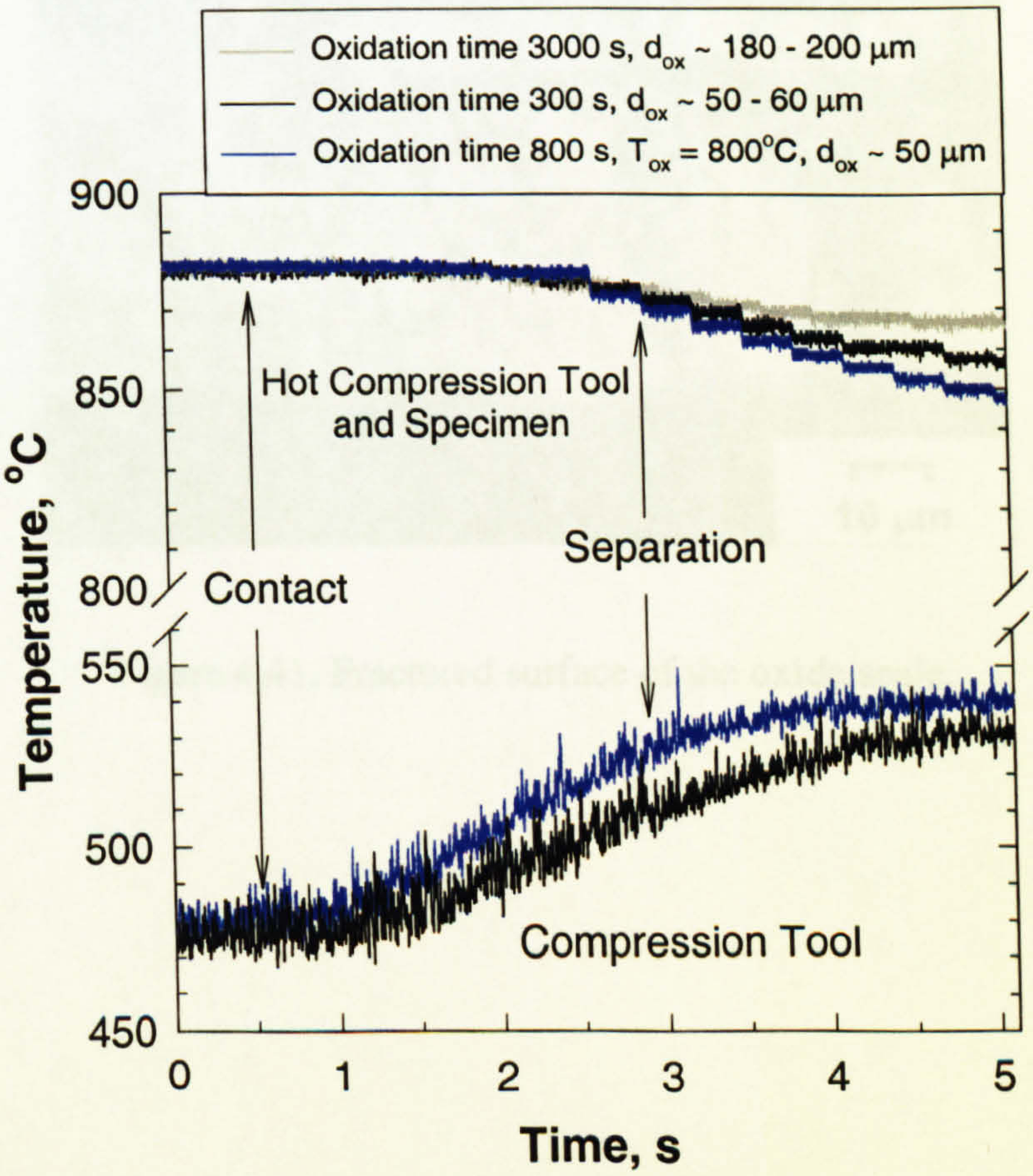

Figure 4.39. Temperature alteration during the tool-specimen contact.

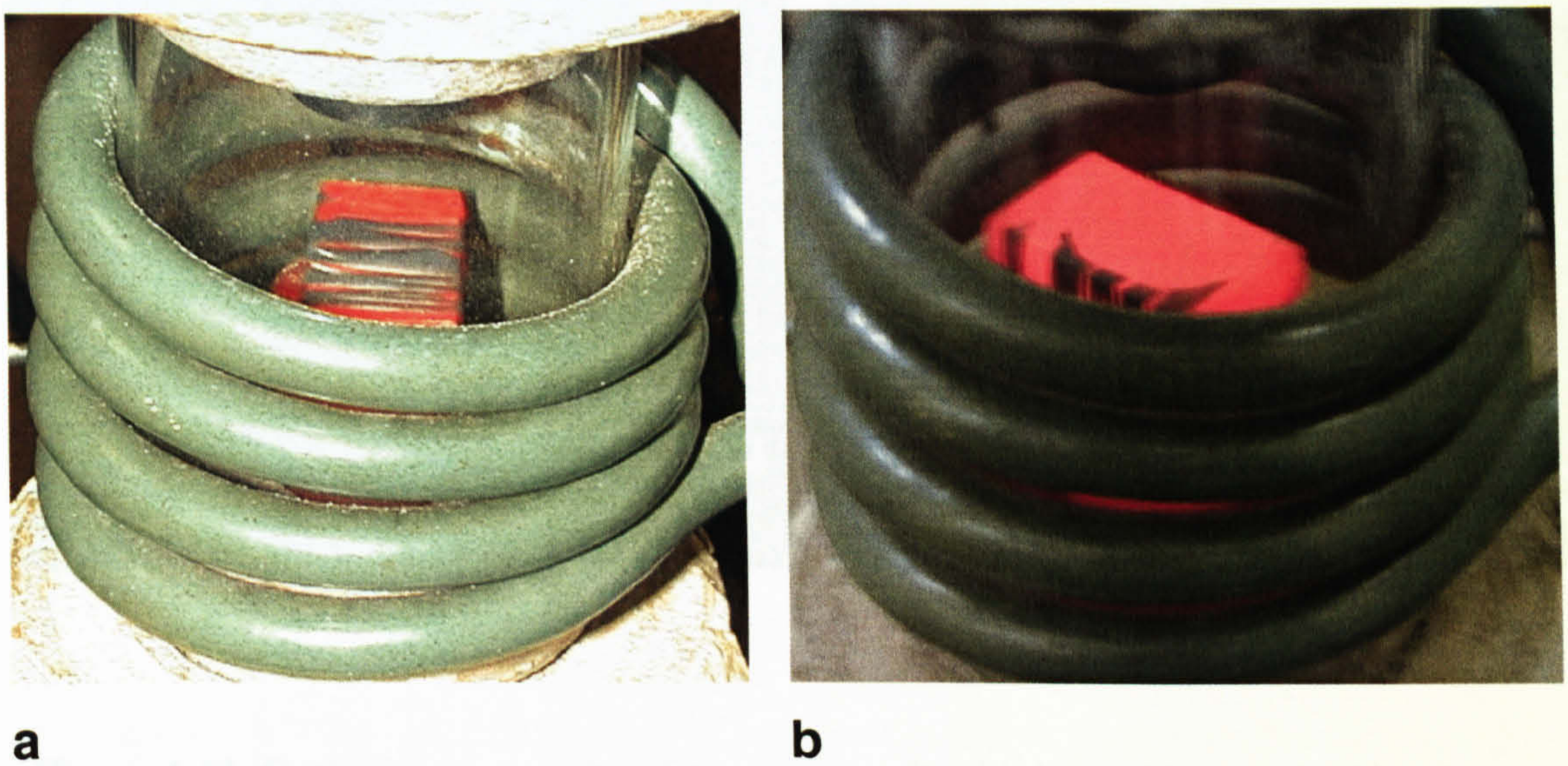

a b

Figure 4.40. Actual view of the specimen inside of the induction coil with cracked oxide scale a) before the compression test; b) after the compression test.

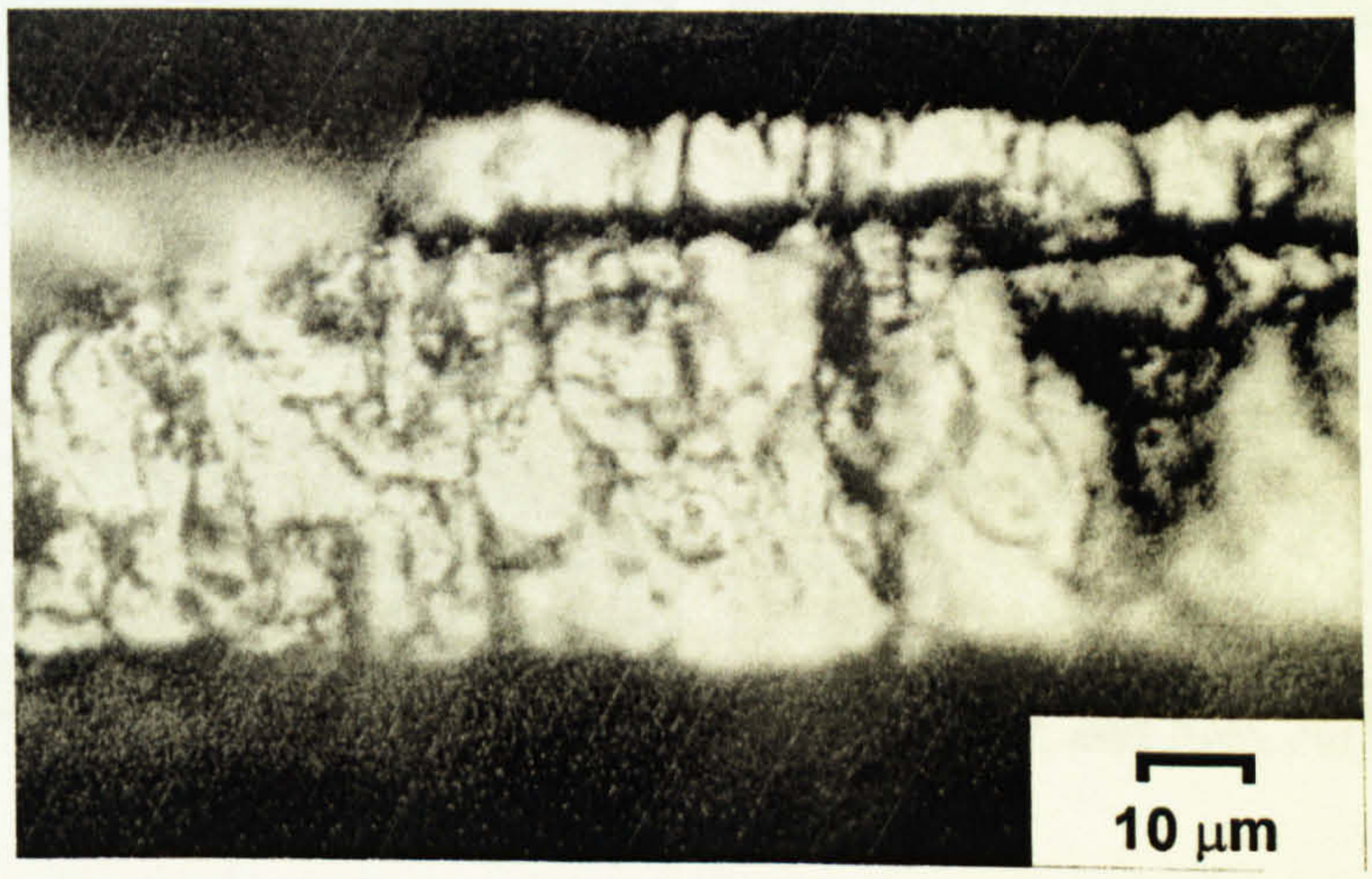

Figure 4.41. Fractured surface of the oxide scale.

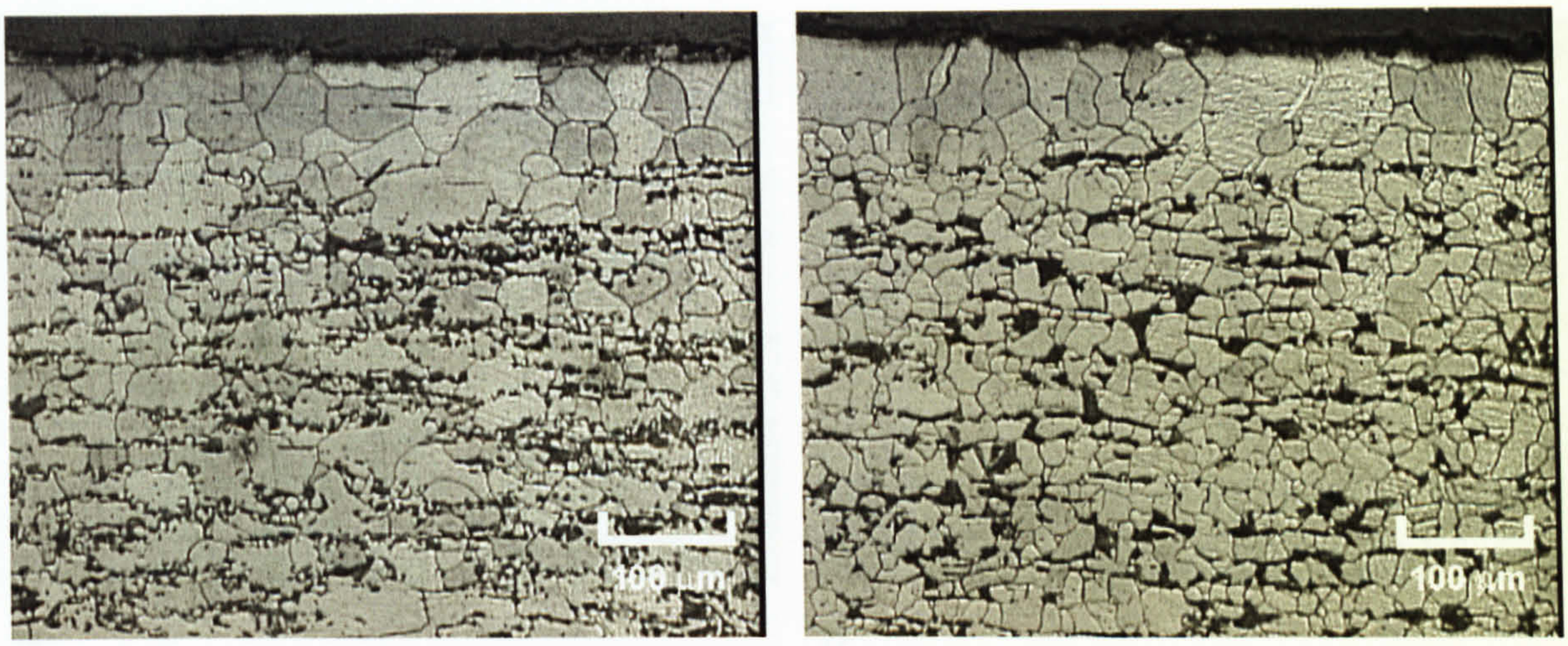

2-mm 4-mm

Figure 4.42. Optical micrographs of specimens after high-temperature tension tests.

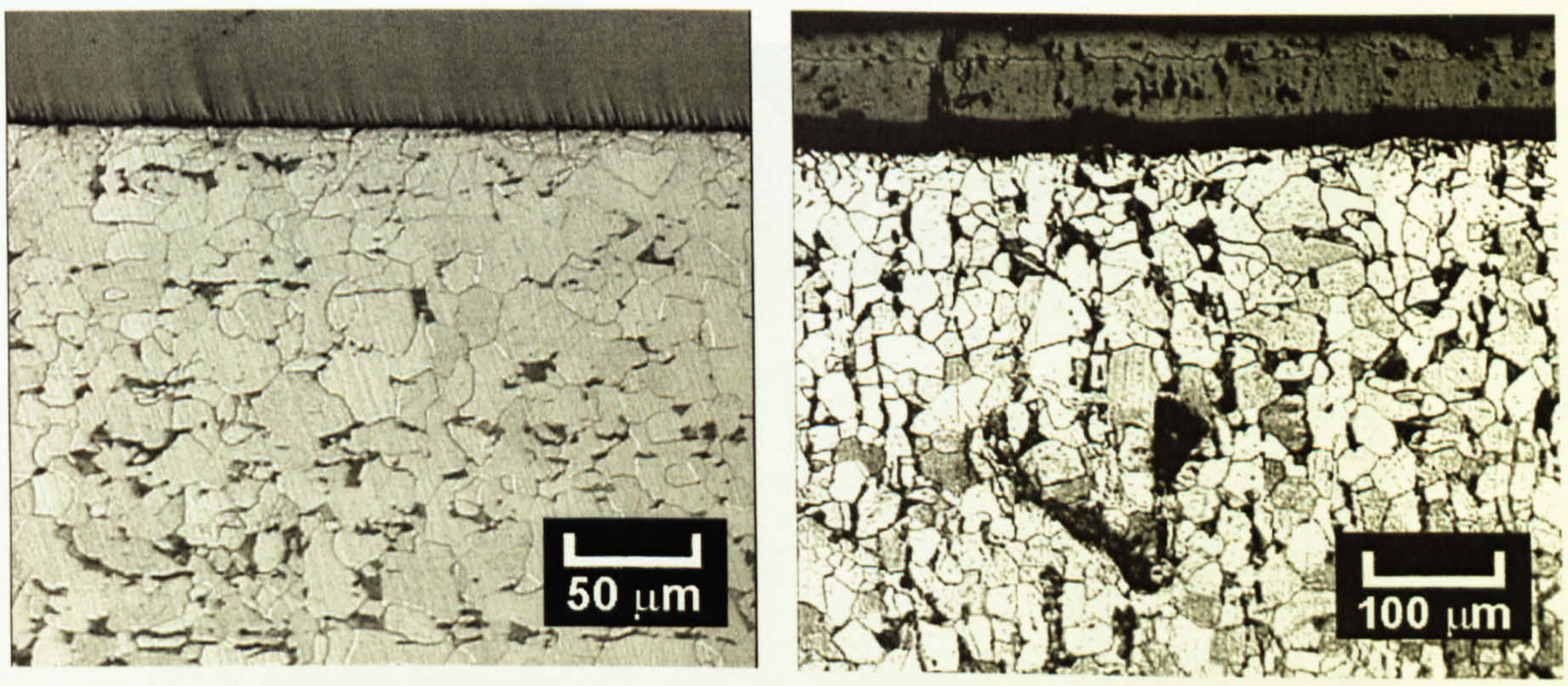

a b

Figure 4.43. Optical micrographs of specimens after high-temperature compression tests: a) T_{ox}= 1070°C, oxidation time is 300s, b) T_{ox}= 870°C, oxidation time is 3000s.

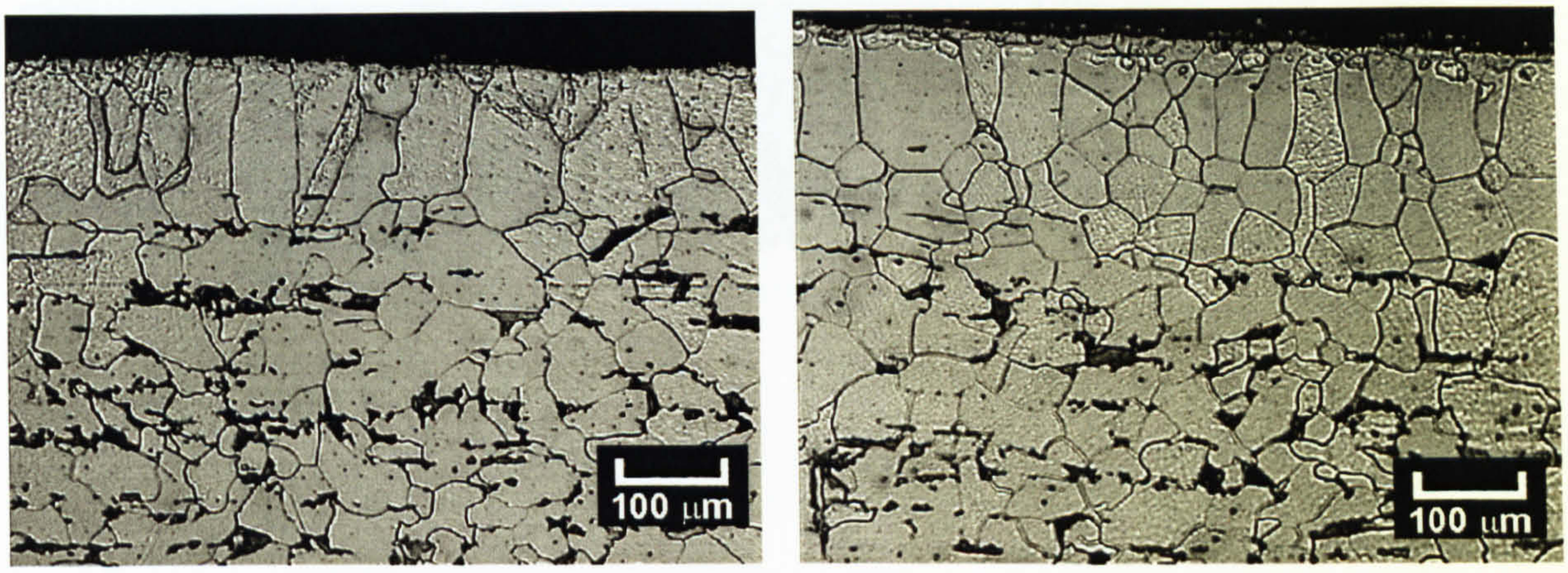

Figure 4.44. Optical micrographs of specimens after high-temperature tensile-compressive tests T_{ox}= 800°C, oxidation time is 800s, $T_{comp\ test}$= 880°C: a) "cold" side, b) "hot" side.

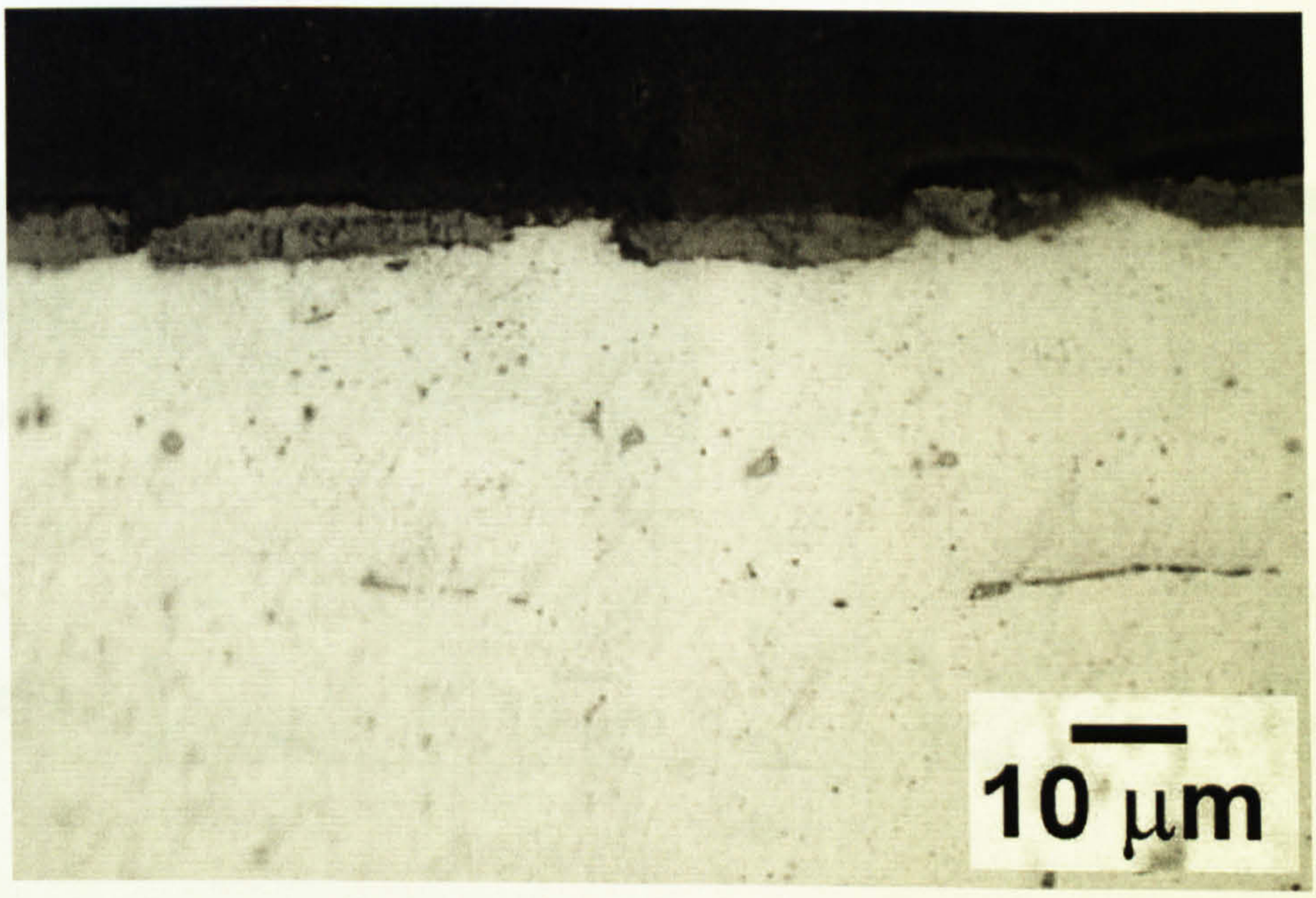

Figure 4.45. Optical micrographs of the cracked oxide scale after high-temperature tensile-compressive tests T_{ox}= T_{tests} = 880°C, oxidation time is 300s.

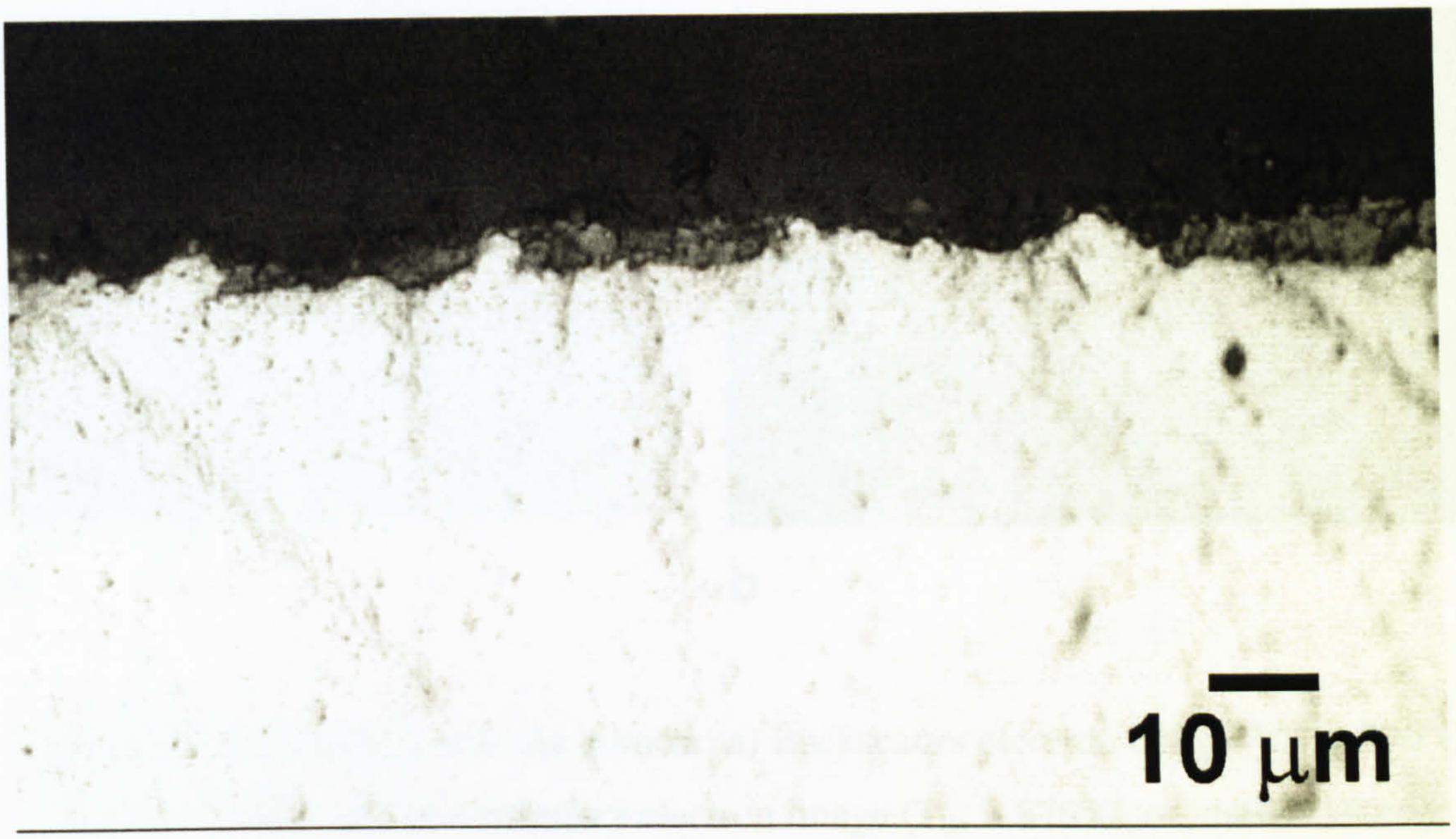

Figure 4.46. Optical micrographs of the remaining oxides and extruded steel after high-temperature tensile-compressive tests T_{ox}= 800°C, oxidation time is 800s, $T_{comptest}$ = 880°C.

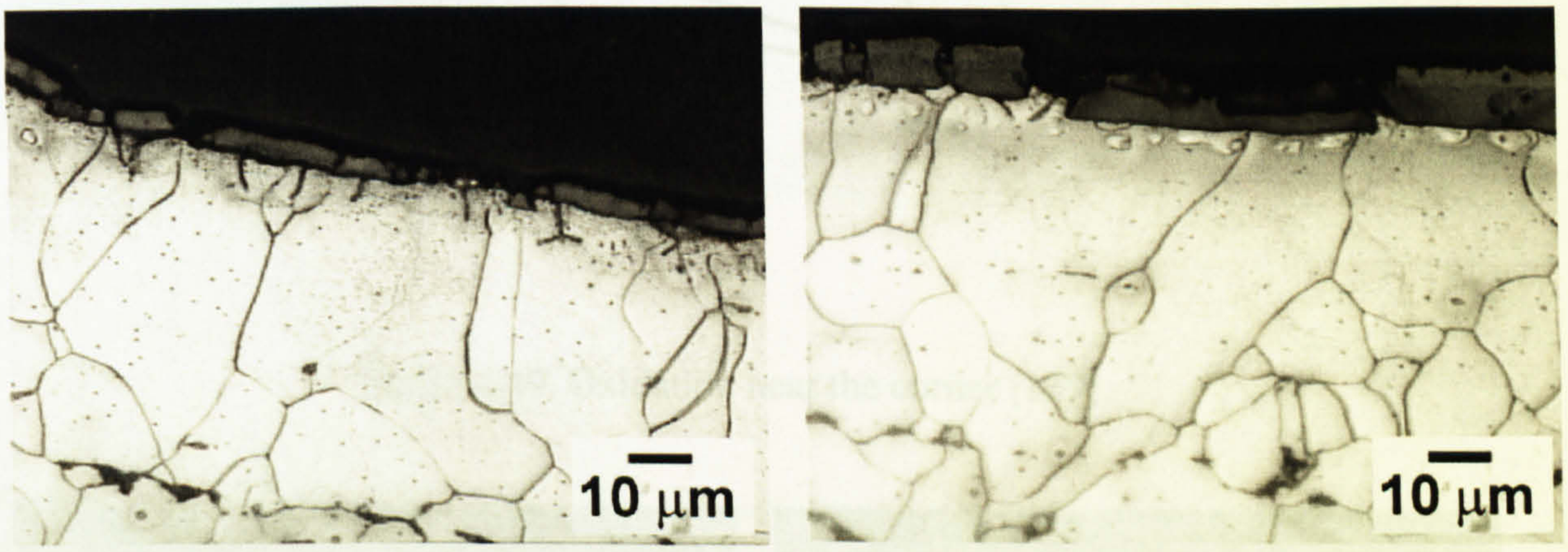

Figure 4.47. Optical micrographs of damage near the oxide-metal interface after compression (T_{ox}= T_{tests} = 880°C, oxidation time is 300s).

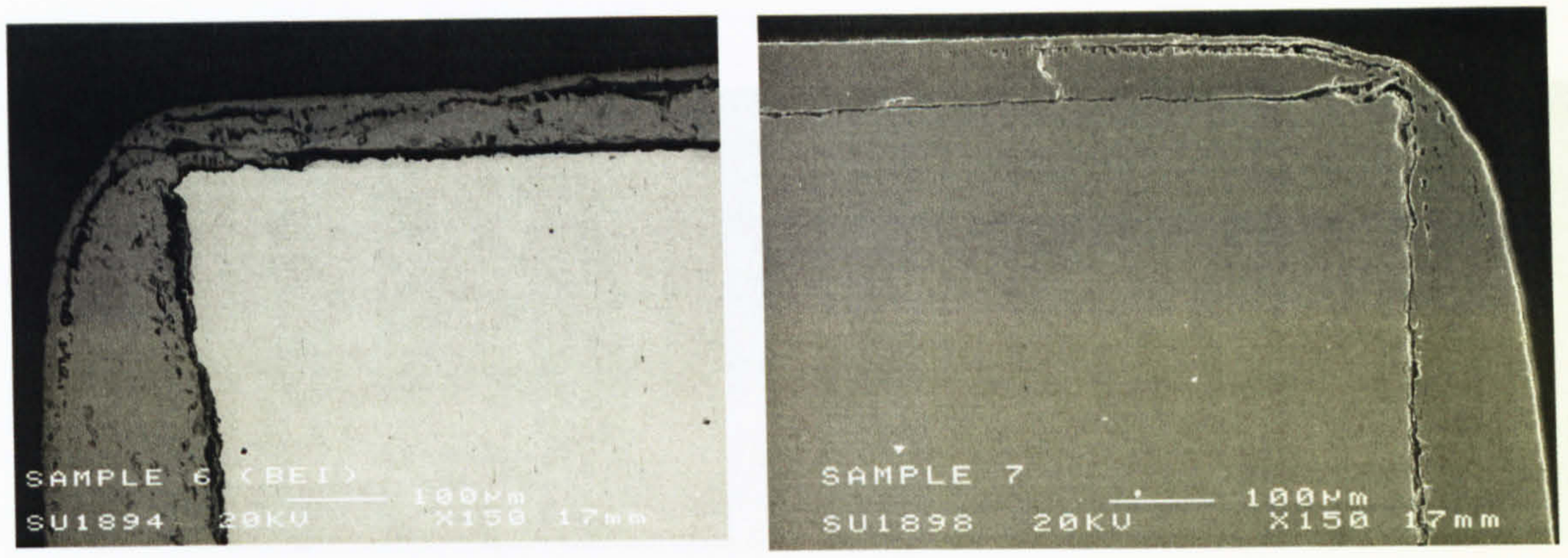

a b

Figure 4.48. Big blisters near the corners: a) Backscatter electron image (T_{ox} = 870°C oxidation 3000s) and b) Secondary electron image (T_{ox} = 870°C, oxidation 1500s).

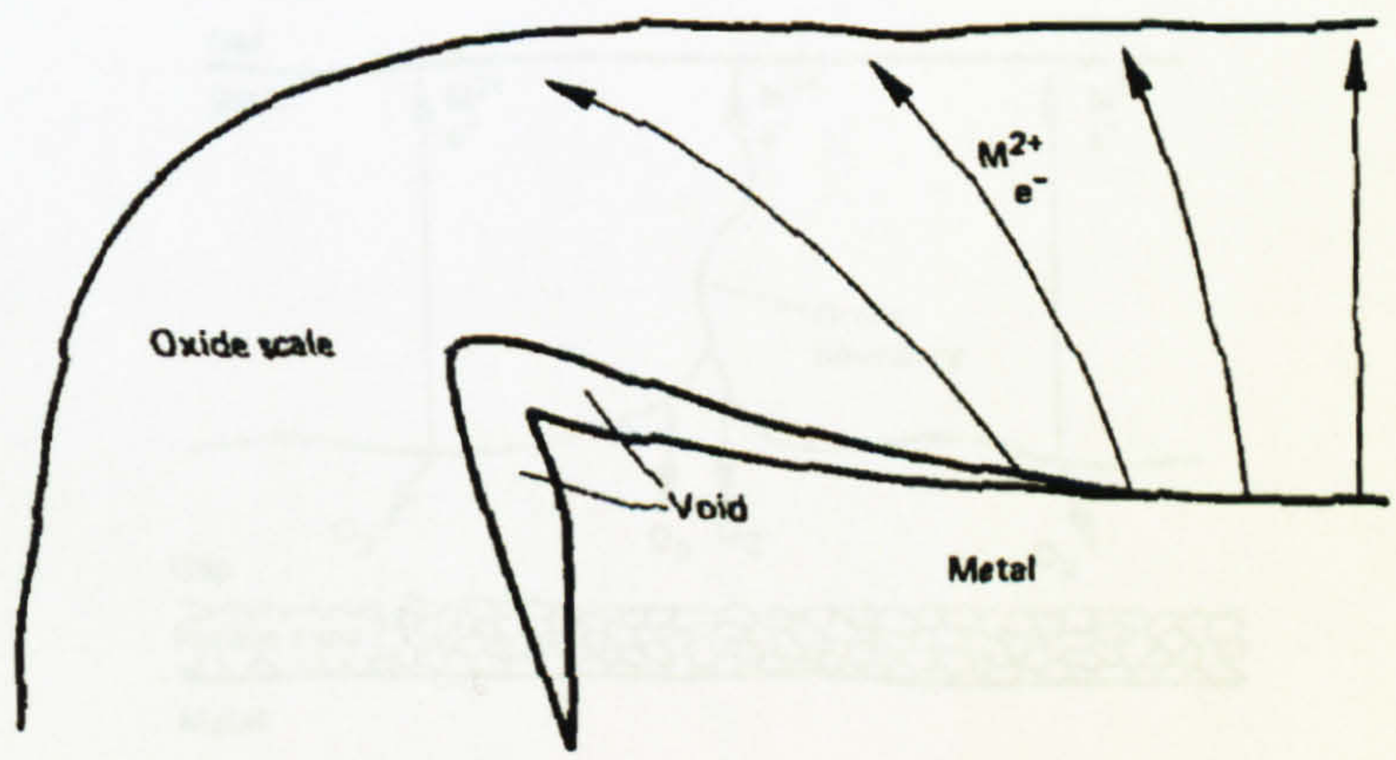

Figure 4.49. Oxidation near the corner [139].

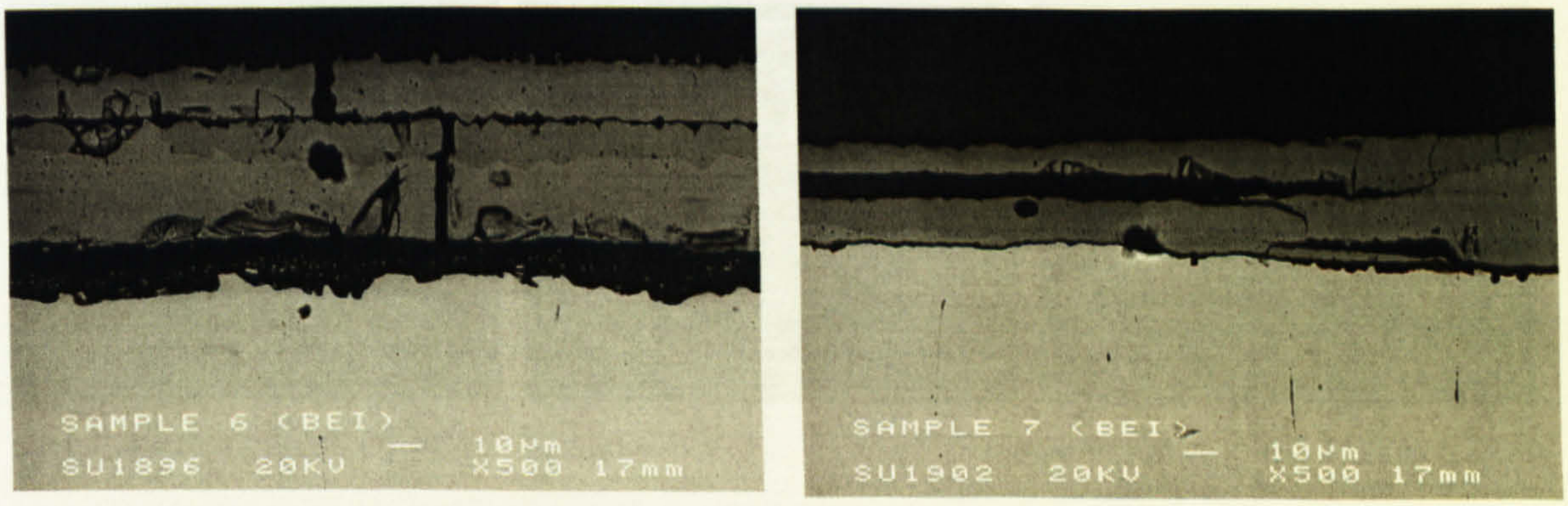

a b

Figure 4.50. a) Through-layers crack and delamination (T_{ox} = 870°C, oxidation 3000s), b) Delamination between layers (T_{ox} = 870°C, oxidation 1500s).

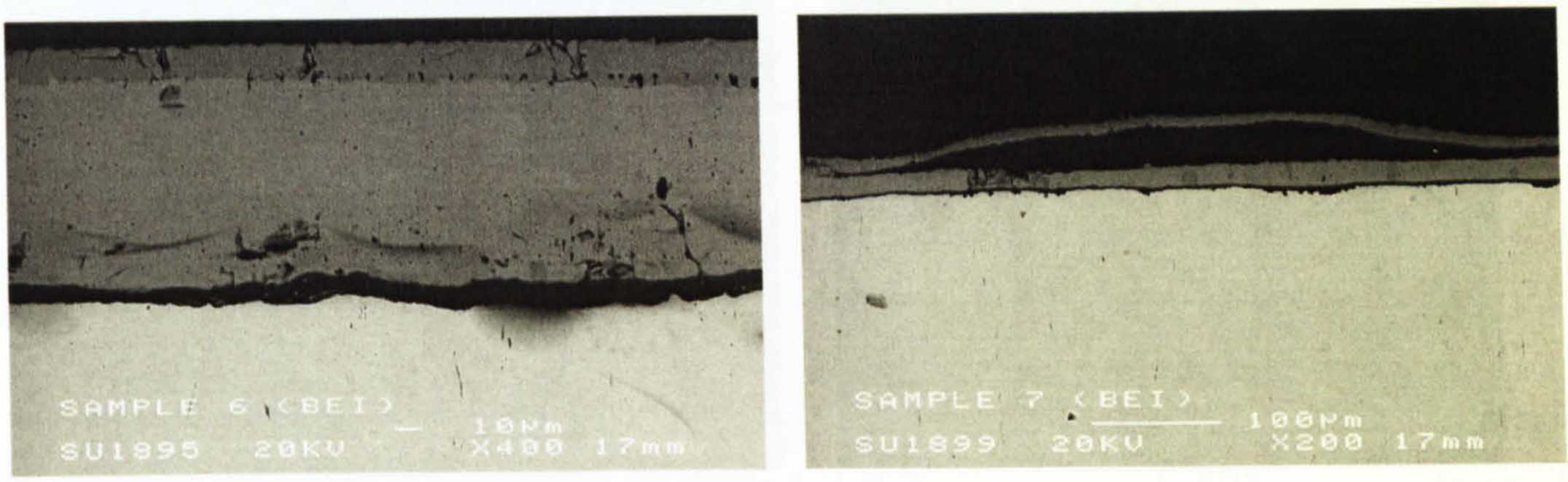

a b

Figure 4.51. a) Morphology of the dense oxide scale (T_{ox} = 870°C, oxidation 3000s), b) Big blister (T_{ox} = 870°C, oxidation 1500s).

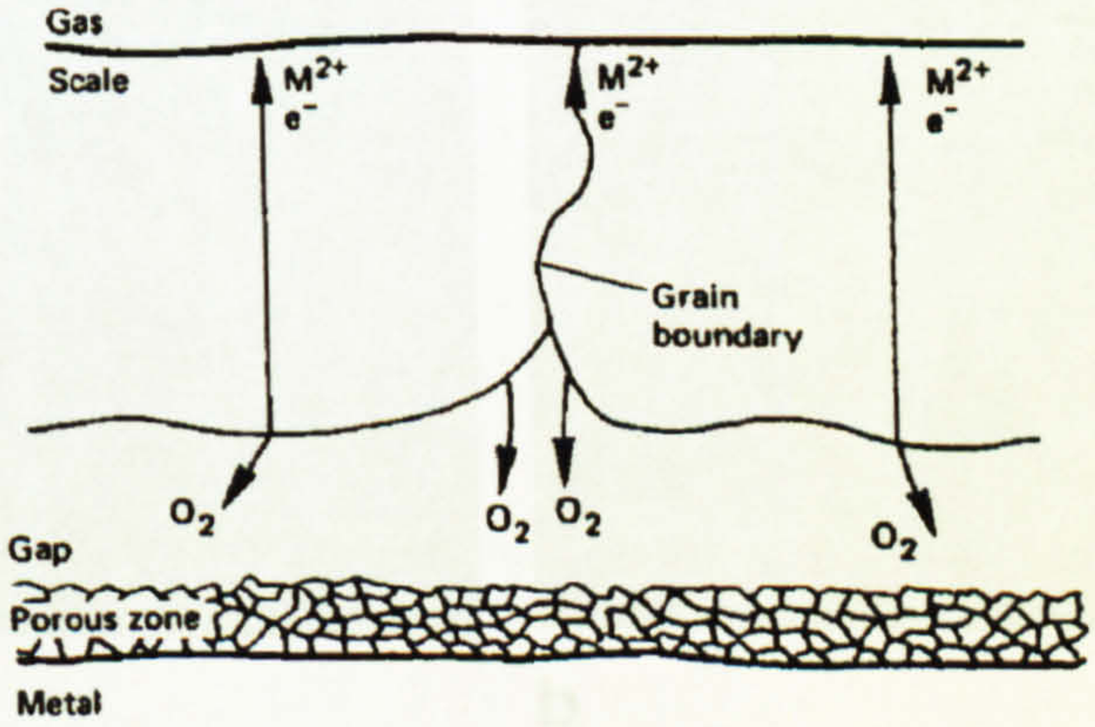

Figure 4.52. Oxidation process [139].

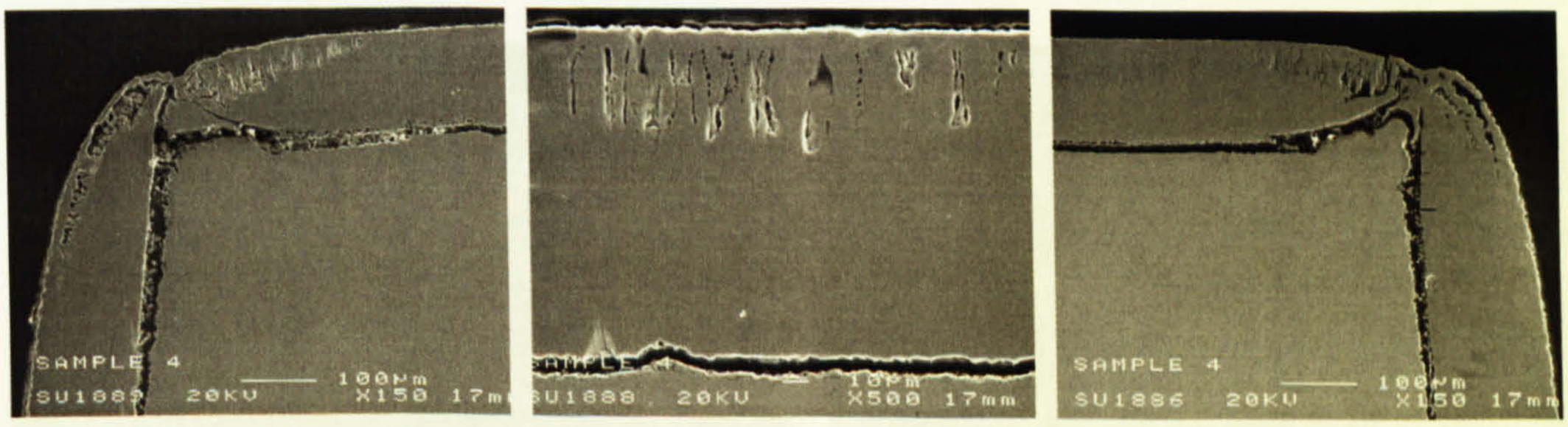

a b c

Figure 4.53. Oxide morphology near the corners and in the centre of the specimen (T_{ox} = 1000°C, oxidation 320s).

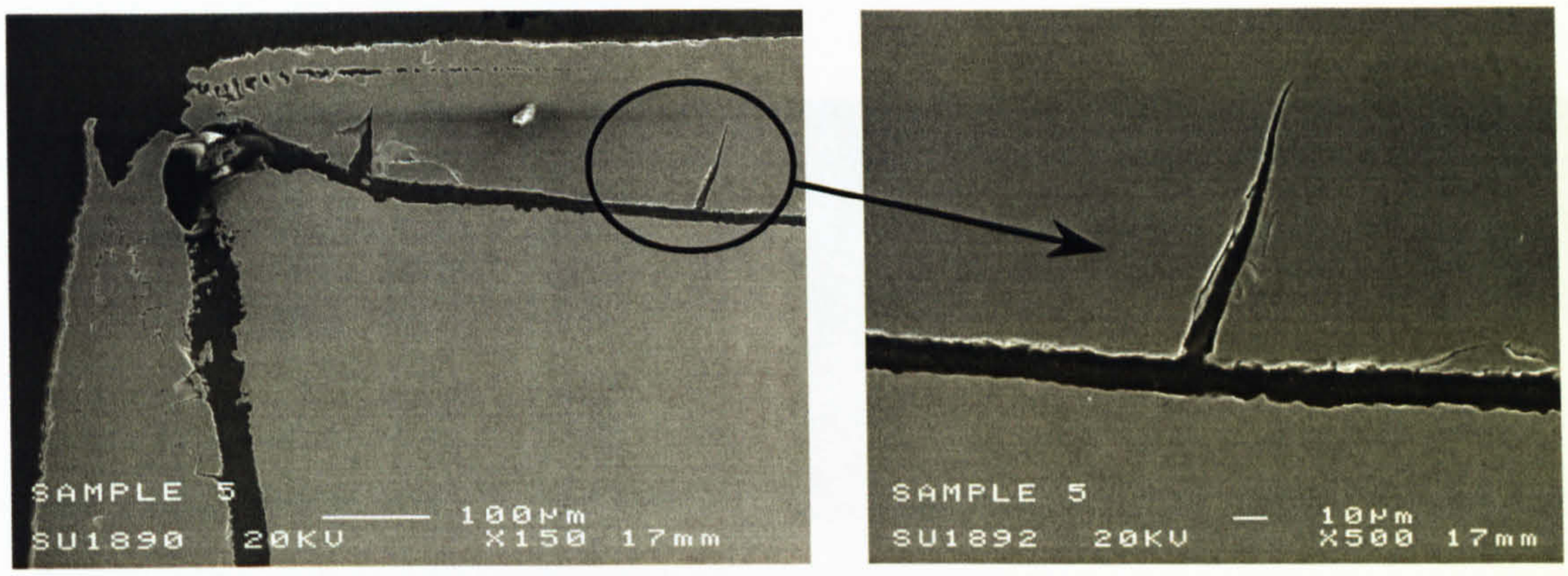

a b

Figure 4.54. a) Oxide scale near the corner with cracks, b) Magnified crack (T_{ox} = 1040°C, oxidation 300s).

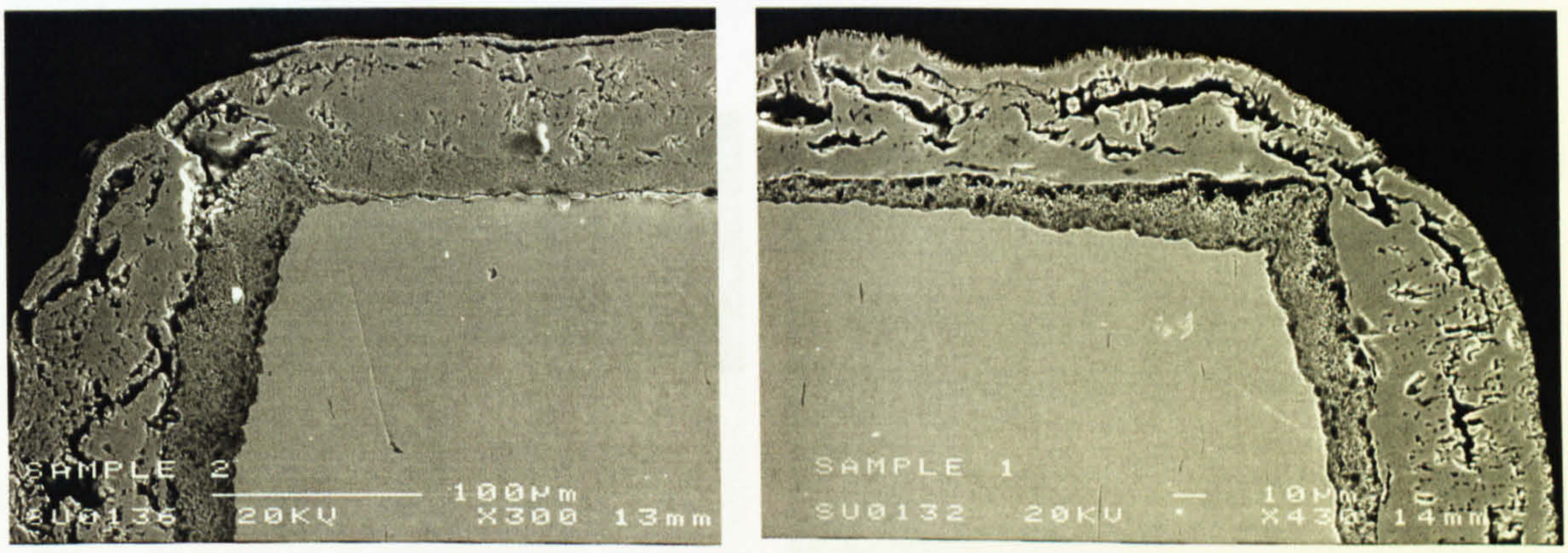

a b

Figure 4.55. Damage of oxide scales near the corner of specimens: a) T_{ox} = 870°C, oxidation 3000s, b) T_{ox} = 870°C, oxidation 1500s.

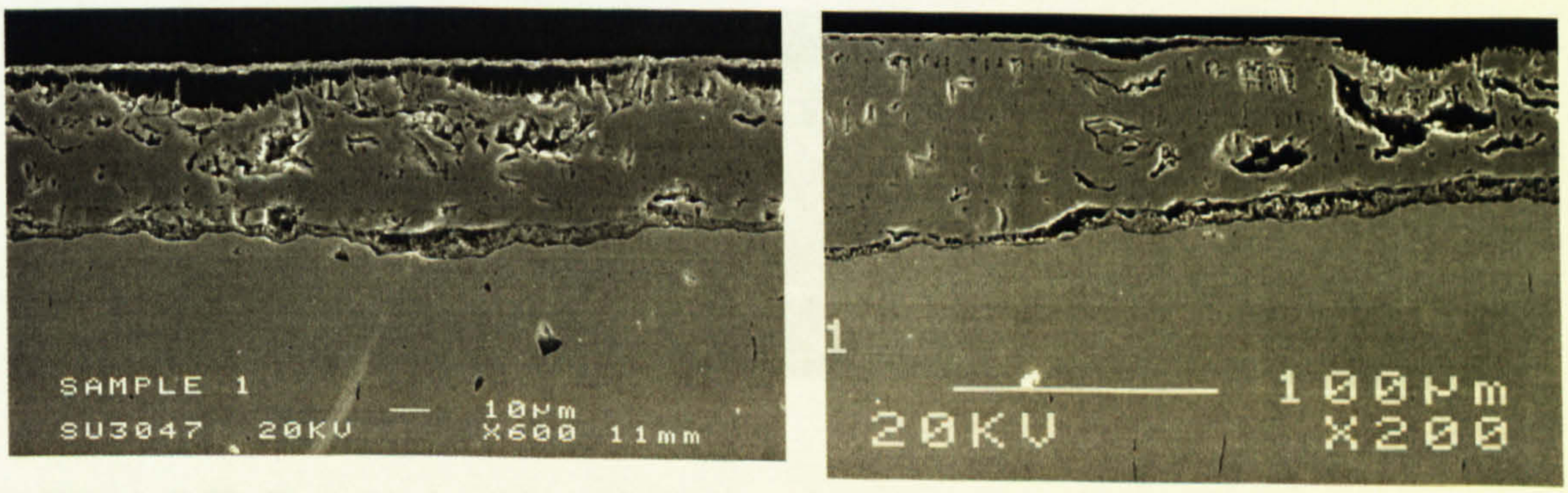

a b

Figure 4.56. a) Two failed blisters, b) Small and big blisters failure (T_{ox} = 870°C, oxidation 1500s).

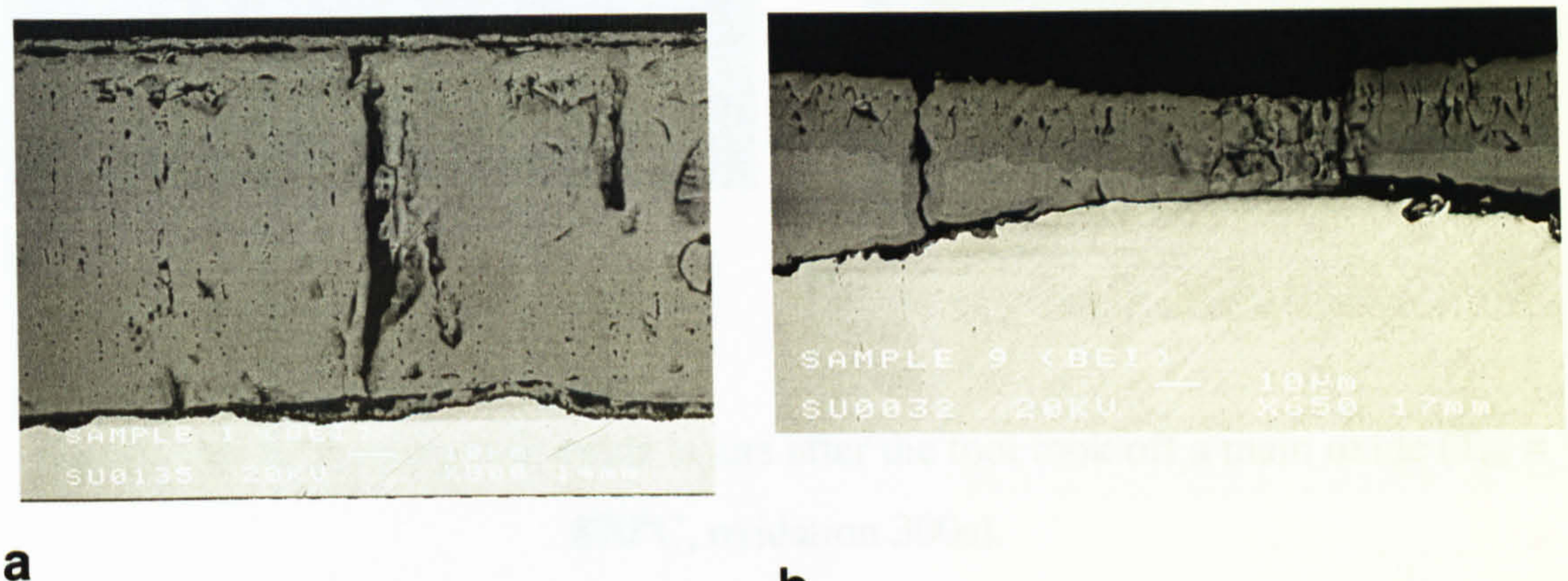

a b

Figure 4.57. Through-thickness cracks: a) T_{ox} = 870°C, oxidation 1500s, b) T_{ox} = 870°C, oxidation 300s.

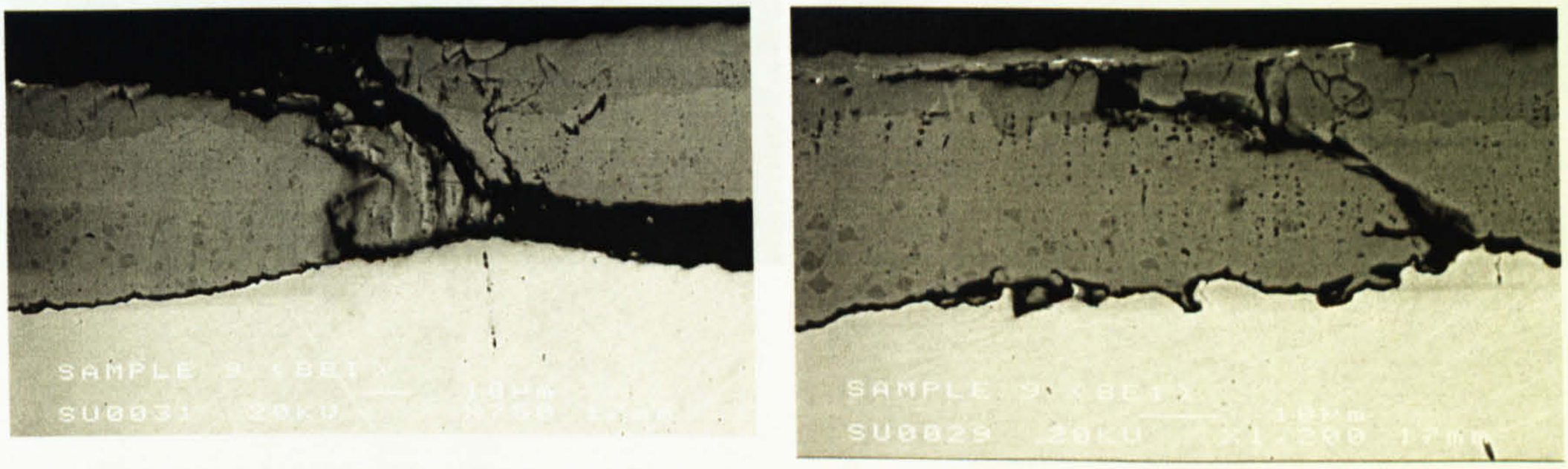

a b

Figure 4.58. Failure of oxide scales (T_{ox} = 870°C, oxidation 300s).

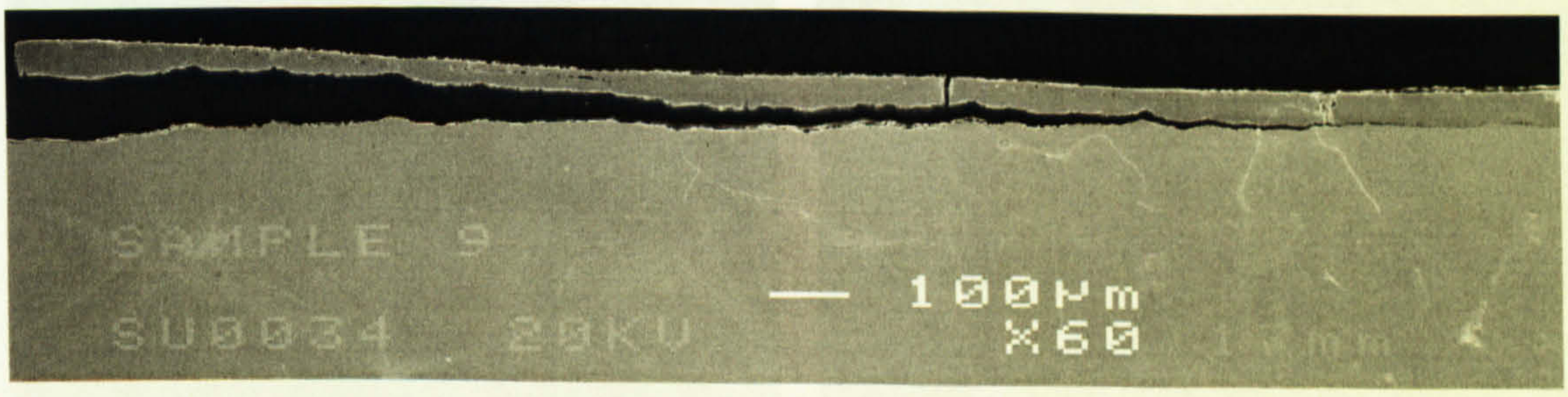

Figure 4.59. Separated oxide scale on the specimen (T_{ox} = 870°C, oxidation 300s).

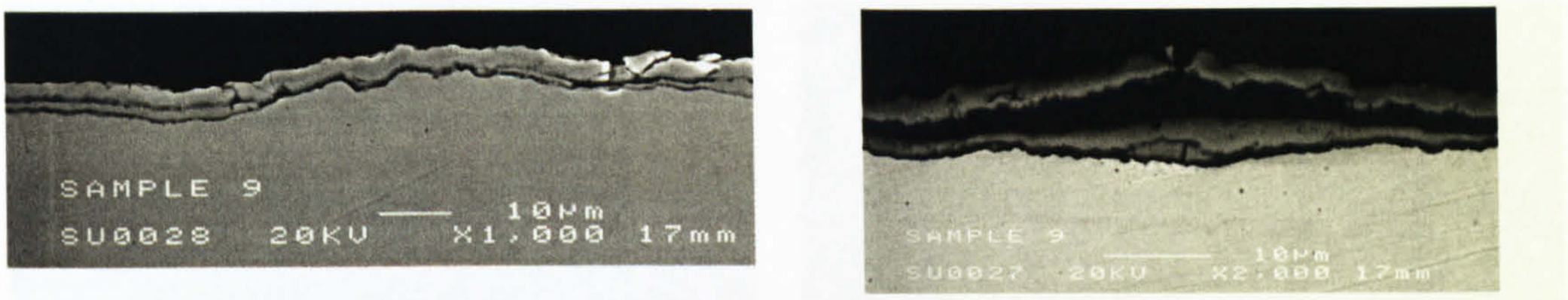

a b

Figure 4.60. Remaining thin oxide layers after the tool took off a main oxide (T_{ox} = 870°C, oxidation 300s).

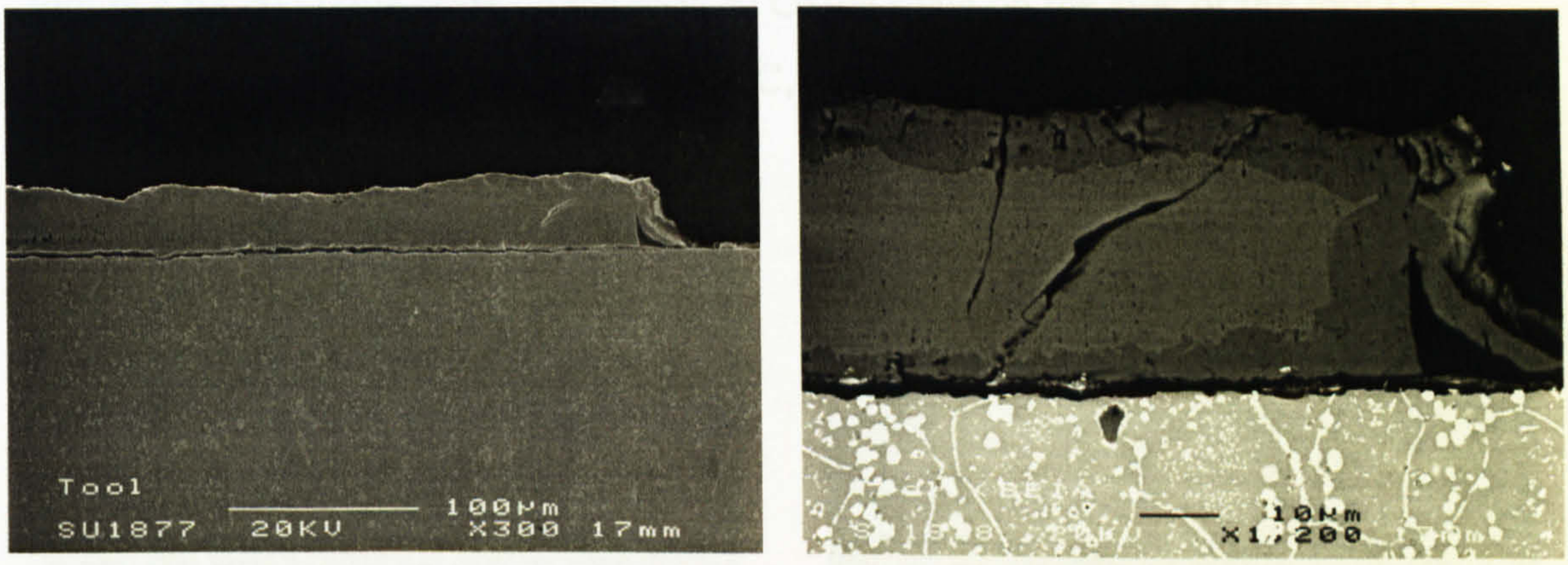

a b

Figure 4.61. Verge of the oxide scale on the tool (T_{ox} = 870°C, T_{tool} = 760°C, oxidation 300s).

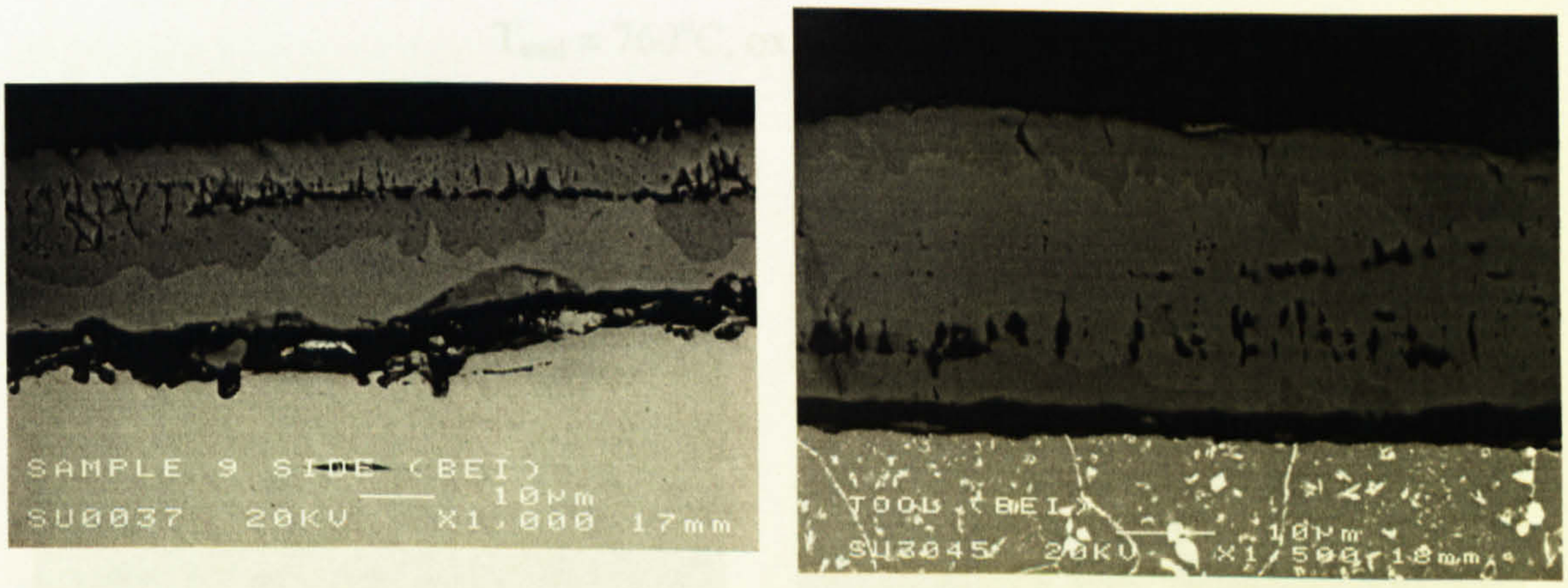

a b

Figure 4.62. a) Oxide scale on the specimen, b) Adhered oxide scale on the tool (T_{ox} = 870°C, T_{tool} = 760°C, oxidation 300s).

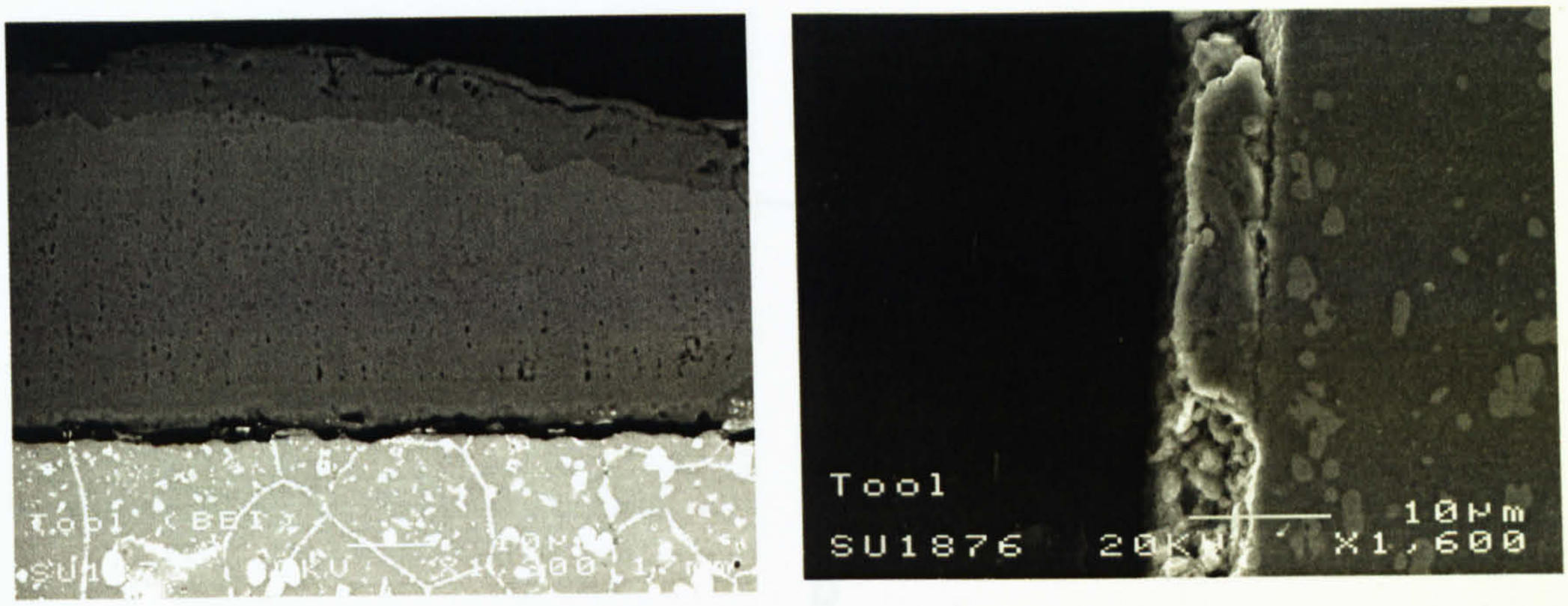

a b

Figure 4.63. a) Oxide scale on the tool, b) Oxide scale on the side of the tool (T_{ox} = 870°C, T_{tool} = 760°C, oxidation 300s).

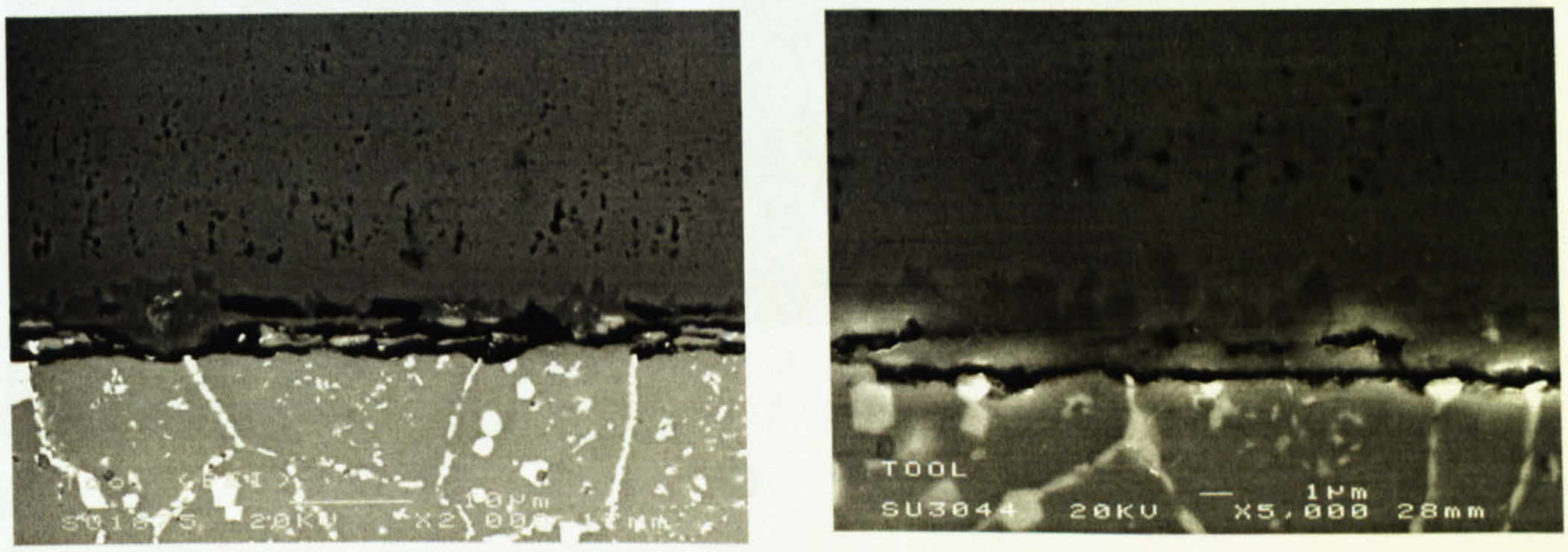

a b

Figure 4.64. Two kinds of oxide scales adhered each other on the tool (T_{ox} = 870°C, T_{tool} = 760°C, oxidation 300s).

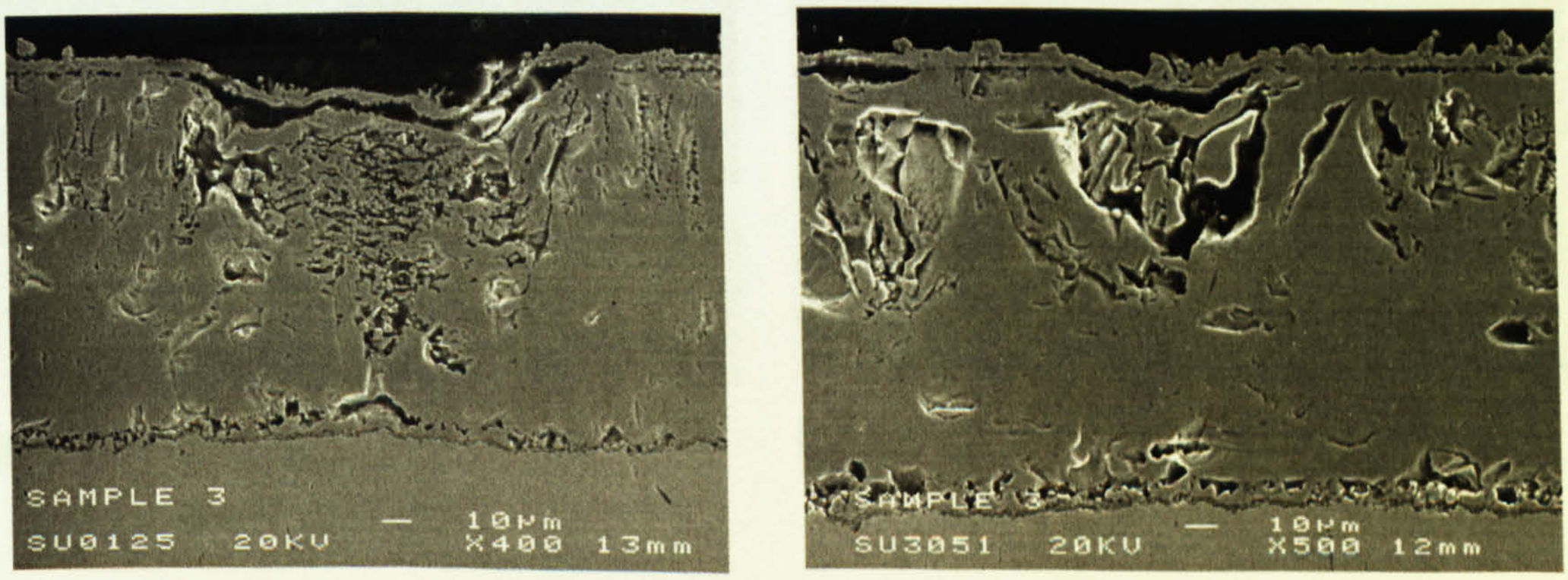

a b

Figure 4.65. a) Big and b) Small blisters failure (T_{ox} = 970°C, oxidation 800s).

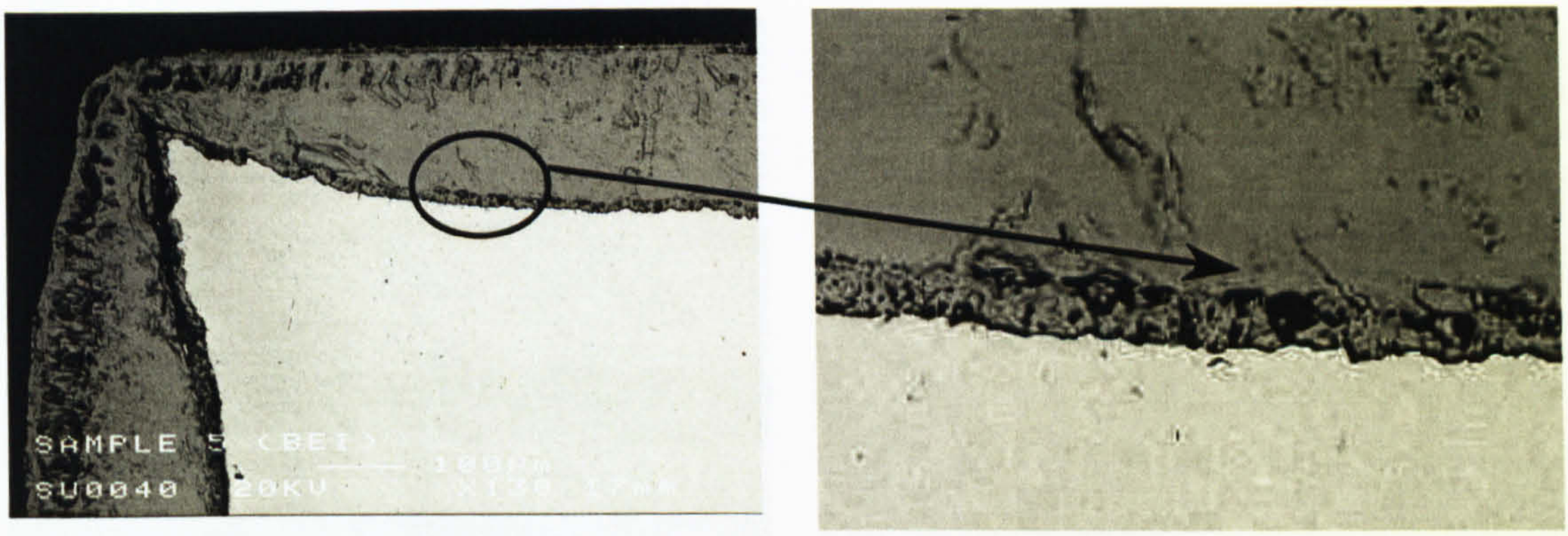

a b

Figure 4.66. a) Damage of oxide scales near the corner and b) Closure of the crack (T_{ox} = 970°C, oxidation 1500s).

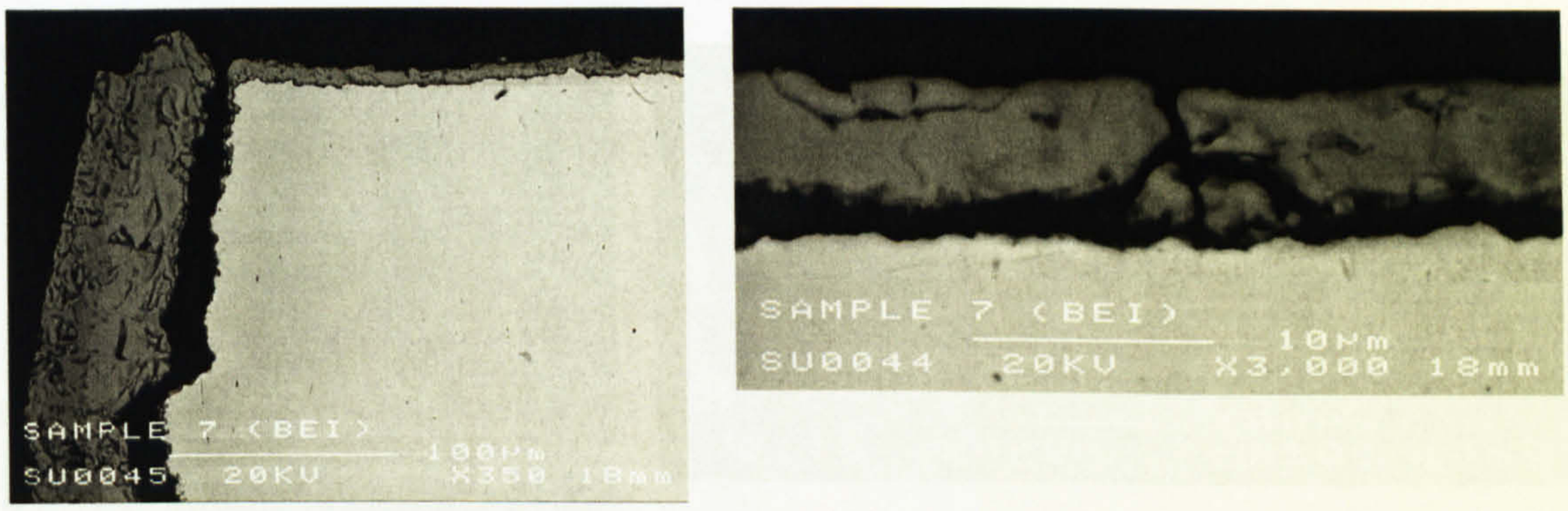

a b

Figure 4.67. Remaining thin oxide layers after the tool took off a main oxide (T_{ox} = 970°C, oxidation 100s).

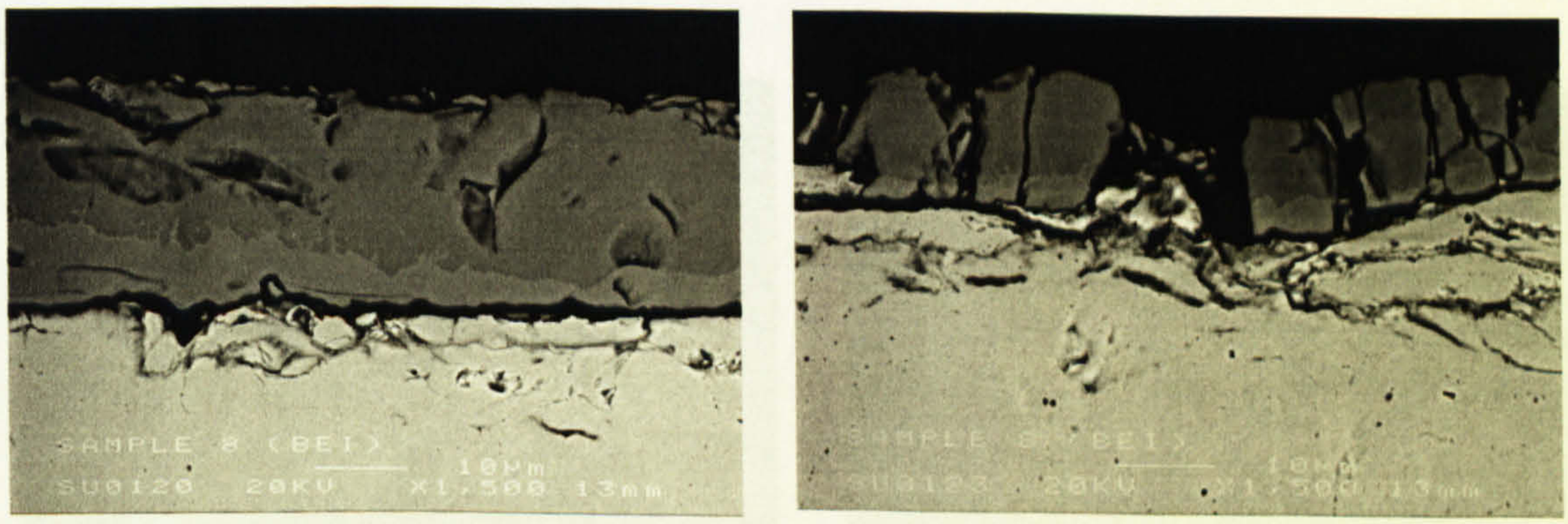

a b

Figure 4.68. a) Morphology of the thin oxide scale and b) Oxide islands and substrate yielding (T_{ox} = 970°C).

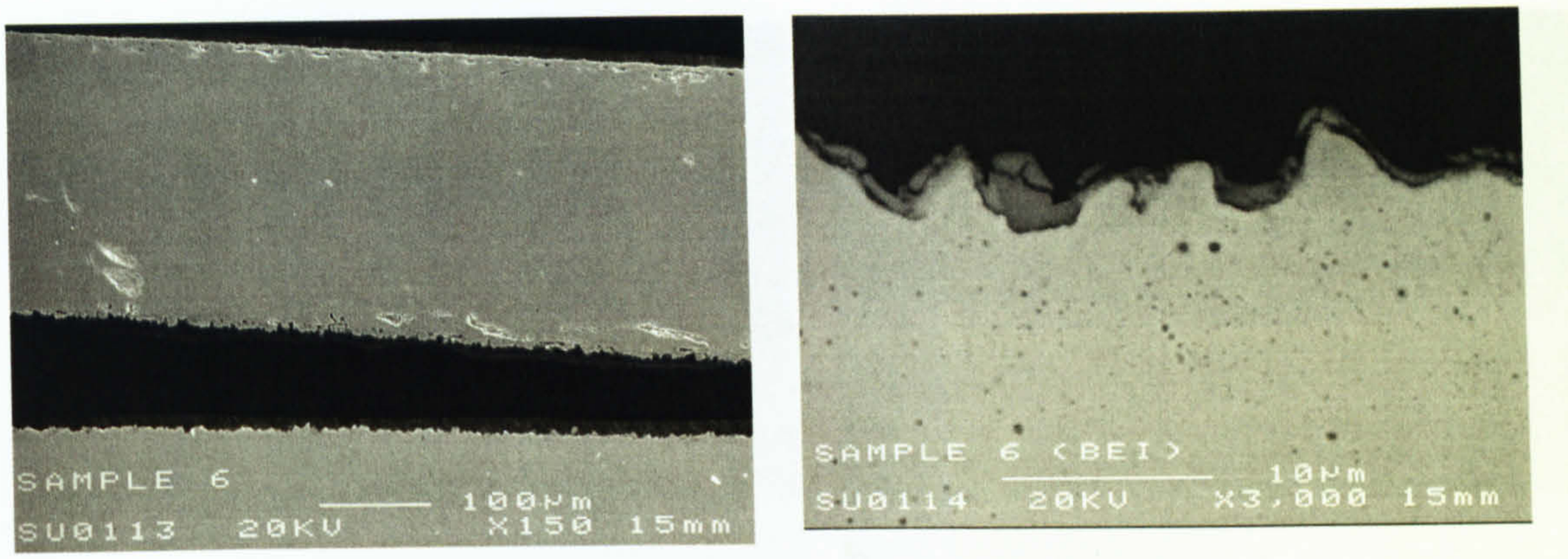

a b

Figure 4.69. a) Spalled thick oxide scale and b) Traces of oxide remains on the metal substrate (T_{ox} = 1070°C, oxidation 800s).

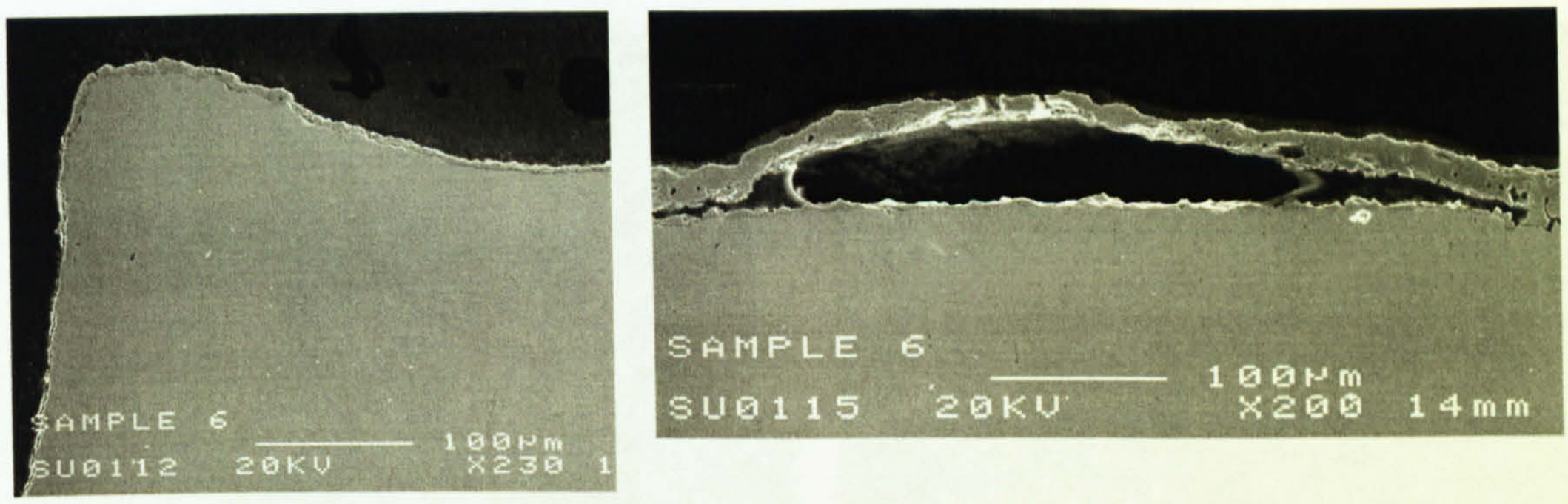

a b

Figure 4.70. a) Specimens corner view with remaining oxide scales, b) The big blister on the surface (T_{ox} = 1070°C, oxidation 800s).

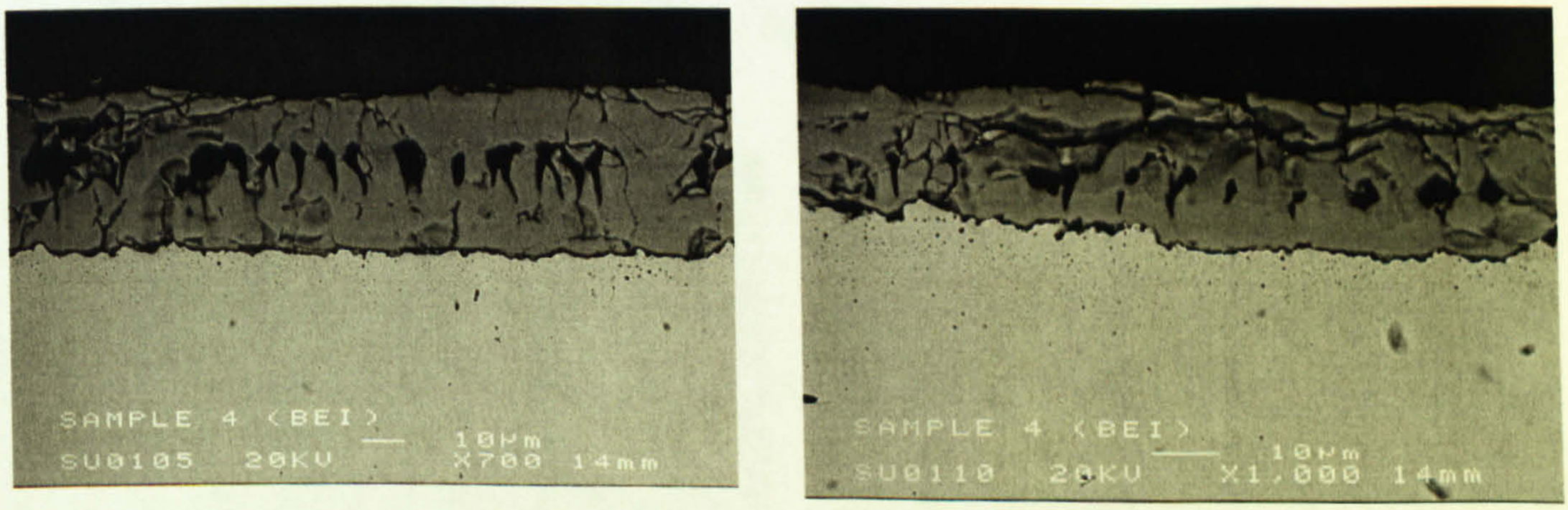

a b

Figure 4.71. a) Scale with vertical cracking and b) Scale with horizontal cracking (T_{ox} = 1070°C, oxidation 300s).

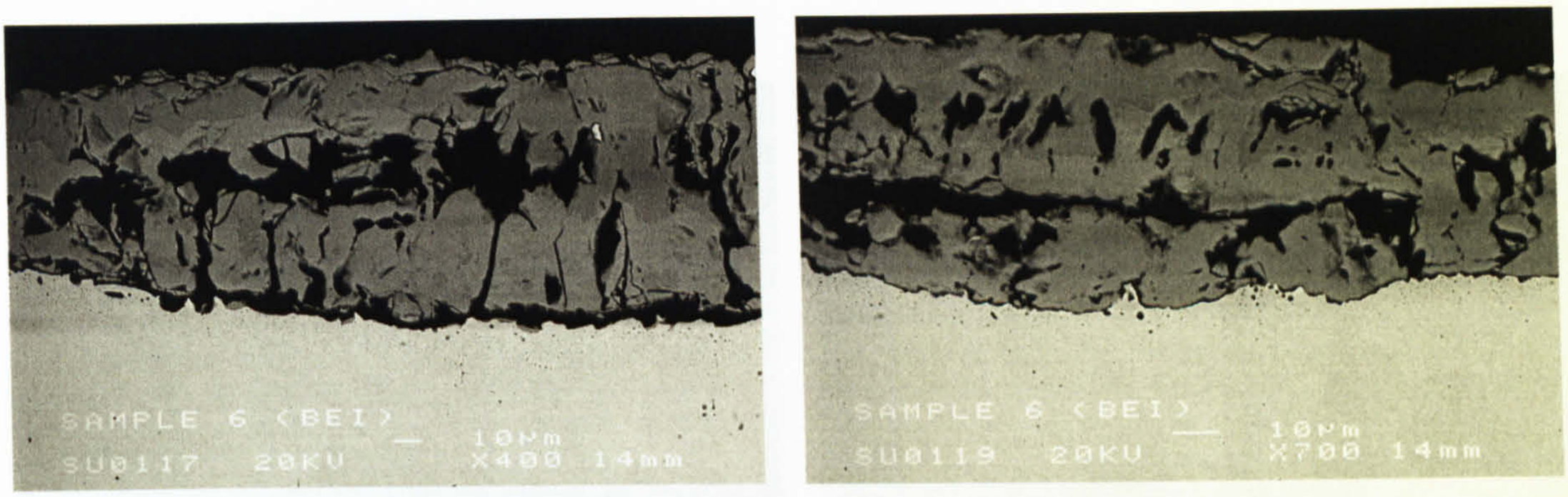

a b

Figure 4.72. a) Damaged oxide scale, b) Delamination inside the scale (T_{ox} = 1070°C, oxidation 800s).

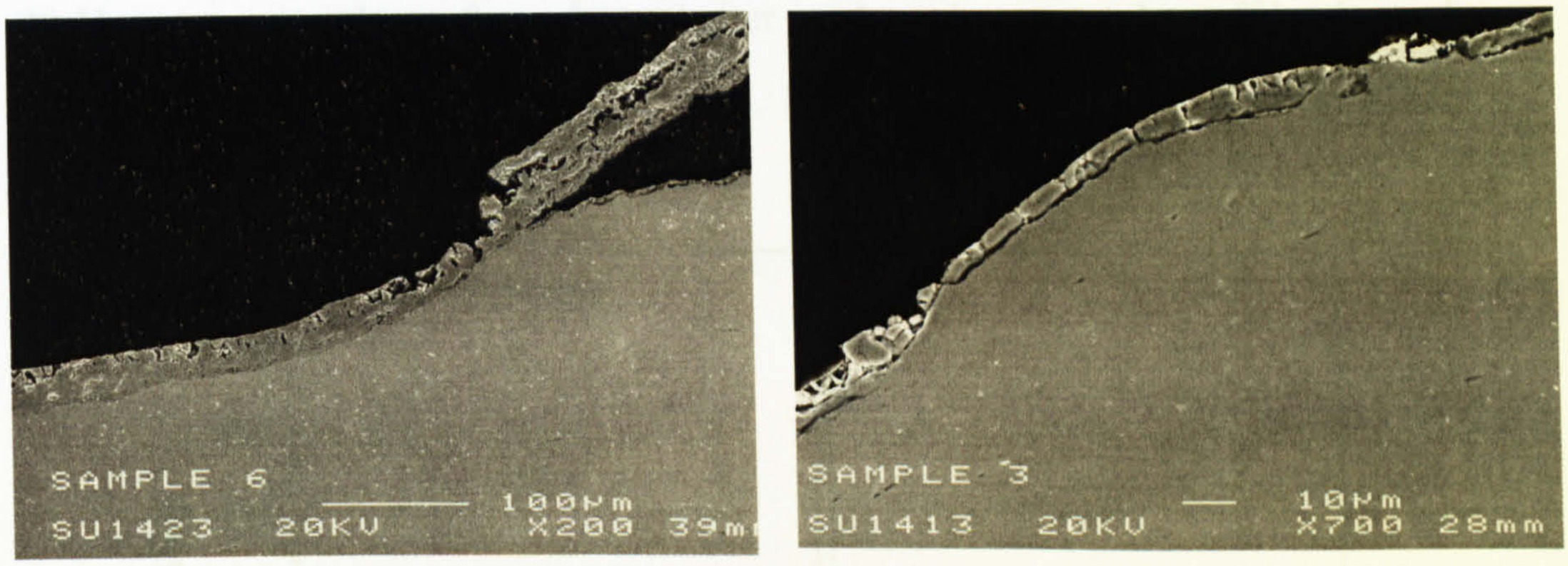

a b

Figure 4.73. Damaged oxide scales in the area of the contact with the edge of the tool (where bending was possible) $T_{ox} = T_{tests} = 880°C$, oxidation time: a) 3000s, b) 300s.

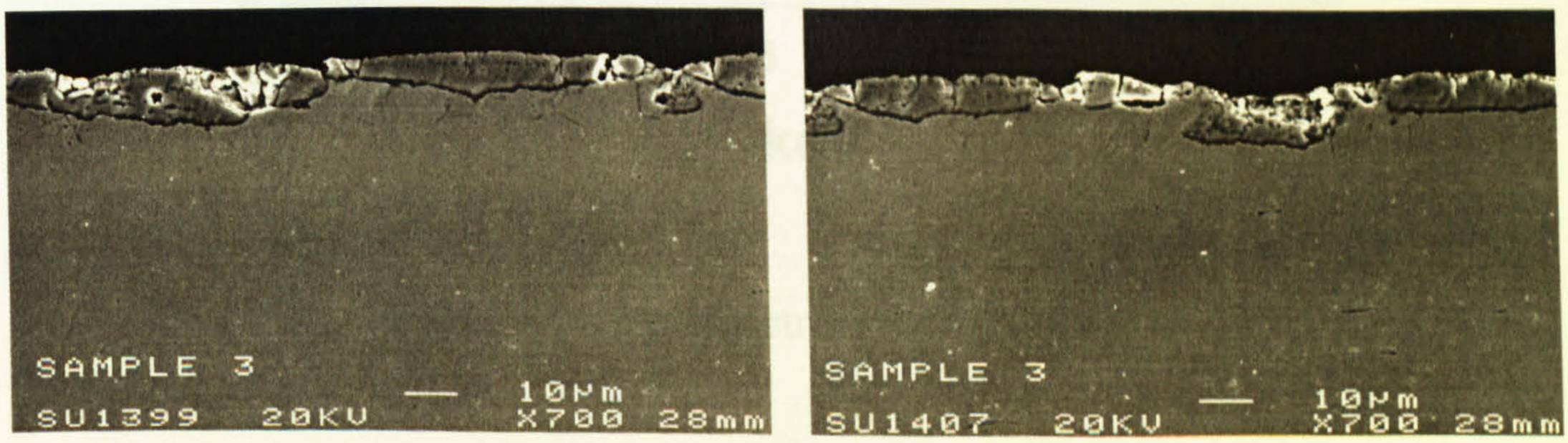

a b

Figure 4.74. Pressed in, cracked oxide scale after compression.

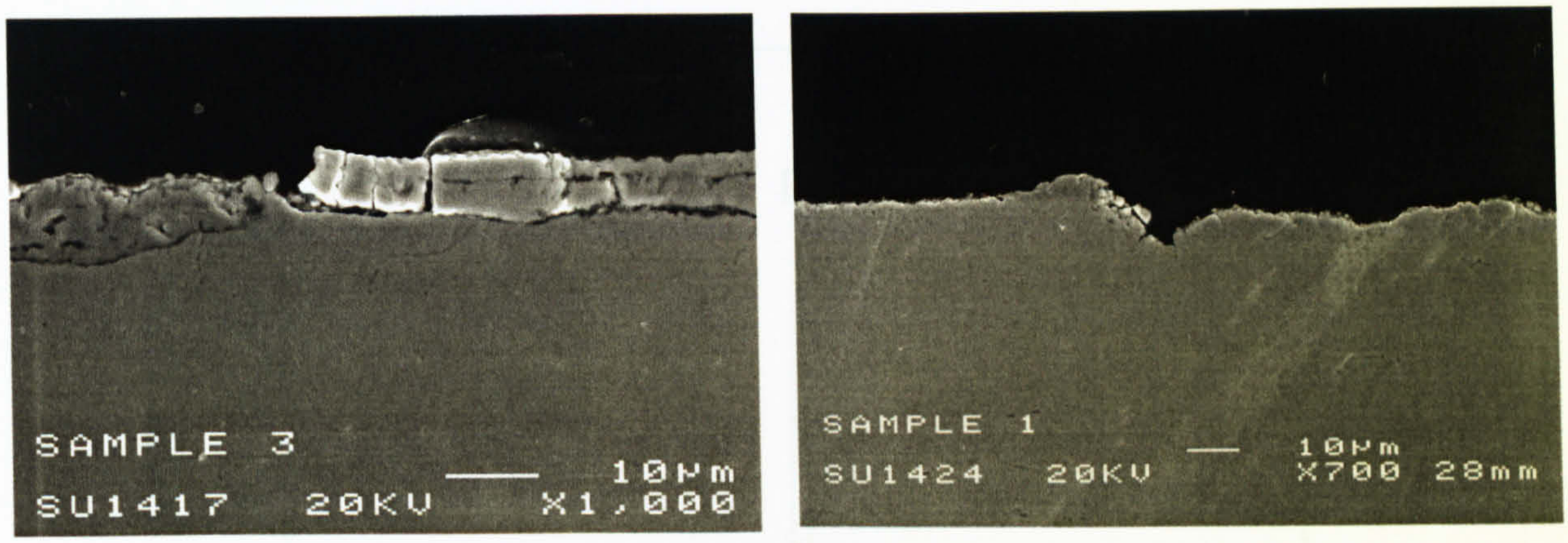

a b

Figure 4.75. a) Delaminated fragment of the oxide scale near extruded metal, b) Unevenness on the surface of metal after oxide scales were taken off by the tool.

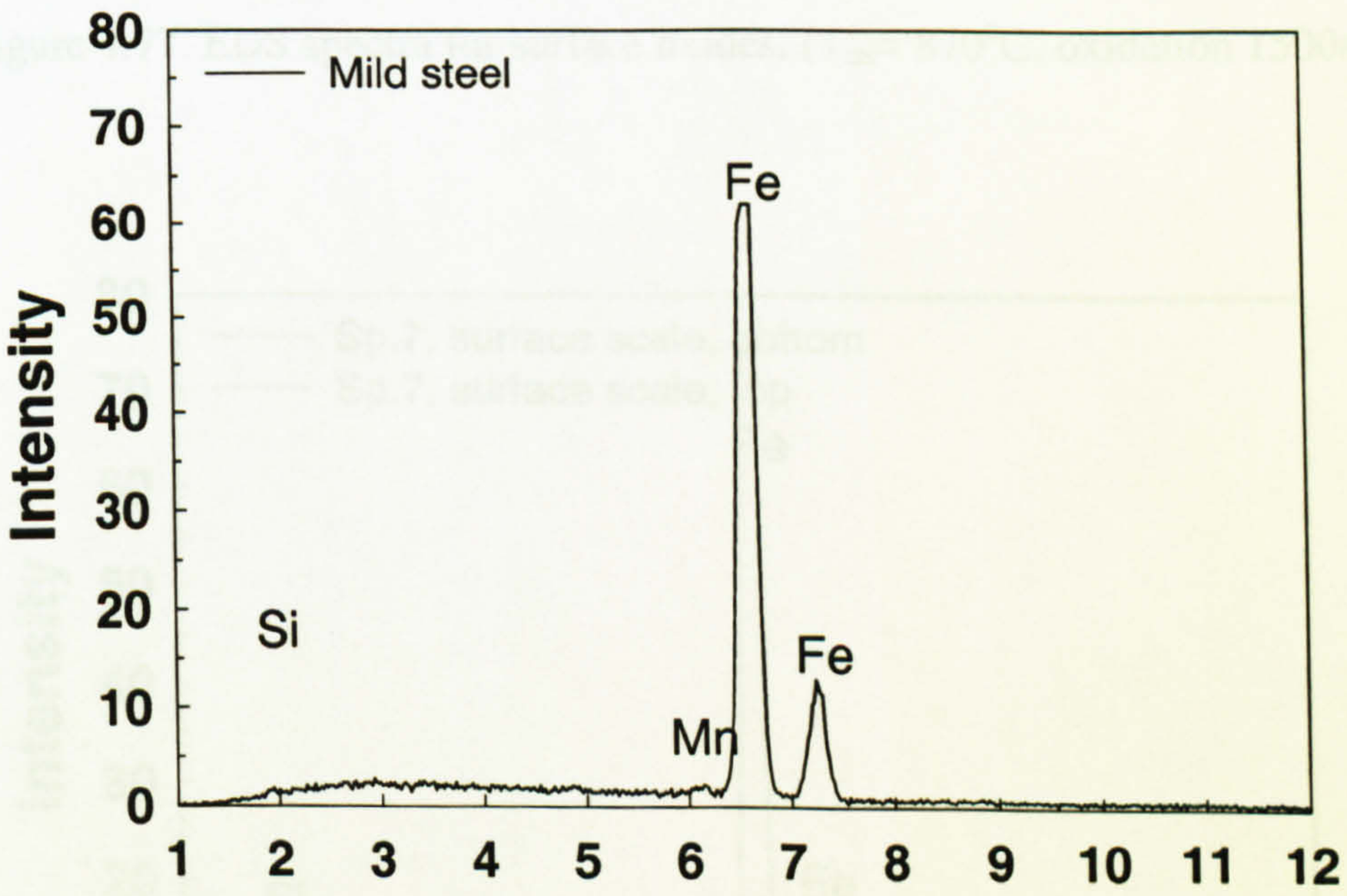

Figure 4.76. EDS spectrum for mild steel.

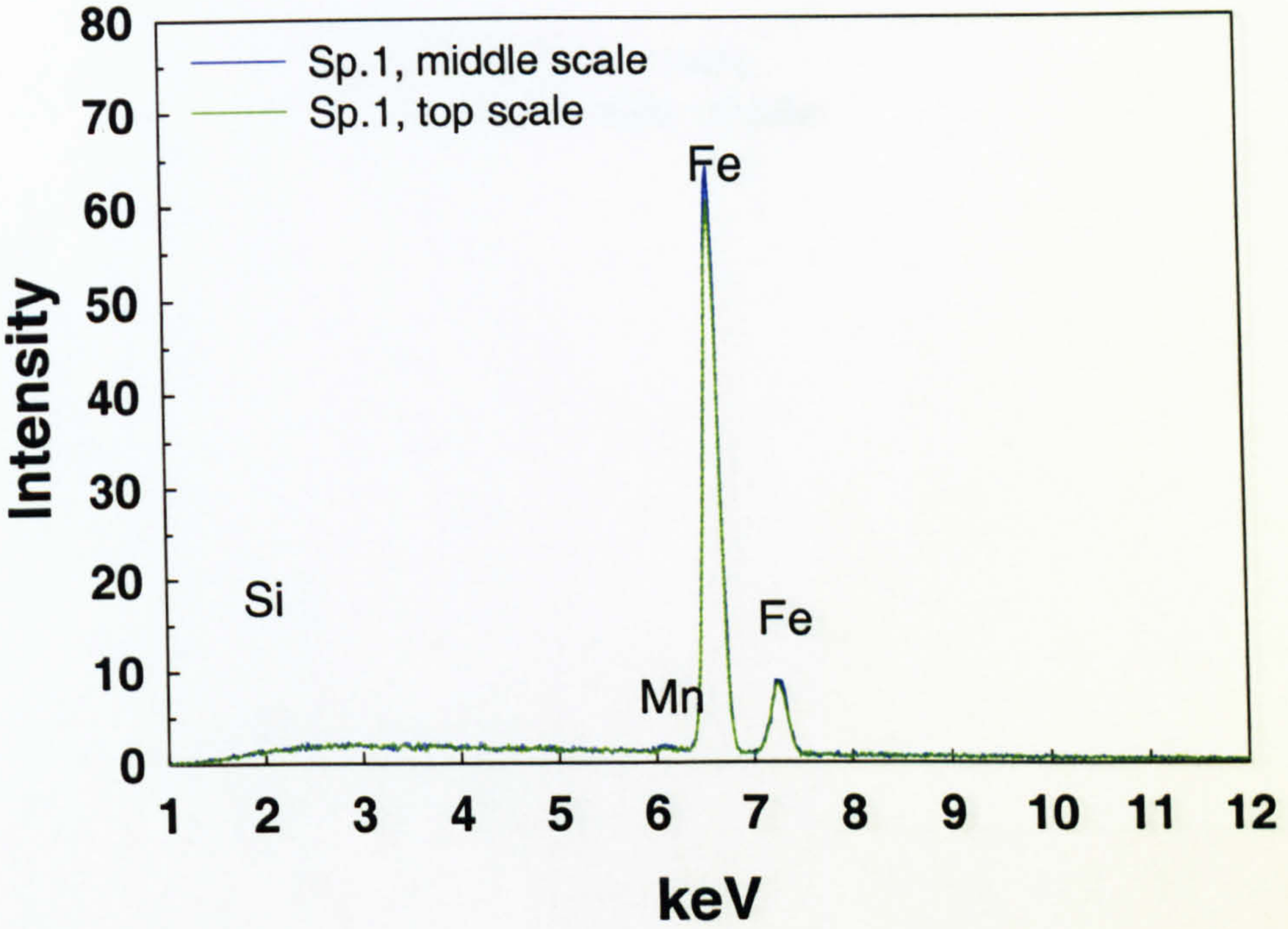

Figure 4.77. EDS spectra for surface oxides. (T_{ox}= 870°C, oxidation 1500s)

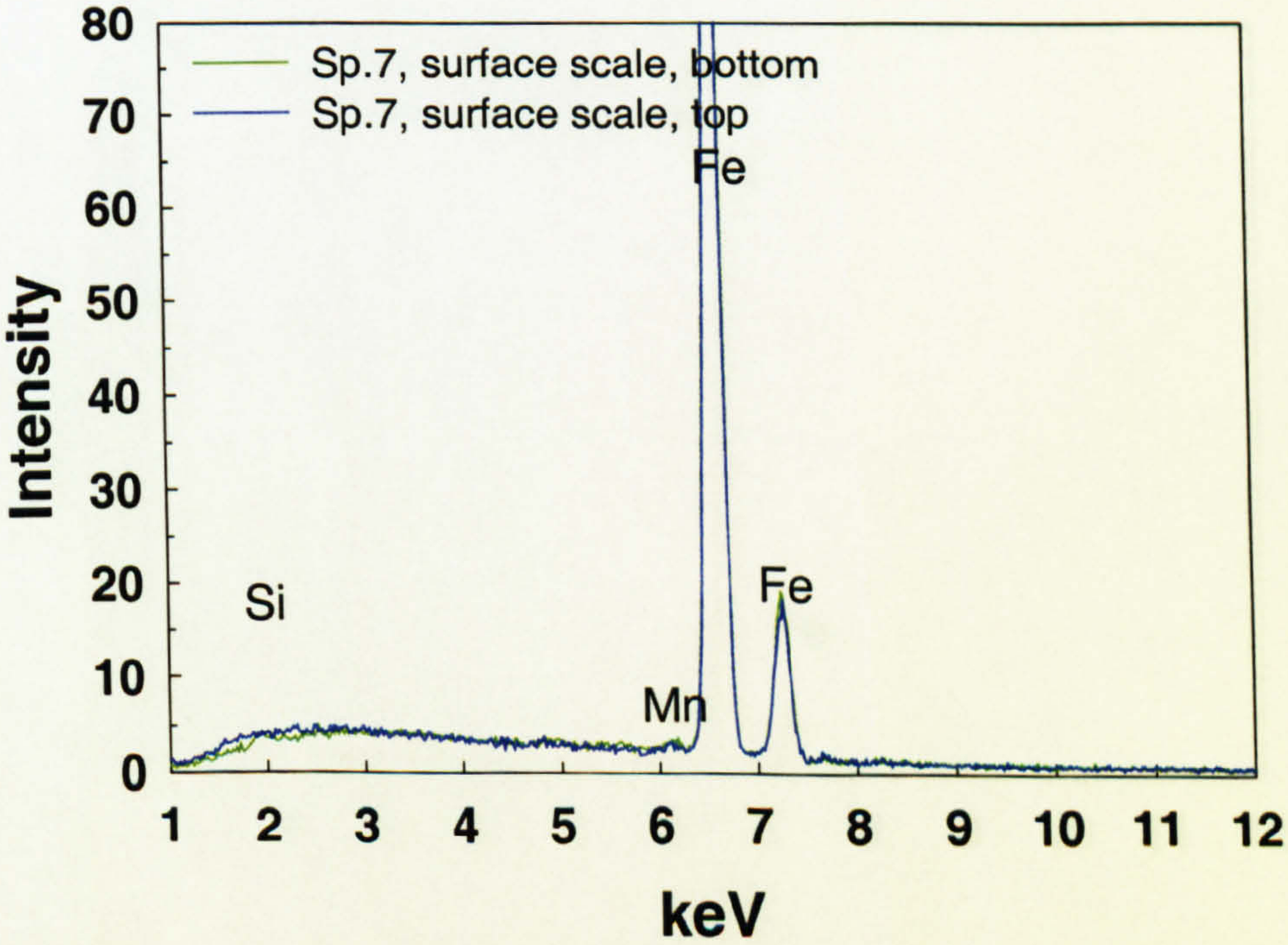

Figure 4.78. EDS spectra for surface oxides. (T_{ox}= 970°C, oxidation 100s)

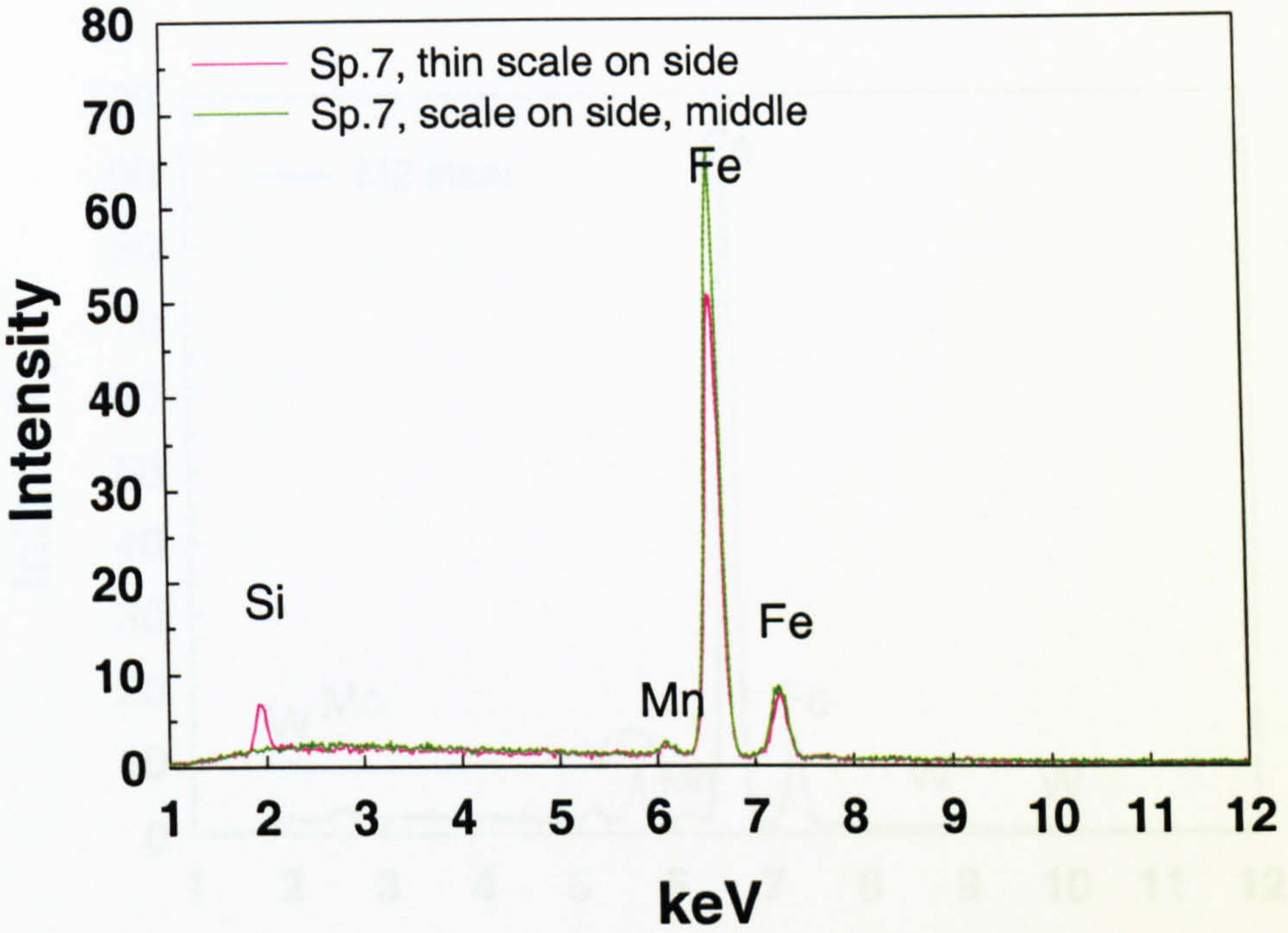

Figure 4.79. EDS spectra for oxides on the side of the specimen. (T_{ox}= 970°C, oxidation 100s)

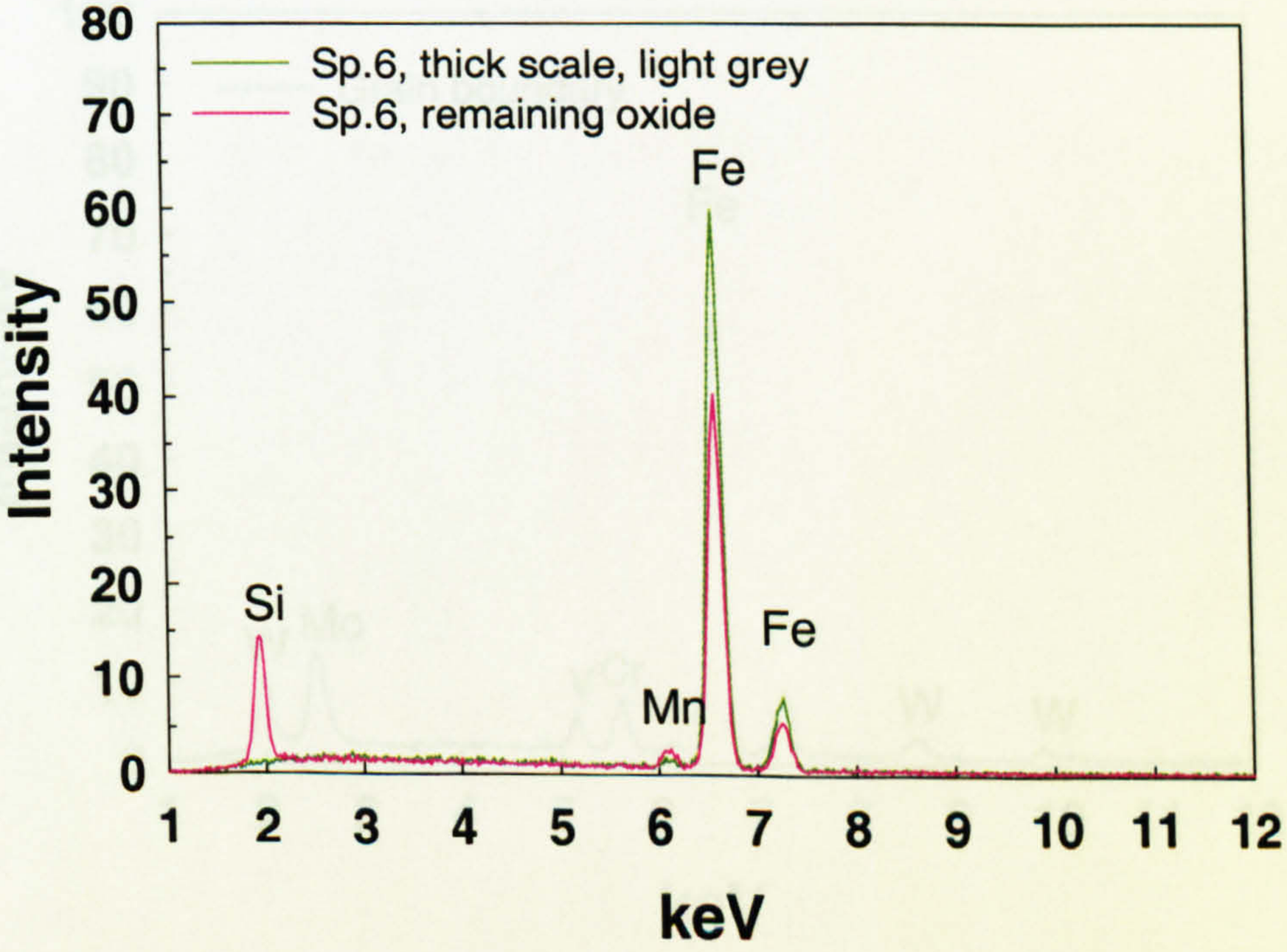

Figure 4.80. EDS spectra for surface oxides. (T_{ox}= 1070°C, oxidation 800s)

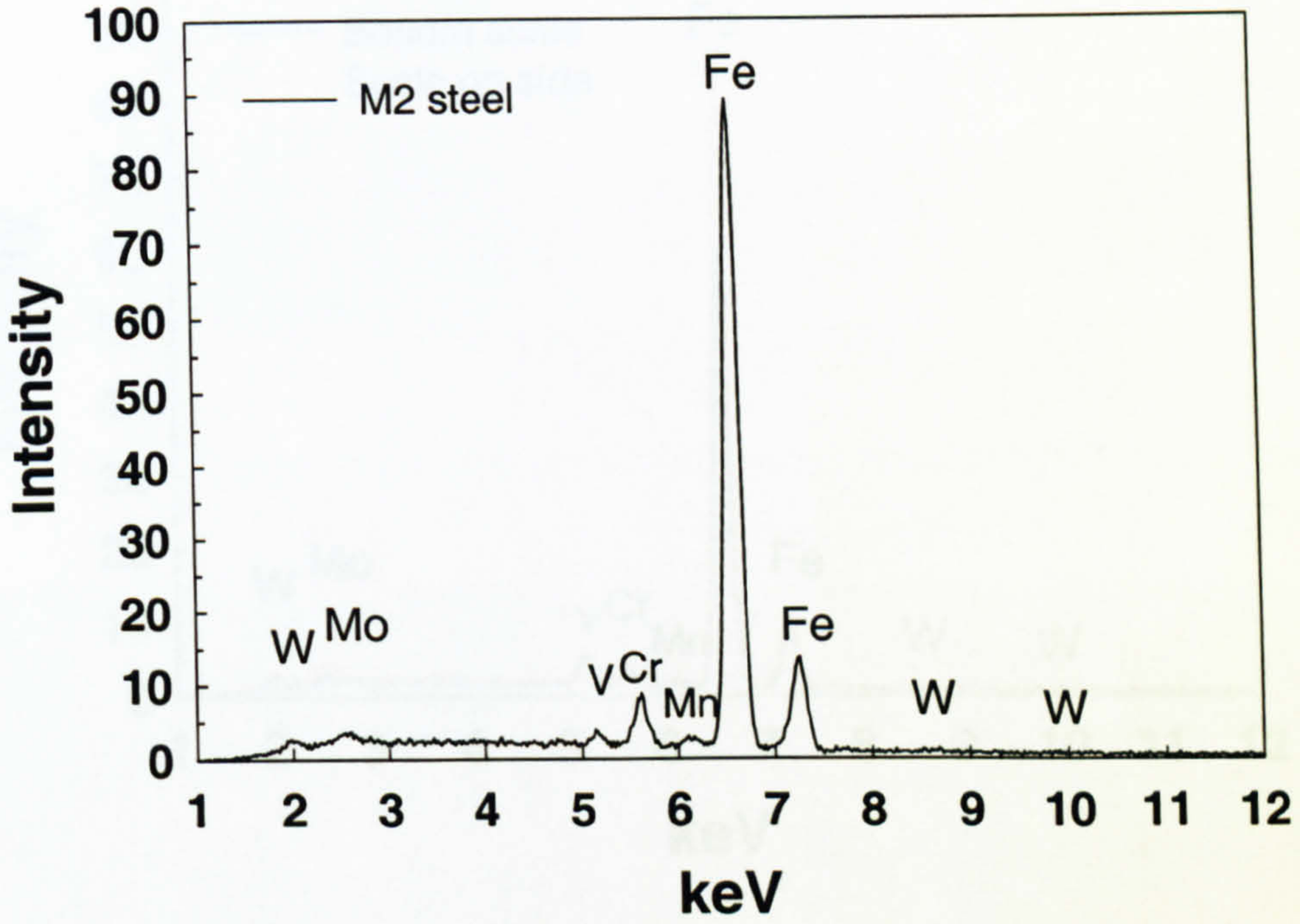

Figure 4.81. EDS spectrum of high-speed steel M2.

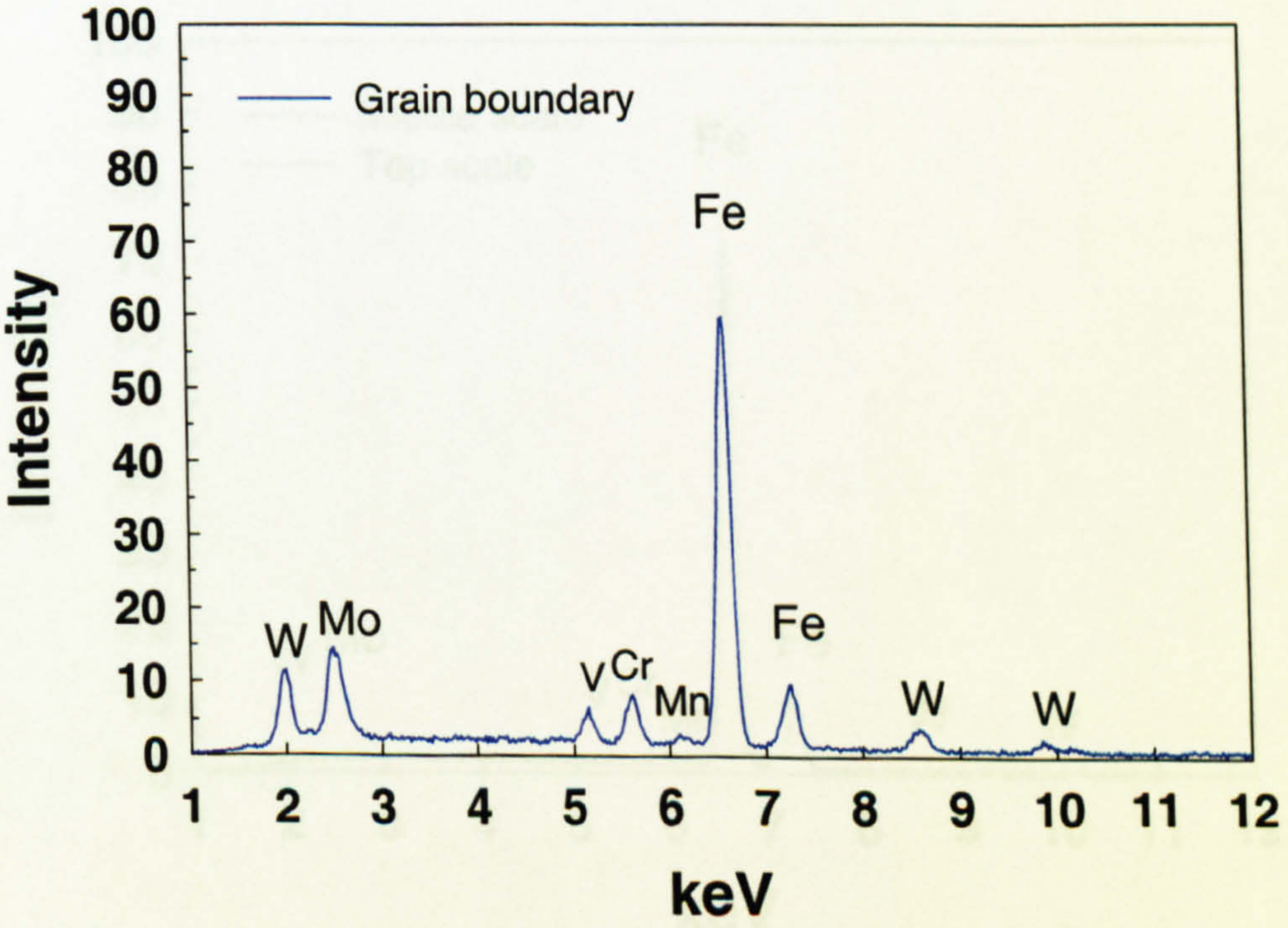

Figure 4.82. EDS spectrum of high-speed steel M2 (grain boundary).

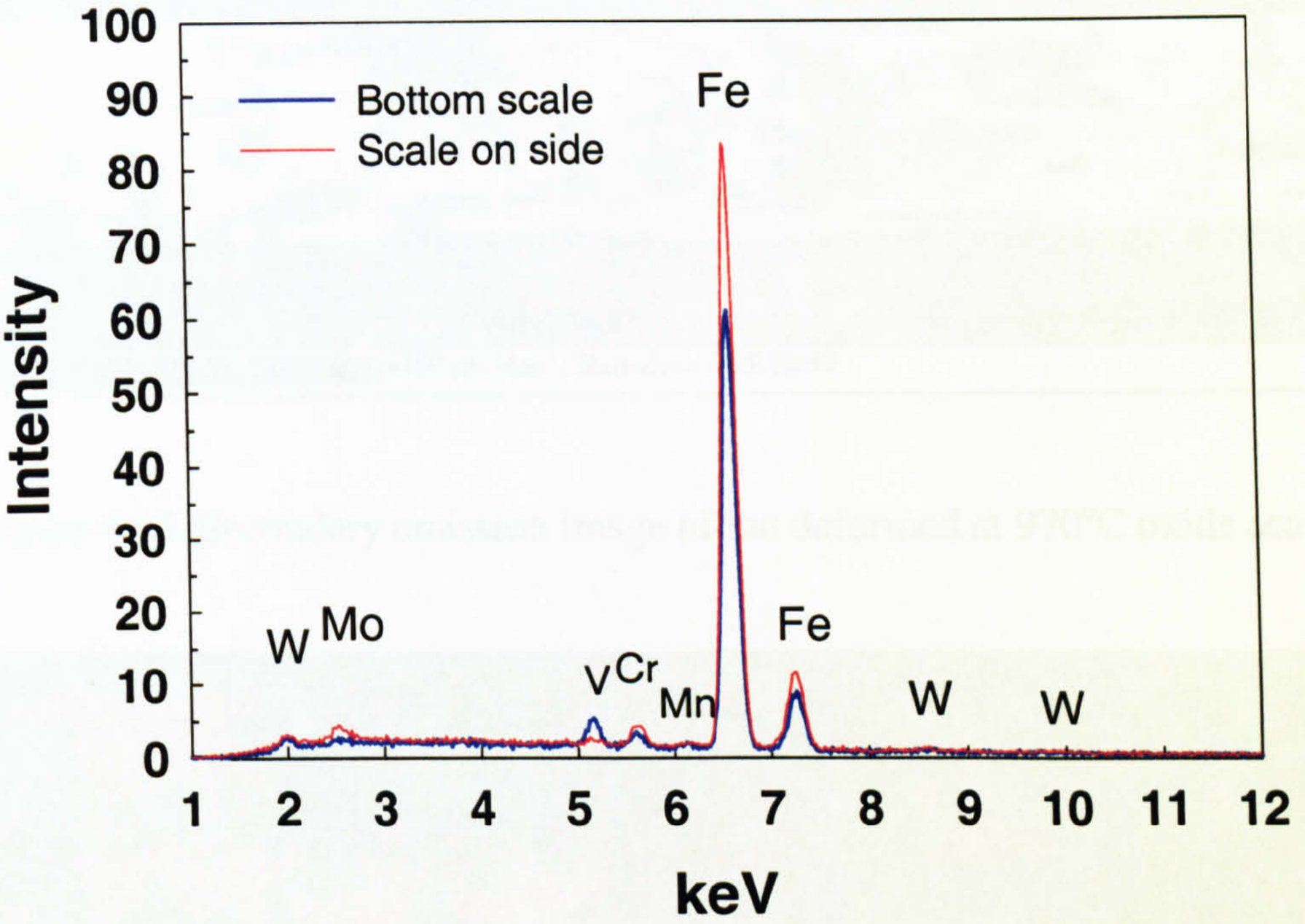

Figure 4.83. EDS spectra for oxide near the scale/metal interface on the tool.

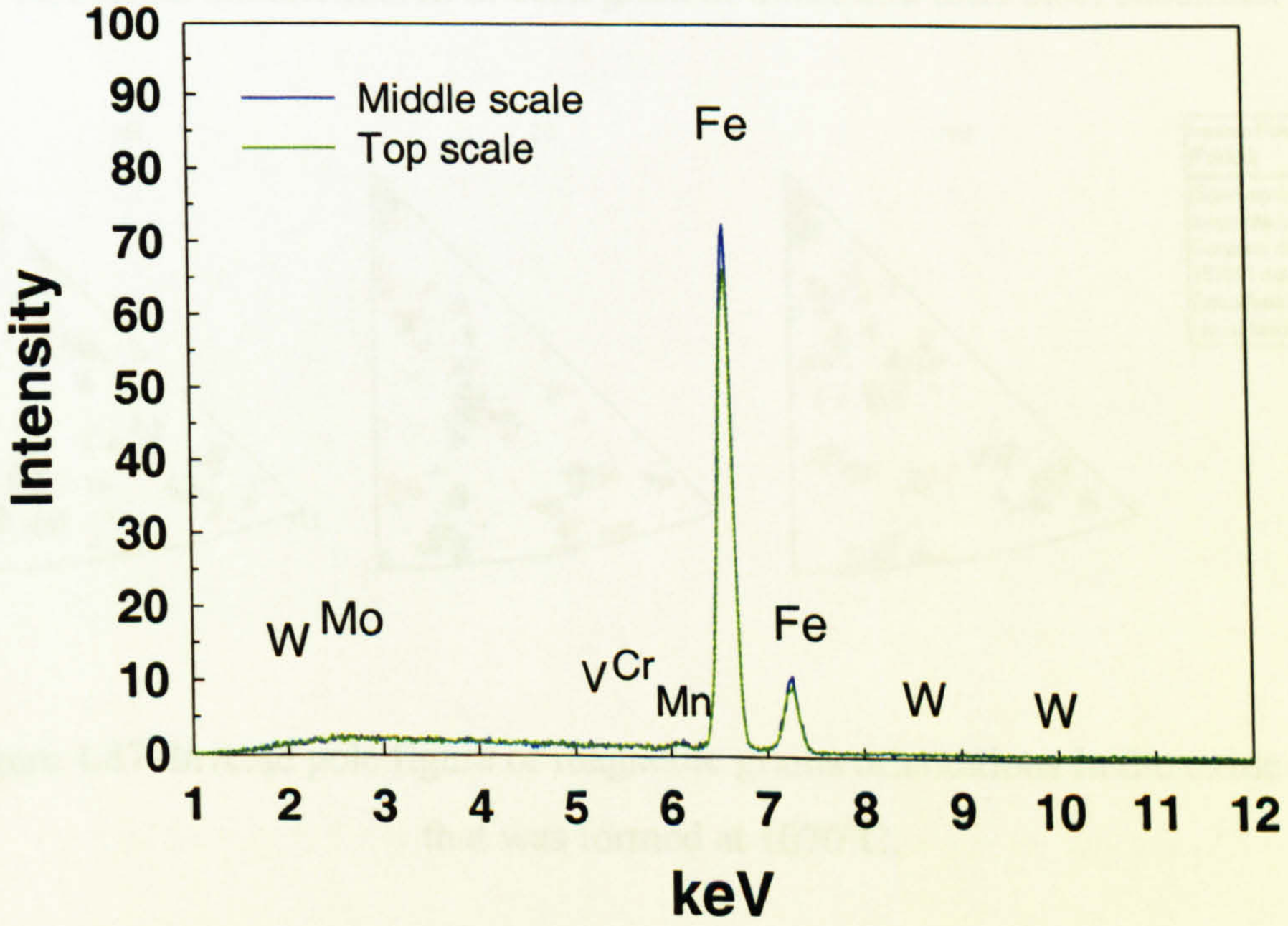

Figure 4.84. EDS spectra for surface oxides on the tool.

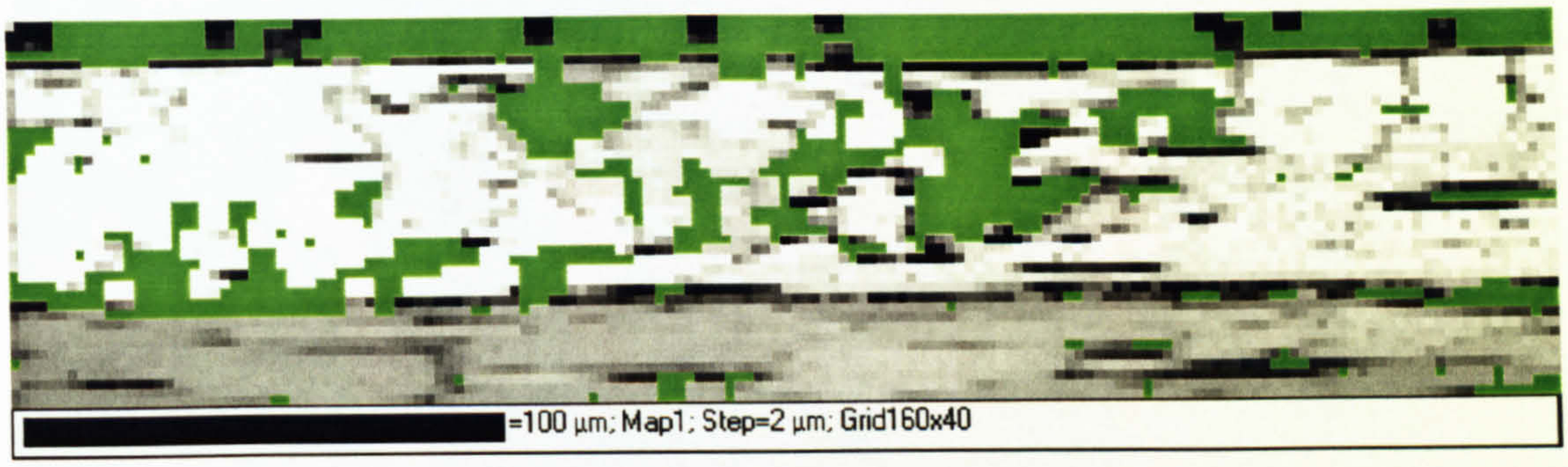

Figure 4.85. Secondary emission image of the deformed at 970°C oxide scale.

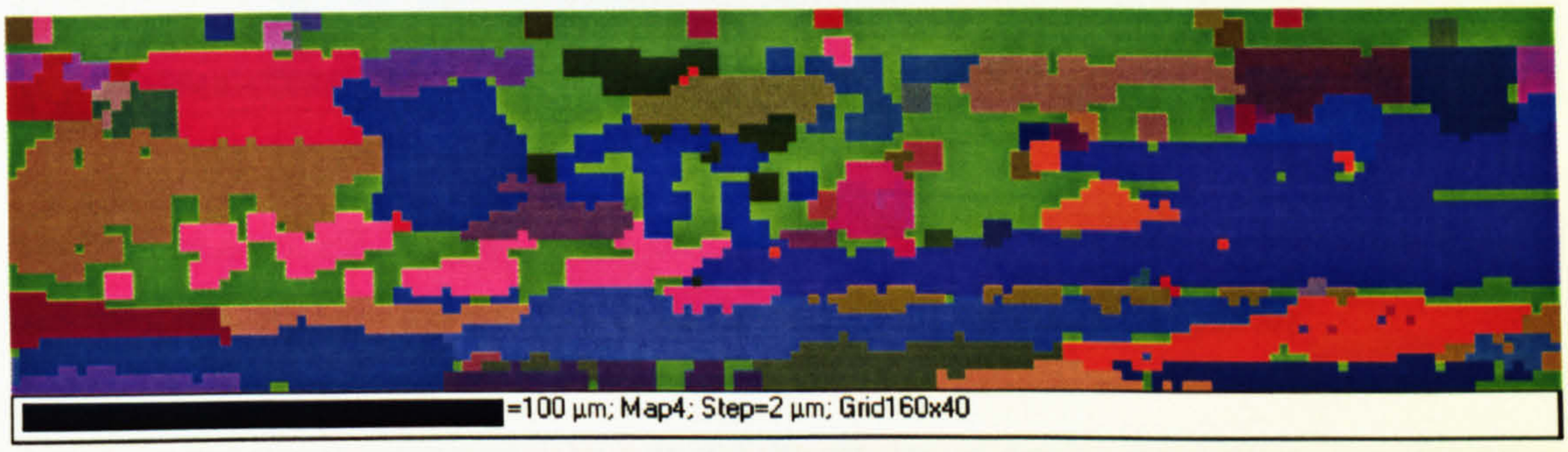

Figure 4.86. EBSD map of the deformed at 970°C oxide scale. Each of the colours represents the orientation of each grain of oxide and mild steel substrate.

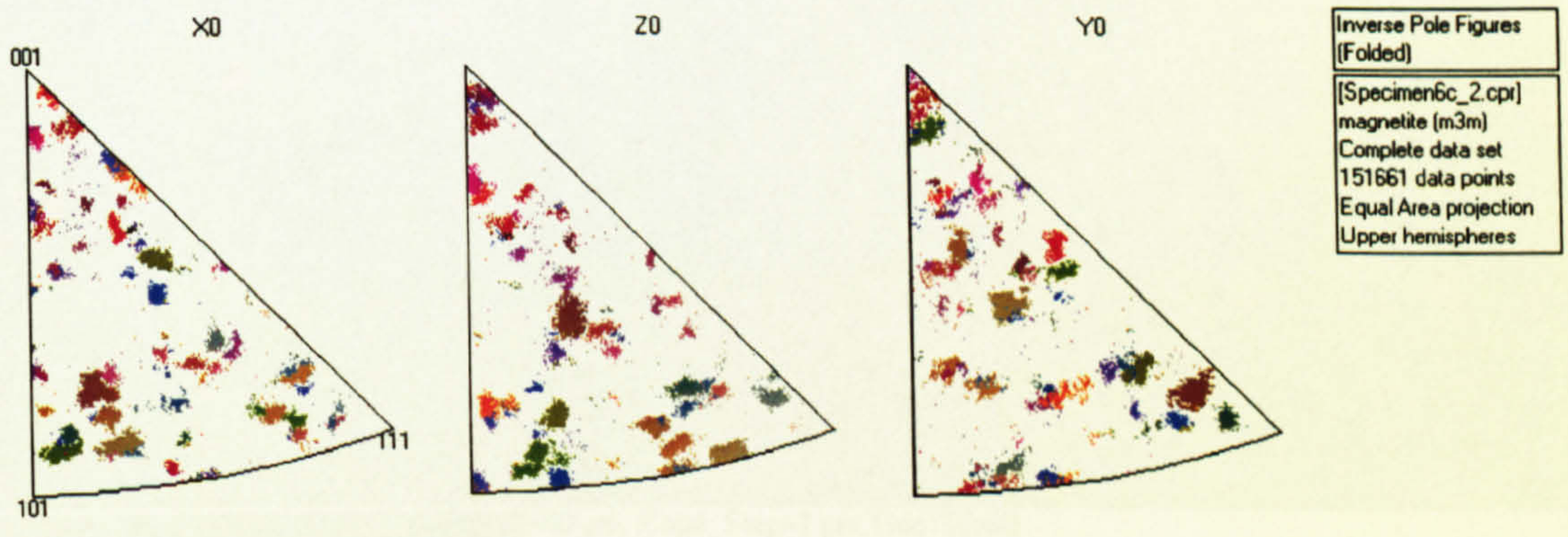

Figure 4.87. Inverse pole figure of magnetite grains orientations in the oxide scale that was formed at 1070°C.

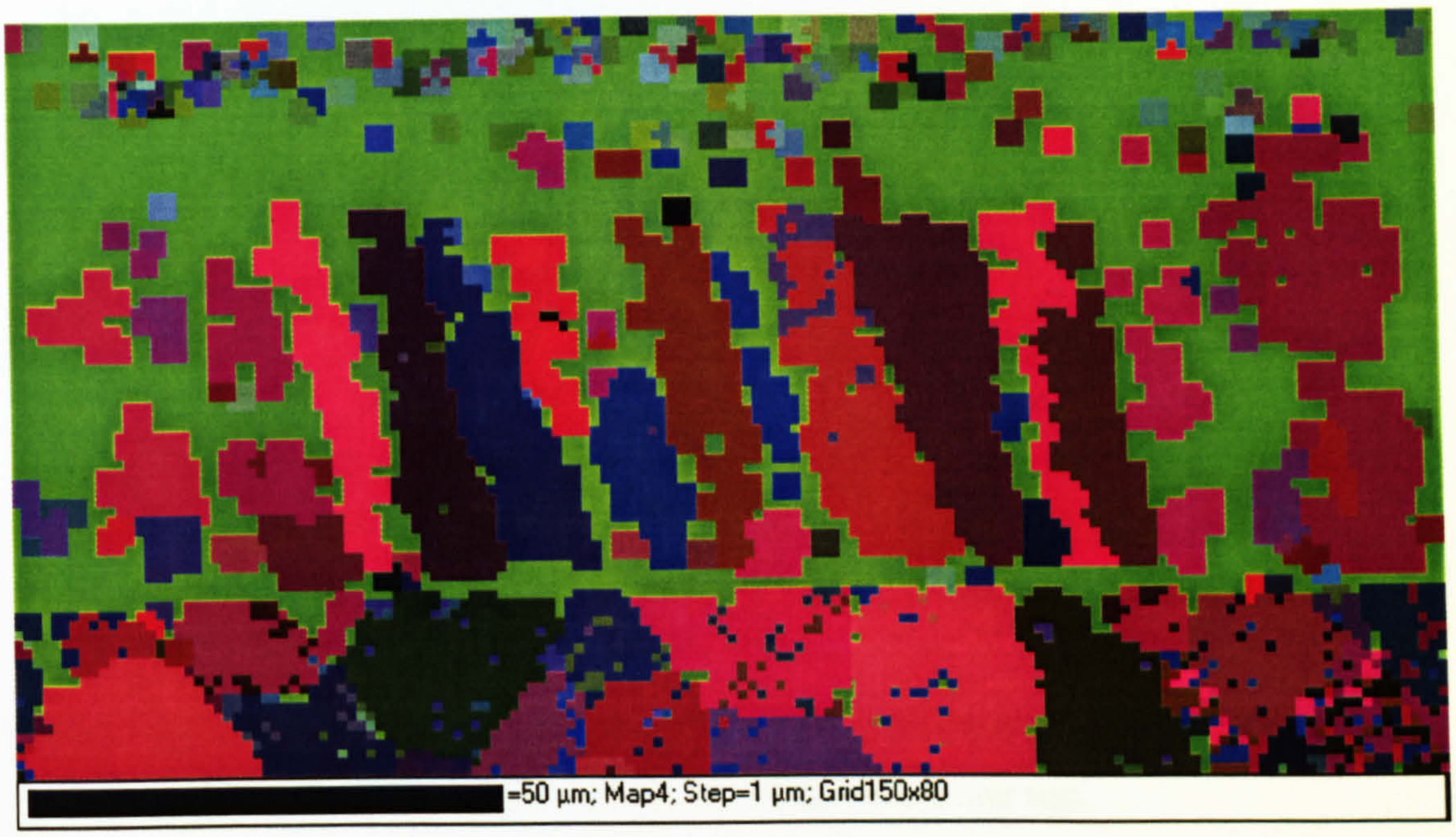

Figure 4.88. EBSD map of the oxide scale. Each of the colours represents the orientation of each grain of oxide and mild steel substrate.

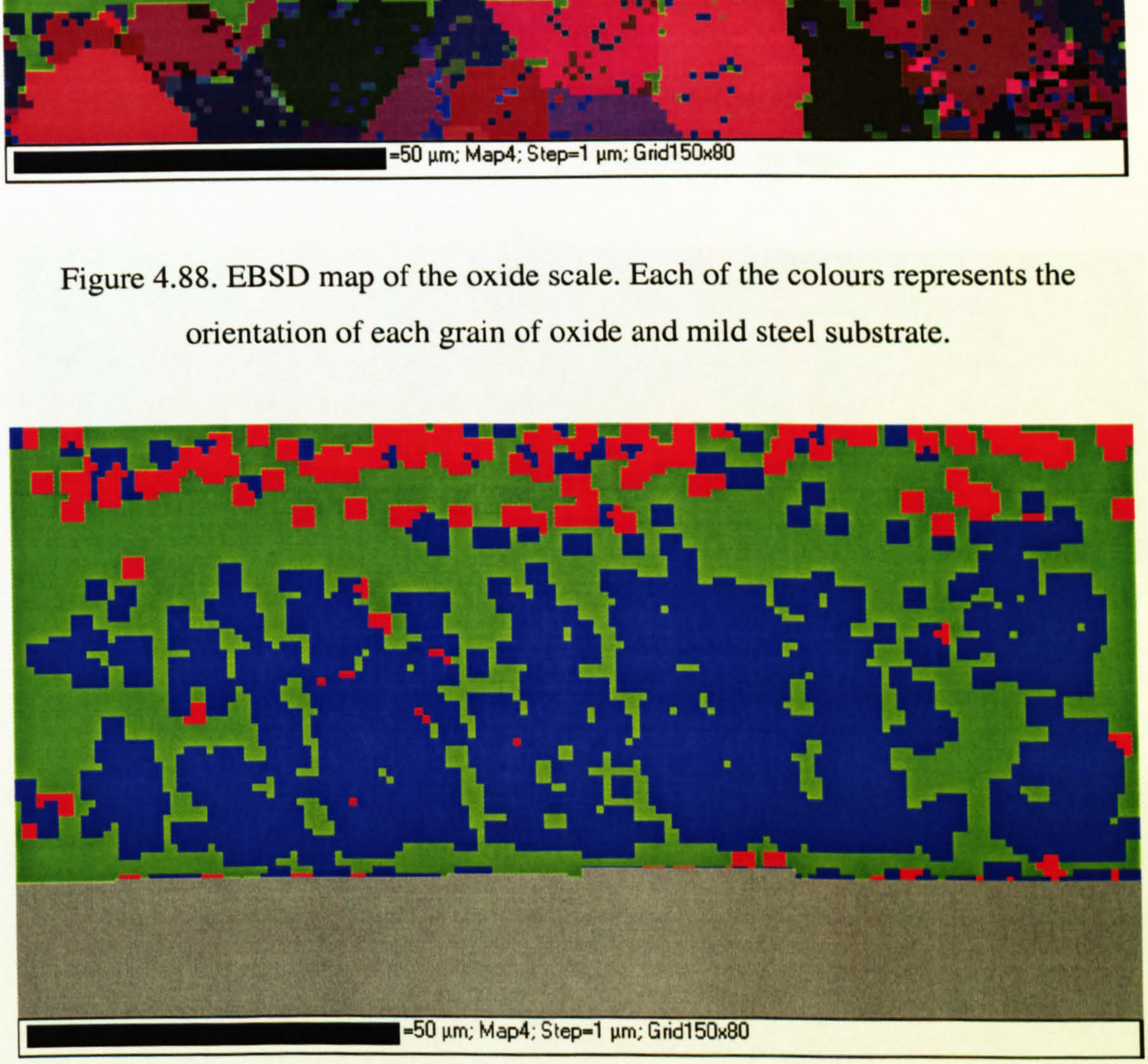

Figure 4.89. EBSD phase map of the oxide scale. Red colour represents hematite, blue colour is magnetite and grey colour is the metal substrate.

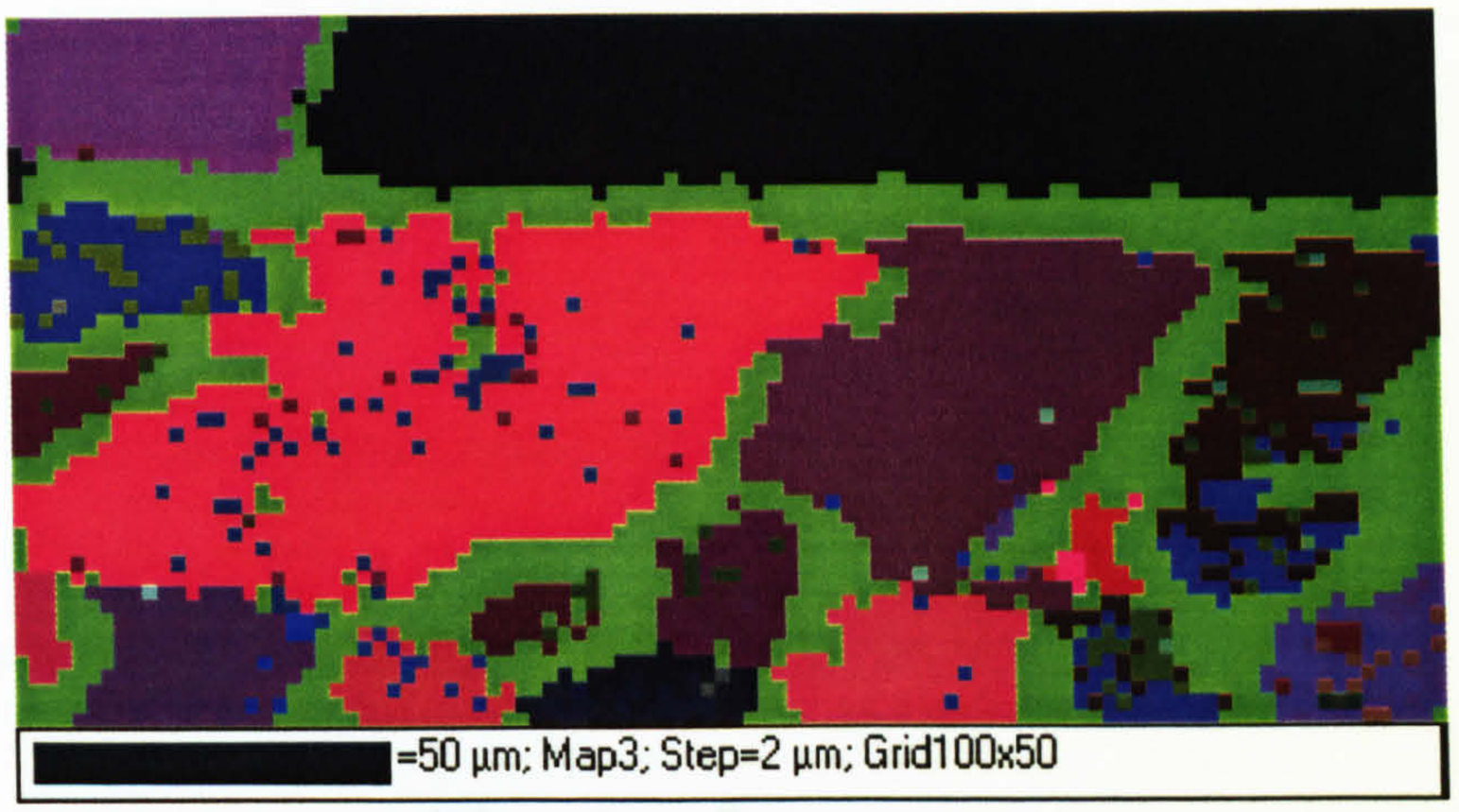

Figure 4.90. EBSD map (Euler angles) of mild steel grains near the oxide/metal interface and two oxide grains at the top.

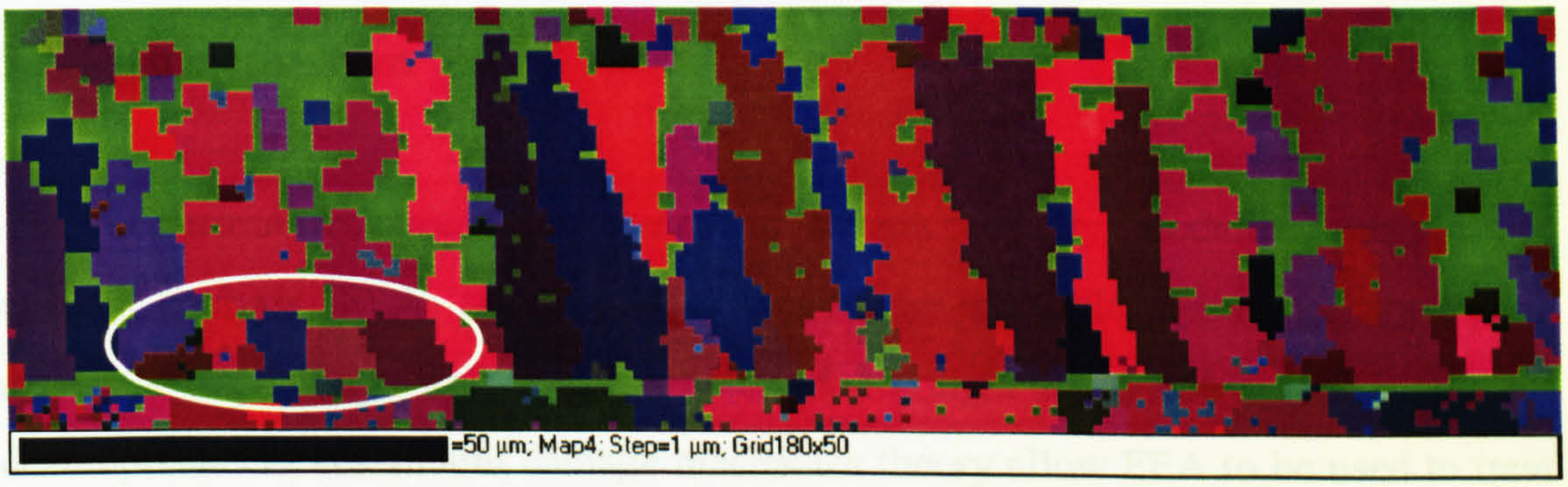

Figure 4.91. EBSD map (Euler angles) of the oxide scale adhered to the tool.

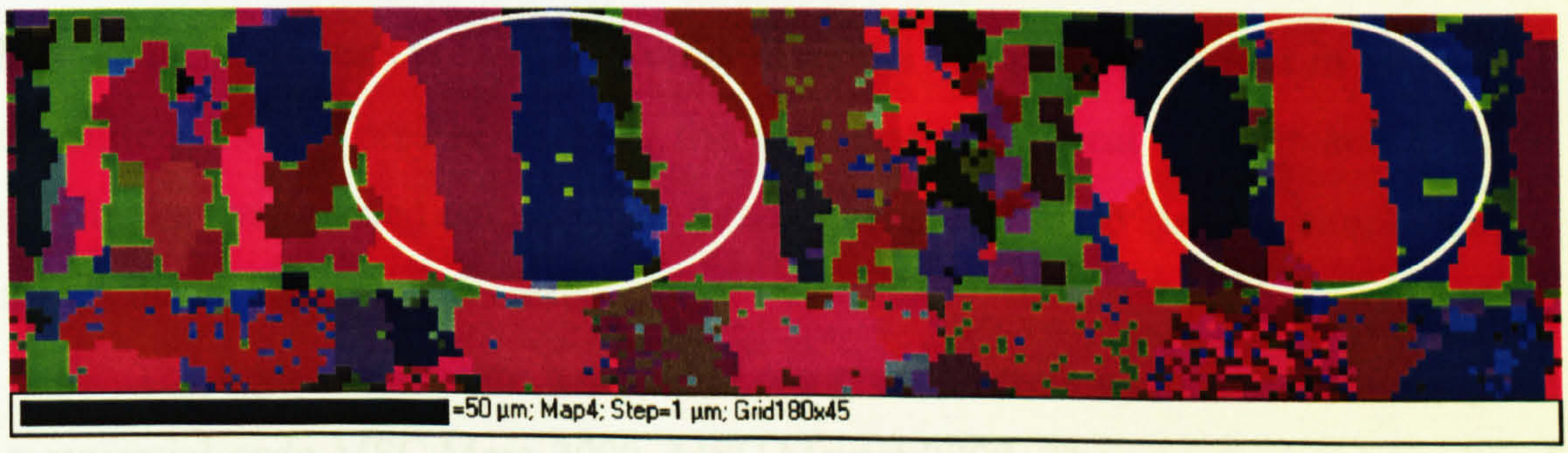

Figure 4.92. EBSD map (Euler angles) of the oxide scale adhered to the tool.

Chapter 5

Finite Element Modelling

5.1. Introduction

Thermo-mechanical processes can be successfully modelled using finite element analysis (FEA) [121]. This is one of the available techniques applied to materials modelling, and is widely used throughout industry today. Recent developments in continuum damage mechanics theory allow FEA to be used to treat fracture, crack growth and related phenomena. FEA is the simulation method usually based on a large database of measured materials properties as input.

In Chapter 4, the results of tension, compression and tension-compression high-temperature tests are given in order to model the oxide behaviour in hot-rolling conditions. In the present chapter, the examination of heat transfer and a strain distribution was carried out using the three-dimensional finite element simulation for the tensile and compression tests.

The high-temperature tensile and compression tests were simulated using the commercial code MSC.Marc 2000, MSC.Mentat 2000. The experimental results of the tensile and compression tests were interpreted using fully coupled, thermo-mechanical finite element analysis.

5.2. Three-dimensional finite element modelling of the high-temperature tensile test

The through-thickness crack mode of failure of oxide scales has been assumed initially based on experimental and published [29] results for low temperatures. It was assumed that the tensile stresses on the surface of the gauge section are transmitted to the oxide scale and cause its cracking. Based on this assumption, a coupled thermo-mechanical 3-D model was developed for two different specimen thicknesses (Figure 5.1 and 5.2) and a range of test temperatures that allows for analysis of stresses at the gauge section. The thicknesses of the gauge section were chosen to be 2 and 4 mm while the temperature was changed within the range 800 - 880°C. Note that the nominal gauge sections were 10 x 5.5 x 1 mm and 10 x 5.5 x 2 mm, because only a 1/8 of the specimens were modelled. The boundary conditions were applied as shown in Figure 5.3. The displacement was included as a table related to the experiment, while temperatures were achieved by heating the surface nodes in the indicated places (Figure 5.3). Although the same displacement was applied to all specified nodes, the variation in movement of the nodes was computed as shown in Figure 5.4.

5.2.1. Two different approaches to the heating of the specimen

The induction heating process was used in all tests to heat specimens as mentioned in paragraph 3.6.1. The general problem when heating steel through to elevated temperature is the variation of the magnetic properties. Hence, the minimum diameter of steel billets should be limited in order to be heated up to forging temperature with good efficiency. In our case, the specimen with the 4 mm thick gauge section was heated with good efficiency. However, the specimen with the 2 mm thick gauge section had insufficient thickness to be heated properly. Therefore, the same temperature (as for the 4 mm thick gauge section) at the thermocouple point was reached by the heat transfer from the cylindrical part of the specimen that was

inside the induction coil (about 5 mm in length) to the gauge section. Figure 5.5 shows the temperature distribution in the central part of the specimen when the gauge section was heated. The temperature at the thermocouple point (Figure 5.5) was about 30°C lower than the measured results. However, this type of a thermal modelling was acceptable for the gauge with 4 mm thickness as shown in Figure 5.6. Figure 5.7 shows the different approach to the heating of the specimen, namely the cylindrical part (about 5 mm) of the specimen was heated. This method produced better results in temperature distribution. The modelling was appropriate since the temperature in the thermocouple point was equal to the measured one.

5.2.2. Sensitivities to materials properties

In finite element analysis, the quality of the material property data has a major impact on the capability of the model to simulate a real process. The thermo-mechanical model is always sensitive to the temperature dependant material properties. Therefore, these parameters should be selected accurately. In the previously described models, Young's modulus and yield stress were very sensitive functions of temperature.

The value of Young's modulus as a function of temperature was obtained from the literature [140] and initially implemented into the models (see Appendix 2, Figure A2.5). However, the modelling results of the stress history did not compare well with the experimental results. The reason for this was the difference among the modelling size (length 100 mm) and the actual distance (between crossheads ~900 mm), where measurements were carried out (see Figure 3.4). In order to prove this supposition, the simple 3D thermo-mechanical model of a rod was developed and computed at room temperature. It should be noted that due to the water-cooling during the experiment most of the test rig was at room temperature. The modelling results are shown in Figure 5.8 as the red line. According to Figure 5.8 the literature Young's modulus value should be optimised in order to satisfy the experimental results to the apparent elastic modulus. The apparent elastic modulus allowed to taken into account the elastic behaviour of the entire rig. The history curves of the equivalent stress after the optimisation are also shown in Figure 5.8.

Another very important parameter that needed to be checked was the yield stress. The experimental results for the yield stress were compared with several empirical equations [131 - 134] and were found to lie within an acceptable range for the value of stresses as shown in Figure 5.9. Based on the consideration of the induction heating (see 3.6.1), only one experimental point in Figure 5.9 was assumed to be the actual surface temperature, namely the point that has a minimum yield stress (maximum specimen thickness). All others points have been computed according to empirical equations: the curve Data 1 using Shida's results (equations in Appendix 1) and curve Data 2 following Hajduk.

The equation of Hajduk et al. [131] was used in the form

$$\sigma = \sigma_0 K_T K_\varepsilon K_u \qquad (5.1)$$

where σ_0, K_T, K_ε, and K_u are the functions of material, temperature (T), strain (ε) and strain rate ($\dot{\varepsilon}$), respectively. The equation for low carbon steel is

$$\sigma = 97.1[20.059\exp(-0.00299T)](1.685\varepsilon^{0.223})(0.696\dot{\varepsilon}^{0.159}) \qquad (5.2)$$

Figure 5.10 shows difference between yield stress at current temperature and yield stress at 880°C with decreasing the temperature. As can be seen from Figure 5.10 the same difference in yield stresses, for instance 20 MPa, might be achieved with the 70 – 120°C temperature drop depending on the equation. In order to satisfy the pyrometer measurements (Figure 4.9), the minimum temperature drop was chosen to be implemented in the finite-element model.

5.2.3. Stress behaviour

The steel stress-strain relationship implemented into the model was obtained during the tests, while other material properties are given in Appendix 2. The elastic-plastic transition was fitted using experimental curves and the yield stress compared with that computed by equations in Appendix 1 (see 5.2.2). However, the equations shown in Appendix 1 cannot be used as a general constitutive law for all conditions. Figure 5.11 shows a stress distribution in the longitudinal, tensile direction on the surface of samples with two different thicknesses of gauge section undergoing tensile loading.

The difference in the maximum value of stress is mainly due to the stress-strain curves' sensitivity to temperature. Following the assumption that was introduced in the previous section, the temperature inside the induction furnace was supposed to be lower for the 2 mm model, namely 800°C on the surface in the centre of the gauge section. The gauge section of the 4 mm model had the higher temperature according to Figure 4.9 for a specimen with the same geometry, i.e., 880°C.

Figure 5.12 shows the experimental and simulated stress-strain curves. Due to large scatter of the experimental strain, the comparison of these curves was complicated. Therefore, a history plot of stresses has been chosen for the evaluation of the model simulation. Figure 5.13 shows stresses for 2 and 4 mm gauge thickness models in the centre of the gauge section. The experimental and modelling results show a good agreement for the specimens with 2 and 4 mm thickness of the gauge section. The difference in stresses is achieved simply by the different temperature of the specimens and using the experimental stress-strain curve.

Figures 5.14 show the corresponding strain distributions on the 2 and 4 mm models. As can be seen from Figure 5.14, the equivalent total strains were very similar for both 2 and 4 mm models which are in good agreement with the experimental results. Figure 5.15 shows elastic and plastic strains separately. The elastic strain was the same at any point of the gauge section, while the plastic strain was varying from the centre to the edge of the gauge section as shown in Figure 5.15. However, the strain distribution was nearly identical for 2 and 4 mm models.

5.2.4. Crack appearance in the oxide scale

The crack appearance in the oxide scale was simulated using the fracture mechanics approach. The finite element mesh of the model is shown in Figure 3.13. Due to the three-dimensional thermo-mechanically coupled finite element analysis demanding large amounts of computer memory and time, only 1/8 of the gauge section was modelled and analysed for crack appearance. The continuous layer of oxide scale with a thickness of 0.1 mm covering the whole gauge length of the specimen was simulated in the model. Generally, two different temperatures and thicknesses were examined similar to the tensile models without oxide scale. For the

evaluation of the crack, MSC.Marc requires calculation of the J-integral. That requires the crack front with nodes, the shift vector, and the nodes of the rigid region as described in detail in section 3.11.1. An automatic geometry based search was used for crack appearance. Since the slipping effect was not observed along the scale/metal interface during the high-temperature tensile tests, the oxide scale was adhered to the metal firmly and slipping was prohibited in the model. The allowed crack paths were directed perpendicular to the applied displacement (X axis) with the radius for the first rigid region equal to 0.05 mm and for the second rigid region equal to 0.1 mm (see Figure 5.16a). A crack developed in the oxide scale perpendicular to the direction of the maximum principal stress if the maximum principal stress in the material exceeds a certain value, σ_{cr} (Figure 5.16b). Cracking stress, σ_{cr}, was calculated according to Equation 2.49 and using the experimental data of the stress intensity factor, K_{Ic}, from Figure 2.17. Unfortunately, a lack of data exists for high temperature properties of oxides and the available data has a wide scatter. Sensitivity of the model to this scatter also was examined. The material loses all load-carrying capacity across the crack unless tension softening (softening modulus - E_s) is included. If tension softening is included, the stress in the direction of maximum stress does not go immediately to zero. Therefore, the material softens until there is no stress across the crack. At this point, no load-carrying capacity exists in tension. The softening behaviour is characterized by a descending branch in the tensile stress-strain diagram (Figure 5.16b) and it may be dependent upon the element size. It was impossible to find any experimental evidence of tension softening of oxide scales in the literature, hence tension softening was not included in the model. It should be noted, that abrupt softening could produce numerical difficulties in stress calculations.

The cracks in the model did not appear in the usual sense, nevertheless it was possible to detect cracking strain and assume that as the crack. Calculations of cracking strain are implemented inside the MSC.Marc finite element code, however they can be found in the literature [159, 160]. These calculations assume that the total strain can be decomposed into an elastic component and a cracking component.

The boundary conditions that were applied in the model are shown in Figure 5.17. The mesh size along the X axis has been chosen to be able to reproduce the maximum number of cracks that were obtained during the experiment. On the other

hand, one should remember that the mesh size influences the number of cracks which could appear. Another parameter that was a constant in the model (as it was in the test), but could be important for cracking behaviour, was the deformation rate. However, more data would be needed in order to include deformation rate dependence in the model.

Figures 5.18 show the crack initiation phase and relative sizes of the scale and the substrate for 4 mm specimen at temperature 850°C. Figure 5.19 shows the stress distribution before the second crack occurs. The stress relaxation zone can be seen where the first crack appeared (Figure 5.19). The second crack appearance is shown in Figure 5.20. The stress map on the surface of the scale with two cracks is shown in Figure 5.21. As can be seen from Figure 5.21, subsequent cracking might happen at the region with maximum stresses.

Figures 5.22 and 5.23 show the crack initiation phase and final crack pattern of the 2 mm specimen at temperature 750°C. According to these figures, the crack pattern appeared similar to that shown in Figure 4.10. As can be seen from Figure 5.22 cracking was initially through-thickness and hence the crack pattern was probably formed almost instantly.

Since the values of stress intensity factor, K_{Ic}, present in the literature, for instance [141], have a wide variation, the sensitivity to K_{Ic} of the simulated cracking behaviour was checked for one particular temperature of 800°C. The minimum and maximum values of K_{Ic} were obtained from Figure 2.17 as 5.8 and 9.5 $MN \cdot m^{-3/2}$ respectively. Figure 5.24 and 5.25 show the component 11 stress distribution on the surface of the oxide scale in the moment when cracking commenced. As can be seen from Figure 5.24 the stresses gradually rise to the maximum value that is quite uniform near the edge of the specimen. In Figure 5.25 the stresses have a steady increase up to the maximum in the centre of the specimen. Nevertheless, cracks were initiated in the similar way for both models. However, further development of cracks was different for the models. Figure 5.26 shows the crack pattern that has appeared on the surface of the model with minimum value of K_{Ic}, while Figure 5.27 shows the fewer number of cracks that were developed on the surface of the model with maximum value of K_{Ic}. Figure 5.28 shows the stress relaxation after the cracks have been appeared, rendering further formation of cracks impossible. Hence, it is possible to summarize that the stress intensity factor, K_{Ic}, was very important in the cracking

phenomena of the oxide scale. Moreover, at elevated temperatures, K_{Ic} can have a large value that will keep oxide scale without cracking and the oxide/metal interface sliding might occur.

5.3. Three-dimensional finite element modelling of the high-temperature compression test

Heat transfer and stress-strain distribution were simulated using a thermo-mechanical coupled finite element model, based on results obtained during the experiment. The model view and the orientation of the compression tool and the slab imitation specimen are shown in Figures 3.15 and 3.16. Thermal and mechanical properties of materials, which were implemented in the finite element code as tables, are presented in Appendix 2. Aside from plotting the stress and strain maps, temperature, stress and strain histories were checked in particular nodes as shown in Figure 5.29. The contact phenomena were modelled, including friction and heat transfer between the tool and workpiece.

5.3.1. Heat transfer during the contact of the specimen and tool

Temperature changes were simulated using the 3-D thermo-mechanically coupled finite element model (Figure 3.15). Since the maximum number of the high temperature compression tests were carried out at 970°C, the finite element analysis, which is able to predict the temperature distribution during the compression test, was performed and compared with experimentally obtained results at the same temperature.

Figure 5.30 shows a comparison between measured and calculated temperatures. The temperatures were checked in the thermocouple points that are shown in Figure 5.29. The heat transfer coefficient at the contact interface ($\alpha_{contact}$) during the simulation of the compression test was supposed to be in the range of 1300 - 2400 $Wm^{-2}K^{-1}$ (depending on oxide scale thickness) to satisfy measured temperature results. According to the literature [119, 132, 142, 143] and [144], the heat transfer coefficient during the hot rolling process appeared to be between 2000

the oxide scale for hot rolling more experimental measurements of the heat transfer coefficient at different oxide scale conditions should be carried out.

5.3.2. Stress and Strain distribution

The high temperature compression test was not a plane strain test. Therefore, it was impossible to measure a strain distribution. However, the finite element simulation of the test assisted in the stress-strain evaluation. The 3-D thermo-coupled finite element analysis was performed for the temperature of 970°C. Figure 5.31 shows the evolution of stresses at the contact nodes (see Figure 5.29). According to Figure 5.31, the difference between the central node and the node closest to the edge of the specimen was about 2 MPa. Figure 5.32 shows the simulated stress-strain curve. The maximum total strain, which was calculated in the finite element model, equals about 0.035. Equivalent plastic strain rate also was computed in the model and typical history plots are shown in Figure 5.33. As can be seen from Figure 5.33 the average equivalent plastic strain rate was approximately 0.1 s^{-1}.

Figure 5.34 shows the equivalent plastic strain map at the cross-section of the compressed specimen. According to this map the maximum of the equivalent plastic strain is situated not at the area of the contact, but somewhere in the middle of the specimen. Therefore, in the place where the oxide scale was situated the plastic strain of the mild steel was 0.02 – 0.03. The equivalent stress was distributed in the slab imitation specimen evenly, as shown in Figure 5.35, although the stresses in the tool varied from the maximum 20 MPa to a minimum about 5 MPa (Figure 5.35). Nevertheless, the longitudinal component (along the X axis) had the maximum values in the contact zone, where the oxide scale is situated, with highest number of 25 MPa near the edge of the specimen, as shown in Figure 5.36. According to Figure 5.36, the minimum of the compressive stresses was in the centre of the specimen where the thermocouple hole was situated.

Since some specimens, especially at temperatures higher than 970°C, have been bent, a second finite element model was built to check any difference in stress-strain behaviour of the specimens during the compression test. The contact under a small angle due to misalignment was simulated in this model. The strain and stress

small angle due to misalignment was simulated in this model. The strain and stress maps of the cross-section of the specimen at the early stage of the contact are shown in Figures 5.37 and 5.38 respectively. As can be seen from Figure 5.38 the equivalent stress map was different from Figure 5.35 and had maxima and minima along different sides which undoubtedly leads to the bending of the specimen. Figure 5.39 shows the final distribution of the total strain along the mild steel specimen and the maximum value of the total strain was approximately 0.06.

Figure 5.40 shows the cross-section of the specimen compressed under a small angle with the equivalent stress map at the end of the compression stage. In spite of the different distribution of stresses, from Figure 5.35, the values of stresses were generally the same as for the first model. Figure 5.41 shows the equivalent stress map on the surface of the workpiece and tool. As can be seen from this figure most stresses on the surface of the workpiece are situated between 10 and 15 MPa with a small zone of slightly higher stresses near the contact (15-20 MPa).

5.4. Summary

In this chapter the results of the 3-D thermo-mechanical coupled finite element analysis have been reported. The finite element simulation of the high-temperature tensile test has helped to evaluate a distribution of stress and heat transfer in a specimen with the flat gauge section. According to the analysis, both 2 and 4 mm gauge thickness specimens had almost uniform distribution of surface stresses. Even heterogeneity of stresses near the edge of the gauge section did not affect too much the crack spacing. However, the modelling of the oxide scale revealed a strong dependence of crack spacing on cracking stress and, hence, the stress intensity factor (K_{Ic}). In its turn, K_{Ic} is strongly dependent on the temperature. The insufficient amount of experimental data and its wide scatter were also mentioned as possible sources of error in the modelling. The finite element simulation of the high-temperature compression test has helped to evaluate heat transfer with respect to the oxide scale effect and to determine a suitable stress-strain distribution in specimens during the contact and compression stage. In addition, the bending phenomenon during the hot compression test also was simulated.

Figures

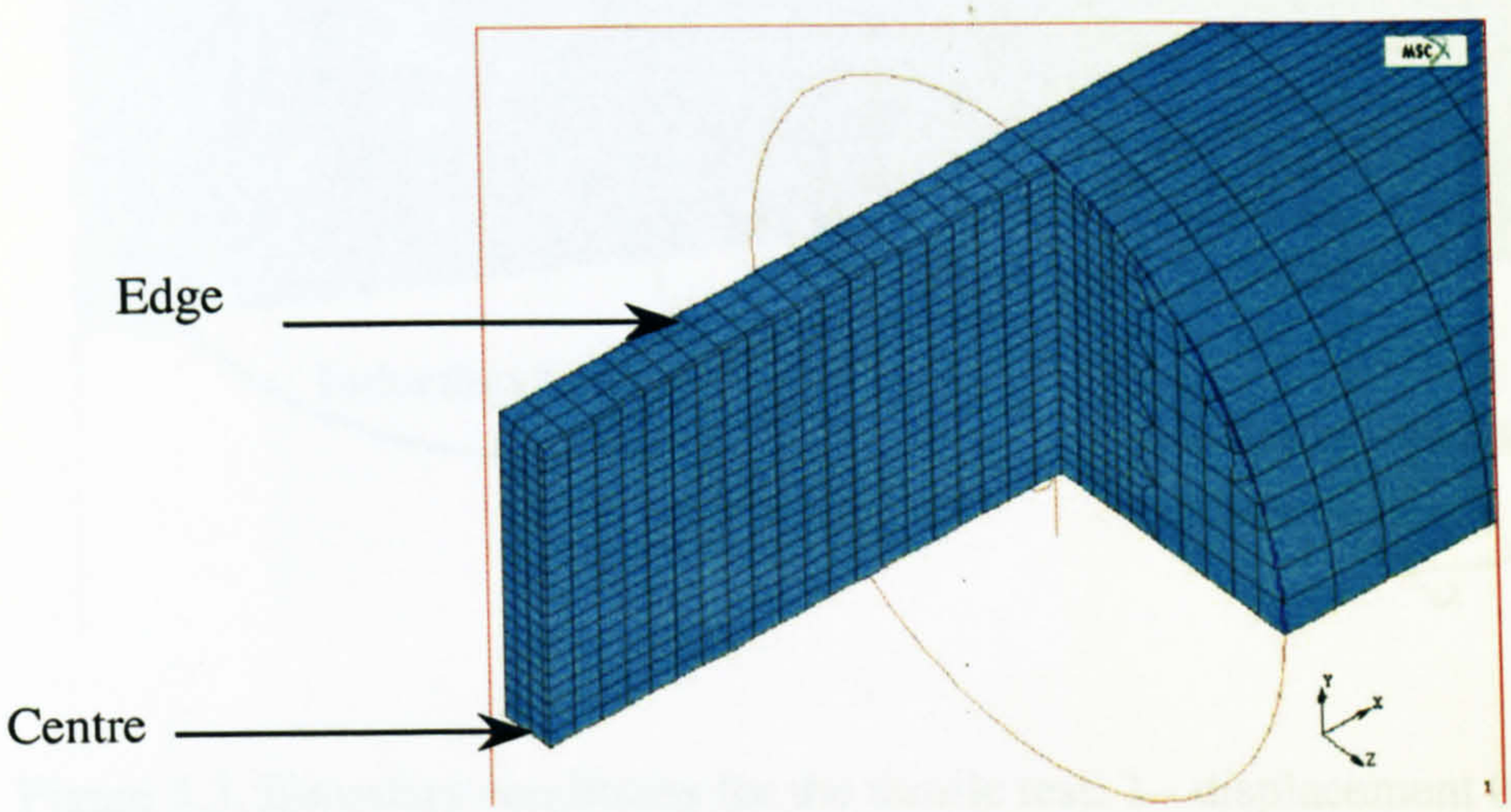

Figure 5.1. The finite element model – 1/8 of the specimen with the flat gauge section of 2 mm.

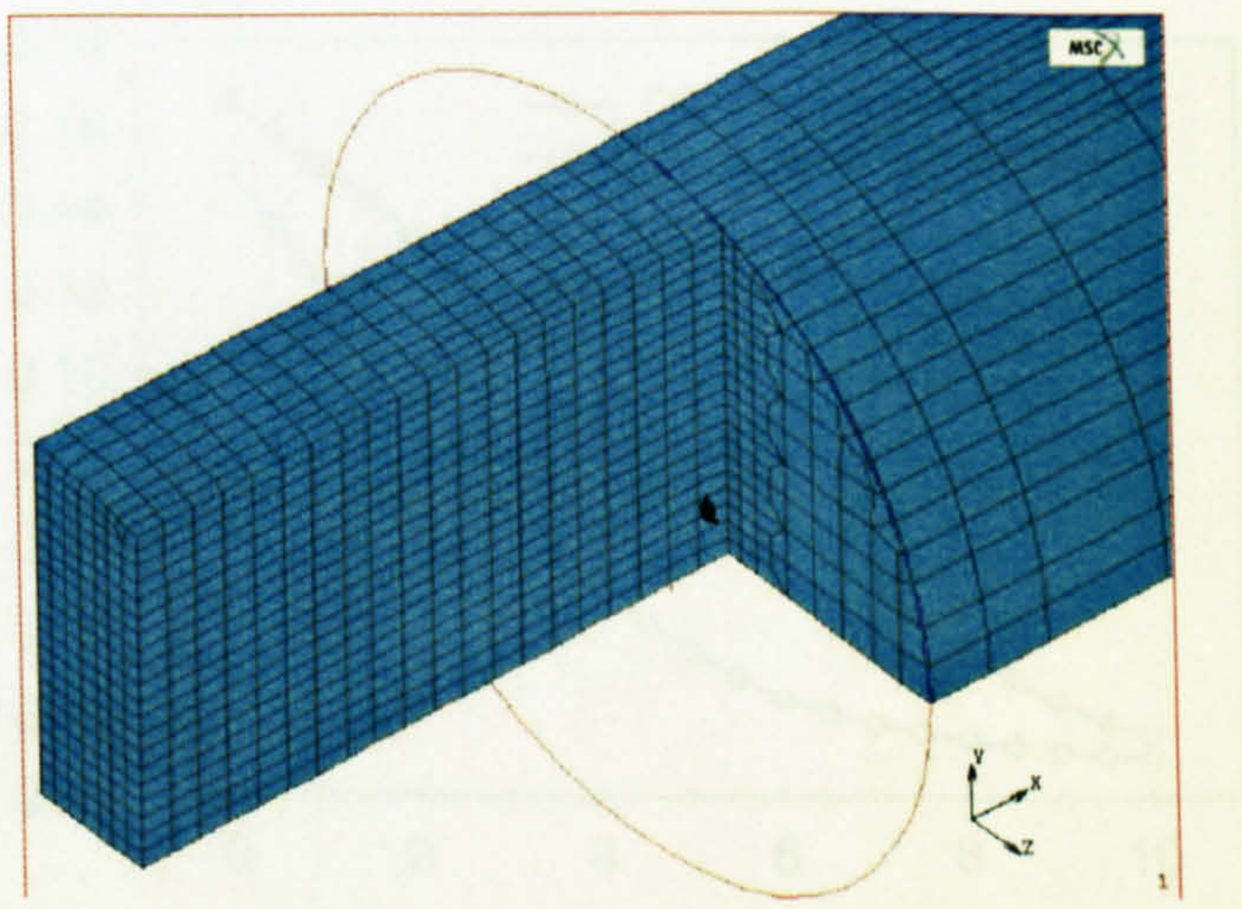

Figure 5.2. The finite element model – 1/8 of the specimen with the flat gauge section of 4 mm.

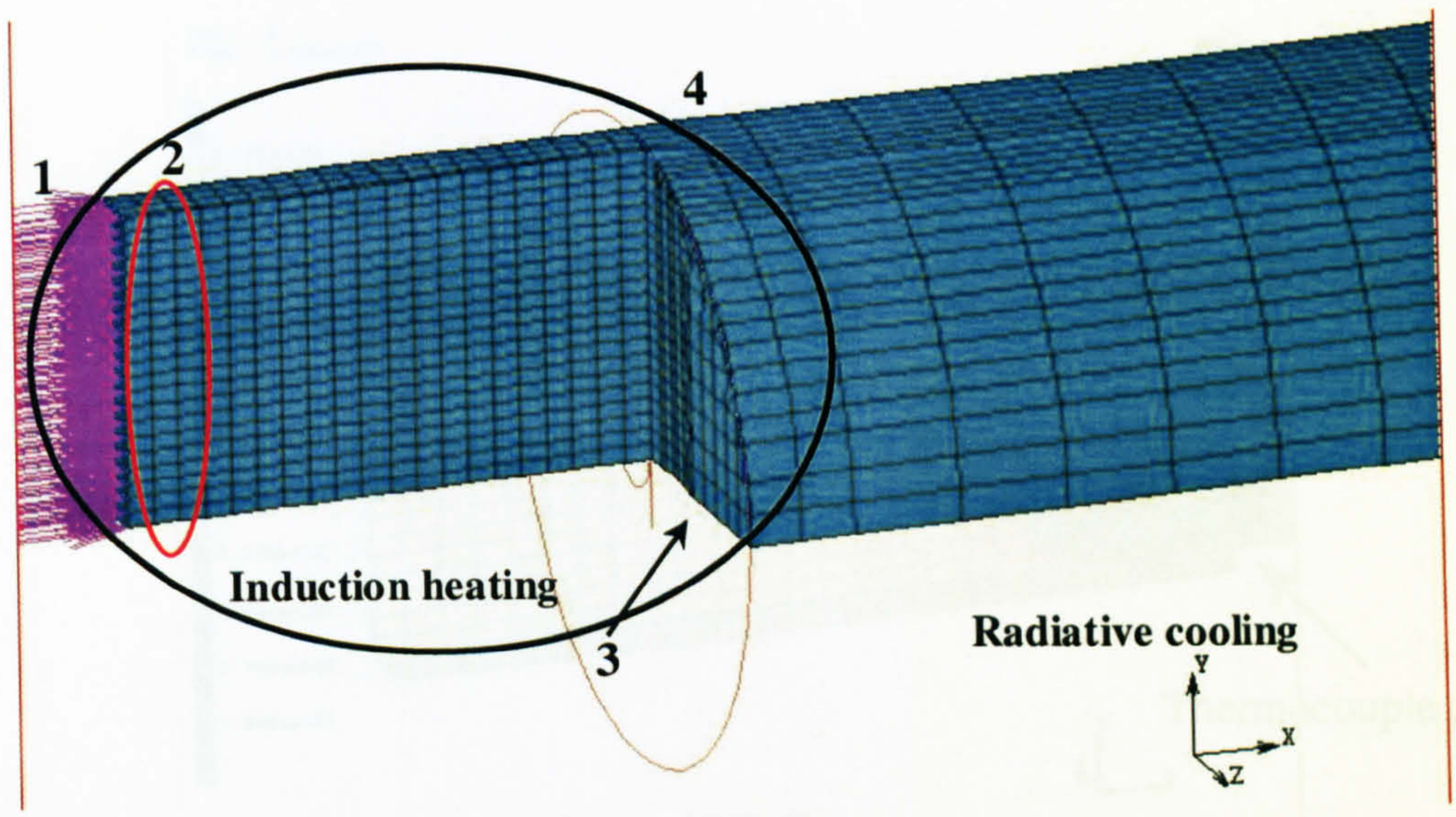

Figure 5.3. Boundary conditions for the tensile test: 1 - displacement 0.15 mm, 2 – maximum/(minimum) temperature for the gauge section 4/(2) mm, 3 – temperature measured by thermocouple, 4 – temperature measured by pyrometer.

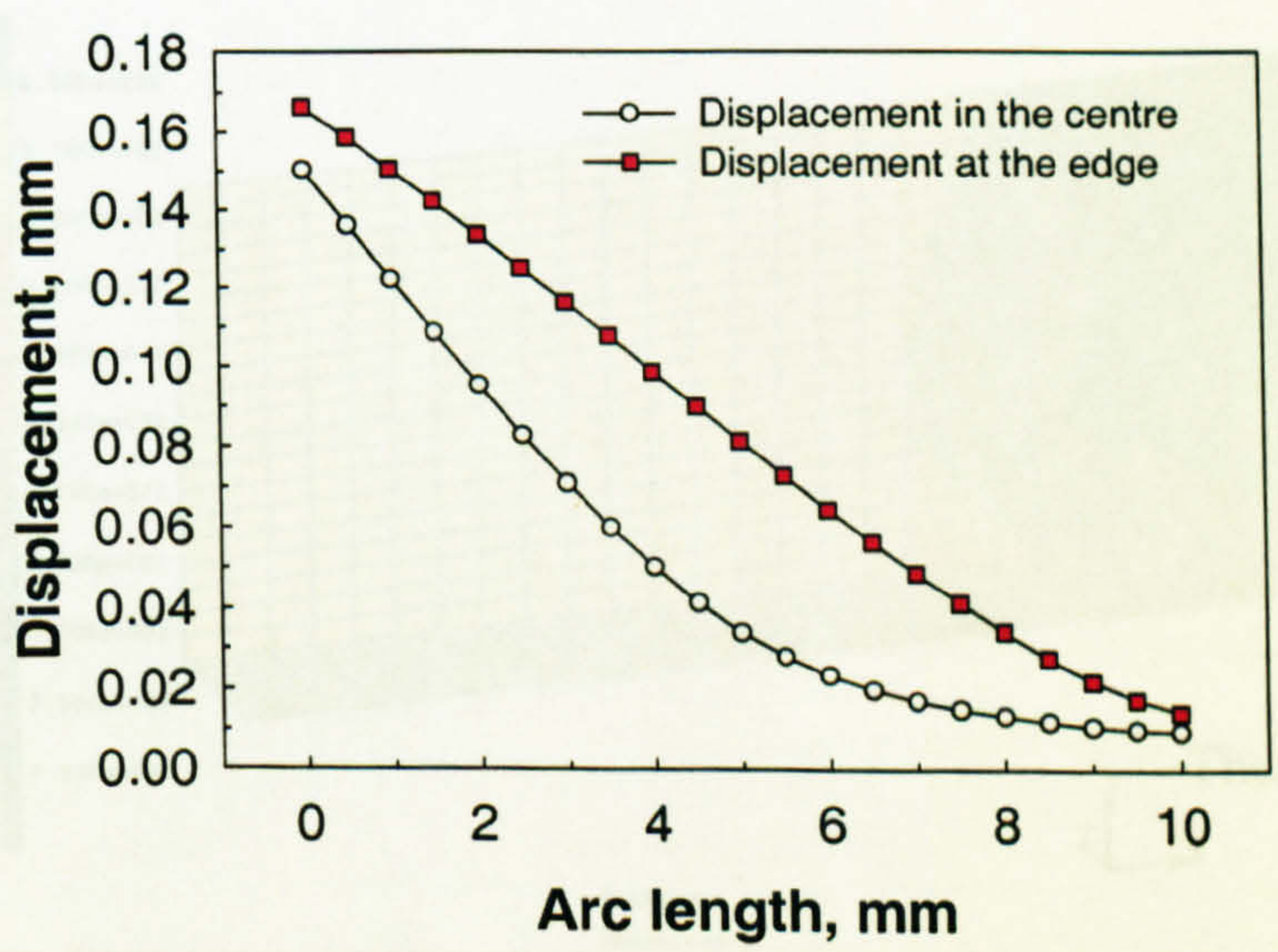

Figure 5.4. Displacement variation in the centre and at the edge of the gauge section.

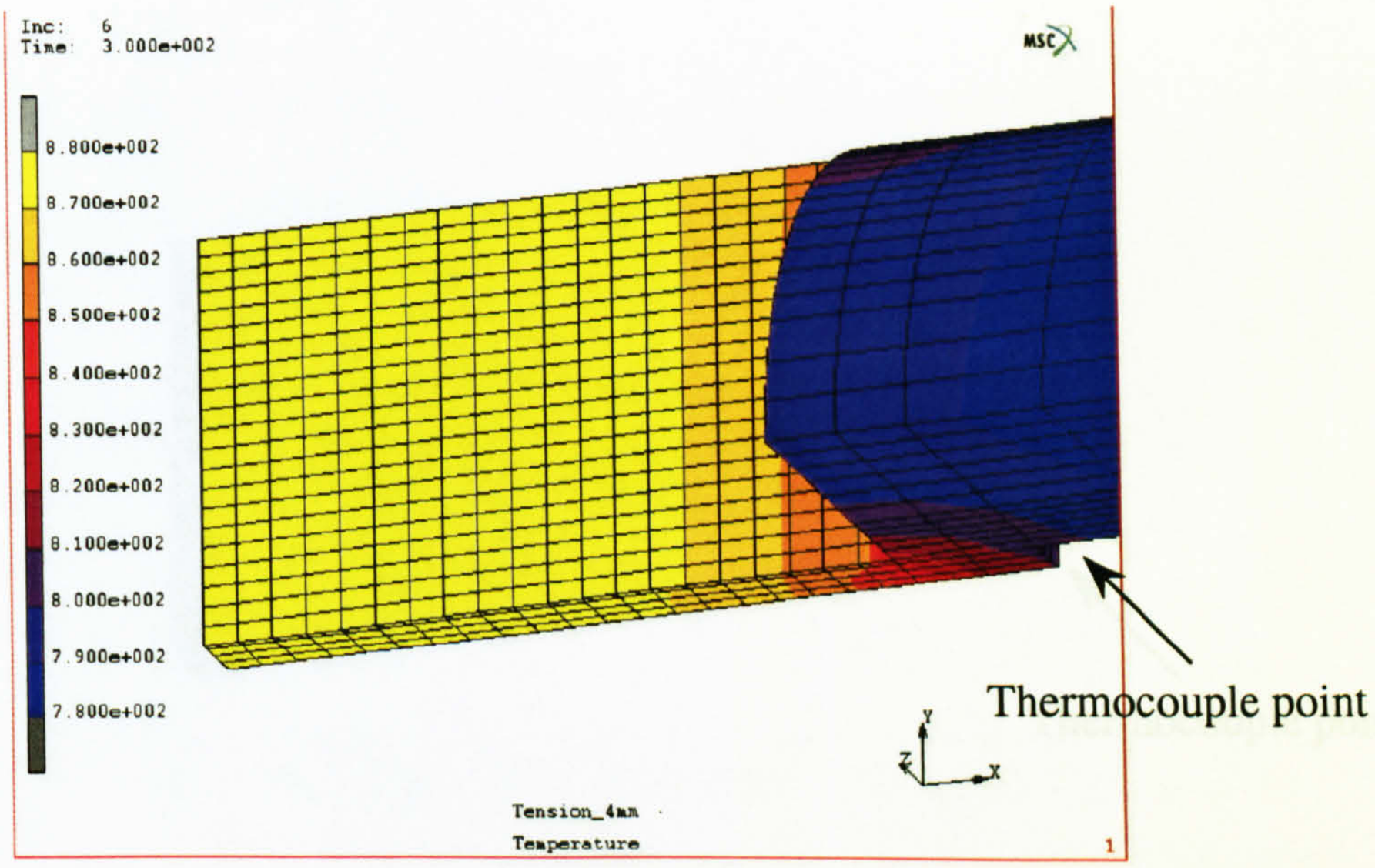

Figure 5.5. Temperature distribution in the gauge section (2 mm), the centre of the gauge section is heated.

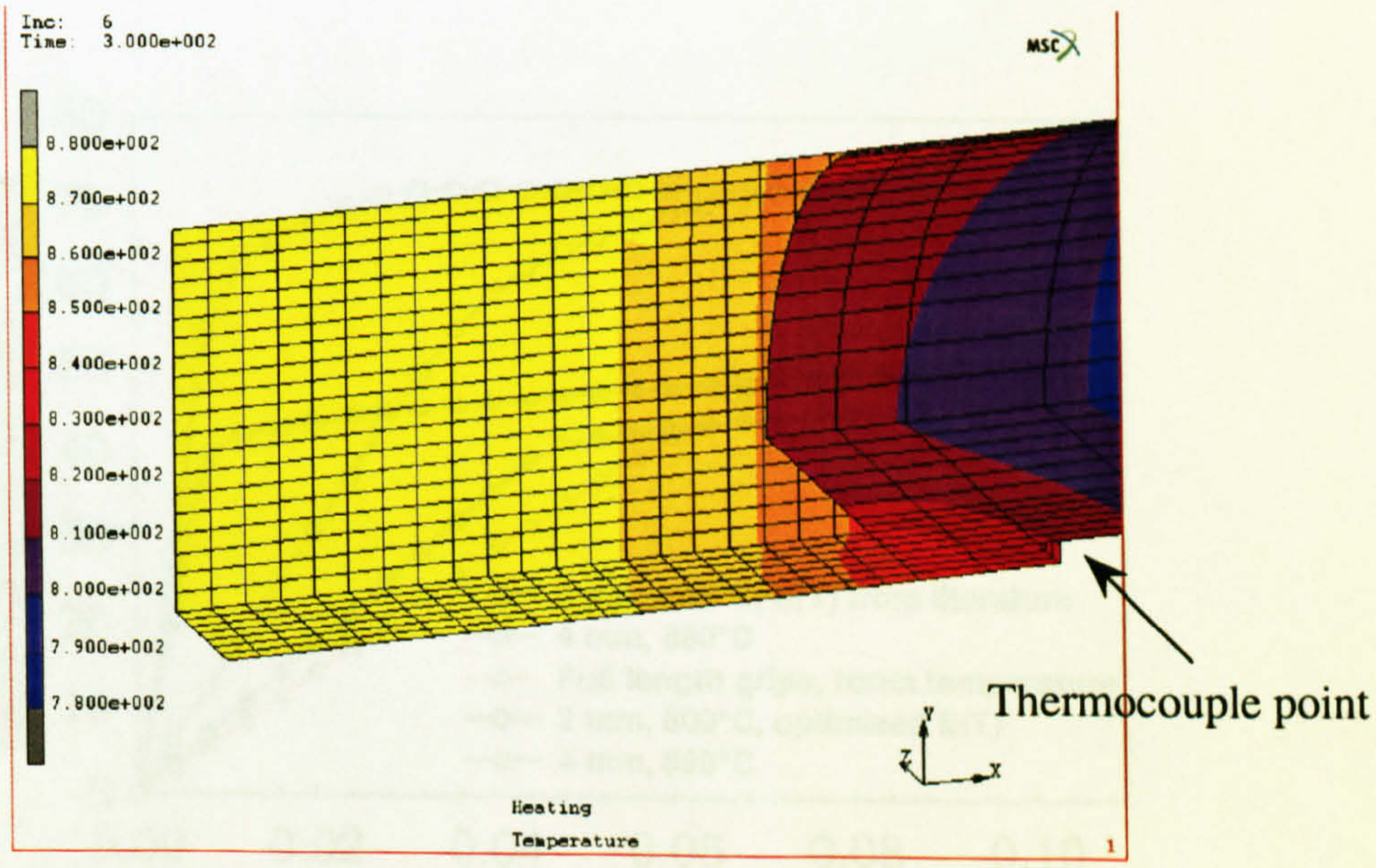

Figure 5.6. Temperature distribution in the gauge section (4 mm), the centre of the gauge section is heated.

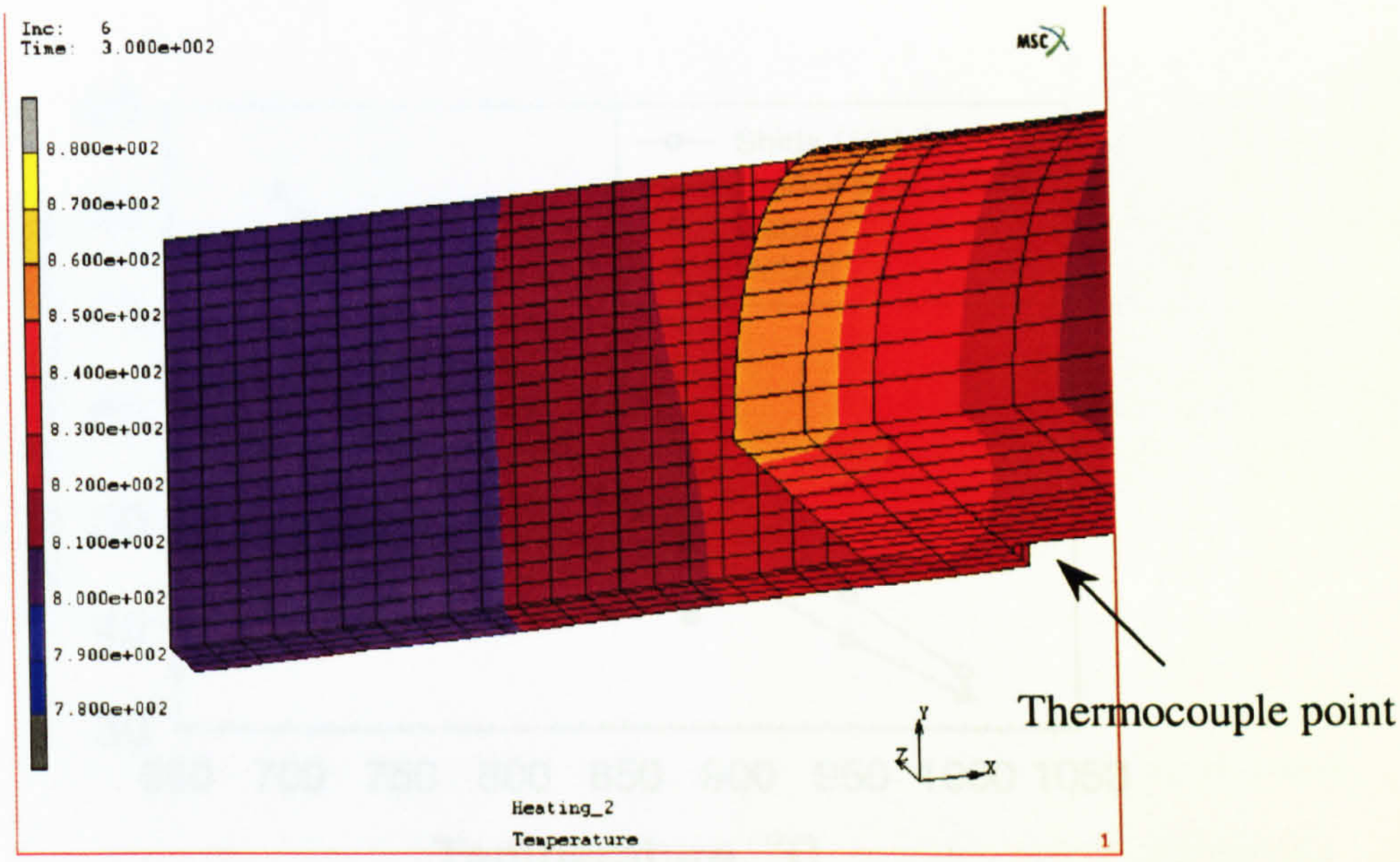

Figure 5.7. Temperature distribution in the gauge section (2 mm), the cylindrical part of the specimen is heated.

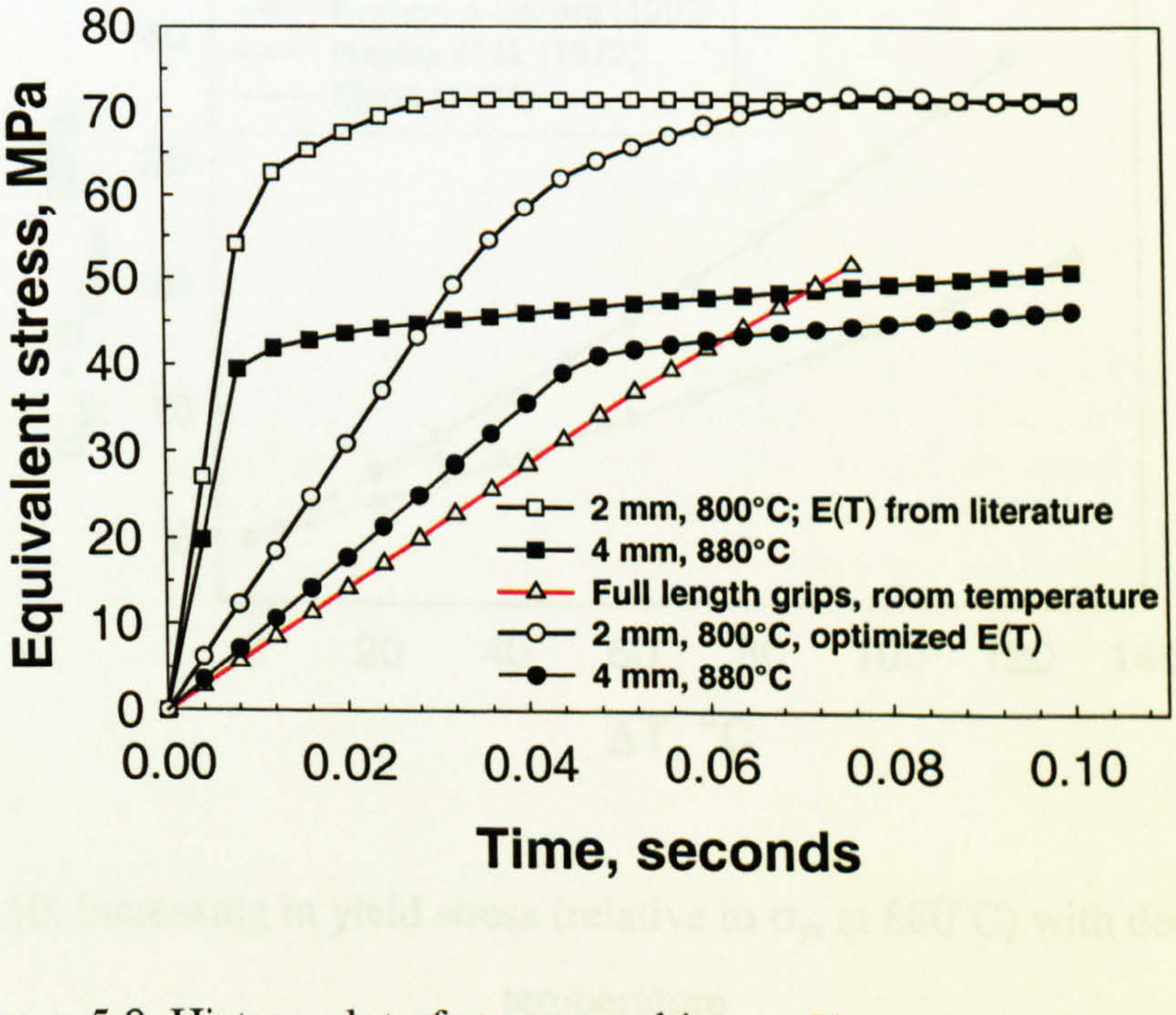

Figure 5.8. History plot of stresses subject to Young's modulus value.

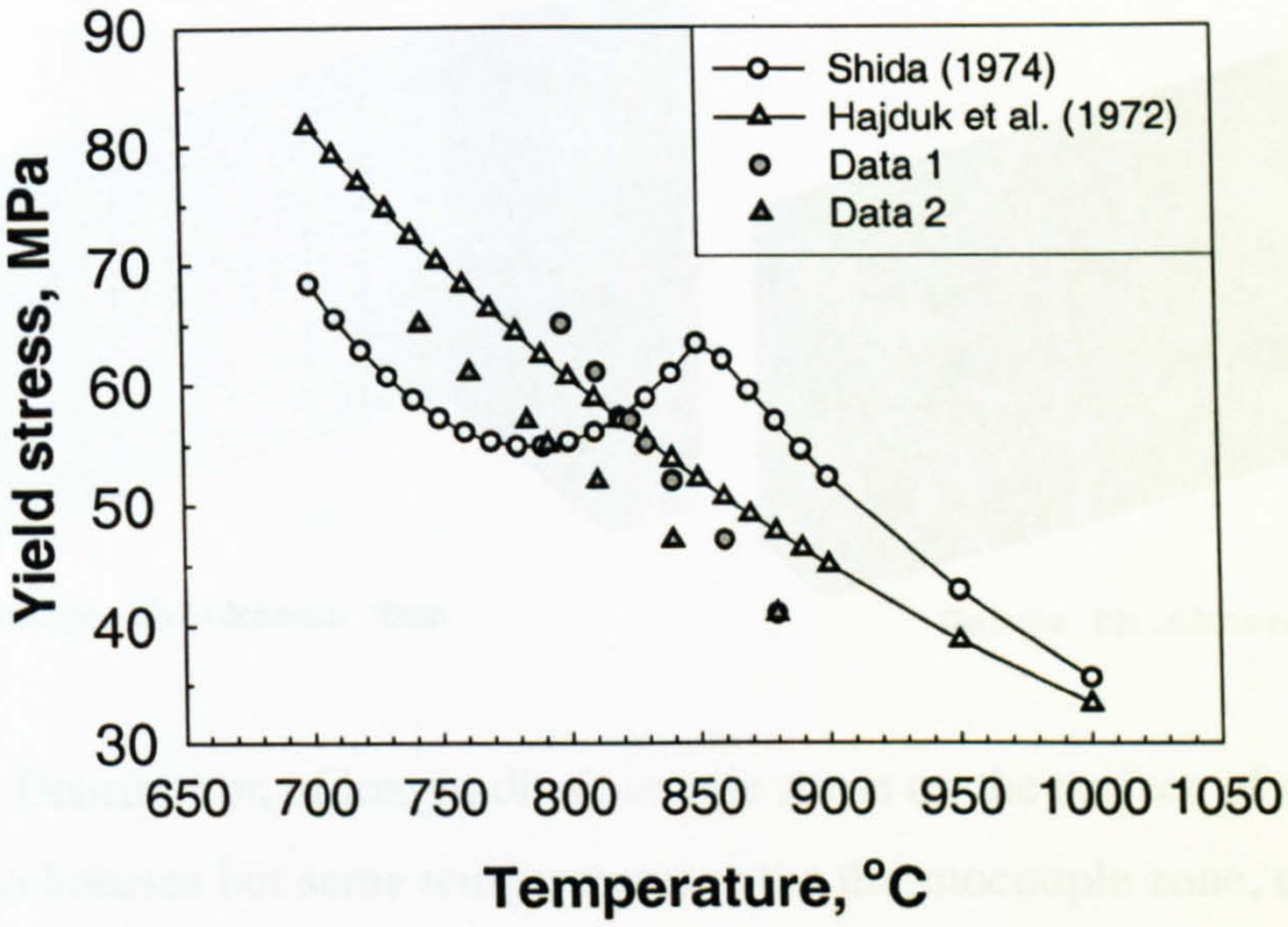

Figure 5.9. Yield stress as a function of the temperature.

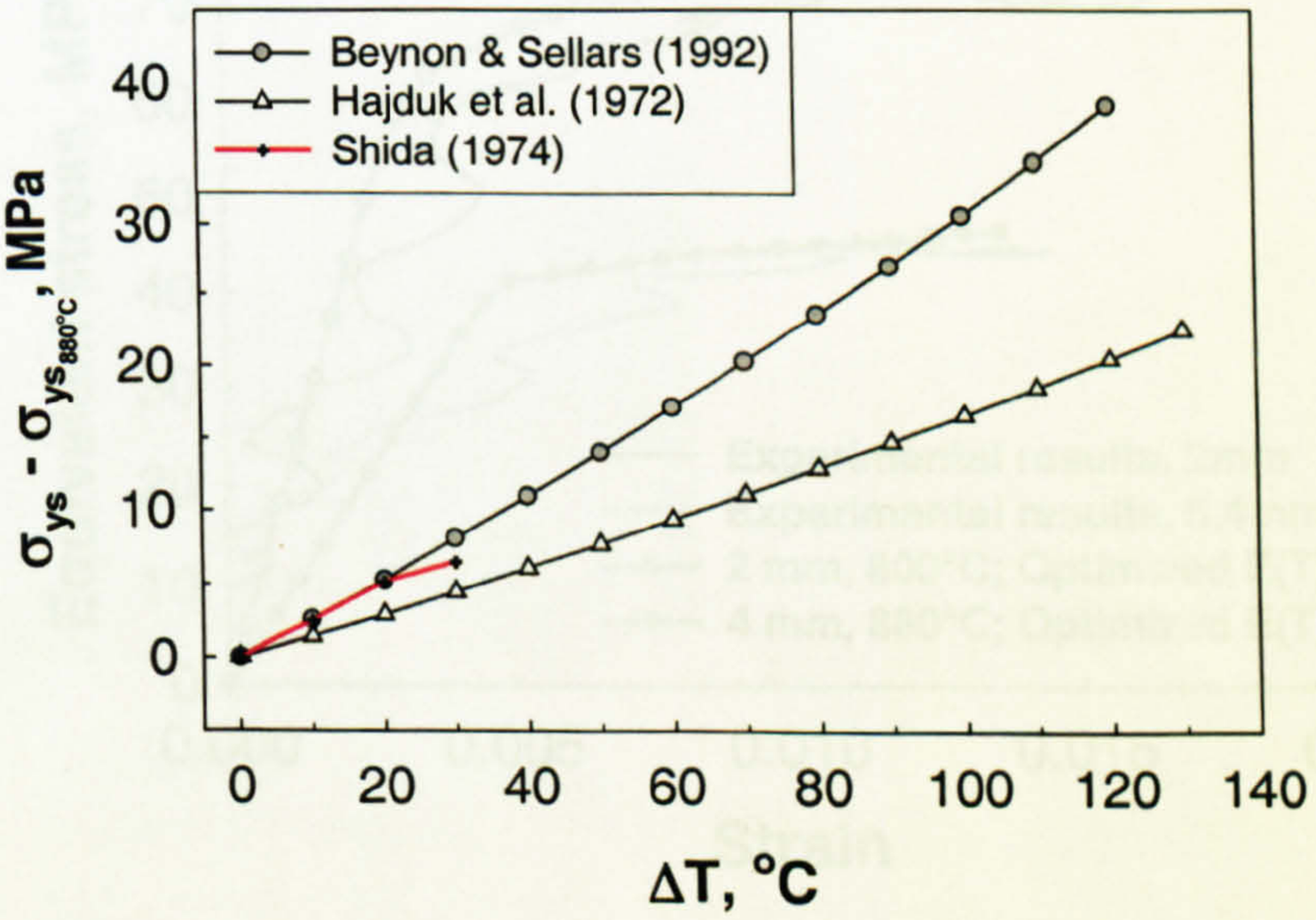

Figure 5.10. Increasing in yield stress (relative to σ_{ys} at 880°C) with decreasing the temperature

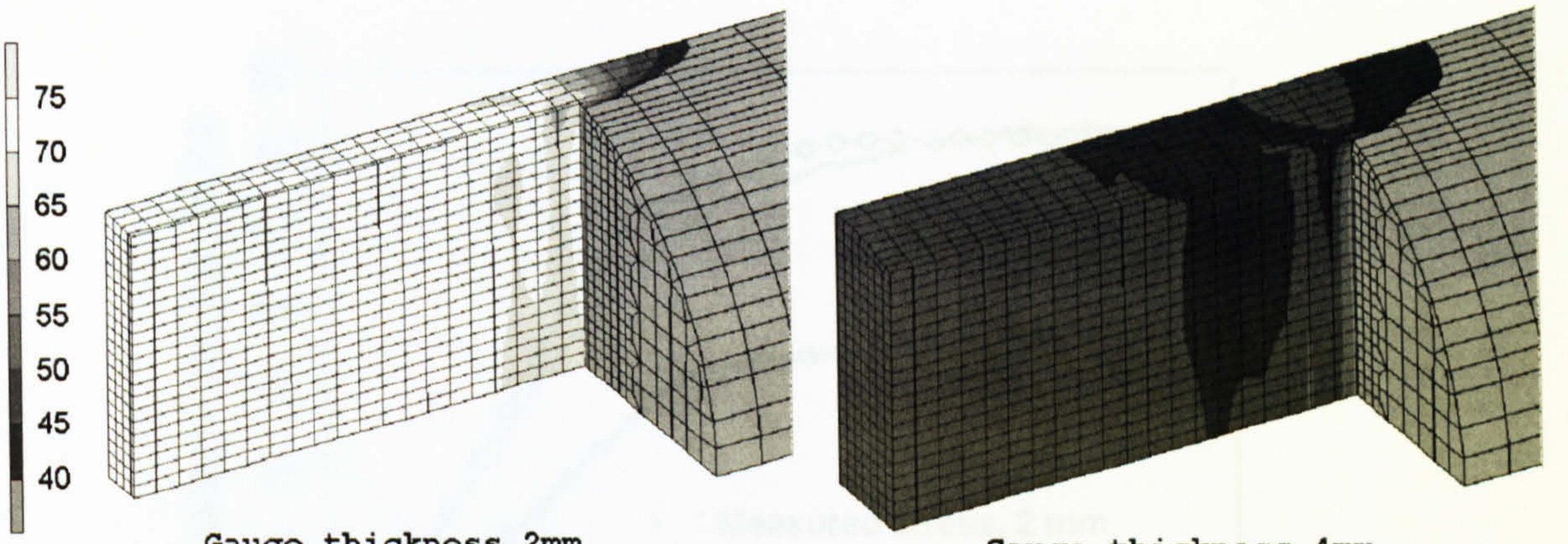

Figure 5.11. Distribution of longitudinal, tensile stress on the surface of models with different thicknesses but same temperatures at the thermocouple zone, total tensile strain is 0.015, average strain rate is 0.2 s^{-1}.

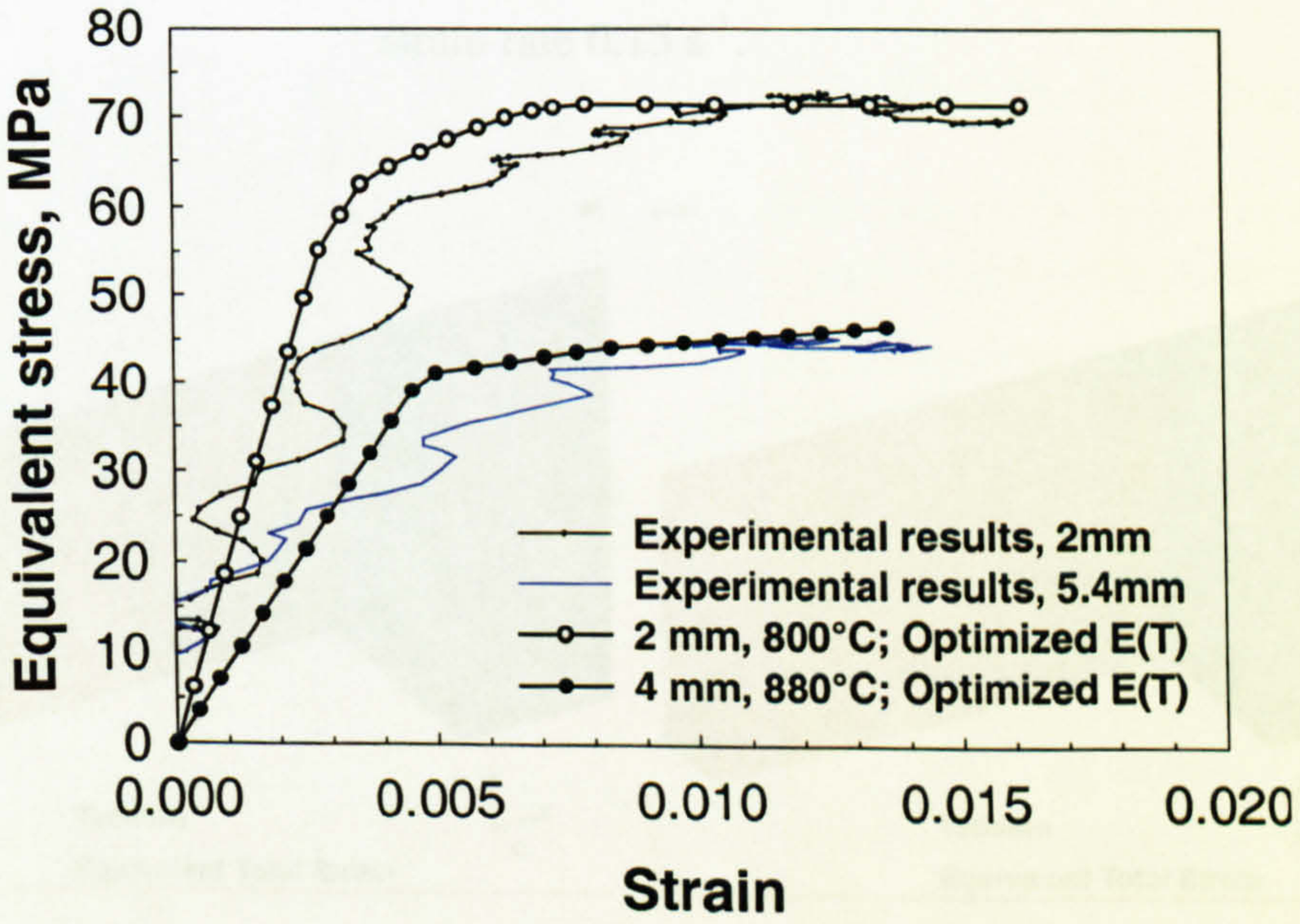

Figure 5.12. Stress - strain curves comparison, average strain rate 0.15 s^{-1}.

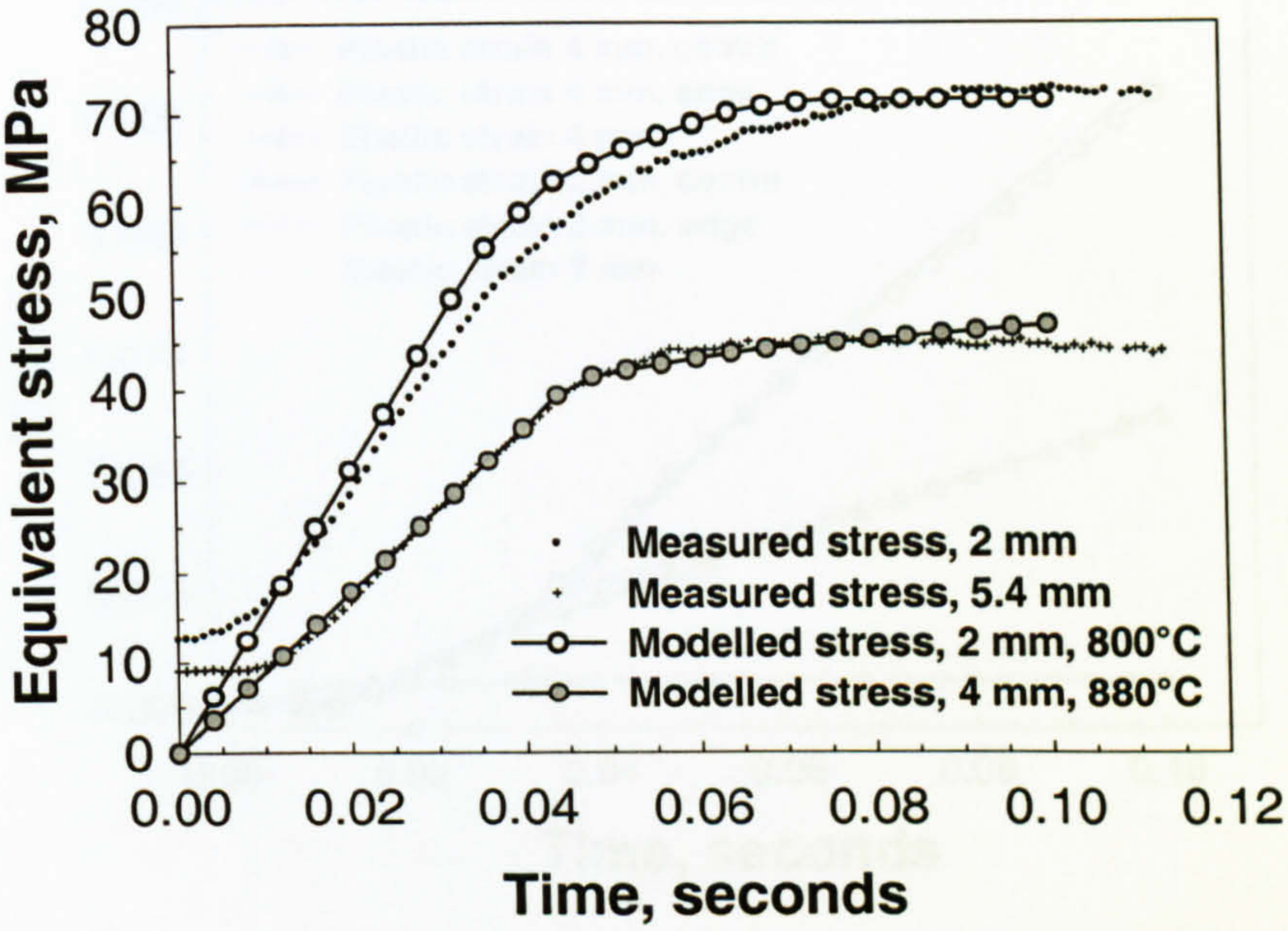

Figure 5.13. History plot showing evolution of stress at the specimen surface, average strain rate 0.15 s^{-1}.

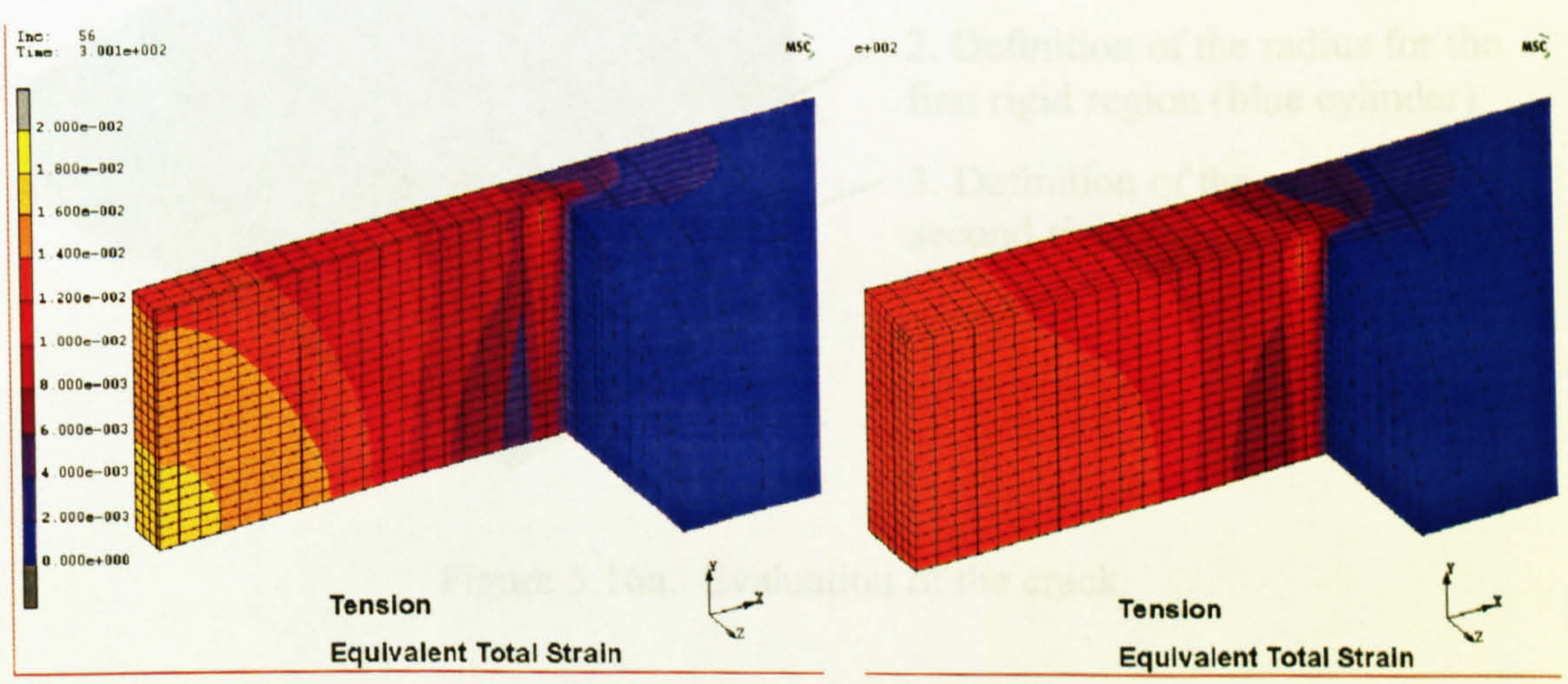

Figure 5.14. Equivalent total strain for a) 2 mm model and b) 4 mm model.

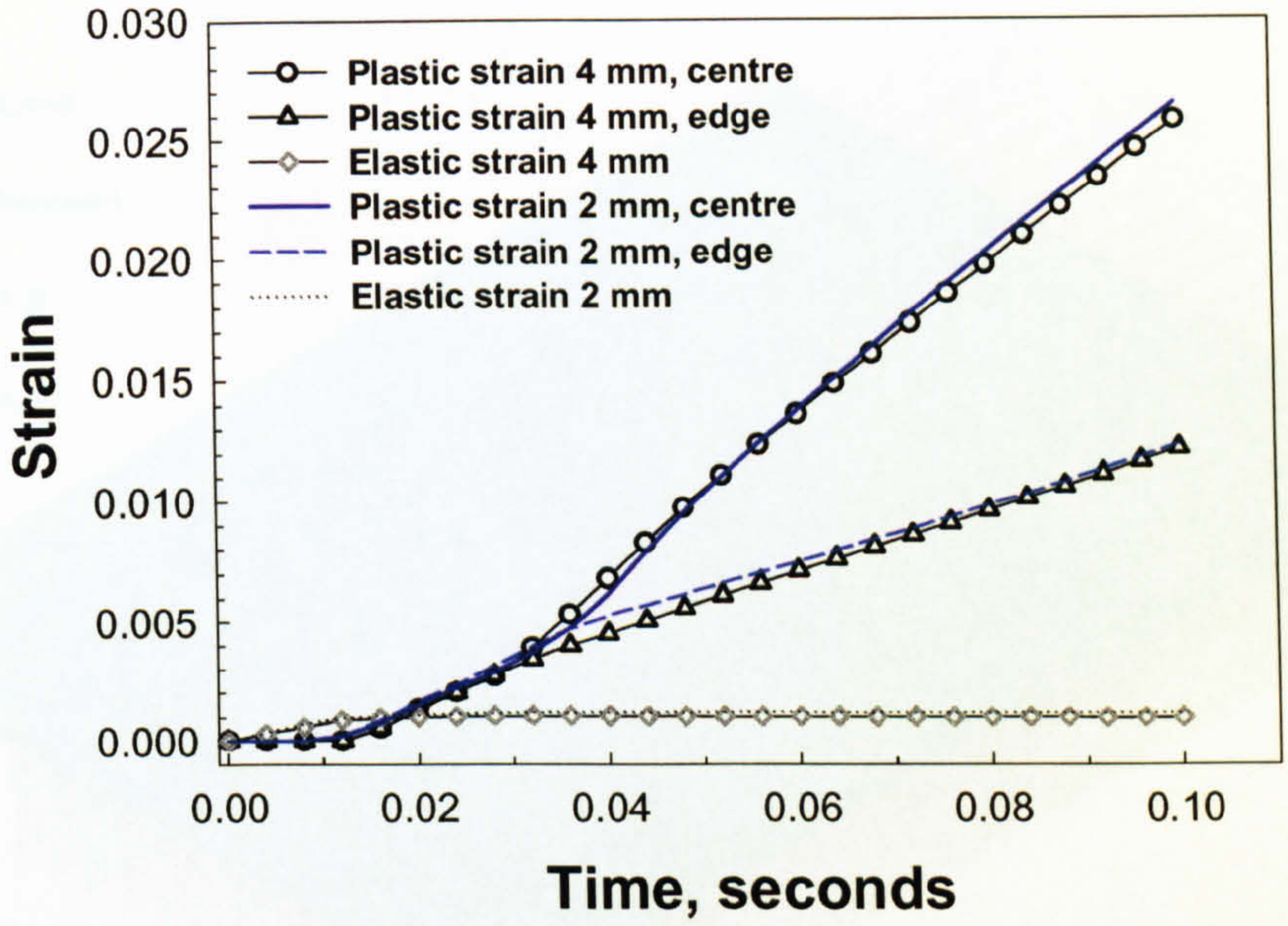

Figure 5.15. History plot of plastic and elastic strains.

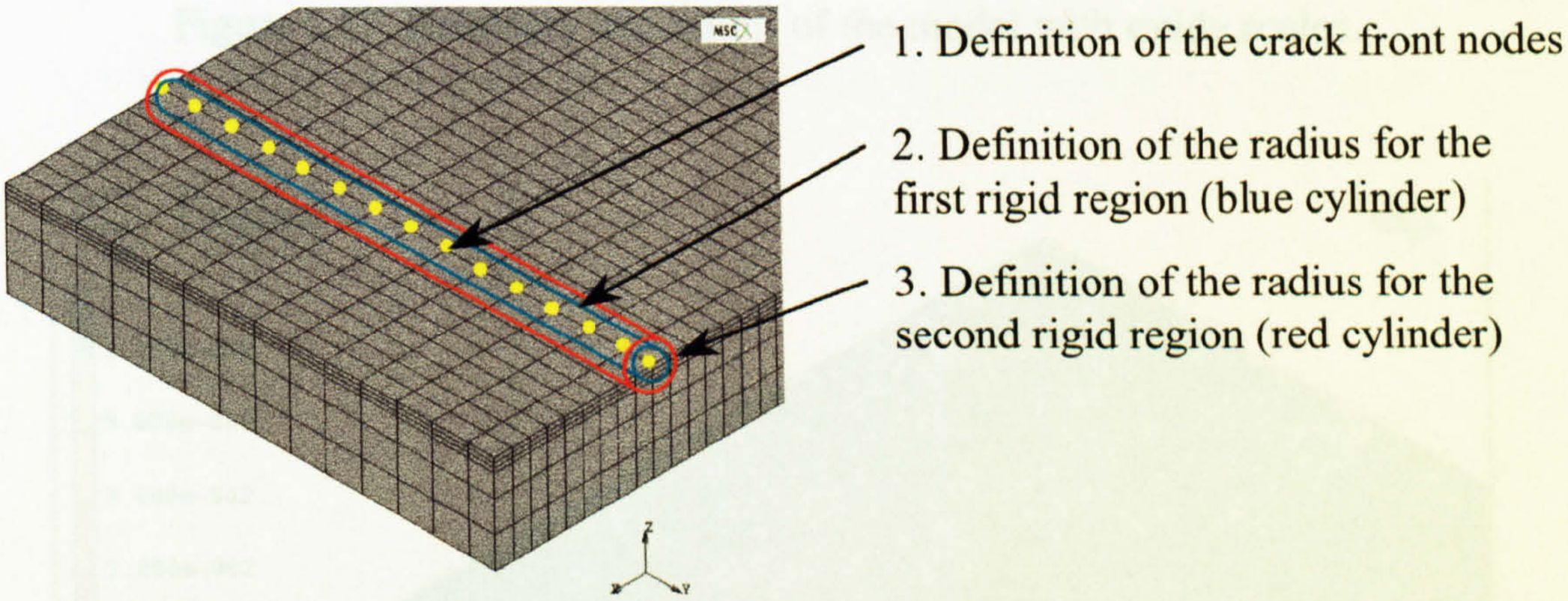

Figure 5.16a. Evaluation of the crack.

Figure 5.16b. Uniaxial stress-strain diagram.

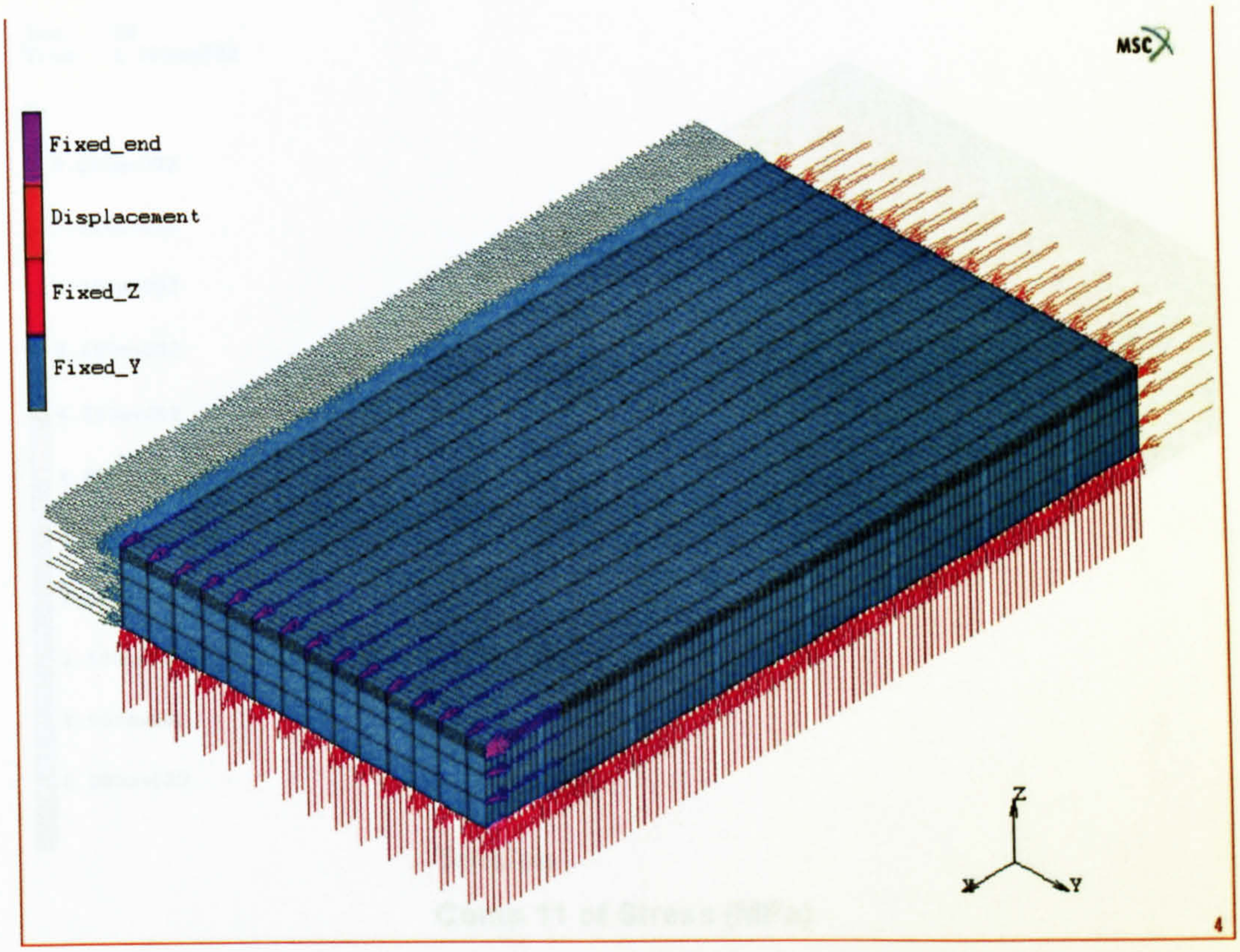

Figure 5.17. Boundary conditions of the model with oxide scales.

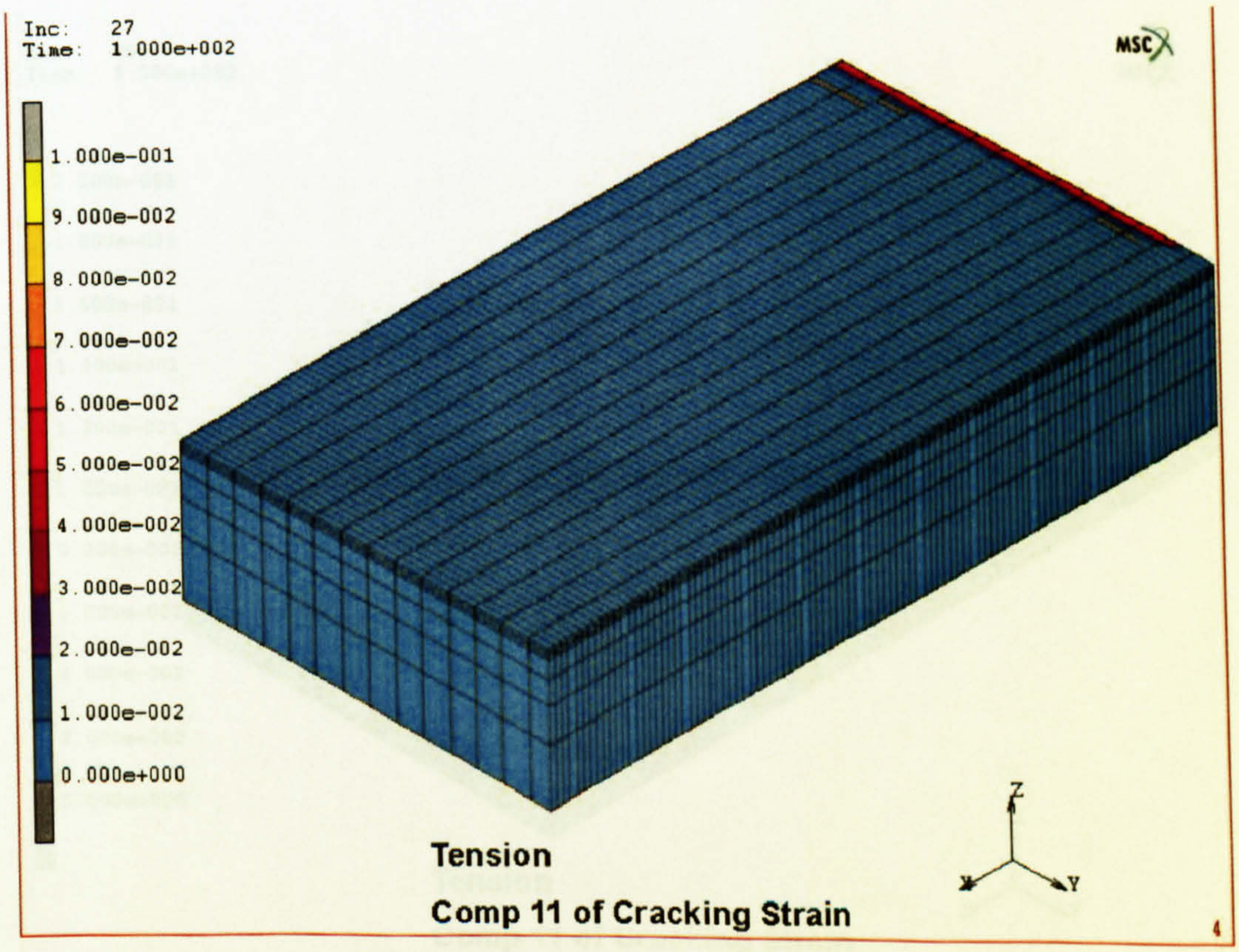

Figure 5.18. Crack initiation at 850°C and K_{Ic} = 12 MN $m^{-3/2}$.

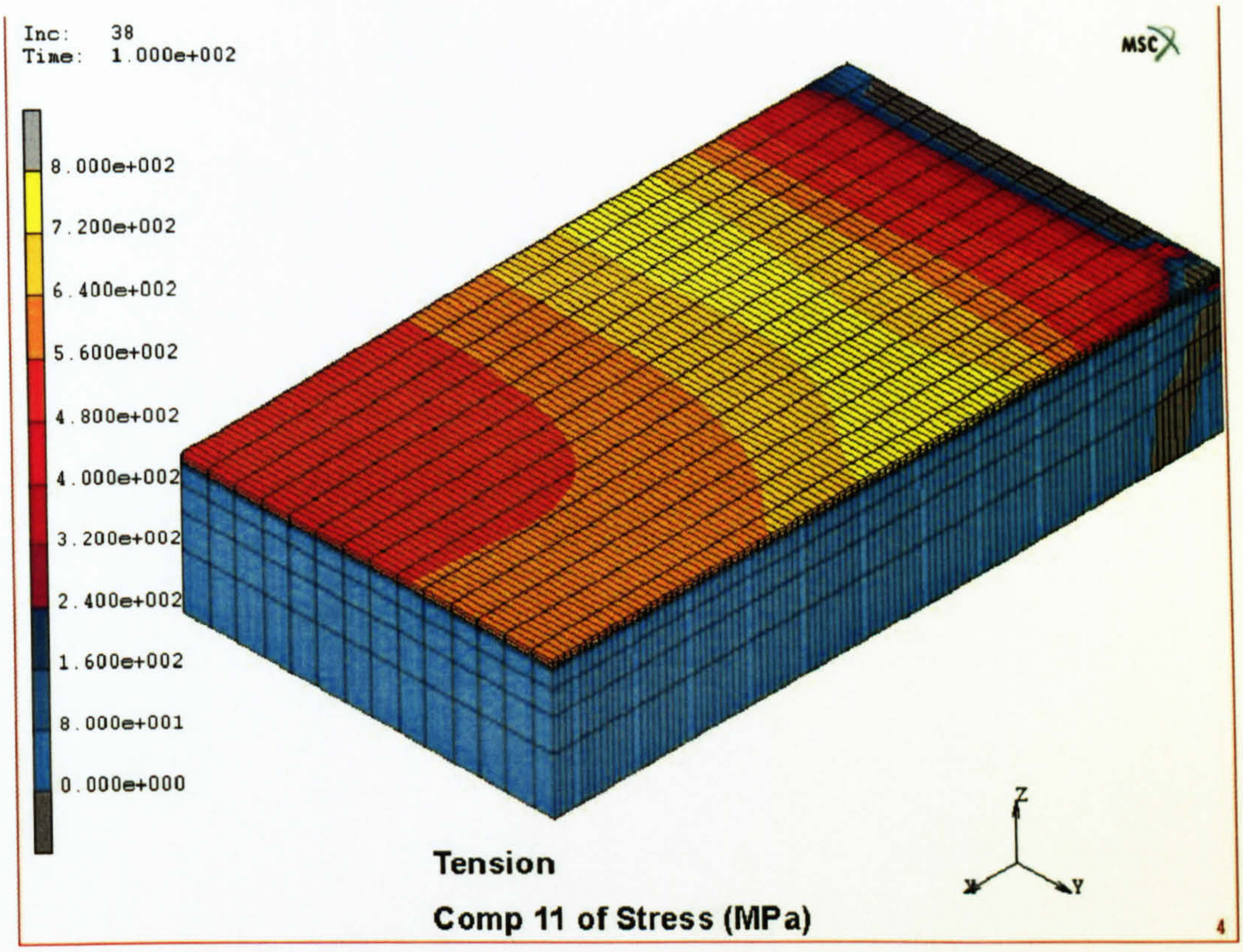

Figure 5.19. Stress distribution in the oxide scale after first crack appears.

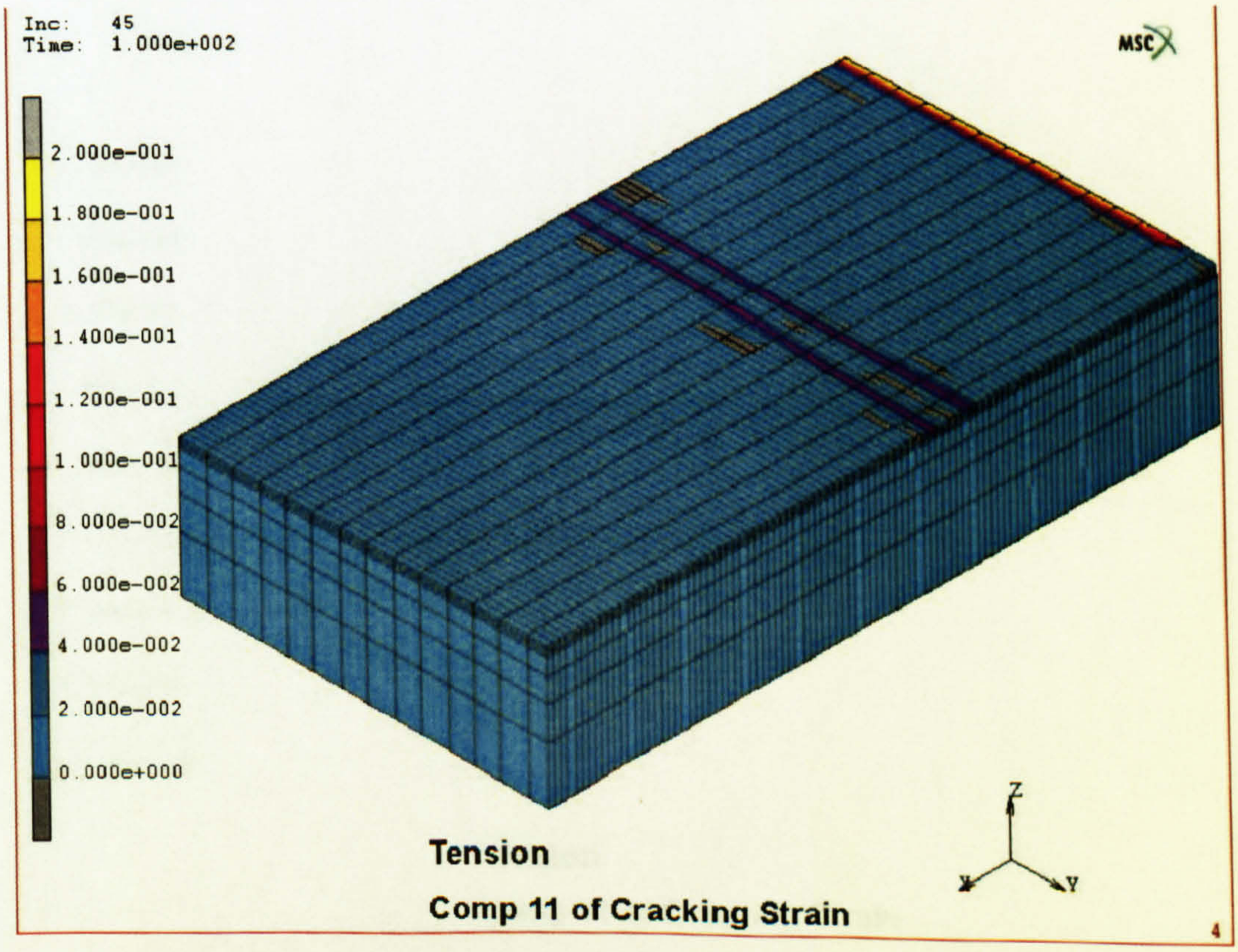

Figure 5.20. Second crack appearance at 850°C and K_{Ic} = 12 MN $m^{-3/2}$.

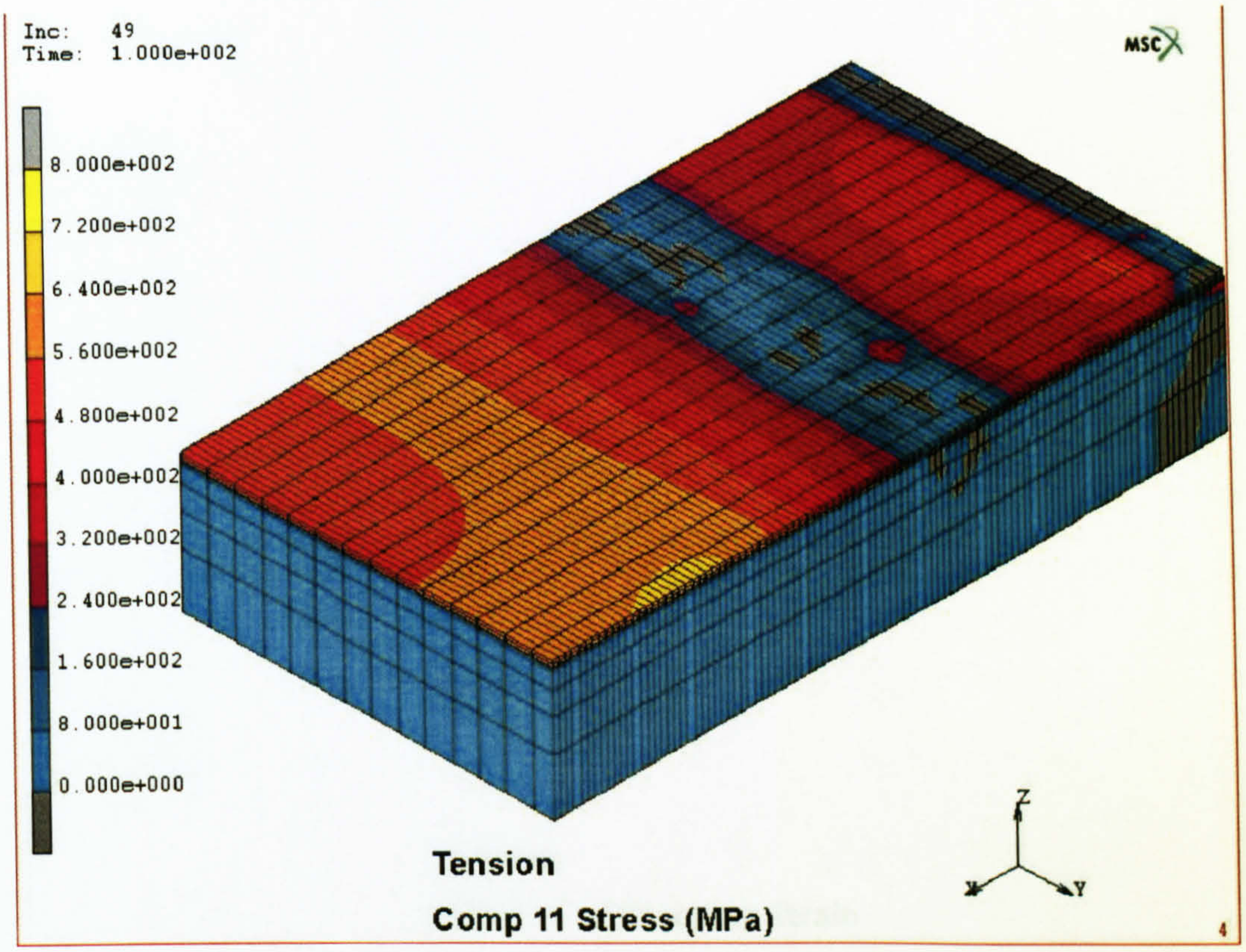

Figure 5.21. Stress distribution in the oxide scale after second crack appears.

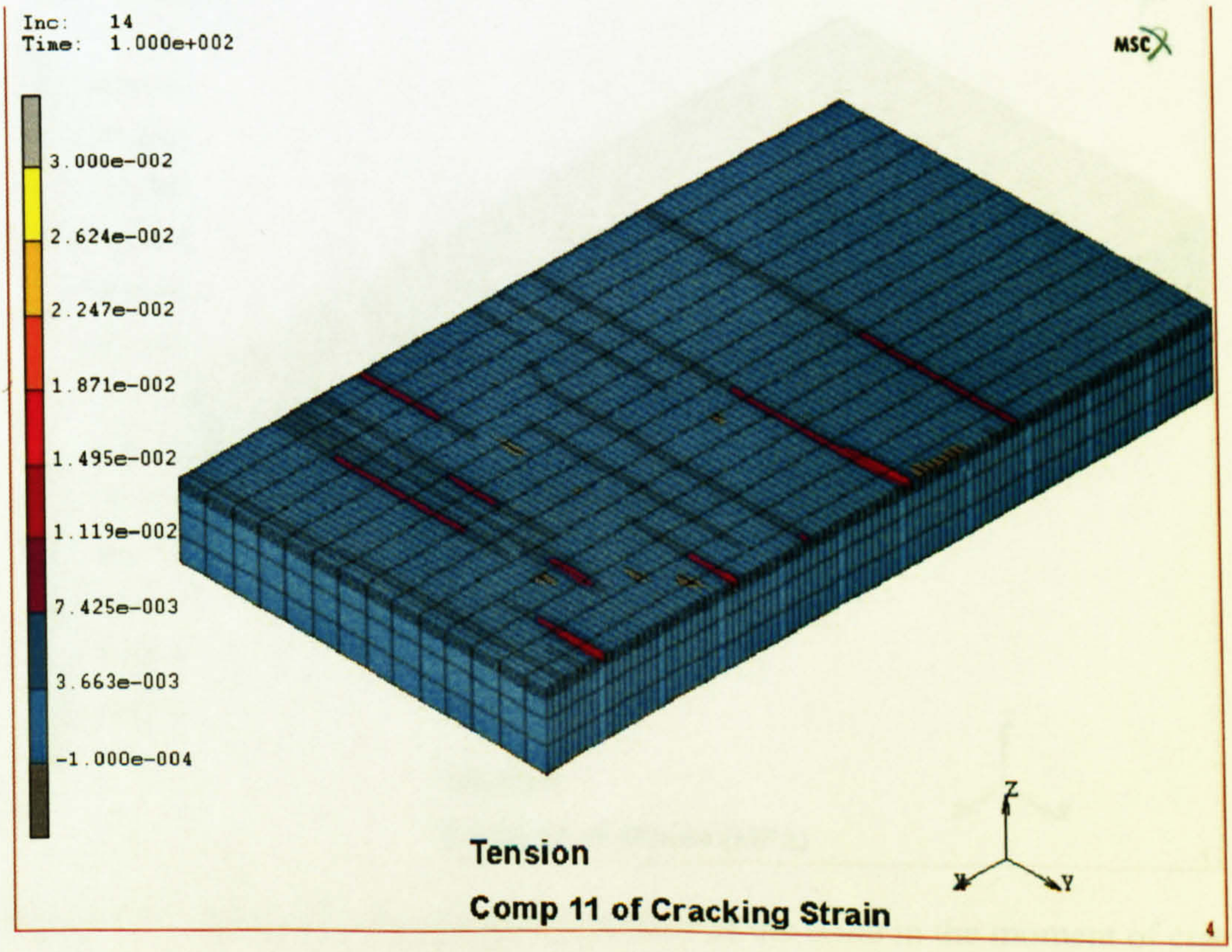

Figure 5.22. Crack initiation at 750°C and $K_{Ic} = 4$ MN $m^{-3/2}$.

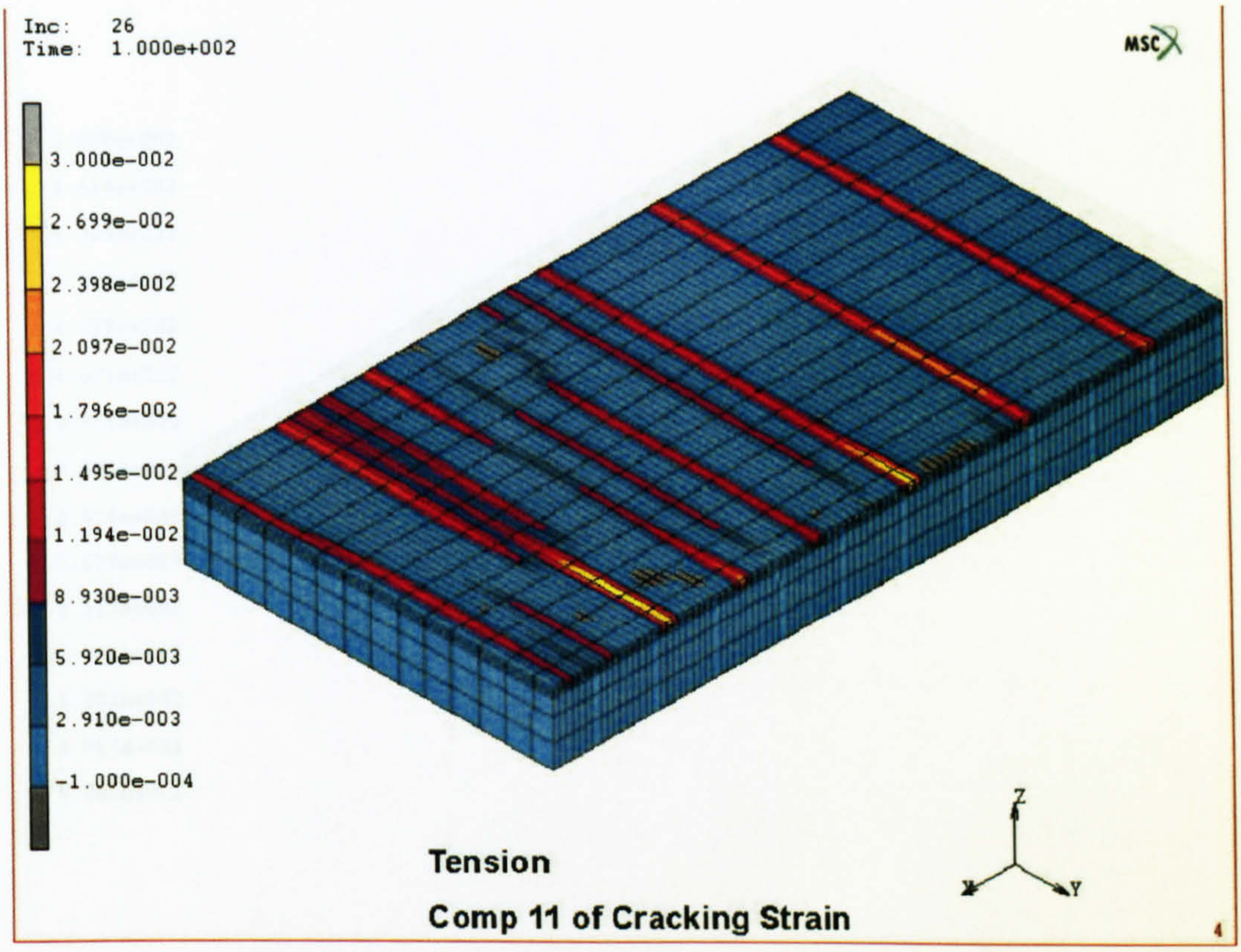

Figure 5.23. Final crack pattern on the oxide scale at 750°C and K_{Ic} = 4 MN $m^{-3/2}$.

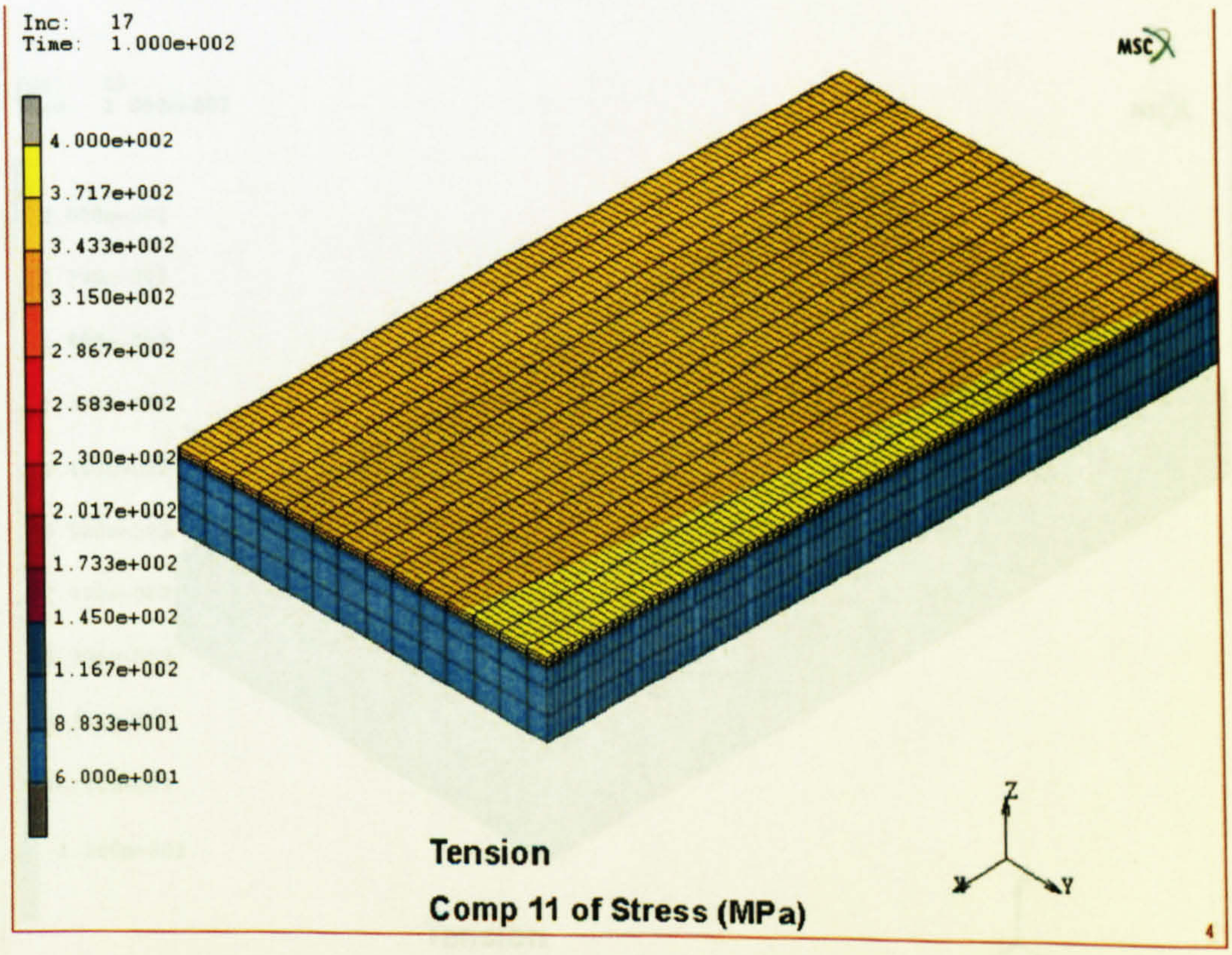

Figure 5.24. Stress distribution on the surface of the scale in the moment of crack initiation. (T = 800°C, K_{Ic} = 5.8 MN·$m^{-3/2}$).

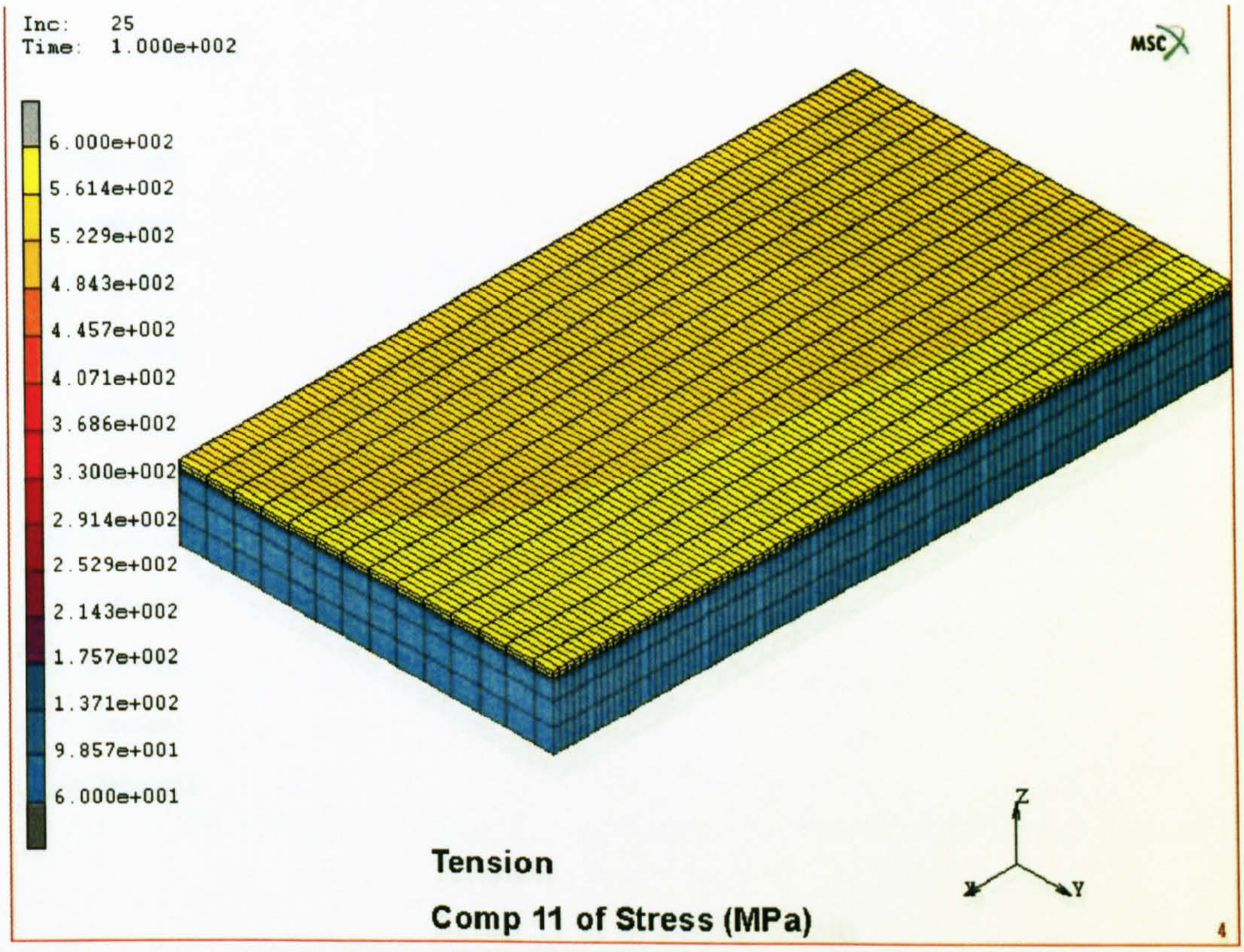

Figure 5.25. Stress distribution on the surface of the scale in the moment of crack initiation. ($T = 800^{o}C$, $K_{Ic} = 9.5\ MN \cdot m^{-3/2}$).

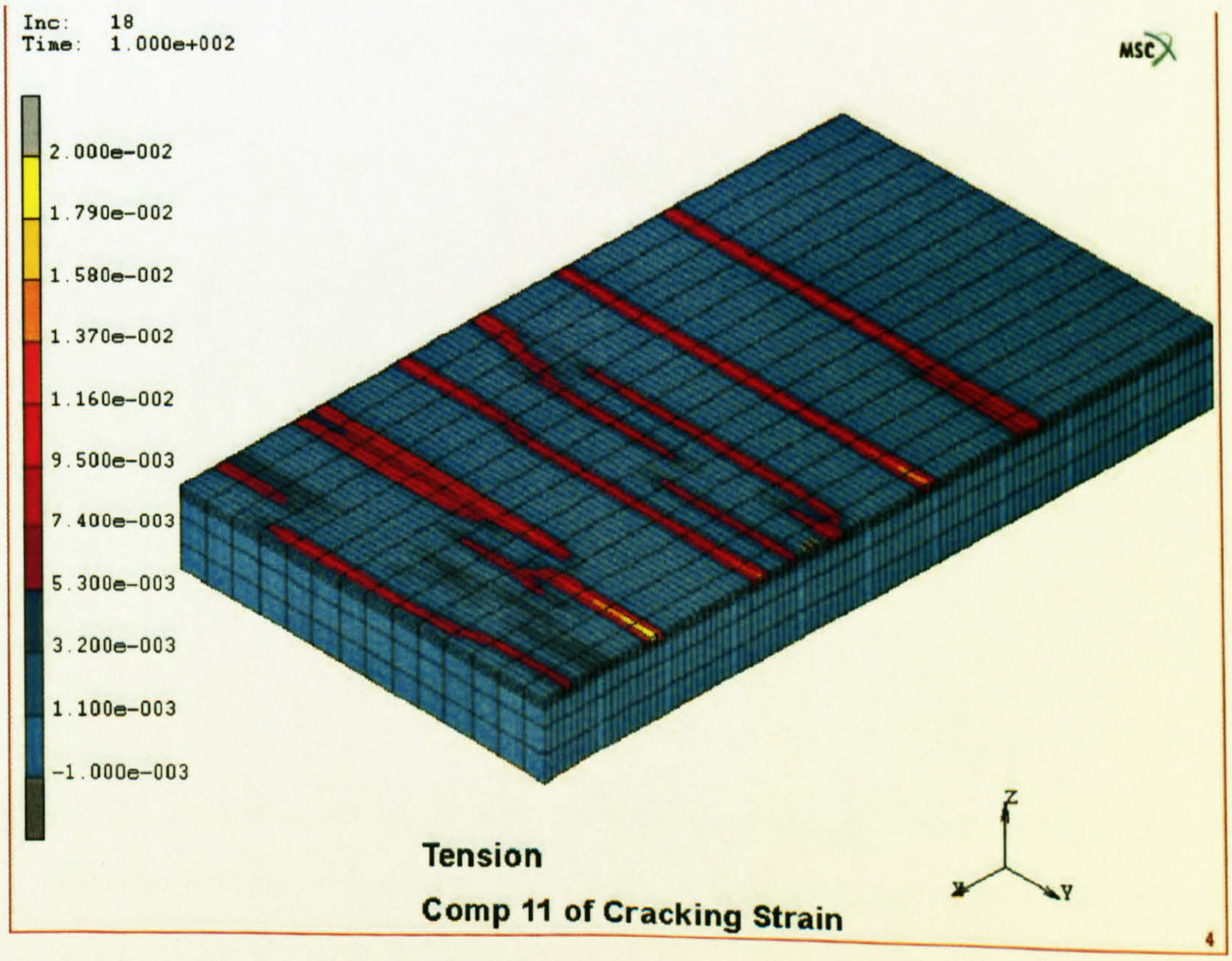

Figure 5.26. Crack pattern formation at $800^{o}C$ and $K_{Ic} = 5.8\ MN \cdot m^{-3/2}$.

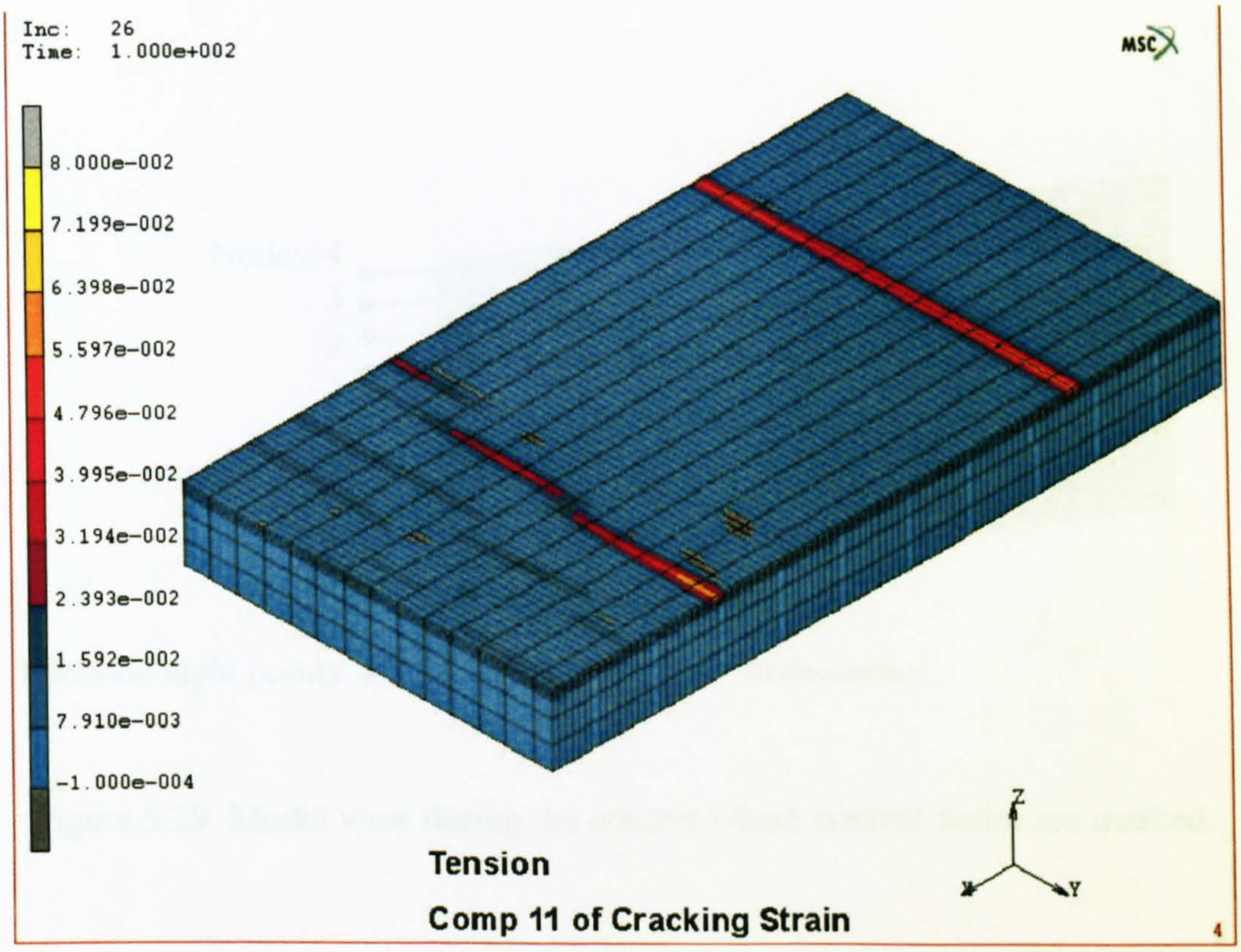

Figure 5.27. Crack initiation at 800°C and K_{Ic} = 9.5 MN·m$^{-3/2}$.

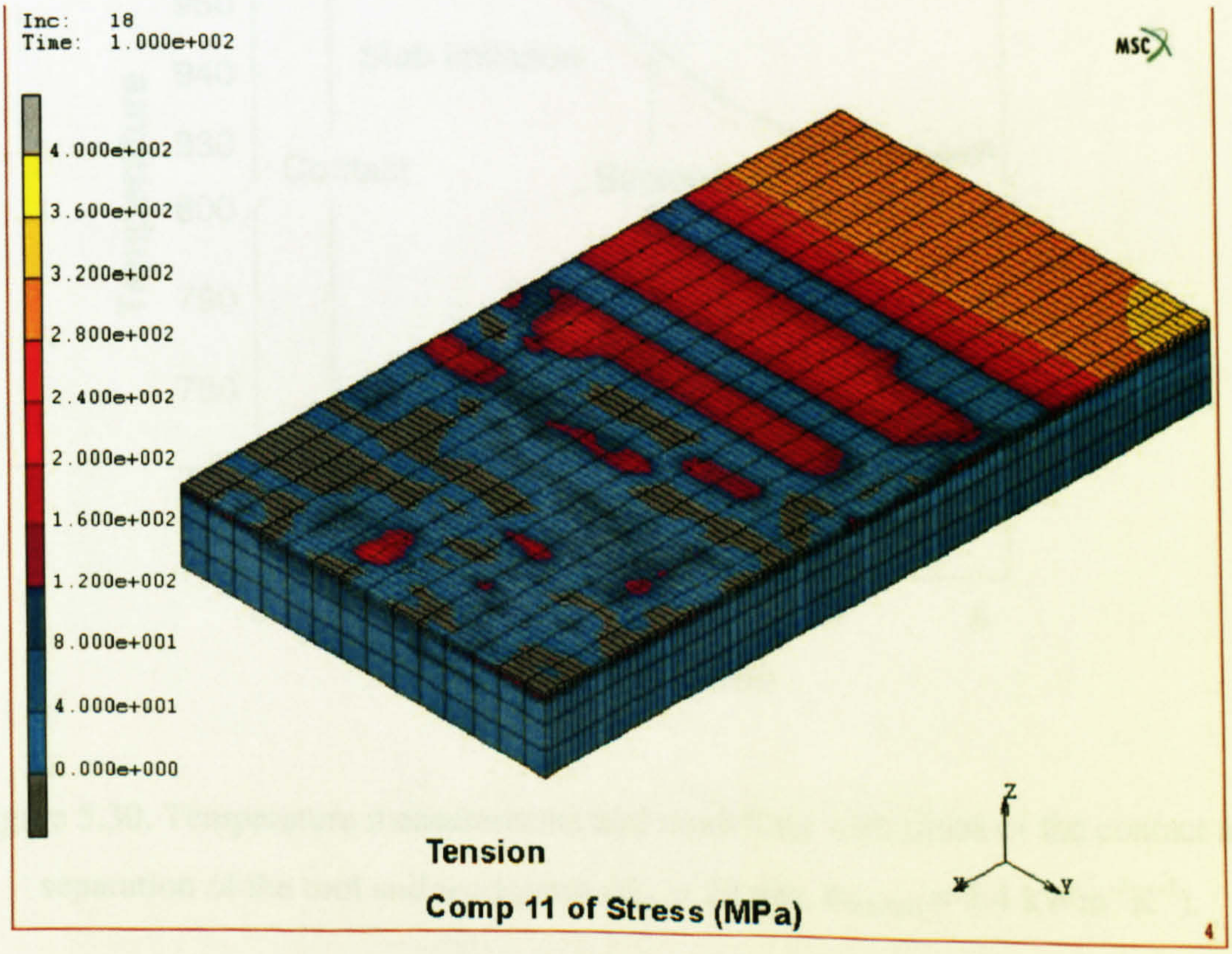

Figure 5.28. Stress relaxation after cracks appeared at 800°C and K_{Ic} = 5.8 MN·m$^{-3/2}$.

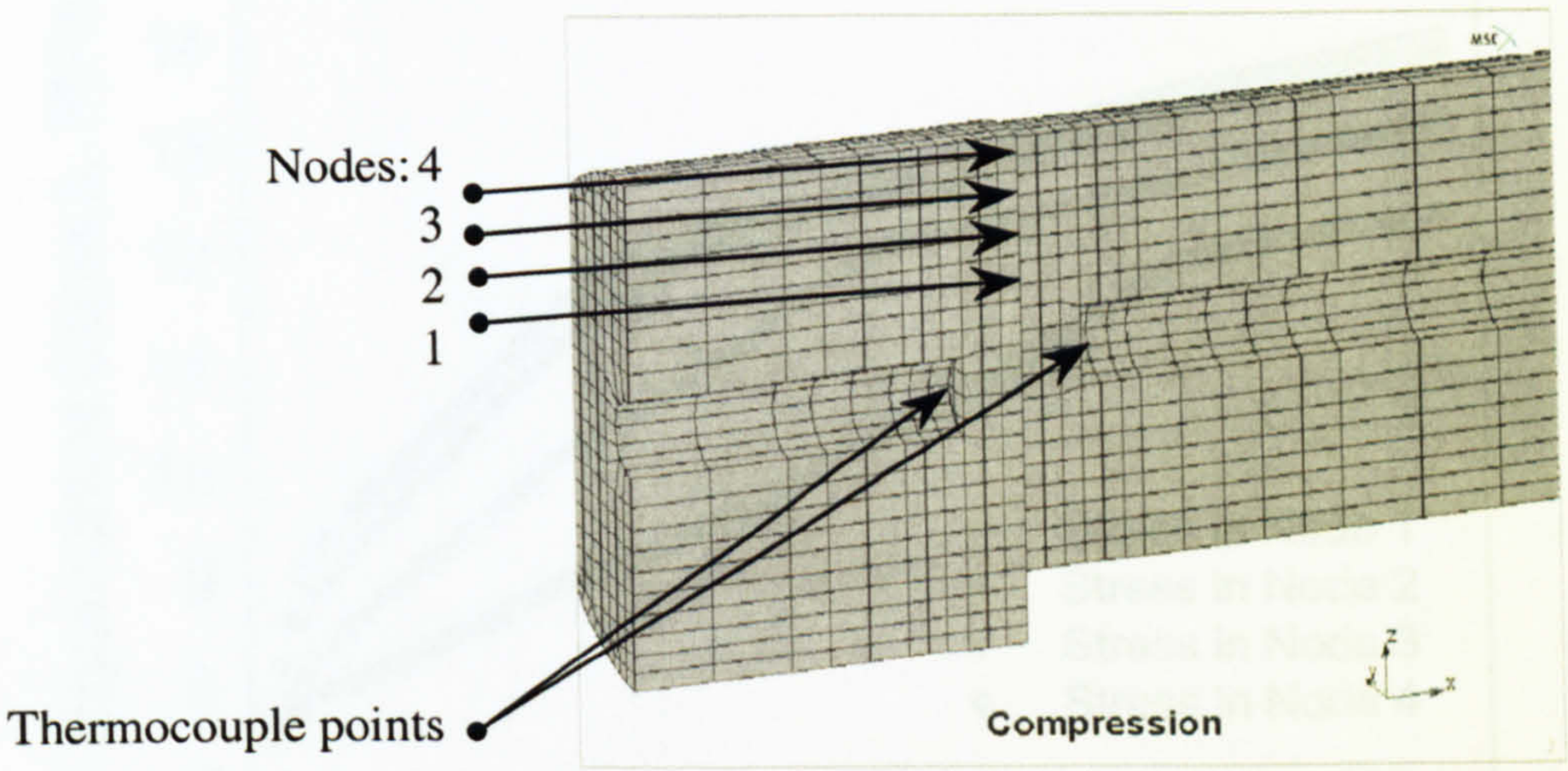

Figure 5.29. Model view during the contact where control nodes are marked.

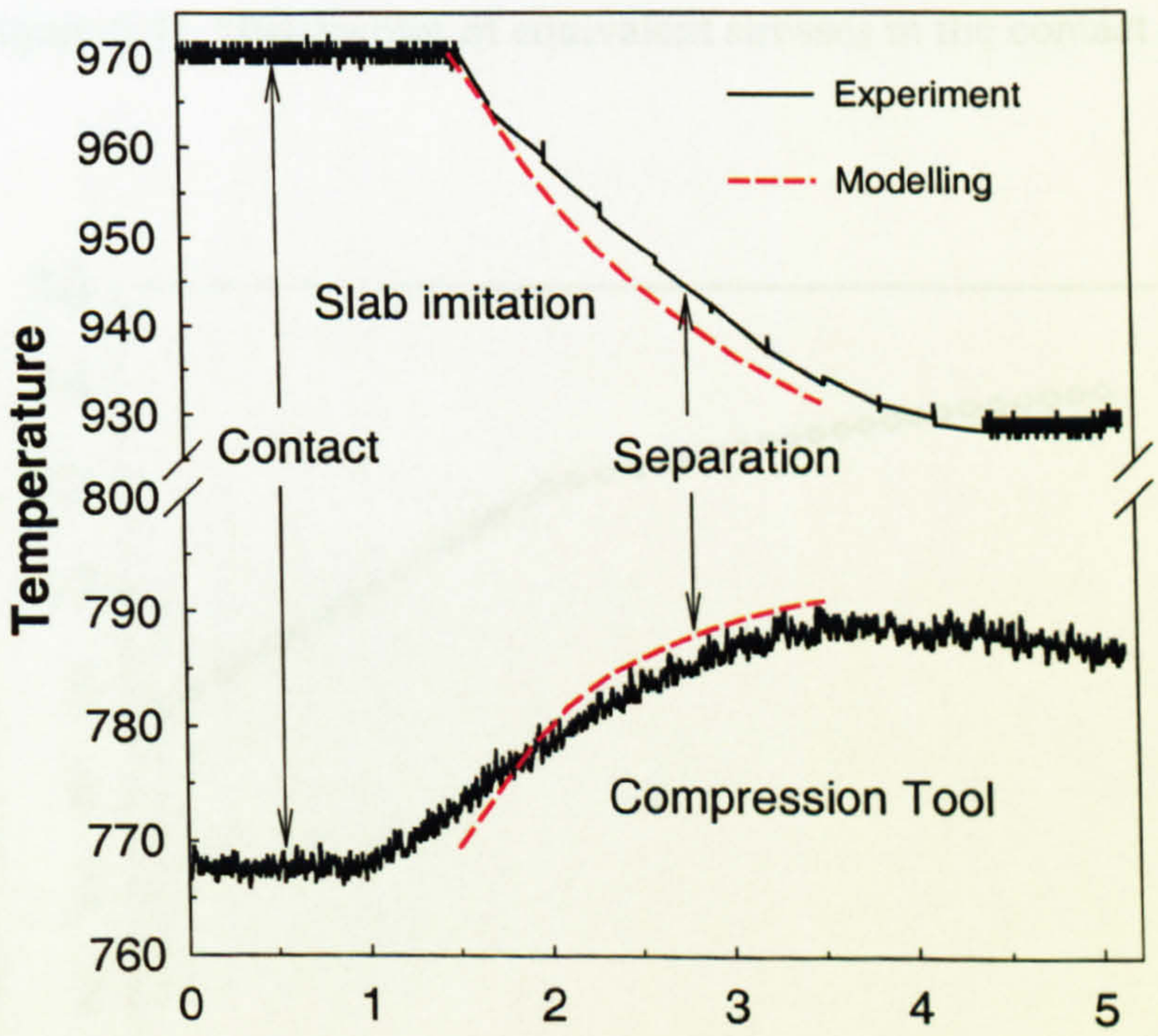

Figure 5.30. Temperature measurements and modelling with times of the contact and separation of the tool and workpiece (d_{ox} = 20 μm, $\alpha_{contact}$ = 2.4 $kWm^{-2}K^{-1}$).

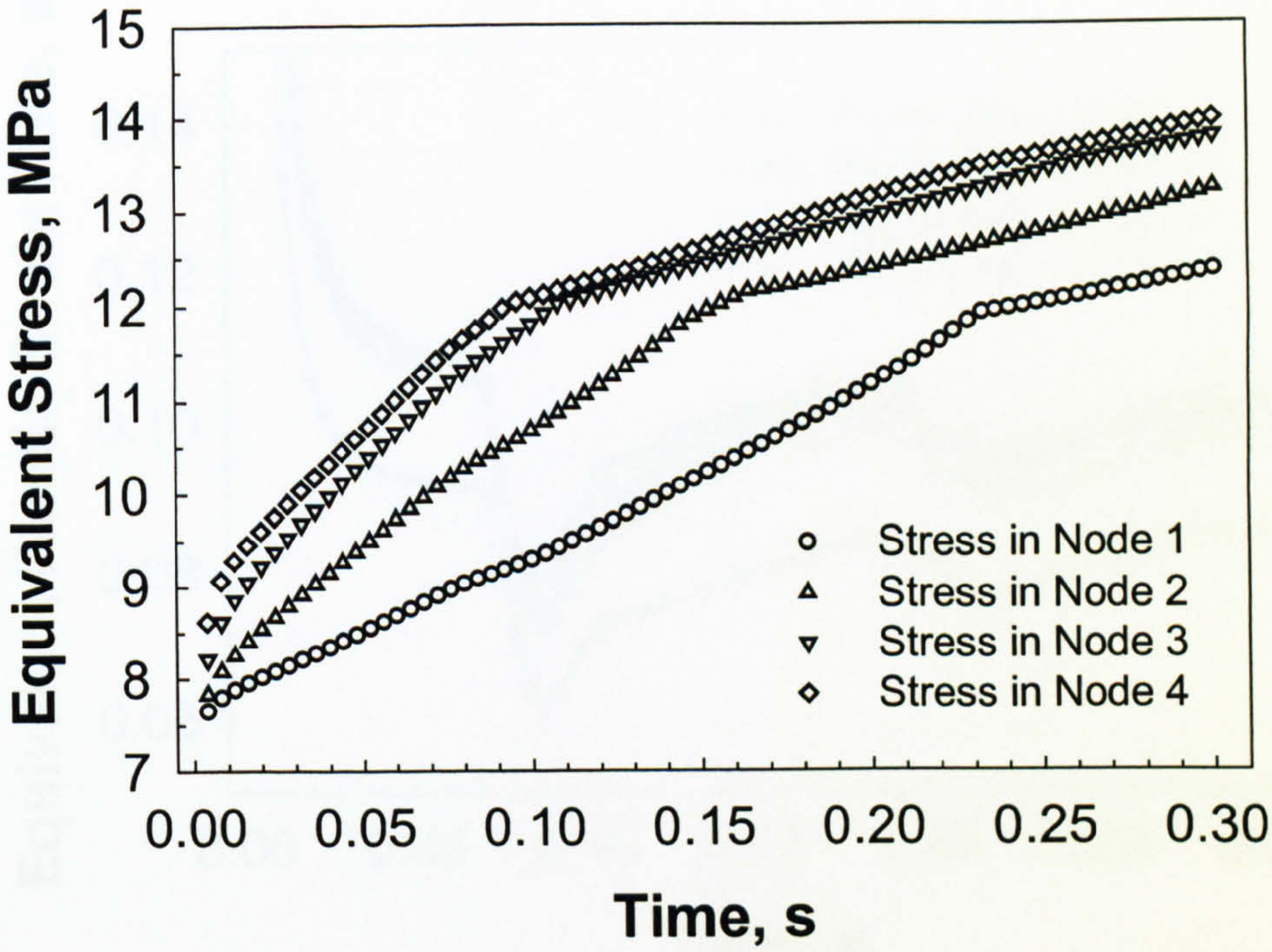

Figure 5.31. History plot of equivalent stresses in the contact nodes.

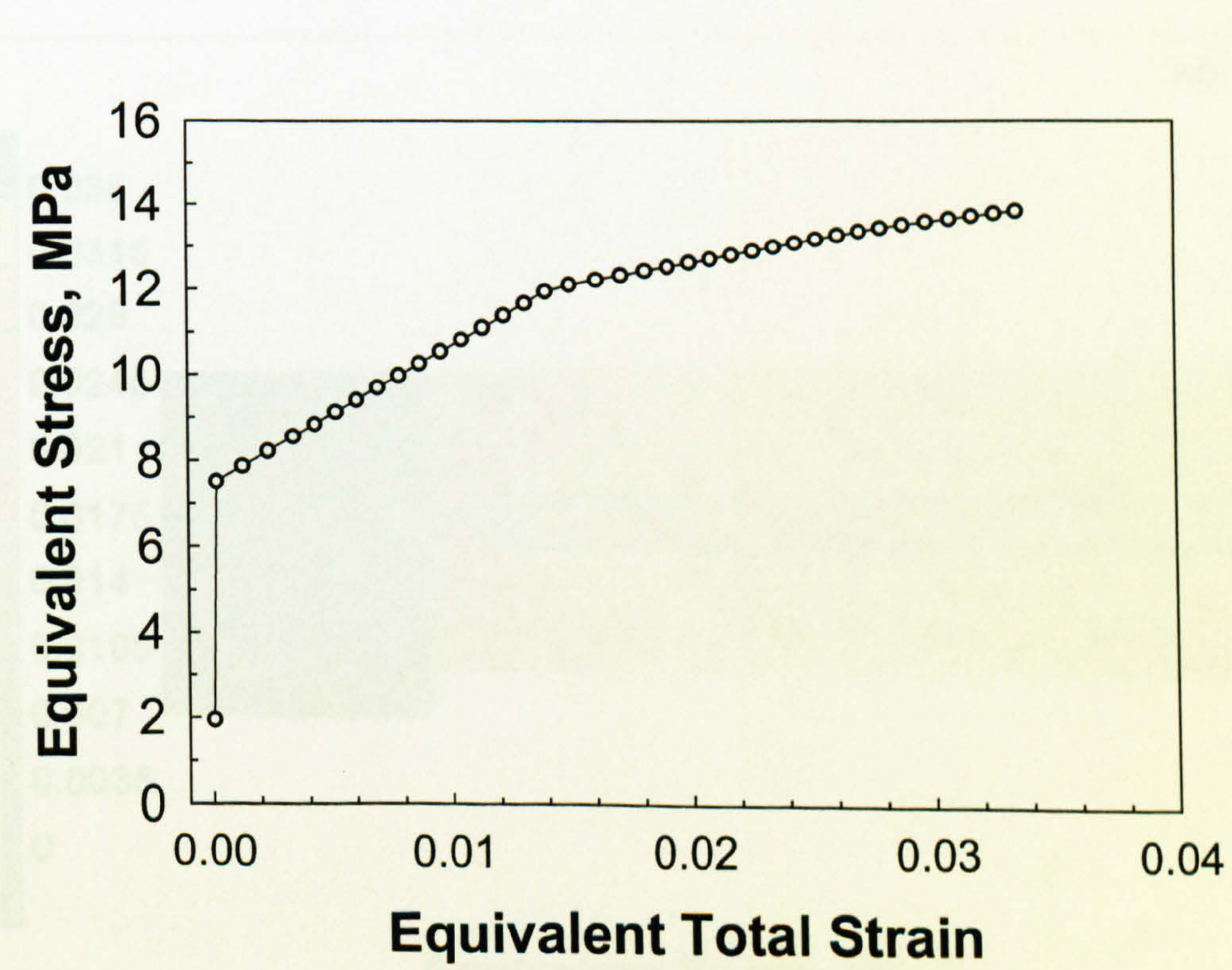

Figure 5.32. Stress – strain curve.

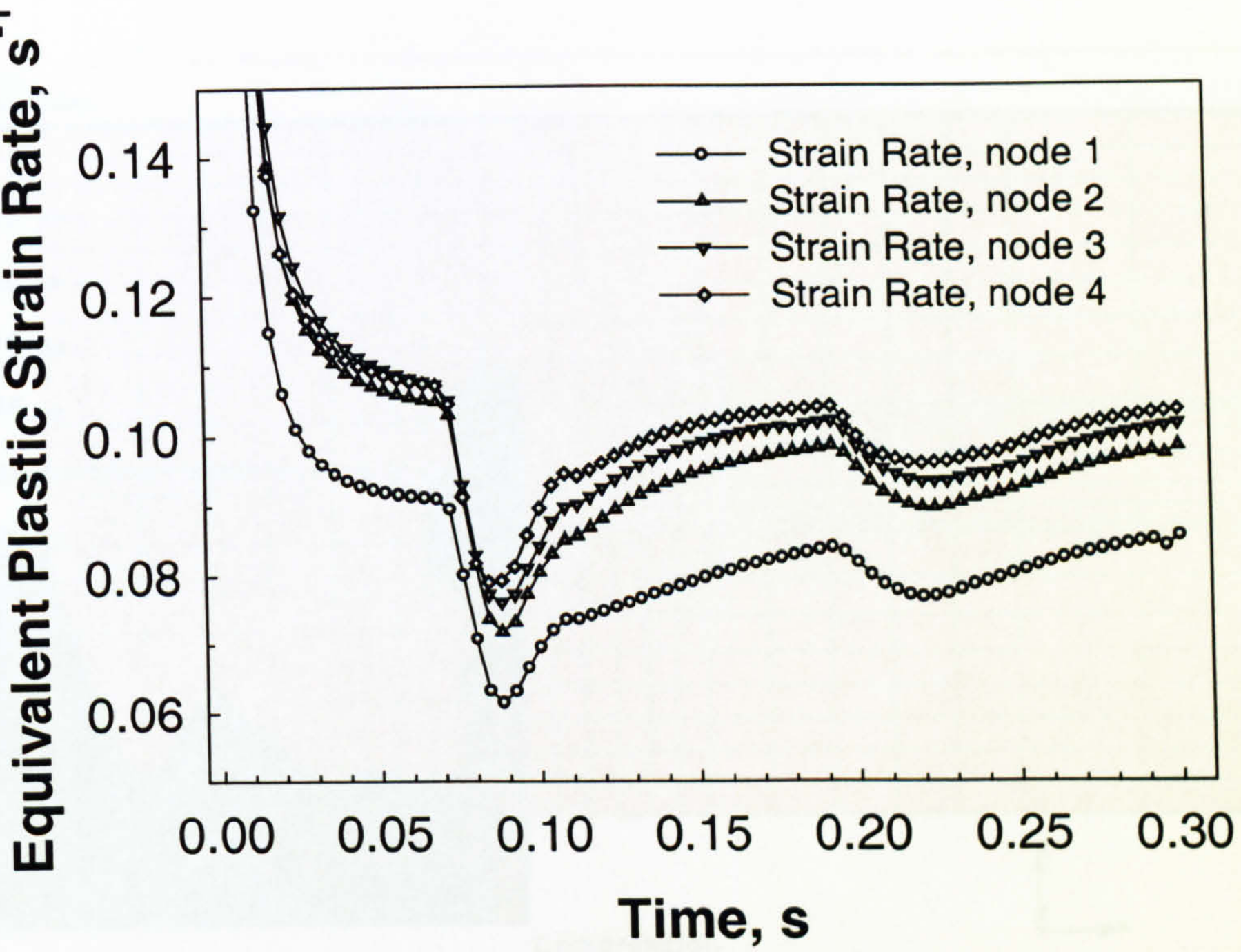

Figure 5.33. History plot of equivalent plastic strain rate.

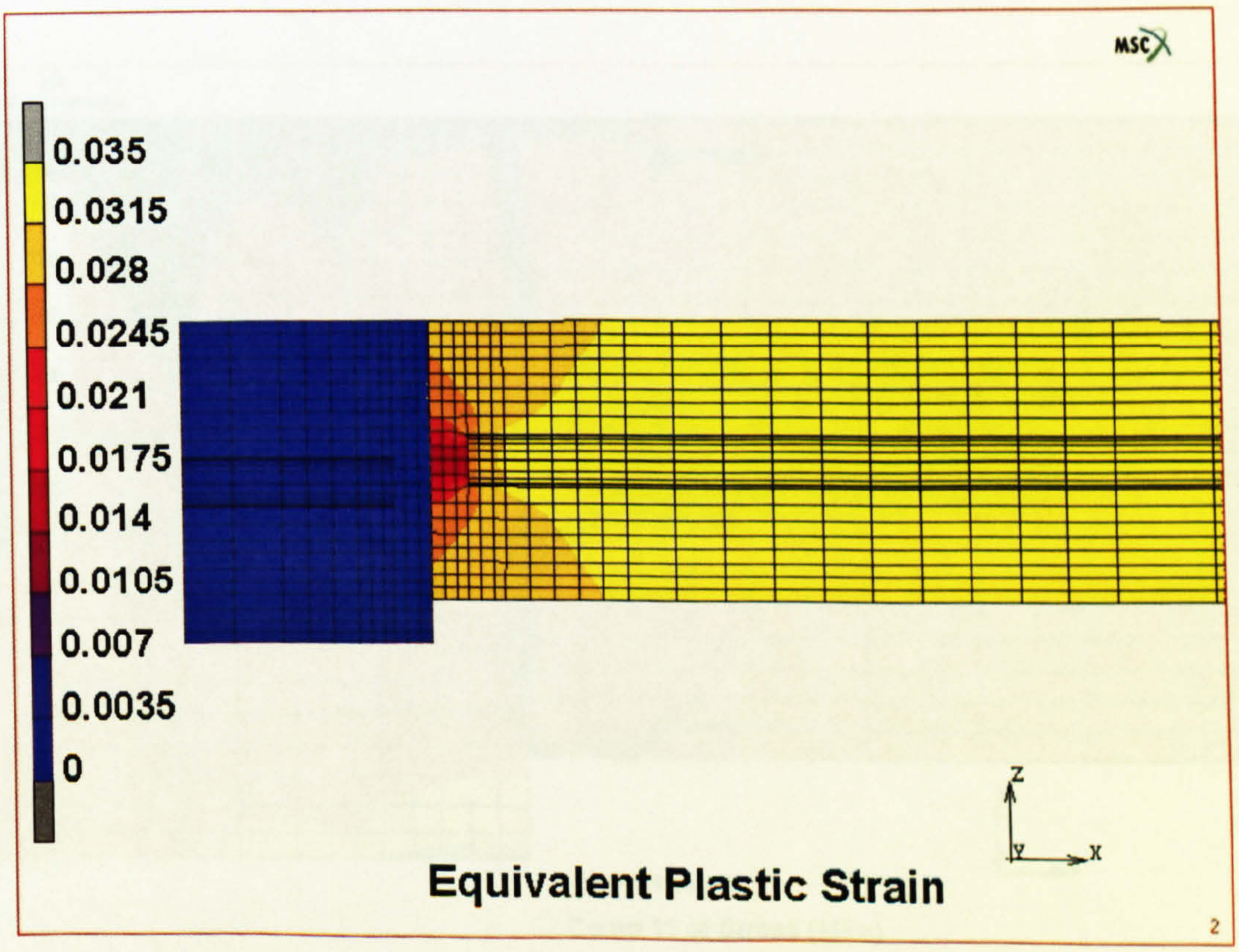

Figure 5.34. Equivalent plastic strain distibution.

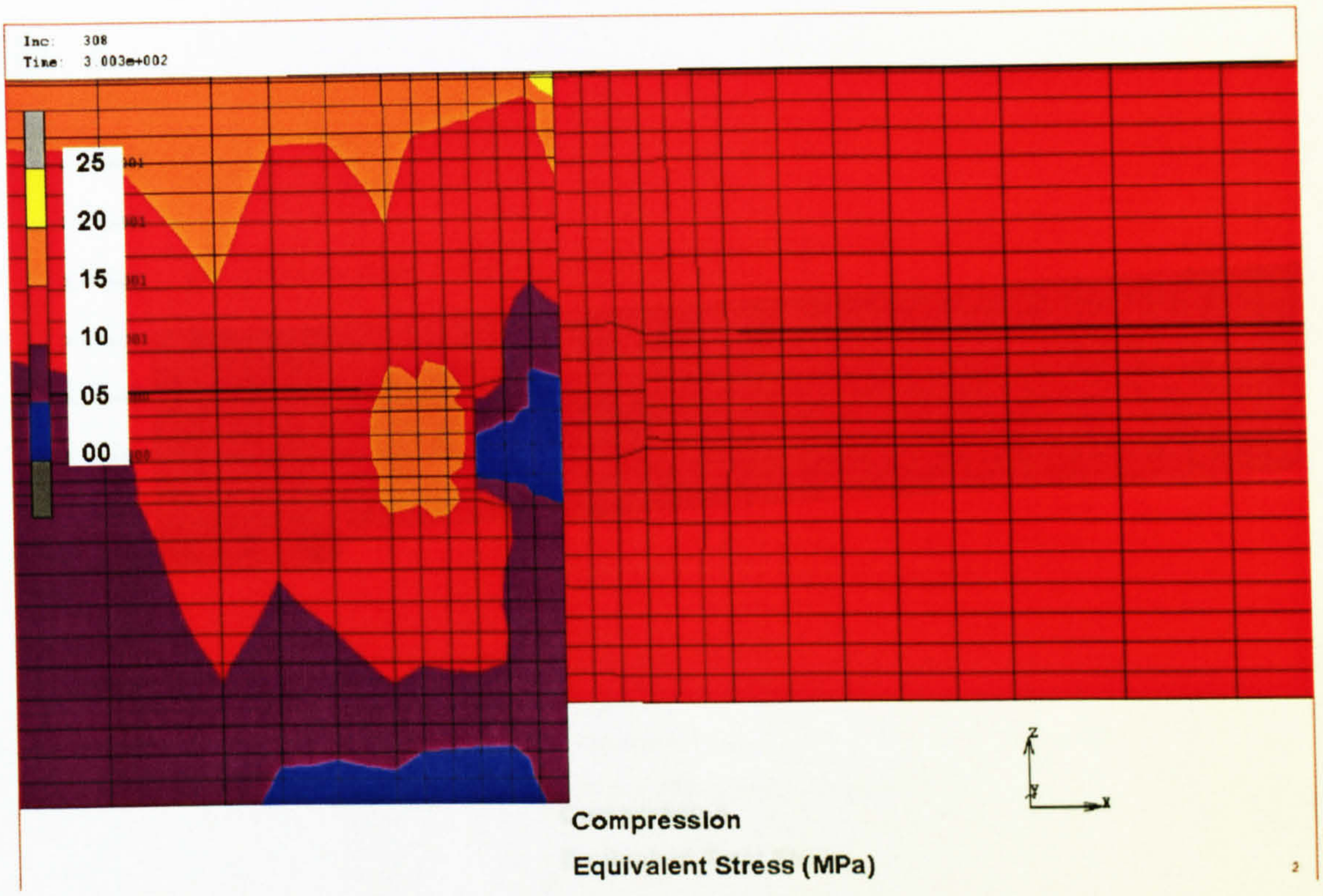

Figure 5.35. Equivalent stress distribution.

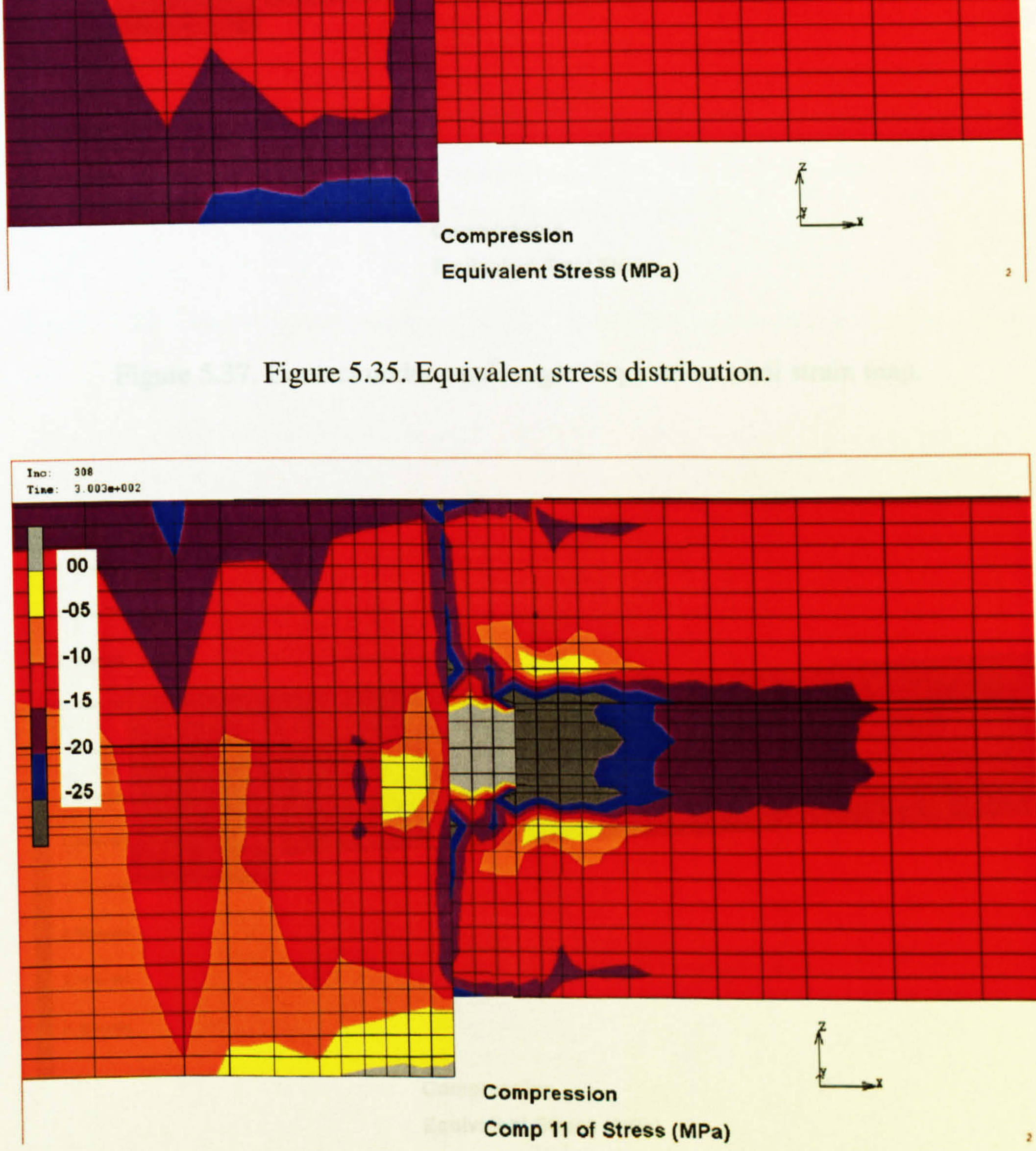

Figure 5.36. Stress distribution along the axis X.

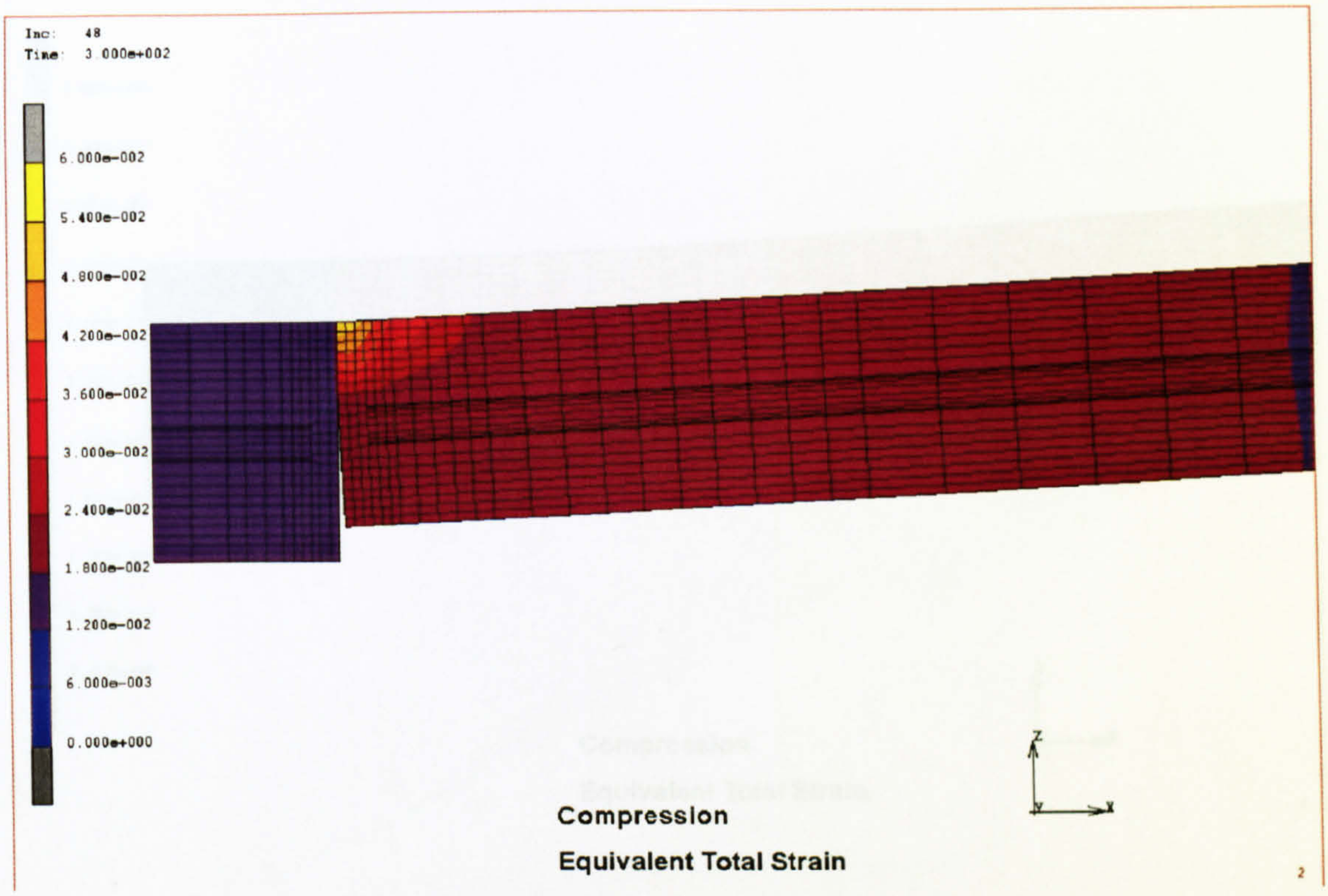

Figure 5.37. Contact under small angle. Equivalent total strain map.

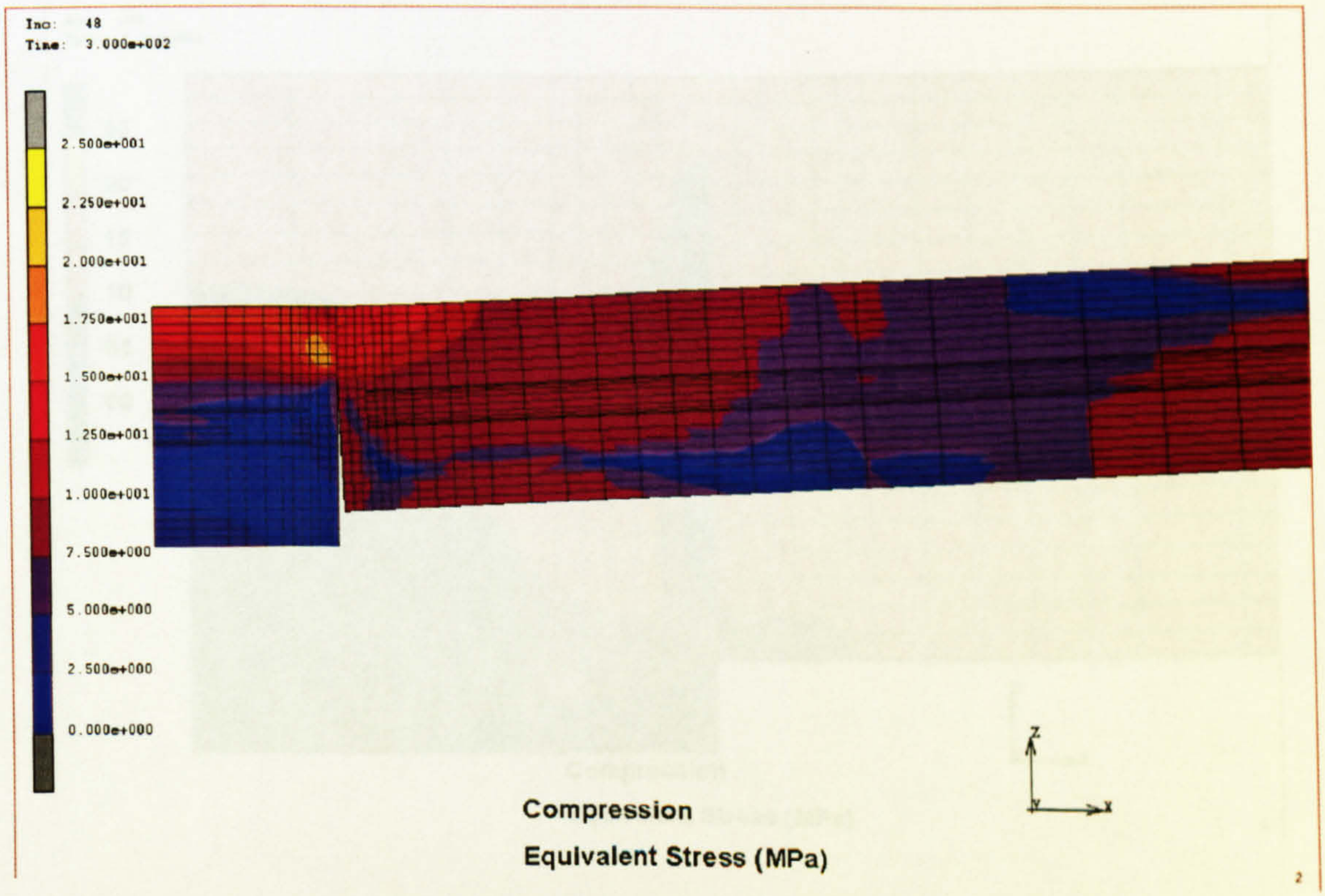

Figure 5.38. Contact under small angle. Equivalent stress map.

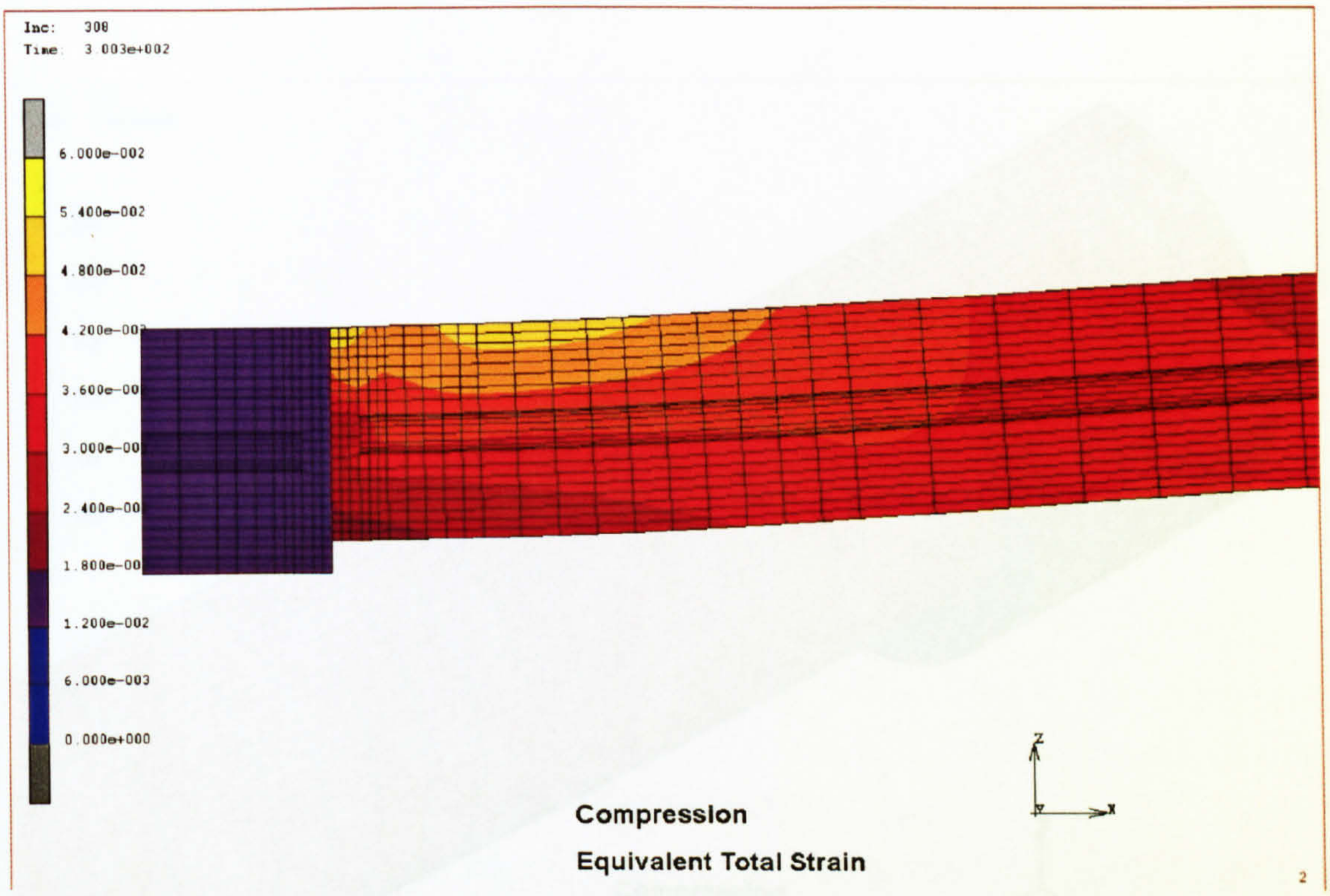

Figure 5.39. Contact under small angle. Equivalent total strain map at the end of the compression test.

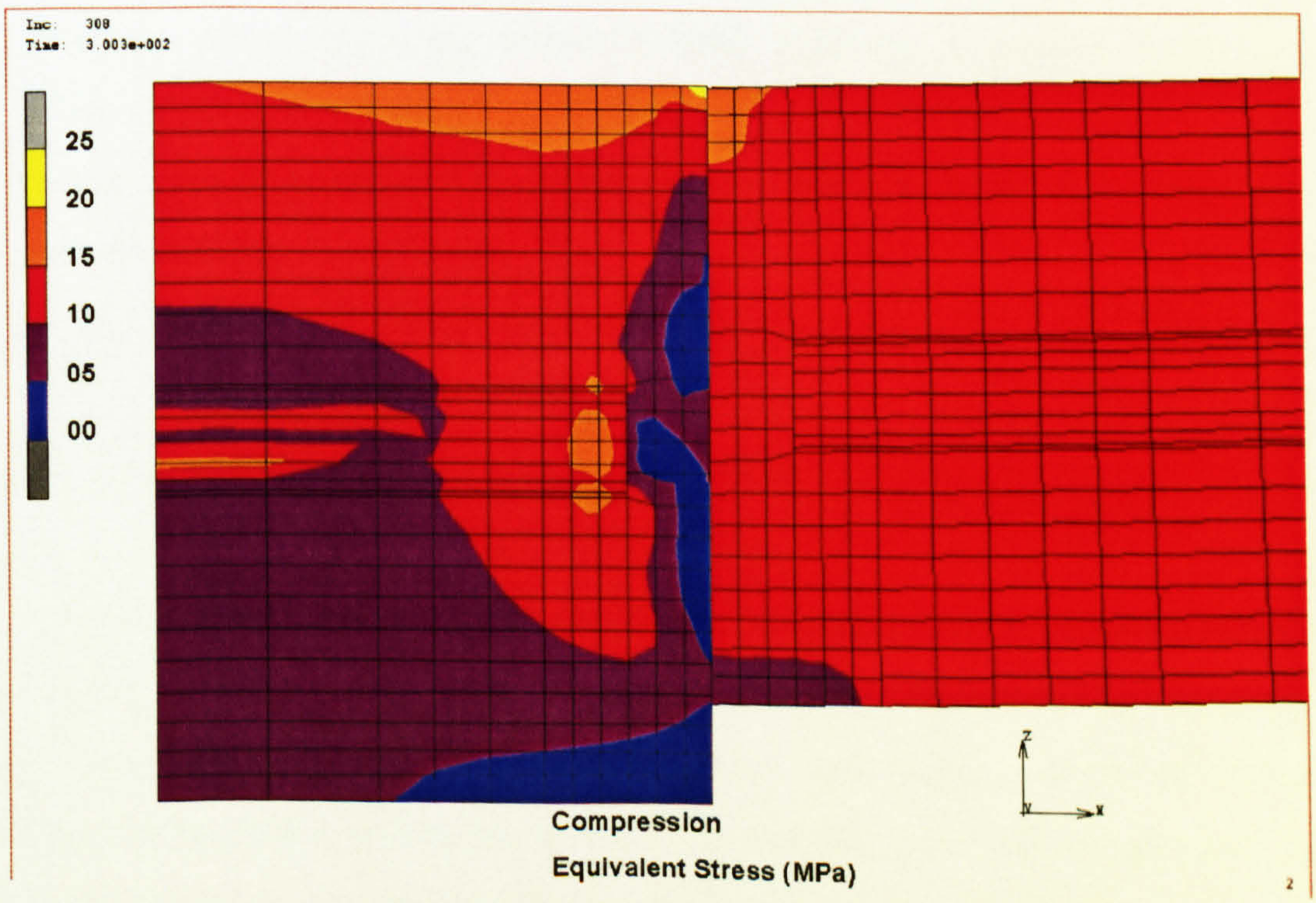

Figure 5.40. Contact under small angle. Equivalent stress map at the end of the compression test.

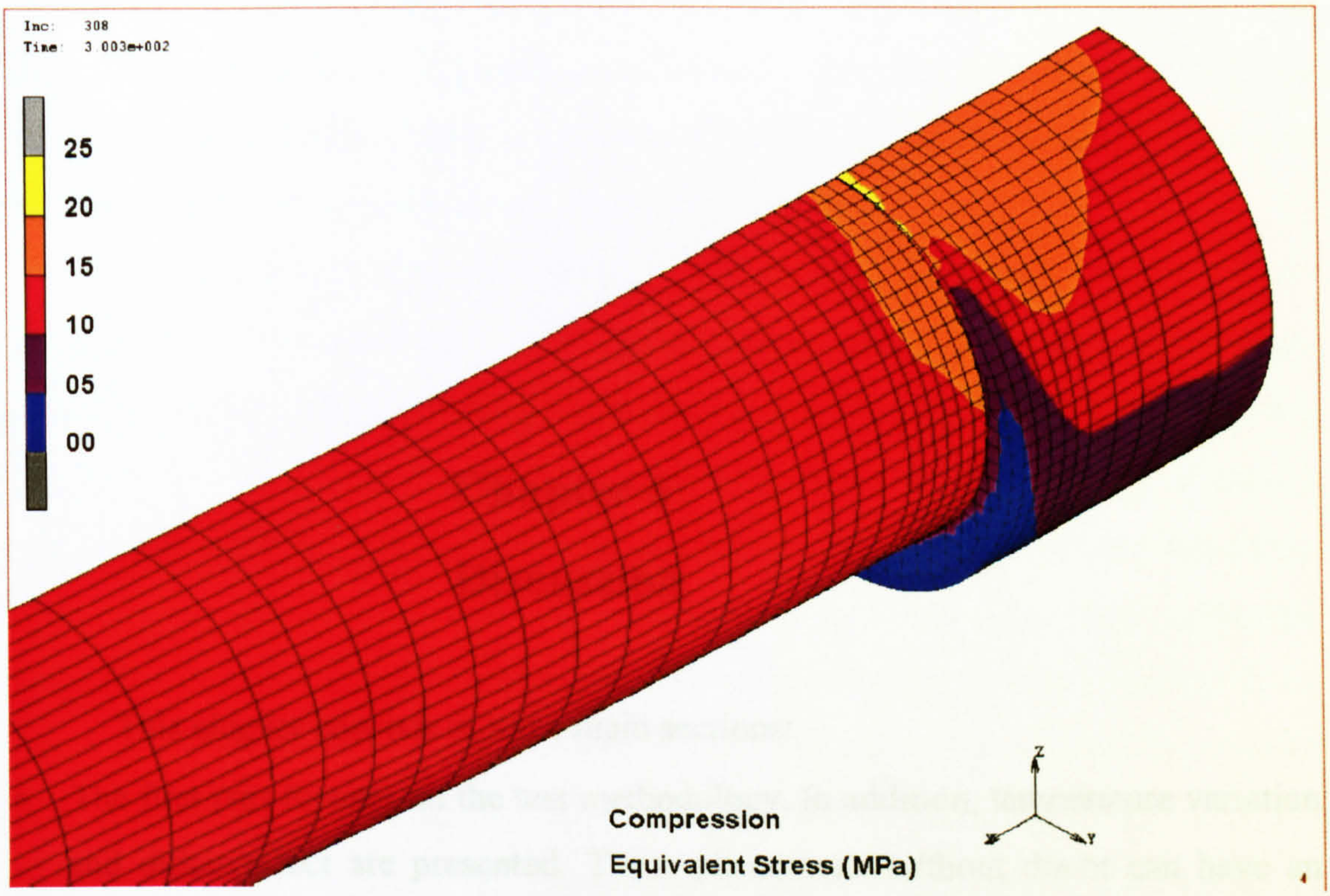

Figure 5.41. Contact under small angle. Equivalent stress map on the surface of the specimen.

Chapter 6

Discussion

This chapter consists of three main sections:

- The first part focuses on the test methodology. In addition, temperature variation and dither effect are presented. These phenomena without doubt can have an influence on the measurements during the tests.
- In the second part the high-temperature tensile and compression test results are discussed. The stress-strain behaviour and the oxide scale failure mechanisms are analysed. After this, the microstructural evidence of oxide failure after deformation is dealt with.
- Finally, the third part of this chapter deals with the finite element simulation of the above tests.

6.1. Test Methodology

As already mentioned in Chapter 3, the deformation of the surface oxide scale during the hot rolling process is too complicated to be reproduced in one detailed test. Therefore, in order to obtain maximum information about the thermo-mechanical behaviour of the oxide scale, several different high-temperature tests were suggested. A standard tensile test methodology was adapted to examine the behaviour of flat mild steel specimens. The gauge section was chosen in parallelepiped shape, despite having used a cylindrical one in previous studies [29].

This choice of the flat gauge section (Figure 3.2) facilitated the crack pattern recognition (Figure 4.10) and a plane strain condition was achieved for the modelling of flat hot rolling. The radial contraction of the underlying steel in the tensile test with a round specimen [29], which could produce behaviour different to that experienced in a flat geometry, was effectively eliminated.

The additional test methodology which was developed involves high-temperature compression tests. The detailed experimental procedure of the high-temperature compression test is given in section 3.7. The major aim of this test was to replicate as closely as possible the hot rolling temperature conditions, whereas a simple plane strain compression test [111] was unable to satisfy these conditions (temperature gradient between the workpiece and the tool and controlled atmosphere). On the other hand, the normal compression test that was developed was able to achieve plane strain conditions for the surface oxide scales. The obvious strength of the proposed high-temperature compression test was its ability to achieve temperature differences of several hundreds of degrees between samples. However, one should be careful with the induction furnace design, because air leakage is possible if the furnace is not hermetically installed. This can lead to undesirable oxidation of the specimen.

6.1.1. Temperature variation during tensile testing

A minor obstacle was found during the tensile testing through heating and temperature measurements. Although temperatures at the thermocouple points were the same in every test, the temperature inside the induction-heating furnace could not be measured with a thermocouple. Measurements that were made by the pyrometer indicated unequal temperatures at the gauge section of specimens with different thicknesses. As was mentioned in section 3.6.1, induction heating efficiency depends on the skin depth of current flow and should be not greater than 25% of the bar diameter [128]. In the present study a minimum calculated square size was approximately 3.3 mm for good (70-75%) and 1.8 mm for acceptable (~50%) efficiency in the high temperature tensile experiment. Therefore, it is logical to conclude that specimens with different thicknesses were heated in the centre of the

gauge to different temperatures. This provides a reasonable explanation for why the stresses also varied, Figure 4.8. According to the pyrometer measurements (Figure 4.9) and with regard to the empirical equations [131], [132], [133] and [134], the temperature difference was about 80-150 K. It should be noted that the minimum value was used in the finite element modelling.

6.1.2. Dither effect

Another surmountable problem was a dither effect, which can cause some inaccuracy in measurements.

Stiction and hysteresis can make controlling a hydraulic valve seem erratic and unpredictable. Stiction can keep the valve spool from moving when input signal changes are small. The spool then tends to overshoot when the signal becomes large enough to free it. The force required for the spool to move initially is more than the force required to keep it moving to the desired position. Friction of a sliding spool causes a reduction in the distance moved. Hysteresis can cause the spool shift to be different for the same command signal input, depending on whether the change is increasing or decreasing. Therefore, dither is a rapid, small movement of the spool about the desired position. It is intended to keep the spool moving to avoid stiction and average out hysteresis. Dither amplitude must be large enough and the frequency slow enough to enable the spool to respond and yet small and fast enough not to cause a resulting pulsation in the hydraulic output [145].

As can be seen in Figure 4.7, the dither effect was evident for both MAYES and INSTRON machines. The testing system produced a wide scatter of the displacement data during position control at the tensile stage. The data collection and control signals were simultaneous with a frequency of 1000 Hz with a dither at 195 ± 10 Hz. According to the results obtained, it is quite possible that the dither was a reason for the wide scatter of the displacement data (Figures 4.5 and 4.6*b*). Therefore, the strain results were smoothed by the 11-point running average technique (Figure 4.8). However, the load data was collected with minimal noise through a different channel and did not need any transformations. It should be noted that the measured loads were of most value to this investigation.

6.2. Tensile testing of flat specimens

The high-temperature tests revealed a variation in the maximum stresses for specimens with different thicknesses and temperatures of the gauge section. However, the measurement of temperature was made only by a thermocouple located outside the induction furnace. As stated above, according to Wright [128] the geometrical size of a heated sample and its temperature are mutually dependent during induction heating. Hence, it was assumed that specimens with different thicknesses had different surface temperatures within the induction furnace. Additional temperature measurements by pyrometer (Figure 4.9) confirmed the initial assumption. The temperature variation appears to be enough to produce a visible effect in failure of oxide scales (Figure 4.10). Failure of the oxide scale during the tension of rectangular sections was according to previous results with cylindrical gauge specimens [29]. Figure 4.10 shows flat specimens with crack distributions on the surface, from which it can be seen that failure of oxide scales for flat and round [29] specimens was similar. In spite of the round sample, the crack spacing of flat specimens was uniform and, therefore, could be easily counted.

One complication is that the crack spacing values depend on the thickness of the flat specimens. The most likely explanation of this phenomenon is the difference in stresses on the surface of the different specimens. These stresses (Figure 4.8) were higher for thinner (cooler) specimens for the moment when the maximum strain (~1.2-1.4%) were reached. It is fairly certain that failure of the oxide scales occurred in that time interval. Therefore, it appears that temperature was the major factor for the crack pattern formation. Nevertheless, one cannot exclude the geometry factor of specimens, which could also play a part in oxide scale failure processes, although the finite element analysis of the 2 and 4 mm gauge thickness models, which had an equal temperature, did not reveal differences in stress-strain behaviour. Finally, the optimal thickness for specimens was found to be about 3 mm (Figure 4.11). The number of cracks is more or less steady around this thickness and the induction heating efficiency is good enough to maintain the elevated temperature inside the

gauge section. The results of the test are more reproducible in the light of all these features.

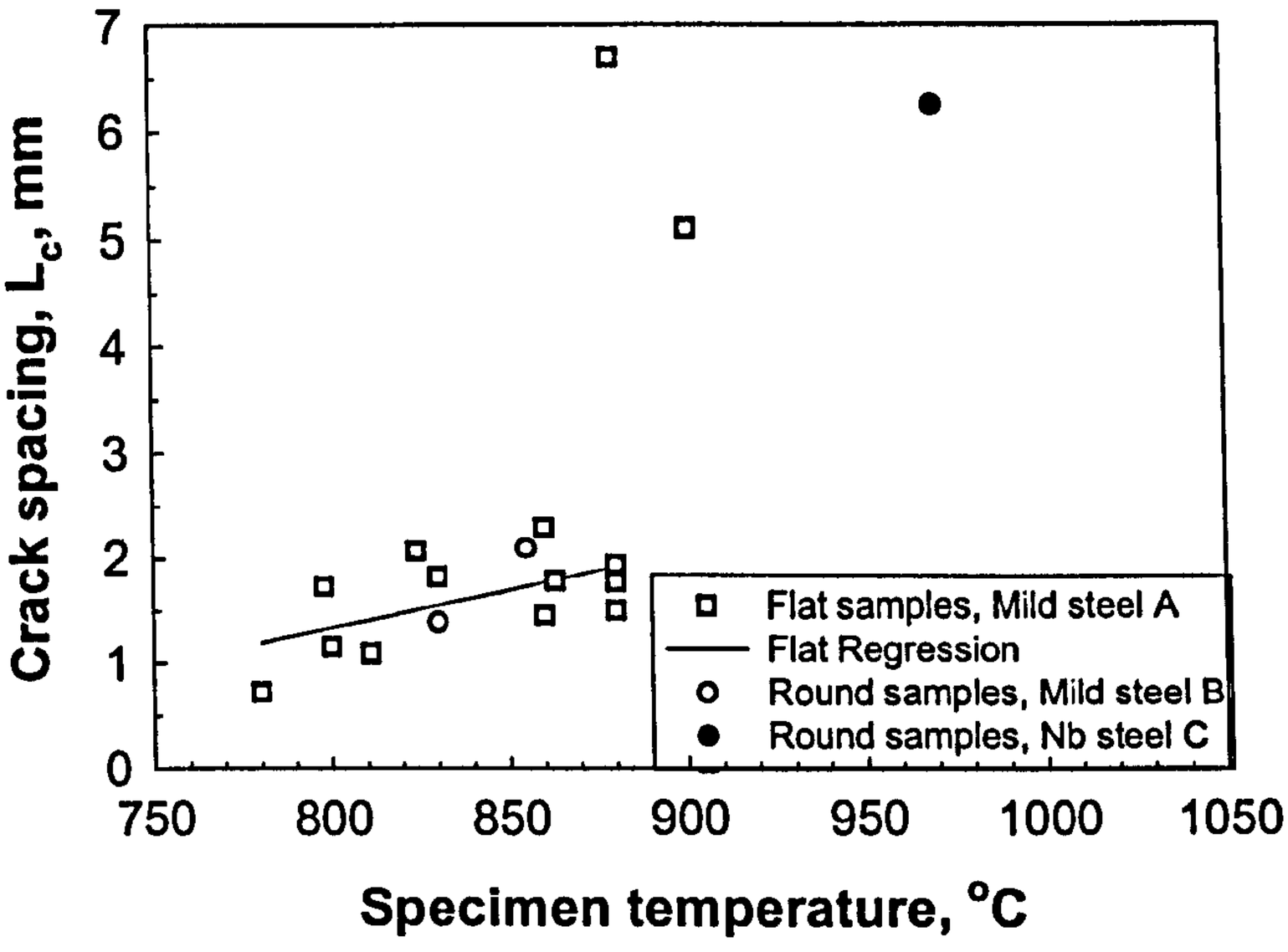

Figure 6.1. Crack spacing variation of specimens with the flat or round gauge section.

In addition, the data for crack spacing versus specimen temperature were plotted for comparison with the round specimen results (Figure 6.1). The flat specimens' results are presented here as square points and the regression line. The regression line shows a gradual rise of crack spacing with increasing temperature, indicating that the higher the temperature, the fewer cracks were observed. The points where the crack spacing equals 6.7 and 5.1 mm (steel A) was not included in the regression, because they are in the transition zone between through-scale cracking and slipping of the oxide scale. According to Krzyzanowski and Beynon [29] and [78], at higher temperatures through-thickness cracking is replaced by slipping of the oxide scale along the metal/oxide interface. Assuming through-scale cracking of the oxide up to 900°C, a simple explanation can be given for this upward trend. During the high-temperature tensile test, shear stresses arise between a metal substrate and the oxide scale. These shear stresses produce tensile stresses in the oxide scale, which lead to the appearance of the through-thickness crack. Therefore, the higher the maximum stress in the metal substrate is, the higher the shear and tensile stresses are in the oxide scale. As the tensile stresses on the oxide scale increase, a larger number

of through-thickness cracks can appear. On the other hand, the critical cracking stress heavily depends on the critical stress intensity factor, K_{Ic}, (Equation 2.49). According to Figure 6.2, the critical temperature should exist where the critical stress intensity factor becomes big enough to prevent through-thickness cracking formation or the crack spacing tends to infinity. From this point of view the influence of temperature on crack spacing (Figure 6.1) and the critical stress intensity factor (Figure 6.2) is similar.

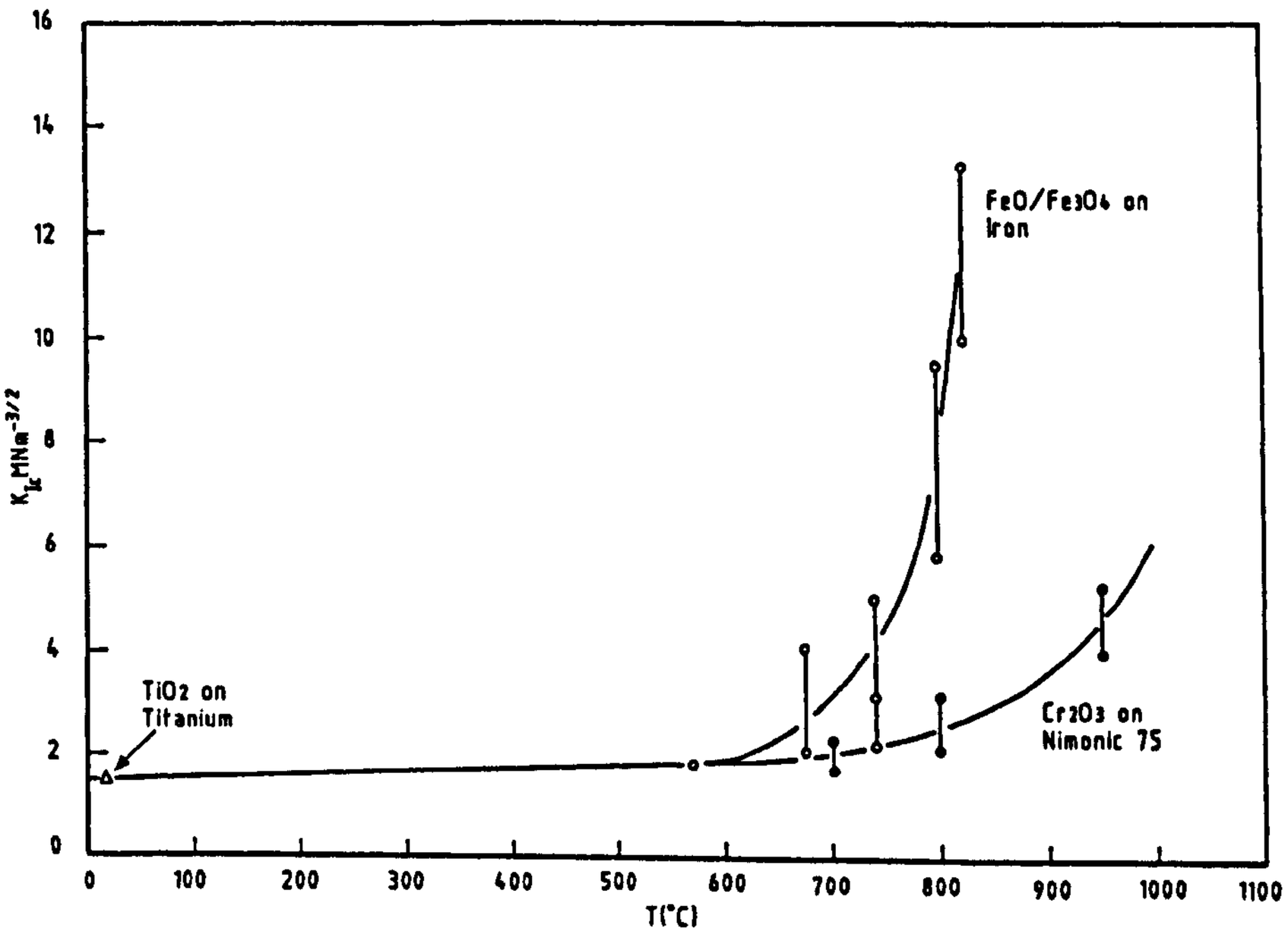

Figure 6.2. Influence of temperature on critical stress intensity factor, K_{Ic}, for oxides [141].

As was assumed above, only temperature variation caused a change in the stresses within the specimens. Hence, the crack spacing rises with increasing temperature, as shown in Figure 6.1. It should be noted that for different steel compositions the temperature range for brittle failure within the oxide scale could vary. An example of such a variation is Krzyzanowski and Beynon's study of oxide scale failure in different steels [78]. There are two steels involved in that investigation: steel B is a mild steel (Table 6.1), similar to steel A (mild steel in Table 3.1), and the upper limiting temperature (T_{cr}) for the appearance of through thickness cracks is about 900°C. Steel C is a niobium microalloyed grade with a

higher content of silicon and manganese (Table 6.1) where T_{cr} is shifted to approximately 1000°C. The steel B data are for the round specimens presented in Figure 6.1 below 900°C. The point at 970°C in Figure 6.1 comes from steel C. Despite the fact that the difference of chemical contents in steels B and C is minimal, the transition zone divergence appears to be about 100 K.

Table 6.1. Chemical contents (weight %) of steel grades used for hot tensile testing by Krzyzanowski and Beynon [78].

Steel	C	Si	Mn	Cr	Ni	Cu	Mo	Nb	Al	V	P	S
B	0.19	0.18	0.79	0.05	0.07	0.14	<0.02	<0.01	<0.005	<0.01	<0.005	0.03
C	0.18	0.36	1.33	0.03	0.02	0.08	<0.02	0.041	0.034	<0.01	0.025	0.01

6.3. Compression test

The behaviour of oxide scales formed on mild steel was studied using a high-temperature compression test technique over the temperature range 870 - 1070°C. The oxide scales were examined between 5 and 250 μm thick. The morphology of oxides is generally the same as was reported by other authors [28], [73]. However, the ratio between layers was different. A number of failures of oxide scales under the compressive stress were observed.

6.3.1. Preliminary oxidation

In order to obtain undamaged oxide scales and information about the oxide growth, the oxidation tests were carried out before the compression test. The acquired results indicate that for the higher temperatures (970 - 1070°C) the oxide scale was thicker than theoretically expected (Figure 4.13). However, according to Figure 4.13, the thickness of the oxide scale after the compression test was often less than the theoretically calculated one. These results might be explained by the heterogeneity of the oxides at high temperatures. Figure 4.14*d* shows the extremely

heterogeneous oxide scale after the oxidation test at 1070°C. Hence, the porous oxide can be very thick although after compression, the thickness could be greatly decreased. Certainly one should recognise that the parabolic law of oxidation is not perfect.

6.3.2. Compressive stresses

The loading conditions during the compression tests had some features that should be discussed. Figures 4.16, 4.17 and 4.18 show the sharp peaks in compressive loading at about 0.8 seconds. Subsequently the load showed a rapid decrease in the following 0.1 s and a gradual decrease afterwards. The appearance of the peak can be explained using Figures 4.15 and 6.3. Figure 6.3 shows the left upper corner of the plot of Figure 4.15, namely the crosshead movement. The raw and smoothed (by the 11-point running average technique) data are shown in Figure 6.3.

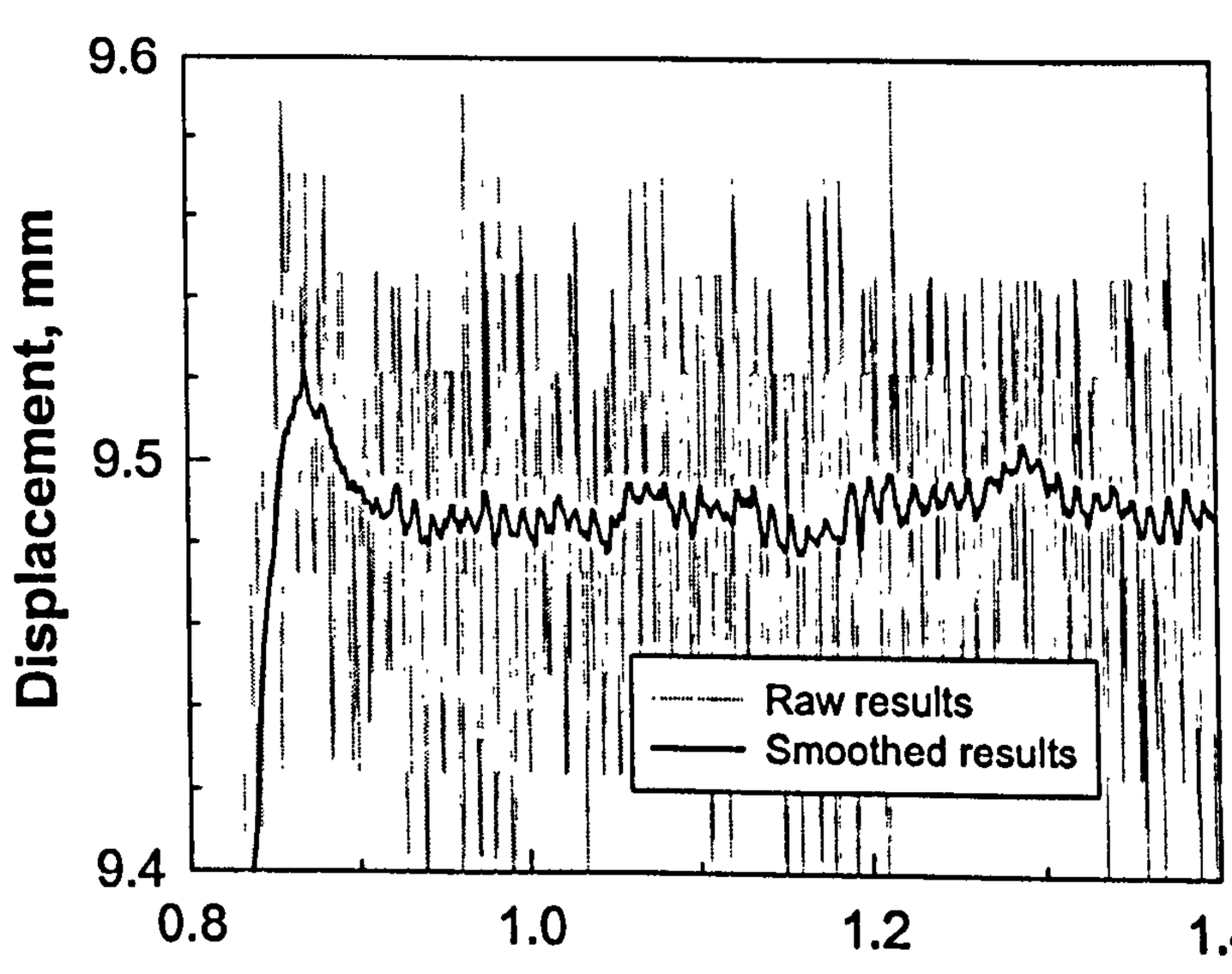

Figure 6.3. Crosshead movement at the end of the compression stage.

It can be seen clearly from the smoothed curve that the crosshead movement brought about the peak (approximately 0.03 mm above the average steady position).

The small backward movement of the crosshead was detected by the abrupt decrease of the load. However, the backward movement of the crosshead was not perceived by relying on the raw displacement data. The compressive stresses were calculated using only the part of the loading curve before the peak load.

In addition, some strong and weak points of the high-temperature compression tests should be noted. Two minor disadvantages were identified: first, due to the geometrical size of the specimens, it was not possible to achieve compressive stresses higher than 20 MPa (Figure 4.21), and second, at temperatures 970 and 1070°C undesirable bending of specimens can take place (Figure 4.29). However, the attained stresses were enough to reveal damage and failure of the surface oxide scale. Moreover, the high-temperature compression test provided information about temperature changes during the tool/specimen contact and allowed the clear detection of the sticking effect.

6.3.3. Heat transfer during the tests

The changing of the temperature was observed in both parts of the specimen during the contact (~3 s). Upward and downward trends of the temperature are present for the roll and slab imitation specimens respectively. The effect of the oxide scale on the overall heat transfer properties has been investigated. According to the temperature measurements, the thinner the oxide scale, the bigger the difference between initial and final contact temperatures (Figure 4.26). This indicates that the thickness of the surface oxide scale is very important for hot rolling. Moreover, the testing (hot rolling) temperature itself obviously exerts influence on heat transfer. For instance, Figure 4.25 shows temperature changes for specimens with approximately the same oxide scale thicknesses. The temperature changes for the slab imitation specimen with the oxide scale thickness of ~50 μm were 40 and 22 degrees at 970°C and 870°C temperatures correspondingly. Therefore, the higher the temperature is, the bigger the temperature drop (or rise) it produces at the same oxide scale thickness. It should be noted that the tool and slab imitation specimens were made from different materials and, hence, had different thermal properties and temperature alterations during the compression test.

6.3.4. General oxide scale behaviour

A general conclusion about the high-temperature oxide scale growth was that at the temperatures above 1000°C, oxides became heterogeneous and grew with a high grade of porosity (Figures 4.27*b* and 4.29*c*). This can lead to the exfoliation and delamination of the oxide scale from the metal substrate with subsequent decreasing of the surface temperature. Oxide scales appeared to be more brittle at the relatively low temperature (870°C), as can be seen in Figure 4.28*a*. The oxide scale was cracked, crushed and fell off the side of the specimens, while at 970°C only a single crack appeared on the specimen's side (Figure 4.28*b*). The oxide scale at 1070°C was harder to analysis due to the exfoliation and the outer layers had lower temperatures and could fail in a brittle manner while the inner layers could be firmly adhered to the metal substrate (Figure 4.28*c*). The visual examination of the specimens at room temperature after the test (Figure 4.29) confirmed the conclusion that was drawn above during the compression at the elevated temperature.

The high-temperature compression test reveals the possibility of studying a sticking effect, which can occur between the tool and the specimen. The sticking effect is strongly related to the hot mill pick-up of oxide scales and can influence the quality of the surface finish. It appeared from the tests that the sticking effect could not occur randomly at any oxide scale thickness. The sticking phenomenon was detected only for the oxide scale with thickness of ~50 μm (Figure 4.30 and 4.31) but not for the range 100 - 250 μm. It seems likely that this would be strongly linked to the surface diffusion and adhesion of the oxide scale. It is certain that this phenomenon depends on the temperature. For example, at 870°C only a small amount of the oxide scale was stuck to the tool from the slab imitation specimen (Figure 4.30), while at 970°C the roll imitation tool captured the oxide scale from the slab imitation specimen completely (Figure 4.31). However, the information obtained about the sticking effect should not be considered as sufficient for a general description and more experiments which involve the study of this phenomenon are essential.

6.4. Tensile-compressive test

The tensile-compressive tests were more complicated than either the tensile or compression tests because the gauge section has to be cut off from one specimen (see Figure 3.9) and later compressed. Moreover, the cracked oxide scale should not be lost during the specimen transformation. Fortunately, it was found that such a procedure was possible without additional damages to the oxide.

Figure 4.35 shows the temperature effect on the crack spacing of the tensile specimens even more clearly than Figure 4.10. Five specimens, which were tested at the different temperatures, are shown in Figure 4.35. The higher the testing temperature the bigger the distance between cracks. On the other hand, if the testing temperature was the same (T_{test} = 880°C in Figure 4.35), the specimens had a similar number of cracks. It is certain that the results obtained during the tensile stage of the tensile-compressive test are in a good agreement with those attained in the tensile test with different thickness of the flat specimens (Figure 6.1).

The compression stage of the tensile-compressive test allowed stresses equivalent to 200 MPa to be reached. This level of stresses was comparable with what can arise during hot rolling. Although it was not possible to calculate stress-strain curves without the finite element modelling, the compressive stresses were computed depending on the crosshead movement, as shown in Figure 4.38. There is a good possibility that the compression of the mild steel specimen between the two high-speed tools is closer to the hot metal forming conditions than is the compression test that is discussed in section 6.3. Despite some technical difficulties (two stage test and possible cutting problems) the higher compressive stresses could be reached easily (compare Figure 4.38 and 4.21). Heat transfer between the "cold" tool and the "hot" tool was obtained in the same way as for the compression test discussed in section 6.3.3. The differences were as follows: the oxide scales were cracked during the tensile stage of the tensile-compressive test and the bottom thermocouple was installed in the "hot" tool, hence about 5 mm below the contact surface of the specimen with the "cold" tool. Therefore, the measurements of the temperature were influenced in two ways: first, the delay of the "hot" tool temperature alteration was approximately 1.5 s (the "cold" tool ~0.5 s); and second, the temperature changes were bigger than for the unbroken oxide scale (Figure 4.39). According to Figure

4.39, the thickness of the oxide scale, even if it was damaged, undoubtedly has an influence on the temperature alteration. The sticking effect also took place during the compression stage of the tensile-compressive test. Figure 4.40a shows the specimen with the cracked oxide scale before the compression test. The oxide scale was cooler than the metal as shown in Figure 4.40a. Figure 4.40b shows the same specimen after the compression test. The oxide scale disappeared from the surface of the specimen and the remaining oxide having the outline of the round "cold" tool can be seen in Figure 4.40b.

6.5. Microstructural investigations of oxide scale failure

Microstructural analysis of the oxide scales provided valuable information about fracture mechanisms. The examination of the scales, which was carried out with the optical microscopy, SEM, EDS and EBSD techniques, allowed consideration of the reasons of failure. Since the behaviour of the surface oxide scale under hot rolling conditions is very complex, only using multiple techniques allowed us to attain the understanding of this process.

6.5.1. Optical microscopy

Initially, optical microscopy of the tested oxide scales has helped to reveal the fracture surface and a number of oxide layers. Figure 4.41 shows the fracture surface of the oxide scale, which failed in a brittle manner. It can also be seen that the scale has at least two layers and the lower, thick layer appeared to have the columnar structure. According to the literature, the scale can consist of three layers: the top outer layer is the hematite (Fe_2O_3), but it might be too thin to be detected with an optical microscope; the middle layer is the magnetite (Fe_3O_4) and the lower layer is wüstite (FeO) [6]. However, another author suggests a different scale composition, the top layer being the hematite and the bottom, thick layer being the columnar magnetite [58]. This suggestion is well linked with other authors' studies, which reveal that at temperatures higher than 900°C the amount of wüstite drops

dramatically from 90 to 20% [64], [65] and [66]. Nevertheless, there is a good possibility that the variation of the chemical composition of steel will result in the different oxide formation at the hot rolling temperatures. On the other hand, the cooling rate is also important. The final scale composition on the surface of the hot rolled strip is not only determined by the composition of the scale formed at high temperature, but also by the fact that oxides might change phase, for instance, wüstite can turn into magnetite for the period of the cooling stage [146] and [147].

Scanning electron microanalysis needs to be carried out for the detailed investigation of the oxide scale microstructure – see next section.

Since the specimens were at elevated temperatures for quite a long period (up to 3000s), measurement of the decarburisation zone in the steel specimens was required. The decarburisation could be another reason, apart from the temperature, for the stress variation during the high-temperature tensile test of different specimens. However, the depth of the decarburisation zone was equal for the thin (2 mm) and thick (4 mm) specimens, as shown in Figure 4.42. Moreover, it was too shallow, in comparison with the thickness of the gauge section, to be the reason for the stress variation. As regards the compressed specimens (Figure 4.43), the decarburisation of the surface layers was not noticeable during the optical observations. One possible explanation of the dissimilarity in the decarburisation depth could be in the different geometry of the compressed specimens from the tensile specimens. The compression specimen was a cylinder with a diameter of 11 mm while the tensile specimens had a rectangular cross-section in the gauge section with thicknesses of 2 - 5.5 mm. However, the optical micrographs of the tensile-compressive specimen revealed the same size of the decarburisation zone as in the tensile specimen (Figure 4.44a). This could be another argument in favour of the above explanation for the near absence of the decarburisation in the cylindrical specimens. Moreover, the difference of the "hot" and "cold" side of the tensile-compressive specimen was noticeable, as shown in Figure 4.44. It is likely that the recrystallisation on the "hot" side of the specimen started and that is why the grain size in Figure 4.44b is smaller than in Figure 4.44a.

Another feature can be seen in optical micrographs, namely the oxide scales could be pressed in the metal substrate and the steel could extrude between the oxide fragments, as shown in Figures 4.45 and 4.46. The damage of the metal substrate under the oxide scale was detected in the form of the microcracks after etching of the

polished cross-section of the specimen, Figure 4.47. There is a strong possibility that these microcracks appeared during the compression stage due to difference in the hardness of the oxide fragments and the mild steel substrate.

6.5.2. Scanning electron microscopy

SEM analysis confirmed a complicated morphology of oxide scales. The surface scale consisted of highly porous oxides at 870°C and 1070°C and also dense oxides at 970 - 1070°C. Due to heterogeneities during the growth, the oxide scale at 1070°C contained both types of structures, porous and dense.

i) Oxide scale at 870°C

Figures 4.48 and 4.51*b* show porous oxide scales for the specimens after oxidation at 870°C. Big blisters are situated in the top layers of the scale and can be crushed after compression is applied, as shown in Figures 4.55 and 4.56. The oxidation near the corner of the specimen followed the literature representation [139] (Figure 4.49), although the morphology of the corners of specimens with oxide scales was more complicated, as shown in Figures 4.48, 4.53, 4.54 and 4.66. Figure 4.50 shows the through-layers crack and delamination between layers and since this was the only oxidation test without compression, all this damage may have appeared during the cooling stage. This is an example that shows that the cooling process is very important and sometimes the dominating factor for the final scale formation.

A number of SEM images indicated through-thickness fracture (Figures 4.57 and 4.58) and hence, brittle behaviour of scales. It should be noted that some through-thickness cracks were not perpendicular to the surface (Figure 4.58). This could be due to grain-boundary sliding in the substrate near to the oxide-metal interface. Figure 4.56 shows the blisters failure at 870°C. The thin top layer of oxide (possible Fe_2O_3) was not fractured, but the middle layers were crushed due to compression. This indicated significantly different mechanical properties at high temperature among different oxide phases. Blisters were inverted and many cracks can be seen inside the oxide. It is also an indication of a brittle failure. Backscattered

electron images (BEI) showed several different phases of the oxide inside a scale (Figures 4.51*a*, 4.57*b* and 4.58). The two main phases were observed: *a*) top oxide (dark grey) and *b*) bottom oxide, which connects to the metal substrate (light grey).

The sticking phenomenon, which was observed during the high-temperature compression tests, was closely examined with SEM analysis and results are shown in Figures 4.59 – 4.64. Figure 4.59 shows the partly separated oxide scale from the slab imitation specimen. It can be seen that the shape of the oxide scale, where it was separated from the metal substrate, was irregular and a thin layer of oxide remains on the metal surface. Thin oxide layers have always remained on the surface of steel after the roll imitation tool has taken off a main scale. Figure 4.60 shows clearly fracture features that can occur in such thin (~5 μm) layers. Cracking and delamination have been found there and, generally, thin layers behave similarly to the thick oxide scale at 870°C. Figure 4.61 shows the oxide scale that stuck to the tool. The cross-section of the scale was identical to the slab imitation specimen scale (shown in Figure 4.59), except that it was the inverted image. Another confirmation that the oxide scale from the specimen adhered to the tool is given in Figure 4.62. Figure 4.62*a* shows the oxide scale on the surface of the slab imitation specimen where voids are positioned in the top layer, while Figure 4.62*b* shows the oxide scale on the tool with similar voids, situated near the oxide/metal interface. Therefore, it is clear that the oxide scale from the specimen was transferred to the tool. In addition, BEI images visibly indicate different oxide phases on the top of both scales (Figure 4.62). Since the scale in Figure 4.62*b* was inverted after the compression stage, the oxide phase transformation almost certainly occurred during the cooling stage. This is another confirmation of the importance of the cooling process. The oxide/metal interface is shown with higher magnification in Figures 4.63*a* and 4.64. As can be seen from these figures, the thin (5-10 μm) layer of the oxide scale, which adhered to the metal substrate, has visibly lower porosity than the rest of the scale. Also, the thickness of the oxide scale on the side of the tool was about 8 μm (Figure 4.63*b*): this suggests fairly certainly that the oxide scale was that of the tool. Therefore, based on Figures 4.63 and 4.64 it is possible to conclude that the oxide scale from the slab imitation specimen adhered not directly to the tool, but to the oxide scale *on* the tool. The chemical contents of these joint oxide scales are discussed later in section 6.4.3.

ii) Oxide scale at 970 - 1040°C

At this range of temperatures the oxides were observed as dense structures with quite big voids and blisters in the upper part of the scale (Figure 4.53). The big voids and blisters could be very destructive for the oxide scale when normal compressive stresses occur. Figure 4.65 shows a blister crushing similar to that shown in Figure 4.56. The blister crushing can be the reason for through-thickness failure of the oxide scale. This failure is not a simple crack and has a complicated structure (Figure 4.65*a*). The top layer of the scale changed shape but remained unbroken. Possibly this scale was fractured in a ductile way with plastic deformation of the oxide layers. Another feature, which could be a sign of plasticity or ductile behaviour of the oxide scale, was detected near the corner of the specimen that was oxidized at 1040°C. As can be seen from Figure 4.54, the crack appeared and has been arrested in the middle of the scale. This crack could grow only at high temperature otherwise (if it grew during the cooling stage) it would be a through-thickness crack similar to that shown in Figure 4.50*a*. At high temperatures the gas pressure in the void (described by [139]), situated near the corner, can be high enough to bend (very smoothly) the oxide scale and produce the crack. It is very likely that the oxide scale fractured in a ductile manner and the crack was not through-thickness. Figure 4.66 also shows the corner of a specimen with a crack in the oxide scale but after the compression test. The corner void is closed as well as the crack. In that case, it is not possible to detect any plastic deformations of oxide scales during the compression test. The sticking effect occurred at 970°C as well as at 870°C. The thickness of the scale was comparable (50 - 55 μm), however, the adherence was stronger. Whole oxide scale from the slab imitation specimen was transferred to the tool after the compression test. Figure 4.67 shows a thin oxide layer, which is remained on the surface of the slab imitation specimen. The thickness of the remaining scale was the same as for the temperature of 870°C. However, the oxide scale on the side of the specimen (Figure 4.67*a*) was almost separated from the metal substrate with only traces of oxide remaining on the metal surface. It is possible to assume that the conditions of separation were different for the top and side oxide scales. The top oxide scale was stuck to the tool and has been taken off at high temperature, while the side oxide scale was quite likely to have separated during

the cooling stage. Since the thickness of the remaining oxide was different, the mechanical properties of the scale layers varied significantly with temperature. The morphology of a thin oxide was shown in Figure 4.68*a*. It is a solid oxide layer without voids. Figure 4.68*b* shows oxide islands that are much harder than the metal substrate and not deformed after the compression test. However, thin oxides can be fractured as a brittle scale and its small pieces easily deform the metal substrate. In this case, even the oxide scale with a thickness of approximately 15 μm (Figure 4.68*b*) will affect the surface finish of the hot rolled slab or strip.

iii) Oxide scale at 1070°C

At the temperature 1070°C, oxide scales are very heterogeneous and have not a precise thickness. Figure 4.71 shows morphology of oxide scales with a thickness of about 100 μm. Unlike oxides, which were formed at 870°C and 970°C degrees, this scale has big regular pores in the middle. Several mechanisms of damage were observed for this type of oxide scale. Figure 4.71*a* shows many vertical cracks, which could appear under compression or during the cooling stage. The horizontal crack in the top part of the scale is shown in Figure 4.71*b*. The cause of such a crack is still not clear. It is quite possible that the horizontal crack was formed during the cooling stage when the different layers of the scale had different coefficients of linear thermal expansion. On the other hand, the scale in Figure 4.71*b* is thin and could be a remaining layer from the thick oxide that had delaminated and fell off. Another damaged oxide scale is shown in Figure 4.72*a*. There is a strong possibility that under the pressure the vertical voids have combined to form one big horizontal cavity. The microstructure of the scale at elevated temperatures often includes long columnar oxide grains (for example [58]). Figure 4.71*a* appears to show that the columnar grains are separated by the vertical voids. The columnar grains can be crushed under the compressive load, which leads to the horizontal cavity formation (Figure 4.72*a*). Figure 4.72*b* shows a resemblance to the oxide scale given in Figure 4.71*a*; however, the scale in Figure 4.72*b* was damaged in a slightly different way: the result of the compression test in this case was the delamination within the oxide scale. Some evidence in Figure 4.72*b* shows that the columnar grains were inclined under the normal compressive load producing shear stresses within the scale (see

Figure 6.4) and a subsequent exfoliation. A similar effect of sliding at phase boundaries has been described by other authors [148] on duplex stainless steels.

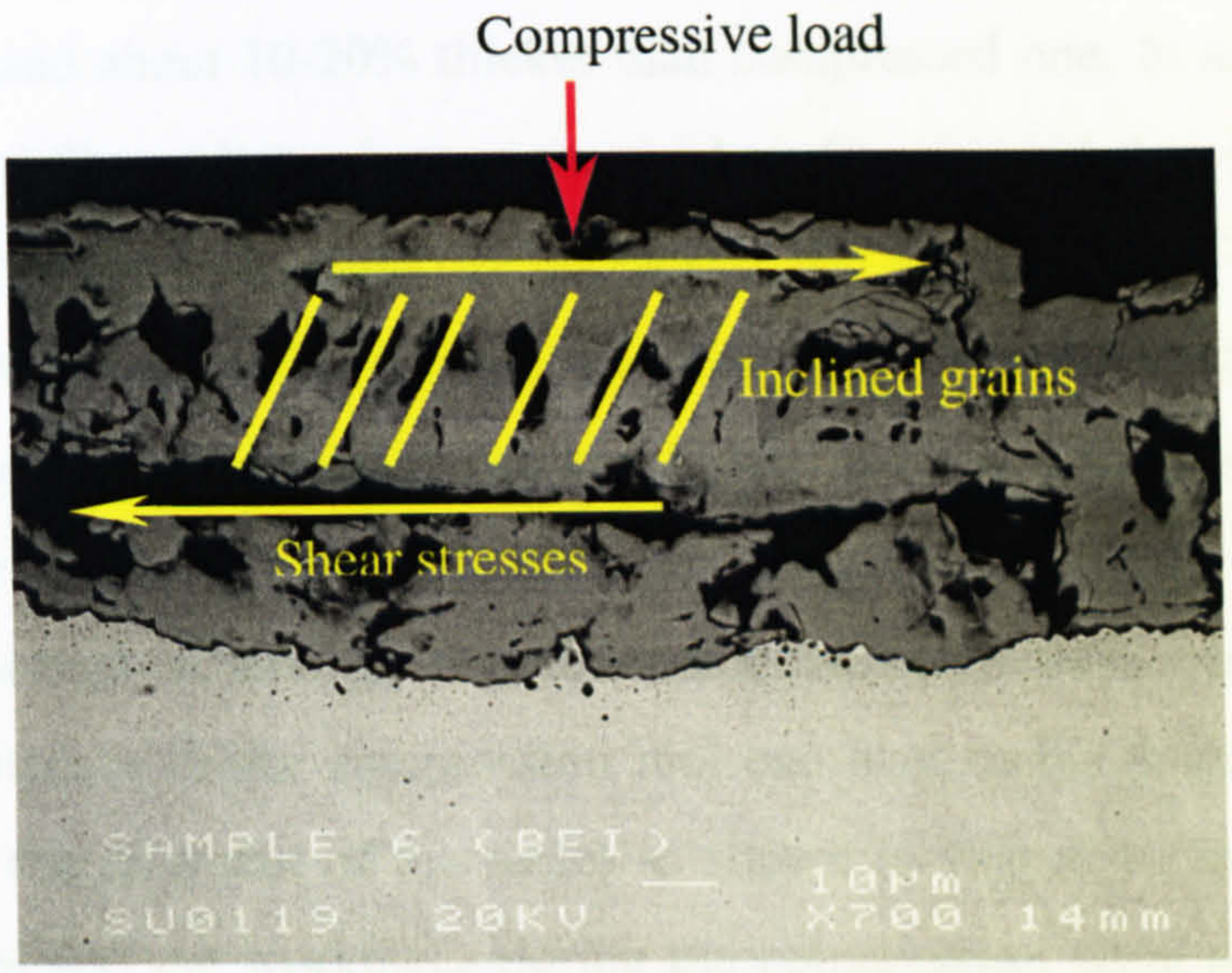

Figure 6.4. Possible mechanism of delamination under compressive load.

When the oxidation time is longer and scales are thicker (Figure 4.69*a*) the vertical pores disappeared. The separation of oxide scales for 1070°C can be of two types. In the first case (Figure 4.70*a*), it is the same as for 870°C and 970°C and the remaining oxide scale approximately 5-10 μm. In the second case (Figure 4.69*b*), when spallation happened for a thick scale, only traces of an oxide were detected. Figure 4.70*b* shows a big blister on a flat metal surface. It indicates that this blister was formed after compression without damaging the metal substrate. As the oxide scale has not fractured, this could be evidence of plastic behaviour at that high temperature.

On the whole, the high-temperature compression test results suggest not only brittle behaviour of oxide scales, but also some signs of plasticity and ductile behaviour.

iv) Oxide scales after tensile-compression testing

The behaviour of the oxide scale after the tensile-compression test was similar to the high-temperature compression test, however, some features were

and should be noted. As can be seen from Figure 4.73a, the thickness of the oxide scale was reduced during the compression stage of the tensile-compressive test. The part of the oxide scale that was outside the tool (right top corner Figure 4.73a) remains porous and about 10-20% thicker than compressed one. In addition, Figure 4.73 shows the different behaviour of the thick (~50 μm) and thin (~8 μm) oxide scales. The thick oxide scale could rise uncracked, if it was outside of the edge of the compressive tool (Figure 4.73a), while the thin oxide scale had many cracks, but remained adhered to the metal substrate (Figure 4.73b). The evidence that the fracture of the oxide scales was brittle is shown in Figure 4.74. Figure 4.74 shows the oxide scales that content through thickness cracks and were even crumbled in some places. The contact with the compression tool can lead to the delamination of the oxide scale (or the fragment of the scale) as shown in Figure 4.75a. The adhesion between the tool and the workpiece during the compression stage perhaps was not strong enough to take off the oxide fragment, but was able to produce the delamination. Finally, Figure 4.75b shows that when the oxide scale was taken off by the tool, it was possible to detect where were the cracks in the surface oxide. The marks of the metal's extrusion between the oxide cracks and the intrusion of the oxides are still on the surface of the metal substrate.

6.5.3. Electron dispersive spectroscopy microanalysis

Energy dispersive spectroscopy microanalysis was used for identifying and quantifying elemental composition of oxide scales. This technique appeared to be very useful for the determination of two different scales where the sticking effect occurred.

At the beginning, the EDS spectra of mild and high-speed steels were obtained. Figure 4.76 shows the EDS spectrum of mild steel (chemical contents in Table 3.1) that includes *Fe* and the poorly recognizable trace of *Mn*. Hence *Fe* and *Mn* are only metals which could be expected in the oxide scale EDS spectra. Figure 4.81 shows the EDS spectrum of high-speed steel (the tool) with several recognizable peaks namely *Fe*, *W*, *Mo*, *V*, *Cr* and even some traces of *Mn*. At the grain boundaries, *W*, *Mo* and *V* have higher concentration as shown in Figure 4.82. It is possible to

expect these four elements (*W*, *Mo*, *V* and *Cr*) to be distinguishing features of the oxide scale that was formed on the tool.

The EDS spectra of the mild steel oxide scales are given in Figures 4.77 – 4.80. The oxide scale examined here contained only a small amount of *Mn* along the full thickness as was anticipated. Besides, a strong peak of *Si* was observed in the thin layers or residue of the oxide scale near the metal substrate (Figures 4.79 and 4.80). These results agreed with literature data that *Mn* is very mobile and *Si* stays at the scale base. The influence of chemical composition of steel on oxide properties was discussed in section 2.2.3 (v). Figure 4.83 shows the EDS spectra of the scale on the side of the tool and the bottom layer of the scale, which adhered to the tool after the compression test at 870°C. *W*, *Mo*, *V* and *Cr* were detected with similar intensities in these two EDS spectra. It is certain that both examined oxides belonged to the tool. However, EDS spectra of the middle and top layers of the adhered to the tool oxide scale did not reveal any elements except *Fe* and some traces of *Mn* (Figure 4.84). Therefore, the conclusion should be as follows: the oxide scale, which was situated on the surface of the tool, contained both the mild steel and the high-speed steel oxides. The EDS spectra results provided conclusive evidence that the oxide scale from the slab imitation specimen adhered to the tool oxide scale.

6.5.4. Electron backscatter diffraction

The oxide scales possess a complex crystal structure coupled with anisotropic materials properties. The phase and orientation of the grains have a large influence on the useful properties and behaviour of oxides. Therefore, the electron backscatter diffraction (EBSD) technique was used to provide information such as the grain size, orientation and phases in the oxide scale.

Figure 4.85 show the SEM image of the oxide scale with a crushed blister, similar to that shown in Figure 4.65. The EBSD Euler map of the same area is shown in Figure 4.86. As can be seen from Figure 4.86 some oxide grains were crushed and fell off in pieces. These grains appeared to be fractured in a brittle manner. The thin black line of hematite on the surface of the oxide scale was detected in Figure 4.85, though in Figure 4.86 it was not possible to identify other phases of oxides.

Therefore, the EBSD technique of the pattern recognition was not sensitive enough in this case and needs improvement perhaps in the data handling and processing software. In addition, inadequate sample preparation can also be the source of poor pattern recognition when EBSD of oxides is undertaken [149].

The column grain orientation in an oxide scale formed at 1070°C was quite random and without an apparent priority as shown in Figure 4.87. This result agreed well with the conclusion that the thicker scales show randomly oriented patterns [150]. Figure 4.88 shows columnar oxide grains (magnetite) with thin hematite layer. Hematite was recognised and shown in Figure 4.89. As can be seen from Figures 4.88 and 4.89, the hematite layer consisted of very small grains. In addition, the interface between magnetite and hematite was not indexed by the software, which probably means that the crystal patterns there were damaged during the compression test or the oxide scale was too porous there. As regards the growth of the oxide grains, the size of the mild steel grains appeared to be smaller than the oxide ones on the oxide/metal interface (Figure 4.90). Therefore, the grains of the oxide and steel were not related in sizes at the oxide/metal interface. Figures 4.91 and 4.92 show the oxide scale that adhered to the tool. It is hard to see on the EBSD map that the two different oxide scales are connected to each other. Figure 4.91 shows the encircled area where two oxide scales were determined based on grain size analysis. On the other hand, two encircled areas (Figure 4.92) show long columnar grains that appeared to grow directly from the metal substrate. These results, obtained from the oxide scale that adhered to the tool, clearly show the complexity of processes, which took place during the contact of the specimen and the tool. The presence of the two kinds of the scale connection probably displayed a boundary state of the oxide behaviour. The scales in Figures 4.91 and 4.92 were magnetite oxide. One could assume that during the cooling stage wüstite in the oxide scale was transformed to magnetite. In that case, the transformation in the oxide scale could leave two separate grains (Figure 4.91 encircled) or perhaps could join two grains in one (Figure 4.92 encircled). However, the sticking phenomenon has not been studied enough and needs more experimental data and particularly microstructural investigations.

6.6. Finite element modelling

6.6.1. Tensile test simulation

The finite element modelling has helped to evaluate heat transfer and a distribution of stress (Figure 5.11) in a specimen with the flat gauge section (Figure 3.12). The problems with specimen heating were described in section 5.1.1. Nevertheless, the finite element model has assisted in the evaluation of the real surface temperature of the thin (2 mm) specimen (Figures 5.5 and 5.7). The temperature distribution could not be correctly interpreted with only the thermocouple and pyrometer measurements. Sensitivity of the modelling to the temperature dependent material properties is shown in Figures 5.8-5.10. The thermo-mechanical finite element model was built far from the place where mechanical measurements were carried out. Therefore, a Young's modulus value was substituted by apparent elastic modulus in order to satisfy the experimental results (Figure 5.8). This replacement was very useful to keep the number of finite elements in the complicated thermo-mechanical model as small as possible and to reflect the experimental results that were observed. Figures 5.9 and 5.10 show the yield stress as a function of the temperature. The closeness of the results in Figure 5.9 suggests that the measurements and calculations were in a good correlation. However, in Shida's equations [133] the yield stress had a sharp drop over the range of 700 – 850°C. This drop was taken place probably due to the phase transformation, but other authors [131] and [132] do not suggest such a dramatic change in the yield stress. Nevertheless, the difference in the yield stress value of mild steel, which calculated in different studies, might vary significantly (see Figure 5.10).

According to the analysis, both 2 and 4 mm gauge thickness specimens had almost uniform distribution of surface stresses. Even heterogeneity of stresses near the edge of the gauge section did not affect the crack spacing very much (see Figure 4.10). Figure 5.13 shows the history plot of stresses in the X-direction on the surface in the centre of the specimen. It should be noted, that due to the dither effect (see sections 4.2.3 and 6.1.2) the stress-strain curve could not be modelled as well as the history plot of stresses (Figure 5.12). The numerical values of stress are very similar

inside the gauge section for each temperature level, but change when higher or lower temperatures are applied. This could lead one to assume that the stresses during the tests were dependent on temperature rather than geometry. At the same time, the distribution of plastic strains does not depend on the thickness of the gauge section (Figures 5.14 and 5.15). Elastic strains are relatively low in comparison with plastic strains. The numerical values of the plastic strain change inside the gauge section of a specimen for one temperature level (due to the displacement variation that shown in Figure 5.4), but there is no difference for higher or lower temperature. Hence, the strains are not dependent on temperature or geometry in the tests reported here.

The cracking of the oxide scale was simulated using the fracture mechanics approach, which is explained in section 3.11.1. The softening modulus (Figure 5.16) was not included in the model because of absence of data. Nevertheless, the crack formations simulated with finite element modelling (Figures 5.20 and 5.23) were very close to those obtained during the experiment (Figure 4.10). The modelling results suggest that the stress intensity factor (K_{Ic}) had major influence on the crack pattern formation. Figures 5.26 and 5.27 show the same specimen at 800°C and the only difference is in the stress intensity factor values. As can be seen from these figures, the number of cracks was visibly different.

6.6.2. Compression test simulation

The thermo-mechanically coupled finite element model was aimed at examining two main problems that were raised during the compression test. The first problem was a simulation of the heat transfer during the contact of the slab imitation specimen and the tool. The second problem was a stress and strain distribution, which were impossible to measure with appropriate accuracy during the compression test. The heat transfer coefficient at the contact interface was the most difficult parameter for evaluation. The values that are published in the literature vary widely from 2 to 200 $kWm^{-2}K^{-1}$ [119], [132], [142], [143] and [144]. The conditions at the interface undoubtedly are very important and influence the variability of the heat transfer coefficient. For example, the presence of the oxide scale between the tool and workpiece almost certainly decreases heat transfer. The finite element simulation

was used in order to evaluate the heat transfer coefficient. Temperature was checked at the thermocouple points (Figure 5.29). The experimental and modelling temperature changes were brought together (by varying the heat transfer coefficient) to be as close as possible, as shown in Figure 5.30. The heat transfer coefficient, which was obtained during the modelling, was between 1.3 and 2.4 $kWm^{-2}K^{-1}$. These values are situated near the lower bound of the published range. Therefore, it might suggest that the oxide scales, which were definitely detected and measured in the present study, were not considered by some other authors. When the oxide scale is under consideration [119], the value of the interfacial heat transfer coefficient was similar to that calculated in the present research. Another important parameter that should be mentioned is the compression stress (or load). The higher the compressive stresses are, the better is the contact between the tool and workpiece (especially in the case of the damaged oxide scale). It should be noted that the modelling was carried out by assuming unbroken oxide scale. If the oxide scale contains cracks and extrusion of metal is possible, the interfacial heat transfer coefficient is going to be different and more complicated to calculate.

Since the high temperature compression test was not a plane strain test, the distribution of strains was simulated by the finite element model, based on the experimental load and displacement. The 3-D thermo-coupled finite element analysis has revealed the distribution of stresses and strains inside the specimen. Figures 5.31 and 5.36 show that stresses in the centre of the specimen were lower than stresses near the edge. This explains why the oxide scale that adhered to the tool at 870°C was not in the centre of the specimen (Figure 4.30). The gauge section size was uncertain in the compression test, hence, it was impossible to calculate the strain and strain rate accurately from the obtained results without using a finite element model. Figure 5.33 shows the history plot of the equivalent plastic strain rate near the surface of the specimen after the contact with the tool. The average strain rate was 0.1 s^{-1} except in the region where the thermocouple hole was situated (near node 1). It is highly likely that the variation of the equivalent plastic strain rate (dropping at 0.08 s and 0.19 s in Figure 5.33) occurred during mathematical calculations to achieve a convergence in the finite element model. Therefore, only an approximate value of the equivalent plastic strain rate can be taken into consideration when relying on the finite element simulation. Similarly, the equivalent plastic strain was obtained as

shown in Figure 5.34. The equivalent stress distribution near the area of the contact did not show differences inside the specimen (Figure 5.35), while the longitudinal stress distribution revealed the local increase of the stresses near the contact (Figure 5.36). Figure 5.36 suggests the places where the damage of the oxide scale could occur with the greatest probability. When the contact occurs under a small misalignment angle, bending of the specimen was possible (Figure 5.39). In this case, the total strain on the concave side of the specimen was about two times higher than in the direct contact. Therefore, there is a strong possibility that the oxide scale damage can appear in the area where the initial contact occurs. Figure 5.40 confirms that the highest possible stress shown be expected to be at the point of the initial contact. In addition, it should be noted that the stress increase was only local as shown in Figure 5.41.

6.7. Summary

In this chapter the thermo-mechanical failure of the oxide scales has been discussed. It is clear that the temperature was the leading factor in the oxide scale behaviour. However, the influence of the surface oxide scales in hot metal forming processes, such as hot rolling and forging, appeared to be quite complicated and many factors should be considered in order to interpret and model these processes effectively. Although a complicated process, hot rolling can be divided into the several relatively simple tests and studied more accurately. At that stage, each important thermo-mechanical parameter and failure mechanism can be detected, measured and simulated using the finite element method. The results obtained can be used for the verification of the global process model (for example hot rolling) and specification of further laboratory tests.

Chapter 7
Conclusions

Several general conclusions about the test methodology have been made.

- When induction-heating equipment is used for the heating of small specimens, a minimum square size or diameter should be calculated as shown in section 3.6.1. The sizes of the specimen should be sufficient for obtaining a good induction heating efficiency.

- The crosshead movement of the tensile (compression) machine should be checked carefully, as a small backward movement of the crosshead was detected during the tensile and compression tests. This backward movement lead to an abrupt decrease of the load.

- Dither frequency and dither effect can influence data measurements during the steady stage of the experiment. If this happens, the data obtained should be smoothed (for example by the running average technique).

Two main mechanisms of failure were distinguished from the complicated deformation of the oxide scales during hot rolling: the first was the failure due to tensile stresses; and the second appeared under compression when the failure occurred due to normal or tangential compressive stresses. The main conclusions from the high-temperature, tensile and compressive tests carried out are given in the following sections.

7.1. Tensile testing of flat specimens

- High-temperature tensile testing of flat specimens has been carried out to compare with previous results for a cylindrical geometry [29]. The failure behaviour of oxide scale during tension at 800-880°C was similar to previous results found with cylindrical specimens.

- A high sensitivity of scales to temperature changes was observed in the experiments and confirmed in the modelling approach.

- Optical microanalyses detected a decarburisation of the surface layer of the steel. However, this zone was too small compared with the dimensions of the gauge section for the decarburisation to be a major reason for the stress variation. Nevertheless, it would appear that the decarburisation might be able to influence stress distribution of thin specimens if the time of the oxidation was long enough.

- The oxide scales fractured in a brittle way. However, oxide scales on the surface of flat specimens were sensitive to the thickness of the gauge section. The thicker the gauge section the wider the distance between cracks. The physical explanation of that phenomenon can be the following, scales on the surface are very sensitive to the level of stresses and, hence, temperature in the gauge section. Therefore, the geometrical size of a heated sample and its temperature were mutually dependent during induction heating. It has been suggested that the specimens with different thickness had different surface temperature within the induction furnace. The variation was supposed to be enough to produce the difference in stresses and a visible effect in failure of oxide scales.

- Some of the experimental evidence (Figure 6.1) shows that the chemical composition of the steel is very important for the mechanical failure of the oxide scales under elevated temperatures. According to Krzyzanowski and Beynon [29] and [78], at higher temperatures through-thickness cracking is replaced by slipping of the oxide scale along the metal/oxide interface. It

seems that the transition zone between through-scale cracking and slipping of the oxide scale can be at the different temperature range depending on the chemical composition of the steel.

- Three-dimensional thermo-mechanically coupled finite element modelling has been used to investigate more precisely the failure mechanism of oxide scales under hot rolling conditions. The 3-D finite element simulation of the tensile test of flat specimens has helped to evaluate a distribution of stresses and heat transfer for different thickness.

- The elastic-plastic behaviour of the flat specimen inside and near to the induction furnace was investigated by 3-D finite element modelling. The results show that the stresses and temperature could have a major influence on the brittle failure of the oxide scales in the 700-900°C ranges of temperatures.

- It has been suggested that only the temperature variation could cause a change in the stresses within the specimens. Also, when the oxide scale was tested in the 700-900°C range of temperatures, the crack spacing rises with increasing temperature, as shown in Figure 6.1. Using the measured values of the stress intensity factor, K_{Ic}, (Figure 6.2) the 3-D finite element model of the tensile test of flat specimens with the simulated oxide scale has appeared to succeed in explaining the different crack spacing at different temperatures.

7.2. Compression testing

- The current investigation has demonstrated the possibility to conduct high-temperature compression test using the same equipment as for the tensile tests.

- Hot rolling conditions can be achieved with different temperatures for the roll and slab imitation specimens.

- A new phenomenon of the failure of oxide scales under the compressive stress was observed. Some fragments of a scale had stuck to the roll imitation tool and were taken off by the slab imitation specimen after the compression test.

- The changing of the temperature was observed in both parts of specimen during the contact. The upward and downward trends of the temperature were present for the roll and slab imitation specimens correspondingly. The thinner the oxide scale the bigger the difference between the initial and final contact temperatures.

- SEM analysis confirmed a complicated multi-layer morphology of oxide scales. The oxide scales formed highly heterogeneous and porous structures particularly during the short oxidation time at temperatures that were higher than 1000°C. Those scales also had the most complicated fractures under the compression stress. However, it seems that during longer periods of oxidation dense scale could be formed (Figure 4.69*a*).

- Some of the evidence (the lack of wüstite in oxide scales) shows that the cooling rate is important for the formation of the surface oxide scale. As mentioned in section 6.4.1, the final oxide scale composition is not only determined by the composition of the scale formed at high temperature, but also by the fact that oxides might change phase during the period of the cooling stage [146] and [147].

- A number of SEM images indicated through-thickness fracture and hence, brittle behaviour of scales. However, some images at 970°C and 1070°C revealed traces of ductile behaviour and plastic deformation of the oxide scales.

- Blisters and big pores failure might lead to the delamination within the scale and the separation of the scale from the metal substrate.

- At temperatures higher than 1000°C there were indications of ductile behaviour and plastic deformation of the oxide scales. For instance, at 1040°C non through-thickness and widely opened cracks were detected (Figure 4.54).

- Chemical contents of steels can have an influence on contact between a roll and a slab at high temperature conditions. The bottom oxide has a more complicated chemical content, which might influence the metal-oxide interface failure and descaling procedure

- The 3-D finite element model of the high-temperature compression test has helped to evaluate the distribution of stresses inside the specimens and heat transfer during the contact of the tool and the workpiece.
- Heat transfer coefficient between the slab imitation specimen and the tool (the roll imitation specimen) has been evaluated using the finite element simulation.
- Since some specimens, especially at temperatures higher than 970°C, have been bent, the contact under a small angle due to misalignment was simulated in 3-D finite element model. The calculations of the stress distribution suggest that the oxide scale damage might be larger in the area where the initial contact occurs.

7.3. Tensile - Compressive testing

- A tensile-compressive test was developed and successfully performed under thermal conditions which were as close as possible to hot rolling.
- The stresses obtained during the testing achieved a higher level than in the compression test and lay in the typical range for metal forming operations.
- SEM images indicated that different fracture is possible for oxide scales with different thicknesses (Figure 4.73).
- The results obtained signified that pieces of the cracked oxide scale might contribute to damage of the metal substrate near the oxide-metal interface (Figure 4.47).
- The high-temperature tensile-compressive test confirmed the possibilities to simulate and study the extrusion of steel between the cracked oxide scales similar to that that can happen during the hot rolling process.

Chapter 8

Suggestions for Further Work

The influence of the electric current on the oxide-metal interface near the surface during induction heating is still unknown. Therefore, it is suggested that oxidation and mechanical testing experiments should be carried out using short-wave infrared heating instead of induction heating. This helped avoid the effect of induced electromagnetic field that produces a circulating current.

The investigations of the mechanisms involved in the sticking between oxide and tool were not the primary aim for the present study; hence, it is suggested that these should be investigated separately. Different materials, temperature conditions, oxide scale thicknesses and presence of lubricants could be studied in order to verify when the sticking is happening and how is possible to avoid it.

According to the literature review, there is not enough data on the thermo-mechanical properties of the oxides at the elevated temperatures. Therefore, hot microhardness measurements of different oxides and precise heat-transfer coefficient measurements of different oxide scale thicknesses (for instance, using the equipment as shown in Figure 8.1) would be very helpful for improving further physical based finite element modelling.

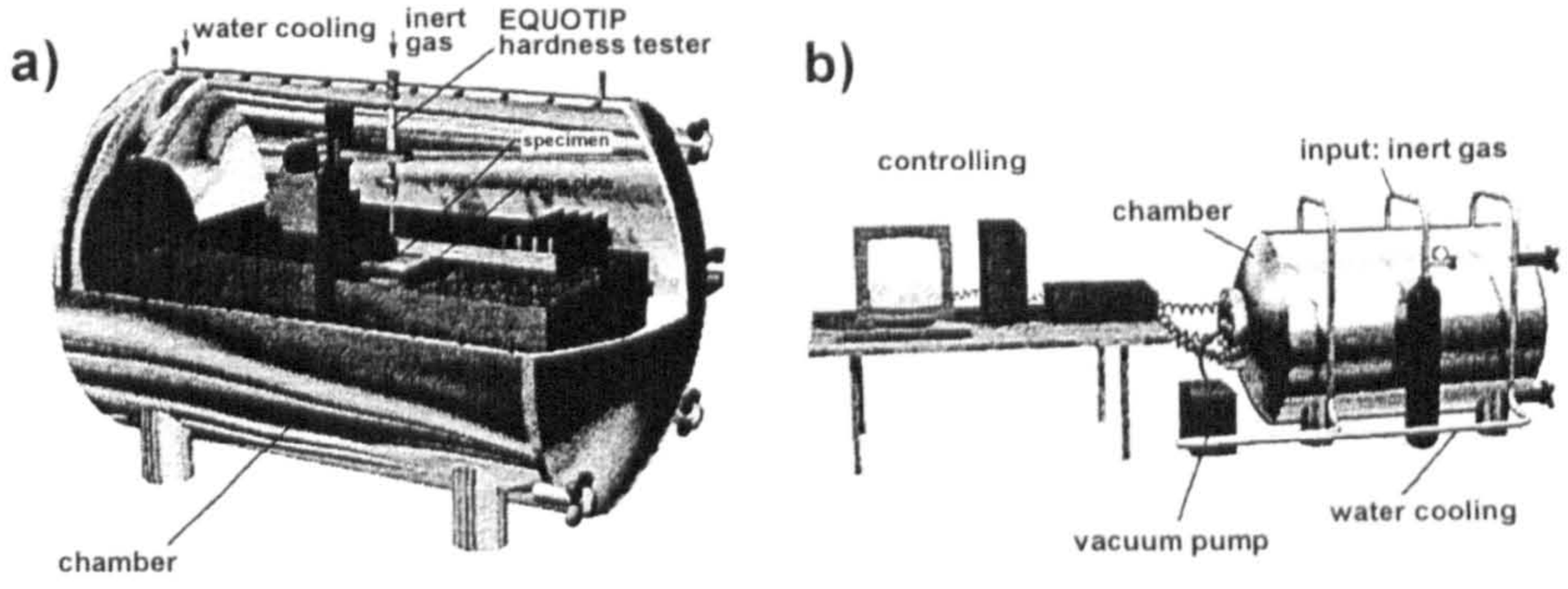

Figure 8.1. Equipment for high-temperature thermo-mechanical measurements [144].

Some of the evidence shows that the composition of the oxide scales and the relative thickness of the oxide layers are changing during the cooling. Finite element modelling relies on the experimental data, but most measurements were carried out at room temperature. In this case, *in-situ* measurements of the oxide scale compositions at elevated temperatures (for example High Temperature X-Ray Diffraction [151]) could be carried out to provide vital data.

Another technique that could supply more information about the composition and perhaps mechanical damages of the oxide scale is the use of EBSD measurements to investigate grain structure and phase compositions of oxide scales. However, the EBSD can provide useful data if the resolution is high enough to detect all layers and features in the scale. It should be noted that the EBSD could be particularly effectively if used as the constituent part of the mechanical (or thermo-mechanical) tests.

References

1. Hollander, F., and Hurkmans, A. (1990). *Flatness and Profile - Development and Predictive Control from Slab to Sheet.* in *5th International Rolling Conference. Dimensional Control in Rolling Mills*. London, UK: Institute of Metals in co-operation with the Association of Iron and Steel Engineers.
2. Le Hay, T., and Quehen, A. (1990). *New Technologies for Dimensional Control of Hot Strip Mill.* in *5th International Rolling Conference. Dimensional Control in Rolling Mills*. London, UK: Institute of Metals in co-operation with the Association of Iron and Steel Engineers.
3. Morgan, H.D., Detry, J.M., Charlier, A., Houyoux, C., Van Daele, C., Tondeur, S., and Cornet, X., (2002), *"Shape and Metallurgical Control in Skin Pass Rolling of Hot-Rolled Coil"*. EUR 20080 EN. European Commission.
4. Freitag, D.W., and Richerson, D.W., (1998), *"Opportunities for Advanced Ceramics to Meet the Needs of the Industries of the Future"*. DOE/ORO 2076. Prepared by U.S. Advanced Ceramics Association and Oak Ridge National Laboratory for the Office of Industrial Technologies Energy Efficiency and Renewable Energy U.S. Department of Energy.
5. Kittel, C., (1996), *Introduction to Solid State Physics*. 7 ed. New York: Wiley.
6. Hauffe, K., (1965), *Oxidation of Metals*. New York: Plenum.
7. Kröger, F.A., (1974), *The Chemistry of Imperfect Crystals*. 2 ed. Vol. 2. Amsterdam: North-Holland Publishing Co. 988.

8. Kofstad, P., (1966), *High-Temperature Oxidation of Metals*: Wiley.

9. Kubaschewski, O., (1979), *Metallurgical Thermochemistry*. 5th ed. Oxford: New York, Pergamon Press.

10. Kofstad, P., (1972), *Nonstoichiometry, Diffusion, and Electrical Conductivity in Binary Metal Oxides*. New York: Wiley-Interscience. 382.

11. Shewmon, P., (1989), *Diffusion in Solids*. 2nd ed. Warrendale, Pa.: Minerals, Metals & Materials Society.

12. Glicksman, M.E., (2000), *Diffusion in Solids: Field Theory, Solid-State Principles, and Applications*. New York: Wiley. 472.

13. Fick, A., (1855): "*Philosophical Magazine*, **10**, p. 30.

14. Zener, C., (1952), *Imperfections in Nearly Perfect Crystals*. New York: John Wiley & Sons.

15. Fisher, J.C., (1951): "*Journal of Applied Physics*, **22**, p. 74.

16. Chen, C., and Tsong, T.T., (1990): "Displacement Distridution and Atomic Jump Direction in Diffusion of Ir Atoms on the Ir(001) Surface", *Physical Review Letters*, **64**(26), p. 3147-50.

17. Sun, B., Suo, Z. and Yang, W., (1997b): "A Finite Element Method for Simulating Interface Motion - I. Migration of Phase and Grain Boundaries", *Acta Materialia*, **45**(5), p. 1907-15.

18. Sun, B., and Suo, Z., (1997a): "A Finite Element Method for Simulating Interface Motion - II. Large Shape Change Due to Surface Diffusion", *Acta Materialia*, **45**(12), p. 4953-62.

19. Chang, C.M., Wei, C.M., and Chen, S.P., (1996): "Modeling of Ir Adatoms on Ir Surfaces", *Physical Review B*, **54**(23), p. 17083-96.

20. Kubaschewski, O., and Hopkins, B.E., (1962), *Oxidation of Metals and Alloys*. 2nd ed. London: Butterworths.

21. Wagner, C., (1933): "*Journal of Physical Chemistry (B)*, **21**, p. 25.

22. Mott, N.F., (1947): "*Journal of Chemical Physics*, **44**, p. 172.

23. Cabrera, N., and Mott, N.F., (1949): "*Reports on Progress in Physics*, **12**, p. 163.

24. Evans, U.R., (1947): "*Transactions of Electrochemical Society*, **91**, p. 547.

25. Himmel, L., Mehl, R.F. and Birchenall, C.E., (1953): "*Journal of Metals*, **5**, p. 827.

26. Davies, M.H., Simnad, M.T. and Birchenall, C.E., (1951): "On the Mechanism and Kinetics of the Scaling of Iron", *Journal of Metals*, **3**, p. 889-96.

27. Davies, M.H., Simnad, M.T. and Birchenall, C.E., (1953): "*Journal of Metals*, **5**, p. 1250.

28. Wrazej, W.J., (1953): "Observation on Scaling of Iron", *Transactions of the American Institute of Mining and Metallurgical Engineers*, **197**, p. 265-6.

29. Krzyzanowski, M., and Beynon, J.H., (1999a): "The Tensile Failure of Mild Steel Oxides Under Hot Rolling Conditions", *Steel Research*, (1/99), p. 22-7.

30. Wood, G.C., (1962): "The Oxidation of Iron-Chromium Alloys for Use at High Temperatures", *Corrosion Science*, **2**, p. 197-202.

31. Peters, F.K., and Engell, H.J., (1959): "Die Haftfestigkeit von Zunderschichten auf Stahl", *Archiv für das Eisenhüttenwesen*, **30**(5), p. 275-82.

32. Rahmel, A., and Manenc, J., (1973), *Mechanische Eigenschaften und Haftung von Zunderschichten - Einfluß auf die Oxidation von Metallen*. Weinheim: Verlag Chemie.

33. Malik, A.U., (1985): "High-Temperature Oxidation of Transition Metal, Carbide-Dispersed Iron-Base Alloys", *Oxidation of Metals*, **25**(5/6), p. 233-63.

34. Sheasby, J.S., Boggs, W.E. and Turkdogan, E.T., (1984): "Scale Growth on Steels at 1200°C: Rationale of Rate and Morphology", *Metal Science*, **18**, p. 127-36.

35. Wei, F.I., and Scott, F.H., (1989): "High Temperature Oxidation of Commercial Austenitic Stainless Steels", *Materials Science and Technology*, **5**, p. 1140-7.

36. Allen, G.C., and Wild, R.K., (1983): "Characterization of the Oxide-Metal Interface at the Surface of a Stainless Steel", *Philosophical Magazine A*, **48**(3), p. 373-86.

37. Taniguchi, S., Furukawa, T. and Shibata, T., (1997): "Failure of Scales Formed on Cu-containing Low Carbon Steels during Cooling", *ISIJ International*, **37**(3), p. 263-71.

38. Seo, S.-J., Asakura, K. and Shibata, K., (1997): "Effects of 0.4% Si and 0.02% P Additions on Surface Hot Shortness in 0.1%C-0.5%Mn Steels Containing 0.5% Cu", *ISIJ International*, **37**(3), p. 240-9.

39. Merz, M.D., (1979): "The Oxidation Resistance of Fine-Grained Sputter-Deposited 304 Stainless Steel", *Metalurgical Transactions A*, **10A**, p. 71-7.

40. Baer, D.R., and Merz, M.D., (1980): "Differences in Oxides on Large- and Small-Grained 304 Stainless Steel", *Metallurgical Transactions. A*, **11A**, p. 1973-80.

41. Hobby, M.G., and Wood, G.C., (1969): "The Role of Nickel in the High Temperature Oxidation of Fe-Cr-Ni Alloys in Oxygen", *Oxidation of Metals*, **1**(1), p. 23-53.

42. Imai, N., Komatsubara, N. and Kunishige, K., (1997): "Effect of Cu and Ni on Hot Workability of Hot-rolled Mild Steel", *ISIJ International*, **37**(3), p. 224-31.

43. Lanteri, V., Mousseaux, L., Henry, P., Di Fant, M., Moulin, G., Salvador, G., and Cleizergues, O., (1996), *"Adhesion Tests at High Temperatures on Low-Carbon Steel Scales"*. Final Report. ECSC research project 7210-EB/306.

44. Grabke, H.J., Leroy, V. and Viefhaus, H., (1995): "Segregation on the Surface of Steel in Heat Treatment and Oxidation", *Iron and Steel Institute of Japan*, **35**, p. 95-113.

45. Seal, S., Nardelli, R., Kale, A., Desai, V. and Armacanqui, E., (1999): "Role of Surface Chemistry on the Nature of Passive Oxide Film Growth on Fe-Cr (Low and High) Steels at High Temperatures", *Journal of Vacum Science and Technology. A*, **17**(4), p. 1109-15.

46. Mitra, S.K., Roy, S.K. and Bose, S.K., (1990): "*Oxidation of Metals*, **34**, p. 101.

47. Moon, D.P., and Bennett, M.J., (1989): "*Materials Science Forum*, **43**, p. 263.

48. Papaiacovou, P., Hussey, R.J., Mitchell, D.F. and Graham, M.J., (1990): "*Oxidation of Metals*, **33**, p. 19.

49. Whittle, D.P., and Stringer, J., (1980): "*Philosophical Transactions of the Royal Society London, Series A*, **295**, p. 309.

50. Mayer, M.G., (1948): "On Closed Shells in Nuclei", *Physical Review*, **74**(3), p. 239-9.

51. Duffy, D.M., Harding, J.H. and Stoneham, A.M., (1992): "Atomistic Modelling of the Metal/Oxide Interface with Image Interactions", *Acta Metallurgica Materialia*, **40**, p. S11-S16.

52. Duffy, D.M., Harding, J.H. and Stoneham, A.M., (1996): "A Calculation of the Structure and Energy of the Nb/Al_2O_3 Interface", *Acta Materialia*, **44**(8), p. 3293-8.

53. Stoneham, A.M., (1994): "Interfacial Modelling", *Materials at High Temperatures*, **12**(2-3), p. 183-7.

54. Duffy, D.M., and Tasker, P.W., (1984a): "A Calculation of the Formation Energies of Intrinsic Defects Near Grain Boundaries in NiO", *Philosophical Magazine A*, **50**(2), p. 143-54.

55. Duffy, D.M., and Tasker, P.W., (1984b): "A Calculation of the Interaction Between Impurity Ions and Grain Boundaries in NiO", *Philosophical Magazine A*, **50**(2), p. 155-69.

56. Finnis, M.W., and Kruse, C., (1994): "Understanding Adhesion Between Metal and Oxide", *Materials at High Temperatures*, **12**(2-3), p. 189-94.

57. Stoneham, A.M., and Harding, J.H., (1998): "Computer Simulation of Interfaces:What Do We Need to Know?" *Acta Materialia*, **46**(7), p. 2255-61.

58. Metcalfe, E. (1989). *Oxide Characterisation for Life Prediction.* in *Surface stability: proceedings of the sixth seminar in a series of seven sponsored and organised by the Materials Science, Materials Engineering and Continuing Education Committees of the Institute of Metals*. London, Institute of Metals.

59. Manning, M.I., and Metcalfe, E. (1979). *Hematite-Magnetite Transformations in Oxide Scales Growing on Steels.* in *Phase Transformations : Spring Residential Conference*. York: Institution of Metallurgists.

60. Schmitz-Niederau, M., and Schutze, M., (1999): "Cracking and Healing of Oxide Scales on Ti-Al Alloys at 900°C", *Oxidation of Metals*, **52**(3/4), p. 241-76.

61. Banovic, S.W., DuPont, J.N. and Marder, A.R., (2000): "Growth of Nodular Corrosion Products on Fe-Al Alloys in Various High-Temperature Gaseous Environments", *Oxidation of Metals*, **54**(3/4), p. 339-69.

62. Gittins, A., (1975): "Fracture in Hot Working of Steel", *The Journal of the Australian Institute of Metals*, **20**(4), p. 184-200.

63. Bernard, J., and Coquelle, O., (1946): "Nouvelle recherches sur l'oxydation du fer aux temperatures elevees par la methode micrographique", *Compte Rendus*, **222**, p. 796.

64. Garber, S., and Sturgeon, G.M., (1961): "Scale on Wire Rod and its Removal by Mechanical Means", *Wire Industry*, (March/June), p. 257-9; 295; 369-76.

65. Sheppard, and Steen, W.M., (1970): "Hydraulic Descaling of Steel: A Preliminary Experimental Study", *Journal of the Iron and Steel Institute*, (September).

66. Schweighofer, A., and Tyas, S. (2000). *VAI's Solutions on Hydraulic Descaling*. in *3d International Conference on Hydraulic Descaling*. London.

67. Abuluwefa, H.T., Guthrie, R.I.L. and Ajersch, F., (1997a): "Oxidation of Low Carbon Steel in Multicomponent Gases: Part I. Reaction Mechanisms during Isotermal Oxidation", *Metallurgical and Materials Transactions. A*, **28A**, p. 1633-41.

68. Abuluwefa, H.T., Guthrie, R.I.L. and Ajersch, F., (1997b): "Oxidation of Low Carbon Steel in Multicomponent Gases: Part II. Reaction Mechanisms during Reheating", *Metallurgical and Materials Transactions. A*, **28A**, p. 1643-51.

69. Nagl, M.M., and Evans, W.T., (1993): "Review. The Mechanical Failure of Oxide Scales under Tensile or Compressive Load", *Journal of Materials Science*, **28**, p. 6247-60.

70. Robertson, J., and Manning, M.I., (1990): "Limits to Adherence of Oxide Scales", *Materials Science and Technology*, **6**, p. 81-91.

71. Schutze, M., (1985): "Deformation and Cracking Behaviour of Protective Oxide Scales on Heat-Resistant Steels under Tensile Strain", *Oxidation of Metals*, **24**(3/4), p. 199-232.

72. Schutze, M., (1995): "Mechanical Properties of Oxide Scales", *Oxidation of Metals*, **44**(1/2), p. 29-61.

73. Chen, R.Y., and Yuen, W.Y.D., (2000): "A Study of the Scale Structure of Hot-Rolled Steel Strip by Simulated Coiling and Cooling", *Oxidation of Metals*, **53**(5/6), p. 539-60.

74. Chen, R.Y., and Yuen, W.Y.D., (2001): "Oxide-Scale Structures Formed on Commercial Hot-Rolled Steel Strip and Their Formation Mechanisms", *Oxidation of Metals*, **56**(1/2), p. 89-118.

75. Chen, R.Y., and Yuen, W.Y.D., (2002): "Oxidation of Low-Carbon, Low-Silicon Mild Steel at 450-900C Under Conditions Relevant to Hot-Strip Processing", *Oxidation of Metals*, **57**(1/2), p. 53-79.

76. Krzyzanowski, M., and Beynon, J.H., (1999b): "Finite Element Model of Steel Oxide Failure During Tensile Testing Under Hot Rolling Conditions", *Materials Science and Technology*, **15**, p. 1191-8.

77. Krzyzanowski, M., Beynon, J.H. and Sellars C.M., (2000a): "Analysis of Secondary Oxide-Scale Failure at Entry into the Roll Gap", *Metallurgical and Materials Transactions B*, **31B**, p. 1483-90.

78. Krzyzanowski, M., and Beynon, J.H., (2000b): "Modelling the Boundary Conditions for Thermo-Mechanical Processing - Oxide Scale Behaviour and Composition Effects", *Modelling Simul. Matter. Sci. Eng.*, **8**, p. 927-45.

79. Picque, B., Favennec, Y., Paccini, A., Lanteri, V., Bouchard, P.O., and Montmitonnet, P. (2002). *Identification of the Mechanical Behaviour of Oxide Scales by Invese Analysis of a Hot Four-Point Bending Test.* in *The 5th International ESAFORM Conference on Metal Forming.* Krakow.

80. Tan, K.S., Krzyzanowski, M. and Beynon, J.H., (2001): "Effect of Steel Compositions on Failure of Oxides Scales in Tension Under Hot Rolling Conditions", *Steel Research*, **72**(7), p. 250-8.

81. Krzyzanowski, M., and Beynon, J.H. (2002a). *Pecularites of Multi-Layer Oxide Scale Behaviour During Hot Rolling Determined Using Matematical Modelling.* in *"KomPlasTech" 2002.* Krakow: Akapit.

82. Evans, H.E., (1988): "Spallation of Oxide from Stainless Steel AGR Nuclear Fuel Cladding: Mechanisms and Consequences", *Materials Science and Technology*, **4**, p. 415-20.

83. Evans, H.E., (1989): "*Materials Science and Engineering*, **A120**, p. 139.

84. Thouless, M.D., (1990): "Crack Spacing in Brittle Films on Elastic Substrates", *Journal of American Ceramic Society*, **73**(7), p. 2144-6.

85. Hu, M.S., and Evans, A.G., (1989): "The Cracking and Decohesion of Thin Films on Ductile Substrates", *Acta Materialia*, **37**, p. 917-25.

86. Beuth, J.L., and Klingbeil, N.W., (1996): "Cracking of Thin Films Bonded to Elastic-Plastic Substrates", *Journal of the Mechanics and Physics of Solids*, **44**(9), p. 1411-28.

87. Xia, Z.C., and Hutchinson, J.W., (2000): "Crack Patterns in Thin Films", *Journal of the Mechanics and Physics of Solids*, **48**, p. 1107-31.

88. Greco, F., Lonetti, P. and Zinno, R., (2002): "An Analytical Delamination Model for Laminated Plates Including Bridging Effects", *International Journal of Solids and Structures*, **39**.

89. Schutze, M., (1988): "Stresses and Decohesion of Oxide Scales", *Materials Science and Technology*, **4**, p. 407-14.

90. Budi Aulia, T., (2000): "Strain Localization and Fracture Energy of High-Strength Concrete under Uniaxial Compression", *Leipzig Annual Civil Engineering Report*, (5), p. 221-40.

91. Meyer, J., (1997): "Deformation Capacity of the Concrete Compression Zone - Stress-Strain Curves for Nonlinear Calculation", *Leipzig Annual Civil Engineering Report*, (2), p. 87-102.

92. Coleman, J., and Spacone, E., (2001): "Localization Issues in Force-Based Freame Elements", *Journal of Structural Engineering*, **127**, p. 1257-65.

93. Wei, Y., and Hutchinson, J.W., (1997): "Nonlinear Delamination Mechanics for Thin Films", *Journal of the Mechanics and Physics of Solids*, **45**(7), p. 1137-59.

94. Audoly, B., (2000): "Mode-dependent Toughness and the Delamination of Compressed Thin Film", *Journal of the Mechanics and Physics of Solids*, **48**, p. 2315-32.

95. Hutchinson, J.W., He, M.Y., and Evans, A.G., (2000): "The Influence of Imperfections on the Nucleation and Propogation of Buckling Driven Delaminations", *Journal of the Mechanics and Physics of Solids*, **48**, p. 709-34.

96. Bruno, D., and Greco, F., (2000): "An Asymptotic Analysis of Delamination Bucklong and Growth in Layered Plates", *International Journal of Solids and Structures*, **37**, p. 6239-76.

97. Bruno, D., and Greco, F., (2001): "Delamination in Composite Plates: Influence of Shear Deformability on Interfacial Debonding", *Cement & Concrete Composites*, **23**, p. 33-45.

98. Balint, D.S., and Hutchinson, J.W., (2001): "Mode II Edge Delamination", *Jpurnal of Applied Mechanics*, **68**(5), p. 725-30.

99. Lemaitre, J., (1996), *A Course on Demage Mechanics*. 2nd ed. Berlin: Springer-Verlag. 227.

100. Tvergaard, V., (1990): "Material Failure by Void Growth to Coalescence", *Advances in Applied Mechanics*, **27**, p. 83-151.

101. Pardoen, T., and Hutchinson, J.W., (2000): "An Extended Model for Void Growth and Coalescence", *Journal of the Mechanics and Physics of Solids*, **48**, p. 2467-512.

102. Feenstra, P.H., and de Borst, R, (1995): "A Composite Plasticity Model for Concrite", *International Journal of Solids and Structures*, **33**(5), p. 707-30.

103. De Borst, R., (2002): "Fracture in Quasi-brittle Materials: a Review of Continuum Damage-based Approaches", *Engineering Fracture Mechanics*, **69**, p. 95-112.

104. Stringer, J., (1970): "*Corrosion Science*, **10**, p. 513.

105. Mizes, R.V., (1928): "*Zhournal of Mathematic Mechanics*, **8**, p. 161.

106. Groves, G.W., (1970): "*Proceedings of the British Ceramic Society*, **15**, p. 103.

107. Schutze, M., (1990): "Plasticity of Protective Oxide Scales", *Materials Science and Technology*, **6**, p. 32-8.

108. Kelly, A., and MacMillan, N.H., (1986), *Strong Solids*. Oxford: Oxford University Press.

109. Goedjen, J.G.S., D.A. and Stout, J.H., (1997): "In-situ Strain Mesurements in the Ni/NiO System during High Temperature Oxidation", *Materials Science and Engineering*, **A222**, p. 58-69.

110. Zhang, Y., Gerberich, W.W., and Shores, D.A., (1997): "Plastic Deformation of Oxide Scales at Elevated Temperatures", *Journal of Materials Research*, **12**(3), p. 697-705.

111. Dieter, G.E., (1988), *Mechanical Metallurgy*. London: McGraw-Hill. 751.

112. Hansen, S.S., (1987), *Microalloyed Plate and Bar Products: Production Technology*, in *Fundamentals of Microallying Forging Steels*, G. Krauss, and Banerji, S., Editor. The Metallurgical Society. p. 155-74.

113. Orowan, E., (1943): "The Calculation of Roll Pressure in Hot and Cold Flat Rolling", *Proceedings of the Institute of Mechanical Engineers*, **150**, p. 140.

114. Alexander, J.M., (1972): "On the Theory of Rolling", *Proceedings of the Royal Society London, Series A*, **326**, p. 535.

115. Lahoti, G.D., Shah, S.N., and Altan, T., (1978): "Computer Aided Analysis of the Deformations and Temperatures in Strip Rolling", *Journal of Engineering for Industry. (Transactions ASME)*, **100**, p. 159.

116. Lahoti, G.D., et al., (1980): "Computer Aided Analysis of Metal Flow and Stresses in the Plate Rolling", *Journal of the Mechanical Working Technology*, **4**, p. 105.

117. Handbook, M., (1988), *Metals Handbook. Forming and Forging*. 9th ed, ed. P.U.t.D.o.t.A.I.H. Committee. Vol. 14. Ohio: Metals Park: American Society for Metals.

118. Krzyzanowski, M., Trull, M. and Beynon, J.H. (2002b). *Numerical Identification of Oxide Scale Behaviour Under Deformation - a Way for Refining of Contact Simulation in Metal Forming Operations*. in *Euromech 435: Friction and Wear in Metal Forming*. Valenciennes, France.

119. Li, Y.H., and Sellars, C.M. (1996). *Modelling Deformation Behaviour of Oxide Scales and Their Effects on Interfacial Heat Transfer and Friction During Hot Steel Rolling*. in *2nd International Conference on Modelling of Metal Rolling Processes*. London, UK: The Institute of Materials.

120. Fletcher, J.D., Talamantes-Silva, J. and Beynon, J.H. (1998). *The Influence of the Roll Gap Interface Conditions on Subsequent Surface Finish*. in *Modelling of Metal Rolling Processes: Symposium 8. Control of External Product Properties*. London: The Institute of Materials.

121. Beynon, J.H., (1999): "Finite-element Modelling of Thermomechanical Processing", *Philosophical Transactions of the Royal Society London, Series A*, **357**(1756), p. 1573-87.

122. Li, Y.H., and Sellars, C.M., (2002): "Cracking and Deformation of Surface Scale During Hot Rolling of Steel", *Materials Science and Technology*, **18**(3), p. 304-11.

123. Blazevic, D.T. (1996). *Tertiary Rolled in Scale the Hot Strip Mill Surface Problem of the 1990's*. in *37th Mechanical Working and Steel Processing Conference and International Symposium on Recovery and Recrystallisation in Steel Processing*. Hamilton, Ontario, Canada: ISS-AIME.

124. Blazevic, D.T. (2000). *Newton and Descaling - Data and Conclusions.* in *3d International Conference on Hydraulic Descaling.* London.

125. Beverley, I., Uijtdebroeks, H. de Roo, J., Lanteri, V., and Philippe, J.-M., (2001), *"Improving the Hot Rolling Process of Surface-Critical Steels by Improved and Prolonged Working Life of Work Rolls in the Finishing Mill Train".* EUR 19871 EN. European Comission: Brussels.

126. Fisher, C.A.J., (2001), *Theory, Simulation and Design of Advanced Ceramics and Composites*, in *European White Book on Fundamental Research in Materials Science.* Max - Plank - Institute Fur Metallforschung Stuttgart: Stuttgart. p. 138-44.

127. Hoyle, G., (1988), *High Speed Steels.* London: Butterworths. 222.

128. Wright, L.G., (1978), *"A new type of induction heater for the heating of small parts in the forge".* Electricity council: London. p. 6.

129. Randle, V., (1992), *Microtexture Determination and its Applications.* London: The Institute of Materials.

130. Fletcher, A.J., (1989), *Thermal Stress and Strain Generation in Heat Treatment.* Elsevier science publishers ltd: London. p. 89.

131. Hajduk, M., Zidek, M., Elfmark, J. and Kopec S., (1972): "*Hutnicke Listy*, **27**, p. 567-71.

132. Pietrzyk, M., and Lenard, J.G., (1991), *Thermal-Mechanical Modelling of the Flat Rolling Process.* Springer-Verlag: Berlin. p. 13-20.

133. Shida, S., (1974), *"Effect of Carbon Content, Temperature and Strain Rate on Compressive Flow Stress of Carbon Steels".* Hitachi Research Laboratory Report. p. 1-9.

134. Beynon, J.H., and Sellars, C.M., (1992): "Modelling Microstructure and its Effect During Multipass Hot Rolling", *ISIJ International*, **32**(3), p. 359-67.

135. Anderson, T.L., (1995), *Fracture Mechanics: Fundamentals and Applications.* 2nd ed. London: CRC Press.

136. Bakker, A., (1983): "*International Journal of Pressure Vessels and Piping*, **C14**, p. 153-79.

137. Key, S.W., and Krieg, R. D., (1982): "On the Numerical Implementation of Inelastic Time-Dependent, Finite Strain Constitutive Equations in Structural

Mechanics", *Computer Methods in Applied Mechanics in Engineering*, **33**, p. 439-52.

138. MSC.MARC, (2000), *Theory and User Information*. Vol. A: MSC.Software Corporation.

139. Birks, N., and Meier, G. H., (1983), *Introduction to High Temperature Oxidation of Metals*: Edward Arnold. 198.

140. BSC-Reports, *"Swinden Laboratories"*. Rotherham, UK.

141. Hancock, P., and Nicholls, J.R., (1988): "Application of Fracture Mechanics to Failure of Surface Oxide Scales", *Materials Science and Technology*, **4**, p. 398-406.

142. Malinowski, Z., Lenard, J.G. and Davies, M.E., (1994): "*Journal of Materials Processing Technology*, **41**, p. 125-42.

143. Beynon, J.H., (1998): "Tribology of Hot Metal Forming", *Tribology International*, **31**(1-3), p. 73-7.

144. Caliskanoglu, D., Al Baouni, M., Volles, R., Leisten, B., Leitner, H., Ebner, R., and Kopp. R. (2002). *Influence of the Heat-Transfer-Coefficient on the Temperature Stress of Hot Forming Tools*. in *Euromech 435: Friction and Wear in Metal Forming*. Valenciennes, France.

145. Pippenger, J.J., (1984), *Hydraulic Valves and Controls: Selection and Application*. Fluid Power and Control. New York: N.Y.: Dekker.

146. Garber, S. (1960). *Observation on the Scale Structure of Mild Steel Strip*. in *Flat Rolled Products II: Semi-finished and Finished, 2nd Technical Conference*. AIME, Chicago: Interscience, New York.

147. Moore, N.E., Oldroyd, P.S., Lewis, P.J., and Westacott, M., (1991), *"An Investigation of the Formation, Constitution and Properties of Scale Formed in the Reheating Furnace and During the Hot Rolling Process"*. Research Project 7210.KB/809. Final Report. ECSC.

148. Pinna, C., Beynon, J.H., Sellars, C.M., and Bornert, M. (2000). *Experimental Investigation and Micromechanical Modelling of Hot Deformation of Duplex Stainless Steels*. in *Mathematical Modelling in Metal Processing and Manufacturing*: Canadian Institute of Mining, Metallurgy and Petroleum.

149. Farrer, J.K., Michael, J.R., and Carter, C.B., (2000), *EBSD of Ceramic Materials*, in *Electron Backscatter Diffraction in Materials Science*, A.J.

Schwartz, Kumar, M. and Adams, B.L., Editor. Kluwer Academic/Plenum Publishers: New York. p. 299-318.

150. Gulbransen, E.A., and Ruka, R., (1952): "Role of Crystal Orientation in the Oxidation of Iron", *Journal of the Electrochemical Society*, **99**(9), p. 360-8.

151. Abuluwefa, H.T., Root, J.H., Guthrie, R.I.L. and Ajersch, F., (1996): "Real-Time Observations of the Oxidation of Mild Steel at High Temperature by Neutron Diffraction", *Metallurgical and Materials Transactions. B*, **27B**, p. 993-7.

152. Boyer, H.E., and Gall, T.L., (1985), *Metals Handbook. Desk Edition*. Ohio: Metals Park, Ohio:American Society for Metals.

153. Devadas, C., and Samarasekera, I.V., (1986): *Ironmaking and Steelmaking*, **13**, p. 311.

154. Ranta, H., Larkiola, J., Korhonen, A.S. and Nikula, A. (1993). in *1st International Conference on Modelling of Metal Rolling Processes*. London, UK: The Institute of Materials.

155. Morrel, R., (1987), *Handbook of Properties of Technical and Engineering Ceramics*. London: HMSO.

156. Kohler, C., Jeschar, R., Scholz, R., Slowik, J. and Borchardt, G., (1990): "Influence of Oxide Scales on Heat Transfer in Secondary Cooling Zones in the Continuous Casting Process, Part 1: Heat Transfer through Hot-Oxidized Steel Surfaces Cooled by Spray-Water", *Steel Research*, **61**(7), p. 295-301.

157. Slowik, J., Borchardt, G., Kohler, C., Jeschar, R. and Scholz, R., (1990): "Influence of Oxide Scales on Heat Transfer in Secondary Cooling Zones in the Continuous Casting Process, Part 2: Determination of Material Properties of Oxide Scales on Steel under Spray-Water Cooling Conditions", *Steel Research*, **61**(7), p. 302-11.

158. Evans, H.E. (1994): "Modelling Oxide Spallation", *Materials at High Temperatures*, **12**, p. 219-27.

159. Simons, J.W., Antoun, T.H. and Curran, D.R. (1997): *A Finite Element Model for Analysing the Dynamic Cracking Response of Concrete. 8th International Symposium on Interaction of the Effects of Munitions with Structures,* McClean, Virginia.

160. Simons, J.W., Kirkpatrick, S.W, Klopp, R.W. and Seaman, J.W. (1999): *Methods for Modelling Damage in Finite Element Calculations. Proceedings of the International Seminar on Numerical Analysis in Solid and Fluid Dynamic.* Osaka University, Japan, p. 79-86.

Appendix 1

Yield Stress Empirical Calculations for Mild Steel

A1.1. Shida's equations of the flow strength [133]

$$\sigma = \sigma_f f\left(\frac{\dot{\varepsilon}}{10}\right)^m \tag{A.1}$$

where for

$$\overline{T} \geq 0.95\frac{C+0.41}{C+0.32} \tag{A.2}$$

$$\sigma_f = 0.28\exp\left(\frac{5}{\overline{T}} - \frac{0.01}{C+0.05}\right) \tag{A.3}$$

and

$$m = \left(-0.019\mathrm{C}+0.126\right)\overline{T} + \left(0.075C - 0.05\right) \tag{A.4}$$

For

$$\overline{T} < 0.95\frac{C+0.41}{C+0.32} \tag{A.5}$$

$$\sigma_f = 0.28q(C,\overline{T})\exp\left(\frac{C+0.32}{0.19(C+0.41)} - \frac{0.01}{C+0.05}\right) \tag{A.6}$$

with

$$q(C,\overline{T}) = 30(C+0.9)\left(\overline{T} - 0.95\frac{C+0.49}{C+0.42}\right)^2 + \frac{C+0.06}{C+0.09} \tag{A.7}$$

and

$$m = (0.081\mathrm{C} - 0.154)\overline{T} - 0.019C + 0.207 + \frac{0.027}{C+0.32} \tag{A.8}$$

The other parameters are defined as

$$f = 1.3(5\varepsilon)^n - 1.5\varepsilon \tag{A.9}$$

and

$$n = 0.41 - 0.07C \tag{A.10}$$

In the above formulae $\overline{T} = (T+273)/1000$, T is the temperature in °C, C is the carbon content in weight percent, ε is the strain and $\dot{\varepsilon}$ is the strain rate. Shida points out that the form of the equation has no physical significance. The range of the applicability of the formulae was given by Shida as

Carbon content	< 1.2%
Temperature	700 – 1200 °C
Strain rate	0.1 – 100 s^{-1}
Strain	< 70%

A1.2. Beynon & Sellars equations of the flow strength [134]

$$\sigma_{ys} = 103.84\sinh^{-1}\left[\left(\frac{Z}{4.92\cdot 10^{13}}\right)^{0.13}\right] \tag{A.11}$$

where Zener Hollomon parameter, Z is:

$$Z = \dot{\varepsilon}\, exp(312000 / RT_{def}) \tag{A.12}$$

where $\dot{\varepsilon}$ is the deformation strain rate, R is the gas constant (8.31 kJ/(kg mol K)) and T_{def} is the deformation temperature (K).

Appendix 2
Thermal and Mechanical Properties of Steels and Oxide Scale

All parameters for heat transfer calculation were presented as function of the temperature, T (°C) using available experimental data [127, 144, 152, 153] and [154]. The mechanical properties of the steel and oxide scale were assumed to be similar to those used in the literature [120, 140, 141] and [155].

A2.1. The properties of steels

Density [152]

$\rho_{\text{mild steel}} = 7850 \cdot (1 + 0.004 \cdot 10^{-6} \cdot T^2)^{-3}$ kg/m^3; $\rho_{M2} = 8160$ kg/m^3

Poisson's ratio [152]

$\nu = 0.3$

Specific heat, c_p (J/kg K)

$$c_p = 422.7 + 48.66 \exp(0.319 \cdot 10^{-5} \cdot T) \quad \text{for} \quad T \leq 700^{\circ}\text{C}$$

$$c_p = 657.0 + 0.084 \, (T \cdot 10^{-3})^{-24.6} \quad \text{for} \quad T \geq 700^{\circ}\text{C}$$

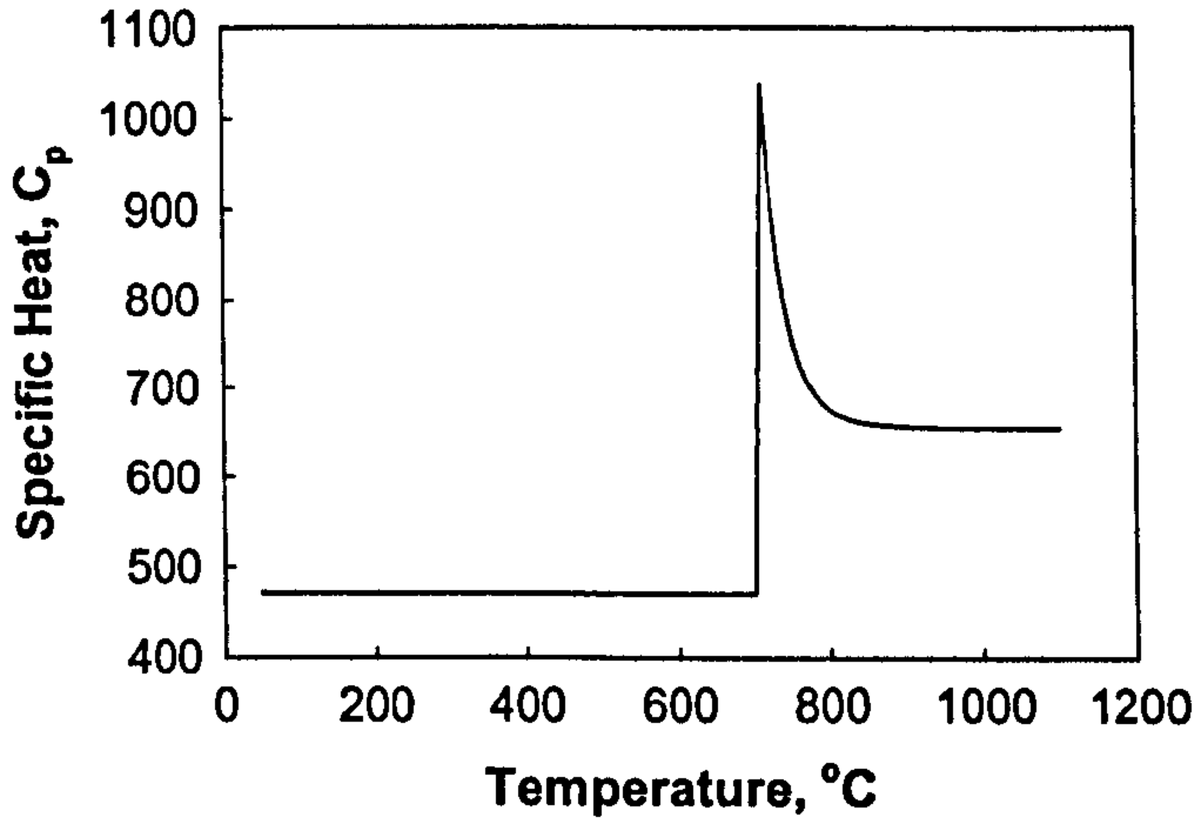

Figure A2.1. Specific heat for steels, after [153].

Thermal conductivity, λ (W/m K)

$$\lambda = 23.16 + 51.96 \exp(-2.02519 \cdot 10^{-3} \cdot T)$$

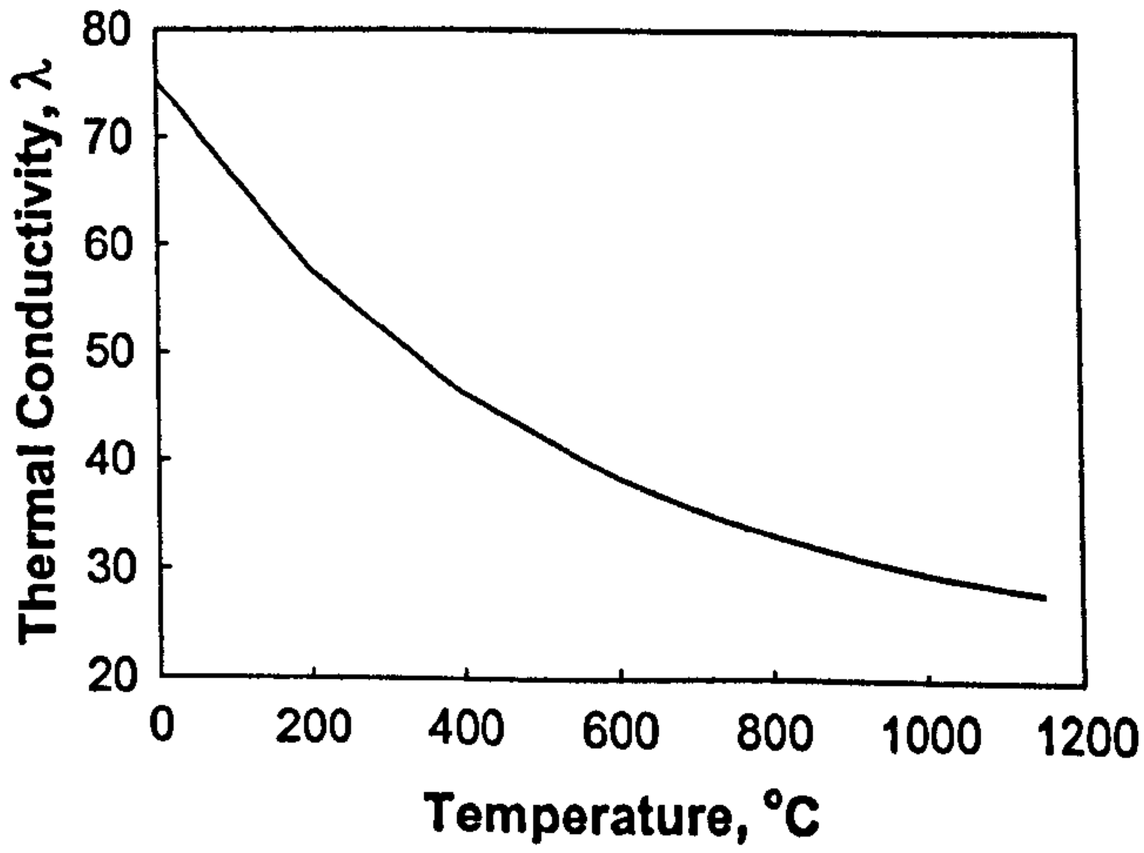

Figure A2.2. Thermal conductivity for steels, after [153].

Heat transfer coefficients [153]

The energy balance for the boundary surface was given by

$$\lambda \frac{\partial T}{\partial n} = \alpha (T_a - T)$$

where λ is the thermal conductivity ($Wm^{-1}K^{-1}$), n is a coordinate normal to the surface, α is the heat transfer coefficient ($Wm^{-2}K^{-1}$), and T and T_a are the boundary surface and the ambient temperature (°C) respectively.

The surface of the specimen was subjected to gas cooling and coefficient of radiative heat transfer was specified as follows

$$\alpha = \left(1.2 - 0.52\frac{T}{1000}\right)\frac{T^4 - T_a^4}{T - T_a}5.675 \cdot 10^{-8}$$

and shown in Figure A2.3. Heat transfer through the grip contact was assume d as α_{gr}= 30 $Wm^{-2}K^{-1}$ [76]. Finally, the heat transfer coefficient at the contact interface during the compression test was supposed to be $\alpha_{contact}$ = 2400 $Wm^{-2}K^{-1}$ to satisfy measured temperature results and literature data [144].

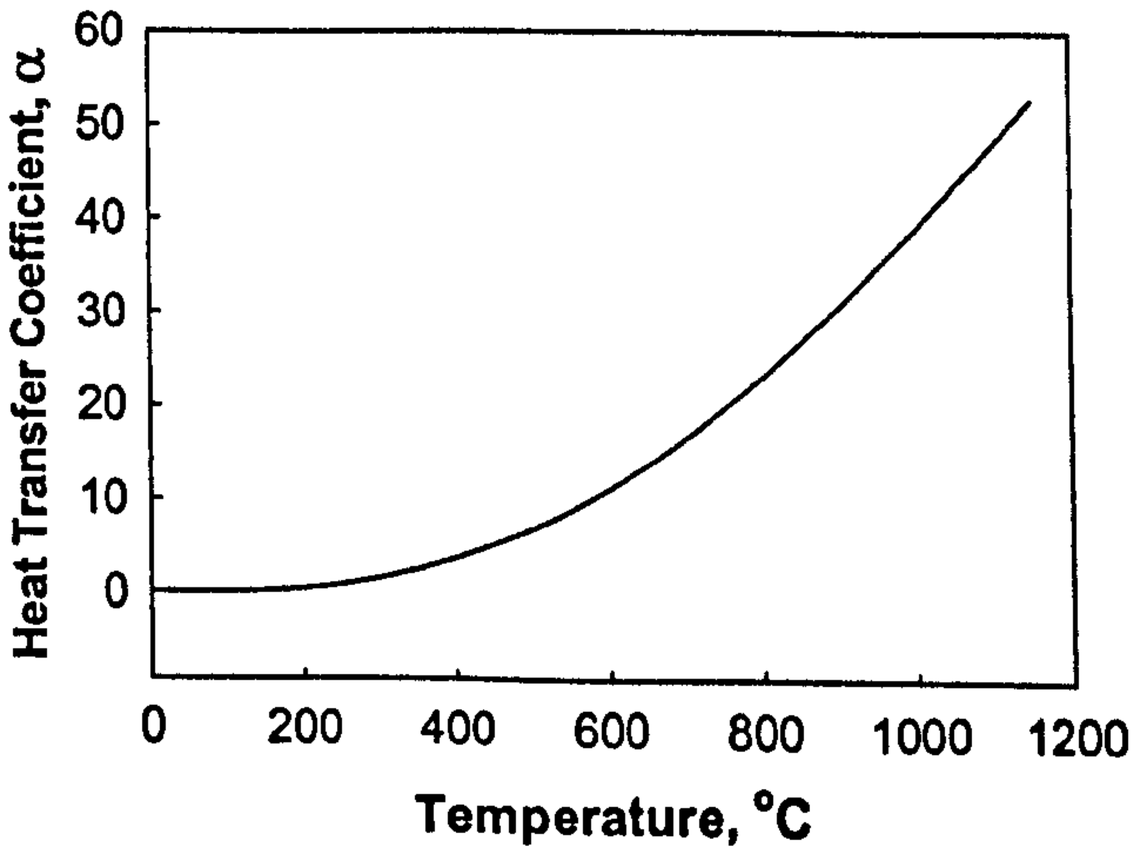

Figure A2.3. Radiative heat transfer coefficient.

Linear thermal expansion [152]

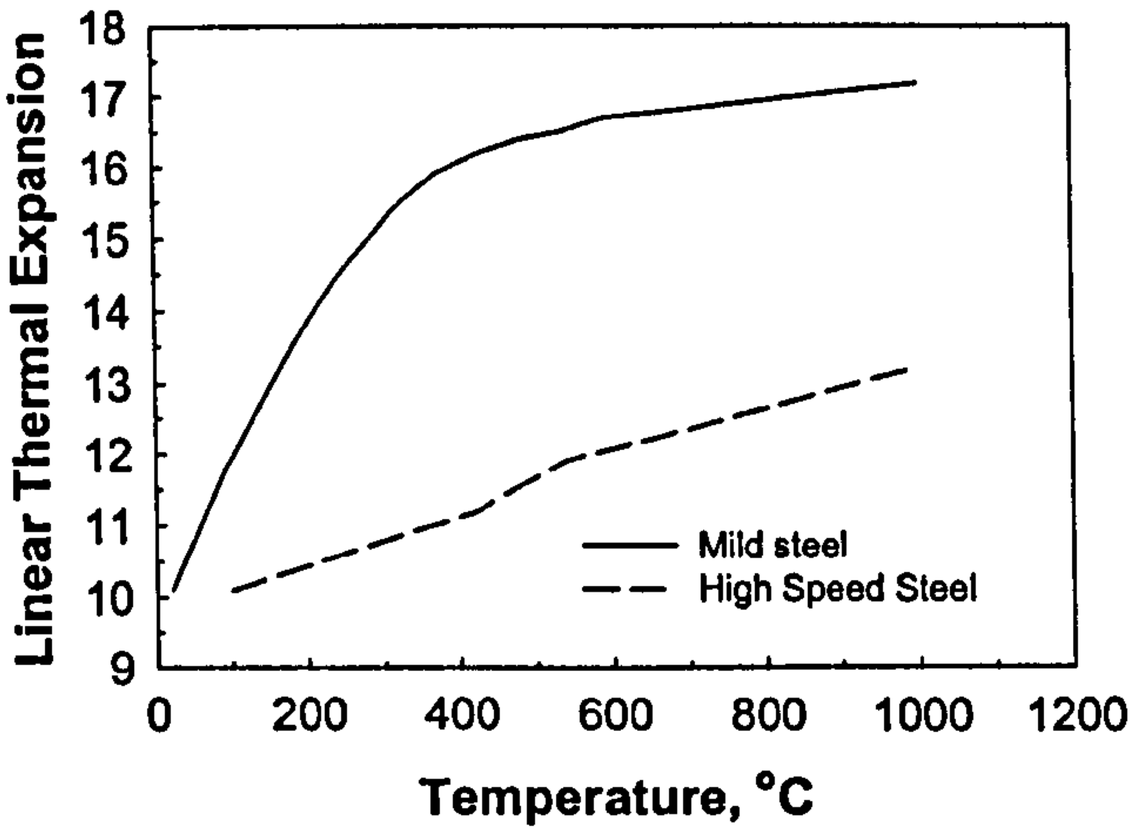

Figure A2.4. Linear thermal expansion (μm/m·K) for low carbon and M2 steels.

Young's modulus

Young's modulus for steels was included as a function of the temperature (Figures A2.5 and A2.6).

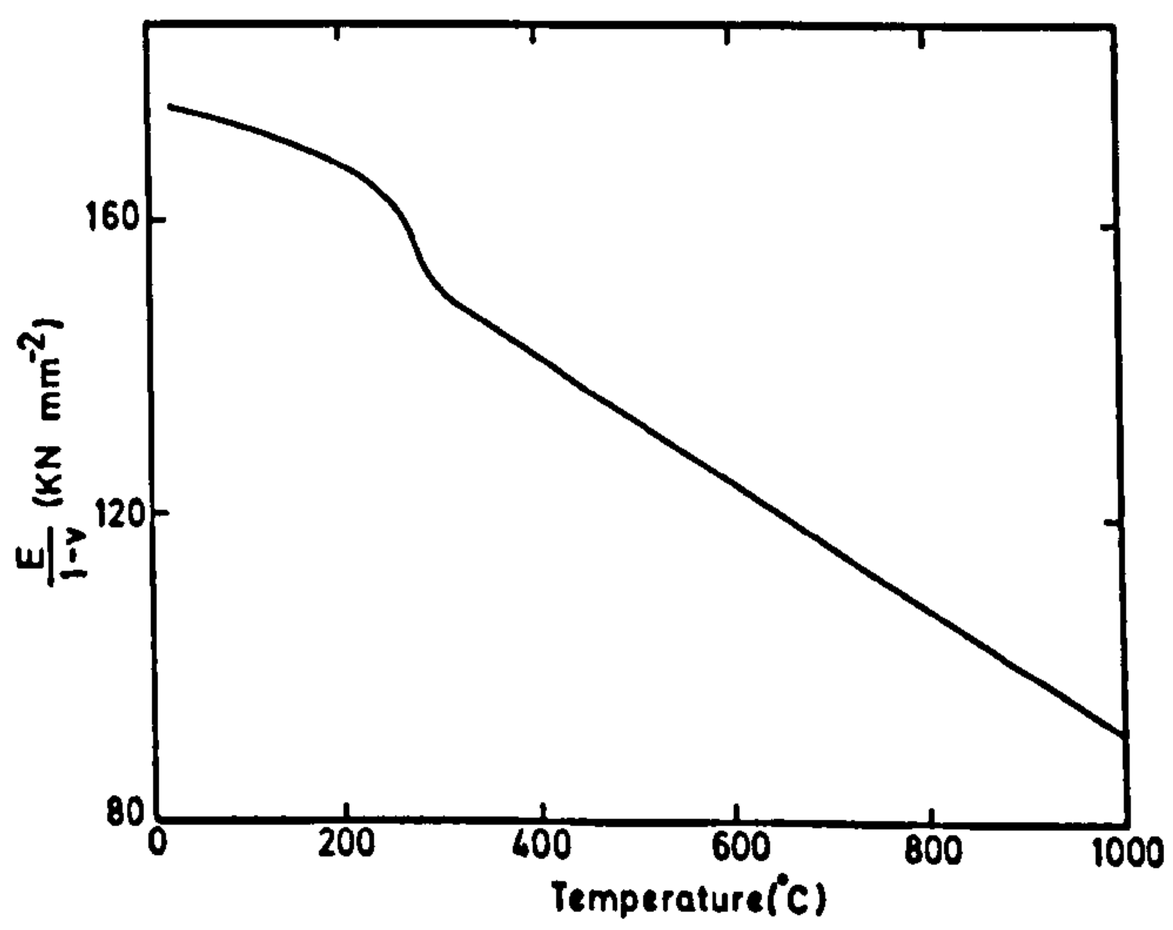

Figure A2.5. The effect of temperature on Young's Modulus (E = Young's modulus, ν = Poisson's ratio) in low-alloy steels [140] as reported in [130].

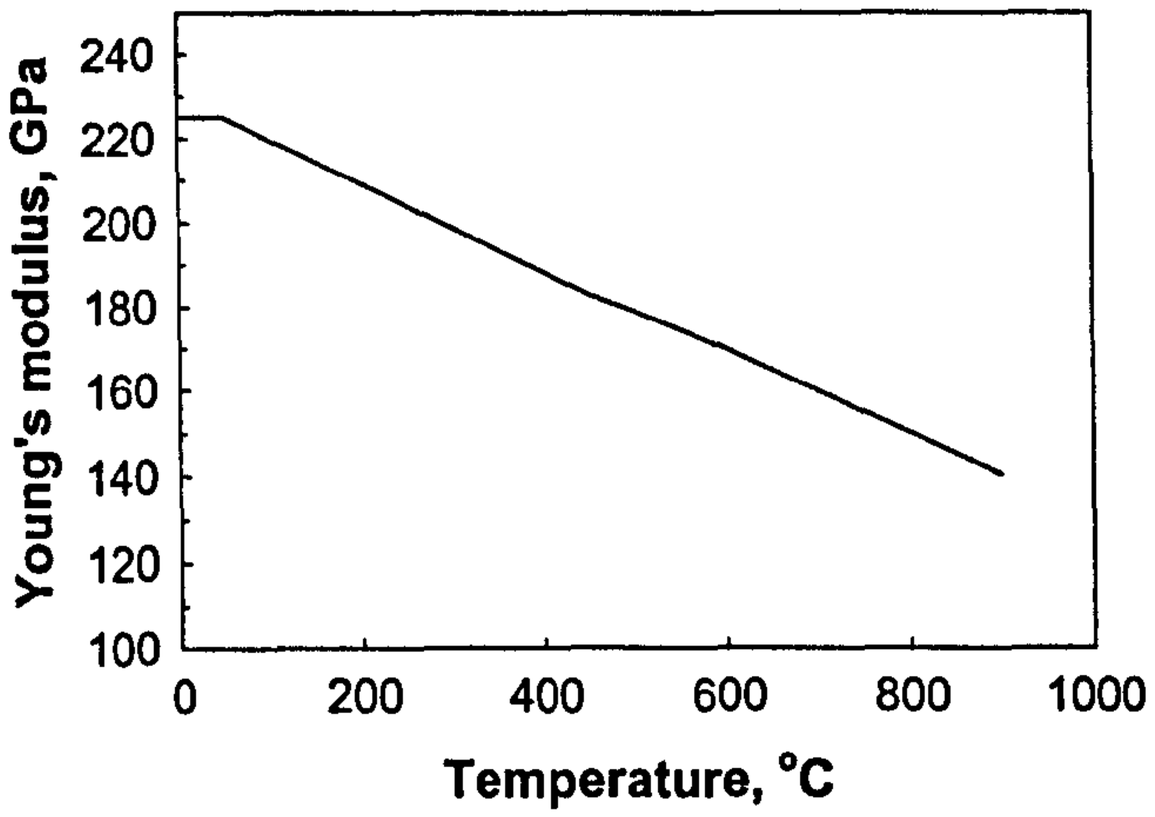

Figure A2.6. The effect of temperature on Young's Modulus in high-speed steels, after [127].

A2.2. The properties of the iron oxide scale

Density [154]

$\rho_{oxide\ scale} = 5700\ kg/m^3$;

Poisson's ratio [70]

$\nu = 0.3$

Thermal conductivity, λ (W/m K) [154]

$\lambda = 1 + 7.83 \cdot 10^{-4} \cdot T$ for $600 \leq T \leq 1200°C$

Specific heat, c_p (J/kg K) [154]

$c_p = 674.96 + 0.30 \cdot T - 4.37 \cdot 10^{-5} \cdot T^2$ for $600 \leq T \leq 1100°C$

Young's modulus (GPa) [155]

$E = E_{ox}^{\circ} (1 + n (T - 25))$ $\quad n = -4.7 \cdot 10^{-4}$, $E_{ox}^{\circ} = 240$ GPa

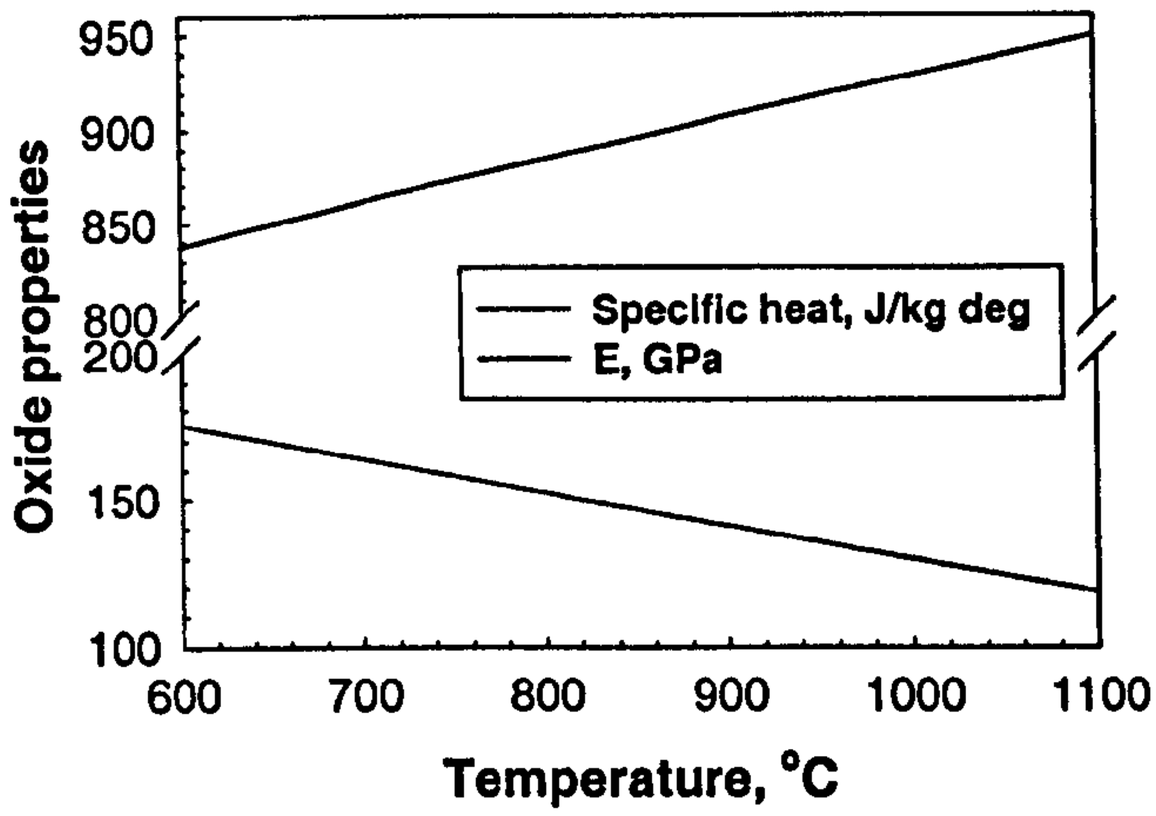

Figure A2.7. The effect of temperature on Young's Modulus and specific heat in iron oxide.

Linear coefficient of thermal expansion (μm/m·K) [70]

FeO – 15.0; Fe_3O_4 – 12.0; Fe_2O_3 – 13.0

Stress intensity factor (fracture toughness), (MN m $^{-3/2}$) [141]

$K_{Ic} = a_0 + a_1 T + a_2 T^2 + a_3 T^3 + a_4 T^4 + a_5 T^5$ $\quad$ for $20 \leq T \leq 850$°C

$a_0 = 1.42$; $a_1 = 8.90 \cdot 10^{-3}$; $a_2 = -8.21 \cdot 10^{-5}$;

$a_3 = 3.18 \cdot 10^{-7}$; $a_4 = -5.45 \cdot 10^{-10}$; $a_5 = 3.44 \cdot 10^{-13}$.

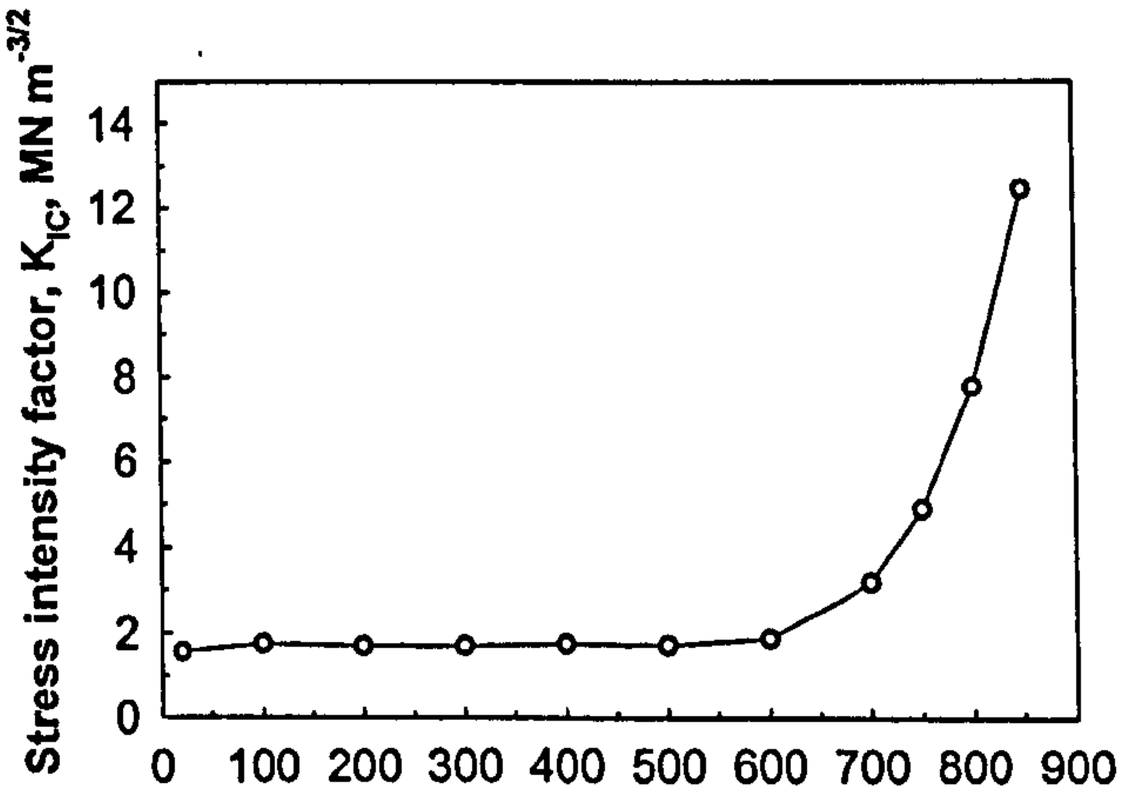

Figure A2.8. Values of the fracture toughness of surface scale oxide as a function of temperature, after [141].

Appendix 3

Schedules for Compression and Oxidation Tests

A3.1. Compression

Test type: Regular 1

Specimen 1; $T_{bot} = 870°$, $T_{top} = 755°$

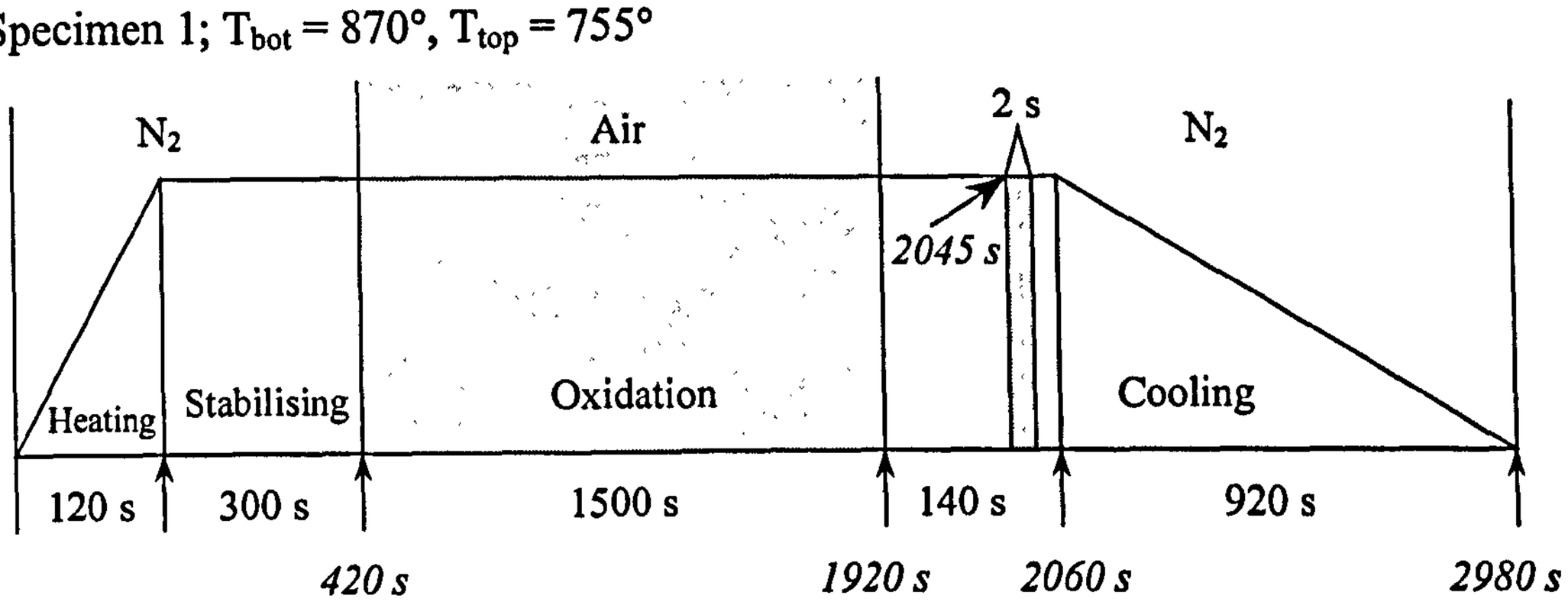

Test type: Regular 2 (Failed to collect the data)

Specimen 2; $T_{bot} = 870°$, $T_{top} = 762°$

Test type: Regular 3

Specimen 3; $T_{bot} = 970°$, $T_{top} = 776°$

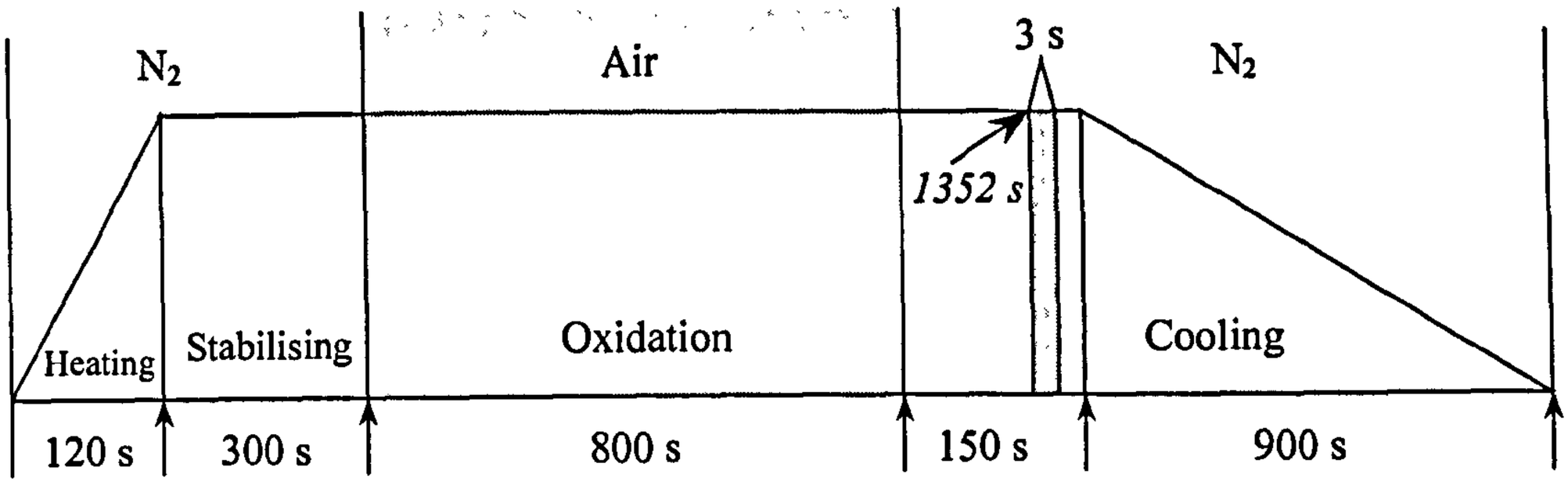

Test type: Regular 4

Specimen 4; $T_{bot} = 1070°$, $T_{top} = 777°$

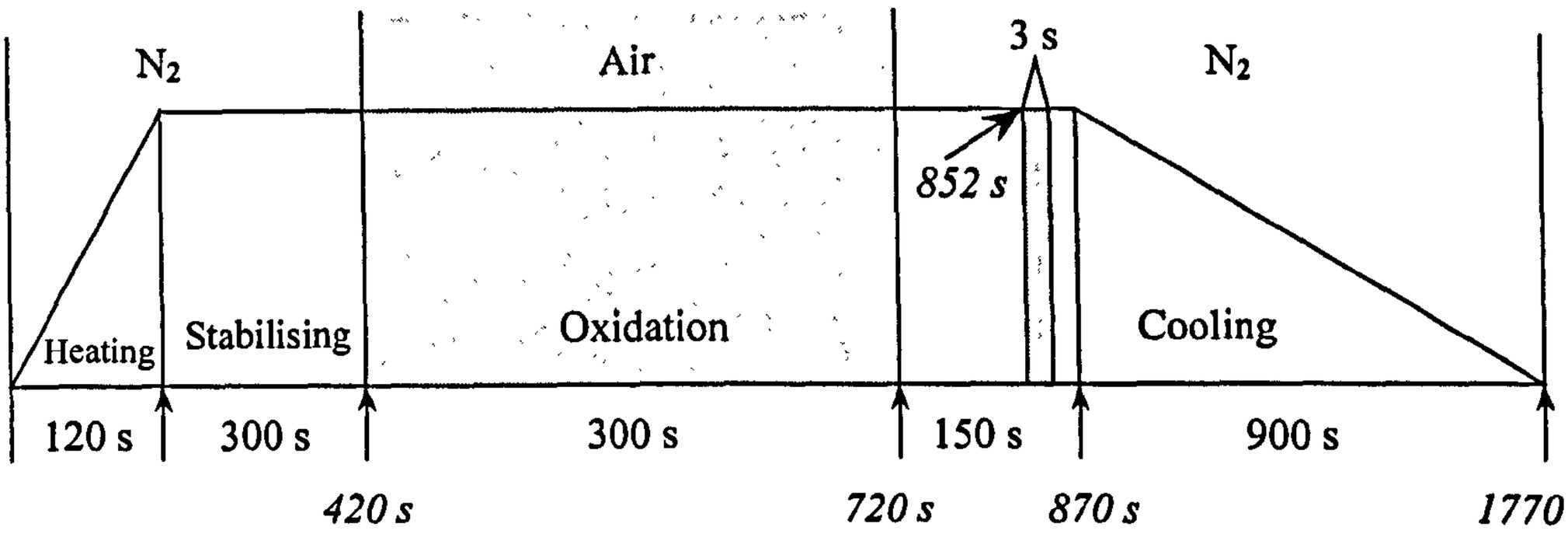

Test type: Regular 5

Specimen 5; $T_{bot} = 970°$, $T_{top} = 770°$

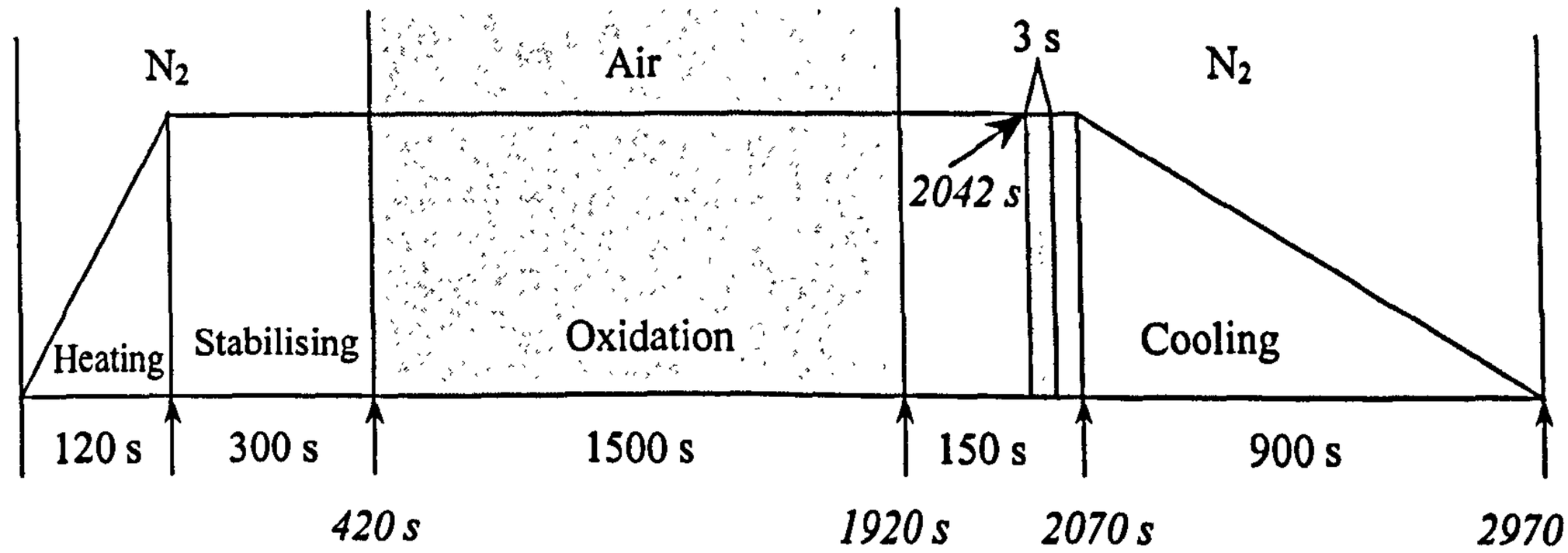

Test type: Regular 6

Specimen 6; $T_{bot} = 1070°$, $T_{top} = 778°$

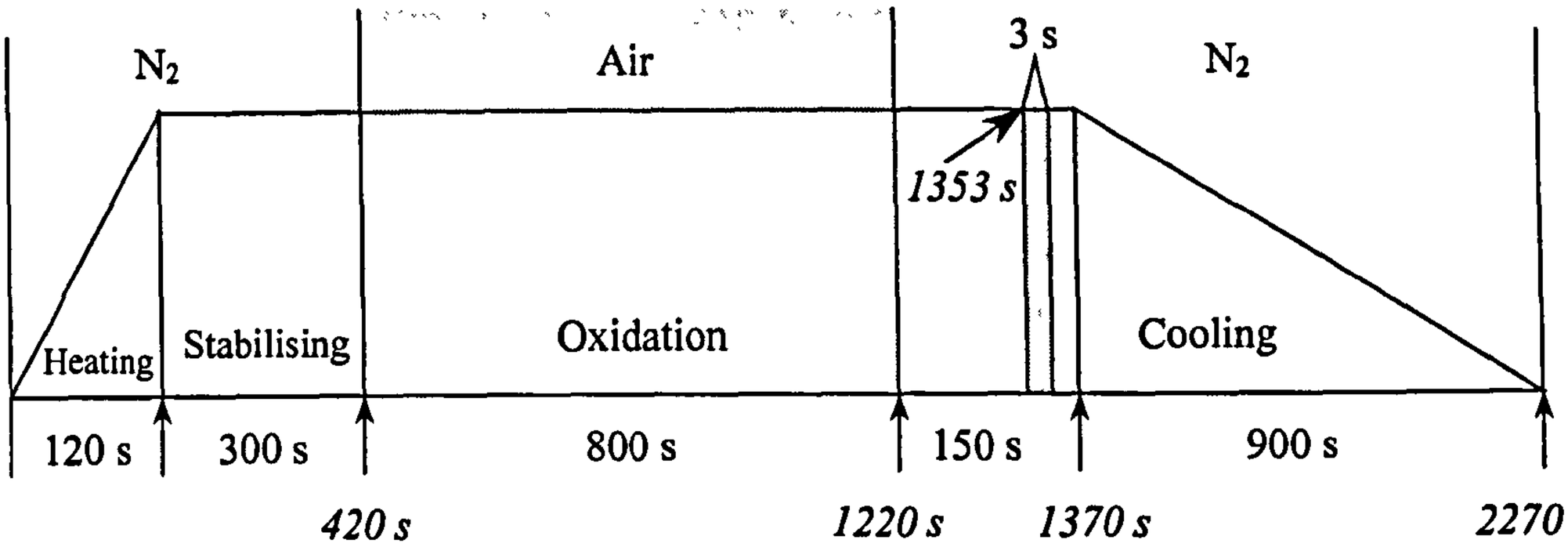

Test type: Regular 7

Specimen 7; $T_{bot} = 970°$, $T_{top} = 764°$

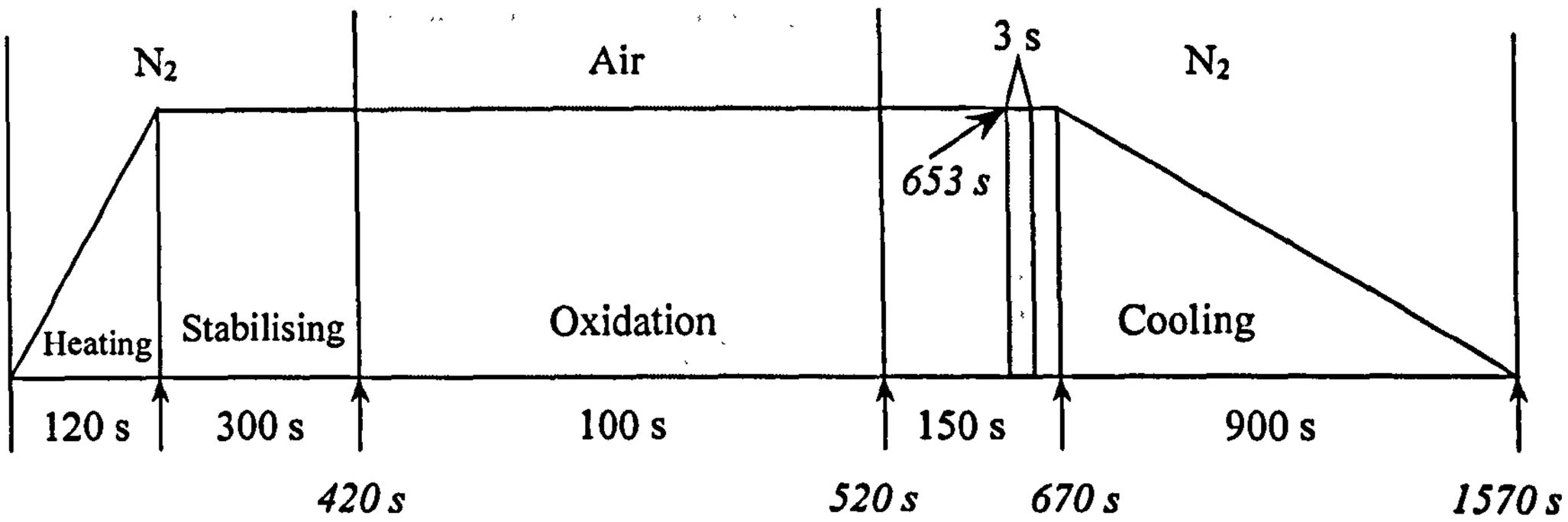

Test type: Regular 8

Specimen 8; $T_{bot} = 970°$, $T_{top} = 766°$

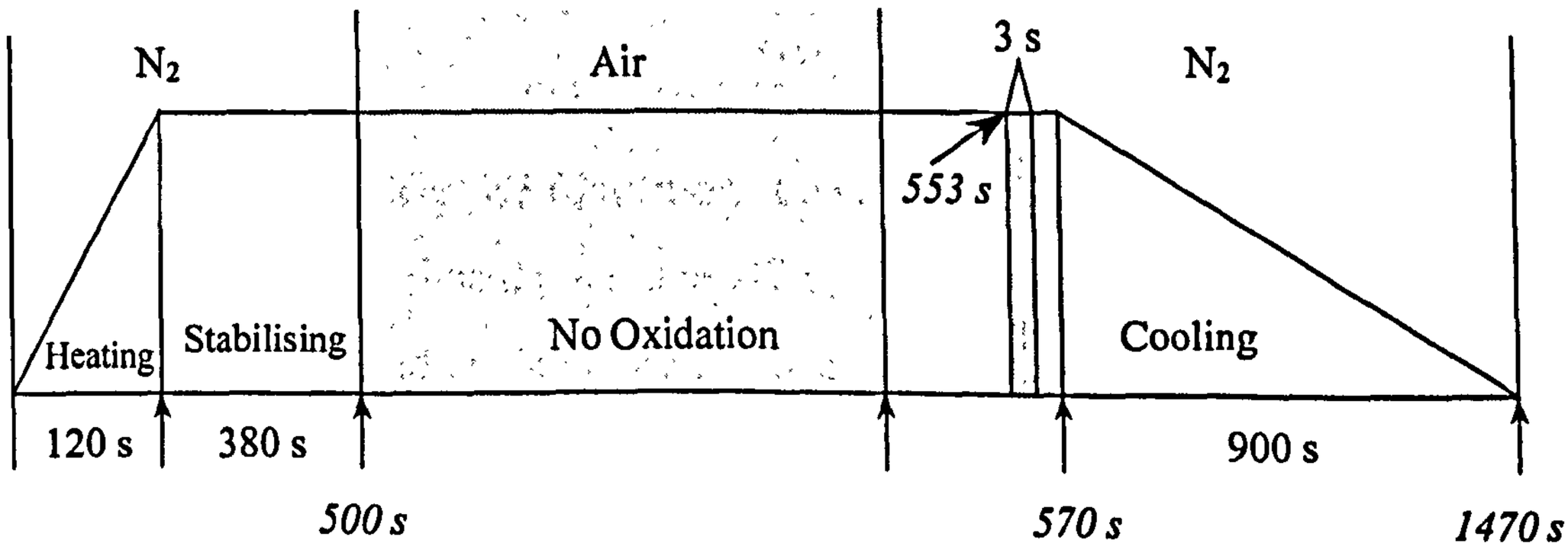

Test type: Regular 9

Specimen 9; $T_{bot} = 870°$, $T_{top} = 744°$

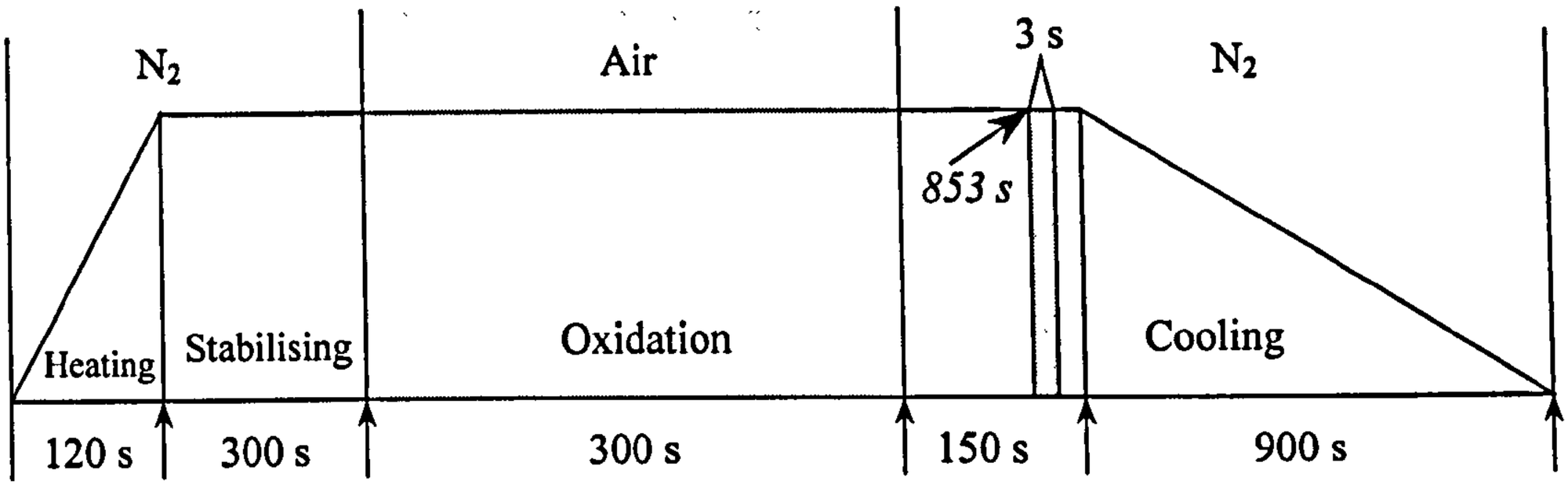

For all tests, T_{bot} is the slab imitation specimens temperature and T_{top} is the tool temperature.

A.3.2. Oxidation

Test 1*; T = 970°

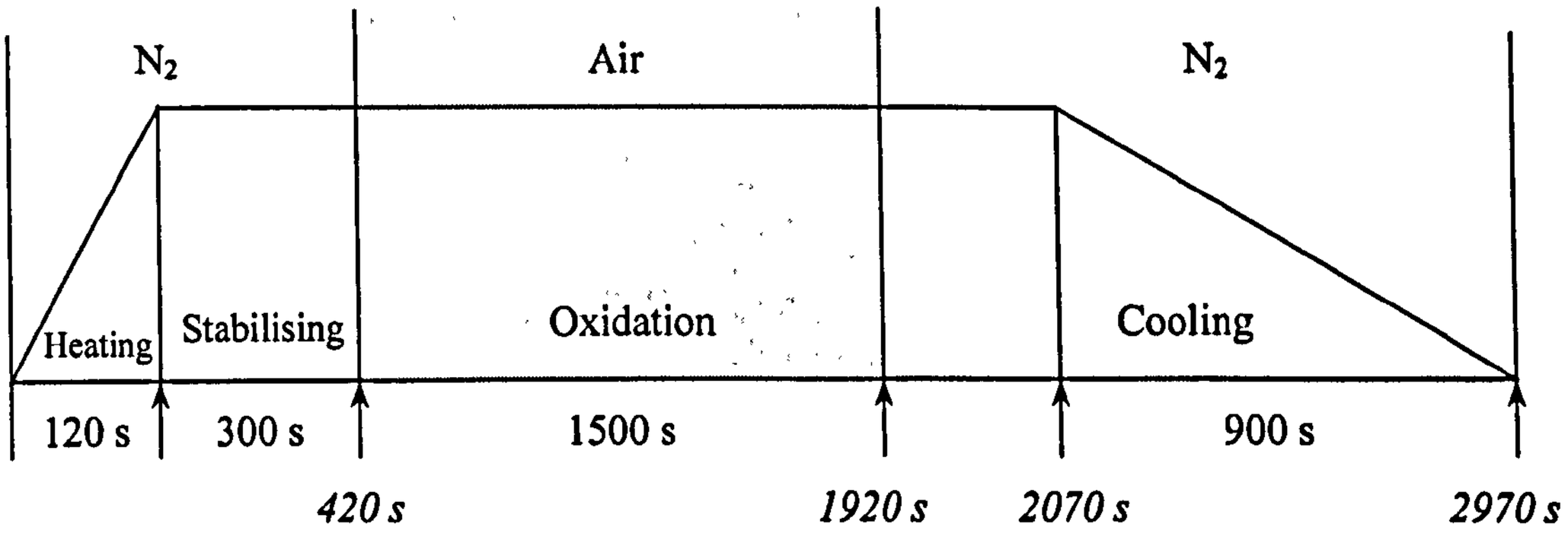

Test 2*; T = 1070° as Test N4 (oxidation 300 s);

Test 3*; T = 970° as Test N3 (oxidation 800 s);

Test 4*; T = 1000° and oxidation time 320 s;

Test 5*; T = 1040° and oxidation time 300 s;

Test 6*; T = 870° as Test N2 (oxidation 3000 s);

Test 7*; T = 870° as Test N1 (oxidation 1500 s).

A.3.3. Tension-Compression

Specimen 1

Test type: Tension

$T_{th} = 750°C$; $T_{ox} = T_{test} = 800°C$

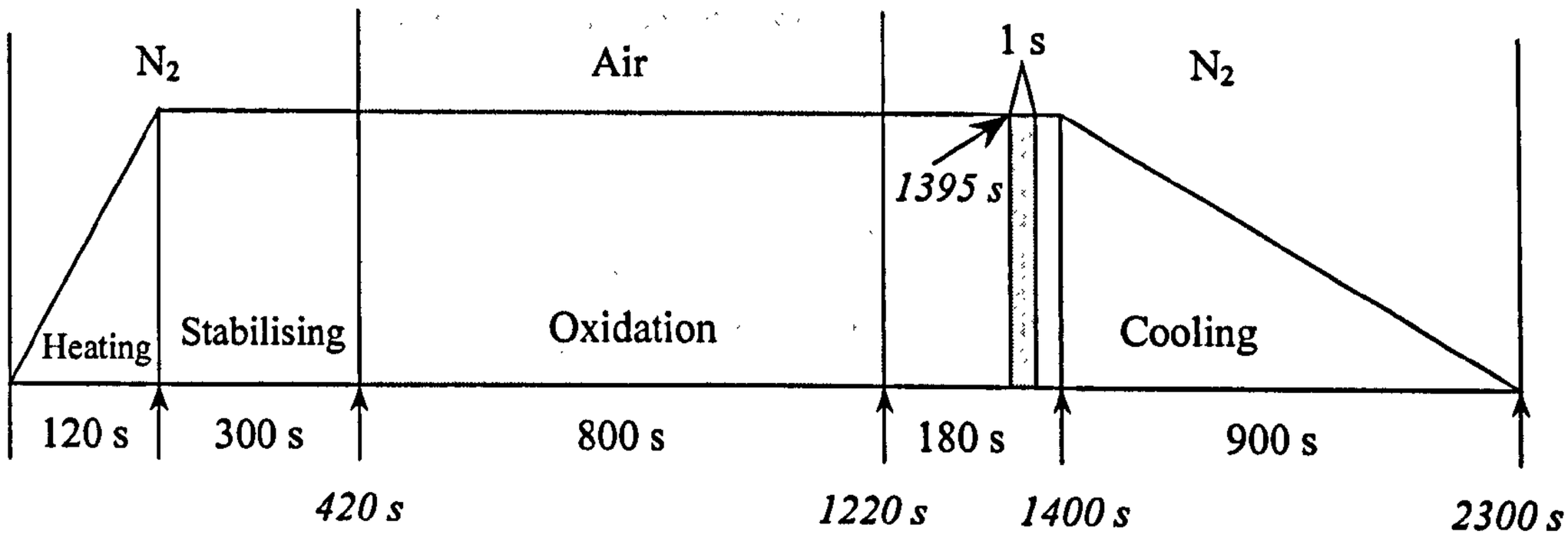

Test type: Compression

$T_{bot} = 880°C$; $T_{top} = 477°C$

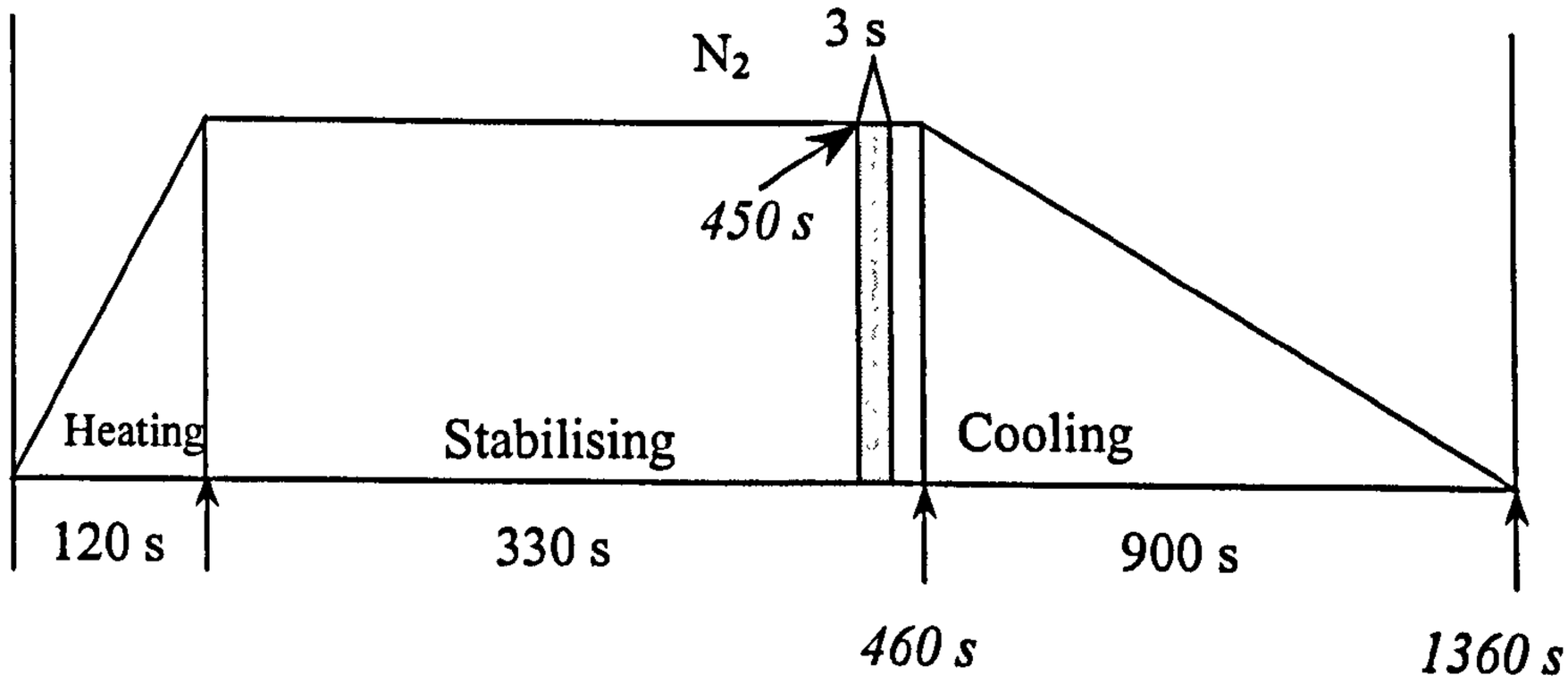

Specimen 3

Test type: Tension

T_{th} = 830°C; T_{ox} = T_{test} = 880°C;

Initial load = 0.05 kN

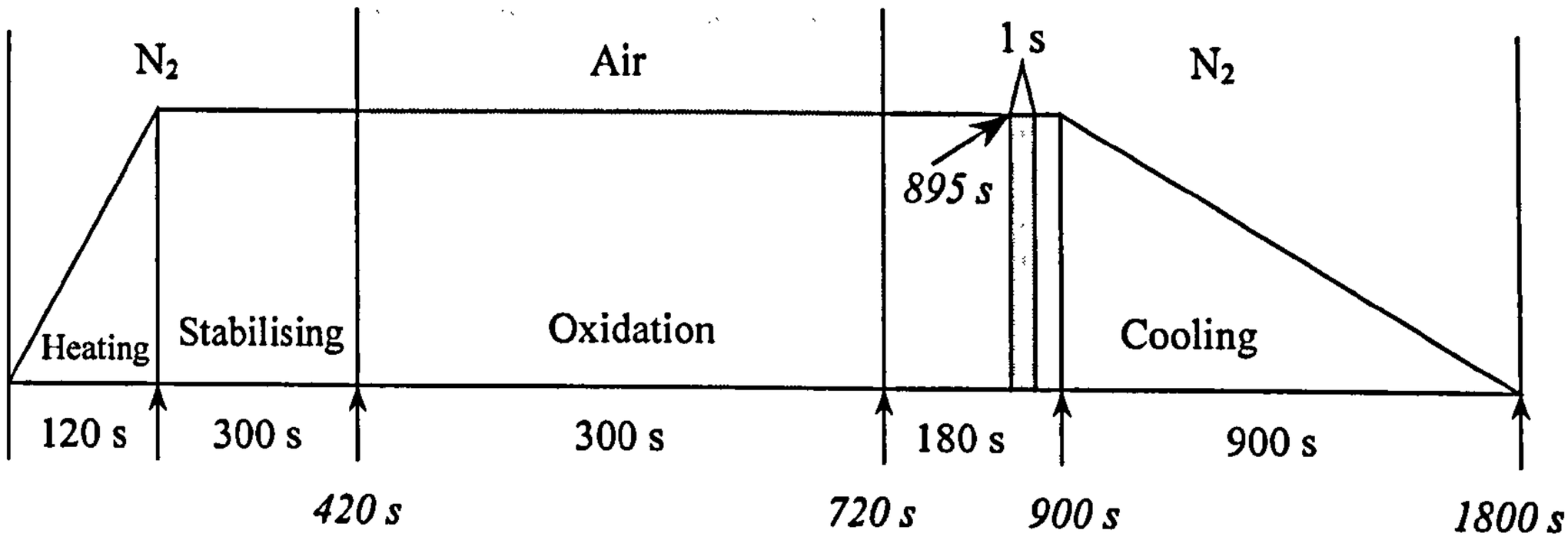

Test type: Compression

T_{bot} = 880°C; T_{top} = 478°C

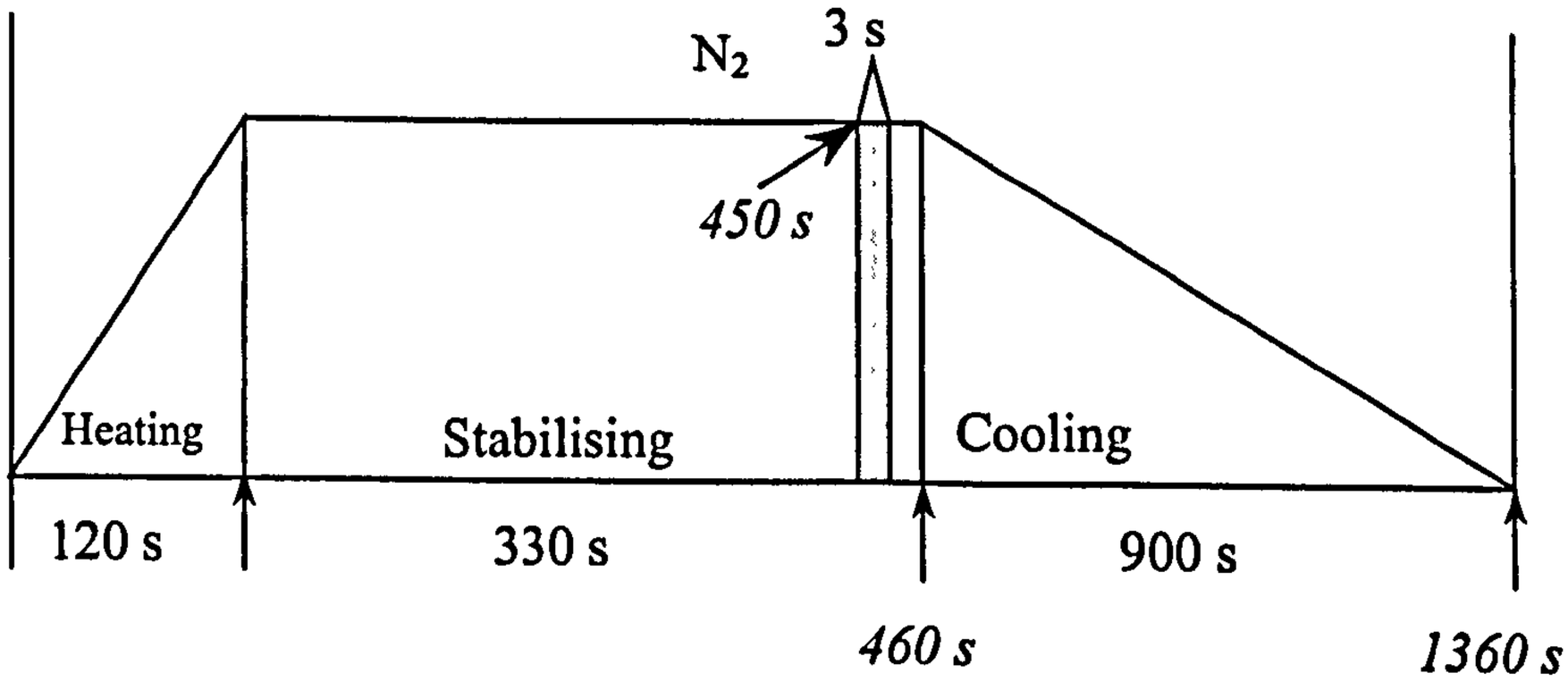

Specimen 6

Test type: Tension

T_{th} = 830°C; T_{ox} = T_{test} = 880°C;

Initial load = 0.05 kN

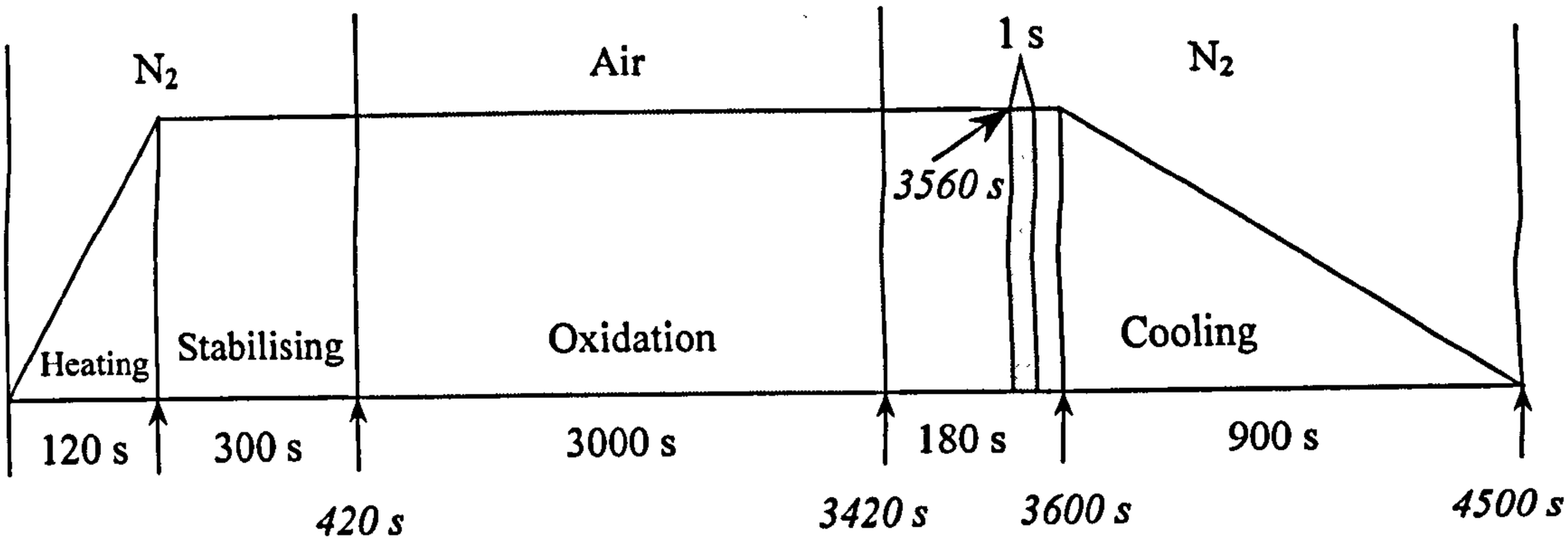

Test type: Compression

T_{bot} = 880°C; T_{top} = 465°C

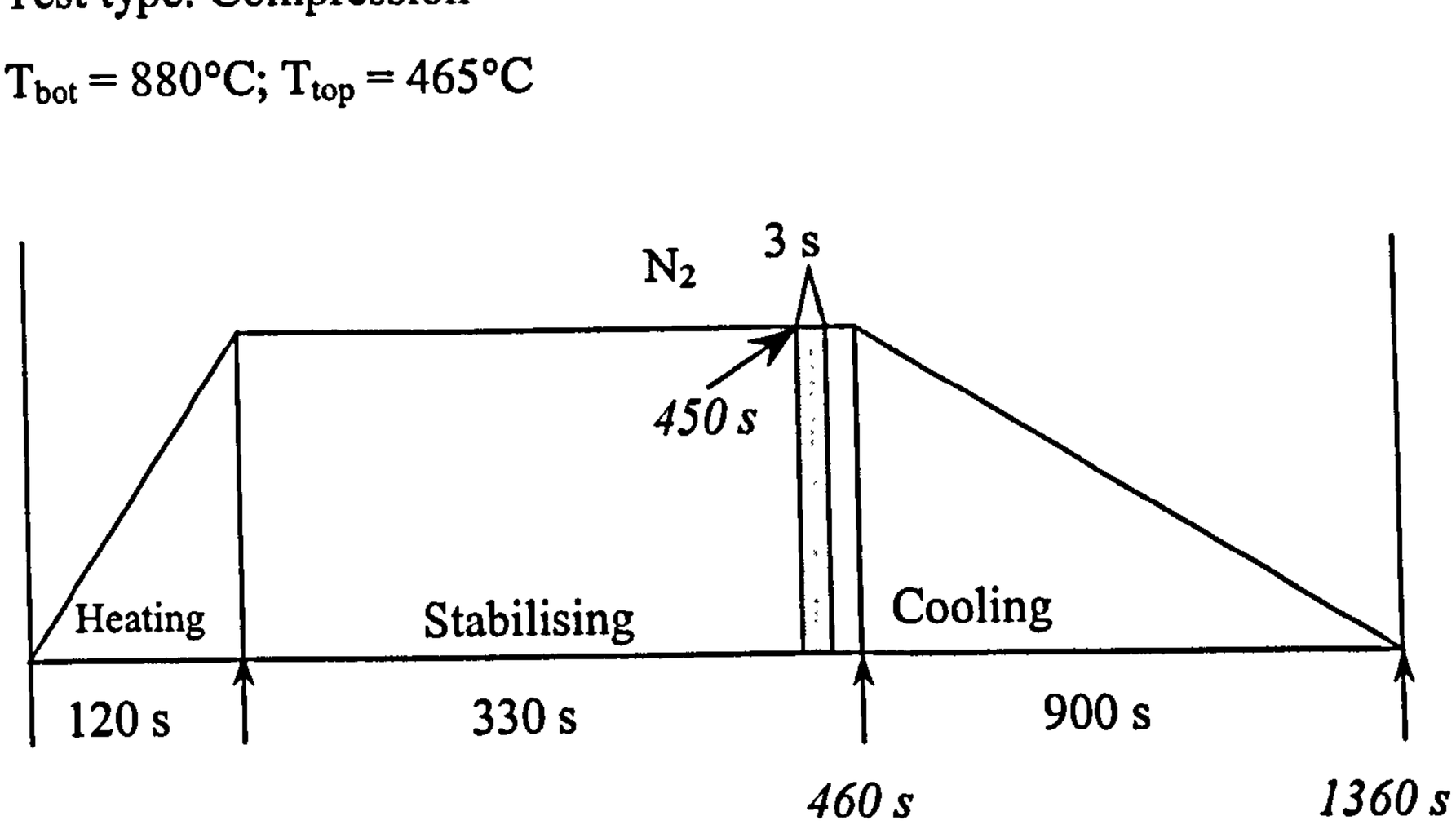

For all tests, T_{bot} is the bottom tool temperature and T_{top} is the top tool temperature.

Specimen 2

Test type: Tension

T_{th} = 800°C; T_{ox} = 850°C; T_{test} ~ 780-790°C, load ~ 2.5 kN

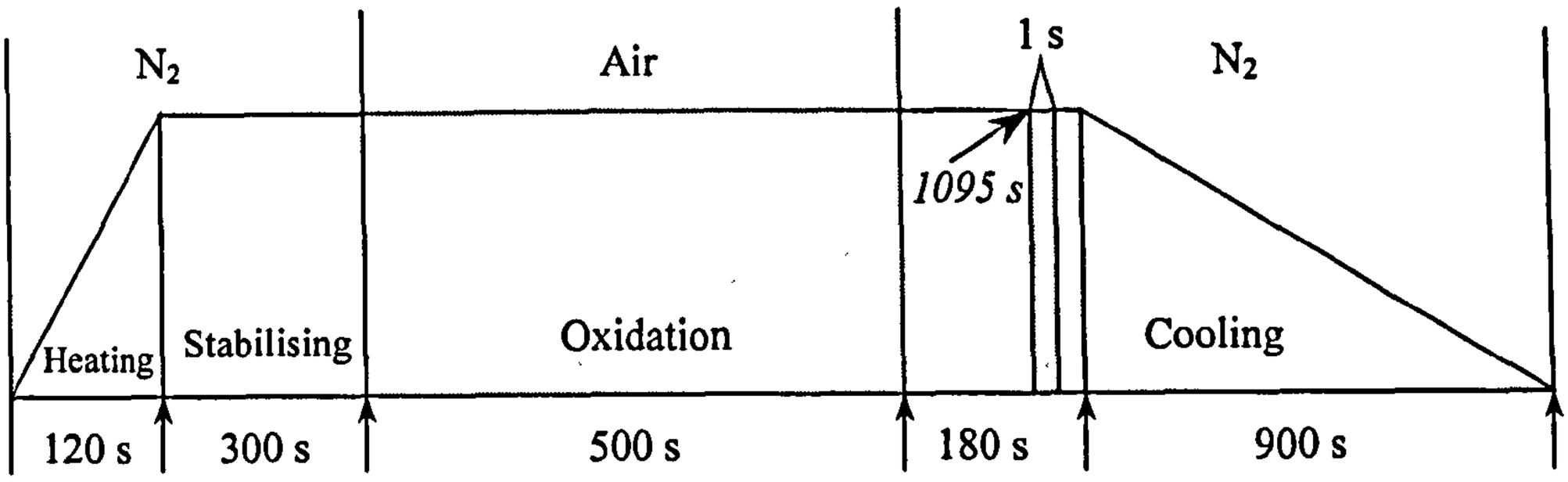

Specimen 5

Test type: Tension

T_{th} = 830°C; T_{ox} = T_{test} = 880°C; Initial load = 0.041 kN

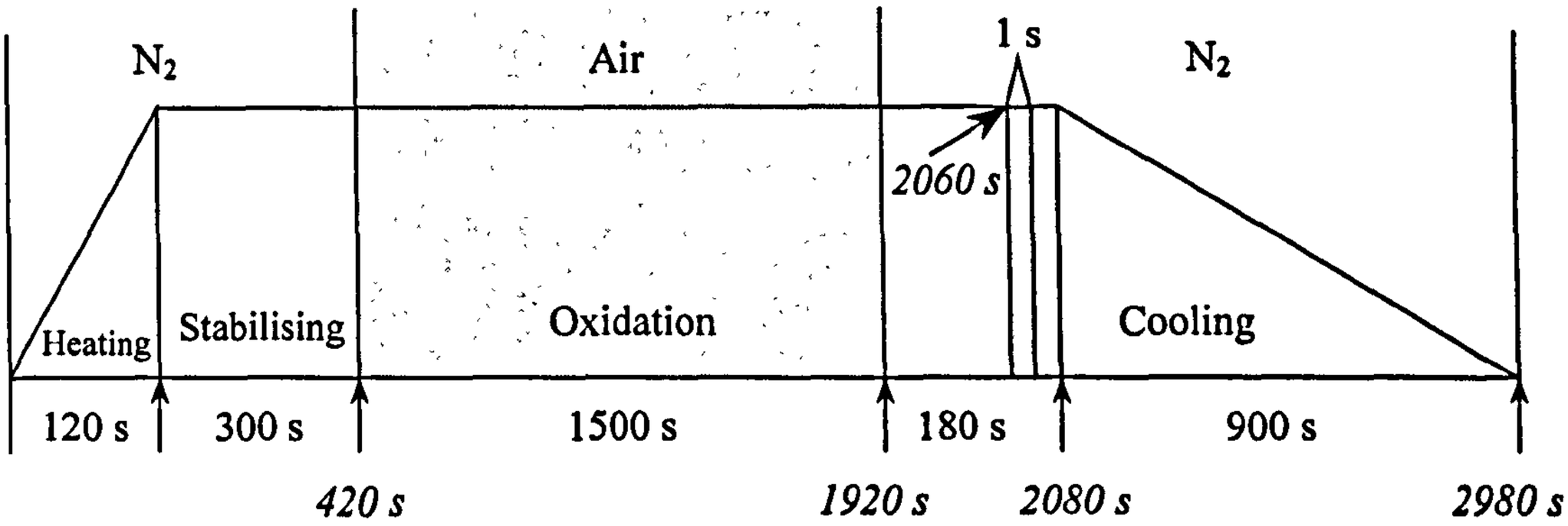

Specimen 7

Test type: Tension

T_{th} = 850°C; T_{ox} = T_{test} = 900°C; Initial load = 0.05 kN